Characterisation of blast loading for shallow buried explosives

Stephen D. Fay

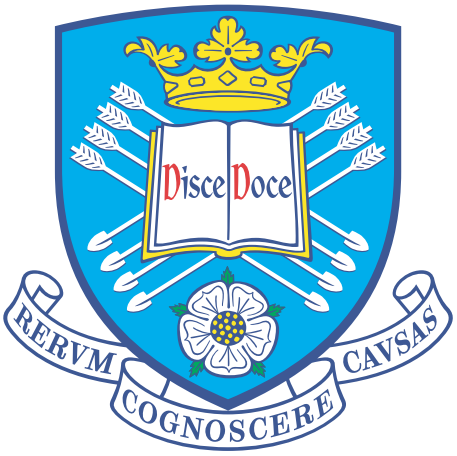

This thesis is submitted for partial consideration towards the degree of Doctor of Philosophy in

The Department of Civil and Structural Engineering

at the University of Sheffield

3rd September, 2020

Dedicated to Francesca and Dotty.

Abstract

This thesis presents the design of a new experimental technique for measuring the spatial and temporal pressure on a rigid target following detonation of a shallow buried explosive device: the Characterisation of Blast Loading (CoBL) apparatus. CoBL was designed to measure the output from a 6 kg TNT cylindrical charge at quarter scale, offering a balance between scientific validity and cost-effectiveness. In total, 91 experimental tests have been performed, which are reported and analysed in detail in this thesis.

Initially, a series of commissioning tests were performed to refine the experimental apparatus, increase the quality and accuracy of the data, and remove sources of error. Following this, a detailed parametric study was conducted to systematically investigate the influence of key parameters on the mechanism and magnitude of loading developed on the target surface, namely: charge encasement and shape; soil confinement and burial depth; soil saturation; particle size distribution of saturated soils; and standoff distance.

Experiments with modified charge cases provide an understanding of the interaction between the charge case and soil and the consequences of this interaction on the pressure-waveform. Two charge shapes were compared to investigate the focusing of detonation products for a spherical and cylindrical charge. Soil confinement and burial depth were investigated to assess the contribution of the confining media at the base, laterally and above the charge. Soil saturation was varied to investigate changes in response behaviour of the soil when the voids between soil particles become filled with water. Two saturated soils with particle size distributions described as 'uniform' and 'well–graded' were tested to compare the influence of the particle size distribution on the loading mechanism. Three standoffs were tested in partially saturated soil to investigate the evolution of the loading in ejected material.

The CoBL test apparatus has been used to produce the first detailed experimental study into the output from shallow buried charges with spatially and temporally resolved pressure histories measured above a shallow buried charge. The observations from these tests can be used to verify the behaviour of soils in numerical models allowing armour designers to accurately assess the mechanisms of loading applied to a protective structure when subjected to a buried IED attack.

Acknowledgements

I would like to thank my supervisors Dr Samuel Rigby and Prof. Harm Askes for the support and guidance and for being there when I've needed you. It has been a humbling experience working with you and I have learnt much about myself in the process. I would like to thank everyone in the Department of Civil and Structural Engineering at the University of Sheffield that have supported me since my undergraduate days, I look forward to working with you again.

I would like to express my sincere gratitude to Dr Samuel Clarke and Prof. Andrew Tyas and Blastech Ltd. for the opportunity to conduct this research and providing me with fascinating and exciting employment. Roy, your technical insights, charm and humour are unparalleled. Danny, Ash and Andy, there are no finer technicians.

I would like to thank Ian Elgy and Matthew Gant for their review of my experimental work and DSTL and EPSRC for funding this project. I would like to acknowledge with gratitude my current employers, Dr Richard Crowther, Dr David Munro and Christopher Nunn who have done so much to facilitate the completion of this thesis.

I thank Gillian and Alfred Oliver for treating me like family and supporting my writing efforts, most of this thesis was drafted at their home for which I am forever indebted. I would like to thank my parents for raising me without limits and allowing me to be a dreamer. I thank Julia, Tim and the girls for their polite efforts to keep me grounded, and everything else. Laura Craig, Andrew Wooff and Lucy Johnson have been great friends and provided a perfect home through the early years of this project. Sally and Dorothy, never has a parent been more proud.

Finally, and most importantly, I would like to thank Francesca for her endless patience and support.

Contents

List of Figures

List of Tables

Chapter 1

Introduction

1.1 Background and motivation

Improvised explosive devices (IEDs) have been used throughout the world by terror groups to great effect on civilian, political and military targets. Between 2002-2014 military operations in Afghanistan and Iraq resulted in 635 deaths of British service personnel of which 271 deaths were a result of IEDs and roadside bomb attacks [1]. Over the same 12 year period a reported 61,937 attacks using explosives were conducted globally resulting in 145,006 deaths and 298,180 casualties [2]. The use of IEDs as a terror weapon can deny access to roads, towns and infrastructure creating an environment of sustained insecurity. The impact of this is a distinctive change in military priorities, tactics and strategy, and equipment leading to significant cost. Sustained IED attacks may impact on the political process causing further instability, disrupting elections or affecting territorial control [3].

Of the injury patterns caused by victim operated IEDs, those associated with the primary[1] blast wave are relatively uncommon in both surviving casualties and fatalities. For example, of the 53 IED related fatalities of British service personnel in Iraq in 2006, only two were as a result of primary blast injury [4]. This is due to the fact that service personnel are typically mounted in vehicles, and detonations which occur in close proximity to the exterior of the vehicle do not lead to the development of significant pressures inside the vehicle. In addition, vehicle mounted personal are provided protection from high velocity fragments and secondary blast injury. Momentum transferred to the vehicle will cause displacement of structural panels resulting in blunt force trauma [4], a tertiary blast injury. In cases where substantial vehicle throw occurs, traumatic brain injury is a significant risk. When large floorpan deflections occur, victims often present with injuries such as bone fracture [5] and traumatic amputation of the lower limbs as a result of crushing syndrome [4]. In each of these scenarios the consequences

[1] Primary, secondary and tertiary blast injuries are caused by a range of effects from an explosive detonation. Primary blast injuries are a consequence of contact with the blast shock wave, secondary blast injuries result from wounds produced by ballistic fragments and tertiary blast injuries relate to blunt trauma from an object striking an individual [4].

for the victims are severe and require immediate and highly specialised medical triage and treatment, without which these injuries are soon fatal [6].

Designing vehicle protection against IED threats is most commonly achieved by deflecting the blast load around the vehicle with an armoured v-shaped form placed some distance from the underbelly of a vehicle. This approach was pioneered in South Africa in the 1970s [7]. The level of protection applied to a military vehicle must be balanced against impeding vehicle effectiveness and mobility [4]. Designing suitable vehicle platforms requires a detailed knowledge of the loading which it is to be designed against. Therefore a definitive understanding of the complex loading from the detonation of a shallow buried charge will assist in armoured vehicle design methods.

1.2 Scope, aim and objectives

Engineers tasked with the design of protection which is to resist the loading from a shallow buried charge are faced with a number of difficulties when assessing a suitable design load. Firstly, there is a range of geotechnical parameters which affect the magnitude and duration of the loading. Therefore, how the loading interacts with the target is dependent not only on the soil material but also on the conditions within the soil. Secondly, small changes in target geometry will significantly affect loading on the target. Therefore application of existing experimental data may not be appropriate to new designs. Thirdly, the mechanisms for enhancement of the blast loading and momentum transfer are currently not clear, therefore fundamental insight is lacking for a proper validation of numerical models and simulations.

Current practice for vehicle platform development is to test vehicles against a standardised threat level such as those described in STANAG 4569 [8]. If a significant number of design iterations are required, the cost and time required for this development rapidly escalate, leaving vehicle manufacturers constrained by budgetary requirements and extending the period before deployment of new protective equipment.

Because of these constraints on vehicle design, it is important to develop methods which will equip engineers to design vehicles with some degree of confidence in loading and response. Currently the experimental and numerical work in this area is not unified in its approach. Therefore the most important part of research in this area is to demonstrate how the coupled ejecta flow and detonation products contribute to target loading.

This thesis presents research that expands and improves existing knowledge of how loading is transmitted from a buried explosive charge to the surrounding soil and how momentum is

transferred when ejected soil and detonation products interact with a target. This is achieved by investigating the spatial and temporal distributions of blast loading, determining the mechanisms which govern this load development, and exploring how these mechanisms are related to the properties of the soil bed. These aims will be achieved by meeting the following objectives:

- Develop and refine the test set-up allowing clear mechanisms to be defined.
- Design and execute a parametric study suitable for the assessment of buried blast loading mechanisms.
- Determine loading mechanisms from experimental results.
- Compare findings with current hypotheses.

The experimental approach developed in this thesis provides the measurement of pressure in an array of discrete points, on a fixed plane, near the surface of a shallow buried charge. The pressure waveforms generated from the experimental work informs of the characteristic mechanisms of the blast loading for a range of granular geological materials at a range of saturation and density states. This provides critical insight into the generation of loading mechanisms for a given geological state.

The Characterisation of Blast Load (CoBL) test apparatus located at the CEDUS Laboratories, Buxton, was developed in partnership with the University of Sheffield Department of Civil and Structural Engineering, Blastech Ltd. and the Defence Science and Technology Laboratory (DSTL). This thesis presents the results from 91 shallow buried explosive tests; the CoBL apparatus has since been used to measure the output from near-field explosive charges, Tyas et al. [9] and Rigby et al. [10]. This thesis was written in support of the Defence Science Technology Laboratory (DSTL) funded Characterisation of Blast Loading project.

1.3 Thesis outline

The remainder of this thesis is organised into the following chapters:

Chapter 2 – Theoretical background and literature review

This chapter provides background information on the detonation process and provides insight into the early stages of blast loading. Aspects of geotechnical parameters and experimental equipment pertinent to this thesis are introduced. A review of literature is used to explore historical and contemporary experimental and numerical efforts aimed at developing an understanding of the mechanisms of momentum transfer from a shallow buried charge.

Chapter 3 – Experimental design and commissioning tests

This chapter describes the development of an experimental apparatus that can be used to measure high-magnitude, short–duration, spatial and temporal pressure distribution. Commissioning tests are used to assess ways to improve repeatability of the experiments, provide confidence in the data, investigate the affect of dispersion and soil container and refine instrumentation locations for further studies.

Chapter 4 – Parametric study

This chapter presents the results and discussion from a detailed and comprehensive parametric study used to evaluate the mechanisms of shallow buried blast loading.

Chapter 5 – Summary and conclusions

This chapter summarises the current work and makes suggestions for further work in this subject area.

1.4 Published work

Work detailed in this thesis has been published in conference and peer–reviewed journal papers and has been repeated with permission from Elsevier, Springer, Jove and Sage Publishing:

- S.D. Fay, S.D. Clarke, J. Warren, A. Tyas, T. Bennett, J. Reay, I. Elgy, M. Gant. Capturing the spatial and temporal variations in impulse from shallow buried charges. *15th International Symposium for the Interaction of Munitions with Structures (ISIEMS15)*, Potsdam, Germany, 2013.
- S.D. Fay, S.D. Clarke, A. Tyas, J. Warren, S. Rigby, T. Bennett, I. Elgy, M. Gant. Measuring the spatial and temporal pressure variation from buried charges. *23rd International Symposium on Military Aspects of Blast and Shock (MABS23)*, Oxford, UK, 2014.

- S.D. Clarke S.E. Rigby, S.D. Fay, A. Tyas, J.J. Reay, J.A. Warren, M. Gant, R. Livesey, I. Elgy. 'Bubble-type' vs 'shock-type' loading from buried explosives. *16th International Symposium for the Interaction of Munitions with Structures (ISIEMS16)*, Destin, USA, 2015.

- S.D. Clarke, S.D. Fay, J.A. Warren, A. Tyas, S.E. Rigby, J.J. Reay, R. Livesey, I. Elgy. Geotechnical causes for variations in output measured from shallow buried charges. *International Journal of Impact Engineering*, 86:274–283, 2015.

- S.E. Rigby, A. Tyas, S.D. Clarke, S.D. Fay, J.J. Reay, J.A. Warren, M. Gant, I. Elgy. Observations from preliminary experiments on spatial and temporal pressure measurements from near–field free air explosions. *International Journal of Protective Structures* 6(2): 175–190, 2015.

- S.D. Clarke S.E. Rigby, A. Tyas, S.D. Fay, J.J. Reay, J.A. Warren, M. Gant, I. Elgy. Reflected pressures from explosives buried in idealised cohesive soils. *24th International Symposium on Military Aspects of Blast and Shock (MABS24)*, Halifax, Canada, 2016.

- S.E. Rigby, S.D. Fay, A.Tyas, S.D. Clarke, J.J. Reay, J.A. Warren, M. Gant, I. Elgy. Localised variations in reflected pressure from explosives buried in uniform and well-graded soils. *24th International Symposium on Military Aspects of Blast and Shock (MABS24)*, Halifax, Canada, 2016.

- S.E. Rigby, S.D. Fay, S.D. Clarke, A. Tyas, J.J. Reay, J.A. Warren, M. Gant, I. Elgy. Measuring spatial pressure distribution from explosives buried in dry Leighton Buzzard sand. *International Journal of Impact Engineering*, 96:89–104, 2016.

- S.D. Clarke, S.D. Fay, S.E. Rigby, A. Tyas, J.A. Warren, J.J. Reay, M. Gant, I. Elgy. Blast quantification using Hopkinson Pressure Bars. *Journal of Visualized Experiments*, 113, doi: 10.3791/53412, 2016.

- S.D. Clarke, S.D. Fay, J.A. Warren, A. Tyas, S. E. Rigby, J.J. Reay, R. Livesey, I. Elgy. Predicting the role of geotechnical parameters on the output from shallow buried explosives. *International Journal of Impact Engineering* 102:117–128, 2017.

- S.E. Rigby, S.D. Fay, A. Tyas, S.D. Clarke, J.J. Reay, J.A. Warren, M. Gant, I. Elgy. Influence of particle size distribution on the blast pressure profile from explosives buried in saturated soils. *Shock Waves*, 28:613–626, 2017.

- S.D. Clarke, S.E. Rigby, S.D. Fay, A. Barr, A. Tyas, M. Gant, I. Elgy. Characterisation of buried blast loading. *The Royal Society – Proceedings A*, 476: 20190791, 2020.

Chapter 2

Theoretical background and literature review

2.1 Introduction

A background of the detonation process is given whilst considering the formation of a blast wave in free–air and confined conditions. A discussion of fundamental geotechnical conditions is required to understand how geo–parameters are defined and what the consequence on the mechanical behaviour might be. The application of Hopkinson Pressure Bars as a pressure measurement technique is discussed with an outline of the benefits and limitations of the technique.

A literature review of experimental and numerical techniques used to asses momentum transfer is outlined later in this chapter. Early work by the community focused on developing empirical models which were only applicable to geometries and soil conditions in which the experiment was conducted. The introduction of early numerical methods changed the focus of experimental work from developing empirical methods to the provision of data for calibrating numerical models. Most recently, advances in numerical modelling and reduction in computation cost have again changed the focus of work towards detailed experimental and numerical studies investigating the mechanisms of load transfer such that more rigorous validation exercises can be conducted. Understanding the physical loading mechanisms allows findings from numerical studies to be applied to a wider set of scenarios that may be encountered in reality and improve the design of vehicles and personal protection. Experimental techniques are fundamental in providing data and insight from which the mechanisms of momentum transfer from a shallow buried charge can be observed.

2.1.1 Problem background

The momentum transfer from a shallow buried charge to a target can be described in five stages and is shown in Figure 2.1.

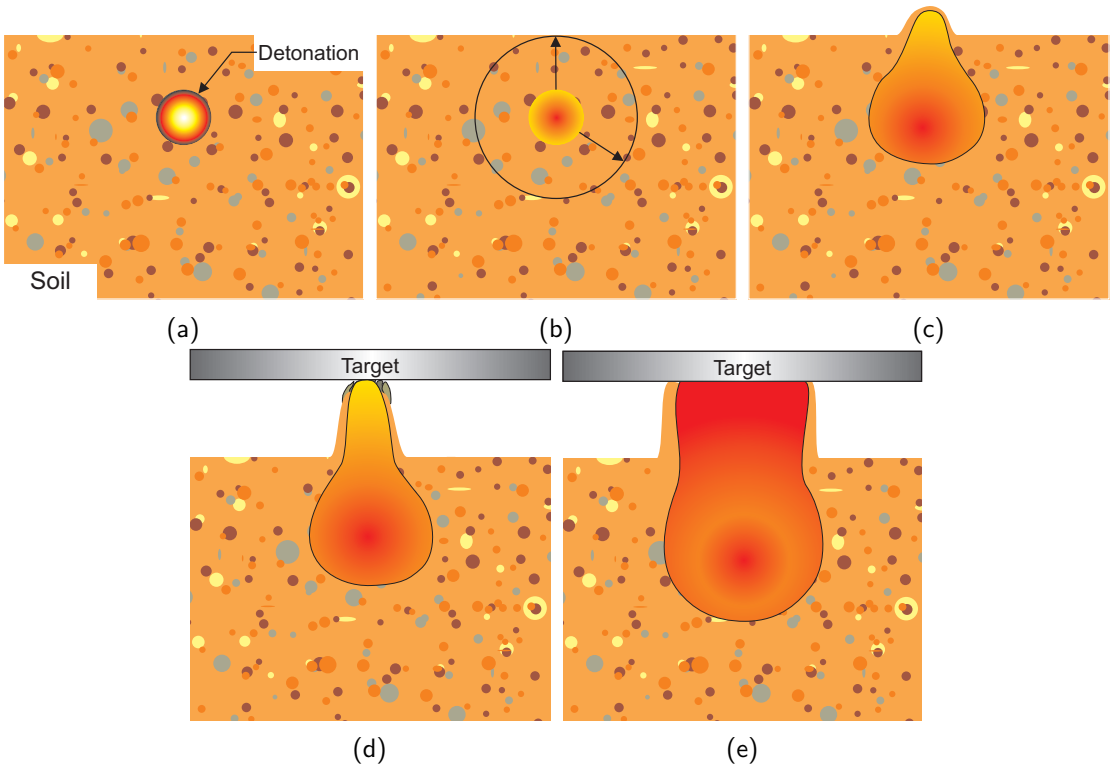

Figure 2.1: Five stages of a shallow buried detonation. (a) detonation of the chemical explosive; (b) interaction between detonation shock wave and expanding detonation products into the surrounding soil; (c) expansion of the soil and detonation products into free air; (d) early time interaction with a target; (e) late time interaction with the target, Bergeron et al. [11]

Empirical predictions for pressure–time histories on a target following the detonation of chemical explosive in free air are well established [12, 13]. However, current computational methods for predicting the pressure on a target for complex scenarios require specialist knowledge and experience, as well as large computational costs. Such situations require complex treatment of the propagation of pressure waves through compressible granular media with multiple phases. Furthermore, numerical methods require significant validation effort from well–controlled multi–parameter data sets. With no accurate numerical or experimental work that can predict the pressure load transferred to a target the subject remains in its infancy.

Figure 2.2 illustrates complexity of introducing a confining medium to a detonation. Subfigures (a) and (b) show two incidental detonation to target geometries pre detonation with air as the confining material in (a) and sand as the confining material in (b). Subfigures (c) and (d) show possible post–detonation behaviour where (c) has air as the surrounding medium and

(d) is confined with sand.

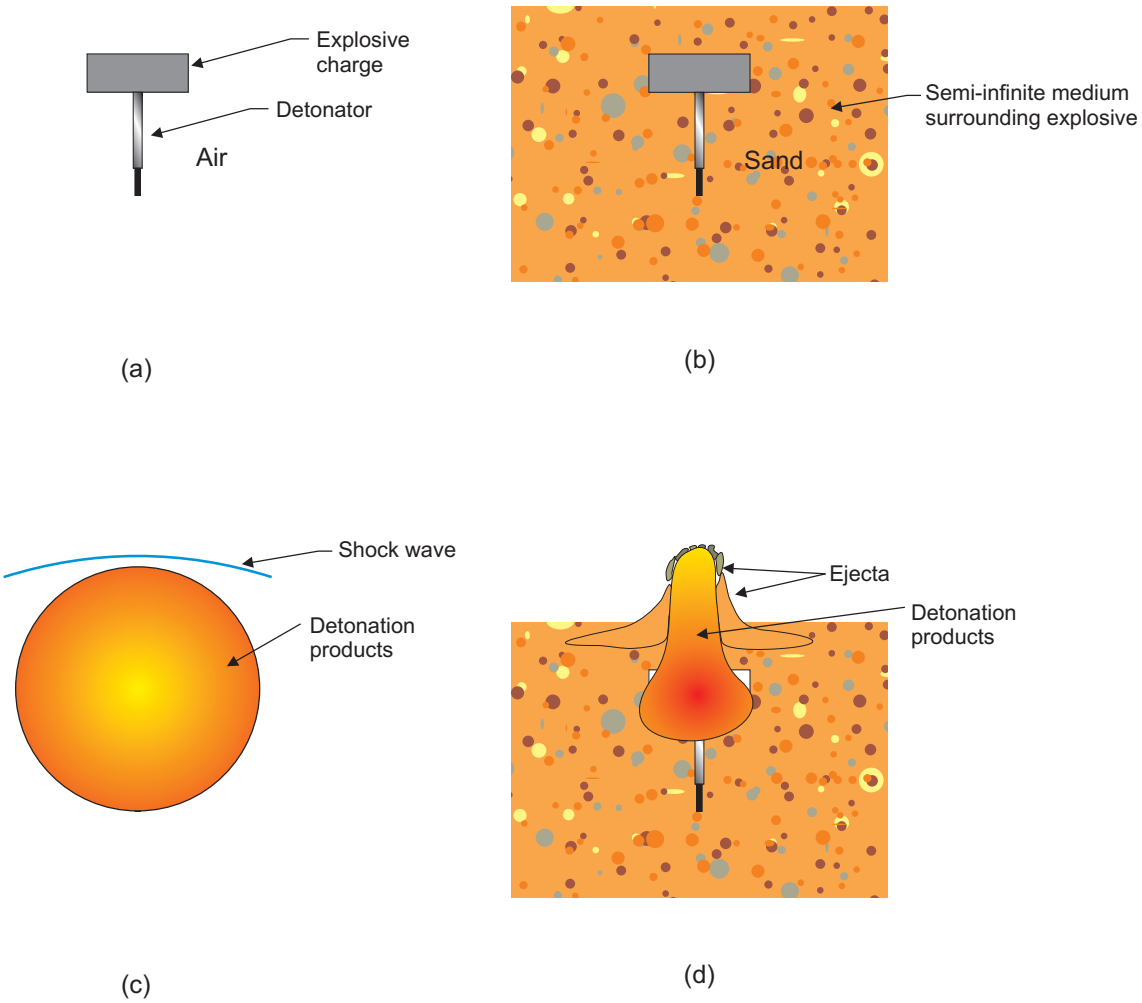

Figure 2.2: Comparison of above ground and shallow buried detonation.

It can be seen from (c) that only the shock wave formed by compressing ambient air around the detonation products will strike a structure some distance from the explosive. The processes involved are detonation of the explosive, compression of the air and increased particle velocity, some thermal radiation and then reaction of the target plate and pressure sensors. In contrast, it can be seen in (d) that when a detonation is surrounded by a confining material the post–detonation phenomena are more complex. The detonating explosive expands by compressing the confining material, confining material and detonation products are ejected from the soil surface.

2.2 Chemical explosives

A chemical explosion is a reaction or change of state over a very short duration (μs range). The exothermic decomposition of a chemical results in the production of heat, gas and vapour [14]. As the reaction is over quickly and the reacted materials do not expand instantaneously, the detonation products occupy the volume previously occupied by the explosive. Relative to the volume that the detonation products would occupy naturally the volume is very small and at very high temperatures and so at very high pressure [15].

Developing an understanding of the detonation and its interaction with its surroundings are fundamental to understanding the mechanisms at the soil–explosive boundary layer. This section will describe the behaviour of explosives when detonating, the effect of confinement, how a blast wave forms in air and considerations of target clearing.

2.2.1 Ideal detonation

The detonation process is complex. Not only is there a jump condition between one physical state to another but a new chemical state needs to be considered. In order to understand the detonation process Zukas et al. [16] proposed some simplifications of detonation behaviour.

- Lateral boundaries are not considered and detonation gasses exit behind the shock front i.e. a one dimensional model.
- Initiation of explosive has taken place and a planar wave front in the explosive has been formed.
- The detonation gasses are in thermodynamic equilibrium and the reaction is complete i.e. fully oxidised.
- The detonation process occurs at a constant velocity i.e. the reactions occur at a steady state, shock front (detonation wave), chemical reaction and rarefaction (Taylor) wave are in equilibrium.

This ideal one–dimensional detonation described by Zukas et.al [16] is presented in Figure 2.3 where three relationships for a detonation are presented. Figure 2.3.1 illustrates the bulk explosive during detonation. Figure 2.3.2 shows the pressure–distance relationship along the length of the explosive. Figure 2.3.3 shows the pressure–volume Hugoniot which describes all equilibrium states in which a material can exist behind the shock front [17].

Four areas A, B, C and D are noted across Figure 2.3 which correspond to:

(A) Pre–detonation

(B) The instant the shock wave interacts with virgin explosive

(C) The instant all chemical reactions are complete

(D) The instant all chemical reactions are complete and post–detonation respectively

At point 'A' the detonation wave is yet to affect the explosive, pressure is ambient and the explosive's volume is unaffected. At A, before the detonation wave interacts with the explosive, the explosive's volume is highest and pressure is lowest

At point B the supersonic wave front compresses the explosive and molecular bonds begin to break. Von Neuman argued that the reaction takes place at a finite rate and width [18]. The implication of this being that between point C and point B (between fully reacted detonation products to the un–reacted shock front) pressure will become significantly higher. This phenomena is known as the Von Neuman spike [18]. The chemical chain reaction continues to release heat energy supporting pressure in the shock front driving it forwards. The physical state of the un–reacted material 'jumps' from A to point B seen in Figure 2.3.3 as the green Rayleigh line. When the Rayleigh line is drawn such that it is tangential to the reacted Hugoniot (at point C) a steady state of detonation is achieved and the assumptions made by Zukas [16] are met.

The Chapman–Jouguet (C–J) point is in a detonation reaction where the reaction has just been completed. The fully reacted explosive occupies the same volume but the chemical state has changed from solid to gas [17]. A number of intermediary Hugoniot lines between B–C as seen in Figure 2.3.3 represent partially detonated explosive. Behind the shock front at point B, a change of physical and chemical state occurs and the explosive compounds evolve into hot gases. Locations bounded between B and C outline where these chemical reactions occur. When all chemical reactions are complete and the explosive has transformed into gaseous detonation products the pressure–volume state at point C is achieved and known as the C–J state.

Beyond point C into the area D, gases begin to expand as they lose the confinement of their solid physical state and a Taylor rarefaction wave is formed. The rarefaction wave direction of travel is opposite to the direction of the detonation shock propagation [19]. Furthermore, the gradient of the rarefaction wave and therefore rate of expansion of gasses is affected by the level of confinement achieved either through the quantity of explosive or level of confinement from surrounding materials. The effect on the Taylor wave due to changing confinement conditions and can be seen in Figure 2.4.

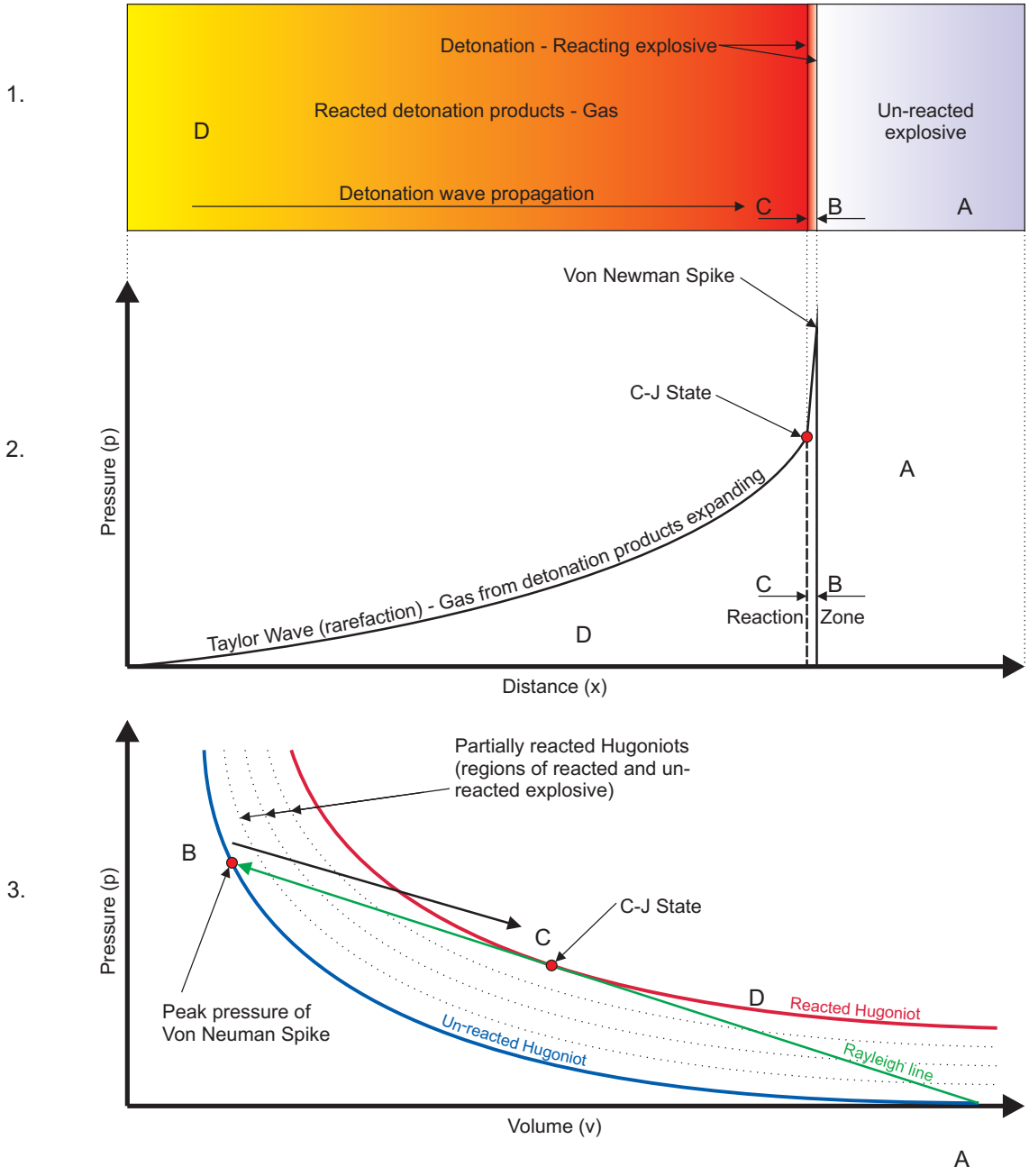

Figure 2.3: Three representations of a detonation showing; (1) diagram of the detonation in an explosive material, (2) graph of pressure–distance showing a detonation wave propagating in an explosive, (3) the pressure–volume Hugoniot showing the jump condition for a detonating explosive.

2.2.2 Detonation wave confinement

The pressure–distance relationship discussed in Figure 2.3 shows an ideal detonation scenario. The effect of explosive thickness or confinement from boundaries such as containing vessels were ignored [17]. In reality it may not be practical to achieve this ideal scenario as explosive thickness, explosive shape and explosive containers may all act to confine detonation products which are then unable to expand away from detonation immediately. Figure 2.4 demonstrates the effect of confinement outlining the behaviour of the Taylor rarefaction wave. As confinement increases, the decay in pressure decreases.

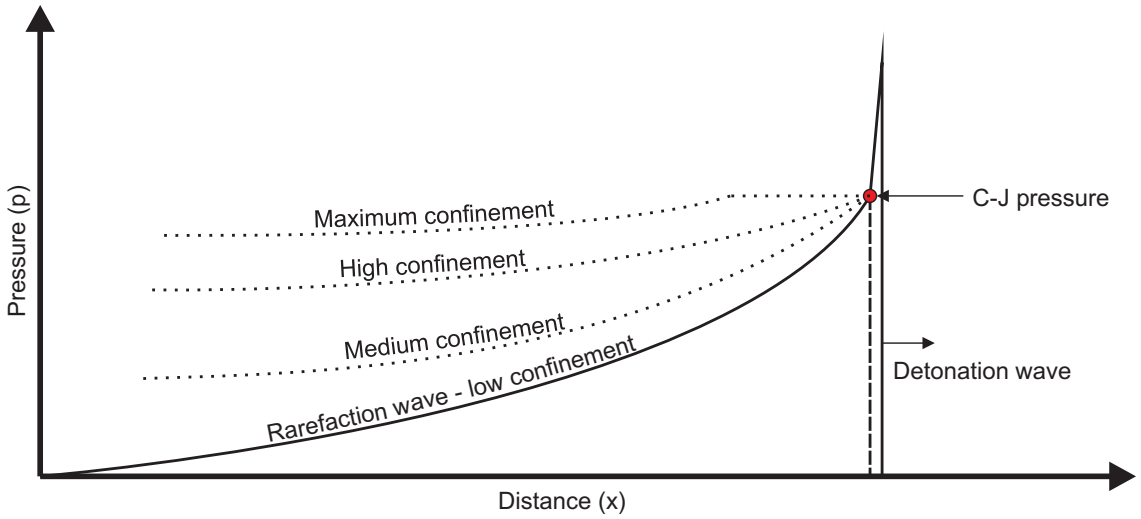

Figure 2.4: Changes to the rarefaction (Taylor) wave with increased confinement, adapted from [17].

Illustrated on Figure 2.4 is a maximum confinement rarefaction pressure–distance line. When confinement of the detonation products is achieved so that the detonation products are contained within the same volume as the unreacted explosive, the rarefaction wave will be flat at its top and equal to the C–J pressure [18] . If the detonation products are able to escape this confinement over time, the rarefaction wave will be prolonged in distance and time.

The characteristics of this rarefaction decay can be significantly affected by a restriction of the reaction products. Surrounding an explosive charge by soil in the case of burial may inertially confine detonation products and it may be possible to affect the pressure–distance relationship as illustrated in the pressure–distance diagram of Figure 2.4.

2.2.3 Transmission of detonation shock waves into free–air

Section 2.2.1 described the process of detonation and the effect of confining the detonation products has been shown. When the detonation occurs in free–air a shock wave begins to form at the explosive–air boundary. There is a transition between the detonation shock wave and subsequent blast wave. This transition is illustrated in Figure 2.5 where high pressure, high velocity components of the detonation shock wave move to the front of the wave forming an air shock wave [12]. As a result the very highest pressure components lead the blast wave to form a characteristic discontinuity as can be seen in Figure 2.5 c.

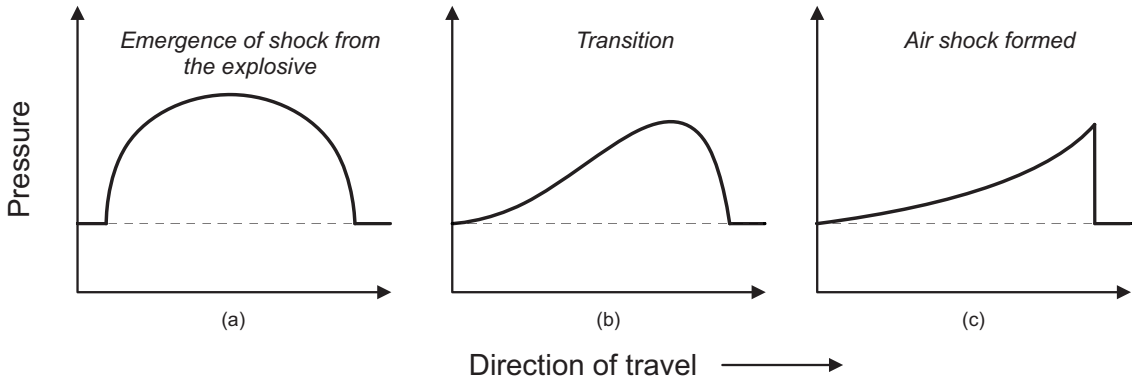

Figure 2.5: Development of explosive shock formation. (a) Initial pressure pulse (b) transient formation of discontinuity due to a range of particle velocities (c) fastest moving particles at the front of the shock wave, adapted from [12].

This newly–formed discontinuity shock front is characterised in Figure 2.6 as an abrupt increase in air pressure at the time of arrival t_a, behind which air particles are compressed together [19]. Behind the thick layer of air, space between the air particles increase and the pressure will decay down to ambient pressure. The area of positive pressure behind the shock front is known as overpressure. The overpressure positive phase is illustrated in Figure 2.6 at time t_d. Momentum of the detonation and air particles is high and the air over–expands creating a volume below atmospheric pressure around the detonation point [12]. This is due to the space between the air particles being greater than when at atmospheric pressure. Over–expanded air will flow back into the volume below atmospheric pressure to maintain equilibrium creating a negative pressure phase, illustrated in Figure 2.6 at time t_n. The form of the blast wave presented in Figure 2.6 is often referred to as the 'Friedlander exponential' after Friedlander suggested a simple formula to calculate pressure waveforms for free–air detonations [20].

As the blast wave continues to expand radially from the explosive the blast energy is absorbed by compressing the surrounding air. Attenuation of the shock by the air decelerates and reduces the pressure of the shock wave with radial distance from the detonation point.

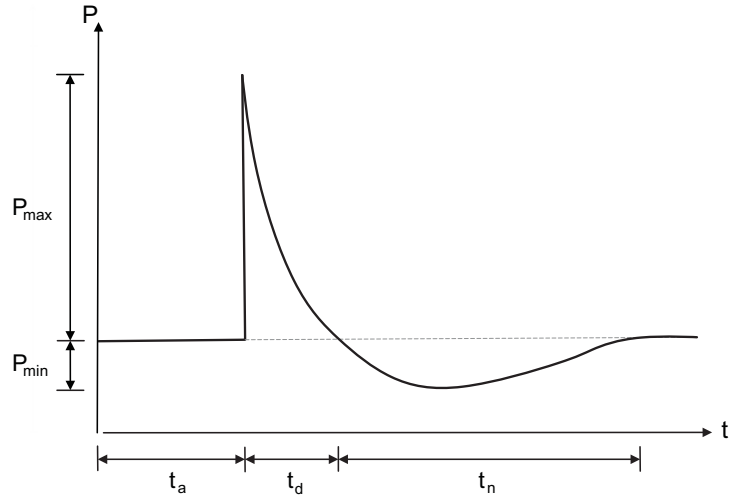

Figure 2.6: Indicative blast shock wave pressure–time history.

2.2.4 Blast wave clearing of finite surfaces

Blast wave clearing describes the phenomena of a blast wave in contact with a rigid surface losing its confinement such that the rate of pressure decrease with volume increase accelerates. This phenomena can occur at the edge of a target plate where confinement of detonation products by the target surface is lost, shown in Figure 2.7. When a propagating blast wave strikes a structure, reflected pressures develop on the target's loaded face (Figure 2.7b). When this blast wave reaches the edge of a finite target (Figure 2.7c), diffraction will occur at the edge (Figure 2.7d). This diffraction causes a low pressure rarefaction wave to propagate along the loaded face (Figure 2.7e), where higher magnitude reflection pressures begin to flow into the lower magnitude pressure regions [21]. Upon the arrival of the rarefaction relief wave a significant reduction in pressure and impulse thereafter will be witnessed on the loaded target face. This phenomenon is featured in structural design guides such as UFC 3–340–02 [22].

An example of clearing can be seen in Figure 2.8, where ConWep [13] predicted reflected pressure for an infinite target and experimental data from a semi–infinite target are compared. In each test a 0.25 kg PE–4 hemispherical charge was detonated on a ground slab 4 m from the target. It can be observed that between 7.25 ms and 8.25 ms the predicted infinite reflected and infinite experimental data are in excellent agreement. However beyond 8.25 ms the reflected overpressure for the finite target shows a significant reduction when compared to the reflected overpressure predicted on the infinite target.

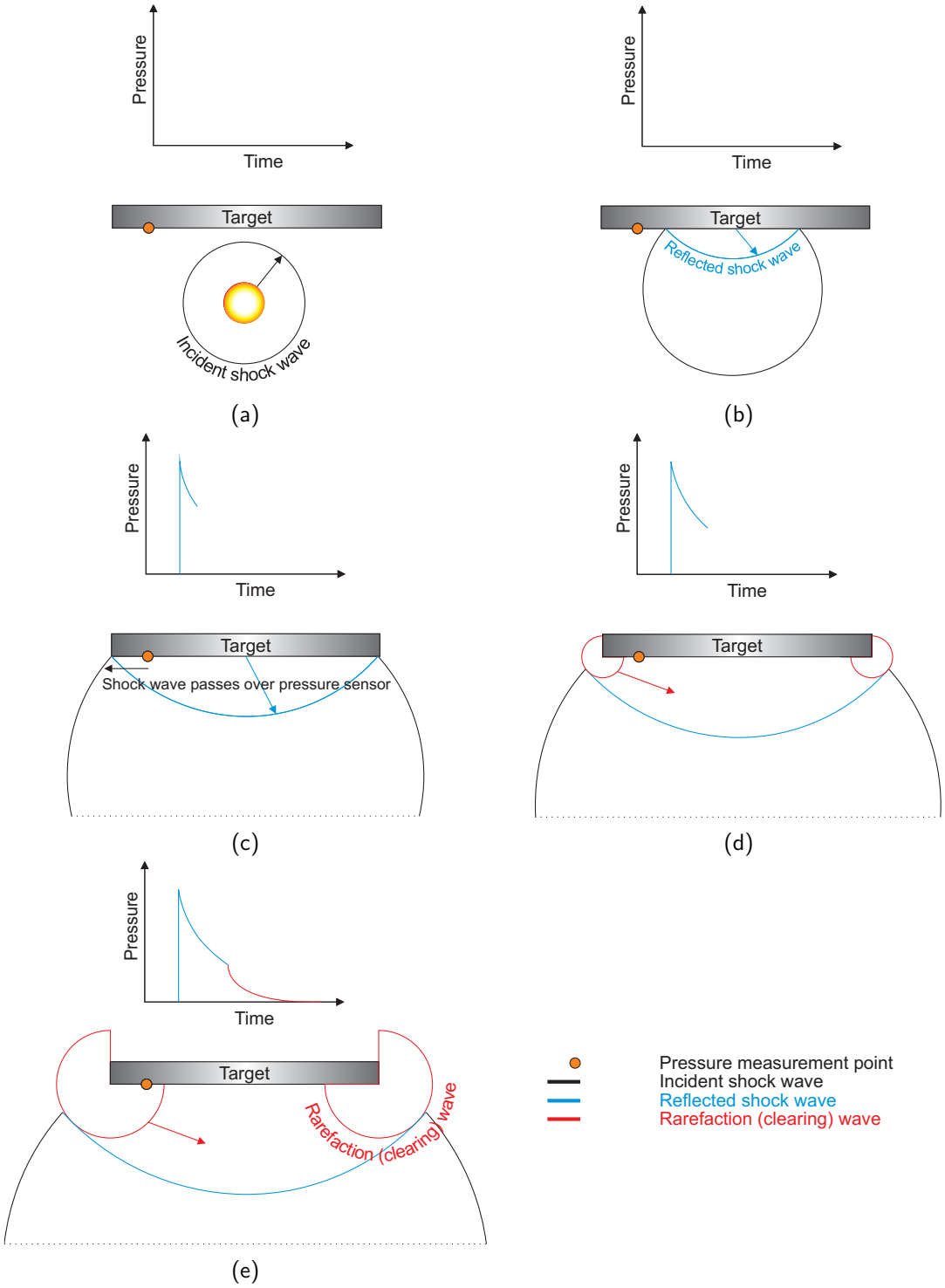

Figure 2.7: Blast wave clearing of a finite target.

This demonstrates the significance of the effect of blast wave clearing and it must be considered in experimental work. Targets used to measure pressure following the detonation of a shallow buried charge should be designed such that the width of the target prevents clearing during the time of interest.

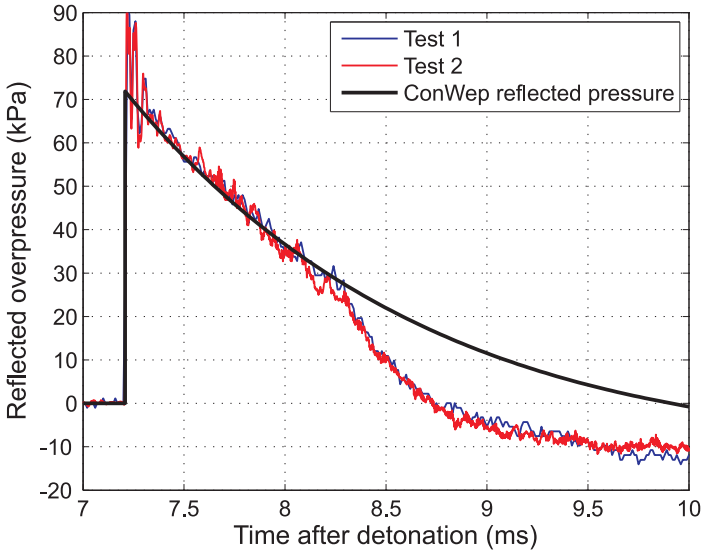

Figure 2.8: Experimental results (Tests 1 and 2) versus empirical model prediction (ConWep). Tests 1 and 2 show clearing pressure on a small target, ConWep prediction shows reflected pressure on an infinite target for identical charge configuration [21].

2.3 Geotechnical materials

Soil is a term which describes unbonded or weakly bonded material overlying harder rock on the Earth's surface [23]. There is a large variety of soil and their creation is due to many factors such as natural geological cycles and the parent material from which the soil came. A soil's physical characteristics are an important factor when understanding soil behaviour and these characteristics are derived from the parent material, weathering, formation method and transport method to a soil's present location. Water transported soils such as sands are typically described as granular, cohesionless and course grained and fall within the particle size diameter of 0.06–2 mm [23, 24].

Sand is often found in three phases where the bulk material contains solid particles, fluids and gases. A physical description of soil can be given by calculating its bulk properties with ratios of solid particles, fluid and gas. These basic parameters provide an understanding of the composition of the material matrix and assessment of the soil's behaviour can be determined [24]. The particle size distribution (PSD) is used to ascertain more complex mechanical properties of a soil and estimate how easily water will flow between soil particles when a soil is under load.

2.3.1 Bulk properties of the geotechncial material matrix

The relationships for the volume and mass of the soil matrix is presented in Figure 2.9.

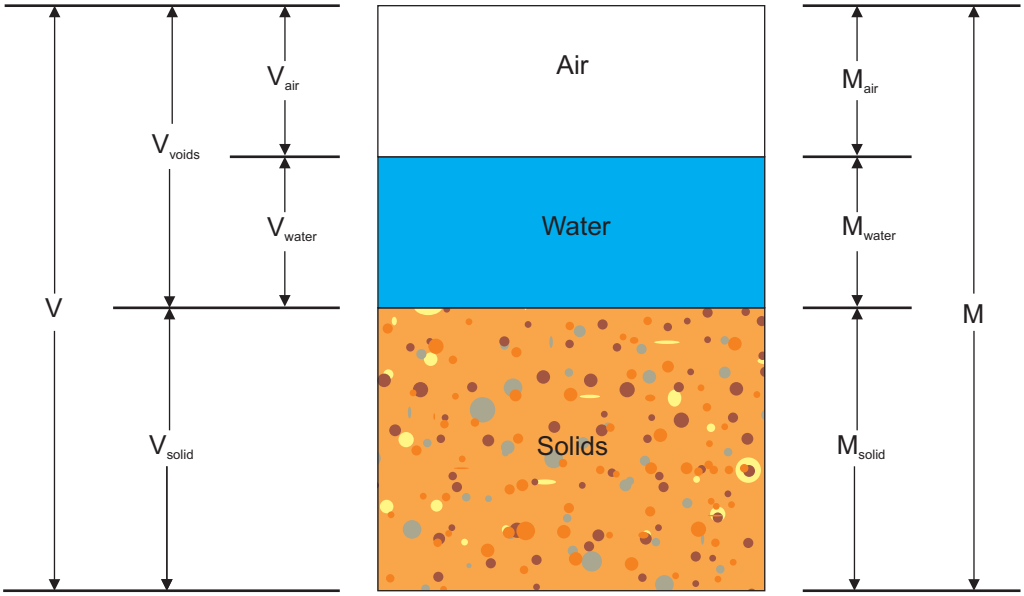

Figure 2.9: Soil solids, water and gas phases of soil [23], showing the conceptual bulk property relationships of volume and mass relating to equations 1.1 – 1.8.

The bulk volume of a soil (V) is made up from the volume of soil particles (V_{solid}) and the void volume (V_{voids}) between the soil particles. From Figure 2.9 the relationship of volumes in a soil can be written as equation 2.1.

$$V = V_{solid} + V_{voids} \tag{2.1}$$

When no water is present in the soil matrix, voids between soil particles are occupied with air, whereas a fully saturated soil has all voids filled with water. When a soil is partially saturated, the voids are filled with both water and air. Levels of saturation are described in Figure 2.10 from dry to fully saturated.

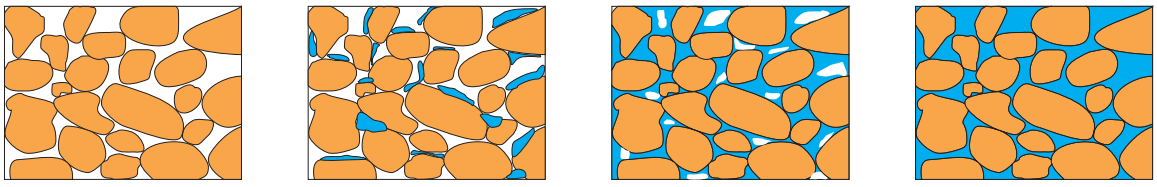

Figure 2.10: The effect of water content on granular soil air voids, adapted from [25].

The volume relationship for the three phases of a soil are presented in equation 2.2.

$$V = V_{solid} + V_{water} + V_{air} \tag{2.2}$$

From Figure 2.9 it can be seen that the bulk mass of a soil is due to the mass of solids (M_{solid}), the mass of water (M_{water}) and the mass of air (M_{air}) as presented in equation 2.3.

$$M = M_{solid} + M_{water} + M_{air} \tag{2.3}$$

However, the mass of air in the soil matrix is negligible and is ignored when calculating the bulk mass, as in equation 2.4.

$$M = M_{solid} + M_{water} \tag{2.4}$$

Using the relationships of volume and mass developed above, it is possible to define two different types of density in a geotechnical contex. The bulk density of a soil accounts for total mass and volume and is written as equation 2.5.

$$\rho = M/V \tag{2.5}$$

The dry bulk density accounts for the mass of soil particles in the total volume of the soil and is written as equation 2.6.

$$\rho_d = M_{solid}/V \tag{2.6}$$

Moisture content is taken as the ratio of water of a soil when compared to the soil particle mass and is defined as equation 2.7.

$$w = M_{water}/M_{solid} \tag{2.7}$$

Whilst the moisture content provides some measure of the amount of water in a soil matrix, it does not describe how the void volume is occupied. The saturation ratio allows the degree of saturation to be understood by observing the volume of voids that contain water as defined in equation 2.8.

$$S_r = V_{water}/V_{voids} \tag{2.8}$$

2.3.2 Particle size distribution

Soil shear strength is determined by inter–particle friction as it is generally accepted that granular soils have no tensile strength. Soil mechanical properties are most strongly influenced by the behaviour of water in voids between soil particles [24] . The main feature which separates gravels and sands from silts and clays is the ease at which water flows between the network of voids between the solid particles [24]. The void size (or permeability) between soil particles is

typically determined by the smallest 10% (by mass) of soil particles because these fit between the larger particles and restrict fluid flow [23]. In sand and soils with larger particles water can flow easily between the voids.

One method of classifying sandy soils is by their particle size distribution (PSD). Figure 2.11 shows the PSD for a well graded (red) and a uniform soil (black). Well graded soils are typically dense and high in strength as the particle distribution enables good packing of the soil particles [23]. Uniform soils are poorly graded consisting of a small band of particle diameters. Uniform soils are less stiff than well graded soils as the particles are less densely packed and so particles shear more easily.

In events where the flow of water between voids is important, the PSD indicates the permeability of the soil [24]. The uniform soil in Figure 2.11 can be seen to have larger diameter particles at 10% mass passing meaning that the flow of water between particles in the LB soil is achieved more quickly when compared to the well graded STANAG soil. A consequence of this is that for short duration high magnitude loading, the more densely packed well graded soil may take longer to drain reducing the strain required to reach hydrostatic lock–up of the particles.

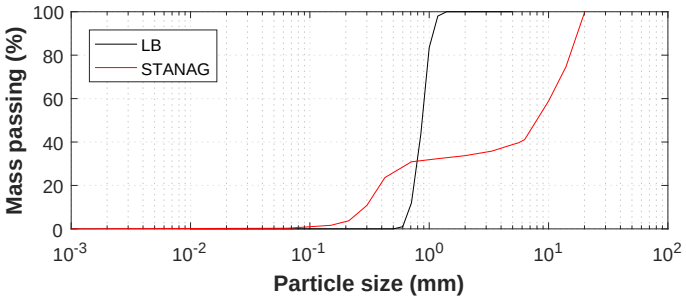

Figure 2.11: PSD of a uniform soil Leighton Buzzard (LB) and well graded soil STANAG. For a comprehensive description of the soils used in the testing presented in this thesis, the reader is directed to Section 3.3.

2.4 High velocity water droplet impacts

Water is a material found in three phases of soil presented in Section 2.3. Therefore the fluid mechanics of water droplet impacts on solid surfaces is of importance in this study. The behaviour of water droplet impacts covers a broad subject area. In this study the primary focus of droplet impact is on the behaviour of the water droplet immediately after impact due to the three behaviours of the water droplet after impact being known to determine the pressure at the water–surface interface.

2.4.1 High velocity water droplet impacts

Rein [26] outlines the impact behaviour of high velocity water droplets on a solid surface. Four distinct phases characterise the behaviour of water droplet impacts that are of interest in this study and are described as initial impact, spreading, splashing and bouncing of the droplet, see Figure 2.12.

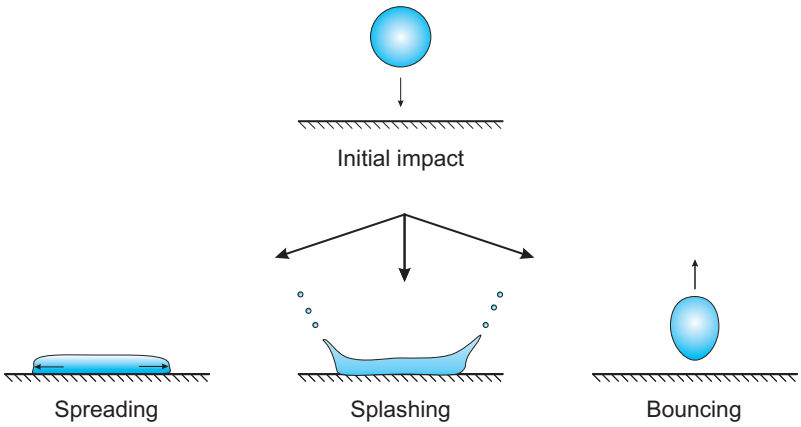

Figure 2.12: Impact of a drop on a solid surface: Initial impact, spreading, splashing and bouncing, adapted from [26].

At impacts above the acoustic limit of the water the pressure is equal to the waterhammer pressure $\rho c u$ where ρ is water density c is the speed of sound in the material and u is the impact velocity. It can be seen in this simple relationship that at high velocities the pressure in the water droplet can rise significantly post impact.

If the impact velocity of the water droplet is higher than $c \sin\beta$ where β is the contact angle, the portion of the droplet yet to contact the plate is undisturbed by the impact and the liquid in contact remains inertially confined. As the water droplet continues to impact the target the contact angle changes up to a critical point where the shock separates from the contact edge and jetting of the fluid begins resulting in spreading or splashing of the droplet. The pressure in this contact zone is not uniform and the highest pressures in this impact are witnessed at the contact edge, where pressures exceed the waterhammer pressure, whereas pressure at the centre of the droplet is lowest. This is attributed to increases in edge pressure with increased obliquity of contact edge slope as the droplet expands [26].

At lower velocity impacts, initial spreading of the droplet is determined by the kinetic energy of the drop where spreading begins the moment that jetting occurs. At higher velocities however, the jetting motion leads to a disintegration of the liquid and splashing occurs. In both high and low velocity impacts the initial expansion of the droplet is similar. The fluid expands into a thin disk reaching a maximum radius where kinetic energy is dissipated into additional surface energy forcing the disk to contract. It is this process that may cause a higher velocity drop

to splash and in some cases the contraction of the water droplet may cause it to 'bounce' off after impact.

2.5 Protection standards for land mine blast protection

The aim of the Standardization Agreement (STANAG) documents are to provide consistent standards between the North Atlantic Treaty Organisation (NATO) members for armed forces equipment providing a minimum performance standard for member states' military capability. Coordination at the equipment level is intended to simplify multi-nation operations where NATO member states' may opt to design their own equipment. Therefore, by all NATO members designing for standardised threat scenarios, it allows combined risk planning and the selection of appropriate protective equipment for any multi–national operation.

STANAG 4569 Edition 2 [8] provides protection levels for occupants of armoured vehicles. By meeting the requirements of the standard a 90% probability of protection is provided for mounted soldiers. Table 2.1 shows the threat levels to which new vehicles must be tested against increasing in the protection required from level 1 to level 4. In this thesis the threat level M2b is used at 1/4 scale; for clarity M defines the threat type (land mine), 2 defines the level (i.e. 6 kg of TNT equivalent mass explosive) and b the relative detonation location on the vehicle (under belly).

Table 2.1: Land mine threat table from STANAG 4569 Edition 2 [8] Protection levels of armoured vehicles for grenade and blast mine threats

<table>
<tr><td colspan="2">Level</td><td colspan="2">Grenade and blast mine threat</td></tr>
<tr><td rowspan="2">4</td><td>4b</td><td>Mine explosion under belly</td><td rowspan="2">10 kg (TNT explosive mass) blast anti-tank mine</td></tr>
<tr><td>4a</td><td>Mine explosion pressure activated under any wheel or track location</td></tr>
<tr><td rowspan="2">3</td><td>3b</td><td>Mine explosion under belly</td><td rowspan="2">8 kg (TNT explosive mass) blast anti-tank mine</td></tr>
<tr><td>3a</td><td>Mine explosion pressure activated under any wheel or track location</td></tr>
<tr><td rowspan="2">2</td><td>2b</td><td>Mine explosion under belly</td><td rowspan="2">6 kg (TNT explosive mass) blast anti-tank mine</td></tr>
<tr><td>2a</td><td>Mine explosion pressure activated under any wheel or track location</td></tr>
<tr><td>1</td><td colspan="3">Hand grenades, unexploded artillery fragmenting submunitions, and other small anti–personnel explosive devices detonated anywhere under the vehicle</td></tr>
</table>

The rationale of selecting this threat level was to allow read across of previous work undertaken at STANAG 4569 Edition 2 level M2B at 1/2 scale [25, 27–32]. This read across would allow understanding of both the spatially and temporally resolved localised loading where the blast products are in contact with a target, versus the response of a deformable structure and the whole body global response of a surrogate vehicle.

Allied Engineering Publication (AEP) 55 Volume 2 Edition 1 [33] is an Annex to STANAG 4569 Edition 2. AEP-55 describes test configuration for the determination of the protection levels defined in STANAG 4569. The depth of burial or overburden for a mine is defined as 100 mm $\pm$ 10 mm and is measured from the top of the mine casing to the surface of the soil.

Shallow buried charges are typically defined as such due to the enhancement caused by surrounding soil on the vertical momentum transfer. The momentum transfer from an explosive charge buried in soil increases with burial depth up to a critical point where the momentum transfer will begin to reduce due to the depth of overburden above the charge confining the charge output. Further increase to the burial depth will continue to reduce the momentum transfer until the output at the soil surface is zero. The term shallow buried in the context of this study means the range of depths at which the momentum transfer from a shallow buried charge is enhanced by its confinement. Providing an explicit depth of burial range to this is difficult because the enhancement is dependent on a number of parameters not investigated in the study. However shallow buried shall be determined as a burial depth of less than 200 mm at full scale, 50 mm at 1/4 scale.

2.6 Blast wave measurement using Hopkinson Pressure Bars

The environment surrounding an explosive charge is aggressive, particularly in the near–field (here, near–field is determined as being within the region of expanding detonation product and shocked surrounding material). It is difficult to make measurements of a blast wave in the near–field with conventional pressure measuring equipment. Measuring the pressure following near–surface detonation of a shallow buried charges adds the further complication of high velocity particle barrage which strike and then flow around measurement equipment. The Hopkinson Pressure Bar (HPB) has been used in high–strain rate measurements for blast pressure [34, 35] in the near field. The use of HPBs has been extended to the study of near–field subsurface detonations with some success [36]. This section will cover some of the basic considerations when developing a HPB for the purposes of measuring near–field blast pressures.

2.6.1 Transducer for measuring near–field blast and particulate impacts

The transducer has many physical forms and is used in a range of applications where mechanical phenomena need to be understood. A transducer essentially takes a mechanical input and 'converts' this to a corresponding electrical output by some means. The HPB is a transducer where mechanical strain caused by axial compression is converted into an electrical output. The HPB, in high strain rate events, is typically constructed from a cylindrical steel rod. Steel is used as it is durable and readily available in many steel grades and relatively inexpensive.

Three components are needed in addition to the steel rod to construct a transducer: strain gauges, which convert strain into an electrical signal; electrical signal conditioning units (a Wheatstone bridge circuit), for balancing resistance in the circuit such that small changes in voltage can be measured; and data acquisition equipment that can record data at suitable resolution for the phenomena of interest. The selection of strain gauges and development of an appropriate Wheatstone bridge is fundamental to developing a HPB which captures data of interest in this study and so fundamental principles of these devices will be discussed further.

2.6.2 Semi–conductor strain gauges

A strain gauge is a variable resistor and is used to measure strain or flexure of a material. When the active element is subjected to strain, resistance in the element will change. As a result a change in the voltage potential in the circuit containing the strain gauge can be measured. This can be used to investigate change in material to which the strain gauge is bonded. Electronically a strain gauge is assembled within a Wheatstone bridge circuit; DC voltage is applied across two terminals to excite the circuit and voltage change is measured across the opposing terminals [37].

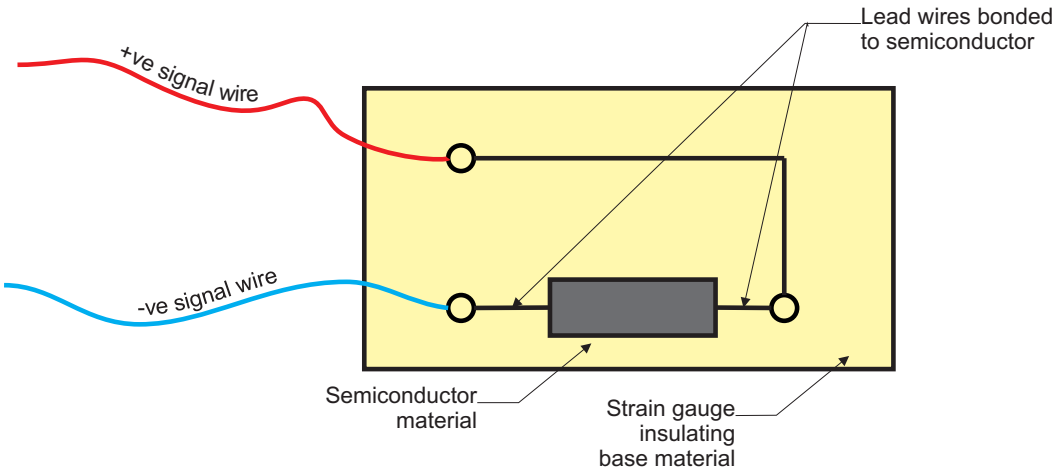

Figure 2.13: A typical semiconductor strain gauge mounted on a base resin.

Modern strain gauges for use outside the laboratory consist of a semiconductor encapsulated within an isolating material, Figure 2.13. Terminals or lead wires are exposed for connection to one leg of the Wheatstone bridge [38]. A semiconductor gauge works with the piezoresitive effect where the resistance of a silicone crystal changes with a change in strain. As the crystal is strained and the resistance changes, a change in voltage potential in the Wheatstone bridge will be witnessed.

The main advantages of semiconductor strain gauges over previous strain gauge designs are:

- High strain sensitivity.
- Low hysteresis[1].
- Ability to attach to small items due to small gauge sizes.
- High in–service life, usually limited by bonding method.

The high strain sensitivity of semiconductor strain gauges means that gauges can measure smaller strains for higher changes in voltage. The two benefits of this are that strain data is measured at a higher resolution and that an increased voltage difference for smaller increments of strain means amplification is no longer needed. Further, any signal noise generated by electronic components or interference is not amplified.

Cyanoacrylate (CA) is an acrylic resin commonly used to bond strain gauges. It is typically used due to its ability to produce a thin film, low hysteresis and high shear strength, compatibility with many materials, and low curing time. These characteristics are highly desirable when selecting a bonding agent for strain gauges [38].

2.6.3 Signal conditioning with the Wheatstone bridge

The Wheatstone bridge is used in many applications where there is an unknown change in resistance [38]. The Wheatstone bridge has two functions, namely providing power to the circuit and allowing measurement of voltage differentials across a circuit [37].

Figure 2.14 shows a half Wheatstone bridge circuit typically used to assess axial loading. Its operation is analogous to a roundabout at rush hour. Consider a multiple exit roundabout where all entrances and exits to the roundabout are full of traffic. No traffic can move onto the roundabout and therefore the flow of traffic is zero. When an exit from the roundabout becomes clear, the resistance to traffic flow is reduced and traffic begins to move. A Wheatstone bridge is similar to this where cars are current (flow of energy) and the blocked exits are resistors (of the same initial resistance value).

When all resistors are at the same resistance, no current will flow across the circuit and the measured voltage across B and D will be zero. However, if the voltage changes in a resistor, R_2 or R_4, current will flow in the circuit and the flow of current can be measured between points

[1] Hysteresis is a non–linear phenomenon where a change in input is not directly proportional to a change in output. Using the example of a strain gauge, this may cause a lag between the input signal, response of the strain gauge and the change in output signal. Mono–crystalline silicone used in semi–conductor strain gauges is perfectly elastic therefore any lag in signal is due to either installation defects, gauge bonding material hysteresis or the gauge construction itself [38].

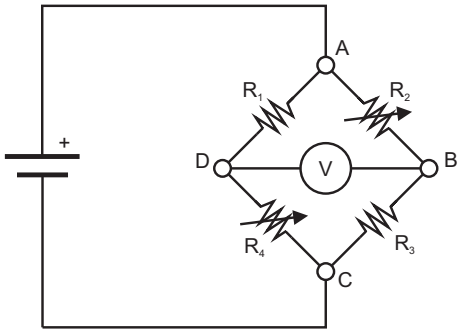

Figure 2.14: A half Wheatstone bridge with two arms unbalanced. Suitable for axial strain, tension and compression [38]

B and D. When strain gauges are placed in the circuit at R_2 and R_4 and strain is applied to the gauge, the strain gauges change resistance resulting in a voltage imbalance in the circuit. It is this voltage change across the Wheatstone bridge circuit that is recorded by the data acquisition equipment. This is a convenient and accurate way of measuring voltage change in a circuit and this method of signal conditioning has been used throughout the experimental work in this thesis.

2.6.4 Hopkinson Pressure Bars

A HPB enables the reconstruction of a blast pressure pulse by transforming mechanical strain into an electrical signal. Figure 2.15 illustrates a typical HPB arrangement. When the HPB is impacted, the resulting stress wave travels along the bar's length as a compression wave. This mechanical displacement of the bar's structure is 'detected' by the strain gauges and converted into voltage which can be recorded by an oscilloscope as a voltage–time history. The voltage–time history can then be processed back into the pressure witnessed across the face of the HPB; and so the input signal is digitally reproduced from this analogue signal. This process is illustrated in Figure 2.15.

When a blast wave meets the reflecting surface of a HPB, it exerts a pressure on the face of the HPB. Stress forms at the bar face for the duration of pressure application corresponding to the force exerted on the bar face. For accurate measurements, the force applied to the HPB must produce a strain response that is within the elastic strain limit of the HPB.

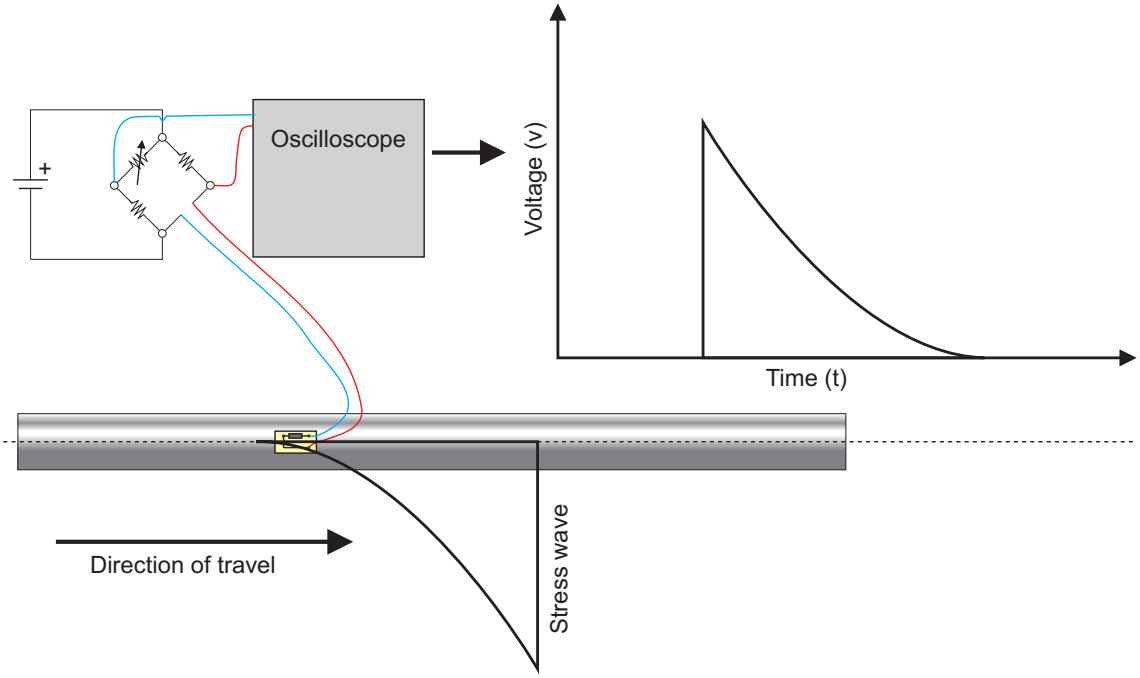

Figure 2.15: Hopkinson Pressure Bar general arrangement.

2.6.5 Hopkinson Pressure Bar dispersion

Rigby et al. [39] authored a state–of–the–art review of HPB techniques where dispersion phenomena and output signal analysis are discussed in detail. Pochhammer and Chree [40, 41] independently derived the equation of motion for an elastic wave in a cylinder for sinusoidal waves, where loading on the face of a HPB can be expressed as a series of sinusoids of varying amplitude and frequency. The Pochhammer–Chree equations show that as phase velocity varies as a function of frequency, low frequency components of an input signal travel along the bar at approximately the wave speed of the bar, and high frequency components will travel more slowly. The effect of different phase velocities is to disperse the input signal, where lower frequency components form the main body of a pulse (as propagation of the wave velocities is approximately similar) and higher frequency components begin to lag behind the main body of the pulse. In a HPB signal, this phenomena may appear as high frequency oscillations overlain and following the peak of a pulse.

It is possible to reconstruct part of the dispersed high frequency input for the first mode of the signal. However for the second and higher modes, it is currently not possible to correct for dispersion beyond the first mode cut–off frequency. Thus, for input signals which are high in magnitude and transient, the input signal currently can not be fully reconstructed.

2.7 Literature review

It is well documented [42–47] that for comparative explosions a shallow buried charge output will be greater than that of a test in free–air. However, the *mechanisms* which causes this enhancement in the transfer of load between the charge surface and a near–field structure remain a topic for investigation. A number of techniques have been developed to assess the output from a shallow buried charge. The choice of method depends on the scaling used, rate and duration of impulse and whether spatial and temporal resolution can be acquired.

Work from the late 1960s reported by Joynt [7] assessed the output from buried charges upon deformable targets and comparatively assessed 'crew cabin' performance for personnel survivability. Some work within the blast community still focuses on the assessment of deformable targets [43, 48, 49]. This approach is useful for assessing the performance of deformable geometries and provides some insight to load transfer but no information of the spatial load distribution nor mechanisms were gained from this methodology.

Bergeron [11] used pressure time–histories and x–rays of a buried charge detonation to outline a number of mechanisms present, namely early interaction with soil, gas expansion and soil ejecta. Since this publication, experimental work and modelling investigations generally seem to have overlooked these distinct loading phases.

In recent state–of–the–art studies [25, 27, 28, 50], impulse data derived from the jump height of a known mass following a detonation has been used to identify first–order geotechnical parameters that further enhance shallow buried charge loading. This approach describes only rigid body target response and provides no information of the spatial and temporal distribution of the target load.

Because the understanding of the buried blast loading phenomenology remains in its infancy, designing protection against such events presents a significant technical challenge due to the understanding of the physics being relatively poor.

2.7.1 Background of buried blast phenomena characterisation

Jack et al. [51] simulated the effects of explosions at altitude by detonating spherical pentolite charges in increasing states of vacuum. Pressure–time histories from these experiments were captured at a 'rigid' boundary several feet from the detonation. This work shows that as ambient pressure decreases the effects on the early pressure wave form increases.

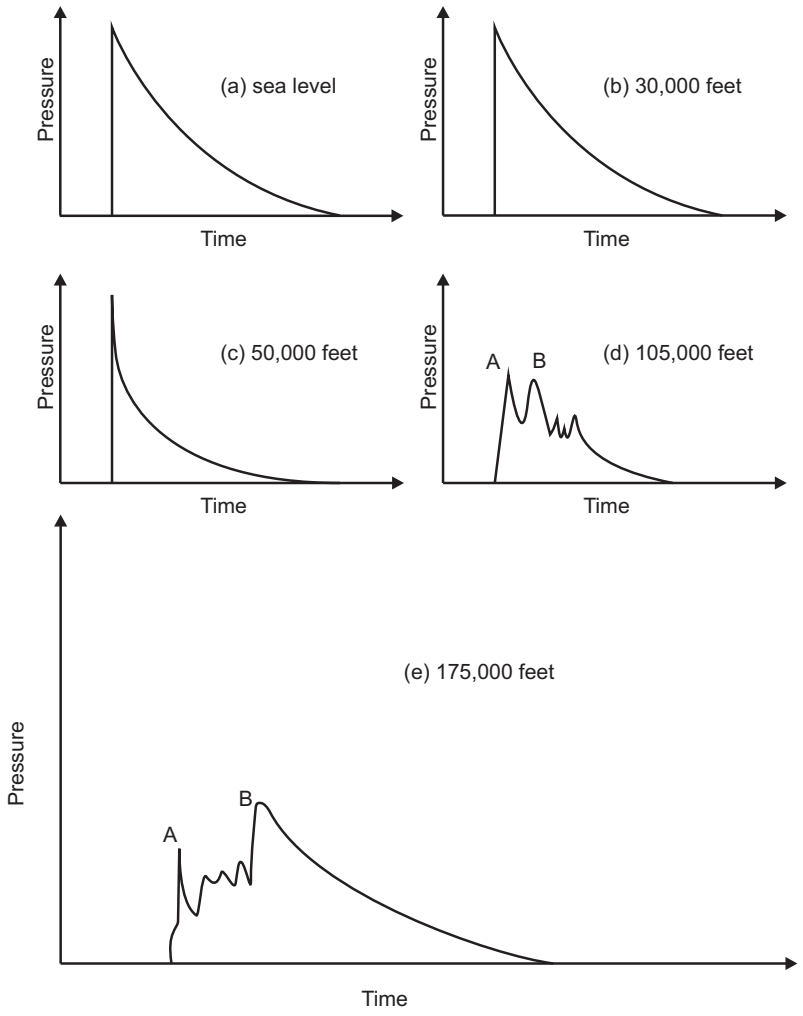

Figure 2.16: Indicative pressure–time histories in reducing atmospheric conditions (a) Sea–level, (b) 30,000 feet (c) 50,000 feet (d) 105,000 feet and (e) 175,000 feet. Adapted from [51].

When there is an atmosphere the Friedlander–type waveform can be seen in the indicative pressure–time histories in Figures 2.16 (a), (b) and (c). When the atmosphere is reduced, illustrated in Figures 2.16 (d) and (e), the Friedlander discontinuity associated with detonation in free air is no longer evident. This change in behaviour indicates that the mechanisms associated with detonation in an atmosphere change when air is no longer present to transmit the shock.

Baker [52] investigated the effects of detonation in low atmospheres at high altitudes. Experimental data produced by Jack et al. [51] was used to assess the reflected impulse on a rigid wall. It was found that Hopkinson's scaling for strong shocks gave accurate predictions when the detonation point is very close to the reflecting surface. Hopkinson's strong shock scaling is independent of atmospheric conditions which implies that the effects of surrounding air is negligible on total impulse transfer. This suggests that energy generated during explosive decomposition in the very near–field is converted almost entirely to kinetic energy. Thus, in the very near–field, impulse is caused primarily by the momentum of the explosive products.

Westine [53] used the pressure histories produced by Jack et al. [51] to confirm that when stand–off is increased and when no atmosphere is available to support a shock wave, momentum transfer is due to detonation product momentum. Westine expands his explanation further and compares the scenario to sub–surface detonation. Referring again to Figure 2.16 e.) features A and B, Westine describes A as a Friedlander discontinuity. However, as there are no air particles to support the initial shock, pressure is due mostly to detonation product momentum. Westine goes further stating that A would disappear entirely in a complete vacuum. There is a gradual rise in pressure between A and B which suggests that peak B is due to the second shock. The second shock is seen more strongly due the presence of gaseous detonation products through which the second shock can expand.

Westine applied Baker's [52] analysis to a shallow buried charge. It was shown that the majority of load from a shallow buried charge was from the mass of detonation products. When the mass for the charge encasement was added to the momentum calculations the impulse calculations were in good agreement, thus strengthening the argument that momentum transfer is predominantly by detonation product, case and ejecta momentum. Westine validated these findings against experimental data and went on to state that this is valid when the target is within the impulsive range of the buried explosive, i.e. loading is applied over a duration considerably shorter than the target response time.

Westine et al. [54] investigated the effects of ground shock pressures from buried detonations of munitions in saturated and unsaturated soils. It was noted that when predicting compressive wave velocity in unsaturated soils, the empirical prediction did not match results taken when the water table was high. Westine calculated the compressive wave velocity in unsaturated soil as 365 m/s whereas in saturated soil the wave speed was 1500 m/s, i.e. the same as the wave speed in water. When the empirical model for dry soil was modified for shocks in water and applied to saturated soil there was significant improvement in predicting the higher pressures generated for sub–surface detonation.

The increase in energy fluence for the saturated soil was attributed to voids between soil particles being filled and therefore becoming almost incompressible. Energy usually used to collapse

voids between soil particles and shear soil particles over one another is reduced as the shock transmits through the fluid component of the soil–fluid mix. Therefore pressures remain higher as the explosive has to do less work on the soil.

Fourney et al. [55] experimentally investigated the mechanisms leading to cratering following the detonation of a buried mine in a bore hole. The post–detonation response of the geomaterial is outlined in Figure 2.17 a–c, the loading can be described in two phases:

- Shock wave loading which quickly transmits through the material.
- A longer duration gas heave caused by the expansion of detonation products.

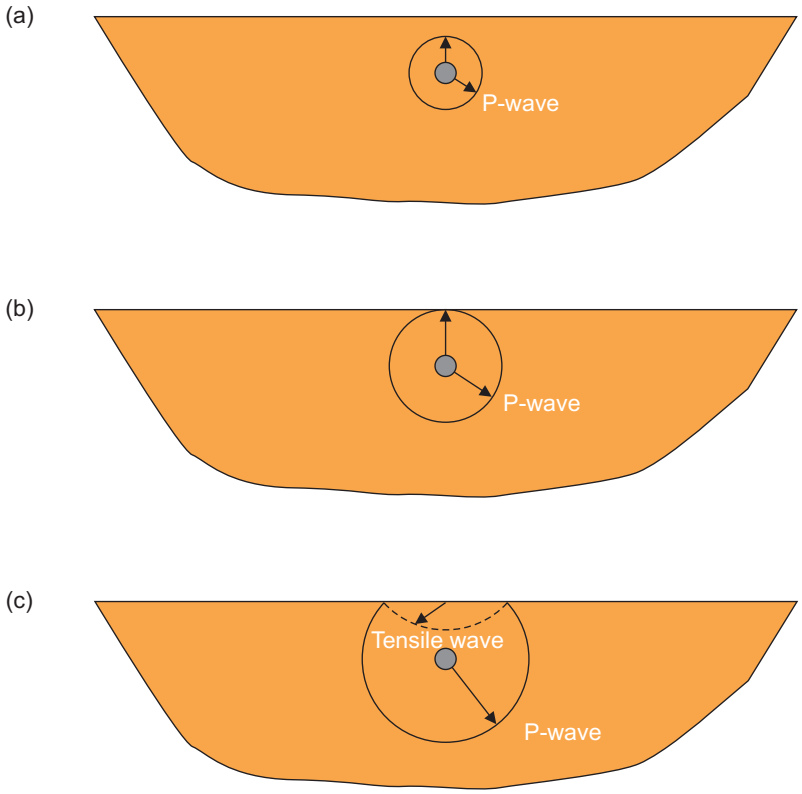

Figure 2.17: Stress wavefronts in half plane with internal point source; (a) Post–detonation, (b) compressive P–wave reaches the free surface (c) tensile reflection of compressive P–wave from free surface, adapted from [55].

The shock wave loading is split into two wave forms, primary (P–wave) and secondary waves (S–wave). The P–wave is compressive and applies force in the direction of propagation moving particles together. An S–wave moves particles side–to–side perpendicular to the direction of travel and shears particles across one another. Generally the modulus of elasticity for compression is greater than shear modulus and so an S–wave propagates more slowly than a P–wave. When a P–wave reaches the free boundary due to the large difference in acoustic impedance between the soil and air most of the wave is reflected back into the soil. One characteristic

of S–waves is that they cannot transmit in fluids. This is due to the shear modulus of fluids being zero and so the fluid will flow rather than being sheared.

Fragmentation of the geo–material is caused when the compressive outgoing wave is reflected and becomes a tensile wave. This is due to the compressive strength of geomaterials being higher than their tensile strength. To maximise particle breakage increasing the outgoing compressive pulse is required. However when crushing begins to occur when the compressive pulse reaches the compressive limit of the geomaterial the stress within the material will reach a peak and will not increase further. With an increase in charge energy (by increasing the charge mass) the crushing zone size around the charge will increase.

2.7.2 Shallow buried blast characterisation techniques

Pressure transducer

Bergeron et al. [11] produced well characterised pressure–time histories following the detonation of cylindrical 0.1 kg C4[2] shallow buried charges in dry sand. Tests were conducted with five pressure transducers placed vertically above and co–axial with the line of detonation at standoffs between 300 mm – 1900 mm. Three distinct phases of post–detonation were noted:

1. The first phase encompasses the detonation and early interaction with the sand where the sand in contact with, and immediate vicinity of, the charge is over–driven but decelerates within 2 charge diameters, see Figure 2.18a.

2. When the compressive wave reaches the soil surface the large drop in acoustic impedance only permits a small amount of shock into free air. As a tensile wave reflects back into the sand and the detonation products, no longer inertially confined, expand, the soil begins to deform at the surface and the detonation products expand in a uniform semi–hemispherical bubble. The initial expansion of the 'soil–bubble' acts as a piston and drives air shock ahead of the expanding soil–bubble, see Figure 2.18b.

3. The soil cap described in 2 is thin as detonation products 'burst' through the top of the ejecta. Following these early events described in 1 and 2 significant ejection of the soil continues. As the in–soil detonation products continue to expand radially and do work on the surrounding material, soil continues to flow upwards within an annulus surrounding the core of gaseous products. This third phase is called the late ejecta flow, see Figure 2.18c.

[2] Composition C4 is a plastic explosive used widely in military applications. The explosive is based on Royal Demolition eXplosive (RDX).

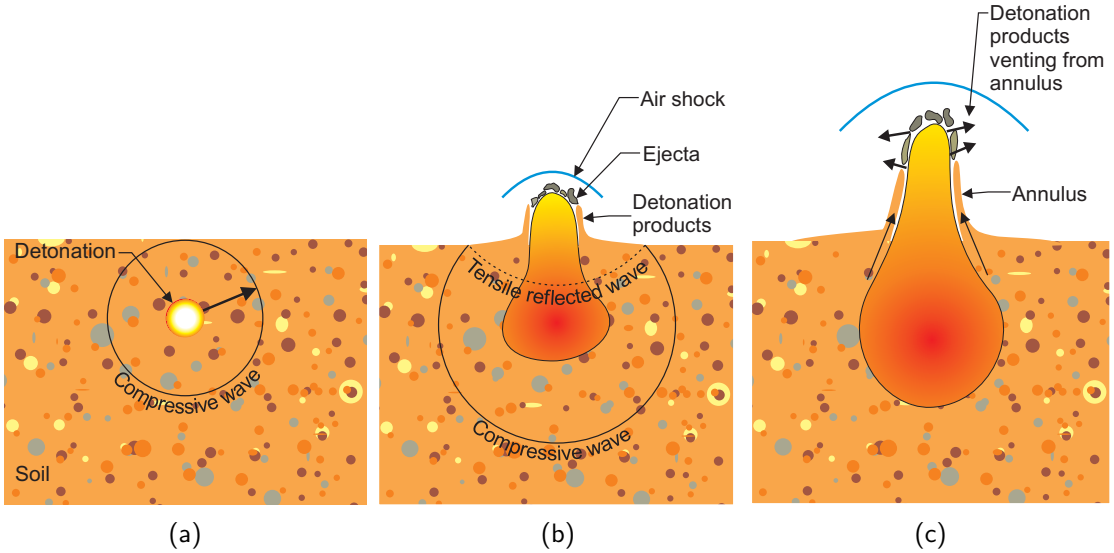

Figure 2.18: Three distinct post-detonation phases highlighted by Bergeron et al. [11].

It was noted by Bergeron et al. that a substantial amount of the explosive energy is transferred in dynamic pressure, and that the soil focuses this flow of energy in the upward direction [11]. These tests show that early soil–explosive interaction are important in the development of the blast loading whilst late time interaction is most affected by burial depth.

Free acceleration method

The Free Acceleration Methodology (FAM) allows a mass to translate freely following the detonation of a shallow buried charge. By accurately measuring displacement of the free flying mass the impulse can be derived through conservation of momentum. Some recent studies have assessed the load imparted onto a target by assessing the movement of a known mass and for assessment of total impulse imparted across the target [25,27,28,44,45,47,49,50,56,57].

Bergeron et al. [44] used a horizontal pendulum to investigate the mechanical effect of moisture content, soil type and burial depth of a shallow buried charge. Whilst investigating burial depth charges were placed on the soil bed, buried flush with the soil surface or buried with overburden at a range of depths. Impulse was lowest for charges that were placed on the soil surface when compared to all other buried tests. When charges were buried with their top flush with the soil surface a significant increase in impulse was seen when compared to the surface charge. Fully buried tests saw further increases in impulse. These findings demonstrate that confinement of dynamic pressure is achieved by the soil around the charge where lateral confinement focuses the detonation products upwards.

It was noted that for nominally similar tests, when moisture content was increased from 7% to full saturation, impulse transferred to the target doubled. Soil type and soil density had a

minor effect on the impulse at the target. Bergeron et al. [44] suggest that confinement of the charge and moisture content are of primary influence on the mechanical response of the soil.

Hlady [45] used the FAM technique where a piston could articulate vertically above a shallow buried charge. Displacement of the target was measured with a linear voltage displacement transducer. A cylindrical 25 g C4 encased charge at approximately 3:1 diameter to height aspect ratio was used in the tests and initiated at the base with an RP–87 detonator. Dry and saturated tests were conducted in prairie soil and concreting sand. The prairie soil is described as well–graded and having a clay component whilst concreting sand was described as containing fine aggregates implying that the prairie soil average grain size and distribution was typically smaller than that of the concreting sand. The charge was buried with an overburden between 0, 20, 50, 75, 100, 125 and 150 mm. Comparison between tests using the two soils showed that energy was increased by approximately a factor of five in the prairie soil compared to the concreting sand. As overburden increased from 0 mm the saturated prairie soil increased energy to the target until 75 mm where the energy transfer began to decrease. In dry soil the energy delivered to the target appeared to remain constant for the burial depths considered in the test series.

Strict soil preparation techniques are not obvious in this work. For example, it was noted that when dry soil containers were transported between the preparation area to the test site, sand levels dropped by 10–20 mm ([45], page 5) This indicates that further compaction occurred during transportation. To rectify this soil was added to the top of the soil bed to ensure soil containers were full for testing introducing soil layers at different densities. The saturation technique was unreliable and inconsistent volumes of water were added to saturate the soil. To increase the moisture content of the soil, containers were top filled with water which has been shown to produce an uneven distribution of water in the soil [28]. A large variance between tests of 50% in energy transfer at the target is most likely a result of the inconsistencies in the soil preparation, therefore only qualitative soil behaviours from this work can be characterised. Issues highlighted in the soil preparation technique used by Hlady [45] will be addressed in Chapter 3.

Fourney et al. [56, 57] conducted a series of experiments at approximately 1/10th scale to STANAG AP 55 [8] level M2 to determine the impulse from shallow buried charges using the FAM approach. It was determined that density and soil type influenced the impulse delivered to the target plate. However, the most important geotechnical parameter was moisture content where an increase in saturation from 0% to 100% resulted in a three and a half fold increase in impulse at the target.

Ehrgott et al. [46, 47] developed a free acceleration Impulse Measurement Device (IMD) to investigate the blast environment from a shallow buried charge. Motion of the mass was

measured with an accelerometer, and displacement via high–speed video and a yo–yo gauge. Further redundancy was achieved with a mechanical scratch gauge. Reflected pressure, ground surface overpressure and overpressure above the charge and laterally along the line of the test apparatus were measured above ground. Soil stress and particle velocity were measured sub–surface. Reflected pressure transducers embedded in the target plate yielded no useful results due to the impact of particulates. Ground surface overpressure measured higher peak overpressure with charges placed above ground than when the charge was buried.

Overpressure measured above the charge and laterally along a plane parallel to the ground surface demonstrated a focusing of impulse for buried charges. Impulse of charges placed on the surface and buried charges were compared. Directly above the buried charge impulse was approximately twice that of the surface charge. At a tangential length of 175 mm from the charge centre impulse from a buried charge in clay and silty soil was a third of the impulse of the surface charge. However, when comparing a charge buried in sand to the surface charge peak impulse was similar. At 535 mm from the charge centre, impulse measured from all buried charges was approximately a third the impulse measured for the surface charge. The reduction in overpressure impulse with increased radial distance from the buried detonation demonstrates a focusing effect of soil. Differences in a radial focusing between sand, silty soil and clay may be due to differing levels of lateral confinement of the detonation products indicating that a partially saturated sand provides less lateral confinement than silt or clay. The data shows that silt and clay had significantly lower void volumes than sand which may suggest that a physical mechanism linked to void volume enables improved focusing of detonation products.

Radial stress–time histories were measured with low–range soil stress gauges, particle velocity was measured by embedding accelerometers in the soil bed and the acceleration–time history integrated to give velocity. Due to the complex reflections induced by a near surface detonation, the soil stress and velocity histories provide limited data. For the range of soils tested soil stress was not sensitive to soil type but peak particle velocity was notably higher in clay soils. The lowest particle velocity was recorded in partially saturated sand. Intermediate velocities were recorded in silty sand where velocity increased with decreasing air voids and shear strength. Impulse measurements of the FAM for surface charges were approximately three to four times lower than for buried charges. Peak impulse for buried charges were higher in clay beds than for silty soil and sand by 40% and 50% respectively.

The large volume of data acquired and various measurement techniques applied in the test series by Ehrgott et al. [46, 47] provides broad insight into the phenomenological behaviour of buried charges. Perhaps most importantly these tests have demonstrated the viability of a range of different instrumentation techniques and how they can be deployed and what levels of success for a phenomenological study each one may bring. Pressure–time data was the most valuable for showing radial distribution of load above the charge and showing that void–volume may be a key geotechnical parameter. However direct measurement on the target

was not possible with off–the–shelf pressure transducers due to aggressive particulate impacts. Surface overpressure–time did not yield useful data due to possible reflections from the trial apparatus overwriting genuine phenomena from reflected shocks. Ground stress did not yield useful data due a lack of compatible data in the field and due to possible surface reflections hypothesised by Ehrgott et al. as overwriting lower magnitude stress histories. Particle velocity showed that shock transmitted more quickly in silt and clay than in partially saturated sand where void volume is highest.

Work conducted by Anderson [50] and Clarke [28] focussed on accurate preparation of the soil bed. Test–to–test variance of load output was reduced to between 0.5%–6% depending on the PSD of the geotechnical material. With the ability to attain clear trends in the data, Clarke was able to perform a parameter study of 70 tests in granular soils, the findings of which were published in [25, 27, 28] and are reported on in detail in Section 2.8.

Pickering et al. [49] performed tests on buried charges with a FAM using deformable and rigid targets. For both target types explosive mass, burial depth and stand–off distance were varied to assess the effect on impulse. The test bed was made up of dry graded concreting sand. PE–4 cylindrical charges were placed on a steel plate and initiated at its base via a hole in the steel plate. Impulse was calculated from maximum jump height recorded by four marker pens tracing transient movement of the FAM.

Explosive mass was varied between 7 g, 14 g and 21 g of PE–4. For the rigid target increasing the charge mass from 7 g to 14 g led to an impulse increase of 40%. An increase of charge mass from 7 g to 21 g increased impulse by 60%. Total impulse at each charge mass was higher for the deformable targets than the rigid plate. The higher impulse seen in the deforming target may be due to geometric changes of the target surface leading to increased loading duration and therefore a higher total impulse.

Charges were buried at a depth of 0 mm (on the surface) up to 70 mm. 5 mm increments in burial depth were used between 0 and 20 mm and increments of 10 mm were used thereafter. All charge masses followed the trend of increasing impulse with increasing depth of burial. Target deflection did not continually increase with burial depth. For all charges between 0 mm and 10 mm burial depth there was a sharp increase in target deflection. Between 10 mm and 20 mm burial, there was a more gradual reduction in deflection with a linear drop–off thereafter. Whilst no explanation is offered by Pickering et al. one hypothesis for this may be that as burial depth increases the confinement of detonation products increases, due to a higher mass of soil above the charge. The additional soil confines the detonation products for longer, increasing global impulse while reducing the peak pressure. The FAM is sensitive to impulse and the deformable target plate is sensitive to pressure. This would allow a higher impulse recorded by the FAM but less deflection of the target. This indicates that as burial depth

increases, global response of a structure begins to dominate rather than localised structural response. As depth of burial increases an increase in late time ejecta is also seen which may indicate that late–time ejecta contributes less to localised structural response.

Pickering et al. [58] used the FAM approach from [49] furthering the study on burial depth and stand–off. A steel plate was placed at the bottom of the sand container. As burial depth was increased, the distance between the charge and the plate was decreased. It was found that charges placed on the steel plate significantly increased impulse transfer to the target when compared to charges buried at the same standoff distance and larger height of burst. This highlights the importance of controlling boundary conditions to remove the influence of the soil container on the output from a shallow buried explosive.

Impulse distribution by free acceleration

Westine et al. [59] conducted 12 shallow buried charge tests in dry sand to investigate momentum transfer to steel armour. The testing aimed to derive functions to predict deformation of a tank floor plate from a cylindrical explosive where the charge mass, burial depth and standoff were varied. Nine impulse plugs were loosely placed in the target along its central axis. Motion of the impulse plug velocity was captured by a high speed video camera. Discrete measurement of impulse was calculated from impulse plug motion post–detonation.

It was observed that impulse is uniformly distributed above the charge but momentum transfer rapidly drops off once outside the charge diameter. Westine argues that for dry sand, loading from a shallow buried charge is impulsive because of the momentum in detonation products and ejecta. The loading is dominated by these inertial effects of the soil and therefore the dominant dry soil property is density. Because of this it is suggested that shock speed in the soil and therefore the compressibility of the soil has a second–order effect.

Joynt's [60] experimental work investigated the spatial distribution of loading on the face of a target following the detonation of a shallow buried explosive by using two steel concentric rings fitted around a central disk. Each section was equal in mass and supported above a buried charge. These tests illustrate the effect of moisture content. In all saturation states tested the distribution of load was focused above the centre of detonation.

Fourney et al. [61] used a similar impulse plug technique as developed by Westine et al. [59]. Tests were undertaken on v–shaped hulls using approximately 1/10th scaling to STANAG AP 55 [8] level M2. The effect of moisture content on load distribution across a target was investigated. Impulse plugs, seen in Figure 2.19, were placed into the target plate and the motion of the plugs post detonation was used to determine the total impulse applied at discrete points on the target. The results of the test are shown in Figure 2.20. The momentum delivered to

the target is highest directly above the charge. As the radial distance from the centre of the charge increased, impulse captured by the plugs decreased.

Figure 2.19: V–shaped hull with impulse plugs [61][3].

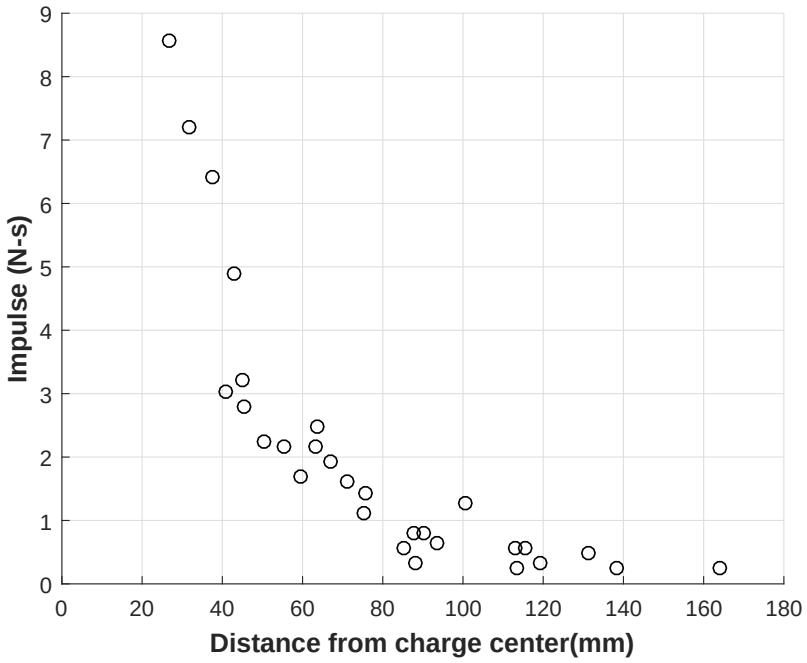

Figure 2.20: Specific impulse vs distance from the charge to impulse plug location for a v–shaped target, adapted from [61].

[3] Reprinted from Proceedings of the IMPLAST 2010 Conference, October 2010, W.L. Fourney, H.U. Leiste, A. Hauch, D. Jung, Distribution of Specific Impulse on Vehicles Subjected to IED's, Page 6, 2010, with permission from the Society for Experimental Mechanics.

Pressure measurement using Hopkinson Pressure Bars

Studies characterising high dynamic loading from impact and blast loads [35, 62] have been conducted on Hopkinson Pressure Bars since their development by Bertram Hopkinson over a century ago [34]. However, until recently it has not been used in buried blast characterisation [36, 63, 64].

Taylor et al. [36] acknowledged the difficulty of measuring pressure at the interface of a target following the detonation of a shallow buried charge due to test–to–test repeatability and lack of symmetry of the detonation products. Work conducted by Taylor et al. [36, 63] has used HPBs to measure the load on a plane above the soil surface following the detonation of a shallow–buried charge. In these works an effectively rigid plate was placed above and parallel to the soil bed surface. An approximate scale factor of 1/10th to STANAG AP 55 [8] level M2 was used throughout the test series.

Analysis of the work published by Taylor et al. confirms the presence of several key features illustrated in the indicative pressure time history in Figure 2.21, including (a) an initial pre–cursor load; (b) a very high magnitude, short duration "shock" pressure; (c) a post–peak plateau with a rapid fall off to low magnitude and finally (d) a long duration very low magnitude pressure.

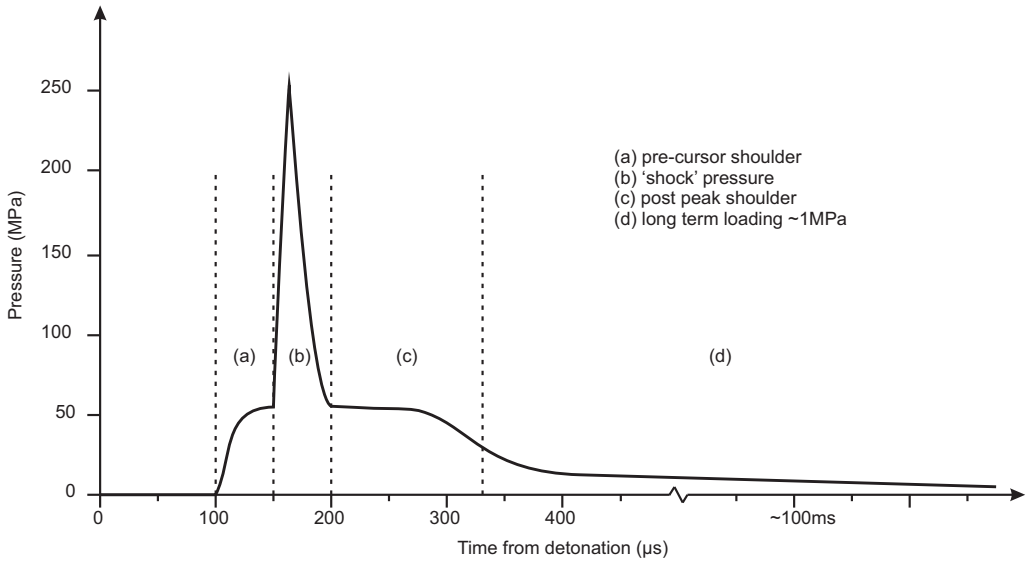

Figure 2.21: Indicative pressure time history (durations will dependent on explosive scaling)

Two loading components were identified by Taylor et al. [36], namely the soil cap over the explosive hitting the target and material from the crater hitting the target as the crater is being excavated. It appears these were identified from high speed video (HSV) and not identified

by the author from features on the pressure–time history. These two features described by Taylor et al. [36] loosely appear to coincide with phases two and three described by Bergeron [11] (as described in Section 2.7.2). This work successfully demonstrates the use of HPBs for measurement of the spatial and temporal loading distribution from shallow buried explosives.

This work is important as it outlines a method where pressure–time histories can be recorded reliably as the instrumentation is robust enough to withstand particle bombardment and high pressures but sensitive enough to capture the significant lower pressure loading features. An outline of some basic trends were shown to agree with the work of Bergeron [11]. However some key limitations of the work are not addressed by the author. Explosive material and length scales are not addressed. At the experimental scale used in these tests the explosive thickness is low and is likely to lead to unstable detonation of high explosive. Therefore secondary explosives were blended with Pentaerythritol tetranitrate (PETN) and a number of detonators to create the charge meaning that the explosive is difficult to characterise in terms of energetics and directionality. Furthermore, geotechnical materials were not scaled. The relative scale of the soil particles would equate to cobbles several hundred millimetres in diameter when expressed at full scale. Equally, the voids between soil particles are not scaled and so compaction of the particles may not scale. Burial depth was in the sub millimetre range which equates to a layer of several sand particles above the charge. At larger scales it has been shown the inertial response of the soil above the charge was a significant factor to detonation product confinement [11, 31, 58].

There are further issues with the application of the instrumentation. Loading pressure is in the region of several hundred kPa and will undoubtedly affect pressure accuracy due to strain–gauge resolution when attached to a steel HPB. Low pressure, short duration features that may indicate important mechanisms would be obscured by the high signal–to–noise ratio. Furthermore, pressure waveforms were typically smoothed with a 20–point average, which could lead to further reduction of resolution in the lower–pressure data.

Tyas used HPBs in a short test series at full scale which was intended to demonstrate the applicability of HPBs to the measurement of buried blast load [64]. The output from this test series successfully demonstrates the use of 5.85 m long 50 mm diameter HPBs for measuring shallow buried blast output at large scales. In his conclusion, Tyas makes suggestions to improve the quality of the pressure–waveforms by reducing the diameter of the HPB to increase signal bandwidth and, due to the load duration, shorten the HPBs to several meters in length.

Confinement of the detonation products

Fourney et al. [57] designed an experimental series focused on determining the contribution of air blast and soil ejecta components of the buried blast loading. Confinement was used to

quantify the level of impulse contributed by detonation products in free air and the contribution of soil–detonation–product ejecta. Confinement was achieved by placing a steel cylinder around the charge and placing the target plate on top of the cylinder. A steel plate was placed below the charge to support the cylinder in free air tests. In two buried charge tests a steel plate supported the cylinder and the charge was placed on the plate. The test configurations are illustrated in Figures 2.22a and 2.22b.

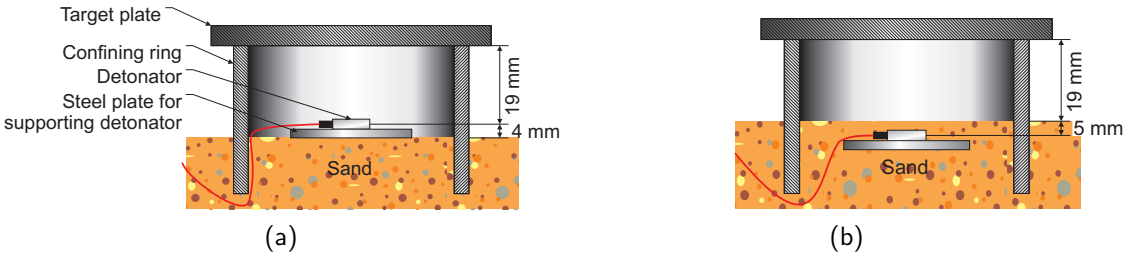

Figure 2.22: The test general arrangement from the experimental series [57]; (a) confinement in air with charge on placed on steel plate supported by dry sand, (b) confinement in saturated soil with charge placed on steel plate.

Test configurations and measured impulse are available in Table 2.2. Tests A and B compare the effect of confinement for free–in–air detonation. A steel plate was placed on the sand surface below the charge in each test. When the charge was confined the detonation products were not permitted to move laterally. For the confined tests B the impulse was approximately 500% higher than unconfined test A.

Tests C–F compare the effect of confinement on a buried charge in saturated sand. For tests C and D, no steel plate underneath the charge was used. Test C was unconfined whilst test D was confined. The output from confined test D was 9.1 Ns and is approximately 7% higher than the impulse recorded in the unconfined test C at 8.5 Ns. This suggests that the detonation products may vent from the soil bubble prior to impact with the target in saturated soil, or that there was some shock interaction from the soil bubble surface with the column of confined air between the target and soil surface, although clearly the reduction in impulse due to the lack of confinement is significantly larger.

In tests E and F buried tests were repeated with a steel plate under the charge, whereby test E was unconfined and F confined. Both E and F produced the same impulse at 10.6 Ns. This suggests that the introduction of the plate under the charge has a large influence in the focus of detonation products upwards towards the target as observed by Pickering et al. [58]. The effect of the introduction of the steel plate means that charge confinement now appears to be a second–order effect and has introduced a mechanism quantified by the author as a 20% increase in impulse at the target for buried tests [57].

The authors then compared the results of the confined above surface test B and below surface test D. It was determined that detonation products can only account for one third of the impulse delivered to target from the buried explosive in this comparison. However the author does not address the different dimensionality of scenarios B and D. In B the detonation products are directed upwards toward the target due to the steel plate and confining ring creating a one–dimensional shock tube problem. In test D only the detonation products and soil ejected from the soil will strike the target and significant shock will transmit into the surrounding geotechncial material i.e. representing a three–dimensional problem.

When comparing tests D and F, it can be seen that approximately 15% of the impulse appears to have been attenuated by doing work on the soil below the detonation. In buried confined tests some possible venting of detonation products or shock of the confined column of air between the target and deforming soil surface was witnessed. The small increase in impulse of 7% between the unconfined test C and confined test D shows that saturated soil provides good confinement of the detonation products. Two tests in this experimental series were geometrically similar, test A and E. From these tests it can be determined that impulse at the target was 70% lower in free air was than from a similar buried test E.

Table 2.2: Test matrix outlined in confinement work by Fourney [57].

Test ID	Charge location	Plate under charge	Confinement ring used	Impulse (Ns)
A	Soil surface	Y	N	3.2
B	Soil surface	Y	Y	16.2
C	Buried	N	N	8.5
D	Buried	N	Y	9.1
E	Buried	Y	N	10.6
F	Buried	Y	Y	10.6

2.7.3 Peak and residual target deformation and digital image correlation

Target deformation has been used as a tool by researchers to study buried blast loading [43, 48, 65–67]. More recently authors have applied spatial and time resolved deformation data captured with Digital Image Correlation (DIC) to estimate plate strain and thereby calculate acceleration and velocity of the target. The application of DIC to blast events in general is challenging because of shock transmitting through the camera support system. Further, light generated by the reacting detonation products and ejecta debris can obscure the camera.

Neuberger et al. [43] used experimental peak dynamic deformation taken at intervals along a circular clamped target following a detonation event to validate a coupled Arbitrary Lagrangian–

Eulerian model using the LS–DYNA solver. The soil material model used in the numerical work was taken from available literature and used a modified Mohr–Coulomb model where maximum yield stress was limited. The rolled homogeneous armoured steel material model, described in a previous paper [42], used the Johnson–Cook constitutive model with the material properties gained from open literature. The TNT explosive was modelled via the Jones–Wilkins–Lee (JWL) equation of state for explosive detonation products where the equation of state (EOS) variables were again acquired from open literature.

Neuberger et al. state that after the numerical model was produced, the soil model was calibrated such that further simulations matched the experimental results. However is not possible to assess whether the soil, target or explosives model or combination of models were capturing the correct physics. As only central peak dynamic deformation was recorded, a single data point was available for validation of all phenomena in the model. This provides low confidence in any phenomenological behaviour described in the numerical model described in this work.

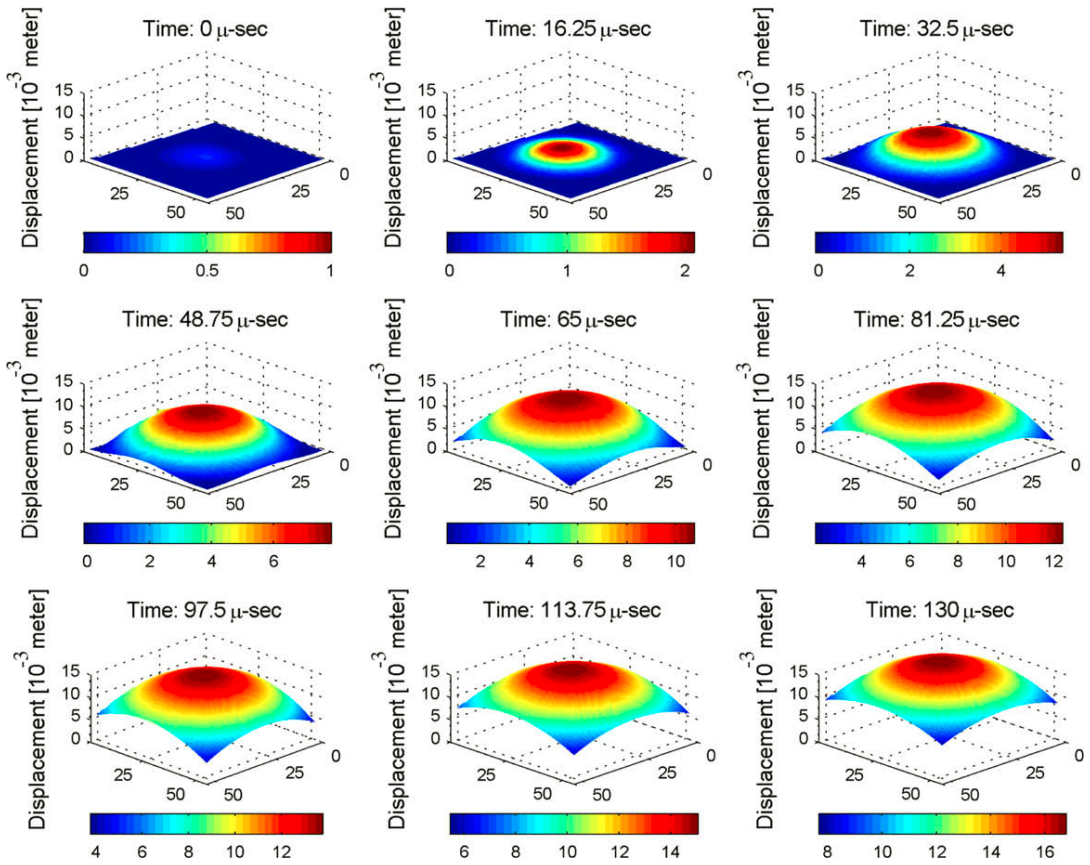

Figure 2.23: Plate displacement profiles – "Full–field transient sheet displacement profile of shallow (7.6 mm) buried test, representing the out–of–plane deformation in the initial part of the impact" [65][4].

[4] Reprinted from International Journal of Impact Engineering, Vol 36, V. Tiwari, M.A. Sutton, S.R. McNeill, S. Xu, X. Deng, W.L. Fourney, D. Bretall, Application of 3D image correlation for full-field transient plate deformation measurements during blast loading, Page 867, 2009, with permission from Elsevier.

Work conducted by Tiwari et al. [65] has resolved the visual obstruction by the use of small charges to approximately a 1/10th scale to STANAG level M2 [8]. An aluminium square target clamped into a steel frame was supported 28.7 mm above the soil surface. The explosive charge was buried at a burial depth between 7.6mm – 25.4 mm. Two high speed video cameras acquired images of the rear face of the targets for DIC analysis. The soil bed was saturated for all tests.

A sample of the deformation profiles from the 7.6 mm depth of burial (DOB) test are presented in Figure 2.23. It can be seen that between 0 μs – 16.25 μs deformation of the target plate is highly localised decreasing rapidly to the target's periphery. Thereafter a full response of the target is mobilised. The early deformation profiles indicate that early time loading is focused above the detonation.

Corresponding acceleration profiles of the deforming targets are available in Figure 2.24. The acceleration profiles show that at 16.25 μs acceleration of the target is localised above the detonation point. At 32.5 μs and up to 65 μs rings of peak acceleration can be seen to spread out from the detonation centre propagating radially to the edge of the target.

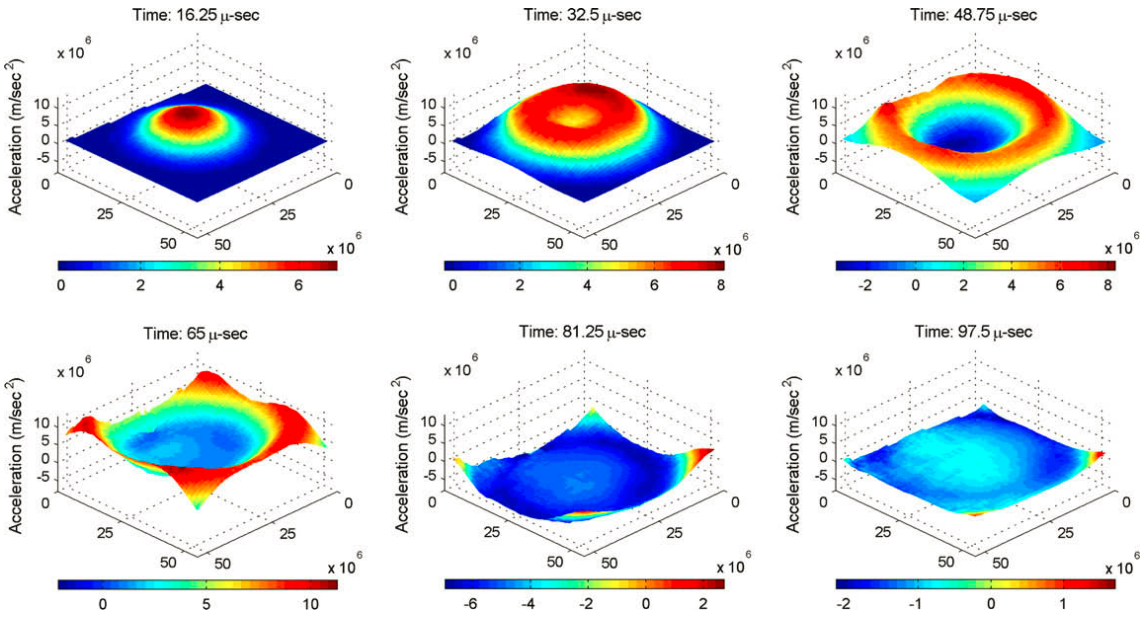

Figure 2.24: Plate acceleration profiles – "Full–field transient out–of–plane acceleration profile for shallow DOB = 7.6 mm" [65][5].

The deformation profile of the target shown in Figure 2.23 illustrates in the early stages of a shallow buried detonation that loading and therefore target response is focused at a point above the charge centre. The acceleration profiles in Figure 2.24 indicate that between 16.25 μs and

[5] Reprinted from International Journal of Impact Engineering, Vol 36, V. Tiwari, M.A. Sutton, S.R. McNeill, S. Xu, X. Deng, W.L. Fourney, D. Bretall, Application of 3D image correlation for full-field transient plate deformation measurements during blast loading, Page 867, 2009, with permission from Elsevier.

32.5 μs a ring of loading spreads across the target from the target's centre to the edge of the target. This agrees with the loading behaviour from shallow buried charges witnessed by Westine [59], Joynt [60] and Fourney [61].

Comparing the estimated deformation and acceleration time–histories it is apparent that target deformation occurs over a longer period than the loading. Target loading appears to be complete between 66.0 μs and 81.25 μs, however target deformation continues beyond 130 μs – approximately twice the time that the target is loaded for. In comparison to the impulse plug and ring experiments of Westine, Joint and Fourney [59–61], full field analysis from DIC showed significant variability in the spatial distribution of strain and accelerations of the target. It is suggested that this transient variation across a number of spatial locations is due to 'sand fingers' and contributes significantly to measurement variation.

Xu et al. [48] used an inverse model approach to identify time–resolved pressure applied to a circular target from a buried detonation. Time and spatially–resolved target deformation data was acquired with DIC for circular aluminium plates subject to a buried blast load. The inverse model in essence estimates distributed blast loading at discrete time steps by applying a pressure distribution to the target and then calculating the deformation profile of the target. When experimentally measured and computed target deformation profiles converge the model proceeds to the next time step.

The inverse model produced by Xu et al. was shown to adequately predict time–resolved loading features from a detonation in water, however no further validation was undertaken for buried charges to which the inverse model was to be applied. Further to this, a Gaussian pressure distribution was assumed in the forward model to estimate plate loading. The simplified stochastic pressure–history profile generated by the inverse model may provide reasonable general estimations of the loading event but does not explicitly describe the actual loading event. For this reason the combination of DIC and pressure–deformation analysis used as the basis for the inverse model approach cannot provide information on the mechanisms of momentum transfer from buried detonations.

Sutton et al. [66] used DIC to investigate the scaling of target deformation following the detonation of a shallow buried charge. Similar to like the work of Tiwari et al. [65]. Sutton overcame the difficulties in using DIC in a blast event by using very small scale experiments estimated between 1/10 and 1/16th scale to STANAG level M2 [8]. Further details of the experimental set–up were not provided.

The testing compared the time resolved deformation of a 'large' 432 mm and 'small' 277 mm target plate following detonation. Post–test, the large target deformation profile was scaled to the dimensions of the small target. Sutton found that there is good agreement during

early time deformation when the target is deforming elastically. However, during later time deformation when deformation becomes plastic, moderate agreement between the scaled large target deformation profile and small target experimental deformation profile was achieved.

Tyler–Street et al. [67] used the DIC approach to validate LS–DYNA models of target deformation following a detonation. The explosive charge used in the experimental work was scaled to STANAG level 2 and buried in sandy gravel or placed in a steel mine pot as specified in NATO STANAG AP 55 [8]. The Toegepast Natuurwetenschappelijk Onderzoek (TNO) mines test apparatus consists of a heavy steel box in which DIC instrumentation is fixed so that high–speed video images of deformation from the rear face of the target can be acquired. The centre of the test apparatus and target plate are aligned parallel to the soil surface and co–axial with the charge centre [67]. User–defined loading models from experimental data acquired during this study and Arbitrary Lagrangian Eularian (ALE) numerical simulations where used to develop load input to the model.

The loading estimated from the time-resolved deformation profiles gained from experimental work was able to predict different loading profiles for each of the charge conditions – an explosive buried in sandy gravel, and an explosive placed in a steel mine pot. However the loading applied to the target in the numerical work is defined as a triangular pulse where the user defines a peak pressure value and duration. Clearly this does not accurately describe the complex spatial and temporal load distributions witnessed by other authors, meaning that for each condition and target geometry experimental work will need to be conducted.

Stored gas and mechanically driven soil to simulate shallow buried charges

As an alternative to small–scale blast experiments, researchers have developed techniques to emulate explosive events. The shallow buried 'blast–loading' is simulated by driving a mass of sand supported above stored gas so that soil is ejected from the soil bed following diaphragm failure [68, 69], or by mechanically driving a column of sand [70].

The application of stored gas for simulation of buried blast oversimplifies the problem by ignoring the air–shock and geometrical and thermal aspects of the loading. Perhaps most critically the work of Hinz [68], McShane et al. [69] and Park et al. [70] focuses only on the sand throw as the mechanism for impulse transfer. This is compounded by the measured velocity of the soil bed being several orders of magnitude lower than reported by other authors – 10's m/s rather than approximately 2000 m/s as reported by Joynt et al. [7]. The relatively low particle velocity recorded by the authors indicates that particle momentum and, consequently, particle strain were significantly lower than that for an event using explosives. Therefore, mechanical response of the soil, such as particle interlock and crushing, which is expected at high strain rates, will not have occurred, thus significantly limiting the validity of this technique.

It was shown by Bergeron et al. [11] that a substantial amount of the explosive energy from a shallow buried charge is transferred in dynamic pressure and that early soil–explosive interaction is fundamental to the development of the blast loading. This is in conflict with the assumptions made in sand column impact tests. It is for this reason that pressure–time histories from soil impact experiments performed by Hinz et al. [68], McShane et al. [69] and Park et al. [70] are fundamentally different to coupled detonation product–ejecta loading from a shallow buried charge.

2.7.4 Barr et al. – Geotechnical behaviour at high strain rates

Barr et al. have produced significant work characterising the behaviour of sandy soils when subject to high strain rates [71–73]. The work aimed to understand the behaviour of sandy soils by varying particle size and moisture content. Three sandy soils were used across the work: a sandy loam with wide particle–size–distribution, a quartz sand of a medium grain structure and a quartz sand of coarse grain structure.

Moisture contents between 0.0% and 15.0% were sampled at 2.5% intervals – 7 moisture contents with 3 repeat tests at each moisture content. Testing was conducted in uni–axial compression with split Hopkinson Pressure Bars (SHPBs) and a confining ring placed around the sample to recorded radial stress [72]. Axial stress in the order of 200 MPa at peak strains between 3000 s^{-1} and 5200 s^{-1} were achieved [73].

For moisture contents between 0 and 7.5% specimens remained partially saturated throughout the HPB impact. An increase in moisture content of the soil had two clear effects; soil stiffness decreased and particle breakage increased [73]. The reduction in stiffness was attributed to a reduction in inter–particle friction which aids rolling and sliding of the particles leading to compaction of the sand. It was reported that the larger strains achieved at higher moisture contents were due to reduced inter–particle friction resulting in more energy being available for compaction and therefore particle breakage. This increase in particle breakage further increases strain on the material as the ability of the soil to compact is aided by the improved particle grading.

For moisture contents between 10.0% and 15.0% [73] the test sample will reach full saturation during impact. It is noted that before the test specimens reached full saturation, the behaviour of samples between 10–15% sample was very similar to the 7.5% sample. However when reaching full saturation, the increase in stiffness witnessed corresponded closely to the equation of state for water. The significance of this is that further strain on the material is dominated by compression of the pore water and further increases in stress are supported by the hydrostatic stress in the pore water.

Barr et al. [73] discussed the importance of the hydrostatic loading component when a sample reaches full saturation. As a sample is compressed and saturation is achieved through a reducing void volume the soil particles change from being loaded via particle–to–particle contact to being significantly loaded by a hydrostatic component from the surrounding pore water. This significantly decreases the deviatoric stress and particle breakage becomes less probable. Consequently, particle breakage occurs prior to the soil reaching full saturation. For higher moisture content soils, full saturation occurs at lower stresses.

The dynamic experiments have shown that there is a significant influence of inertial radial confinement on the behaviour of the soil when subject to a high strain rates [71]. In quasi–static testing the initial Poisson's ratio of a sample approached 0.5. However in the SHPB tests the Poisson's ratio increased from zero to 0.22 for dry–sand tests. At moisture contents of 2.5% and 5.0% the Poisson's ratio remained at zero for longer increasing to a maximum of 0.16. The reduction in Poisson's ratio suggests an apparent stiffening of the sand is due to inertial confinement rather than strain rate dependencies. The apparent increase in stiffness of the material can be explained by considering the radial stress of the sample and apparent reduction in Poisson's ratio [71]. At the strain rate investigated the axial component of the material is subject to high stresses. However the radial stresses must be released by an inward travelling shock wave from the sample's periphery to its centre before the stress can be fully redistributed around the sample. The radial inertial confinement the sample is subject to during high strain–rate events indicates that the apparent increase in axial stiffness is not a true strain–rate effect, but a transient event which will occur for the duration of the release wave between the radial surface to the samples centre and not the full impact event.

2.7.5 Contributions to the understanding from numerical analysis

Based on numerical simulations, Grujicic et al. [74] proposed that the difference between partially and fully saturated sand pressure waveforms is due to a fundamental difference in loading mechanism. Grujicic defines two clear mechanisms, 'shock–type' and 'annulus–type', which are defined as follows:

- *Shock–type loading*: Dry sands have a lower cohesive strength and less ejected volume making up the soil annulus. The annulus ruptures relatively early, allowing the detonation products to escape and impact the target. The loading therefore mainly comprises an air shock load from the detonation products with reduced momentum imparted to the soil. Furthermore, rupture of the soil bubble allows the detonation products to vent in the radial direction, reducing the directionality of the event, see Figure 2.25a.
- *Annulus–type loading*: Saturated sand has a lower compressibility and higher cohesive strength, resulting in a larger volume of soil ejecta and delayed annulus rupture. This annulus confines the detonation products completely until it impacts the target, and the loading is mainly comprised of momentum transfer from the soil, Figure 2.25b.

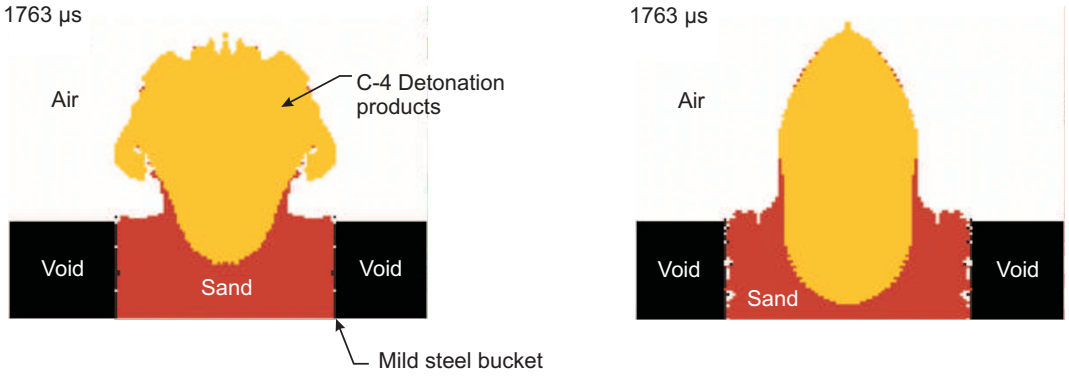

(a) (b)

Figure 2.25: Diagrams taken from the numerical output from work performed by Grujicic showing (a) "temporal evolution of material deformation during landmine detonation in the case for dry sand.", (b) "temporal evolution of material deformation during landmine detonation in the case of fully saturated sand." Grujicic et al. [75][6].

2.7.6 Fox et al. – Modelling of detonation in soil

Fox et al. conducted a body of numerical work [76–79] investigating the effect of changing soil parameters following the detonation of an approximately $1/10^{th}$ scale shallow buried charge to STANAG level M2 [8]. Motivation for this work was due to computational analysis and experimental work being divided in its approach and failing to provide a satisfactory description of a shallow buried detonation. Extensive work in the field focuses on the behaviour of water, air and explosives as primary loading mechanisms but neglects the relationship between momentum transfer and various soil conditions. Because of this, the mechanisms of momentum transfer from a shallow buried charge cannot be clearly explained [77]. Fox et al. [76] argue that the behaviour of shallow buried explosives is also not only a characteristic of the explosive but is also a function of the soil properties, in particular its moisture content.

Experimental and numerical work focused on the response of rigid plates to shallow buried explosive detonations [76]. The initial velocity of the target was measured using high–speed video and specific impulse was calculated from this velocity providing validation data for the numerical models. Numerical work was constructed with an arbitrary Lagrangian–Eulerian approach for fluids and soil coupled with a Lagrangian approach for the solid target [77]. The target was modelled as a rigid solid. The Detasheet C[7] explosives were modelled using the JWL equation of state. The air was modelled having Newtonian viscosity with an ideal gas

[6] Reprinted from Soil Dynamics and Earthquake Engineering, Vol 28, M. Grujicic, B. Pandurangan, R. Qiao, B.A. Cheeseman, W.N. Roy, R.R. Skaggs, R. Gupta, Parameterization of the porous-material model for sand with different levels of water saturation, Page 34, 2008, with permission from Elsevier.

[7] Detasheet C is a sheet explosive and contains rubberised–polymers in the binder such that the explosive maintains its from during handling. The high explosive is a combination of PETN, nitrocellulose and acetyltributylicitrate.

equation of state. The water was modelled as having Newtonian dynamic viscosity and Mie–Gruneisen equation of state with the fit by Steinberg [80].

To complete this body of work Fox et al. [79] conducted a numerical parameter study to investigate the mechanisms of momentum transfer for shallow buried charges. The work focused on the reasons of enhancement to a blast load with the addition of water and a reduction in air voids to the geo–matrix. Concrete sand constitutive models were used with air filled void volumes of 1% and 5%. It can be seen in Figure 2.26 that a reduction in void volume from 5% to 1% increases momentum transfer to the target by approximately 40% [76]. Void volume is dependent on either achieving total compaction of soil particles or filling the voids with water [77]. Therefore, Fox et al. have shown numerically that the effect of either compaction or saturation (both mechanisms reducing void volume) will increase the output from a shallow buried charge.

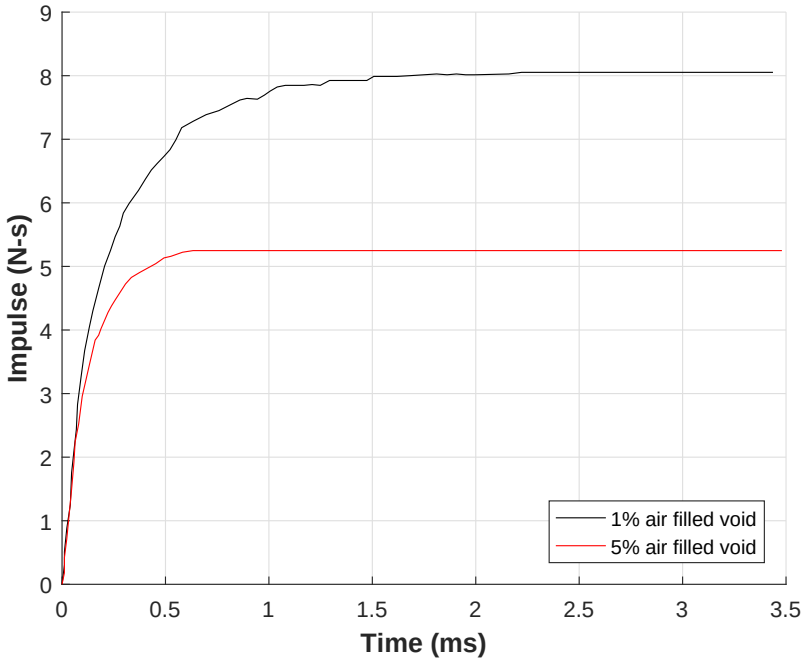

Figure 2.26: Computation of impulse–time histories from shallow buried charges comparing 1% and 5% air filled voids in concreting sand, adapted from [76].

Fox et al. [77] numerically derived the volumetric strain behaviour of three soils of different PSDs (poorly graded sand, clayey sand and silty sand) for a range of moisture contents. Moisture content was selected such that before loading was applied, the soil was wet but not saturated. When pressure was applied to the soil, it reached saturation, similar to the SHPB work of Barr et al. [71] discussed above. As the sample compresses the void volume reduces due to compaction of the soil particles resulting in a reduction in the soil's bulk volume and therefore reducing void volume. As void volume reduces, the pore water still at its original volume occupies a higher percentage of the void volume between the sand particles.

Figure 2.27 illustrates the bimodal behaviour of the three soils as the void volume reduces to zero [77]. At lower volumetric strain the soil is more compliant. At strains exceeding the point at which the void volume is compressed to zero the soil reaches saturation and becomes significantly stiffer. The level of strain at which this change in stiffness occurs is determined by the initial air–fill void content of the soil.

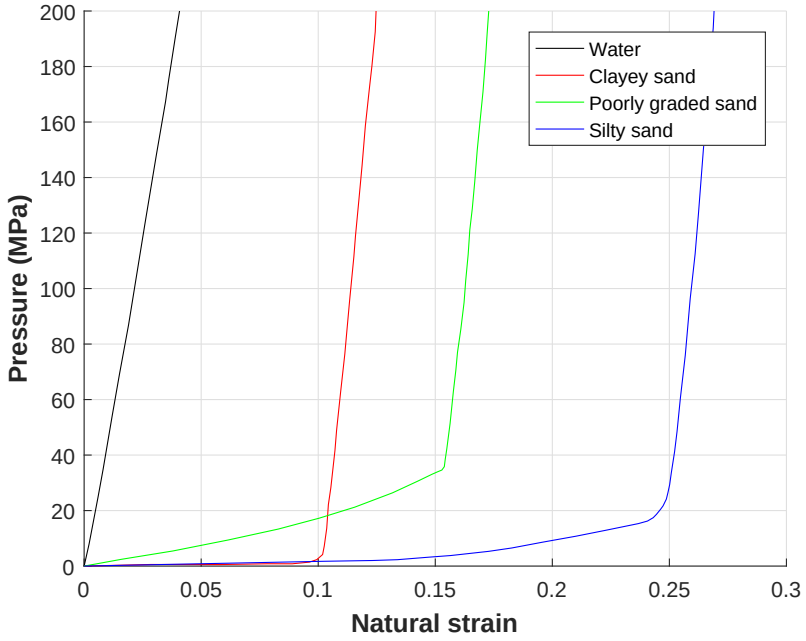

Figure 2.27: "Typical soil hydrostats for pressures up to 200 MPa. Example hydrostats are shown for water, clayey sand (9.6% air filled voids, 13.5% water content), poorly graded sand (14.2% air filled voids, 17.3% water content), and silty sand (21.9% air filled voids, 6.8% water content)", adapted from [77].

Fox et al. [77] noted that for partially saturated soils when pressures were below saturation pressure the strain and yield behaviour is similar to dry sand. At pressures above this, yield behaviour is defined by effective pressure (the pressure acting on the soil skeleton), and the remaining pressure is supported by water in the voids (hydrostatic pressure). An example of this is seen in Figure 2.27 for a poorly graded soil (cf. the green curve). Beyond 0.16 volumetric strain, a significant increase in pressure is required to achieve a small increase in strain. The change in behaviour is attributed to full compaction of the soil i.e. the air–filled voids are zero. In partially saturated soils this means that voids previously filled with water and air are now filled with water and crushed soil particles. Therefore the hydrostatic component of further increases in stress are supported primarily by water. Mechanically this means that for significant increases in total pressure there is a small increase in material strain.

It was observed in the numerical analyses that target momentum increased when less strain was required to reach the hydrostatic lock–up point [77]. This was achieved by using a lower initial void volume. When the hydrostatic lock–up point is reached the bulk modulus makes a significant jump and requires much higher pressures to change the soil volume. When the

hydrostatic lock–up point of a soil is reached, a soil becomes significantly stiffer and less compliant. Therefore more soil is ejected from the soil bed. This was confirmed in the small scale experiments that accompanied the numerical study, where for fully saturated soils, more material is ejected from the soil bed when compared to partially saturated soils.

When the hydrostatic lock–up point has been reached, further increases in the effective stress (the stress on the soil skeleton) happen at a lower rate. The change in effective stress behaviour can be seen on the yield surface for the partially saturated poorly graded soil in Figure 2.28 at a pressure of approximately 37.5 MPa. A consequence of this is that much higher pressures are required to increase the deviatoric stress on the soil particles. This results in much higher pressures being required to yield the material where the shearing or rolling of the soil particles as described by Barr [71] needed to achieve soil further compaction is less likely to occur resulting in lower particle breakage.

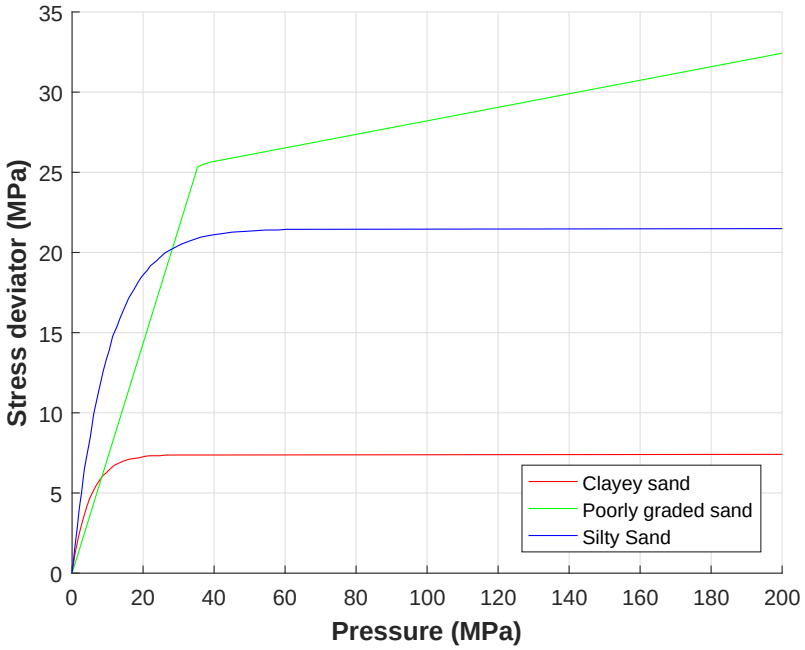

Figure 2.28: "Typical soil yield surfaces for pressures up to 200 MPa. Example yield surfaces are shown for poorly graded sand (14.2% air filled voids, 17.3% water content), and silty sand (21.9% air filled voids, 6.8% water content), and clayey sand (9.6% air filled voids, 13.5% water content)", adapted from [77].

The effect of moisture content on deviatoric yield strength was believed to be the most influential factor in the work performed by Fox et al. [76, 77, 79]. Soils with lower yield strengths imparted higher momentum to the target, whereas dry sand having the largest yield strength produced the lowest loading. Wet but unsaturated sand produced intermediate results and water which has no yield strength produced the largest transfer of momentum. Fox et al. [77] have shown numerically that an increased water content in the soil matrix leads to compaction of the soil being achieved at significantly lower strain. When full compaction is achieved,

hydrostatic stresses support further increases in stress in the soil meaning that significantly more pressure is required for small increases in strain.

2.8 Shallow buried blast experimental work undertaken at The University of Sheffield

Clarke et al. have conducted extensive experimental work investigating the momentum transfer from shallow buried charges using the FAM approach [25, 27–32]. The work was conducted with the aim of studying which geotechnical parameters influence the loading developed on a target surface following the detonation of shallow buried charges, and was performed at 1/2 scale to STANAG AEP–55 [8] level M2.

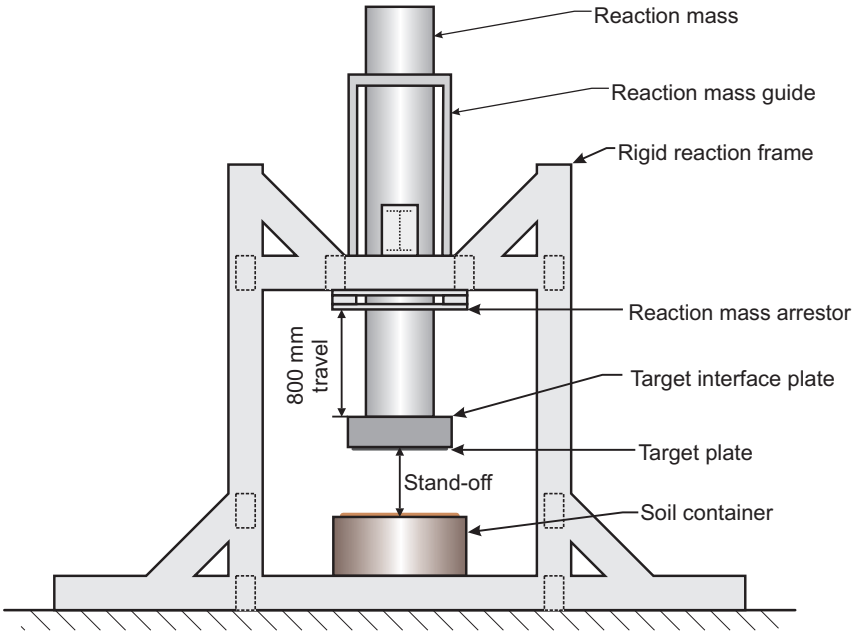

Figure 2.29: Free accelerating mass apparatus used by Clarke et al., adapted from [25][8].

The test appartus used in Clarke's work utilised a free accelerating mass constructed from a large steel frame from which a 1500 kg ballast mass and target interface plate were suspended [25], shown in Figure 2.29. The free flying mass was allowed to travel up to 800 mm vertically, following detonation of a shallow buried explosive, before the mass was arrested by gravity or by contact with rubber bushings fitted to an arrestor plate on the lower flange of the supporting frame. Upward movement of the mass was recorded using high speed video. Momentum transfer was calculated post–test using the ballast mass and maximum jump height to calculate the initial velocity. Steel targets were attached to the interface plate with wooden pegs

[8] Adapted from International Journal of Impact Engineering, Vol 86, S.D. Clarke, S.D. Fay, J.A. Warren, A. Tyas, J.J. Reay, R. Livesey, I. Elgy, Geotechnical causes for variations in output measure from shallow buried charges, Page 278, 2015, with permission from Elsevier.

to permit rotation of the target at the supports. The target plate measured 600 mm square on plan and spanned 500 mm between supports. Dynamic deformation was recorded using aluminium honeycomb crush block, and residual deformation was recorded post–test.

Soil was contained in 1000 mm diameter internal diameter 750 mm deep cylindrical steel bins [25]. Before water was added to the soil the moisture content was checked, and the required mass of water was calculated. Moisture was distributed evenly through the soil with a forced action pan mixer, when moisture visually appeared evenly distributed the moisture content of the soil was checked. Soil bins were filled in three lifts each of appropriate mass for the required bulk density. Compaction of each lift was achieved by placing a steel plate on the surface of the sand and placing a vibrating compactor on the plate until the correct density was reached. Very tight control was of the geotechnical soil bed was achieved with a tolerance on the moisture content of $\pm$ 0.1% and a tolerance on soil density of $\pm$5 kgm^{-3}.

The 0.625 kg PE4 cylindrical charge with 3:1 (diameter to height) aspect ratio was encased in a 3 mm PVC casing. The charges were buried with 50 mm of overburden. Care was taken not to disturb the soil surface during the burial of the charge. A cavity was excavated beneath a cylindrical form work which would allow soil removal below the form until it was undermined. When the soil under the form was undermined the form could be pushed lower into the hole; this was continued until the form top was flush with the soil surface. At this point the charge could be test fitted and adjustments made to align the charge at the correct depth $\pm$ 1 mm. The use of the formwork provides a defined geometry above the charge. Therefore the correct mass of overburden can be placed on top of the charge at the correct density.

The effect of moisture content

Tests conducted with saturated Leighton Buzzard sand 14/25 (LB) show that momentum transferred to a target is doubled when compared to the same detonation in dry sand [29]. Clarke et al. [25] conducted 12 experiments to investigate the effect of moisture content on momentum transfer from a shallow buried explosive in LB sand. Bulk density was kept constant at 1.6 Mg/m^3 throughout testing whilst moisture content was increased – as moisture content increases dry density decreased. Four moisture contents were tested, namely 0, 2.5, 5.0 and 7.5% .

An increase in moisture content of 7.5% led to an increase in impulse of 7% despite a constant bulk density. This indicates that density of a soil is not an indicator of the soil response to blast loading on its own but how the density is achieved i.e. compaction or moisture content have different effects. Clarke et al. [25] tentatively suggest a number of mechanisms that may explain why moisture content affects soil response from sub surface–detonations:

- Water has a greater confining effect than soil.

- Due to the lower density of water, the volume required to replace the same soil mass removed to achieve a constant bulk density will result in a net reduction in void volumes if soil mass is replaced with water mass.
- The relative stiffness of the confinement could be affecting momentum imparted to the target.

Clarke et al. [25] conclude that density alone is inadequate in predicting the momentum transfer from a shallow buried charge. They have shown that with tight control of the soil bed preparation and experimental set–up, it is possible to develop highly repeatable momentum transfer with variances of no more than $\pm$ 3%.

The effect of bulk density, dry density and void volume

Experiments were conducted to observe the interaction between density and moisture content [27,31]. In an initial series bulk density was kept constant and moisture content was increased. To achieve this, LB soil was used where the dry soil mass was replaced by adding water. It was shown that as moisture content increased impulse at the target increased with no change to the overall mass of the soil bed. A lower initial dry density can achieve saturation at lower bulk densities due to the volume of water being lower in mass than the equivalent volume of soil. It was therefore possible to achieve significantly higher impulse from low bulk density saturated soil than low moisture content high density soil.

Further work was conducted to assess the interaction between dry and bulk density [31]. LB soil was held at a constant dry density and bulk density was increased by adding the water to the soil. Moisture contents were varied from 0% to full saturation at 25%. A weak positive correlation was seen between bulk density and imparted impulse. However a much stronger correlation was seen between moisture content and imparted impulse.

An assessment of the relationship of air–voids and density was undertaken where dry density decreased with increased moisture content for a number of soils with different PSDs. To achieve this, soil mass was removed and water added keeping bulk density constant, enabling control of the air void volume in the soil [31]. A correlation was seen for increasing impulse with decreasing air–void volume. However, when the soil becomes fully saturated and air–voids become zero, moisture content has a much stronger correlation to the impulse generated which was attributed to different soils having different moisture contents at full saturation.

The effect of particle size distribution and scaling of soil particles

It was shown that for LB and Leighton Buzzard Fraction 25B Grit (LBF) soils that there was no significant change in impulse measured with variation in PSD for a given moisture content

[27, 28]. However, it is noted that the PSD in LBF sand is still quite narrow and wider PSDs may have a more significant effect. Greater variation in impulse was witnessed for the more well–graded soil LBF at all moisture contents tested with a maximum of 5% variance. This is in comparison to the 3% recorded in [25] with the single fraction LB. To ensure repeatability of experimental work, it was concluded that a single fraction soil should be used [28]. The most repeatable explosive tests were conducted with fully saturated LB 14/25 giving the most repeatable impulse and target deflections [30].

The half scaling of geotechnical materials was addressed by testing soils of two different soil grain sizes with a similar range of PSD. LB and 2LB are single fractions of Leighton buzzard sand where 2LB's particle sizes are approximately twice that of LB. This means that the particle geometries of LB at half scale are approximately the size of 2LB soil at full scale. This means that the effect of scaling of the particles can be assessed. It was shown that there is no clear difference in impulse from LB and 2LB tests meaning that at half scale no scaling of the particle is required.

2.9 Summary

This chapter has focused on the formation of a blast wave in free air and when subject to confinement. Geotechnical parameters of significant influence on buried detonation output have been highlighted and the behaviour of water particle impacts was discussed. Instrumentation suitable for the measurement of a blast wave was introduced and limitations of this method were noted.

Research in the subject area of shallow buried blast is extensive, yet the causes for variations in magnitudes and mechanisms of load transfer for a shallow buried charge remain unclear. This in part is due to experimental and numerical approaches not being unified in their approach. Experimental work in this field falls into three categories:

- Specific impulse measurements achieved through FAM – specific impulse measurements provide good evidence for geological parameter sensitivity to shallow buried charges but do not provide conclusive evidence for the mechanistic evolution of loading at the target.
- Direct pressure measurement – pressure data was collected, however insufficient coverage of the parameter space, inaccuracies in test sample preparation which impose a wide variation in results, or very small scale tests make it difficult to separate surrogate explosive characteristics from real phenomena.
- Simulated blast loading – the 'blast load' is simulated through a mechanically driven column of soil or bursting diaphragm negating the dynamic pressure. This is in conflict

with the findings of [11, 46] which have shown using pressure measurements that a significant body of loading from a shallow buried charge is due to dynamic pressure.

Numerical studies have shown promising lines of investigation, however as stated by Fox in 2014 there is a disconnect between numerical and physical testing, which leaves many numerically derived hypothesise unvalidated [76].

The most important part of the research in this area is to demonstrate how the coupled ejecta flow and detonation products contribute to target loading at a suitable scale. Therefore experimental work in this thesis will aim to combine successful aspects of previous experimental work to investigate the hypotheses of numerical work. It has been shown that pressure waveforms are key to a phenomenological study in this subject area. The HPB array technique was demonstrated to reliably acquire pressure waveforms from very small scale experiments and will be used in the experimental work in this thesis. Clarke [28] and Anderson [50] have shown that with careful sample preparation, test–to–test variance of total impulse can be reduced to five percent allowing strong correlation of momentum transfer between identical tests. The experimental work in this thesis will further develop the soil preparation techniques outlined by Clarke [30] to allow accurate preparation of the soil bed.

Bergeron's hypothesis for the mechanism of the pre–cursor shoulder will be investigated by variation of the charge geometry and geotechnical moisture content. Fox's [79] numerically derived hypothesis of hydrostatic loading dominating soil compaction behaviour in the initial stages of the soil response will be investigated by changing moisture content of the soil. Grujicic's [74] numerical work predicting 'shock–type' and 'annulus–type' formations depending on moisture content will be investigated. The insights of Rein's [26] high velocity fluid particle droplet impact will be considered when investigating the mechanisms of loading from high moisture content soils.

Through this literature review it was shown that, charge geometry, burial depth and standoff distance, soil type, soil density, void volume, particle size distribution and soil saturation all affect the output from a shallow buried charge. The mechanisms of loading from a shallow buried charge will be investigated through experimental work varying these parameters forming a fundamental study into the mechanisms and magnitudes of buried blast loading. Test apparatus will be developed at an appropriate scale allowing the experimental study to form a detailed and comprehensive parametric study aimed at developing a holistic and comprehensive understanding of blast loading based on well controlled scientific testing.

Chapter 3

Experimental design and commissioning tests

3.1 Introduction

This chapter outlines the design of the test apparatus and considers soil choice, soil preparation and explosive engineering design. The testing performed in this chapter verifies results from the test apparatus and continually refines test parameters until an optimum test configuration is chosen. The general structure of this chapter is outlined below:

- Test apparatus design.
- Geological material selection.
- Geological material preparation.
- Explosive engineering design: charge; charge placement; and alignment and transport.
- Commissioning and initial study tests.
  - Tests 1-6, free-air tests informing detonator use and providing comparison to ConWep [13] empirical predictions.
  - Tests 7-18, shallow buried charge tests investigating detonator initiation and orientation.
  - Tests 19-28 quantifying the spatial resolution of the HPB array.
  - Tests 29-34 investigating the effect of the boundary of the soil container on the pressure waveform.
  - Tests 35-40 outlining the effect of HPB dispersion.

3.2 Test apparatus design

The first decision to be made regarding the experimental setup was the scale at which to conduct the experiment. To remove environmental factors one requirement of the experimental programme was that it should be conducted under cover, in a partially buried concrete structure. Budget and project duration constraints required that the experiment should be conducted at as small a scale as possible whilst allowing suitable geotechnical material and explosive engineering scaling.

The NATO standard for buried charge testing (STANAG level M2 [8]) specifies a burial depth of 100 mm in full scale tests. With very shallow depths less than 20 mm, the soil overburden becomes difficult to accurately prepare. To allow for tight control over the soil bed preparation and to be compatible with the explosives engineering implications, 1/4 scale tests have been opted for. This lowers the amount of material required in each test (the size of the soil container is directly proportional to scale) while giving a controllable burial depth (25 mm). At full scale, the charge is described as a 6 kg TNT cylinder with a 3:1 ratio of width to depth [8]. The 1/4 scale charge used in these tests is discussed in Section 3.5.

Work conducted by Taylor et al. [36,63] observed the presence of several key features illustrated in the indicative pressure time history in Figure 3.1:

(a) An initial pre-cursor load.

(b) High magnitude, short duration "shock" pressure.

(c) Post-peak plateau followed by a rapid decay in pressure.

(d) Long duration, very low magnitude pressure.

With reference to Figure 3.1 it is apparent that any instrumentation scheme must be robust to endure pressures exceeding several hundred MPa in an environment of air shock and particulate impact: areas (a) and (b). The transition between areas (a) and (b) requires sufficient instrument time resolution to identify changes in load over the microsecond range. The instrumentation must also be sensitive enough to measure low magnitude pressure: area (d). The instrumentation must be capable of measuring pressures in these ranges for several hundred milliseconds to capture the whole event. This is an extremely onerous set of requirements for a single instrumentation type.

Hopkinson Pressure Bars have a proven ability to record high magnitude load pulse at high temporal resolution [34,36]. High bandwidth can be achieved with a sufficiently small diameter bar and spatial resolution can be achieved when HPBs are placed close together in an array. For these reasons HPBs were selected for use in this study.

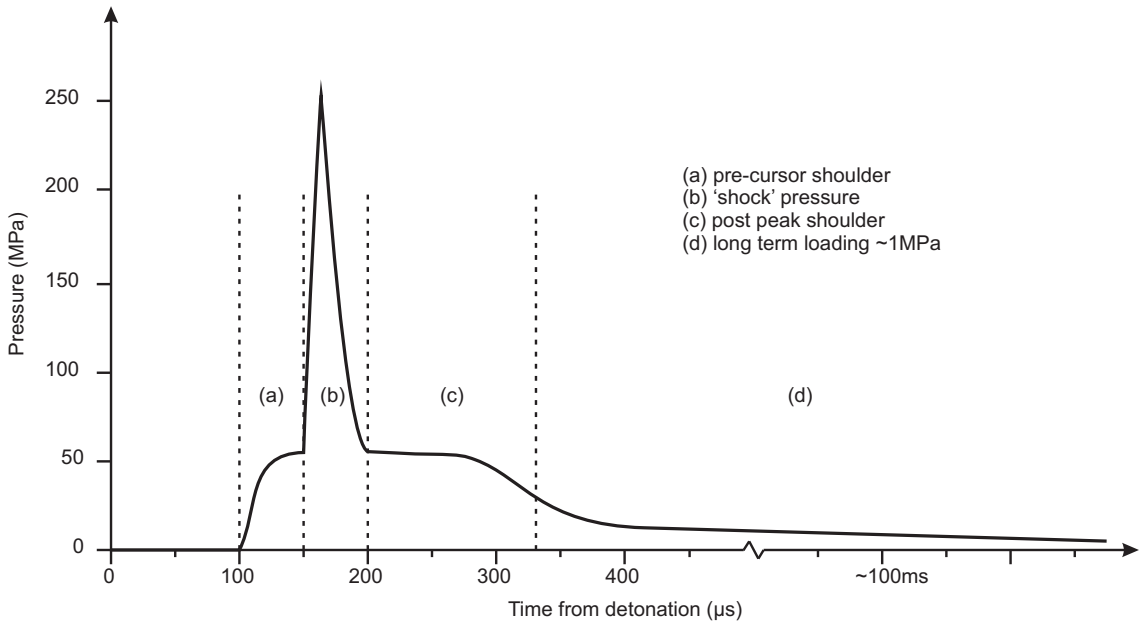

Figure 3.1: Indicative pressure waveform from shallow buried charge.

As the instrumentation is selected, the infrastructure can be designed around the HPB array and an appropriate process of soil preparation and charge placement accurately aligned with the test apparatus can be developed.

3.2.1 Hopkinson pressure bar design

The HPB is a well-established approach for measuring moderately high magnitude, short duration transient loading pulses. The advantages of HPB are robustness and high load capacity. However, consideration must be given to the design of a suitable HPB scheme so that sufficient pulse duration and bandwidth of the pressure pulse is captured.

In Figure 3.1 it can be seen that longer duration low magnitude loading continues into the mid or possibly high hundreds of microseconds (depending on geological condition of the soil bed) requiring a record duration of approximately 1.0 ms to ensure that the whole loading event is captured. The load duration that can be recorded using a HPB is limited by the time taken for the elastic stress pulse to reach the distal end of the bar and return to the strain gauge station close to the loaded face of the bar. After this time, the strain gauge station records a superposition of any still-incoming load and reflections of the earlier stages of the loading pulse. Due to existing infrastructure in which the instrumentation would be housed the maximum practical HPBs length was 3.25 m. With the strain gauge station located 250 mm from the loaded face of the bar, allowing for a thick target plate, the record length of the HPB can be calculated by dividing the bar length between gauge stations by the wave speed of the bar material.

The equation for calculating wave speed is shown in equation 3.1 where C is the wave speed (ms^{-1}), E is the elastic modulus (n/m^2) and ρ is the mass density (kgm^{-3}). A length of 3 m from the gauge to the distal end of the bar gives a recording duration of 1.0 ms[1].

$$C = \sqrt{\frac{E}{\rho}} \tag{3.1}$$

A more problematic issue in HPB use is that propagating waves in a HPB experience dispersion due to the fact that the propagation velocity in the bar is a function of the frequency of each Fourier component of the loading [39]. As a recording station on the bar is typically several bar diameters from the loaded face of the bar (in this case the strain gauge station exceeds this to enable the strain gauge station to be positioned above the steel target plate and thus be protected from the air shock/particle barrage loading) dispersion may mean that the recorded signal differs significantly from the actual load applied to the bar face. The practical effects of dispersion are that loading features with timescales of the order of a few microseconds are difficult to determine from the dispersed loading record, and the dispersed signal typically displays several characteristic forms of oscillation, due to the phase shift in the Fourier components. Whilst it is possible in principle to correct for dispersion effects, using frequency domain phase-shift methods developed in the 1980s [81, 82], Tyas [62, 83] demonstrated that there is currently a practical upper bound to the frequency range over which these can be applied, limiting the bandwidth of a steel HPB to around $1250/r$ kHz[2], where r is the bar radius in mm. There is thus a benefit to using bars of as small a radius as practically possible. In the current work, a radius of 5 mm was chosen, giving an effective bandwidth of 250 kHz.

HPB dispersion will be demonstrated experimentally with the use of two strain gauge stations on the bar at intervals of 250 mm from the loaded face and will be discussed in Section 3.6.5.

An array of HPBs will be used to obtain the pressures at multiple locations at any given time. The degree of spatial variance of pressure is unknown, hence the target plate will be pre-drilled with a hole arrangement to allow variations in the spacings of the HPB array at 25 mm intervals allowing space for both multiple bars and cable umbilicals. The bars fit to the holes with a 0.25 mm tolerance preventing coupling of the bars with any deformation and flexure of the target plate. The bottom end of the HPBs lies flush with the blast face of the target plate and so HPBs must be supported by some means. A receiver frame attached to the main reaction frame serves two functions. Firstly, by supporting the bar by its distal end, the bar is free to displace vertically upwards during the loading period, coming to rest again on the receiver

[1] Taking twice the distance from the gauge to the end of the bar and dividing by the wave speed.

[2] The upper bandwidth limit on a steel HPB bandwidth for radius r was derived by Tyas et al. [62]. The maximum frequency component (r/L) where r is the bar radius and L is the wavelength was shown to be in the range of 0.25–0.30. The limiting bandwidth can be calculated as the maximum frequency component multiplied by the HPB wave speed C_0 divided by the bar radius i.e. $0.25C_0/r$. Conservatively for experimental HPB design, using a maximum frequency component of 0.25 and a wave speed C_0 of 5000 ms^{-1} the relationship of maximum bandwidth is shown to be $1250/r$.

frame post test reducing stress on the bar. Secondly, the distal bar ends will be threaded with a 10 mm diameter 1 mm pitch thread so that the HPBs can be accurately aligned flush with the target plate.

Prior to fabrication of the HPBs a comparison from commissioning testing indicated that foil strain gauges were prone to signal noise, possibly caused by ionisation from the detonation products. Semiconductor strain gauges were therefore used, with the benefit of increased output and reduced signal noise [84].

Kyowa uniaxial KSP-2-120-E4 strain gauges were selected for use in this study due to their availability and small size permitting accurate placement on the bar. Kyowa CC-33A cyanoacrylate cement was used to bond strain gauges to the bar. Two gauges were mounted axially on the surface of the bar around its circumference at 180 degree intervals and connected together in a circuit to form one arm of a Wheatstone bridge. By placing the strain gauges on either side of the HPB, it compensates for bending in the bar and the gauge station will output voltage changed from a change in resistance due to axial strain.

Instrumentation settings

HPB strain data were recorded using 14-bit digital oscilloscopes at a sample rate of 3.12 MHz. The voltage is converted to pressure via equation 3.2 where P is pressure, E is the elastic modulus of the bar material (determined in-house), V_0 is the powering voltage and GF is the strain gauge factor (120).

$$P = \frac{2E}{V_0 \times GF} \tag{3.2}$$

As the stress pulses would propagate 250 mm from the bar face to the strain gauge location at approximately 5,000 m/s, 50 microseconds have been subtracted from the timebase of every recording. Hence, the arrival time of each pressure pulse corresponds to the arrival time at the bar face rather than the arrival time at the strain gauge location as recorded.

Instrumentation is triggered by a breakwire (Figure 3.2) cemented to the internal diameter of the charge case into the charge case. The breakwire circuit triggers the instrumentation from a drop-out of 5 V DC when the circuit is broken by the detonation. A 10% pre-trigger is used to prevent data loss from false triggering caused by the fire set, radio frequencies and other electrical noise from the power supply.

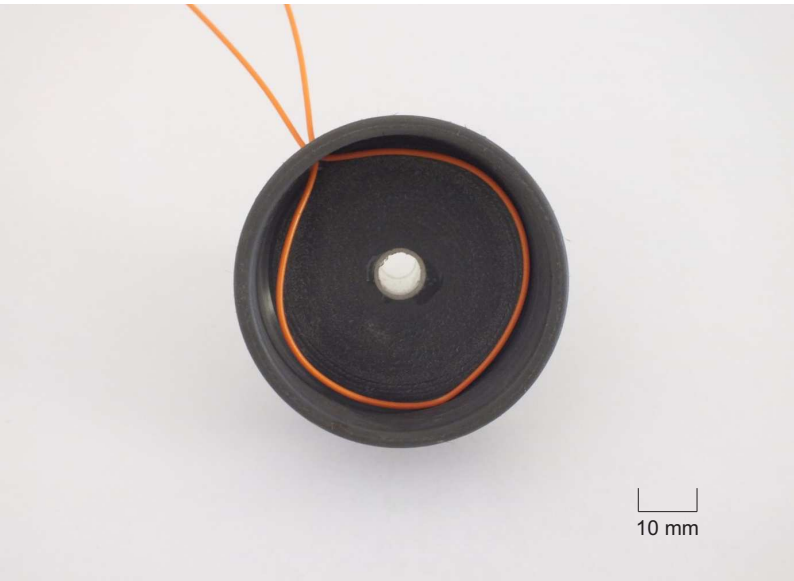

Figure 3.2: Breakwire in the charge case.

3.2.2 Test frame and instrumentation support design

Following the selection of a suitable instrumentation scheme, a test frame and supporting structure can be developed. The test frame must be effectively rigid over the duration of each test to remove potential artefacts generated by dynamic excitation of the supporting structure. Secondary and tertiary structures used to support the bar array should be robust enough to survive repeat testing and protect vulnerable components of the HPBs and load transducers from shocked detonation products and high velocity partials from soil ejecta.

Steel structures have the advantage of precision fabrication and quick erection times. In addition it is easier to engineer connection details between interfacing objects made from metal. Steel frames have a high strength to weight ratio when compared to other building materials – an advantage in standard construction. However, because of this, a test frame which would be capable of enduring repeat blast loading is likely to respond dynamically to very short duration high intensity loads because the mass required to dampen shock loads is not available. It is for this reason that a steel test frame was not used.

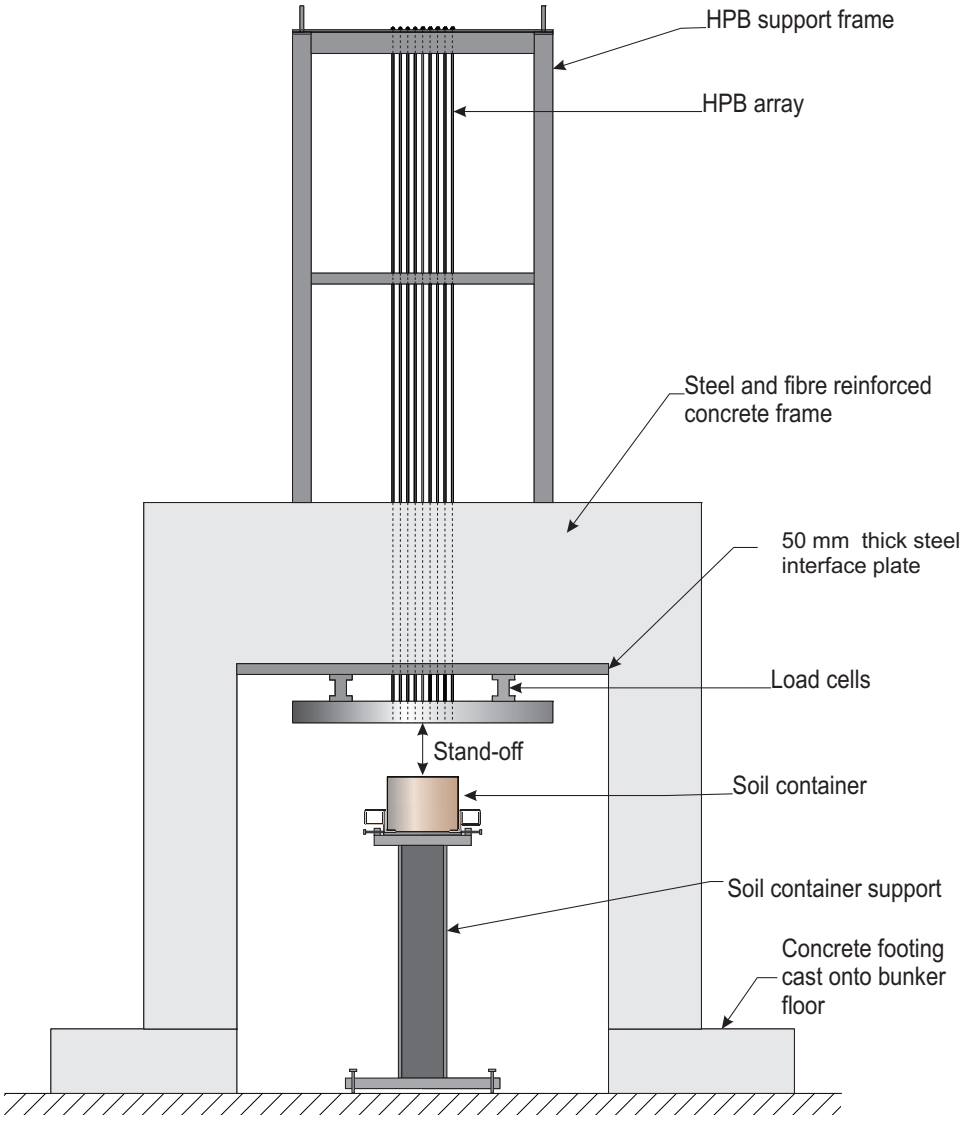

Figure 3.3: Elevation of the Characterisation of Blast Load (CoBL) test apparatus - Full technical drawings available in Appendix D

A concrete test frame allows for the addition of mass that is more economical than is possible with a comparable steel structure. In order to increase a concrete frame's inertial resistance, large amounts of concrete can be used to ballast and therefore dampen the frame and produce an effectively stiff frame system. For the reasons outlined a concrete test frame is developed to support the instrumentation.

Consideration of the apparatus' life cycle and forecasting of future studies influenced the size and geometry of the test frame. Following the completion of this study the frame may be used for increased scale tests (up to 500 g TNT equivalent), geotechnical beds may significantly increase in size or a targets with more complex geometries may be tested. A further consideration is that plant required for moving heavy test samples into the test frame and clearing debris would need sufficient room to track into and around the test frame.

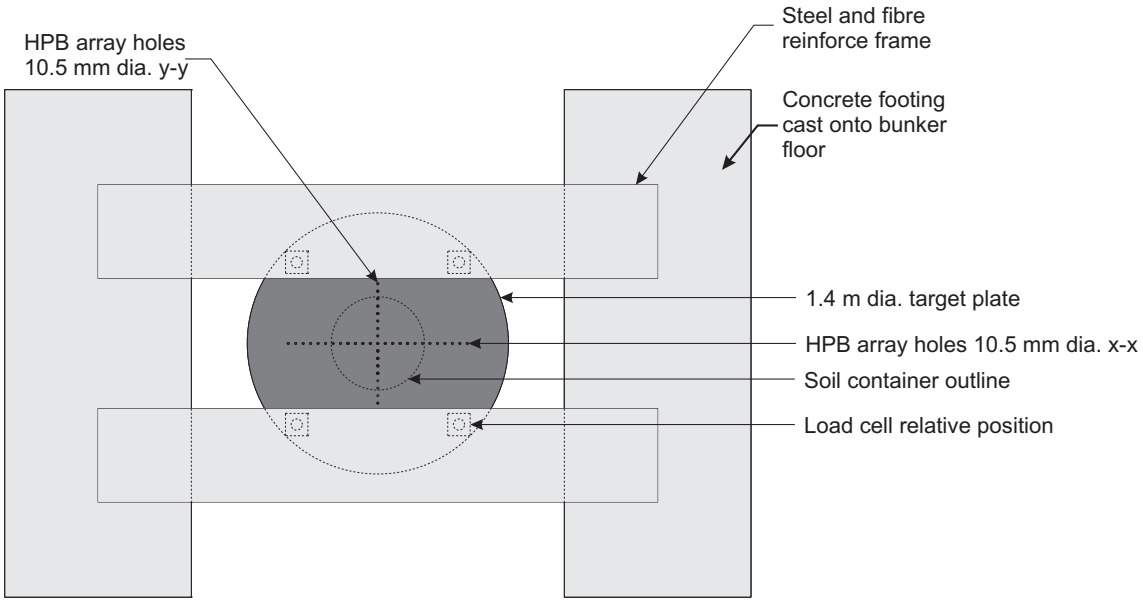

Figure 3.4: Plan view of the Characterisation of Blast Load (CoBL) test apparatus - Full technical drawings available in Appendix D

The experimental setup is based around two large concrete test frames constructed from RC45 fibre and steel reinforced concrete designed to BS 8110-1:1997 and BS 8666:2005 [85,86] with guidance from Arya [87]. Columns are 500 mm square and attached with shear links to a 750 mm deep, 500 mm wide beam spanning between the columns, see Figure 3.3. Shear links cast into the lower face of each of the beams which are welded to a 50 mm thick steel interface plate. The interface plate serves two purposes, namely to shield the concrete from blast products, fragmentation, soil ejecta and also to allow for further instrumentation to be easily affixed.

The bases of the columns were cast into the test frame footing with L-bars at 3 external faces (to the detonation), see Figure 3.4. To maintain the integrity of the floor slab on which the test frame is placed, the frame footing was cast onto the existing bunker slab. To prevent lateral shear of the footing, ragging bars were drilled into the existing slab at 250 mm centres on-plan and resined in position. The footing was then cast around the ragging bars and the column base L-bars.

3.2.3 Target plate

Target plate material selected was mild steel plate grade S355. Previous experience has shown that a target plate's attack face can become pitted and significantly roughened by impacts from soil ejecta and the cable umbilical used to initiate and trigger instrumentation. Mild steel allows for relatively simple repair of the target plate where voids are filled with weld and ground flat without the need for specialist welding equipment or removal of the target. This allows relatively quick repair and reduces risk to technical staff.

A target plate of 1400 mm in diameter was selected for the apparatus as shown in-situ in Figure 3.5. A minimum radius of 550 mm was estimated to prevent target clearing affecting the measurement of blast pressures during the event, which is known to cause venting which reduces pressure and specific impulse acting on the target, see Tyas et al. [88]. The additional radius of 150 mm was added to ensure conservatism on this estimate and to ensure geological materials for which no data is available and longer stand off free-air tests did not clear the target.

Numerical simulations were conducted to check target plate deflection when subjected to the blast pressures [84]. A 1400 mm diameter plate (with boundary conditions approximately representing those of the test rig, i.e. full translational and rotational constraint at nodal locations corresponding to parts of the plate in contact with the load cells) was evaluated under LS-DYNA [89] routine LOAD_BLAST_ENHANCED [90] (100 g TNT at 75 mm free air spherical blast). A target thickness of 100 mm provided a peak displacement of less than 0.3 mm. An increase of target thickness to 125 mm would have exceeded on-site lifting capabilities, and so, this small target deflection was accepted and a 100 mm thick target plate fabricated.

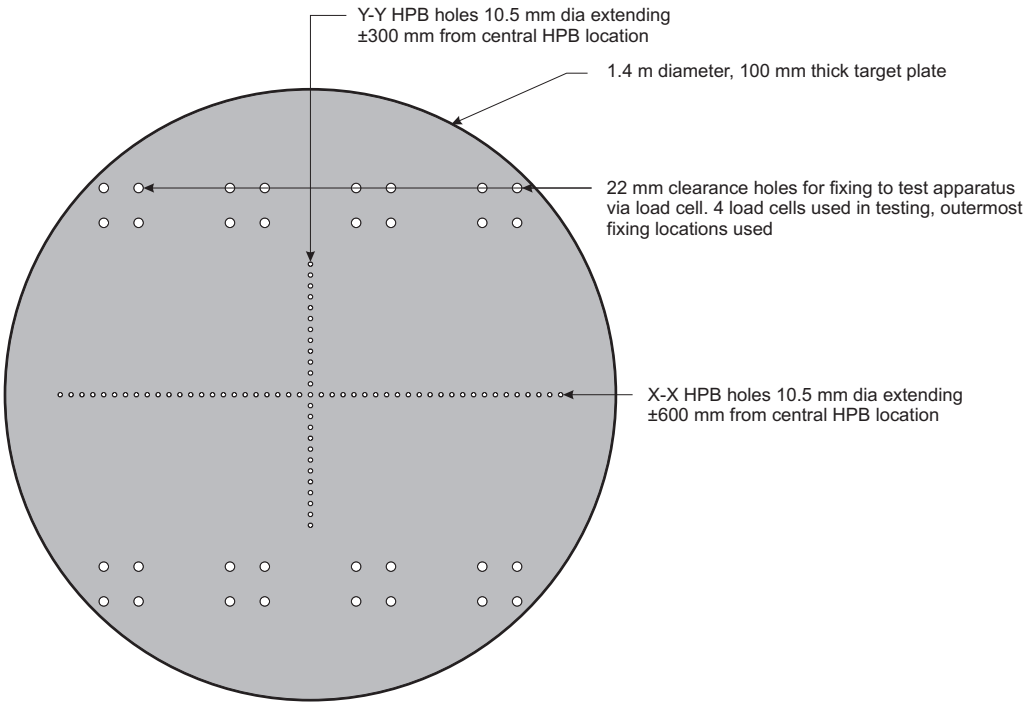

Figure 3.5: Plan view of target plate

10.5 mm diameter holes are drilled through the plate in two perpendicular arrays at 25 mm centre-to-centre spacing. Holes are drilled out to $\pm$300 mm from the central hole, which is common to both arrays. The target plate is attached to the test frame via four load cells which in turn are bolted onto the steel interface plates on the underside of the concrete beams. Due to the ultra aggressive environment that the load cells operate in, they frequently require

service and repair. Due to the risk of removing the target, the load cells will effectively become rigid target supports and record no pressure at the end of their service life. For this reason no load cell data is not presented herein.

3.3 Selection of geological material

Results from buried blast testing performed by Clarke et al. [30] indicated that varying the particle size by a factor of two for uniformly graded soils had little effect on the output from buried explosives. Clarke et al. [30] used Leighton Buzzard 6/14 (2LB) and 14/25 (LB) sands in the study, amongst other soils. LB and 2LB are identical in terms of chemical and sand grain physical appearance; the British Standard BS 5930:1999+A2:2010 soil characterisation [91] describes LB as sub-angular to rounded quartz sand. Particle sizes of 2LB are approximately double that of LB with particles between 0.60-1.18 mm. The distribution of 2LB particles is again approximately double that of LB but still within the bounds of a single fraction. Therefore, using LB soil at 1/4 scale is the equivalent of 2LB soil used in the 1/2 scale tests of Clarke. This demonstrates that at a 1/4 scale LB geological bed requires no further scaling of the soil particles.

Further benefits of LB are that it minimises any effects of particle size distribution removing suspicion of PSD variance causing any effects witnessed. The sand is graded, dried and bagged by the supplier, therefore no variance occurs between batches of soil, meaning that effects witnessed are from the soil-explosive phenomenon and not caused by test variance. There is significant familiarity with LB preparation techniques for compaction and hydration in the literature [27–30, 32]. Mechanical properties of the soil are also beneficial. High particle strength and rounded geometry reduces the probability of particle breakage (due to rounding of angular particles) affecting the behaviour of the sand [30].

Some risk is associated with using a single size particle for a phenomenological study. For example, results may not capture conditions found naturally where it is difficult to achieve large variations in dry bulk density due to difficulty in achieving particle packing through compaction. In addition to this moisture contents between 6-20% are difficult to achieve due to water flowing into lower voids creating a moisture gradient within the soil. Despite these limitations, due to the repeatability possible from LB soil beds, LB was selected for the main body of the research project.

A requirement of the research project was to provide a comparison of LB to STANAG soil. STANAG soil is a very well graded mix of quartz silica materials and is recommended for use in buried charge tests in STANAG 4569 [8] and AEP-55 [33]. Granular materials such as LB and STANAG rely on mechanical interlock from the friction between particles to remain stable; the soils have no tensile strength and are cohesionless. The inclusion of STANAG will enable

the influence of particle size and distribution on the output from shallow buried explosives to be investigated in this study. A comparison of the PSDs for LB and STANAG are presented in Figure 3.6 as a cumulative frequency curve.

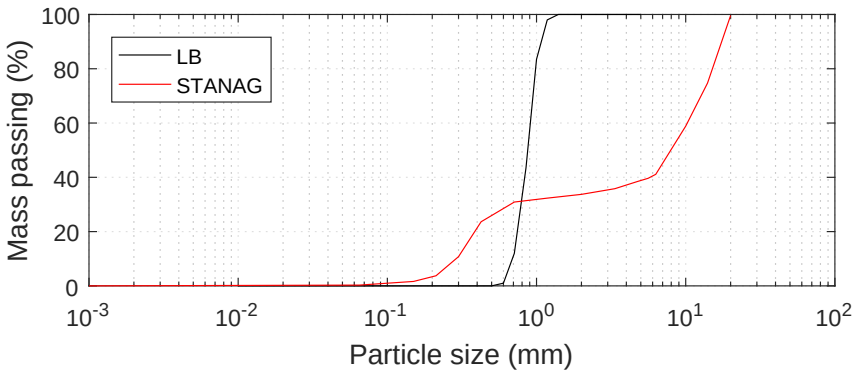

Figure 3.6: Comparison of LB and STANAG PSD

3.4 Geotechnical soil bed preparation

3.4.1 Geological parameters

LB tests were conducted at moisture contents (as a percentage of total mass) of 2.45, 4.76 and 25%. In the Leighton Buzzard sand with moisture contents above 6%, the water no longer adheres to the surface of the soil particles. Instead, it percolates to the base of the bin leading to a saturated base layer and top layer of indeterminable moisture content, the exception being the 25% test where the entire soil mass is saturated. For this reason moisture contents between 5–25% were not tested. Dry density of the soil was fixed at 1600 kgm^{-3} for all LB soil preparation. At moisture contents of 2.45, 4.76 and 25% target bulk densities were 1635, 1670 and 1990 kgm^{-3} respectively. A tolerance of $\pm$0.1% was applied to moisture and a tolerance of $\pm$5 kgm^{-3} applied to the bulk density.

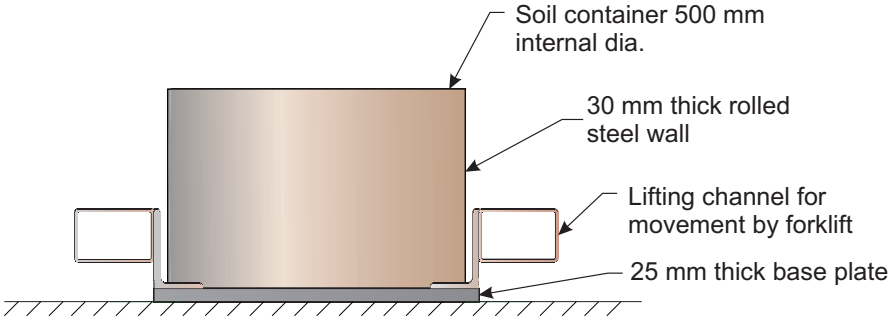

Figure 3.7: Steel soil container used to prepare soil samples – elevation.

STANAG tests were conducted at the point of full saturation where the moisture content is approximately 14%. The dry density of the material is 1806 kgm^{-3} with a saturated bulk density of 2100 kgm^{-3}.

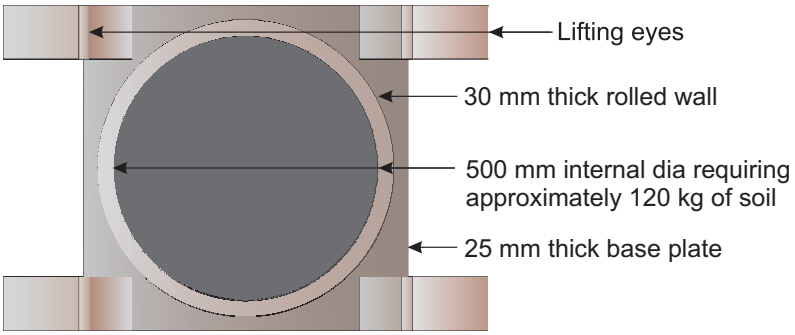

Figure 3.8: Steel soil container used to prepare soil samples – plan.

To create repeatable test beds with varying soil types and geological parameters (and hence levels of compaction), an effectively rigid container was used. Soil was prepared in 30 mm thick mild steel containers formed into a 500 mm diameter, 375 mm tall cylinder illustrated in Figures 3.7 and 3.8. The soil container's diameter and depth are an adapted quarter scale of the recommendations in AEP-55 [33], mirroring the approach of the half scale work of Clarke et al. [28]. A 25 mm thick plate is welded at the base of each cylinder. Four lifting channels were attached to the base plate to allow transport via forklift.

3.4.2 Soil preparation

Soil arrives from the supplier (Garside Sands [3]) kiln dried and heat wrapped in one tonne bulk bags. Typical supplied moisture content of the soil is between 0.1 and 0.3%. The correct mass of soil and water needed to achieve the required soil bed conditions is calculated following an initial moisture content assessment. The moisture content assessment is achieved by heating the soil until there is no further mass loss from water boil off. Then, a comparison of the dry and wet mass is made allowing for an assessment of the water content. When the moisture content is known, a hopper above a forced action mixer is loaded with a bulk bag of soil. An illustration of the preparation equipment is shown in Figure 3.9.

The forced action mixer sits upon a three tonne capacity scale accurate to $\pm$50 g. The forced action mixer is started and the hopper is opened, filling the mixer from above. The required mass of water is then added to the mixer. Mixing typically takes five minutes, but will continue until the water appears evenly distributed from a visual inspection. A sample is then taken

[3] Garside Sands can be reached at the business address Garside Sands, Eastern Way, Heath and Reach, Leighton Buzzard, Bedfordshire, LU7 9LF. Further details of Garside Sands products my be gained from the Aggregate Industries website www.aggregate.com

from the mixer and the moisture content is checked. If this is within tolerance, the mass and moisture content are recorded.

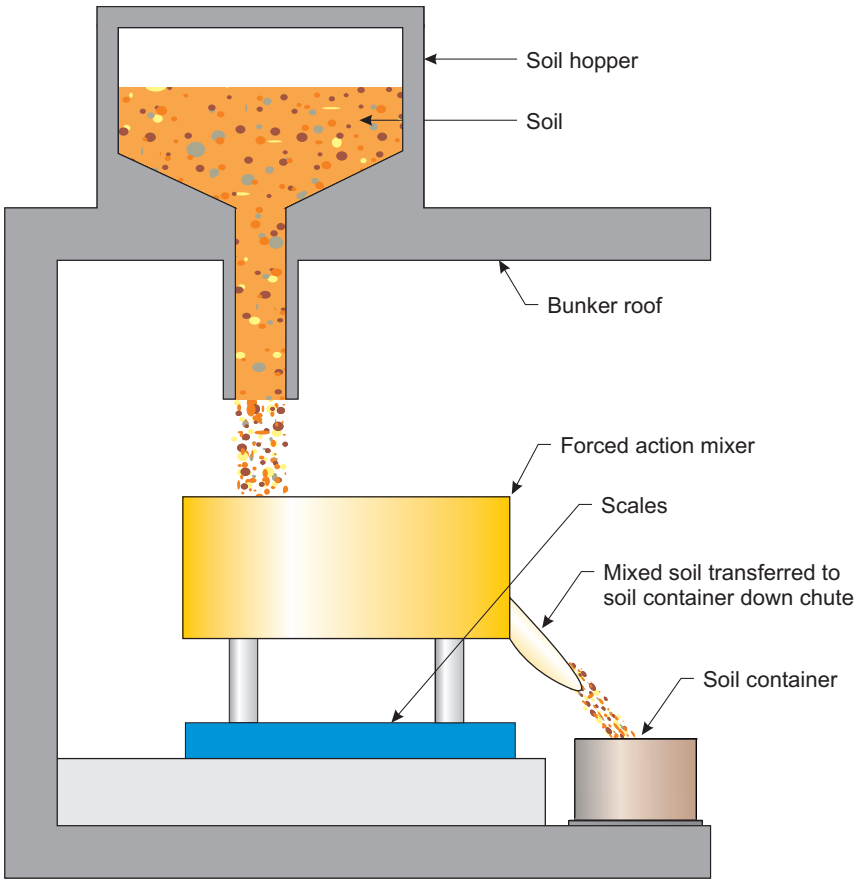

Figure 3.9: General arrangement of soil preparation.

The soil container sits below the mixer and is filled in two lifts to ensure even compaction. 60 kg of material is poured into the steel container for the first lift. A timber plywood board cut to the internal diameter of the soil container is placed on the sand surface as shown in Figure 3.10a, and the sand height is recorded and checked. A stiffened steel compaction tool, see Figure 3.10b, is placed on top of the plywood board and mechanically struck until the sand surface reaches the required height for the specified bulk density. Measurements of the final sand level are recorded and the compaction tool and plywood board are removed from the container.

The un-compacted height of the second lift will exceed the height of the steel container, so a laterally braced 150 mm deep, 500 mm internal diameter steel spill collar, shown in Figure 3.10c, is seated on the top lip of the soil container. A further 60 kg of LB is poured into the container, which is then levelled and compacted as per the first lift. After the plywood board, compaction tool and collar are removed, a small amount of LB (less than 1 kg) should be left protruding from the soil container. This excess material is tamped into the soil bed with a flat steel screeding bar. A polythene sheet seals each soil container so that no moisture is lost during storage. This sheet is removed immediately before the charge is buried and the firing

sequence begins, so that the container remains uncovered for no longer than 15 minutes to minimise wicking of moisture from the soil surface.

(a) Plywood compaction board. (b) Steel compaction tool. (c) Steel spill collar.

Figure 3.10: Soil container preparation equipment.

Saturated soil is prepared much like partially saturated soils, but with some modifications. A helically wound perforated hose is placed at the base of the soil container using a timber spacer to ensure an even hose distribution, see Figure 3.11a. The spacer is removed once enough soil has been added to secure the hose location, as indicated in Figure 3.11b. The container is then filled in the usual manner with the hose being led up the inner wall to allow for saturation prior to firing. One litre of water is added to the mixer to aid lubrication of the sand particles during compaction, the sand is compacted to the appropriate density such that further water achieves target density.

(a) (b)

Figure 3.11: Location of base saturation perforated hose; (a) perforated hose with timber spacer in soil bin base, (b) perforated hose held in place with soil and timber spacer removed.

The balance of water required to saturate the soil is supplied in-situ prior to firing. The primary reason for this is that vibrations from transporting soil containers caused liquefaction and therefore further compaction of the soil bed. Furthermore, accurate in–situ charge placement and overburden replacement was technically difficult and inaccurate. The chosen method of saturation has been found to give a more uniform distribution of moisture content through the soil mass, significantly reducing the possibility of trapping air in the voids between soil particles. The top filling method was checked by comparing the void volume of the soil to the mass of water required to fill the void volume using Equations 2.2 and 2.3. It was shown that base filling with water achieved 100% saturation whilst top filling achieved lower than 30% by mass.

3.5 Explosives engineering considerations

AEP 55 [33] level 2 requires a 6 kg TNT equivalent charge in a cylinder of 3:1 aspect ratio fully encased charge buried at a depth of 100 mm between the uppermost surface of the charge and the soil surface. Using cube root scaling described in Cooper ([17], page 408) the 1/4 scale equivalent TNT charge is 94 g. It was decided to use PE-4 due to the constraints of handling TNT which include hot pouring into the appropriate form and associated fumes, inconsistencies in the detonation profile due to imperfections in the bulk explosive due to entrained air and faults which may occur during cooling and handling. PE-4 by comparison is simple to prepare consistently and less hazardous to the firing officer. A PE-4 equivalence ratio of 1.2 [88, 92] modifies the full scale explosive mass to 5 kg, so that at quarter scale the PE-4 charge is 78 g. The overburden (soil between top of the charge and the soil-air boundary) is reduced from 100 mm to 25 mm.

Detonators used to innate PE-4 are relatively large due to the shock fluence required to initiate detonation in the bulk explosive. Booster materials in combination with lower yield detonators were considered but these would complicate numerical modelling efforts where an accurate source term would need to be developed to consistently compare experimental and numerical work. With no option to reduce the length of the detonator the reduction in scale meant part of the detonator extends above the soil bed which could affect the explosive product break out from the soil bed. Commissioning trials were conducted to assess the performance of the test apparatus and select the most suitable charge configuration. Two free air and two sub–surface charges were proposed in these initial stages, see Figures 3.12 and 3.13.

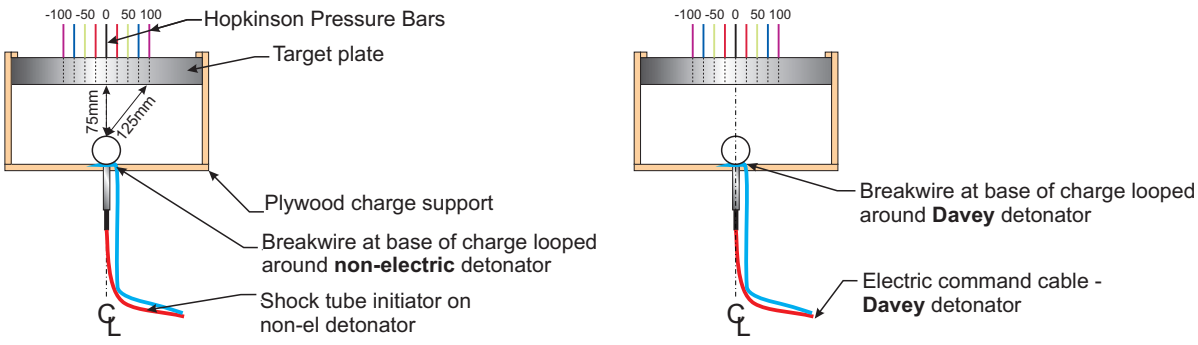

Figure 3.12: Diagrams of test set-up for comparison of charge initiation with a non-electric and electric detonators in free-air. Note that these diagrams are not to scale and the relative dimensions of the target and charge are indicative only.

Figure 3.12 shows the spherical 100 g PE-4 free-air charges were placed on a plywood board under-slung from the target plate at a standoff of 75 mm to the charge centre with detonators inserted into the charge base. Timber ply was selected to support the charge due to the low cost of the material, stiff but frangible and does not combust following interaction with the shock wave. When using plywood it is possible that reflections from the ply my be witnessed

in the pressure–waveform. Lower density options were considered with the aim of reducing reflections with materials such as low density polystyrene. However it has been shown that in the strong shock environment, low density polystyrene foams can combust or detonate [93] adding to the output of the charge. Tyas et al. [94] has used a method of tensioning glass fibre fabric between metal clamps like a 'drum skin' in order to provide the support necessary for accurate charge positioning whilst having the minimum impact on secondary reflections from the base of the charge. Whilst this method appeared successful, it was decided that the additional complexity and therefore turn-over time between tests were higher risk to the test programme than the potential for reflections in pressure–waveforms. It appears that there is a lack of research in the area of explosive charges supports.

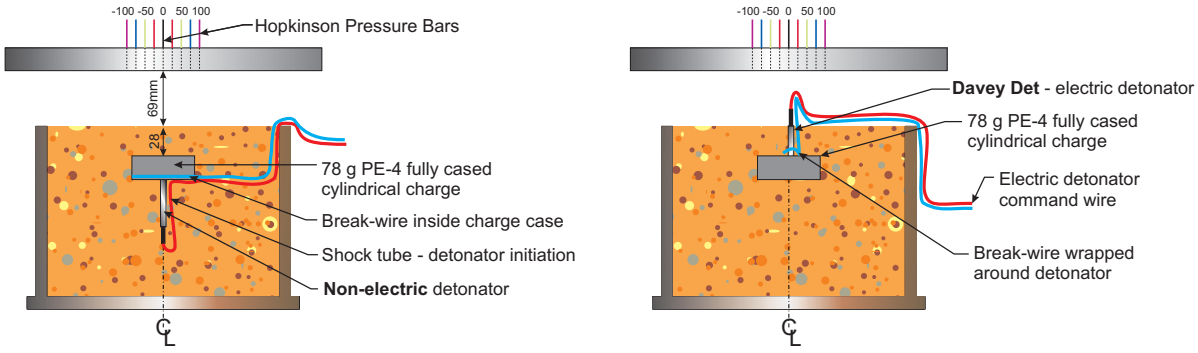

Figure 3.13: Diagrams of test set-up for comparison of charge initiation with a non-electric and electric detonators for shallow buried charges. Note that these diagrams are not to scale and the relative dimensions of the target and charge are indicative only.

The sub-surface explosives show in Figure 3.13 were encased in a 3 mm thick PVC container, formed into 3:1 cylinders with a diameter of 57.1 mm and a height of 19 mm. Base initiated charges used a nylon 66 stanchion resined at the charge's base to reinforce the detonator's position during burial. The charge was buried to a depth of 25 mm from the top of the charge case to the soil surface.

3.5.1 Charge placement and alignment with trials apparatus

The detonator, break wire and charge are configured prior to placement in the soil container. The soil surface is marked for placement of the charge hole shuttering, as shown in Figure 3.14a. A 100 mm deep, slotted plastic shutter which is 5 mm greater in diameter than the charge is aligned with the centre of the soil bed, see Figure 3.14b. Sand is removed from within the shutter as it is pressed into the soil. When the shutter top is flush with the sand surface, excavation is complete. A flat steel bar is used to place a hole at the base of the excavation for the detonator command line and breakwire umbilical. An inclined channel is prepared from the base of the shutter to the edge of the container, see Figure 3.14c. The charge and umbilical can now be buried, Figure 3.14d, and the shutter removed, Figure 3.15a. The charged is measured for lateral and depth alignment to check for disturbance during shutter removal,

shown in Figures 3.15b and 3.15c. The excavated material is weighed, Figure 3.15d, and placed in a sealed bag in order to backfill to the correct density and moisture content, Figure 3.15e, the overburden is carefully placed above the charge, Figure 3.15f, and the soil surface is made good with a screeding level ready for firing. An image of the complete soil container is presented in Figure 3.15g.

(a) (b) (c) (d)

Figure 3.14: Images taken from charge burial process; (a) marking of the soil at centre, (b) excavation shuttering used to prevent side walls from collapse, (c) slot cut into shuttering to allow burial of cable umbilical and sand moved to allow burial of cable, (d) charge placed into excavated hole.

The soil container was transported between explosives preparation area and test apparatus with a forklift. The Firing Officer chaperones the soil container and buried charge between sites to prevent hazard to the forklift operator and ensure safe delivery of the test sample.

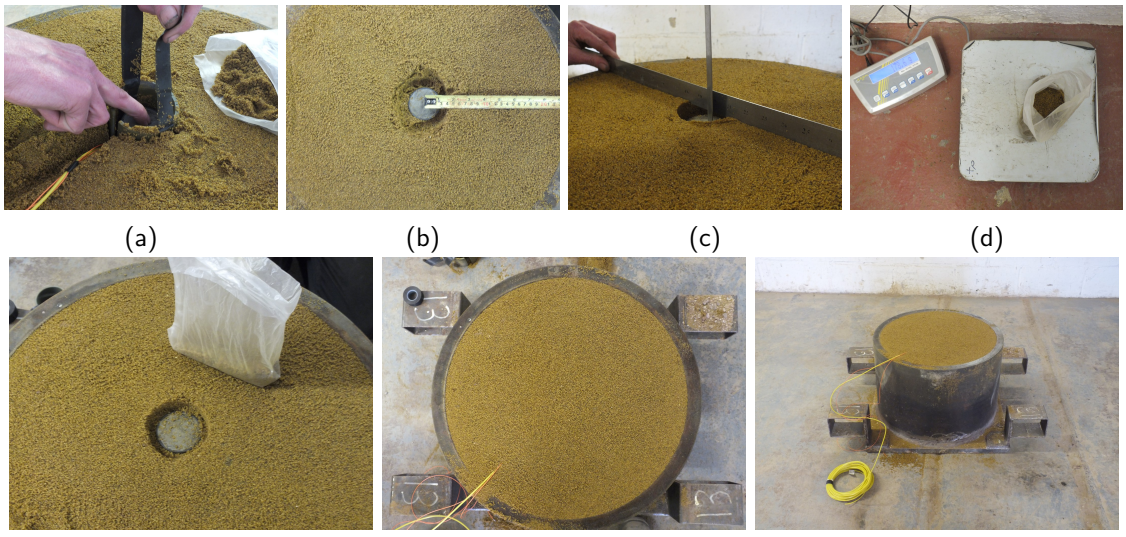

(a) (b) (c) (d)

(e) (f) (g)

Figure 3.15: Images taken from charge burial process; (a) removal of shutter keeping the charge in place, (b) check on lateral alignment, (c) check on vertical alignment, (d) soil removed during burial is weighed accounting for charge volume, (e) correct soil mass is tamped in above charge, (f) the soil surface screeded and ready to fire, (g) final configuration ready for transport to the test site.

The soil container was placed on a supporting frame elevated from the floor slab. Initial 'dry runs' of placing the soil container in the test frame presented some problems. The floor slab in the test structure was cast uneven and had been damaged over the years. Structures developed to support the soil container were fabricated with vertical and horizontal components perpendicular. On the uneven floor the soil container support would lean displacing the soil

container to one side. Furthermore, placement by forklift was often within 25 mm of centre, with bar spacings of 25 mm a more accurate alignment was required.

Both issues were solved with modifications to the soil container support. To ensure the soil container aligned vertically, a 50 mm thick plate was welded to the base of the support and four 20 mm threads cut into each corner of the plate. The plate was aligned vertically by placing M20 bolts into the threaded holes allowing for small vertical adjustments in alignment and height ensuring standoff can be achieved within ± 1 mm. A similar method of alignment was used to ensure the soil container was co-axial with the central HPB. Three 50 mm bars were welded to the top plate, rear and sides, leaving the front open to allow placement and removal of the soil container. 16 mm tapped holes were drilled horizontally at the bar centres allowing an M16 bolt to push the soil container. A plum line attached to the central HPB by a cylindrical neodymium magnet was used to indicate alignment with a small mark on the soil bed, alignment was achieved by pushing the soil container laterally, and from back to front across the soil container top plate using the M16 bolts. The soil container support is illustrated in Figures 3.16 and 3.17.

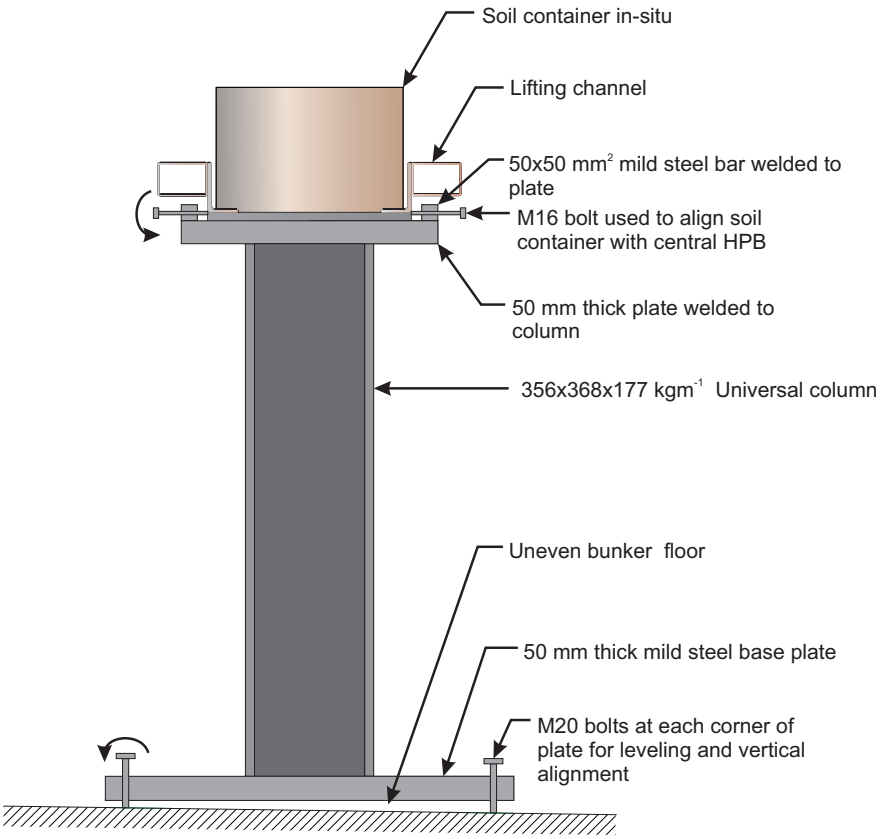

Figure 3.16: Elevation of soil container stand used to align and level soil containers relative to the target plate.

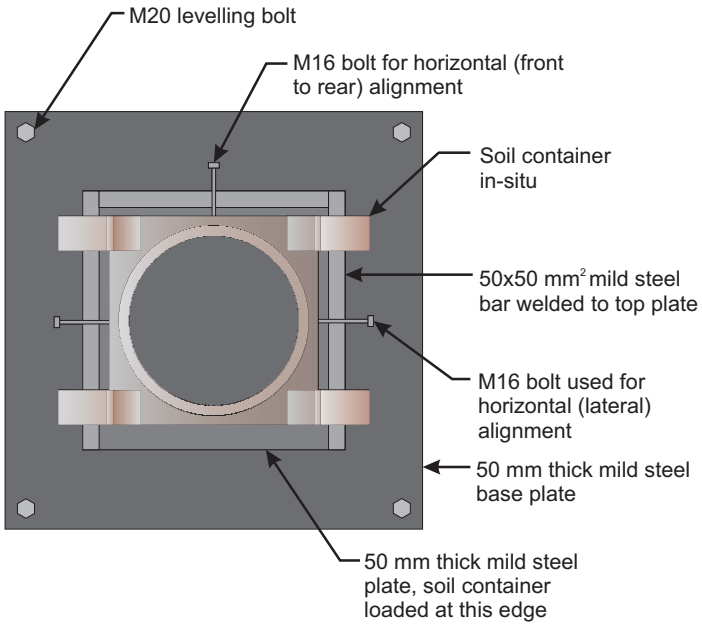

Figure 3.17: Plan of soil container stand used to align and level soil containers relative to the target plate.

3.6 Commissioning of the CoBL test apparatus and testing

3.6.1 Introduction

The following sections present the results and discussion from commissioning tests aimed at demonstrating that the CoBL trials apparatus functioned correctly. Once achieved, further tests were conducted to improve the reliability of the apparatus and repeatability of tests, to determine sufficient spatial resolution and to investigate the test boundary conditions.

This initial study comprises of five main parts for which 40 tests were conducted, summarised in Table 3.1. Tests 1-6 provided confidence in the test apparatus where free-air detonations were compared to empirical data; these tests were also used to investigate the behaviour of electric and non-electric detonators. Tests 7-18 were performed in soil and investigated the orientation of initiation for electric and non-electric detonators. Tests 19-28 investigated the spatial resolution requirements of the HPB array used to determine a suitable HPB configuration for the parameter study in Chapter 4. Soil container boundary conditions were investigated in Tests 29-34. The effect of HPB dispersion on pressure waveforms and specific impulse was investigated in Tests 35-40. In Table 3.1 and subsequent tables spherical (Sph), stand off (SO) and overburden (OVB) are abbreviated to minimise column width.

Table 3.1: Summary of tests in Chapter 3.

Test number	Soil condition	Mass (g)	Case/ geometry	Detonator orientation	Detonator type	SO (mm)	OVB (mm)	Refinement
1–3	Air	100	Sph	Base	Non-el	75	-	Non-el
4–6	Air	100	Sph	Base	Electric	75	-	Electric
7–9	LB	78	Full	Top	Electric	69	25	Det orientation
10–14	LB	78	Full	Base	Non-el	69	25	Det orientation, case top
15–18	LB	53	No top	Base	Non-el	69	28	Charge mass
19–28	LB	53	No top	Base	Non-el	69	28	HPB array
29–34	LB	78	No top	Base	Non-el	140	28	Charge mass, stand off, soil container
35–40	LB, air	78	No top	Base	Non-el	140	28	Dispersion

3.6.2 Free-air commissioning tests and comparison with ConWep

The primary aim of commissioning tests on the CoBL apparatus was to check consistency of results produced by the test apparatus against empirical predictions. To do this, a free air blast load is required for comparison against ConWep [13], an empirical database of air blast data. A secondary aim of commissioning tests was to assess any difference between electric and non–electric detonators. Six free air tests were conducted as specified in Table 3.2.

Table 3.2: Free air commissioning Tests 1–6 – Central HPB and 4 radial HPBs 100 mm from centre.

Test number	Soil condition	Mass (g)	Case/ geometry	Detonator orientation	Detonator type	SO (mm)	OVB (mm)
1–3	Air	100	Sph	Base	Non–el	75	–
4–6	Air	100	Sph	Base	Electric	75	–

Five HPBs were used in tests 1–6 where a single HPB was placed at the centre co–axial with the charge, and four radial bars were placed at 100 mm from the centre. Tests 1–3 were conducted as Figure 3.12 a with a 100 g PE–4 charge 75 mm to the charge centre and 125 mm radially to 100 mm HPBs. For tests 1–3 non–electric detonators were used to initiate the charge, whereas in tests 4–6 electric detonators were used. Central bar results are presented in Figures 3.18a and 3.18b, 100 mm radial bars are excluded for brevity, however full results and accompanying schematic of the test configuration are provided in Appendix B.

The ConWep tool was run using TNT mass scaled by 1.2 for a PE–4 peak pressure equivilance of a spherical charge. Comparison of the various curves in Figures 3.18a and 3.18b would suggest that the ConWep pressure waveforms are in very good agreement with the experimental data. It should be noted that arrival times of the ConWep waveforms are time shifted by 0.015 ms for test 1–3 and 0.005 ms for tests 4–6 due to different breakwire locations being used (as shown in Figure 3.13). Variance between detonator types is clear, peak pressures at the central HPB for electric detonators (Tests 4–5) are consistently higher than the pressures in non–electric tests (1–3).

The mass of primary explosive in the detonator is not accounted for in the ConWep prediction. It was noted that electric detonators used 800 mg of PETN in these tests which is 100% more primary explosive than non–electric detonators. This may explain the increase in pressure seen in tests 4, 5 and 6 when compared to the non–electric detonators used in tests 1, 2 and 3.

Comparison of data acquired from the test apparatus and ConWep provides confidence in the validity of data acquired from the test equipment and data processing. With high confidence in the results, commissioning tests progressed onto buried explosives.

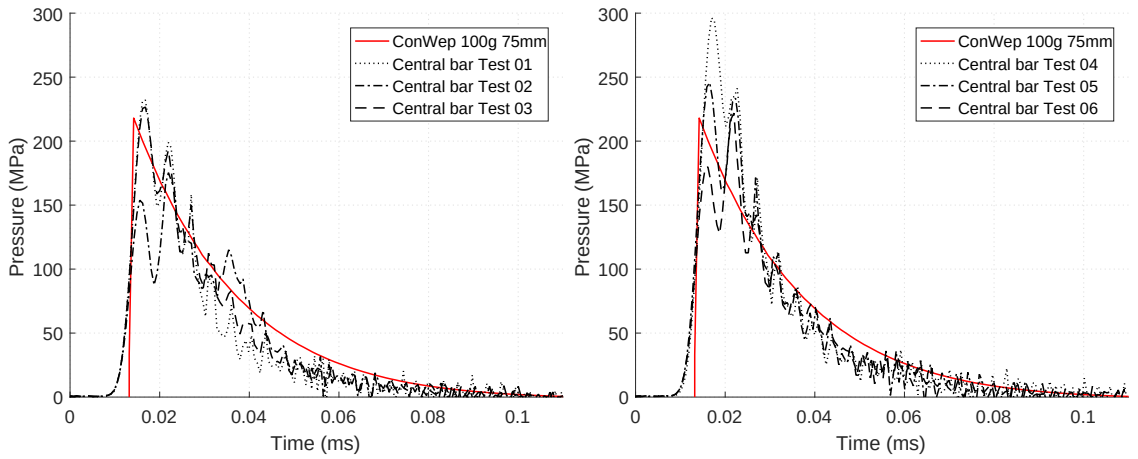

(a) Tests 1–3 vs ConWep prediction – non–electric (b) Tests 4–6 vs ConWep prediction – electric

Figure 3.18: Comparison of data from the central HPB with 100g PE–4 charge at 75 mm from the central HPB; (a) central HPBs from tests 1,2 and 3 with non–electric detonator, (b) central HPBs from tests 4,5 and 6 with electric detonator.

3.6.3 Commissioning tests with shallow buried explosives

Commissioning tests with shallow buried explosives were conducted to observe the implication of explosive engineering choices made during experimental design and observe the performance of the test apparatus. The intention of these tests is to make adjustments to the experimental set–up where needed to maximise data quality and improve work flow and address any arising safety issues.

Shallow buried charges are typically initiated at their top for both safety and practical reasons. Top detonation reduces the time needed for burial therefore reducing exposure of the Firing Officer to live explosive. This was a significant consideration in this body of work, but will be weighed against the tests as explained below. At full scale tests to STANAG level 2 [8] 100 mm overburden is required, covering the top of the charge, detonator and command umbilical. However, at 1/4 scale, the top of the detonator and the command umbilical will extend beyond the soil surface and risk direct impact with the measurement surface. Furthermore, accurately burying an explosive with a clearance reduced to 69 mm was not practical.

Tests 7–14

To reduce the risk of fragment strikes from the detonator and command umbilical and reduce difficulty in charge burial, the explosives were initiated from the base. As this approach has not been used in the literature, shallow buried commissioning tests 7–14 investigate the behaviour of top verses bottom detonated charges as outlined in Figure 3.13 and Table 3.3.

Table 3.3: Buried explosive commissioning Tests 7–14 – Central HPB and 4 radial HPBs 100mm from centre.

Test number	Soil condition	Mass (g)	Case/ geometry	Detonator orientation	Detonator type	SO (mm)	OVB (mm)/Notes
7–10	LB	78	Full	Top	Electric	69	25
11–13	LB	78	Full	Base	Non–el	69	25
14	LB	78	No top	Base	Non–el	69	28

In these tests the HPBs were deployed with a central HPB co–axial with the charge and 4 HPBs 100 mm radially from the centre bar, see Figure 3.19.

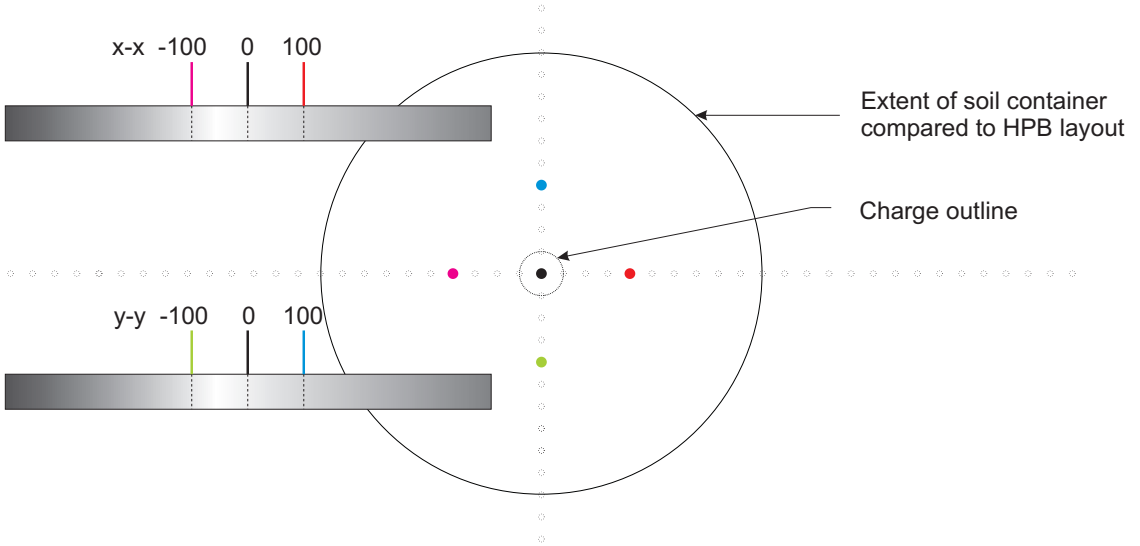

Figure 3.19: HPB set–up for tests 7–14.

Tests 7–10 were conducted with the charge detonated from the top such that the detonator and cable umbilical protruded from the soil surface. The cable umbilical consists of a command line umbilical used to detonate the charge and a break wire. A large amount of signal noise and artefacts were generated by this test setup, a sample of test data from Test 8 is presented in Figure 3.20a. It was hypothesised that these artefacts and signal noise were caused by detonator fragments striking the HPB loading face and electrical noise from the break–wire carrying 5 V DC power striking the target plate.

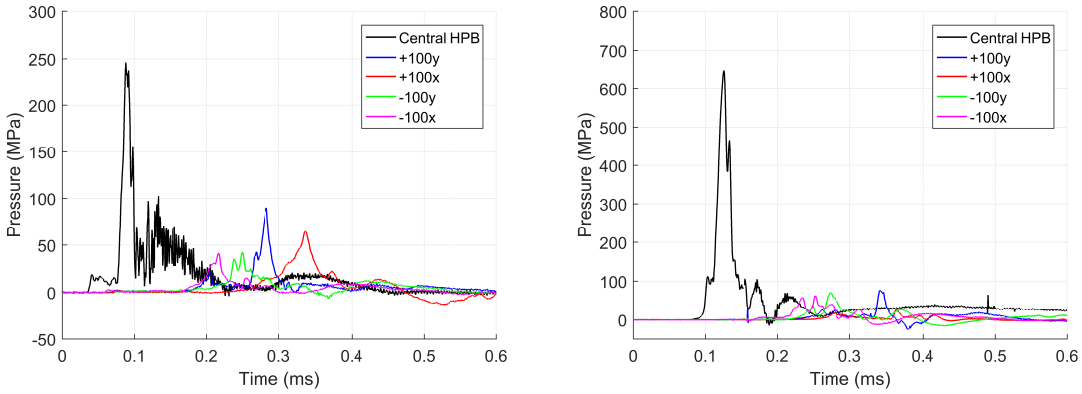

Figure 3.20: Pressure–time data from; (a) Test 8, (b) Test 11.

Tests 11–14 were conducted with the charge detonated from the base such that the detonator and cable umbilical were buried from the charge centre to the soil container wall. A significant reduction in artefacts and signal noise were seen in these tests. Sample data from Test 11 can be seen in Figure 3.20b. When compared to the pressure waveform of Test 8, Figure 3.20a, a more clearly defined pressure waveform is presented which facilitates clearer interpretation of the test results.

In all tests, base detonated charges produce significantly higher peak pressure than that of top detonated charges. Peak pressure in Test 11 is significantly higher than in Test 8, approximately 650 vs 250 MPa. Conversely, it was seen in free air tests that the electric detonator used for top donation consistently produced significantly higher pressures than the non–el detonator used for base detonation. Due to the increase in signal quality gained from base detonation, all further tests with shallow buried charges are base detonated.

Feature (a) (Pre–cursor shoulder, Figure 3.1) seen in the work of Taylor [36, 63], can be seen to reach a value of 20 MPa and act between 0.025 and 0.05 ms in Test 8 (Figure 3.20a), and reaches a value of 100 MPa between 0.09 and 0.10 ms in Test 11 (Figure 3.20b). It is hypothesized that this feature is caused by some interaction between the detonation, charge case and surrounding soil. This theory is investigated in Test 14 where the top of the charge case is removed.

Test 14 was conducted with base detonation using a non–electric detonator and an overburden of 28 mm. The relative charge height in the soil container is identical to Tests 7–13 where the additional 3 mm of overburden accounts for the removal of the 3 mm thick lid of the casing. The pressure–time history from Test 14 in Figure 3.21a is very similar to that of Test 11, Figure 3.20b, an otherwise identical test. However, a distinct difference in the pre–cursor shoulder can be seen. It may be argued that this feature seen in previous work is due to the

case containing the explosives. Further comparison of the central HPBs from Tests 11–14 is provided in Figure 3.21b and illustrates a consistent and significant reduction in pre–cursor shoulder when the charge case top is removed.

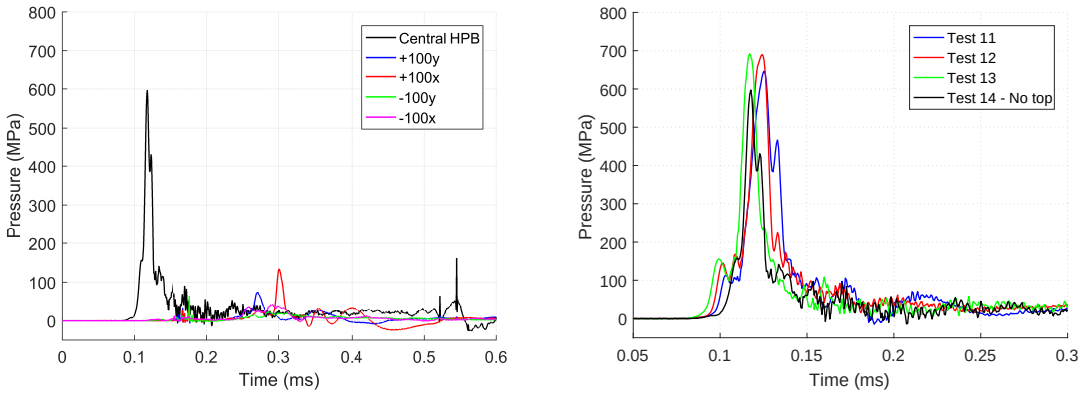

(a) (b)

Figure 3.21: Pressure–time data showing; (a) Test 14, (b) a comparison of central HPB data, i.e. co–axial with charge, for Tests 11–14.

Tests 15–18

After Test 14 the HPBs were inspected due to a number of signal–noise issues. It was found that several of the strain gauges had de–laminated from the HPBs. Whilst gauge and bar were undamaged, it appeared that the bonding cement had failed due to excessive strain. Damage to the HPB has obvious implications for test–to–test repeatability, thus alternative set–ups were considered.

Two options were available to reduce axial strain on the HPB. The explosive mass can be reduced, thus reducing the pressures witnessed by the HPB and, in turn, reducing the axial strain. Alternatively, the standoff between the soil surface and the measurement plane can be increased. Increasing the standoff would require fabrication work to the soil container stand at significant additional costs. For this reason, a reduction in charge mass from 78 g to 53 g of PE–4 was investigated in Tests 15–18.

Table 3.4: Buried explosive commissioning Tests 15–18 – Central HPB and 4 radial HPBs 100 mm from centre.

Test number	Soil condition	Mass (g)	Case/ geometry	Detonator orientation	Detonator type	SO (mm)	OVB (mm)
15–18	LB	53	No top	Base	Non–el	69	28

The charge configuration for tests 15–18 was a 53 g PE–4 cylinder cased without top, stand-off remained at 69 mm, and overburden increased to 28 mm without. The charge was base detonated with a non–electric detonator, as shown in Table 3.4. The test HPB configuration was a central HPB co–axial with the charge and 4 radial HPBs 100 mm from the central HPB, see Figure 3.22.

Data from tests 15–18 are presented in Figures 3.23a, 3.23b, 3.23c and 3.23d. Consistency at central HPB (black) is excellent with little variance of arrival time and peak pressure between tests. Significant variance is seen at the radial 100 mm HPBs between tests. Perhaps more concerning is the variance of pressure at 4 radial locations in the same test.

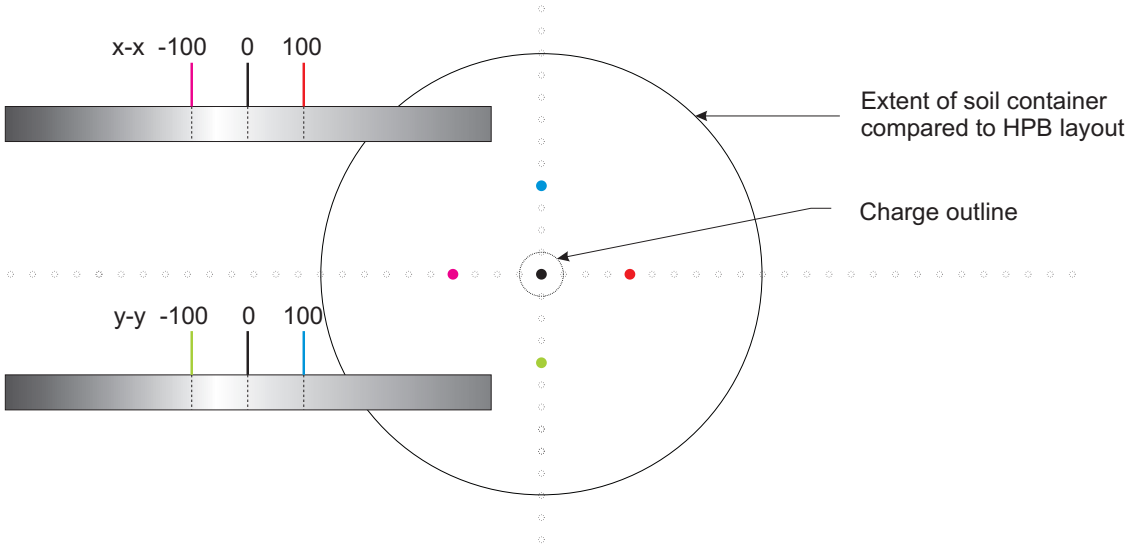

Figure 3.22: HPB set–up for tests 15–18.

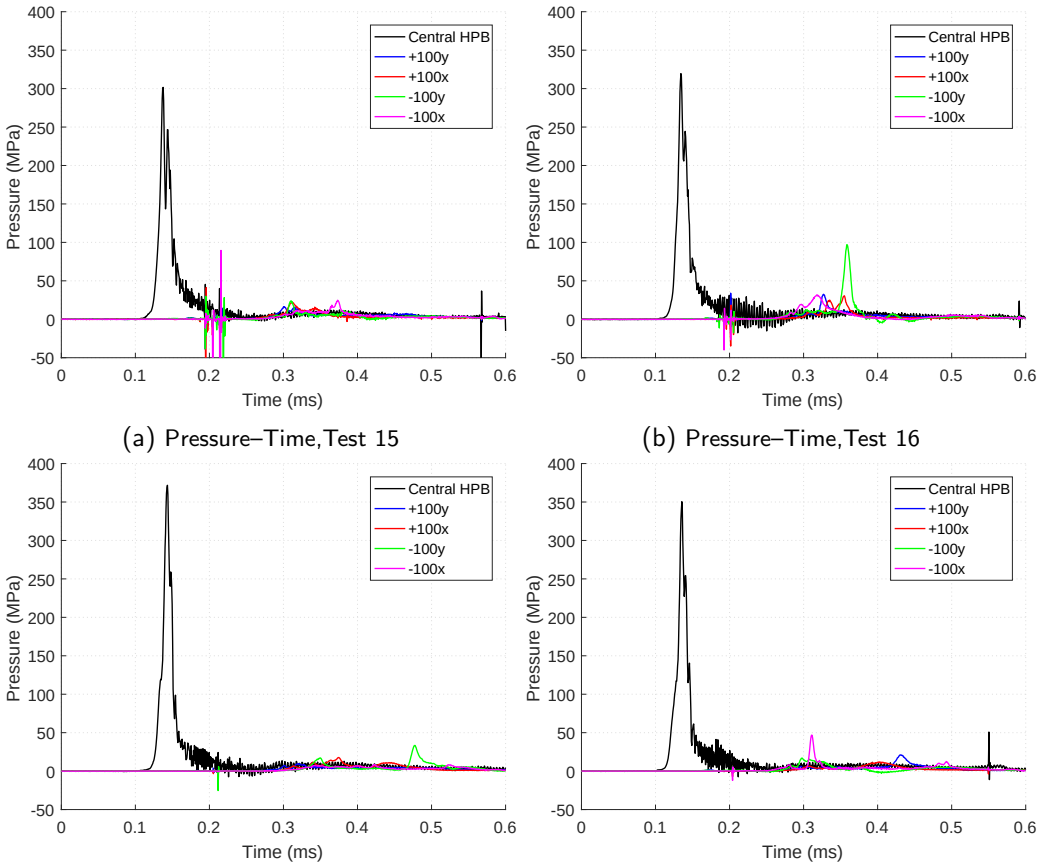

(a) Pressure–Time, Test 15

(b) Pressure–Time, Test 16

(c) Pressure–Time, Test 17

(d) Pressure–Time, Test 18

Figure 3.23: Pressure–time histories of Tests 15, 16, 17 and 18 showing consistency between tests at the central HPB and greater variance at the 100 mm radial HPBs.

The repeatability of the central HPB provides confidence that modifications to the test set–up have significantly improved data quality. However, further investigation was required to assess the variance of pressure with increased distance from the central HPB informing the HPB array layout for the parameter study.

Tests 19–24 and 25–28

Tests 19–28 investigate the variance in pressure with increased distance from the charge. This was achieved by placing the HPBs in a single radial array from the charge centre at 25 mm intervals between 0 and 200 mm. In tests 19–24, the HPB locations were at 25 mm spacing on a single radial array from 0 mm to 125 mm (6 HPBs), Figure 3.24. In tests 25–28, the HPB arrangement was a central HPB at 0 mm then HPBs at 25 mm spacing from 100 to 200 mm (6 HPBs), see Figure 3.25.

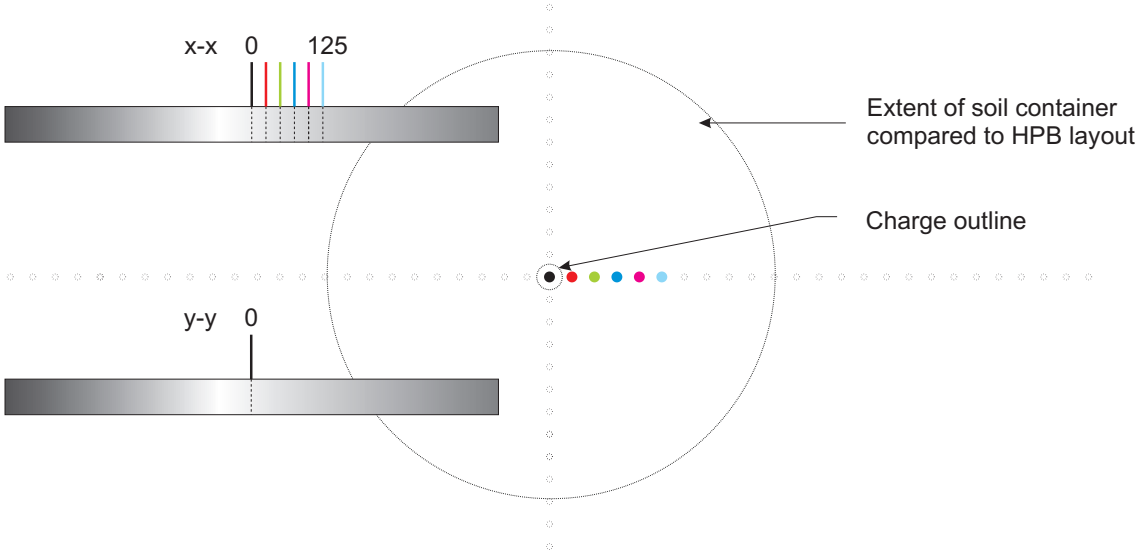

Figure 3.24: HPB set–up for tests 19–24.

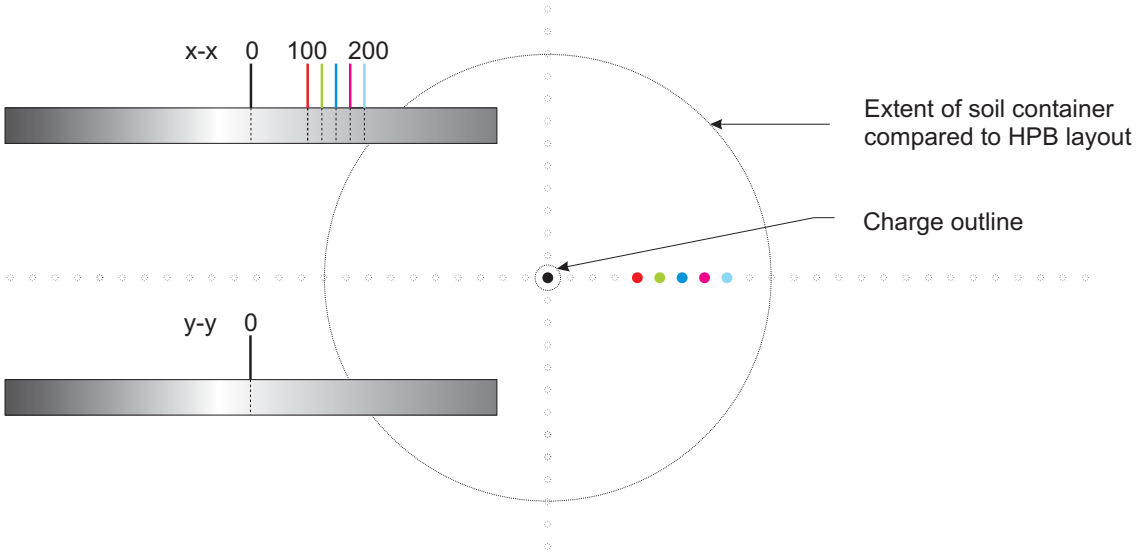

Figure 3.25: HPB set–up for tests 25–28.

The charge configurations for all tests were identical, and are given in Table 3.5. The 53 g PE–4 charge with case top removed was initiated at the base with a non–el detonator. Stand-off remained at 69 mm with an overburden of 28 mm.

Table 3.5: Buried explosive commissioning Tests 19–28.

Tests	Soil condition	Mass (g)	Case/ geometry	Detonator orientation	Detonator type	SO (mm)	OVB (mm)
19 – 28	LB	53	No top	Base	Non–el	69	28

The central and 25 mm HPB fall within the radius of the charge case (27 mm). Figure 3.26a demonstrates that a majority of pressure develops within the boundary of the charge. Pressure measurements outside the charge diameter drop off rapidly between 25 and 50 mm where peak pressure is approximately 30% of the central HPB with a progressive reduction thereafter.

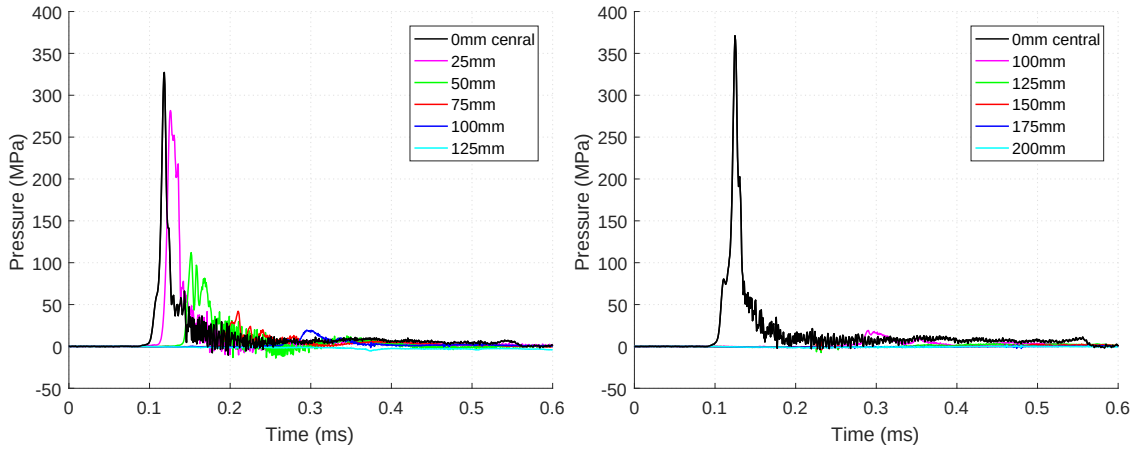

(a) Pressure–time,Test 24

(b) Pressure–time,Test 28

Figure 3.26: Pressure–time histories of Tests 24 and 28 showing consistency between tests at the central HPB and significant drop off in pressure at bar locations between 100–200m.

Figures 3.27a, 3.27b, 3.27c, 3.27d, show pressure–time data from Tests 25, 26, 27 and 28 where the results of the central bar have been left out, so that data at 100–200 mm bars is seen more easily. At 100 mm pressure drops consistently to below 10% of that at the central HPB falling between 20–30 MPa. Pressure histories at 125 mm are significantly lower in magnitude (approximately 10–20 MPa peak pressure) but longer in duration. From 125 mm variance in peak pressure at identical radial lengths from the target centre significantly increases. Pressure measurements at 175 mm and beyond fall below 500 kPa where signal–noise may begin to overwrite genuine pressure features.

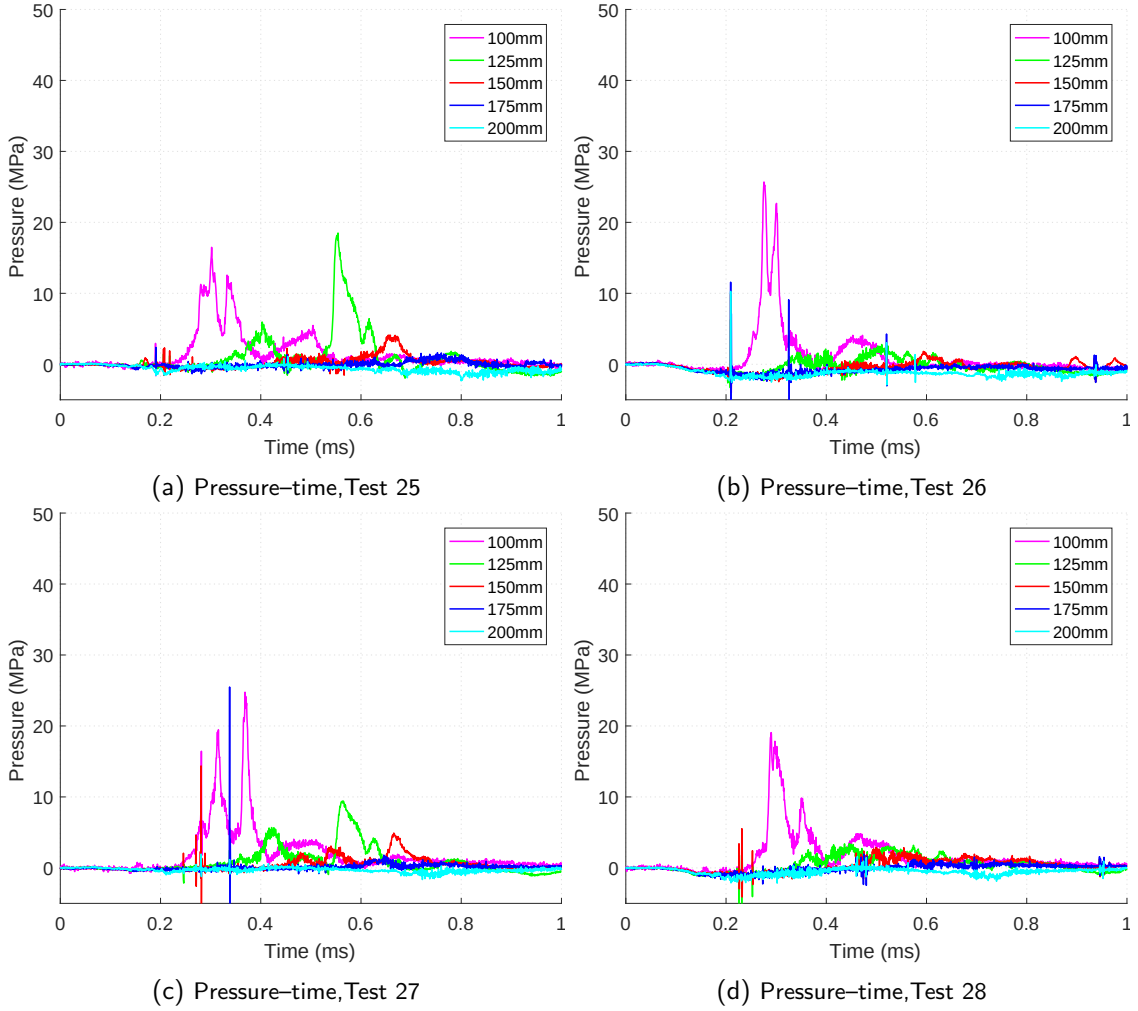

(a) Pressure–time, Test 25

(b) Pressure–time, Test 26

(c) Pressure–time, Test 27

(d) Pressure–time, Test 28

Figure 3.27: Pressure–time histories of Tests 25–28 showing variation in pressure distribution at bar locations between 100–200m.

Repeatability and consistency at the 100 mm bar locations has been significantly less than in Tests 11–14 with a 78 g charge. This may, in part, be due to the 'output geometry' of the smaller 53 g charge where the depth of detonator embedment is lower which may be affecting initiation of the charge. This becomes disproportionately important when the lower shock intensity produced by a non–electric detonator is compared to the output from a high intensity electric detonator. For this reason, returning to the larger 78 g charge with a greater standoff will protect instrumentation and improve scaled resolution between HPBs with the aim of improving data quality.

Tests 29–33

Tests 29–33 repeat the investigation of pressure variance with increased distance from the plate centre, as studied in Tests 19–28. The charge mass and standoff were increased to 78 g and 140 mm, test conditions are presented in Table 3.6. The rationale behind increasing the charge size was to improve scaled resolution between HPBs and overall data quality. Increasing standoff was done to protect the instrumentation, as explained above in the preamble to Tests 15–18. HPBs were arranged in a single radial array from the charge centre at 25 mm intervals between 0 and 175 mm, Figure 3.28.

Table 3.6: Buried explosive commissioning Tests 29–33.

Test number	Soil condition	Mass (g)	Case/ geometry	Detonator orientation	Detonator type	SO (mm)	OVB (mm)
29-33	LB	78	No top	B	Non–el	140	28

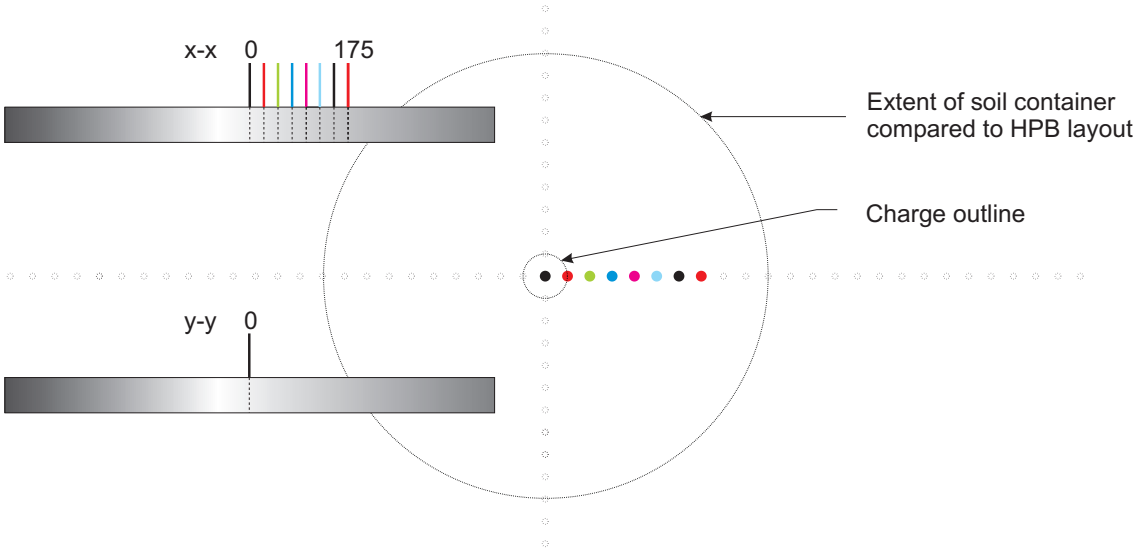

Figure 3.28: HPB set–up for Tests 29–33.

From the observations discussed in Tests 19–28, the charge mass and standoff were changed to 78 g PE–4 at 140 mm for Tests 29–33. It was hoped that increasing the net explosive quantity (NEQ) and standoff would increase data quality, whilst the detonations are almost certainly more consistent. No notable improvement in test–to–test consistency was seen when compared to tests 19–28.

Tests 29, 31 and 32 (Figures 3.29a, 3.29c and 3.29d) show similar features and maximum peak pressures. This peak pressure has been characterised consistently in earlier tests as being

localised at the centre, particularly within the charge diameter. In Tests 30 and 33, the peak pressures at the target centre and around the charge are approximately 50 MPa lower when compared to tests 29, 31 and 32.

By increasing the standoff in Tests 29–33, small inaccuracies in charge placement may be more pronounced than in previous test series. For example, if the vertical axis of the charge and central HPB are not coaxial, the peak pressure will not be recorded at the central HPB. Furthermore, arrival times may be affected and the pressure distribution may change. Issues with co–axial alignment of the charge and HPB could be resolved if the pressure distribution was known in two axes.

Consistent trends appear to emerge when viewing the data from Tests 29–33 as a whole. The pressure waveforms show fairly consistent pressure and arrival times between 0–25 mm, subsequently a rapid drop off at 50 mm and finally a progressive fall off beyond this. With a 78 g charge and 140 mm standoff, pressures decay in a progressive manner with arrival times more evenly spaced when compared to shorter standoffs. Loading produced by the 78 g charge appears more consistent between tests. This can be seen particularly beyond 75 mm where the pressure witnessed at further radial bars is brought out of the signal–noise loading range of the HPB, improving the scaled resolution between HPBs and improving data quality when compared to tests with a 53 g charge at shorter standoffs. In both the 53 g and 78 g tests arrival time and peak pressure becomes more variable with increasing distance from the target centre.

Data recorded at the 0–100 mm bar locations has been the most consistent throughout the commissioning tests. Furthermore, the quality and magnitude of these results are such that features from the interaction between soil ejecta, detonation products and target plate are most easily observed. Beyond 100 mm, pressure–time histories vary more in both magnitude and time of arrival. Moreover, the ratio of signal–noise present in the data increases as the magnitude of the recorded signal is reduced which may begin to obscure genuine artefacts. For these reasons, further tests in this study will deploy HPBs up to a maximum of 100 mm radius from the centre of the target. Some variance between tests still occurs at radii between 0–100 mm and it is not clear if this variance is local to the measurement location or distributed identically for the same swept radius. For this reason four radial arrays at 90 degree intervals will be used in the parameter study (see Chapter 4). Bars will be placed along the x axis between -100 to -25 and 25 to 100 mm with a central bar at 0 mm. Similarly, along the y axis, bars will be placed in the -100 to -25 and 25 to 100 mm locations, leading to 17 HPBs in total. This increase in resolution of instrumentation directly above the charge provides additional data points which can be used to highlight loading variation above the charge increasing data quality and redundancy.

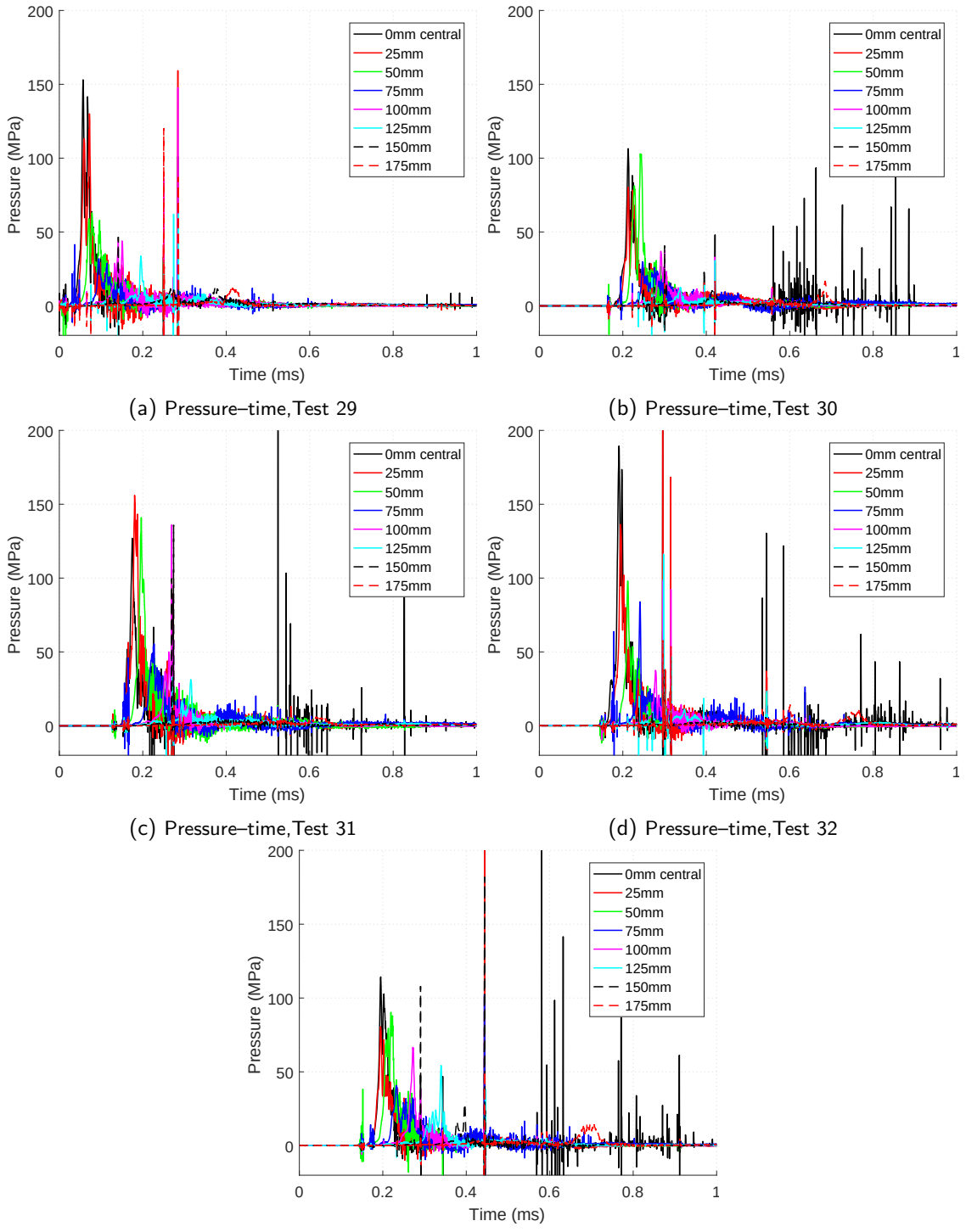

(a) Pressure–time, Test 29

(b) Pressure–time, Test 30

(c) Pressure–time, Test 31

(d) Pressure–time, Test 32

(e) Pressure–time, Test 33

Figure 3.29: Pressure–time histories of Tests 29–33 showing consistency between 0–75 mm and significant drop off and increased variation in pressure at bar locations between 100–175 mm.

3.6.4 Soil container boundary conditions

Test 34 investigated the effects of the soil container boundary conditions on pressure–time histories to confirm that scaling of the soil container was suitably applied. A soil container of 1/2 scale dimensions (to STANAG [8] level 2) was used, increasing the diameter from 0.5 m to 1.0 m and depth from 0.375 m to 0.75 m. The HPB layout was a single radial array at 25 mm resolution between 0 and 100 mm (5 bars), cf. Figure 3.30. The charge configuration from Tests 29–33 was repeated in Test 34 with a 78 g PE–4 charge with cap removed, base detonated with a non–electric detonator with an overburden of 28 mm and 140 mm standoff. This will allow a direct comparison of the 1/4 scale soil container used in Tests 29–33 against the larger 1/2 scale soil container used in Test 34.

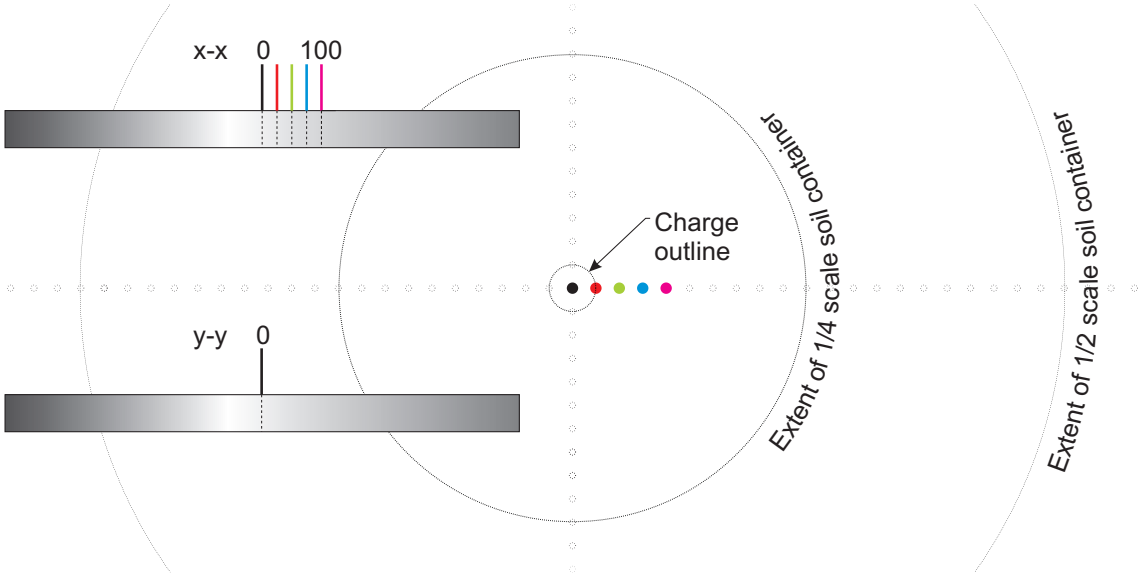

Figure 3.30: HPB set–up for Test 34.

The data from Test 34 was mapped onto the 0 mm, 25 mm 50 mm, 75 mm and 100 mm bars from Tests 29–33 to observe the effect of increasing the soil container volume at the measurement locations of interest to this study 0–100 mm. An inspection of the pressure–time histories in Figures 3.31a to 3.31e shows no notable differance between the 1/2 scale soil container in Test 34 and the 1/4 scale container used in Tests 29–33. Magnitude, arrival time and duration of Test 34 are bounded by the data from Tests 29–33 with the exception of the 25 mm HPB location, Figure 3.31b. At this location, the pressure feature arrives approximately 0.01 ms later than the pressure data from the 1/4 scale tests. A time correction of -0.01 ms was applied to the 25 mm bar of Test 34, which is within typical test–to–test arrival time variance. Pressure histories from a 1/2 and 1/4 scale soil container at measurement locations between 0–100 mm have shown no notable difference confirming that, over the measurement area of interest, the soil container does not affect the output from a 78 g PE–4 shallow buried charge.

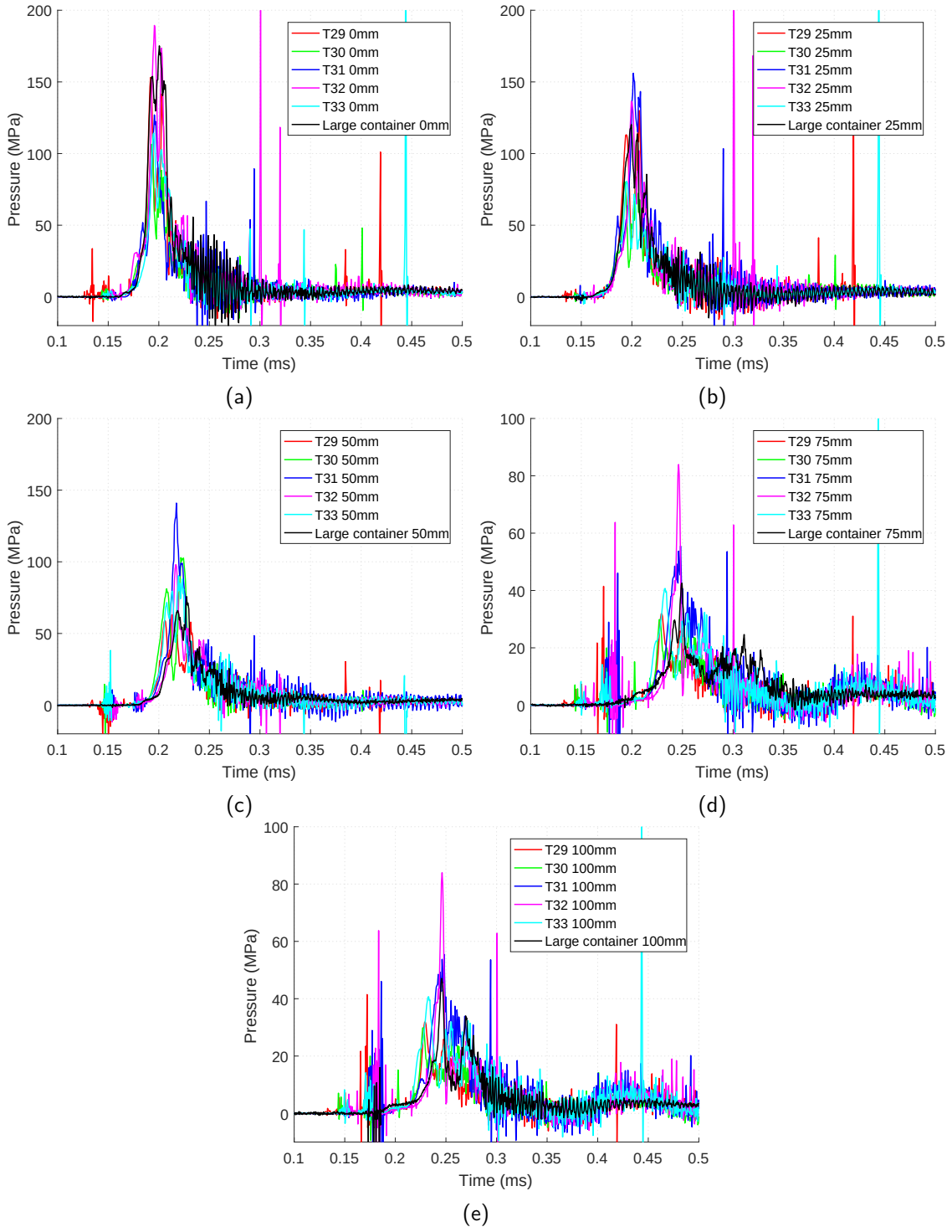

Figure 3.31: Pressure–time histories of Tests 29, 30, 31, 32, 33 and 34 comparison of bar locations at the central bar and 25 mm , 50 mm 75 mm and 100 mm bar locations; (a) Central HPB for Tests 29–34, (b) 25 mm HPB from tests 29–34, with time correction of -0.01 ms to Test 34, (c) 50 mm HPB from tests 29–34, (d) 75 mm HPB from tests 29–34, (e) 100 mm HPB from tests 29–34.

3.6.5 Dispersion in the Hopkinson Pressure Bars

Dispersion of the signal in a HPB was investigated in tests 35–40. A HPB was fabricated with two gauge stations at different distances from the impact face. The gauge station typical of all HPBs used in this study is at 250 mm from the impact face of the bar, whereas the second gauge station was placed at 500 mm from the impact face.

The signal will be dispersed differently between 0–250 mm and 250–500 mm. Higher frequency components, travelling down the bar at lower velocities, will have moved behind the faster moving components. For input signals with frequencies above the mode two cut–off frequency, the original input signal cannot be fully recreated by redistributing the frequency packets from the most advanced techniques available [39]. Whilst dispersion correction is possible for frequencies below the mode two cut–off, the exact energy in higher modes is unknown. The intent therefore is to demonstrate the effect of dispersion for this particular test set–up and comment on the impact that dispersion phenomena have on the results of this study.

In Tests 35–39 a 78 g PE–4 charge was buried with 28 mm overburden at 140 mm standoff, see Table 3.7. The charge was initiated at its base with a non–electric detonator, and the case top was removed. LB soil was used as the confining medium with a bulk density of 1650 kg/m^{-3} and a moisture content of 2.45%. In Test 40 an identical charge was used as Tests 35–39, however a free–air charge detonation was used, likely resulting in a high frequency, short duration peak pressure where the effects of dispersion might more clearly be seen.

Table 3.7: Dispersion within the HPBs – Tests 35–40.

Test number	Soil condition	Mass (g)	Case/ geometry	Detonator orientation	Detonator type	SO (mm)	OVB (mm)/ notes
35	LB	78	No top	Base	Non–el	140	28
36	LB	78	No top	Base	Non–el	140	28
37	LB	78	No top	Base	Non–el	140	Power failure
38	LB	78	No top	Base	Non–el	140	28
39	LB	78	No top	Base	Non–el	140	28
40	air	78	No top	Base	Non–el	168	No soil

Figures 3.32a–3.32e provide a comparison of data at the 250 mm and 500 mm gauge location for Tests 35–40. It is a useful concept to interpret the pressure in these graphs as a stress wave in the bar travelling from the right to the left of the graph, where the lowest frequency components of the stress pulse make up the leading edge of the pressure pulse. Meanwhile, higher frequency components travelling at lower velocities in the bar will arrive progressively later behind the leading edge the further down the bar the stress pulse travels. This separates

the high and low frequency components out in time as the stress pulse travels along the bar. One effect of this may be that the magnitude of peak pressure appears to reduce the further away from the impact face the stress is measured.

In Test 36, 38, 39 the initial peak seen at the 250 mm gauge station appears to have dispersed and translated in time to the second peak. Test 35 appears to have been more significantly affected by dispersion at the second peak, which indicates much of the second peak is made up of higher frequency components that have dispersed between the 250–500 mm gauge stations. Much of the second peak at 0.2 ms appears to have dispersed to approximately 0.21 ms at the 500 mm gauge station implying that the second peak is made up of higher frequency components.

Test 40 had an identical charge to tests 35–39 but was detonated in free–air. In this test more significant dispersion between the 250 and 500 mm gauge stations is seen than in shallow buried tests. The initial peak pressure is reduced from 150 MPa to 65 MPa. This may indicate that frequency components contained at the leading of the air blast contain some very high frequency components. These higher frequency components will separate more over a shorter duration or distance in the HPB.

The frequency of input pressure in soil tests appears to be of a more narrow bandwidth when compared to the free–air test. Therefore, the impact of dispersion on the shallow buried charge tests appears to be lower than in the free–air test. An argument could be made that this is due to the soil dampening the frequency output of the explosive. Increasing the standoff of the buried tests may have further increased the accuracy of the measurement when dispersion is taken into consideration. By reducing higher peak pressures and therefore higher frequency components (when compared to shorter standoffs in Tests 7–28), there is a reduction in the dispersion witnessed using the longer stand–off.

The pressure waveforms of the dispersed signal show that the general form is relatively unaffected and, for buried tests, peak pressure remains similar. The specific impulse history for each test is shown in Figure 3.33 demonstrating little difference between the 250 and 500 mm bar location, meaning that momentum transfer is largely unaffected by dispersion. This demonstrates that in this study, where a primary aim is identification of general features in the load, HPBs provide robust, reliable and accurate measurements. For minimal dispersion effects, the gauge station 250 mm from the impact face of a HPB is suitable. This distance was derived from target thickness, protection requirements for cables and the need for access for in–situ repairs.

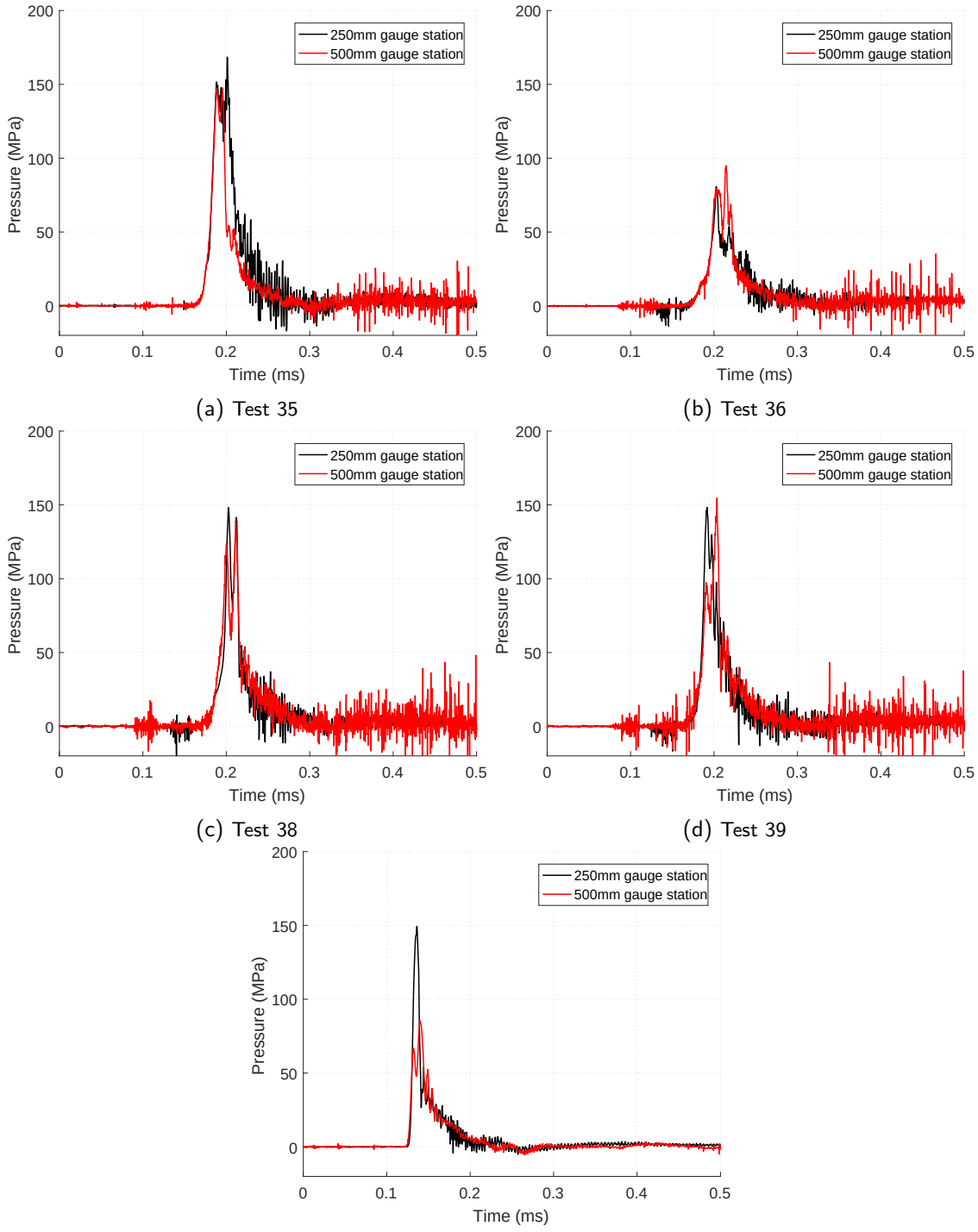

(a) Test 35

(b) Test 36

(c) Test 38

(d) Test 39

(e) Test 40

Figure 3.32: Pressure waveforms of Tests 35, 36, 38, 39 and 40 at the central HPB. Two gauges placed on each gauge station at 250 mm and 500 mm from impact face. These data provide comparison of dispersion at the HPB for soil (Tests 35–39) and air, Test 40. Arrival time of the 500 mm bar has been corrected by 0.05 ms such that the pressure waveforms are overlain.

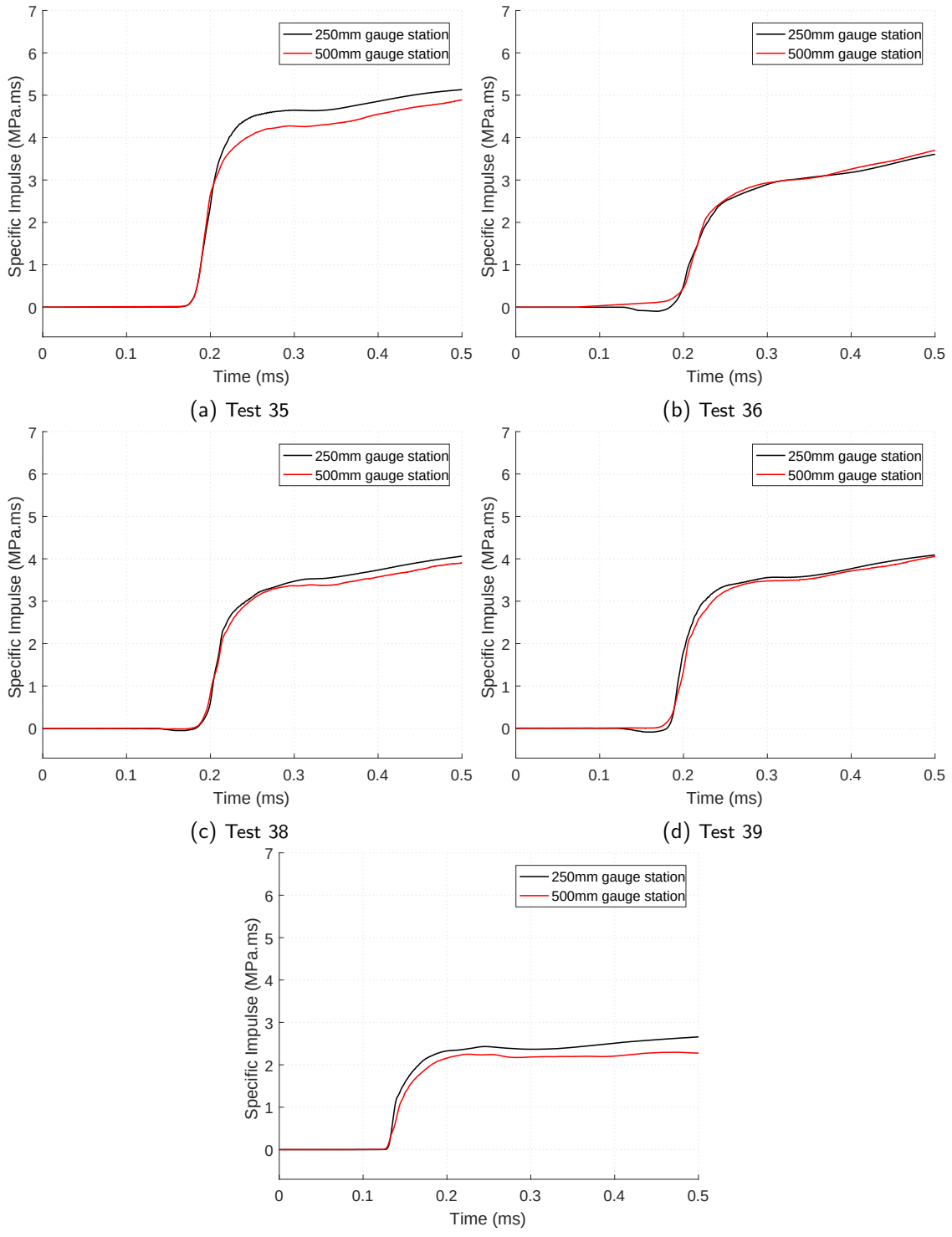

(a) Test 35

(b) Test 36

(c) Test 38

(d) Test 39

(e) Test 40

Figure 3.33: Specific impulse histories of Tests 35, 36, 38, 39 and 40 at the central HPB. Two gauges placed on each gauge station at 250 mm and 500 mm from impact face. These data provide comparison of dispersion at the HPB for soil (Tests 35–39) and air, Test 40. Arrival time of the 500 mm bar has been corrected by 0.05 ms such that the impulse histories are overlain.

3.7 Discussion of final equipment and charge configuration

This chapter has described the development of a test apparatus for the characterisation of shallow buried blast loading where discrete spatial and temporal resolution of blast pressure was achieved using an array of HPBs. The CoBL apparatus has been verified against the empirical air blast predictive tool ConWep [13] showing good agreement between predicted and test data. It was shown that non–electric detonators more closely resemble the pressure data from ConWep than electric detonators. The detonator yield was not included in the ConWep prediction, and so this variance may be due to the higher yield of the high intensity detonator. Non–electric detonators will be used for all further tests in this study due to the closer match with predicted results and for the significant increase in safety when using base detonation.

At a $1/4$ scale, the charge specified at STANAG level 2 [8] requires a 78 g PE–4 charge in a 3:1 aspect ratio formed into a cylinder with full encasement. Standoff between the soil surface and target is 69 mm with 25 mm burial depth. Explosive engineering was scrutinised to develop the most suitable charge configuration for this study. Consideration was given to instrumentation survivability, data quality and repeatability resulting in six iterations of the charge design informed by test data. The final charge configuration is a 78 g PE–4 charge formed into a 3:1 cylinder. Two variations of the charge specified in STANAG level 2 [8] were necessary for data quality and instrument survivability. The charge encasement top was removed as it appears to obscure data in the pre–cursor shoulder. Burial of the charge will continue with 28 mm of overburden – the charge is at the same relative position in the soil container but accounts for 3 mm of the removed case top. Standoff was increased to 140 mm increasing survivability of the instrumentation, data quality and effectively increase resolution of the measurement plane.

The Hopkinson Pressure Bar array has been refined for the charge configuration developed in this study. The bar array was developed over 4 iterations informed by test data. It is not clear if variance in pressure and arrival time beyond the charge diameter is local to the measurement location or distributed similarly for the same swept radius. For this reason, bars will be placed in four radial rays at 90 degree intervals at 25 mm intervals between 0–100 mm. 17 HPBs will be used in total increasing spatial resolution directly above the charge, increasing redundancy and providing more data points for assessment of the pressure distribution across the measurement plane. This array configuration, pictured in Figure 3.34, will be tested in Chapter 4.

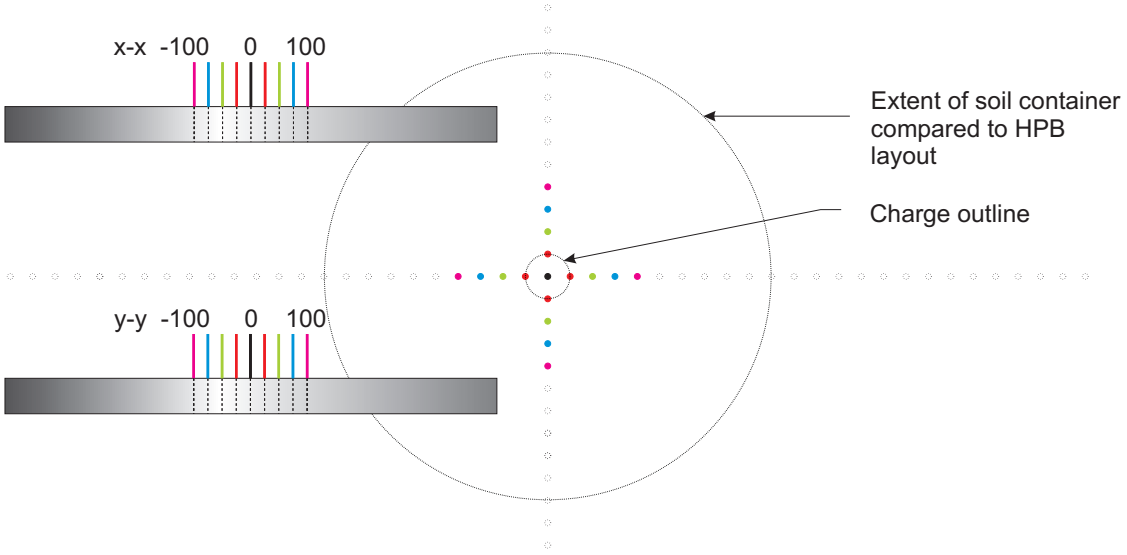

Figure 3.34: Final HPB arrangement.

Significant consideration was required to develop soil preparation, charge burial and soil container alignment of the test sample. Soil moisture content and bulk density are controlled within $\pm$ 0.1% and $\pm$ 5kgm^{-3}, respectively. This is the tightest control in a study of this kind and soil containers outside of these final tolerances were rejected from testing. Integrity of the soil properties was maintained during charge burial by strict control of the overburden material used to replace soil removed from the soil bed for charge placement. Alignment of the charge in the soil bed was achieved with a tolerance of $\pm$ 1 mm. Alignment of the soil container in the CoBL apparatus was achieved with alignment screws ensuring soil container alignment was achieved within $\pm$ 1 mm.

The 1/4 scale soil container boundary conditions were checked for the measurement plane of 0–100 mm by comparison of a 1/2 scale soil container test. It was confirmed that the 1/4 scale soil container does not appear to affect measurement between 0–100 mm radii. Dispersion was checked by placing multiple gauge stations on a single HPB. It was observed that some dispersion occurs in the soil tests. For this reason, the gauge station is placed as close as practical to the impact face of the HPB. More significant dispersion was witnessed on the free–air tests where it may be necessary to apply dispersion correction to fully assess the impact of dispersion on the test.

Continuation of this study will provide baseline data on the typical soil configuration used in commissioning tests but will include the four ray HPB array. Following this, the study will progress by investigating the effects geotechnical parameters, burial depth and standoff in Chapter 4.

A table of baseline parameters used in the continuation of this study are presented in Table 3.8.

Table 3.8: Standard parameters used in parameter study. The parameters presented will be make up Series D as baseline tests. Other series will see a variation of these parameters.

Parameter	Value	Unit
Soil	Leighton Buzzard 14/25 grit	-
Density	1635	kgm^{-3}
Dry density	1600	kgm^{-3}
Moisture content	2.45	%
Burial depth	28	mm
Stand off	69	mm
Explosive material	PE-4	-
Charge geometry	3:1 cylinder	-
Charge mass	0.078	kg
Charge diameter	57.1	mm
Charge height	19	mm
Case	3 mm thick PVC with no top	-
Detonator	Non-electric	-
Detonator orientation	Base	-
HPB array x–x	9 HPB $\pm$ 100	mm
HPB array y–y	8 HPB (excluding central) $\pm$ 100	mm

Chapter 4

Parametric study and discussion

4.1 Introduction

This chapter contains the results and discussion from a detailed parametric study aimed at providing clear, definitive experimental evidence of the exact mechanisms present at the loaded face of a target following the detonation of a shallow buried charge.

The parametric study comprises five main parts, labelled Part One – Part Five, based on 11 distinct test series, labelled Series A–K. In Part One, experiments investigate the effect of the charge case and influence of charge shape. Part Two investigates the interaction of the detonation products in soil with increasing levels of soil confinement. In Part Three the effect of increased moisture content is studied. Part Four will investigate the effect of changing particle size distribution of a saturated soil. Part Five will investigate behaviour from changing the standoff between the soil surface and target.

4.2 Parametric study test general arrangement

The parameter study will use the four perpendicular arrays of HPBs at intervals of 25mm from 0-100mm co-axial with the target plate centre (17 HPB in total). Increasing the HPB array to four radial rays increases the statistical significance of each tests, whilst allowing observations on the probabilistic nature of the soil/air breakout to be observed, see Figure 3.34.

Prior to beginning the parametric study a short series of free–air tests (41–44) were conducted to assess case confinement, the test configurations are presented in Table 4.1.

Table 4.1: Part one tests - Influence of charge encasement and shape.

Test number	Encasement	Charge shape	SO (mm)
41	No case	3:1 cylinder	168
42	No top	3:1 cylinder	168
43	Full case	3:1 cylinder	165
44	No case	Sphere	168

In the parametric study, a PE-4 cyclindrical charge with a mass of 78 g was used throughout testing. Non–electric Davey–detonators were used to initiate the PE–4 charge at its base, and nylon 66 stanchion resined at the charge's base was used to fix the detonators position during burial. The baseline charge was formed into a 3:1 cylinder in a 3 mm thick PVC case with an internal diameter of 57.1 mm and a height of 19 mm.

The baseline soil conditions for the parameter study will mirror those developed in Chapter 3. Table 4.2 provides an overview of the eleven test series. Baseline LB tests in Series D were conducted at moisture contents 2.45%. A dry density of 1600 kgm^{-3} and bulk density 1635 kgm $^{-3}$ was consistent throughout testing with baseline soil parameters (Series B, C, E, J and K). In Series F and G, LB moisture contents of 4.76 and 25% were used where dry bulk density was maintained at 1600 kgm^{-3} with bulk densities of 1670 kgm^{-3} and 1990 kgm^{-3} respectively. STANAG soil used in Series I was prepared with a dry density of 1806 kgm^{-3}, when fully saturated the bulk density was 2100 kgm^{-3}.

A baseline burial depth of 28 mm was used throughout the parametric study. In Series E the burial depth and therefore overburden thickness was increased to 53 mm. Standoff between the soil surface and target was set at 140 mm. Stand off was reduced in Series J to 105 mm and increased in Series K to 175 mm.

Table 4.2: Series A-K - Investigation of explosive-sand interaction.

Tests	Series	Soil type	w(%)	Bulk density	Dry density	Variable
45-46	A	Air	-	-	-	No soil
47-48	B	LB	2.45 %	1635	1600	Soil to charge base
49-50	C	LB	2.45 %	1635	1600	No overburden
51-57	D	LB	2.45 %	1635	1600	Baseline
58-62	E	LB	2.45 %	1635	1600	Overburden
63-67	F	LB	4.76 %	1670	1600	Moisture content
68-72	G	LB	25.0 %	1990	1600	Full saturation
73-74	H	Water	100 %	-	-	Water
75-81	I	STANAG	14.0 %	2100	1806	Soil type
82-86	J	LB	2.45 %	1635	1600	Standoff reduction
87-91	K	LB	2.45 %	1635	1600	Standoff increase

4.3 Data capture and processing

HPB strain data were recorded using 14-Bit digital oscilloscopes at a sample rate of 3.12 MHz. Recordings were triggered via a voltage drop in a breakwire embedded in the charge to synchronise the traces with the time of detonation. 50 microseconds have been subtracted from the timebase of every recording such that the arrival time of each pressure pulse corresponds to the arrival time at the bar face rather than the arrival time at the strain gauge location as recorded.

In all tests, pressure was recorded at each radial location by four separate bars, with the exception of the central bar which was common to each array. In the pressure histories presented in this chapter, indicative results are provided for a single array for each series for clarity of presentation. The specific impulse was calculated from cumulative numerical integration of the pressure traces with respect to time.

High-frequency oscillations can be seen in the traces as a result of Pochhammer-Chree dispersion [39]. At this stage, this physical dispersion effects have not been corrected for: although for this arrangement, Pochhammer-Chree dispersion results in a loss of definition of transient pressure features with durations in the order of 4 μs (along with the oscillations noted previously), the general forms of the pressure-time and impulse-time traces remain unaffected.

The high frequency oscillations due to bar dispersion and signal noise seen in Chapter 3 are addressed in the signal processing of the pressure waveforms for the parameter study in this chapter. The rationale behind using a filter in these results is to highlight the general pressure

waveform of each series. A Butterworth filter was selected due to its flat frequency response meaning that the amplitude of passband frequencies components remains unaffected by the filter [37]. A consequence of this flat passband is that the transition between passband and stopband has a significant gradient when compared to a Chebyshev filter [37]. This means that some stop band frequencies pass the filter at a lower amplitude. However, the pressure waveform frequencies are orders of magnitude lower than the signal noise frequency. Therefore, the filter frequency can be trimmed lower than the noise frequency components such that they are fully removed. Whilst this is not the intended use of the filter, this achieves a noise free signal whilst maintaining the original amplitude of the passband/ pressure waveform signal.

A fourth-order Butterworth filter with a cutoff frequency half that of the noise frequency was used to process the signals from the HPBs. The frequency of the signal noise component was calculated for each test by taking the reciprocal of a single noise oscillation[1]. A fourth-order filter was selected due to its compromise between sharper cutoff than lower order filters and simplicity of implementation when compared to higher orders. Halving the noise frequency was necessary as some frequencies at or above the filter frequency pass through the filter albeit at a lower amplitude due to the gradient between passband and stopband roll off.

High-speed video (HSV) equipment was available on loan from DSTL-Porton Down for some tests. Filming was conduced with a Photron SA-Z HSV camera with a 105 mm f2.8 Nikon lens which was housed in a protective structure in each of the tests. The events were filmed at a resolution of 1024x184 at an aperture of f/11 with a frame rate between 100,000 and 140,000 and an exposure time of between 1/400,000 s and 1/4,032,000 s. The framing rate of the camera was determined from the estimated velocity of the soil ejecta and exposure duration was determined form an estimate of the light available, both from the halogen lighting and from incandescence of the detonation products. The HSV camera was positioned level with the soil surface and triggered with a break wire embedded in the explosives. Here, HSV data is used to support the analysis of pressure waveforms as a visual diagnostic for the observation of general behaviours in the loading phenomena.

[1]Single oscillations were determined by visually inspecting the time between noise peaks.

4.4 Part One – Influence of charge encasement and shape

4.4.1 Introduction

Part One of this parametric study is focused on quantifying the effects of confinement of the charge from 3 mm thick PVC encasement and observing the effect of detonation product shaping and channelling towards the target. Four tests outlined in Table 4.3 assess the effect of charge case confinement and shape.

Table 4.3: Part One - Investigating the effect of charge confinement and shape.

Test number	Encasement	Shape	SO (mm)
41	No case	3:1 cylinder	168
42	No top	3:1 cylinder	168
43	Full case	3:1 cylinder	165
44	No case	Spherical	168

All charges were constructed from 78 g of PE-4 with a stand-off, measured between the top of the charge and measurement plane, of 168 mm. In all tests, the explosive was initiated at its base with a non-electric detonator. All explosives were supported on a 18 mm thick timber plyboard frame supported from the target plate by ply hangers, see Figure 4.1.

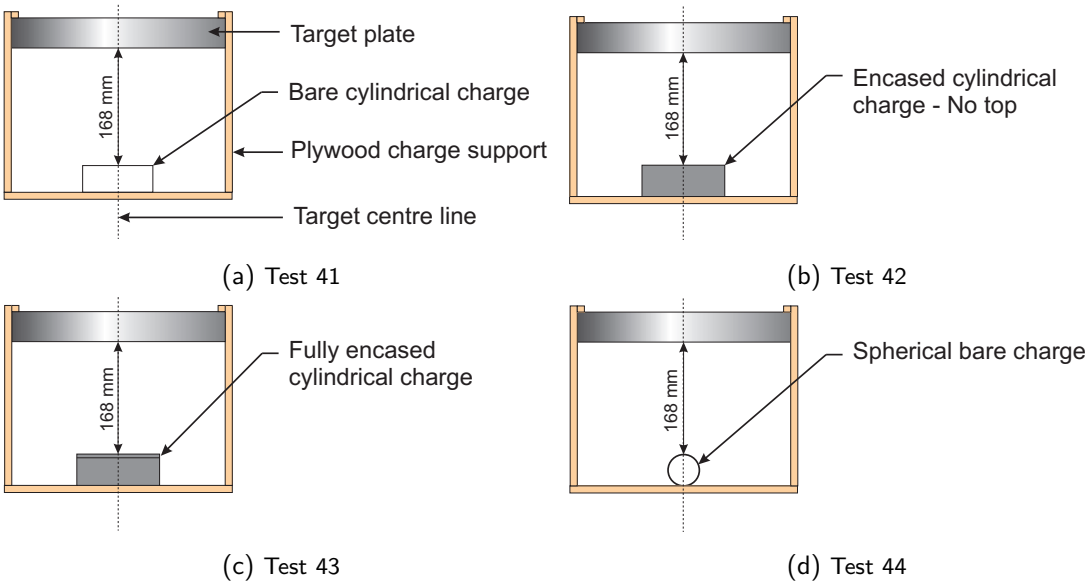

Figure 4.1: Investigation of charge encasement confinement and shape, charge configuration for tests 41(a), 42(b), 43(c) and 44 (d). Note that these diagrams are not to scale and the relative dimensions of the target and charge are indicative only.

Test 41 used a bare cylindrical charge without encasement and serves as the 'null' condition with no confinement of the charge other than that offered by the plywood charge support (which was judged to be negligible), see Figure 4.1a. This test aims to highlight the early stage expansion of the detonation products without the confinement of the charge case used in the buried charge tests. Test 42 serves as the control test with the charge encased at the base and sides with the case lid removed, and is shown in Figure 4.1b. This forms the standard charge configuration used in all buried explosive tests. As discussed in Chapter 3, the lid was removed to reduce signal noise caused by interaction between the detonation products and charge case shown in Tests 14-18. Test 43 aims to highlight the confinement effects of the fully encased charge at the final test geometry, cf. Figure 4.1c; this test identifies the effect of the case top which led to the decision to remove the case top in Chapter 3 tests. Test 44 uses a spherical charge without case to show the influence of charge geometry, shown in Figure 4.1d.

4.4.2 Pressure waveforms

Figures 4.2 and 4.3 show example pressure-time and specific impulse-time traces from a single array for each test. Specific impulse was calculated from cumulative numerical integration of the pressure traces with respect to time.

The pressure-time histories for Tests 41, 42 and 44, plotted in Figures 4.2a, 4.2c, 4.3a and 4.3c, resemble the well-known 'Friedlander' exponential waveform typically associated with free air blast events [12, 20, 51]. The blast pressures generally exhibit a rapid rise to a single, well-defined peak, followed by an exponential decay afterwards. The pressure waveforms and impulse histories for Tests 41 (bare charge) and 42 (partially confined charge) are very similar. In Test 41 the peak impulse at the 25 mm bar location is higher than that of Test 42 which is due to the longer duration of loading at this bar location. In both Tests 41 and 42 the pressure waveform at the 100 mm bar location appears to resemble more of a static stagnation pressure than a dynamic shock pressure with a more gradual temporal decay.

The pressure waveforms of the fully encased charge in Test 43 appear different to those of Test 41 and 42. The peak pressures at the 0, 25 and 50 mm bar locations are in the order of 3 times greater at the 0 and 25 mm bar locations and 5 times greater at the 50 mm bar location. This indicates that the fully cased charge is significantly more efficient at channelling detonation products towards the target post detonation. The duration of each pressure waveform at the central 50 mm of the target are significantly shorter than the waveforms of Tests 41 and 42. Despite the shorter loading duration, impulse across the central 50 mm of the target is approximately 1.5 times higher. The significance of this impulse increase is that it demonstrates true load enhancement by introducing the charge case top rather than just a modification to the pressure waveform. Therefore more loading is transferred to a target for a fully encased charge. At the 75 mm bar location the pressure is approximately two times

greater than that of Tests 41 and 42. The waveform is approximately half the duration of that in Test 41 and 42. There is a steeper gradient of the impulse history at the at the 75 mm bar location indicating a short duration high frequency load. However, peak impulse is similar to that of Tests 41 and 42. At the 100 mm bar location the pressure waveform resembles the stagnation pressures in magnitude and duration as seen in Tests 41 and 42 which indicates that at this region of the target the stagnated pressure is flowing across the target.

The pressure waveform of a spherical charge, i.e. Test 44 shown in Figure 4.3c, shows a radial distribution of pressure at the target demonstrated by the Friedlander exponential shock waveform seen at each bar location. This wider distribution of loading appears to reduce peak pressure, loading duration and impulse at the target when compared to Test 41, owing to an increase in volume and corresponding decrease in pressure of the detonation products. Further comparison between the spherical and cylindrical charge shows that a there is greater focusing of detonation products towards the centre of the target between 0 and 75 mm from the target centre.

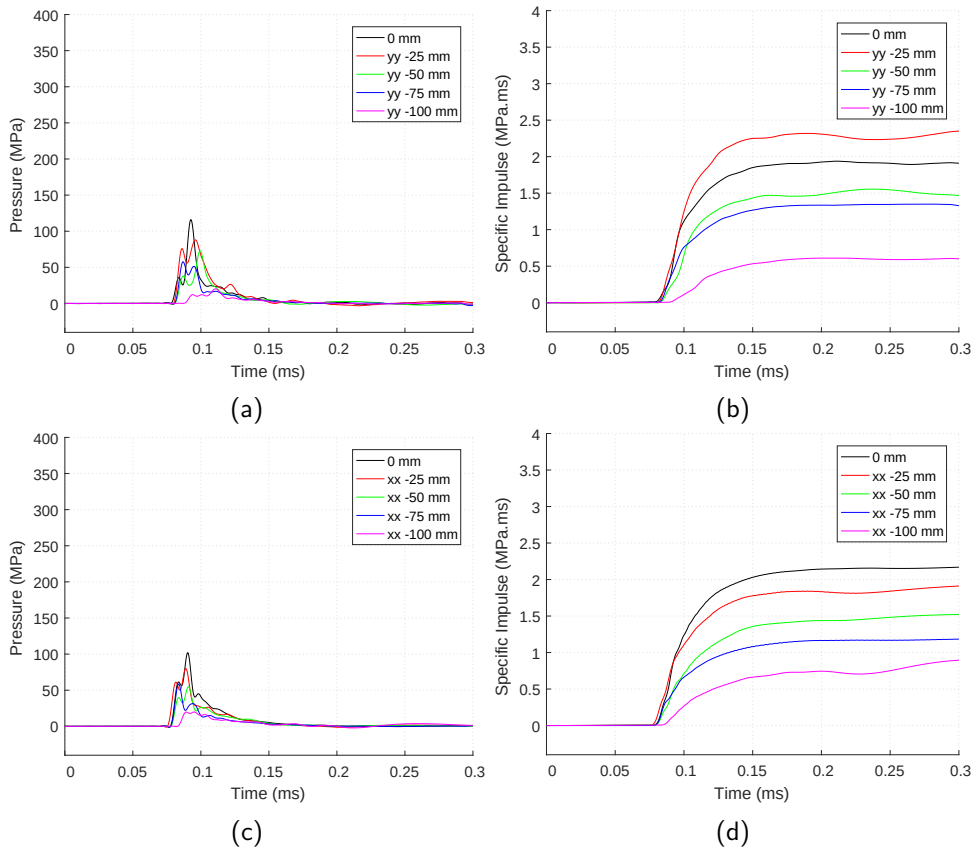

Figure 4.2: Single array pressure waveform and impulse histories for the confinement and shape effect of explosives. Tests 41 pressure (a), specific impulse (b). Test 42 pressure (c), specific impulse (d).

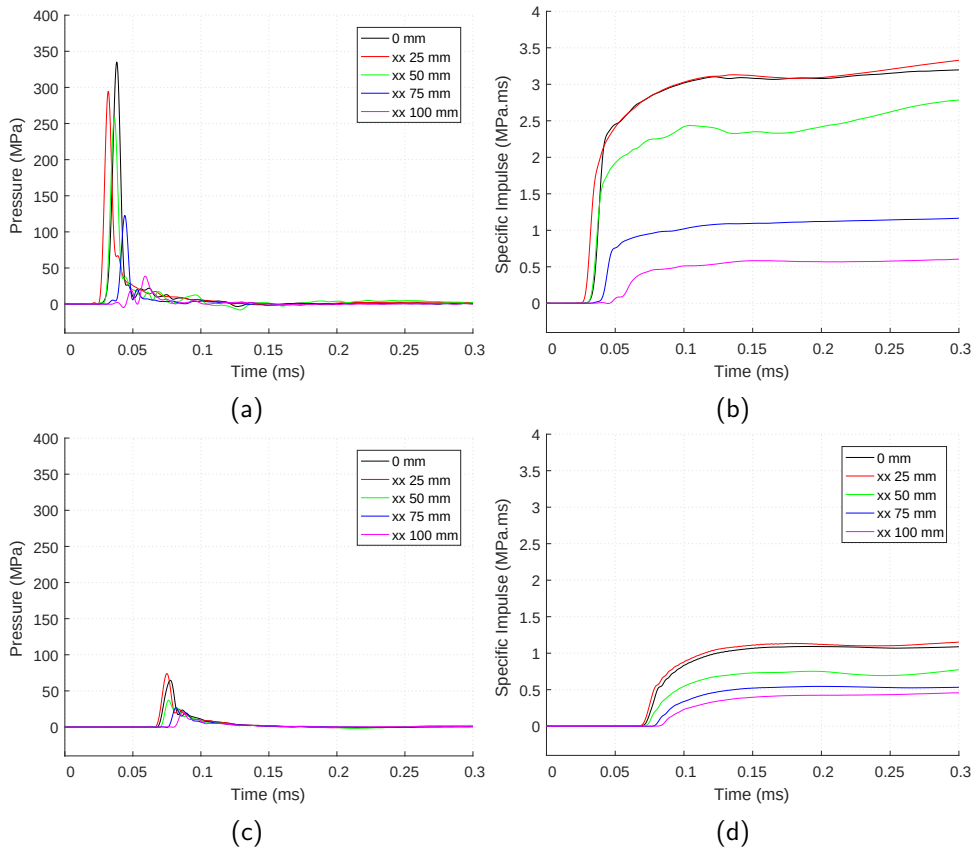

Figure 4.3: Single array pressure waveform and impulse histories for the confinement and shape effect of explosives. Test 43 pressure (a), specific impulse (b). Test 44 pressure (c), specific impulse (d).

4.4.3 High speed video

Figure 4.4 shows select frames from the HSV camera results captured for Tests 41, 42, 43 and 44. The inter-frame time of frames 1–6 is 0.01 ms and for frames 7–11 an inter-frame time of 0.02 ms was used showing each event up to 0.18 ms after detonation.

The HSV shows a clear difference in the emerging shape and luminosity of detonation products for each test configuration. For the cylindrical test without encasement (Test 41) the luminosity and lateral expansion of the detonation products appears to be significantly higher in the region at the diameter of the charge case in Tests 42 and 43. One explanation for reduction of luminosity in this region of the detonation products is that the opaque fragmented charge case reduces light fluence in this region. However, the luminosity and vertical channelling of the detonation products appear similar to that of the partially cased charge of Test 42.

There is significant difference between the partially and fully cased charges from Tests 42 and 43. In the fully confined test (Test 43) vertical channelling occurs over a smaller radius, meaning a reduced volume of detonation products. Furthermore, the luminosity of the detonation products in this vertical channel is lower with exception of the uppermost region. A hypothesis

is that the fragmented charge case confines the lateral and vertical distribution of detonation products. The effect of this is to reduce the volume of the reacting detonation products, thus increasing peak pressure.

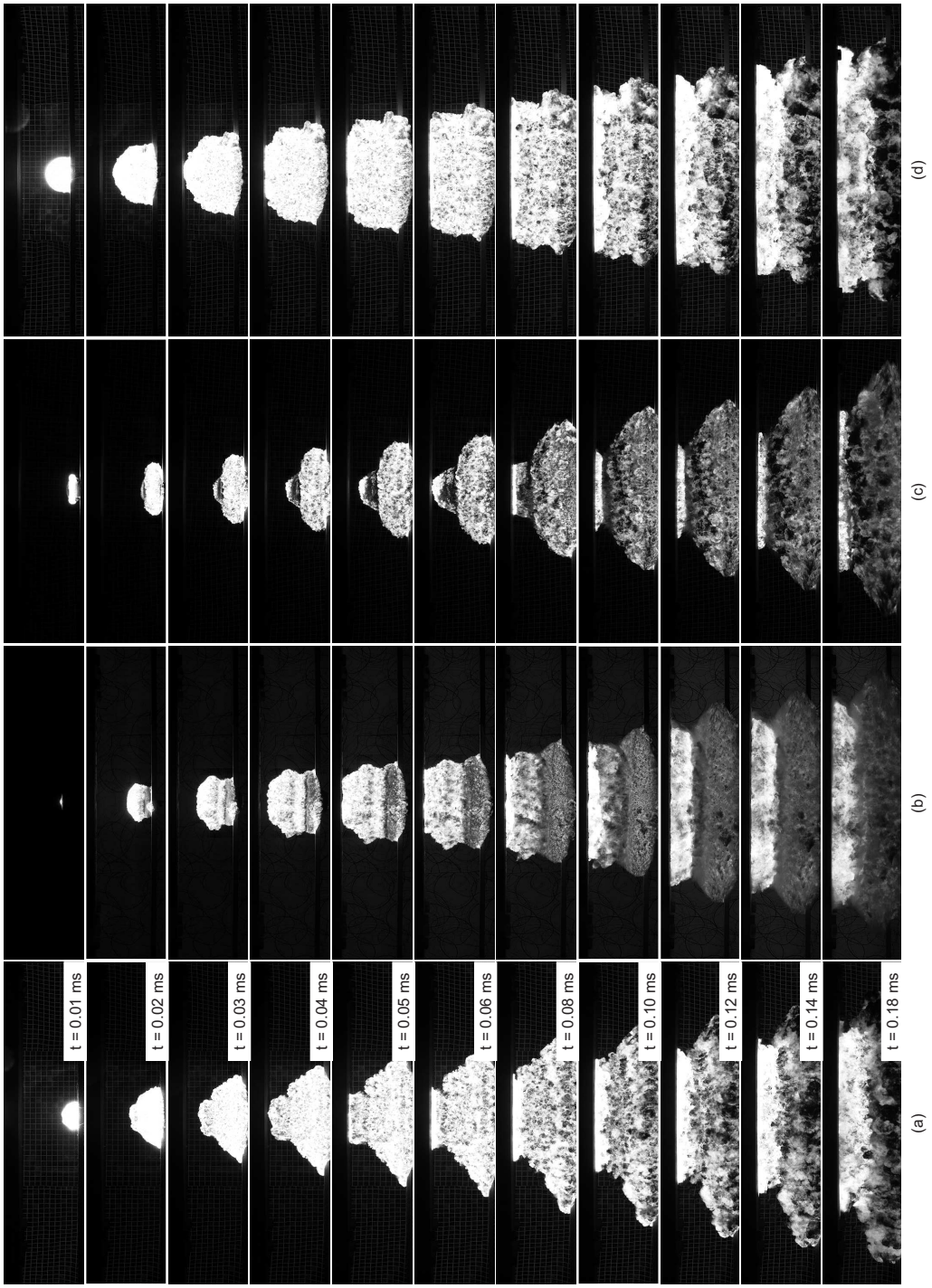

Figure 4.4: HSV results for the confinement and shape effect of explosives, (a) Test 41, (b) Test 42, (c) Test 43, (d) Test 44.

Comparing the bare cylindrical and spherical charges from Tests 41 and 44 it can be seen that cylindrical charge focuses the detonation product over a smaller area of the target plate. In comparison the detonation products of the spherical charge expand radially from the detonation. Due to this, the waveform of the spherical charge appears to distribute across the target more quickly than the cylindrical charge. These observations are consistent with the analysis of Figure 4.3c where a reduction in peak pressure and load duration was witnessed.

4.5 Part Two – Effect of soil confinement on buried explosive output

4.5.1 Introduction

Part Two of this parametric study investigates the effect of lateral confinement of detonation products offered by the surrounding soil mass and how this may affect the loading from a buried charge.

The experimental test plan is summarised in Table 4.4 and shown schematically in Figure 4.5. 18 tests were conducted in total for Part Two of this parametric study; two tests were conducted in each of Series A–C, seven tests were conducted in Series D and five tests conducted in Series E. As a result, there is a total of 34 individual bar recordings for Series A, B, and C, 119 bar recordings for Series D and 85 recordings for Series E.

Table 4.4: Part Two - Tests used to investigate the effect of soil confinement on buried explosive output.

Tests	Series	Soil type	w(%)	Bulk density	Dry density	Variable
45-46	A	Air	-	-	-	No soil
47-48	B	LB	2.45%	1.635	1.6	Soil to charge base
49-50	C	LB	2.45%	1.635	1.6	No overburden
51-57	D	LB	2.45%	1.635	1.6	Base line
58-62	E	LB	2.45%	1.635	1.6	Increased overburden

Series A serves as the 'null' condition with no confinement offered other than the PVC case on the sides and base of the charge, which is common to all tests. Test 34 in Chapter 3 demonstrated that the soil container offers no confinement to the early-stage expansion of the detonation products when confined in soil. Series A therefore is used to demonstrate the effect of an empty soil container on a free-in-air charge. The charge was supported by placing the charge on a 10 mm diameter timber prop within the container, see Figure 4.5a. Series B serves to show the effect of confinement below the charge with the charge seated directly on the soil

surface 190 mm below the measurement plain allowing for 3 mm PVC charge case, cf. Figure 4.5b. In Series C, the effect of lateral confinement was investigated where the soil container is filled but material above the charge is removed, which is shown in Figure 4.5c. Series D provides the control series with lateral and vertical confinement common to all buried tests. This test series overlaps all parametric studies for confinement, saturation and PSD studies, and is shown in Figure 4.5d. In Series E the burial depth of the charge is increased to 53 mm to provide increased vertical confinement of the charge, see Figure 4.5e.

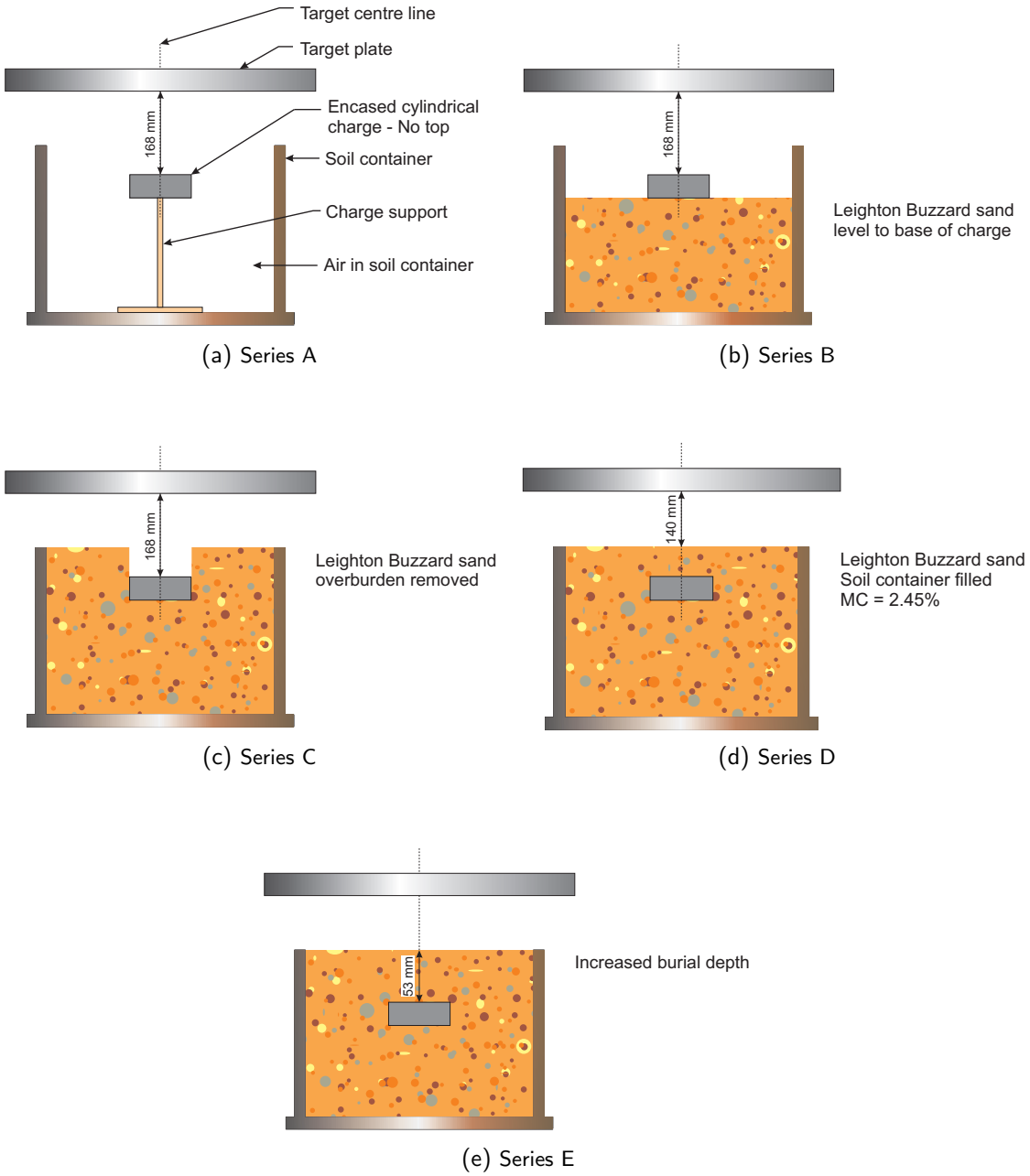

Figure 4.5: Charge configurations Series A, B, C, D and E - Investigation of the effect of soil confinement on buried explosive output. Note that these diagrams are not to scale and the relative dimensions of the target, soil container and charge are indicative only.

4.5.2 Pressure waveforms

Figures 4.6–4.7 show examples of pressure-time and specific impulse-time traces from a single array for one test within each series. Specific impulse was calculated from cumulative numerical integration of the pressure traces with respect to time.

The pressure-time histories for Series A, B and C, shown in Figures 4.6a, 4.6c and 4.6e, resemble the well-known 'Friedlander' exponential similarly to preliminary Tests 41–44. The pressure waveforms in Series B appear higher in magnitude than in Series A, however the specific impulse indicates that the momentum transfer is approximately similar at each bar location. Therefore the soil underneath the charge in Series B may modify the peak pressures but does not appear to increase impulse at the target. The waveforms in Series C generally appear higher in magnitude and longer in duration than those in Series A and B. Impulse in Series C appears significantly higher than Series A and B, indicating that lateral confinement of the charge by the surrounding soil significantly increases the momentum transfer to the target.

The effects of lateral flow and pressure equalisation across the target can be seen in the waveforms from Series A and B, with the reflected blast pressures converging to the same pressure at all HPB locations approximately 0.125 ms after detonation and following the same decay thereafter. The waveforms in Series C at 75 and 100 mm from the plate centre appear to resemble more of a stagnation pressure than a dynamic shock pressure where pressures at 75 and 100 mm are comparatively low in magnitude with a more gradual temporal decay.

Conversely, when soil overburden is introduced in Series D, see Figures 4.7a and 4.7b, the pressure-time histories are similar in magnitude to those in Series A and B, however the arrival time is delayed. This is due to the inertial confinement of the soil overburden serving to slow vertical expansion of the detonation products. With the exception of the short duration pressure spikes, the pressure in the fully confined soil exhibits a sharp rise to peak pressure followed by a fairly gradual decay to ambient pressure. The waveforms appear to follow an 'modified Friedlander' [12, 51] exponential seen in the free-air tests in part two Series A–C, with random pressure spikes overlain. It appears that this exponential waveform represents the detonation product contribution to the loading, and the pressure spikes represent discrete soil particles striking the HPB locations. The observation of a 'shock-type' loading agrees with hypothesis of Bergeron et al. [11] and numerical observations of Grujicic et al. [75].

In Series E the depth of burial is increased form 28 to 53 mm. The pressure waveforms of Series E, Figure 4.7c, show a similar magnitude at the central HPB location as Series D, however 25 and 50 mm bar locations show a significant reduction in peak pressure and instead form several discreet pressure peaks and increased duration when compared to Series D pressure

waveforms. At the 75 and 100 mm bar locations the pressure waveforms indicate a reduction in peak pressure where the discrete pressure peaks are spread further out in time when compared to Series D. Series E impulse histories show that the majority of impulse is delivered to the target at the 0 and 25 mm bar locations.

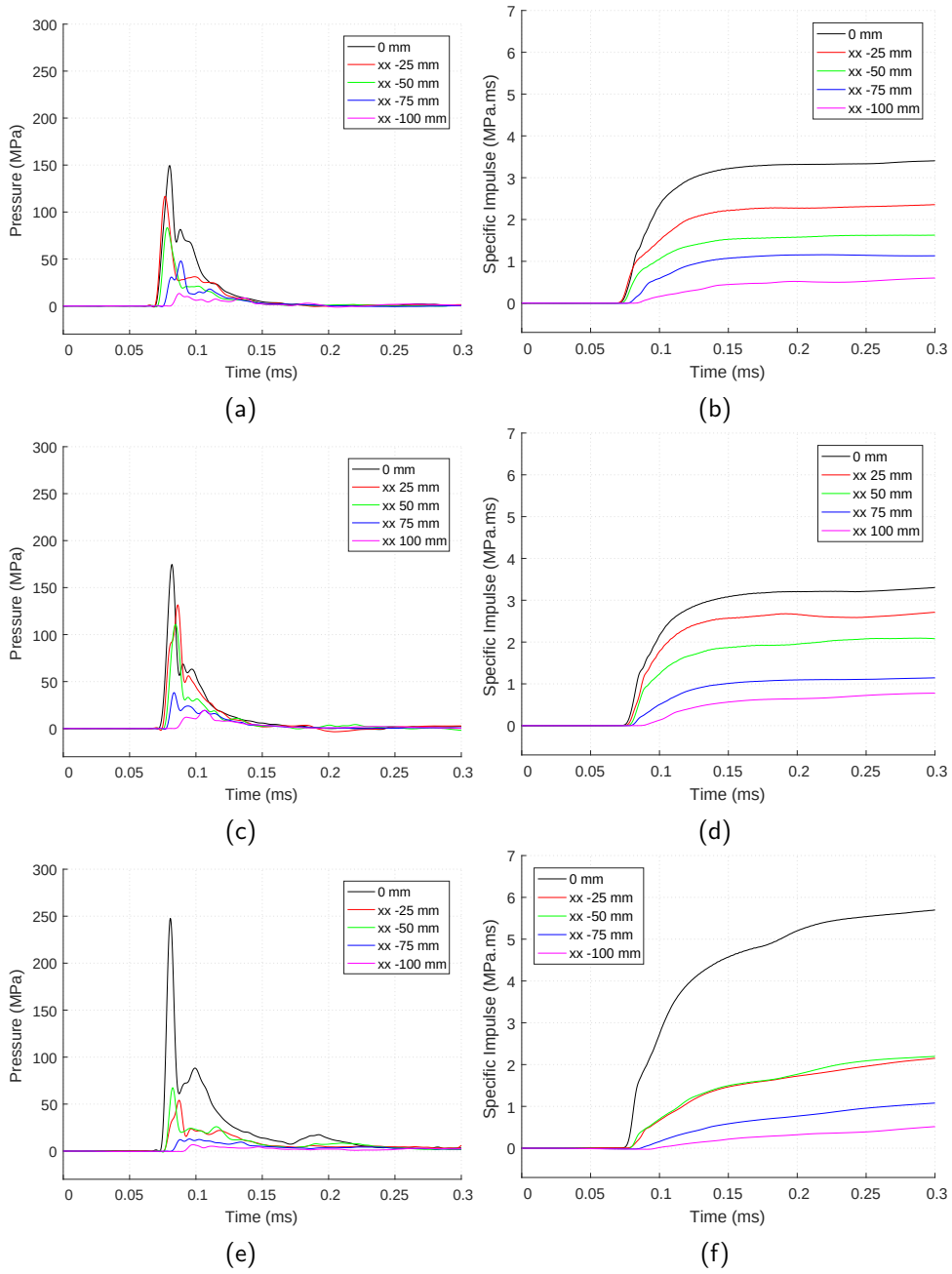

Figure 4.6: Single array pressure-time and impulse histories explosives in increased states of confinement from Leighton Buzzard sand. Series A pressure (a), specific impulse (b). Series B pressure (c), specific impulse (d). Series C pressure (e), specific impulse (f).

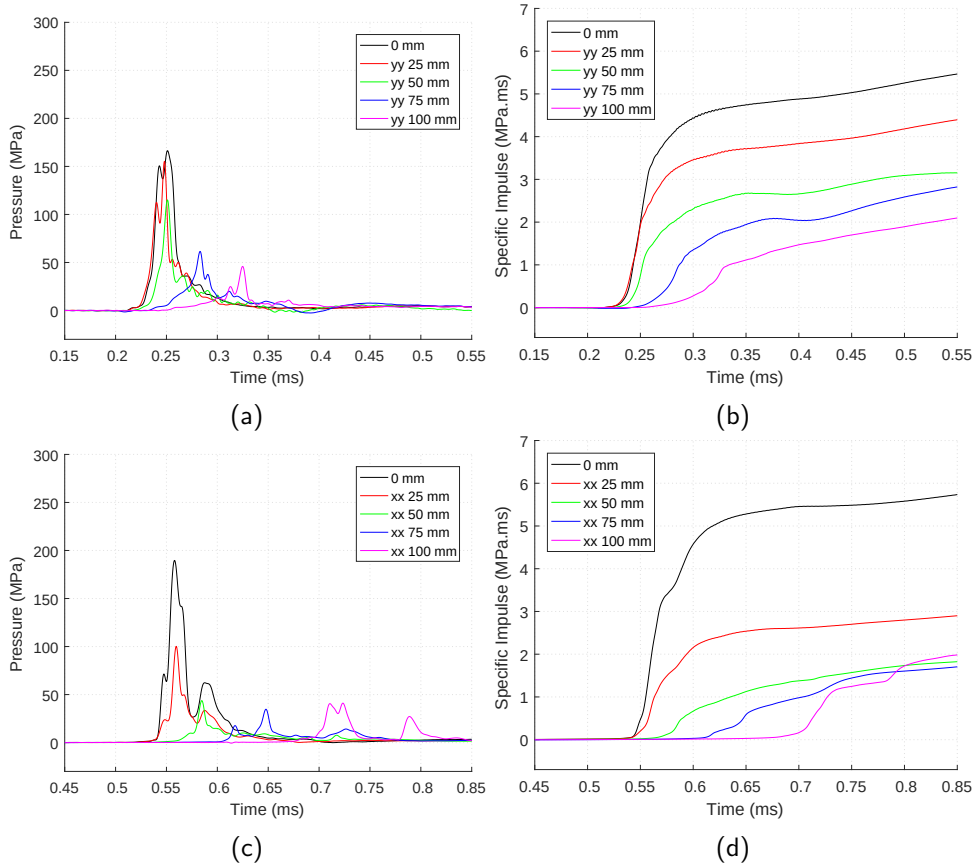

Figure 4.7: Single array pressure-time and impulse histories explosives in increased states of confinement from Leighton Buzzard sand. Series D pressure (a), specific impulse (b). Series E pressure (c), specific impulse (d).

4.5.3 Peak reflected pressure and impulse distribution

Figures 4.8–4.9 show the values of peak pressure and peak specific impulse for all HPB recordings in Series A–E. The variation of peak pressure and impulse with distance from the plate centre can be seen. The mean peak pressures and mean peak specific impulses have been calculated for each soil type at 0, 25, 50, 75, and 100 mm from the plate centre. The mean pressure and impulse at each radial ordinate for each series is given by the solid black line allowing trends to be observed.

There is little difference in the peak reflected pressure and, in particular, peak specific impulse distributions between Series A and Series B tests. This suggests that the presence of a soil surface beneath the charge has little effect on channelling the explosive. With reference the individual pressure-time and impulse-time traces in Figures 4.6a and 4.6c, it can be seen that the magnitudes do not differ significantly between a cased charge in free-air and a cased charge situated on the soil surface.

The peak pressures acting between 0 and 25 mm from the plate centre are higher for Series C

than for Series A and B, however the peak pressures at the 75 and 100 mm bar locations are lower than the corresponding peak pressures from Series A and B. Despite this, the mean peak specific impulse is higher at all bar locations for Series C than for Series A and B. This indicates that the lateral confinement provided by soil sounding the Series C charge increases the changeling of detonation products vertically towards the target centre. Furthermore, the sand ejected from the soil container serves to increase specific impulse due to the longer loading duration at the 75 and 100 mm HBP locations, see Figure 4.6e.

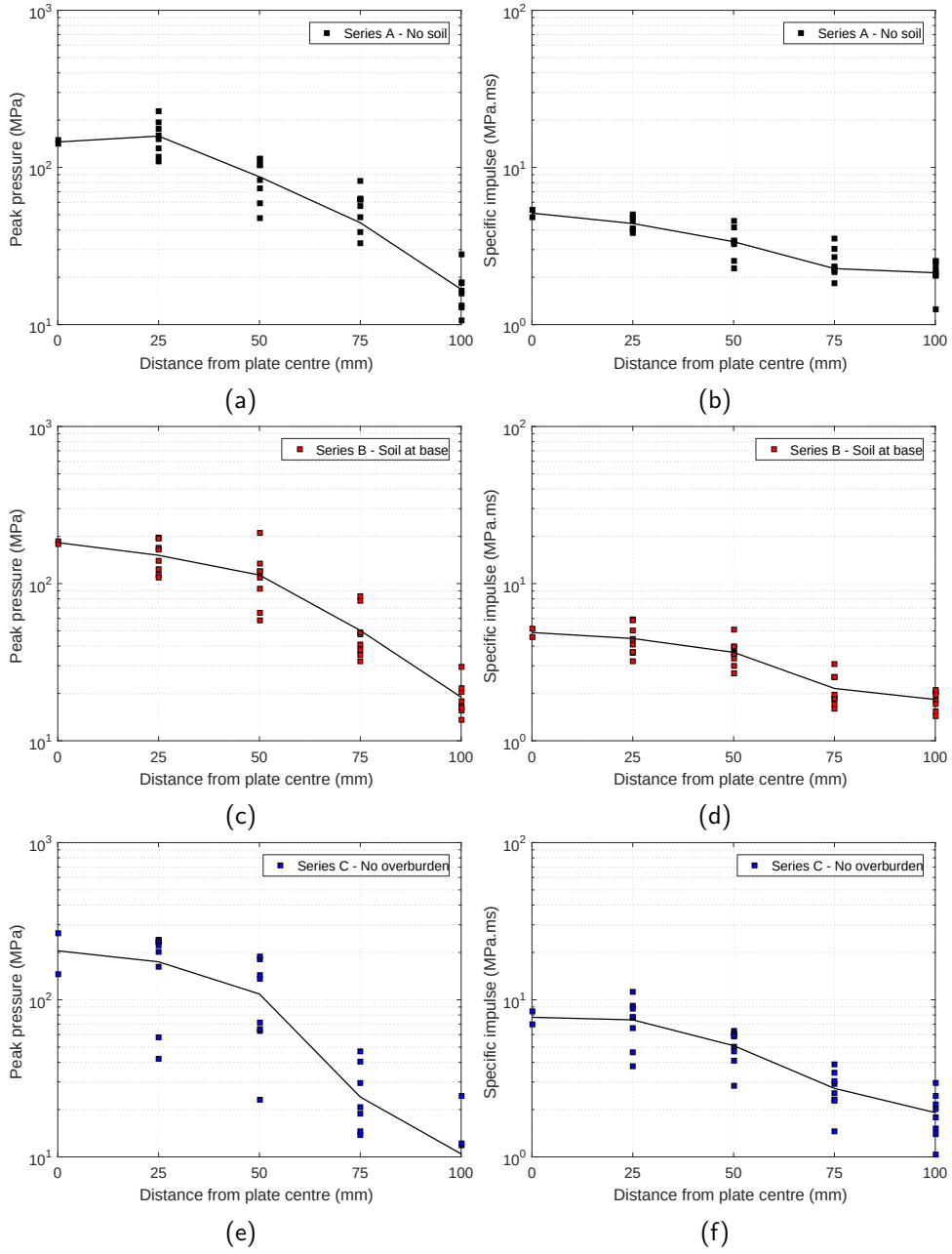

Figure 4.8: Pressure and impulse distributions in increased states of confinement from Leighton Buzzard sand. Series A peak pressure (a), peak specific impulse (b). Series B peak pressure (c), peak specific impulse (d). Series C peak pressure (e), peak specific impulse (f).

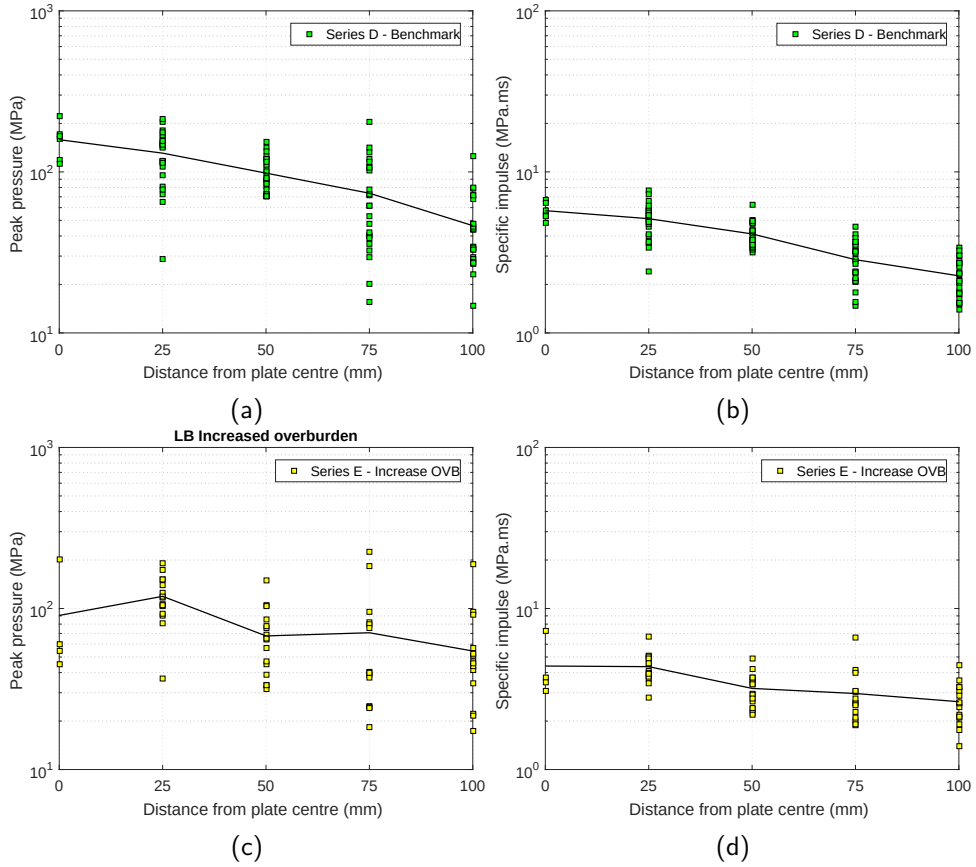

Figure 4.9: Pressure and impulse distributions in increased states of confinement from Leighton Buzzard sand. Series D peak pressure (a), peak specific impulse (b). Series E peak pressure (c), peak specific impulse (d).

Overburden is introduced above the charge in Series D and E such that the charge and detonation products are fully confined post detonation in the soil bed. Peak pressure and therefore momentum transfer at 0, 25 and 50 mm HPB locations is lower than uncovered charges in Series A, B and C. Conversely, at 75 and 100 mm bar locations the peak pressure and specific impulse is higher in Series D and E with overburden than charges without overburden. It appears that as the overburden is introduced and as burial depth increases this acts to distribute the load more evenly and across a wider diameter of the target. As burial depth is increased in Series E, a lower mean peak pressure is witnessed at 0 mm bar when compared to Series D then increasing at the charge periphery at the 25 mm HPB location.

It is worth noting that whilst the number of experiments conducted in each series increases from two in Series C to five in Series D, this is not followed by an increase in spread of peak pressure and peak specific impulse, as perhaps should be expected when increasing the sample size by a factor of 2.5. Taking this into account, it is likely that the relative spread in loading would be higher in Series C, relative to Series D, if more tests were conducted.

4.5.4 High speed video

Figure 4.10 shows select frames from the HSV captured for Series A, B, C and D. The camera was unavailable when conducting Series E. Frames for Series A, B and C are presented between 0.01 – 0.10 ms at an inter–frame time of 0.01 ms. Due to the increase in duration of the buried charge in Series D inter–frame times are presented at 0.04 ms.

For the unconfined and partially confined cases in Series A, B and C, the difference in emerging shape of the detonation products is clear. The confinement offered by the surrounding soil enforces an inherent directionality in the shape of the fireball. As a result, the volumetric expansion of the detonation products is considerably less in Series C than in Series B. At $t = 0.06$ ms, for example, the detonation products in Series C occupy a cylinder with an approximate radius of 100 mm. In contrast, at the same time the detonation products in Series B occupy a cylinder of radius $\sim$150-175 mm. Assuming approximate radial symmetry of the detonation products, this suggests that the detonation products in Series C occupy a volume some 32–44 % of that occupied by the detonation products in Series D. This confinement lengthens the pressure duration and hence increases the specific impulse at the centre of the plate by over 50 % when compared to the free air events of the previous two test series.

The Series C column offers an explanation for the low-magnitude, 'flat-topped' waveforms seen at the 75 and 100 mm bar locations in Series C. It appears as though the detonation products form an effectively flat front which appears to be $<$75 mm radius the moment it impacts the target. Hence, the pressures away from this impact front are almost entirely as a result of lateral pressure flow across the target and hence are more akin to incident rather than reflected pressures.

When overburden is placed on the charge in Series D, some luminosity can be seen at the soil surface at 0.00 ms. After this time there is no luminosity in the ejecta, indicating that no fireball is produced therefore there is no afterburn of the uncreated explosive. The soil forms a smooth annulus as it ejects from the soil surface until 0.12 ms when detonation products can be seen weeping from the soil shown more clearly at 0.16 ms, seen as a black gas. The surface of the ejecta now appears like a turbulent flow of detonation products and soil particles. It can be observed that Series D is at an approximate time factor of 3.5 behind Series C tests; the buried explosive follows a similar volume and profile despite exhibiting different loading characteristics. This implies that the increased loading seen at the 75 and 100 mm bar locations is due to an extended loading period and therefore increased impulse. It is also clear that loading is due to a combination of detonation products and sand throw in a turbulent detonation product flow.

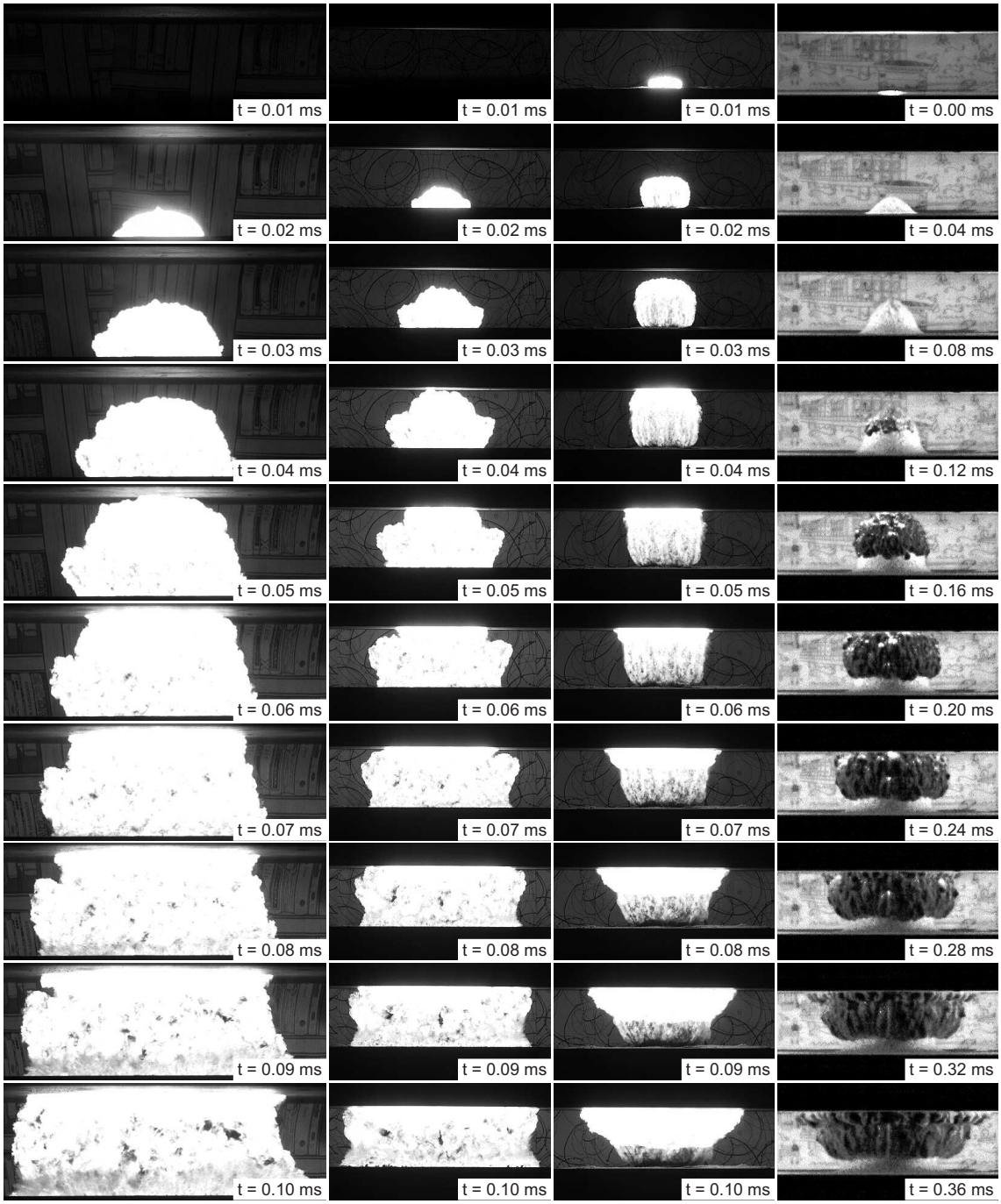

Figure 4.10: HSV for the effect of soil confinement on buried explosive output, (a) Series A, (b) Series B, (c) Series C, (d) Series D. It should be noted that the field of view in Series A tests is different to those of Series B, C and D giving the impression of a 'larger' fireball than in comparative series.

4.6 Part Three – Effect of saturated and partially saturated sand on buried explosive output

4.6.1 Introduction

Part three of the parameter study investigates the influence of moisture content of the surrounding soil and to what extent the presence of water in the soil skeleton fundamentally alters the loading mechanism.

The experimental test plan is summarised in Table 4.5, and testing arrangements are shown in Figure 4.11. Series D provides the control series with a moisture content of 2.45% common to all tests unless specified, see Figure 4.11a. In Series F the moisture content was increase from 2.45% in Series D to 4.76%. For a granular soil, a moisture content of 4.76% moisture content will not fill the pores in the soil matrix, however the volume of water coating the soil particle will increase, cf. Figure 4.11b. Series G tests were performed in fully saturated LB soil at 25% moisture content where the voids between soil particle are fully filled, shown in Figure 4.11c. Series H used the standard charge geometry, however only water is placed in the soil container, as depicted in Figure 4.11d. Series G and H are aimed at quantifying any differences in loading mechanism from partially to fully and saturated soils, and to show any similarities between a fully saturated LB soil and the behaviour of water. Determining the physical reason for any differences observed may be possible by isolating the soil saturation states in this way.

Seven tests make up Series D forming the baseline behaviour for the parametric study with 119 bar recordings available for analysis. Five tests were conducted in Series F and G with 85 bar recordings available for analysis. Two tests were conducted in Series H where 34 bar recordings available.

Table 4.5: Part Three - Test series used to investigate the effect of saturated and partially saturated soil on buried explosive output.

Tests	Series	Soil type	w(%)	Bulk density	Dry density	Variable
51-57	D	LB	2.45%	1.635	1.6	Base line
63-67	F	LB	4.76%	1.670	1.6	Moisture content
68-72	G	LB	25%	1.990	1.6	Full saturation
73-74	H	Water	-	-	-	Water

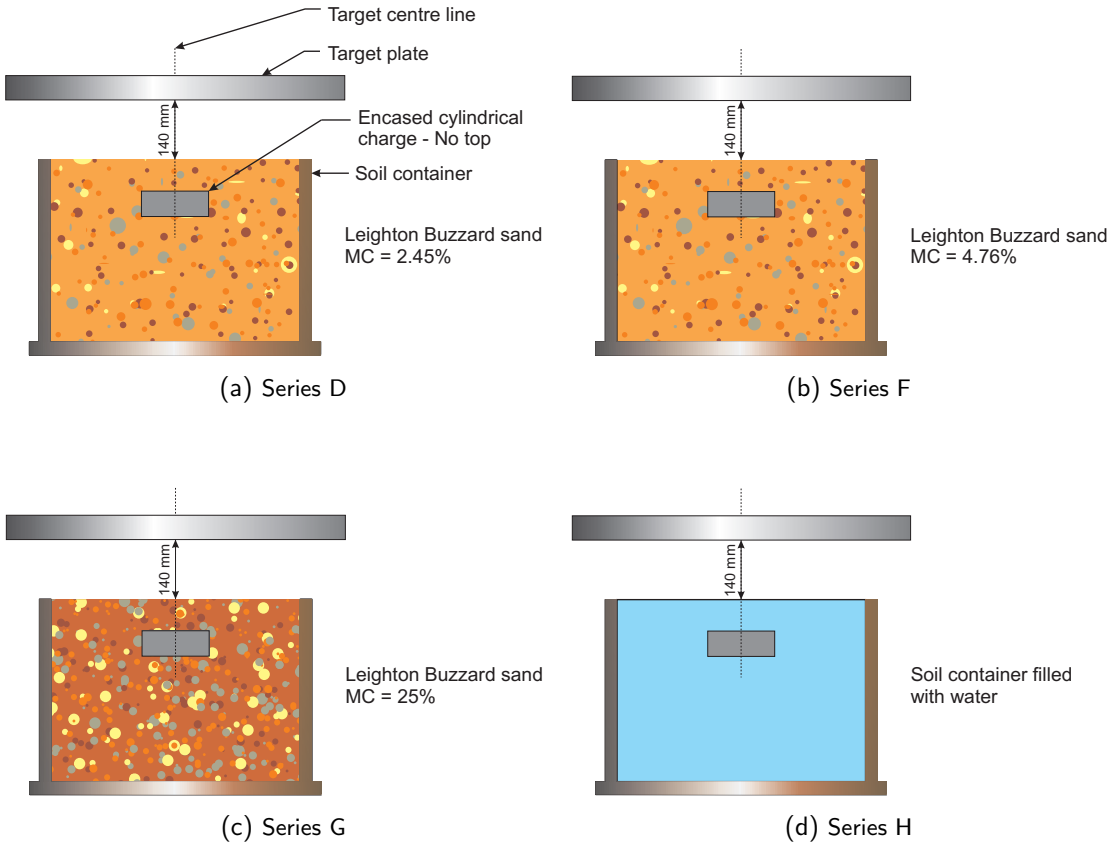

Figure 4.11: Charge configuration Series D, E, G and H - Investigation on the effect of saturated and partially saturated sand on the loading from a shallow buried charge.

4.6.2 Pressure waveforms

Figure 4.12 show example pressure-time and impulse-time traces from a single array for one test within each series for Series D, F, G and H.

The pre-cursor shoulder (described in Chapter 2, Figure 2.21, region a) is perhaps best seen in Series F, Figure 4.12c. However this shoulder only appears to accompany the loading in the partially saturated test and does not appear in fully saturated or water tests in Series G and H. Bergeron [11] theorised that the pre-cursor shoulder was formed by ejected material compressing the air in front of the expanding annulus of material. However, if this theory were correct, the pre-cursor shoulder would appear in the fully saturated soil and water pressure waveforms of Series G and H, cf. Figures 4.12e and 4.12g. Due to the inconsistency between partially and fully saturated soil waveforms, the pre-cursor shoulder may be formed by a different mechanism that does not occur in fully saturated soil detonation events.

For partially saturated soils from Series D and F, pressure magnitude and specific impulse appear similar. As the pressure propagates over the target face, the pressure acting at the

radial bars can be seen to briefly rise above the pressure acting on the more central bars before decaying to a pressure similar to that of the more central bars, indicating equalisation of the blast pressure within the loaded region shortly after passing of the wavefront. At any moment in time after the shock front has passed, therefore, the instantaneous pressure acting on the loaded portion of the target is relatively uniform, however the peak pressure and peak specific impulse decreases considerably with increasing distance from the plate centre.

The pressure waveform from the explosives buried in saturated soil in Series G exhibits an effectively temporally symmetrical rise to peak pressure and decay back to ambient pressure with no evidence of the shock-type loading or short duration loading spikes seen in low moisture content soils. This is consistent with Grujicic's observation that two distinct mechanisms dictated the behaviour of partially and fully saturated soils [75].

The behaviour of the fully saturated soil and water tests is consistent with the initial phase phenomena associated with the problem of impact of a high velocity fluid drop with a solid surface. As the radius of the contact surface between the droplet and the target expands, the highest pressures are generated just inside the contact annulus [26]. With increasing radial spreading of the fluid annulus, the angle between the fluid drop, or soil annulus, and the wall increases and the contact edge velocity decreases, reducing the magnitude of the peak pressure. This reduction in radial velocity of the annulus is evidenced by both the decreasing peak pressure and increasing time to peak pressure for the example HPB traces in Figure 4.12e. The waveform therefore indicates that the soil bubble remains intact, fully confining the detonation products throughout the loading duration.

The pressure-time waveforms from Series H were gained from tests in potable water. The general form of the pressure traces in Series G and Series H are very similar, indicating that saturated LB soil behaves like a fluid following a buried explosive detonation. This again confirms the 'annulus-type' loading mechanism hypothesised by Grujicic et al. for saturated soils [75]. However, loading generated by 'annulus-type' impacts appears to be dominated by fluid in the soil-water mixture resulting in high velocity fluid impacts as described by Rein [26]. The magnitude of the imparted pressure and the rate of radial spreading is a function of the fluid density, sound speed, and compressibility and velocity of the impacting soil bubble [26], hence the differences seen in the pressures and durations in Series F and G.

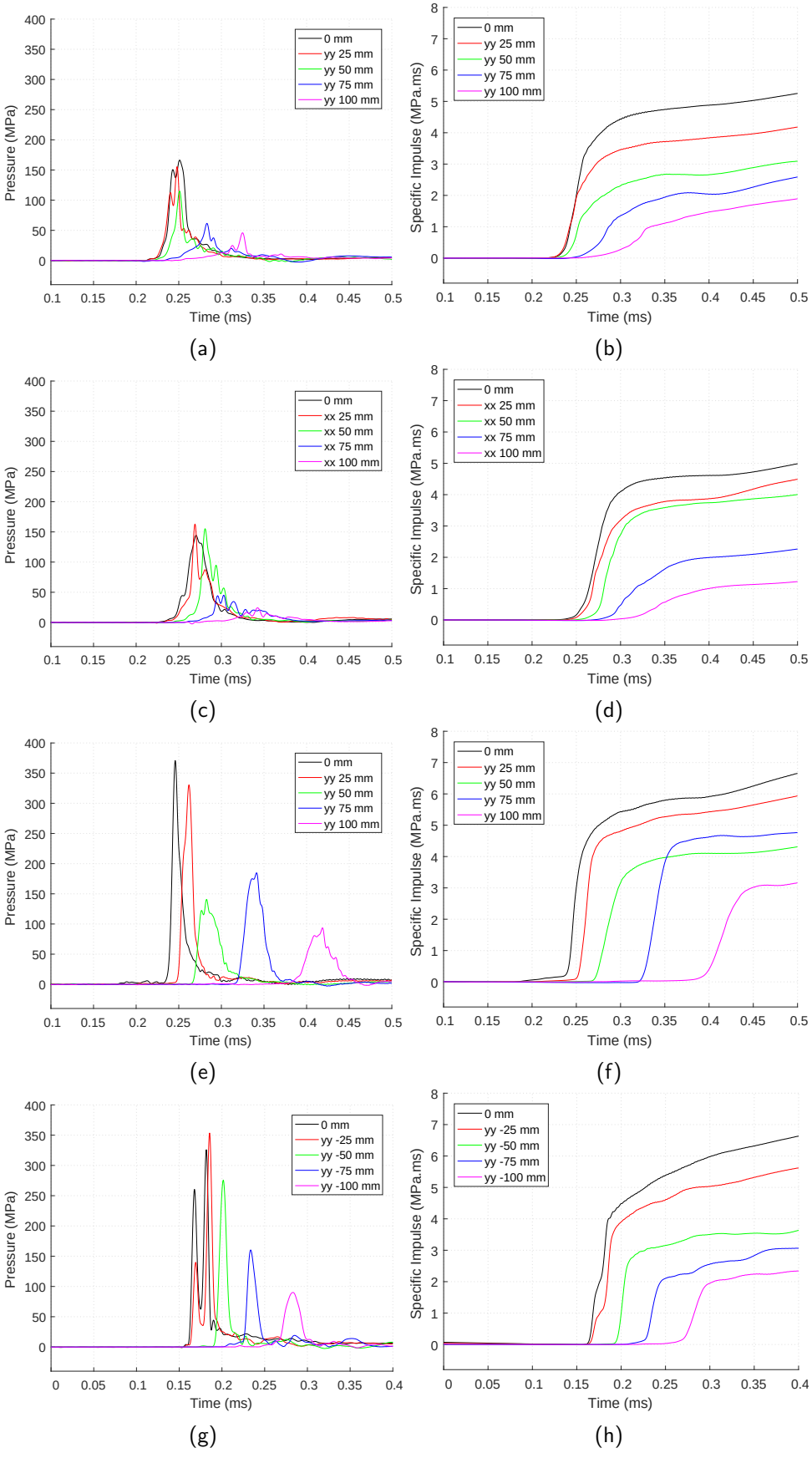

Figure 4.12: Single array pressure-time and impulse histories explosives in increased states of saturation in Leighton Buzzard sand and potable water. Series D pressure (a), specific impulse (b). Series F pressure (c), specific impulse (d). Series G pressure (e), specific impulse (f). Series H pressure (g), specific impulse (h).

4.6.3 Peak reflected pressure and impulse distribution

Figure 4.13 shows the values of mean peak pressure and mean peak specific impulse for all HPB recordings for Series D, F, G and H.

There is no significant difference between Series D and Series F reflected pressure and reflected impulse distributions, suggesting that an increase in moisture content from 2.45% to 4.75% and bulk density from 1,640 kg/m^3 to 1,670 kg/m^3 has a negligible effect on the output from buried explosives over the central region of the target.

The mean peak pressure for the saturated soil (Series G, Figure 4.13e) is in the order of 100% larger than the peak pressure for the partially saturated soils (Series D and F Figures 4.13a 4.13c) at all bar locations. At this central bar location, the specific impulse is 25% larger at the central bar increasing to 85% larger at the 100 mm bar. The results for saturated LB and water (Series G and H) are largely similar in magnitude.

It was shown in Section 4.5.3 and 4.6.2 that the distribution of pressure from a buried explosive event is intrinsically linked to confinement and soil moisture content. In both cases the loading mechanism was fundamentally changed by increasing the level of confinement on the detonation products and the soil moisture content in which the charge is buried. It can be seen from the pressure and impulse distributions for Series G and H (Figures 4.13e, 4.13f, 4.13g and 4.13h respectively) that the distribution of pressure across the target is more evenly distributed than for the partially saturated soils. This suggests that there may be a fundamentally different mechanism for partially and fully saturated soils, providing further confirmation of the observations made by Grujicic et al. [75].

Variability in peak pressure at each bar location appears to be significantly lower in the fully saturated and water tests, see Figures 4.13e and 4.13g. It is hypothesised for partially saturated soils that discrete particle strikes give higher variability in loading, particularly for the value of peak pressure. Particle impacts do not appear to occur in the fully saturated soil where the ejected material appears to act homogeneously. Due to the similarity between the water and partially saturated test it is hypothesised that the fully saturated soil behaves in a similar manner to water, again supporting the observations of a annulus-type loading mechanism. Hence, the fully saturated event has no discrete particle impacts and therefore reduced test variance.

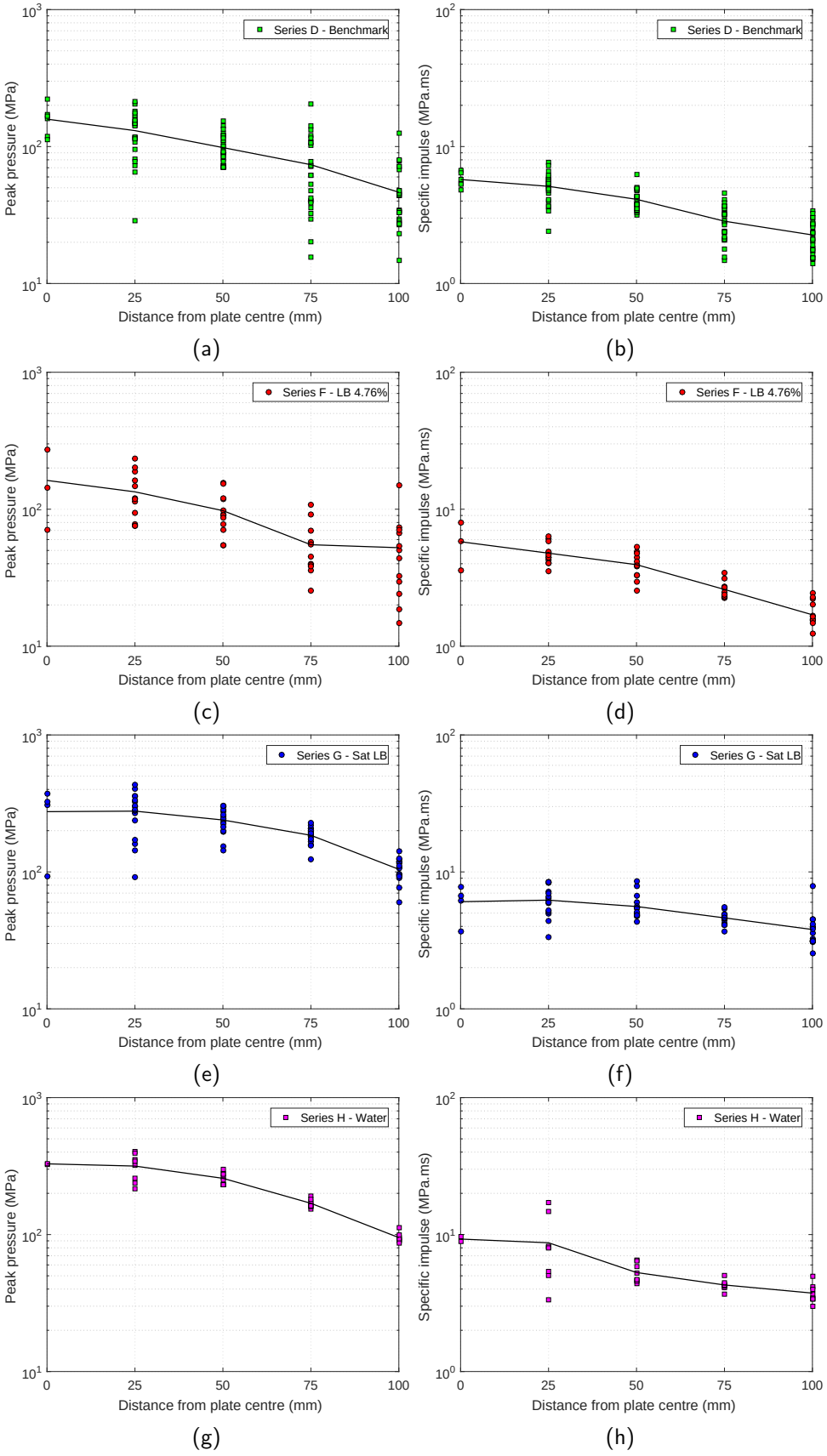

Figure 4.13: Pressure and impulse distributions in increased states of saturation in Leighton Buzzard sand and potable water. Series D peak pressure (a), peak specific impulse (b). Series F peak pressure (c), peak specific impulse (d). Series G peak pressure (e), peak specific impulse (f). Series H peak pressure (g), peak specific impulse (h).

4.6.4 High speed video

Figure 4.14 shows select frames from the HSV captured for Series D and H. The camera was unavailable when conducting Series F and G. Frames for Series D are presented at 0.04, 0.08, 0.12, 0.16 and 0.20 0.24, 0.28 0.32 and 0.36 ms after detonation. As the duration of loading was unknown for charges submerged in water the frame rate of the event was increased meaning that the frame times between Series D and H do not align. It can be seen that the higher frame rate was necessary as the submerged event occurs approximately 1.4 times more quickly. Inter-frame times of 0.02858 ms were selected where the ejection height most closely matched the partially saturated soil from Series D.

Bergeron et al. [11] hypothesised that the pre-cursor shoulder was due to air compressed above the ejecta for dry soils. The pre-cursor shoulder was witnessed in Series D and F tests, and can be seen in Figures 4.12a and 4.12c. However the pre-cursor does not feature in the pressure-time waveforms of the saturated soil nor the water test. As the water ejecta is of a higher velocity and therefore higher pressure than that of the partially saturated soil, the hypothesis of Bergeron should mean that a larger pre-cursor shoulder is seen in these cases. However, the shoulder is not seen in either test. Comparing the HSV for the partially saturated soil and water, it can be seen that for partially saturated soil, detonation products vent from the soil annulus impacting the target at 0.16ms. In the case of water, only the water annulus is seen to strike the target where the water annulus remains intact, thus fully confining the detonation products through the duration of loading. These two different mechanisms observed provide crucial evidence to why the pre-cursor shoulder is seen only in the partially saturated soil: the pre-cursor shoulder is due to venting detonation products impacting the target plate before the main body of ejecta.

It was discussed in Section 4.5.4 for the partially saturated soil in Series D that the soil forms a smooth annulus until 0.12ms. In subsequent frames, detonation products can be seen weeping from the soil surface meaning that the soil annulus has ruptured allowing detention products to vent. It is this venting that forms the 'shock-type' loading mechanism described by Grujicic [75] with particle strikes overlain leading to additional discrete peaks in the pressure-time waveforms. Comparatively, for Series H, the HSV shows that the water forms an annulus confining the detonation products entirely from break out at the soil container and through the interaction with the target plate confirming the annulus-type mechanism described by Grujicic et al. [75]. This indicates that the soil bubble remains intact, fully confining the detonation products throughout the loading duration.

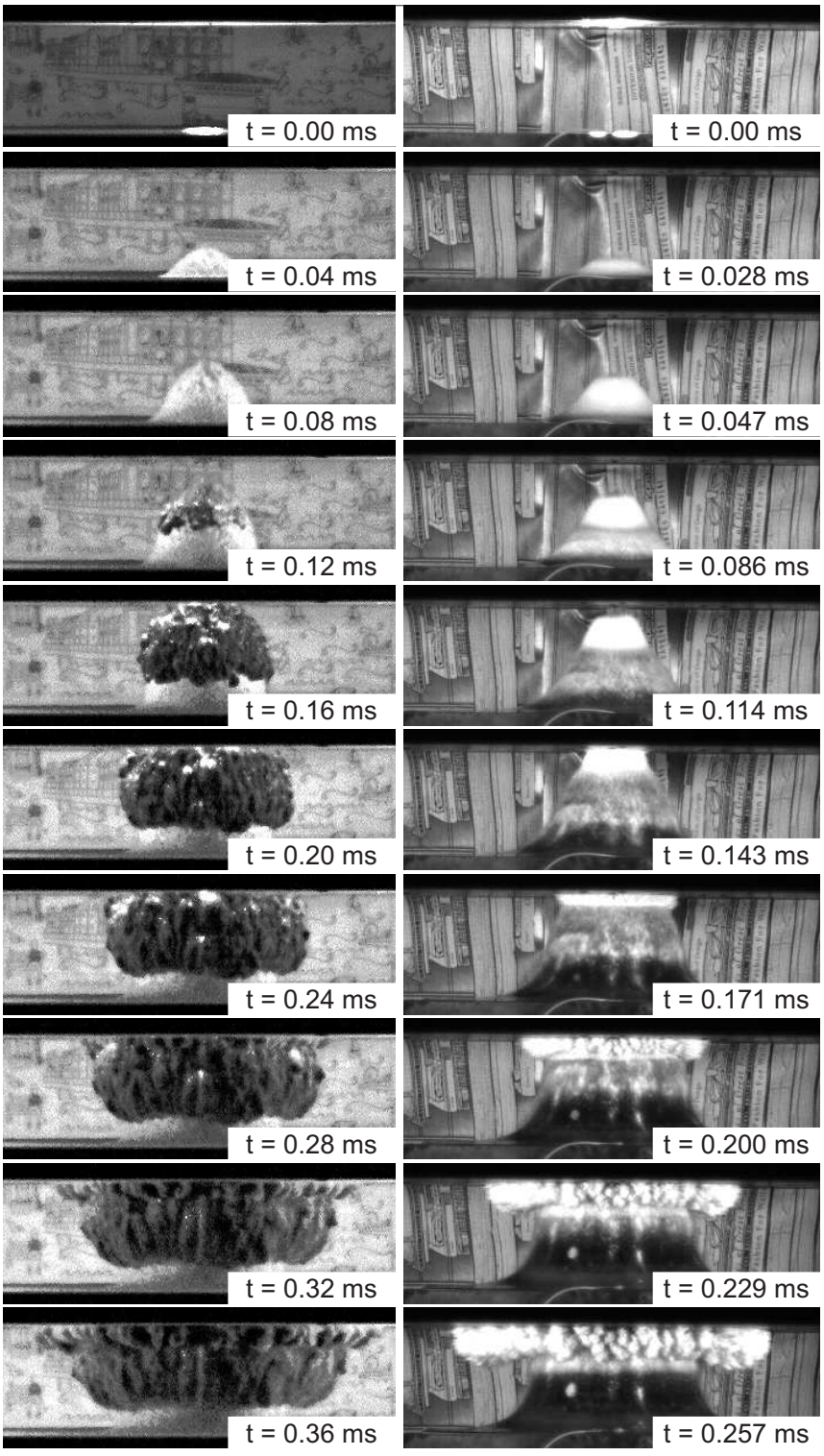

Figure 4.14: HSV for the effect of saturated and partially saturated sand on buried explosive output, (a) Series D, (b) Series H.

4.7 Part Four – Effect of particle size distribution in saturated sand

4.7.1 Introduction

Part Four of this parameter study investigates the effect of Particle Size Distribution (PSD) in saturated soil on the loading formed at the target. The experimental test plan is summarised in Table 4.6 and test arrangements are shown in Figure 4.15. 10 tests make up Part Four of this parametric study. Series G, seen in Part Three of this study, was performed in fully saturated LB soil at 25% moisture content. Series I confined the detonation with a fully saturated well graded STANAG soil at 14% moisture content. The largest particles in STANAG are two orders of magnitude larger than that of LB soil. Five tests were conducted Series G with 85 data points available for analysis. Seven tests were conducted in Series I with 119 data points available.

Table 4.6: Part Four - Test series to investigate the effect of particle size distribution in saturated soil on buried explosive output.

Tests	Series	Soil type	w(%)	Bulk density	Dry density	Variable
68-72	G	LB	25%	1.990	1.600	Full saturation single--fraction
75-81	I	STANAG	14%	2.100	1.806	Full saturation well--graded

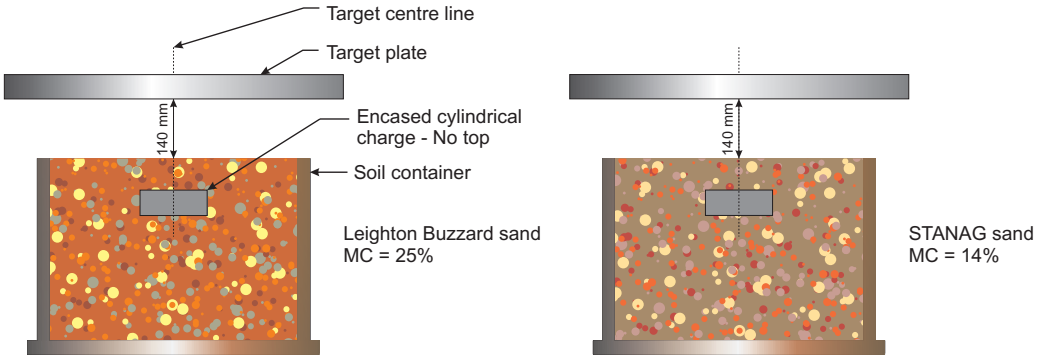

(a) Series G (b) Series I

Figure 4.15: Charge configuration of Series G and I - Investigating the effect of particle size distribution in saturated soil on shallow buried explosive output.

4.7.2 Pressure waveforms

Figure 4.16 shows example pressure waveform and impulse histories for a single HPB array for fully saturated LB sand for Series G. Figure 4.17 shows the pressure waveforms and impulse histories for the full HPB array from a single fully saturated STANAG soil test, i.e. Series I. In Figure 4.17 the central bar (0 mm) is common to all four arrays and hence appears the same in each of the subplots for a given test. As per previous tests, 50 μs has been subtracted from the timebase.

In general, the magnitudes of the fully saturated STANAG soil pressure waveforms are broadly similar to, but more variable than, saturated LB, while the loading for any given bar appears more complex. The STANAG pressure waveforms in Figure 4.17 appear different from the fully saturated LB. The underlying form of the loading appears similar to the annulus-type loading of saturated LB i.e. impact and spreading of a pressurised fluid annulus. However, there are features of the loading which were characterised in the 'shock-type' loading of the partially saturated soil of Series D. Two examples of the pre-cursor shoulder are seen at the 25mm bar location on the x axis, see Figure 4.17a and 4.17c, indicating that some venting of detonation products occurs prior to impact with the target. Furthermore, the temporal decay of pressure, where equalisation across the instrumented area of the target is characteristic of stagnated detonation products, is a feature seen in partially saturated 'shock-type' loading. Discrete pressure peaks associated with particle impact are distributed across the pressure waveforms leading to significant increases in impulse and 'step-like' impulse history with the 75 mm bar in the negative x direction offering a clear example, Figure 4.17c.

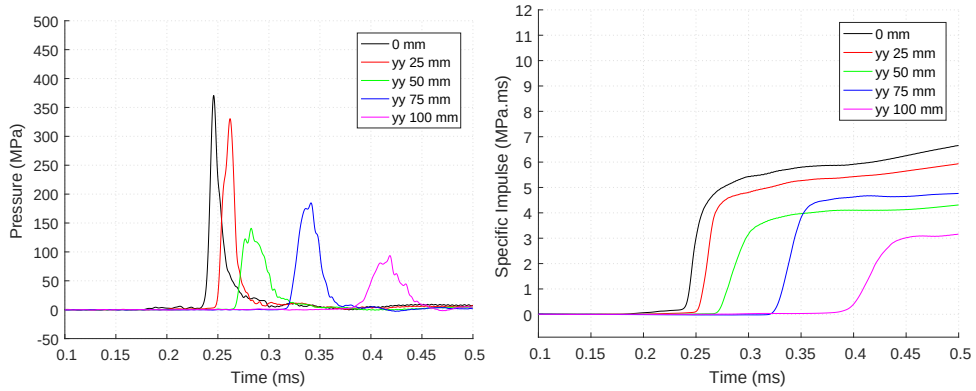

(a) (b)

Figure 4.16: Single array pressure-time and impulse histories investigating the effect of particle size distribution in saturated soil. Series G pressure (a), specific impulse (b).

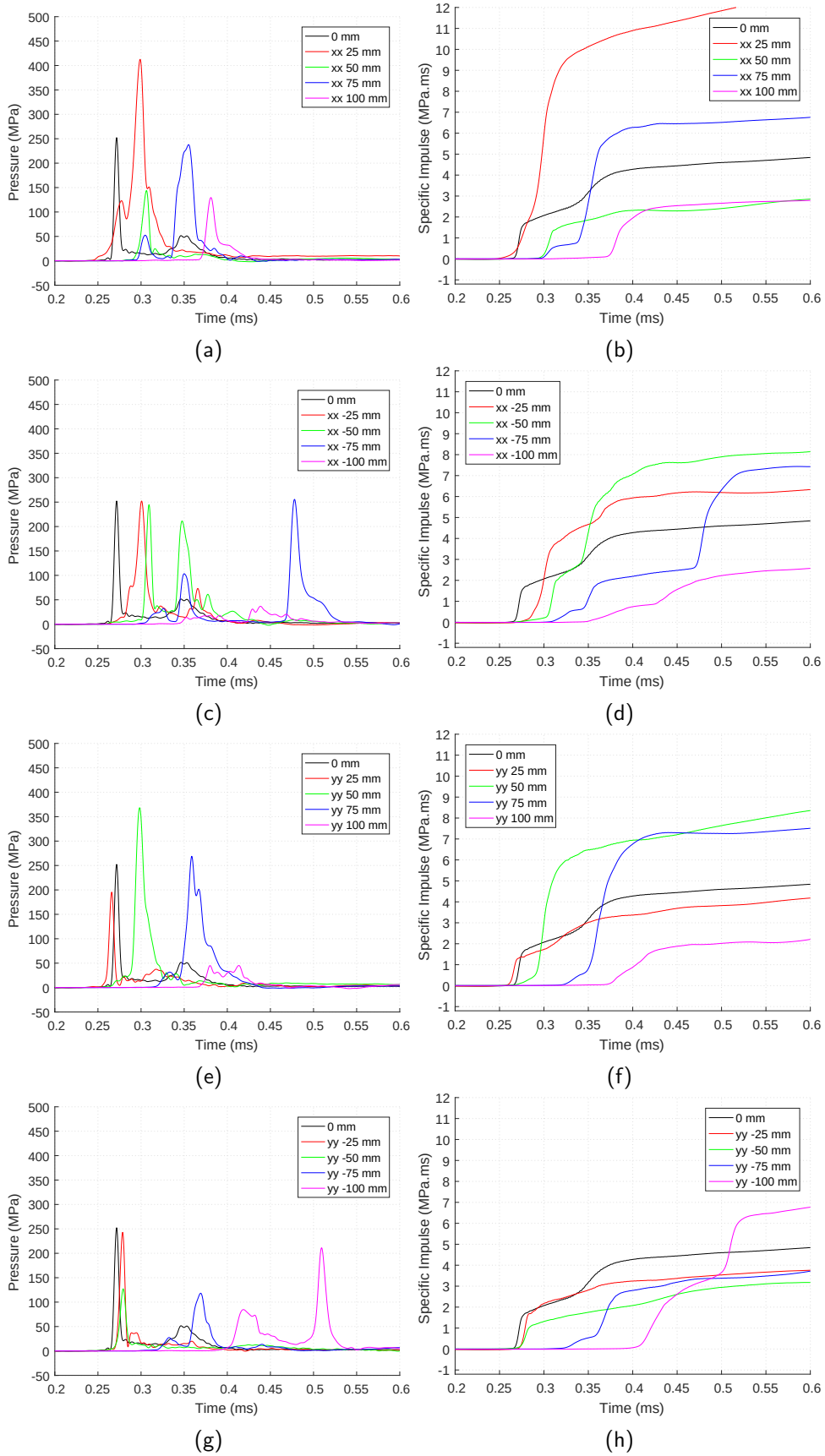

Figure 4.17: Single array pressure-time and impulse histories investigating the effect of particle size distribution in saturated soil. Test 75: Series I (x–x) pressure (a), specific impulse (b). Series I (-x–x) pressure (c), specific impulse (d), Series I (y–y) pressure (e), specific impulse (f). Series I (-y–y) pressure (g), specific impulse (h).

4.7.3 Peak reflected pressure and impulse distribution

Figure 4.18 shows the peak pressure and peak specific impulse compiled for Series G and I. It can be seen in Figure 4.18a that the saturated STANAG mean peak pressure is less evenly distributed across the face of the target indicative of the 'shock-type' loading witnessed in saturated LB and water tests. It was concluded that 'shock-type' loading is due to high velocity fluid impact. Furthermore, variance at discrete measurement locations is high which is indicative of 'shock-type' loading witnessed in partially saturated LB tests. In Section 4.6 it was hypothesised that this variance is caused by a combination of venting detonation products and particle impacts.

The largest particles in STANAG are up to twice the diameter of the recording HPBs rather than an order of magnitude smaller as with LB. It appears that the presence of a well-graded distribution of particle size within the STANAG soil causes a more complex stochastic loading distribution to develop on the loaded face when compared to tests conducted with more uniform soil grading such as LB.

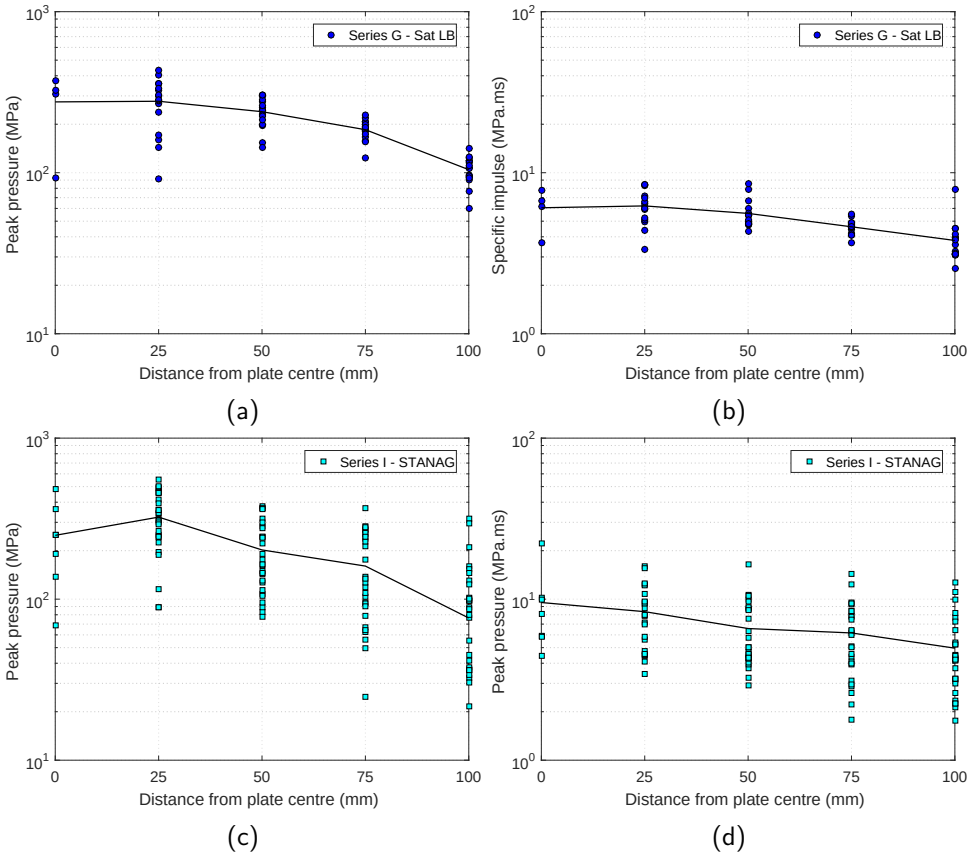

Figure 4.18: Pressure and impulse distributions investigating the effect of particle size distribution in saturated soil. Series G pressure (a), specific impulse (b). Series I pressure (c), specific impulse (d).

4.7.4 High speed video

HSV footage of Series I is presented in Figure 4.19 for saturated STANAG. In saturated STANAG soil there is a large range of particle sizes situated above the charge. The HSV shows that some smaller particles pick up a higher velocity and escape ahead of the main body of the soil ejecta at between 0.028–0.047 ms after detonation. These particles are likely to impart some momentum to the target; their significance however is that the void left in the annulus presents a pathway for the detonation products to vent. This venting can be seen to begin at 0.143 ms with a particularly prominent emergence of the detonation products on the left-hand field of view at 0.200 ms after detonation (seen as black detonation products in Figure 4.19). This shows the complex early-time regime of expanding detonation product gasses interacting with the still-expanding soil annulus. It is suggested that this early loading phase will more closely resemble the combined air-shock/soil impact loading observed in partially saturated tests. The ejecta appears to make full contact with the target at 0.229 ms, and the right-hand field of view appears to show the soil-water annulus intact with the detonation products fully contained within this part of the ejecta. This would indicate that the loading in this region of the target plate is due to 'annulus-type' loading.

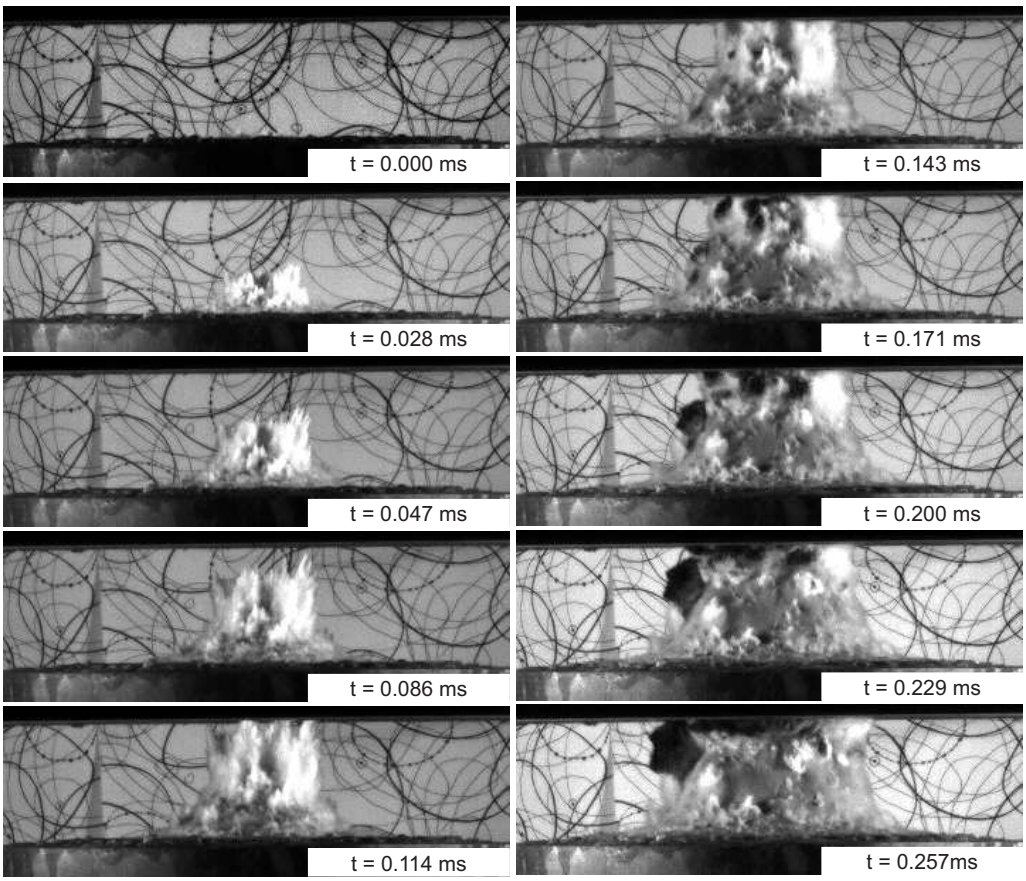

Figure 4.19: HSV for Series I (showing STANAG soil), the effect of particle size distribution in saturated sand on buried explosive output.

The HSV demonstrates that the well graded STANAG soil has been shown to form a complex loading mechanism than cannot simply be described by annulus or shock type loading. Both mechanisms were evident in pressure waveforms and demonstrated in HSV in Figure 4.19. The loading mechanism for a well graded soils therefore appears to be a hybrid of shock and annulus loading. It is for this reason that the loading from a STANAG soil is more complex, because the soil exhibits two distinct behaviours concurrently. The significance of this is that for numerical work, further statistical analysis will be required to account for large variances in loading at any discrete point.

4.8 Part Five – Effect of change to standoff

4.8.1 Introduction

Part Five of this parameter study investigates the effect of increasing and decreasing the standoff upon the loading formed at the target. The experimental test plan is summarised in Table 4.7, and test set-ups are shown in Figure 4.20. 17 tests make up Part Five of this parametric study, Series D, J and K used a single fraction LB soil with a moisture content of 2.45%. Series D employed the baseline standoff used throughout the parametric study of measuring 140 mm between the soil bed and target. Series J tests were performed at a reduced standoff of 105 mm and Series K tests were conducted at an increased standoff of 175 mm. Seven tests were conducted in Series D with 119 data points available from the series for analysis. Five tests were conducted in each of Series J and K with 85 data points available per series.

Table 4.7: Part Five - Test series to investigate the effect of change to standoff on shallow buried explosive output.

Tests	Series	Soil type	w(%)	Bulk density	Dry density	Variable
51-57	D	LB	2.45%	1.635	1.6	Base line
82-86	J	LB	2.45%	1.635	1.6	Reduction in standoff
87-91	K	LB	2.45%	1.635	1.6	Increase in standoff

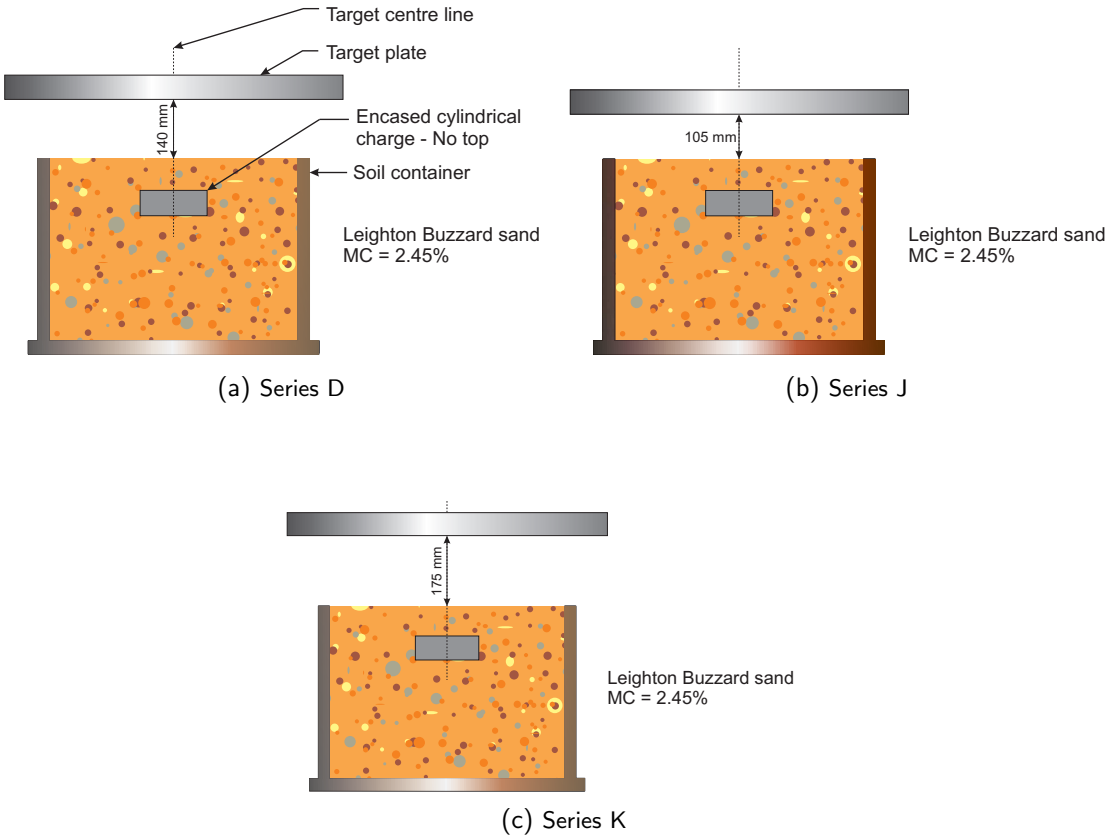

(a) Series D

(b) Series J

(c) Series K

Figure 4.20: Charge configuration of Series D, K and J - Investigation of standoff.

4.8.2 Pressure waveforms

Figures 4.21 and 4.22 show example pressure-time and impulse-time histories for partially and fully saturated LB from Series D and G.

The waveforms of Series J (at 105 mm standoff) show an increase in peak pressure compared to Series D. The waveform, given in Figure 4.21c, is consistent with the 'shock-type' mechanism associated with the loading from detonation products. Fewer discrete pressure spikes are overlain in the waveform than seen in Series D. Loading over the central 50 mm appears more intense and the Friedlander exponential is more clearly defined at bar locations over this region when compared to Series D. This sharp increase in pressure at the target is strong evidence to support the hypothesis that a significant portion of loading is due to detonation product loading. If the loading from a shallow buried charge in partially saturated soil was primarily comprised of particle strikes then the velocity of those particles would be maintained over greater distance. Irrespective of the small distance the standoff has been adjusted in this test, a twofold increase in pressures indicates that the most significant contribution for a shallow buried charge in partially saturated soil is due to detonation product momentum as described by Westine [53]. This finding contradicts the hypothesis of Park et al. [70]. The

impulse history of Series J shows a significant increase in impulse over the central 25 mm of target where the magnitude of momentum transfer has more than doubled when compared to Series D, strengthening the observations of Westine [53]. At 75 and 100 mm bar locations the pressure waveform resembles less of a shock load with discrete pressure peaks overlain. In general, it can be said there is less evidence of particle strikes at this shorter standoff of 105 mm.

When the standoff is increased to 175 mm in Series K the peak pressure is approximately half that of Series D at each bar location, cf. Figure 4.22a. The 'shock-type' loading seen in Series D and J is no longer clear in Series K and it cannot be said to form a Friedlander exponential. The pressure waveform appears 'noisy' with a significant number of particle impacts at all bar locations. The impulse history, given in Figure 4.22b, shows a more even distribution of loading across the instrumented area of the target with lower variance of peak impulse than for Series D and J. Here, the volume between the target and the soil surface has increased, therefore pressure will significantly decrease as the detonation products lose their momentum through expansion into a larger volume. Soil particles however do not have their velocity altered significantly by the increased volume, so at a stand–off of 175 mm the loading appears primarily to be from sand throw. This finding confirms that in the near–field, the primary mechanism of momentum transfer in a partially saturated soil is from detonation product momentum in a 'shock-type' load.

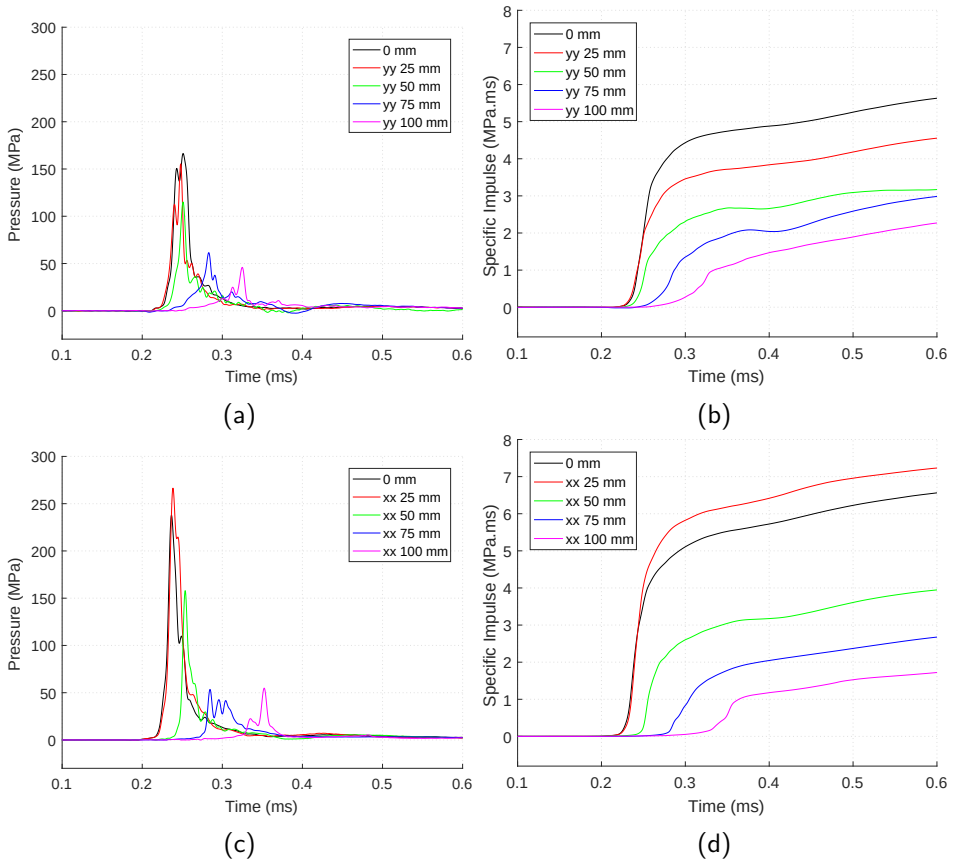

Figure 4.21: Single array pressure-time and impulse histories explosives for changes in standoff. Series D pressure (a), specific impulse (b). Series J pressure (c), specific impulse (d).

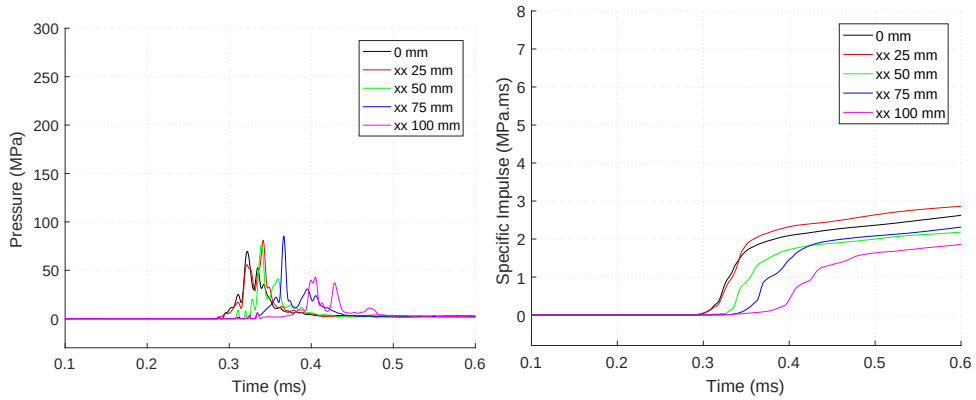

(a) (b)

Figure 4.22: Single array pressure-time and impulse histories explosives for changes in standoff. Series K pressure (a), specific impulse (b).

4.8.3 Peak reflected pressure and impulse distribution

Figure 4.23 shows the peak pressure and peak specific impulse compiled for Series D, J and K. Peak pressure and peak impulse are plotted against distance from the plate centre for each soil condition. The mean peak pressures and mean peak specific impulses have been calculated for each soil type at 0, 25, 50, 75, and 100 mm from the plate centre. The mean pressure and impulse at each radial ordinate for each series are given by the solid black lines.

The trend of pressure distribution seen in Figure 4.23a is for the baseline partially saturated soil of Series D. When the standoff is decreased in Series J, a significant focusing of the loading occurs within the central 25 mm of the target plate, with a rapid drop off to 50 mm and a progressive stagnated drop off thereafter, see Figure 4.23c. This is indicative of shock-type loading and demonstrates that the majority of momentum transfer is due to the pressure contribution of detonation product. Soil particle velocity and therefore soil momentum are relatively unchanged over the 35 mm reduction in standoff and therefore would not account for any significant increase in pressure at the target.

When standoff is increased to 175 mm in Series K, the pressure is reduced at each bar location and the mean shows a near even distribution of pressure at all bar locations compared to Series D and J. Soil particle velocity and therefore soil momentum are relatively unchanged over the 35 mm increase in standoff and therefore would not account for any significant reduction in pressure at the target. The significant reduction in pressure at the central 50 mm of the target therefore appears to be due to the detonation products, again indicating that the most significant contribution of 'shock-type' loading is due the pressure-volume relationship of the detonation products.

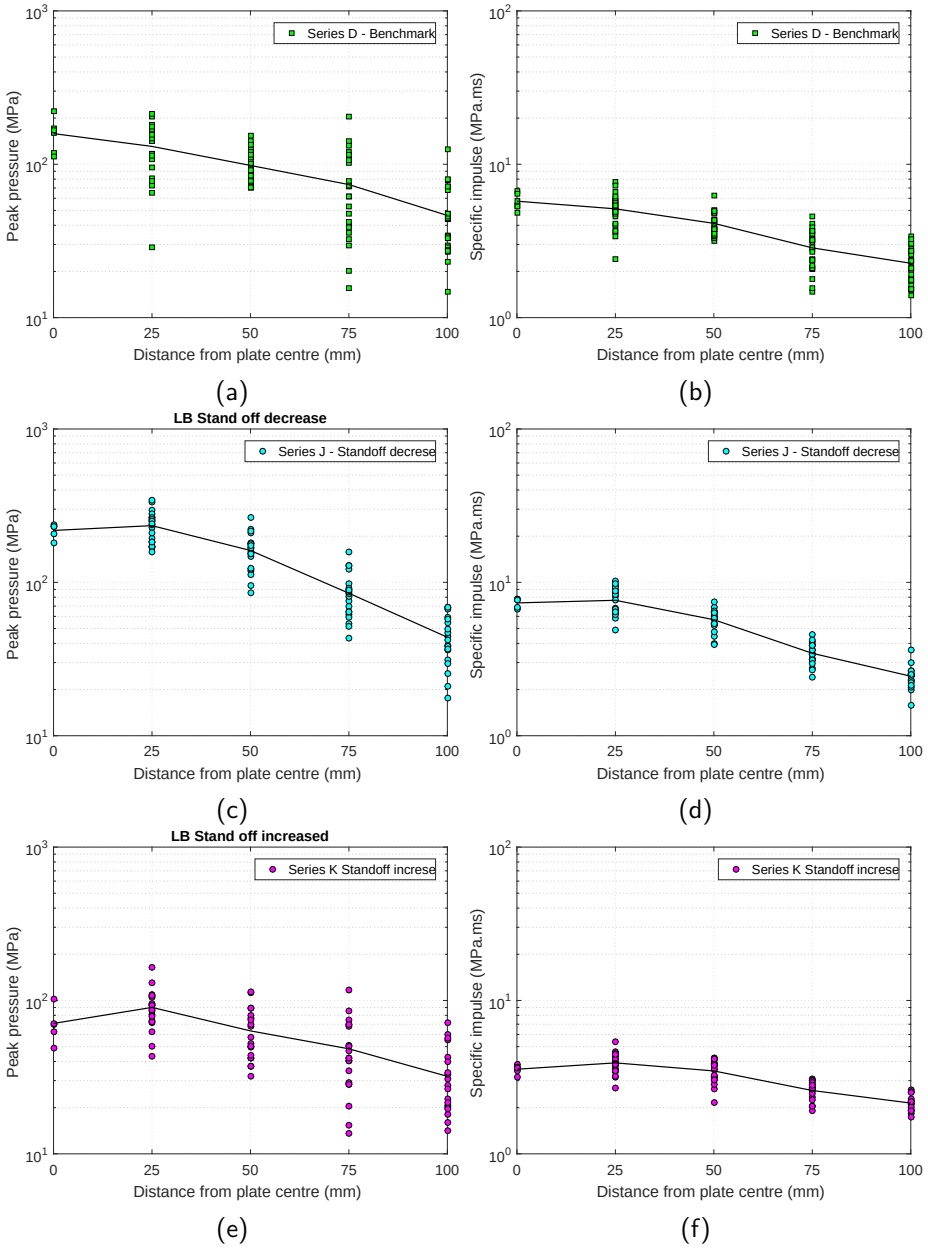

Figure 4.23: Pressure and impulse distributions, effect of change in standoff. Series D pressure (a), specific impulse (b). Series J pressure (c), specific impulse (d). Series K pressure (e), specific impulse (f).

4.9 Parametric study summary

It has been shown that for a fully cased charge, the pressure waveform and subsequent impulse history and therefore momentum transfer are significantly modified. This 'modification' to the input shockwave was hypothesised in Chapter 3 and demonstrated in Test 43. In comparison, for a partially cased charge used throughout testing in this work, it was shown that there is no significant influence on loading mechanisms when compared to a bare charge where pressure waveforms and impulse were similar. The significance of this is that a partially cased charge can be used in place of bare explosive without significantly affecting the results or observed loading mechanisms. The partially cased charge has the practical benefit of being more easily and accurately positioned whilst maintaining the geometry and integrity of the charge and detonator during burial and post burial compaction. A comparison of mean peak pressure and peak impulse for Series A–D is provided in Figures 4.24a and 4.24b

Tests without overburden (Series A, B and C) show similar pressure-time characteristics to a Friedlander exponential waveform. The inclusion of sand at the base of the charge in Series B does not appear to significantly increase momentum transfer to the target. When the charge is laterally confined in Series C, a significant increase in momentum transfer is seen at the target due to confinement focusing the detonation products, an observation consistent with the experiments of Bergeron et al. [44]. It is possible that the vertical channelling caused by the presence of soil around the circumference of the charge is exaggerated by a 'free-path' being available for the detonation products to expand into above the charge.

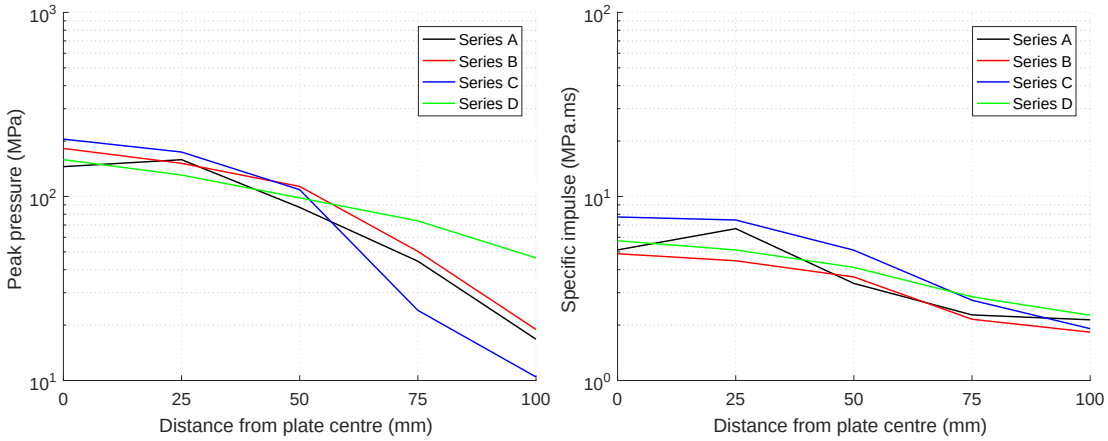

Figure 4.24: Mean peak pressure (a), and mean peak impulse (b) for Series A, B, C and D.

When overburden is placed on the charge in Series D, peak pressures are approximately similar to Series A and B, however the arrival time is more than an order of magnitude later and pressure duration significantly increases. In contrast to the work of Fourney et al. [57], a 20% increase in impulse was seen for charges detonated in partially saturated soil (Series

D) compared a charge placed on a soil fill (Series C). A comparison of mean peak specific impulse is provided in Figure 4.24b were Series D buried tests fall between the mean peak values for various confinement states. Evidence provided by pressure waveforms and HSV has demonstrated for fully confined, partially saturated soil, that loading is due to a combination of detonation products and sand throw.

Increasing burial depth from 28 to 53 mm was shown to affect only the loading distribution where pressure was more evenly distributed across the measurement surface of the target plate as shown in the mean peak pressure and impulse distributions in Figures 4.25a and 4.25b. A decrease in standoff from 140 mm to 105 mm demonstrated that the peak loading significantly increased and distribution of peak loading was more focused towards the target centre. Conversely, when standoff was increased from 140 mm to 175 mm peak loading significantly decreased with a more even distribution of peak load across the target. These results of small changes in length scale provide evidence to the hypothesis that the most significant contribution to loading in partially saturated shallow buried detonations is from the detonation products. Individual particle strikes, whilst visible in the pressure histories, contribute little to the evolution of specific impulse (although they do influence peak pressure distributions, as explained below). One implication of this is that testing aimed to simulate landmine donations which only account for soil particle loading, for example Park et al. [70], may significantly underestimate the loading seen in scaled tests.

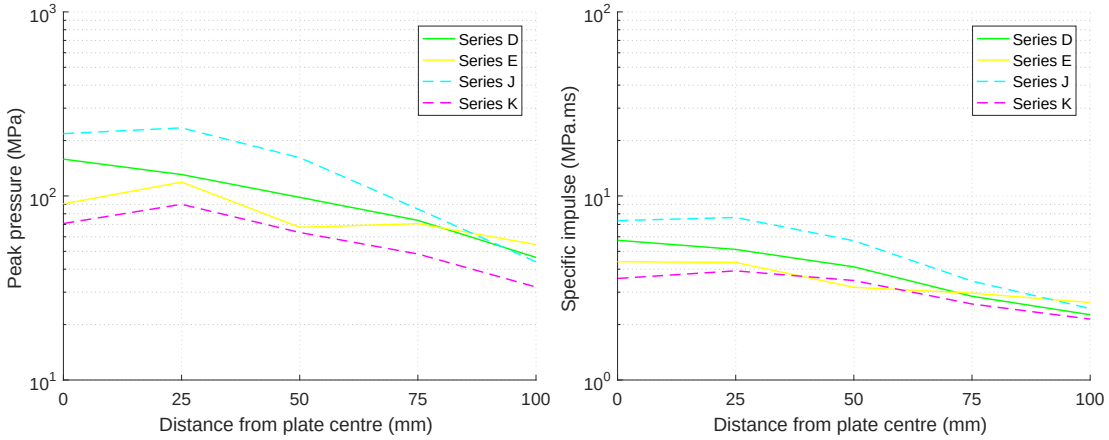

Figure 4.25: Mean peak pressure (a), and mean peak impulse (b) for Series D, E, J and K.

The pressure waveforms of partially saturated soils (Series D) show a 'pre-cursor shoulder' consistent with tests conducted by Bergeron [11] and Taylor [36]. Bergeron hypothesised that this initial loading was due to air compressed in front of the expanding soil ejecta. However, it was seen in the saturated soil and water tests that the pre-cursor shoulder does not form, which indicates that this loading may be caused by another mechanism. HSV of partially saturated soil (Series D) and water (Series H tests) has shown two different forms of ejecta. HSV of partially saturated soil shows the ejecta forming a soil annulus where a significant amount of detonation products are seen weeping from the soil at 0.16 ms. Conversely, in the case of the

charge submerged in water HSV has shown that detonation products remained fully confined within an annulus of water throughout the interaction with the target. Pressure waveforms for fully saturated LB soil and water have been shown to be very similar, indicating that the same mechanism of loading exists for a detonation event in saturated soil and water. Therefore it is hypothesised that the cause of the pre-cursor shoulder in partially saturated soils is due to high energy detonation products weeping though the soil annulus and impacting the target in advance of the main ejecta body.

Saturated soil shows a significant increase in pressure and momentum transfer particularly at the 25–100 mm HPB locations when compared to partially saturated soils. This increase is shown in peak mean data from Series D, G and H in Figures 4.26a and 4.26b. This finding agrees with numerical work of Fox et al. [77] where the weakest soil produced the highest target loading.

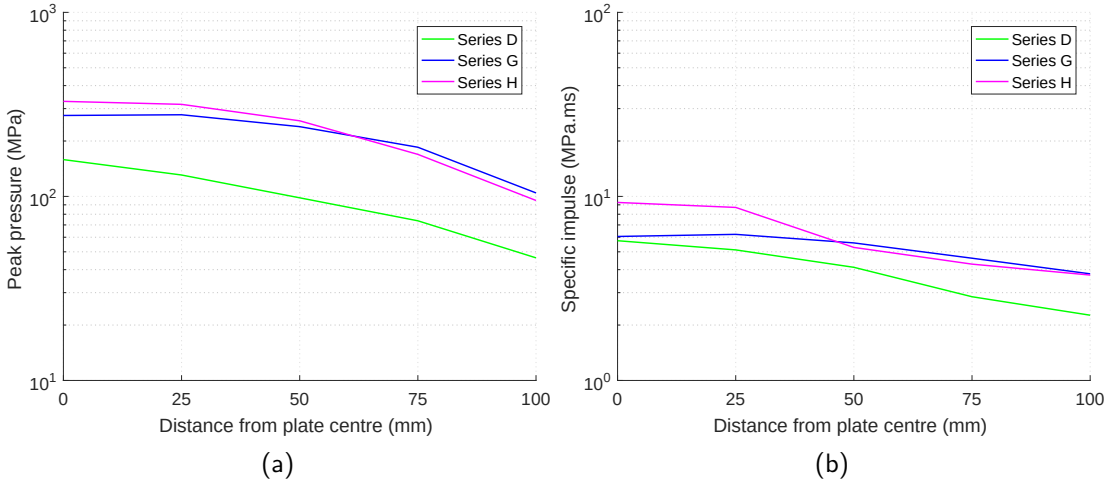

Figure 4.26: Mean peak pressure (a), and mean peak impulse (b) for Series D, G and H.

Evidence of two distinctly different loading mechanisms for partially saturated and fully saturated LB are shown earlier in Chapter 4. The pressure-time waveforms of the partially saturated soils form a Friedlander exponential with discrete pressure spikes overlain which it is hypothesised are due to sand particle impacts. The mean distribution of peak pressures for partially saturated soil appear less evenly distributed with higher variance at each discrete bar location when compared to the fully saturated and water tests. This increased variability in peak pressure is likely due to discrete particle impacts on the HPBs. The extended Friedlander which is the main component of the loading represent the contribution of loading associated with detonation products. The waveform from partially saturated tests agrees with numerical work by Grujicic [75] where the waveform was described as 'shock-type' loading.

Saturated LB and water tests show a much reduced variability at discrete bar locations indicating that particle impacts were significantly reduced or do not occur. As explained above,

HSV footage of submerged tests showed that the annulus surrounding the explosive products remains intact. The pressure waveform of saturated soil forms an approximately temporally symmetrical rise to peak pressure and decay to ambient pressures which is in agreement with the 'annulus-type' mechanism numerically described by Grujicic et al. [75]. The loading of the impacted soil-water is consistent with the initial phase phenomena from the impact of high velocity fluid on a solid surface described by Rein [26]. The pressure waveforms for saturated soil and water are very similar, indicating that saturated LB behaves as a fluid after detonation. The similarity in behaviour of shocked saturated soil and water has been observed at full scale by Westine et al. [54] and by an alternative experimental approach by Barr et al. [73] .

The shock-type and annulus-type mechanisms occur depending on the moisture content of the soil matrix, an observation which is again supported by the numerical work of Fox et al. [77]. In a dry soil when a stress wave is introduced, the soil compacts into the available voids, at high strain particles will crush and fill smaller voids. When water is introduced into the soil matrix, water will fill the voids between soil particles in this compaction process. When total compaction is achieved, further increases in stress are supported by the pore water. At this point of hydrostatic lock-up the bulk modulus of the material increases significantly requiring much larger increases in stress to affect similar increases in strain. Soils with high moisture content reach this hydrostatic lock-up much earlier meaning that compaction is achieved at a much lower strain than in partially saturated soils, see Barr et al. [71–73]. The lock-up of the saturated soil leaves only one response available: to immediately deform and eject from the soil bed. It is this difference in the compaction behaviour between partially and fully saturated soil which appears to cause these two fundamentally different loading mechanisms.

Well–graded STANAG soil exhibits a complex loading which appears as two separate mechanisms which act concurrently, namely shock and annulus type loading. Annulus loading occurs when the annulus remains intact. Shock–type loading is caused by particles in the soil ejecting from the annulus. Where this occurs, the void left by the particle allows venting of the detonation products. The loading profile around this ejection site in the annulus will appear as 'shock-type' loading with discrete particle strikes overlain. The mechanism of loading from a well–graded soil therefore is a hybrid of shock-type and annulus-type loading. In well–graded soils, the loading mechanism that develops from early soil response is determined not only by moisture content of the soil alone but the ability to maintain confinement of the detonation products between the soil bed and target. In the well–graded STANAG soil used in these tests a hydrostatic lock-up of saturated soils described by Fox [77] appears to have occurred due to the presence of annulus type loading. However ejection of particles from the soil has disrupted the annulus mechanism forming a 'shock-annulus hybrid' mechanism. Figures 4.27a and 4.27b show that the mean peak pressure distribution of Series I varies more significantly than that of Series G.

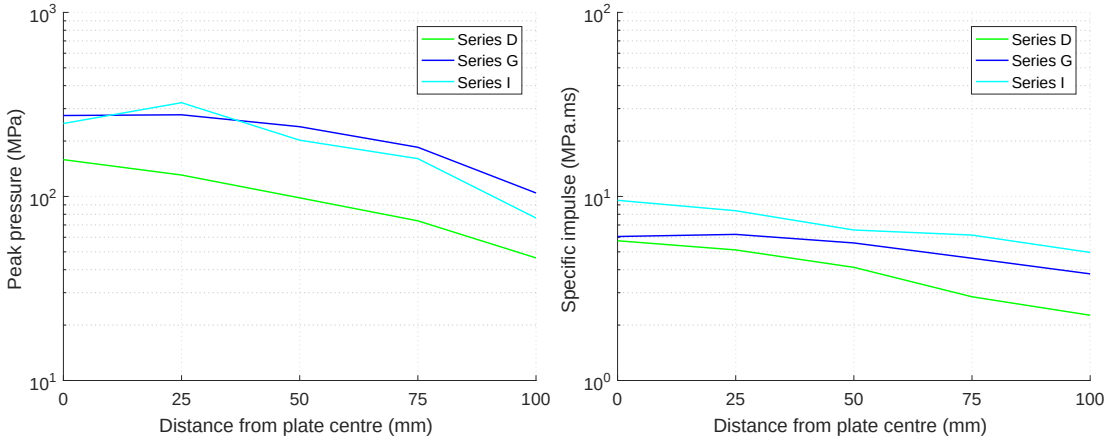

(a) (b)

Figure 4.27: Mean peak pressure (a), and mean peak impulse (b) for Series D, G and I.

Chapter 5

Summary and conclusions

5.1 Summary

The aim of this thesis was to investigate the spatial and temporal distributions of blast loading, determine the mechanisms which govern this load development, and explore how these mechanisms are related to the properties of the soil bed.

This thesis presents the design of a new experimental technique for measuring the spatial and temporal pressure on a rigid target following detonation of a shallow buried explosive device: the Characterisation of Blast Loading (CoBL) apparatus. CoBL was designed to represent STANAG AEP-55 threat level M2 at quarter-scale, offering a balance between scientific validity and cost-effectiveness. In total, 91 experimental tests have been performed, which are reported and analysed in detail in this thesis.

Initially, a series of commissioning tests were performed to refine the experimental apparatus, increase the quality and accuracy of the data, and remove sources of error. Following this, a detailed parametric study was conducted to systematically investigate the influence of key parameters on the mechanism and magnitude of loading developed on the target surface, namely: charge encasement and shape; soil confinement and burial depth; soil saturation; particle size distribution of saturated soils; and standoff distance.

Experiments with modified charge cases provide an understanding of the interaction between the charge case and soil and the consequences of this interaction on the pressure-waveform. Two charge shapes were compared to investigate the focusing of detonation products for a spherical and a cylindrical charge. Soil confinement and burial depth were investigated to assess the contribution of the confining media at the base, laterally and above the charge. Soil saturation was varied to investigate changes in response behaviour of the soil when the voids between soil particles become filled with water. Two saturated soils with particle size

distributions described as 'uniform' and 'well–graded' were tested to compare the influence that the particle size distribution has on the loading mechanism. Three standoffs were tested in partially saturated soil to investigate the evolution of the loading in ejected material.

The use of an array of discrete time resolved pressure measurements has allowed the first detailed insight into the evolution of shallow buried blast loading for a range of geotechnical materials and saturation states. This study has unified a range of hypothesis from both the experimental and numerical communities which aimed to understand how load is formed at the target. Understanding the loading immediately above the charge informs designers of the service environment, and aids numerical modelling efforts for phenomenology verification, ensuring that the fundamental physics are captured in models. The pressure—waveforms contained in this these have been used in numerical models to simulate blast loading which reduces the technical and computational expense of modelling the detonation event itself. By understanding and accurately applying the load to a protective structure, there can be higher confidence in the local response of a target and therefore response connections between armour and the body of the vehicle. Furthermore this will improve the estimates of global response which significantly affects vehicle occupants. Further work in this area should be conducted by numerical computation where the problem is geometrically similar. If there is a need to modify soil type, soil parameters, charge configuration or any of the test geometry further testing is needed.

Following Hopkinson scaling [95] will allow reproduction of the tests contained herein numerically and experimentally allowing the momentum transfer from a range of threats to be estimated. A limitation of this is that the test geometry cannot be altered, for example applied to an inclined target. The level of scaling possible is limited to the validity of scaling the soil particle size requiring further experimental work. This work is not appropriate for estimating the output from shallow buried fragmentation devices. The target used in this research was effectively rigid and infinite over the duration of the test. Whilst it is generally accepted that the loading on a target following the detonation of a landmine is impulsive i.e. the loading has passed by the time significant deformation takes place, it should be noted that significant deformation of a target plate would alter the loading witnessed.

The CoBL test apparatus has been used to produce the first detailed experimental study into the output from shallow buried charges with spatially and temporally resolved pressure histories measured above a shallow buried charge. The observations from these tests can be used to verify the behaviour of soils in numerical models, allowing armour designers to accurately assess the mechanisms of loading applied to a protective structure when subjected to a buried IED attack.

5.2 Conclusions

- The deployment of an array of HPBs in appropriately scaled shallow buried explosive test has been successful in providing detailed pressure waveforms which provide sufficient information regarding the mechanisms of momentum transfer for shallow buried charges in partially and fully saturated soils.

- Good agreement was found between empirical pressure-time histories generated in ConWep and the experimentally measured spherical free-air blast with the CoBL test apparatus.

- The encasement and detonator configuration as specified in AEP55 was shown to significantly modify the output from a shallow buried charge at a 1/4 scale due to the case confining the detonation products and by extension of the detonator above the soil surface. The charge case was modified by removing the case lid and moving the detonator to the charge base. With a modified charge configuration for 1/4 scale level M2 to STANAG AEP-55 [8], no scaling of the soil was required.

- Removal of the soil overburden directly above the charge resulted in a significant increase in peak pressure with a focus of the detonation energy towards the central HPB, an observation consistent with the observations of Bergeron et al. [44]. Comparing the mean peak pressure for a detonation without overburden (200 MPa) and with overburden (160 MPa) shows significant focusing of detonation products above the charge. Between 50–75 mm pressure and therefore momentum transfer significantly drops for charges without overburden demonstrating significant radial confinement of the partially saturated soil.

- For partially saturated soil, small increases in overburden and standoff were shown to decrease peak pressure and increase the distribution of pressure across the measurement surface. When standoff was decreased, peak pressures increased significantly. Here, pressure was highly focussed into a circumference approximately equal to the size of the charge. The focusing of detonation products is consistent with the observations of Ehrgott [46,47] who used pressure transducers on a plane above the soil surface, Tiwari et al. [65] who used DIC and Westine [59], Joynt [7] and Fourney [61] who used the Free Acceleration Methodology with a range of spatial sensitivity. From a protective design perspective, this demonstrates that rigid body experiments that determine impulse from jump height can not fully describe the behaviour of a shallow buried charge. Further testing should be conducted with discrete measurements to allow assessment of the pressure distribution in order to fully understand the loadings applied to protective structures.

- The pre-cursor shoulder first described by Bergeron [11] was hypothesised to be due to air compressed in front of the soil ejecta. This hypothesis was shown to be invalid based on the comparison of partially and fully saturated soil tests. Partially saturated soil tests

demonstrate the pre-cursor shoulder as described by Bergeron, however in fully saturated tests the pre-cursor shoulder was not seen. It is hypothesised that the pre-cursor shoulder is due to detonation products weeping from the ejected soil and striking the target in advance of the main body of soil throw.

- Test-to-test variability of pressure distribution was shown to be similar to that achieved by Anderson [50] and Clarke [28]. This demonstrates that with good control of the soil bed and test setup a large reduction in test–to–test variation is possible. Pressure distribution from a detonation in partially saturated soil was more variable than that of fully saturated soil. This is due to break–out of the detonation products from the soil confining body occurring when the soil annulus became fragmented, with the break–out pattern varying between tests.

- Two distinct behaviours were witnessed according to the saturation state of the soil which match the numerically derived observations of Grujicic [75]. In partially saturated soil a 'shock–type' mechanism was witnessed. In saturated soil an 'annulus–type' mechanism was seen. The shock–type and annulus–type mechanisms are described below:

  - The 'shock–type' mechanism develops due to the soil annulus rupturing relatively early in the ejection from the soil bed, allowing the detonation products to escape and impact the target. The loading therefore mainly comprises a detonation product shock load with reduced momentum imparted to the soil. Rupture of the soil bubble allows the detonation products to vent in the radial direction, reducing the directionality of the event.
  - The 'annulus–type' mechanism develops due to saturated sand having a lower compressibility and higher cohesive strength, resulting in a larger volume of soil ejecta and delayed annulus rupture. This annulus confines the detonation products completely until it impacts the target, and the loading is mainly comprised of momentum transfer from the soil–fluid composition of the soil.

- The soil annulus is formed in both the case of a saturated and partially saturated soil and is a thin shell of soil surrounding the expanding detonation products. The shock–type mechanism evolves in partially saturated soil due to a disruption of the soil annulus where multiple breaches in the annulus wall occur allowing venting of the detonation products which was witnessed as shock type loading. The annulus–type mechanism occurs due to the continued confinement of the detonation products between the detonation location through to the interaction with the target, this is witnessed by the uniform rise and fall of the peak pressures which is indicative of a fluid impact. In well graded saturated soils, the soil annulus was seen to be disrupted in some areas by the annuls breaching due to the movement of larger stone fragments moving out of the annulus. This allowing detonation products to vent around these locations. At the target, the loading appeared to be of an annulus type mechanisms with the exception of where the detonation products had vented, here the pressure—waveforms appeared to resemble shock type loading.

- Observation of the shock–type and annulus–type loading demonstrate that the assumptions of particle barrage being a primary mechanism of momentum transfer following the detonation of a shallow buried charge is not valid. Experimental work that focusses on driving soils mechanically or with stored gas as described by Hinz [68], McShane [69] and Park [70] cannot be said to represent the loading from a shallow buried charge. As predicted by Baker [52] in the late 1960s impulse is caused primarily by the momentum of the explosive products, while the behaviour of the soil serves to modify the profile of this momentum transfer. Baker's hypothesis was confirmed analytically by Westine [53] who demonstrated that the majority of loading from a shallow buried charge in partially saturated soil was from the mass of the detonation products.

- The numerical work of Fox [77] and SHPB experiments of Barr [71] support the hypothesis of a shock–type and annulus–type mechanism with descriptions of the early compaction behaviour of partially and fully saturated soils. In partially saturated soils the soil will compact, crush the soil particles and fill voids between the soil particles. In fully saturated soils when compaction of the soil–fluid is achieved, further increases in stress are supported by the pore water [71,77]. At this point of the hydrostatic lock–up, the material's bulk modulus increases significantly. As the soil response stiffens due to the increase in bulk modulus the soil must begin deforming and eject from the soil bed.

- The initial phase phenomena of water droplet impacts on a solid surface described by Rein [26] were consistent with HSV of saturated soil and water. It was noted in the footage for saturated soil and water that the impacted ejecta may rebound from the target following impact, suggesting that splashing of the water has occurred. This may be due to the fluid expanding into a thin disk after impact, reaching a maximum radius where kinetic energy is dissipated into additional surface energy, which forces the disk to contract. This contraction of the water droplet causes it to 'bounce' off after impact.

- The PSD for uniformly graded and well–graded soils has a significant affect on the mechanisms and therefore loading of the soil. The well–graded saturated STANAG soil demonstrated a more complex loading where the shock–type and annulus–type loading appear to occur at the same time. This is attributed to larger particles disrupting the soil–fluid annulus allowing a pathway for detonation products to flow. This behaviour of the well–graded saturated soil is termed the shock-annulus-hybrid mechanism.

5.3 Future work

Further refinement of the test CoBL test apparatus should include the introduction of smaller diameter HPBs. A primary benefit of reducing the bar diameter is that a closer spacing of the bars could be achieved, allowing more detailed measurements in the region directly above the charge and the area in the transition between vertical and lateral flow of ejecta across the target. A secondary benefit of reducing bar diameter is an increase in the bandwidth capacity of the bar and reduction of dispersive effects, which is likely to be necessary for investigating higher frequency components typically found in free–air tests.

The soils in this study did not include silts, clays or organic matter. Due to the significance of soil saturation to the loading output, soils in areas most likely to be saturated, for example river crossings, should be considered. The loading behaviour of clay has since been investigated with the CoBL test apparatus in a separate study [96], but the behaviour of silts and organic matter when subjected to blast loading remain topics for study.

Thermodynamic principles derived by Fermi [97] are the basis of many numerical codes where pressure-volume and temperature-entropy allow accurate simulation of the behaviour of a material. To develop an exact understanding of the behaviour of a shallow buried charge and to provide data which allows numerical simulation of a buried blast load, the next development stage in characterising blast loading should be to understand the pressure-volume and temperature relationship of the ejected soil at the target. Approaching experimental work with an understanding of numerical analysis will increase the integration between experimental and numerical communities and develop data which can be used for detailed numerical mechanistic studies accelerating understanding of shallow buried detonations.

Bibliography

[1] Ministry of Defence. *UK forces: Operations in Afghanistan*. www.gov.uk/guidance/uk-forces-operations-in-afghanistan-casualty-figures, accessed on 18/12/2015, 2015.

[2] National Consortium for the Study of Terrorism and Responses to Terrorism (START). *The Global Terrorism Database (GTD) gtd–96to13–0718dist.xlsx and gtd–14to17–0718dist.xlsx*. University of Maryland, www.start.umd.edu/gtd, accessed on 26/08/2019, 2018.

[3] United Nations. *Impact of IEDs*. www.un.org/disarmament/convarms/impact-of-ieds/, accessed 01/08/2019, 2019.

[4] H. Champion, J. Holcomb, and L. Young. Injuries from explosions: Physics, biophysics, pathology, and required research focus. *The Journal of Trauma*, 66:1468–1477, 2009.

[5] L. Dong, F. Zhu, X. Jin, M. Suresh, B. Jinag, G. Sevagan, Y. Cai, G. Li, and K. Yang. Blast effect on the lower extremities and its mitigation: A computational study. *Journal of the Mechanical Behaviour of Biomedical Materials*, 28:111–124, 2010.

[6] J.O. Jansen, G.O.R. Thomas, S.A. Adams, N.R.M Tai, R. Russell, J. Morrison, L. Clasper, and M. Midwinter. Early management of proximal traumatic lower extremity amputation and pelvic injury caused by improvised explosive devices (IEDs). *International Journal of Injury*, 43:976–979, 2011.

[7] V. Joynt. STANAG protection levels for landmines. *Lecture to the Armour Symposium, Shrivenham, UK*, 2009.

[8] C.Aksit. STANAG 4569: Procedures for evaluation the protection level of armoured vehicles – Mine threat. *North Atlantic Treaty Organization (NATO)*, 2012.

[9] A. Tyas, J.J. Reay, S.D. Fay, S.D. Clarke, S.E. Rigby, J.A. Warren, and D.J. Pope. Experimental studies of the effect of rapid afterburn on shock development of near-field explosions. *Internation Journal of Protective Structures*, 7:452–465, 2016.

[10] S.E. Rigby, A.Tyas, R.J. Curry, and G.S. Langdon. Experimental measurement of specific impulse distribution and transient deformation of plates subjected to near-field explosive blasts. *Experimental Mechanics*, 59:163–178, 2019.

[11] D. Bergeron, R. Walker, and C. Coffey. Detonation of 100-gram anti-personnel mine surrogate charges in sand – A test case for computer code validation. *Defence Research Establishment Suffield, Alberta, Canada*, Report No. 668, 1998.

[12] G.F. Kinney and K.J Graham. *Explosive shocks in air – Second Edition*. Springer-Verlag New York Inc., USA, 1985.

[13] D.W. Hyde. Conventional weapons effects (ConWep). *U.S. Army Engineer Waterways Experiment Station*, ATTN: CEWES–SS–R, 1991.

[14] J. Köhler and R. Meyer. *Explosives – Fourth Revised and Extended Edition*. VCH Verlagsgesellschaft, Weinheim, Germany, 1993.

[15] J Akhavan. *The Chemistry of Explosives – Third Edition*. Royal Society of Chemistry, Cambridge, Cambridgeshire, UK, 2001.

[16] J.A. Zukas and W.P. Walters. *Explosive effects and applications*. Springer-Verlag New York Inc., 1998.

[17] P.W. Cooper. Explosives engineering. *Wiley-VCH, Inc., USA*, 1996.

[18] R Winter. *An Introduction to some key concepts of shock hydrodynamics*. AWE, Aldermaston, UK, 2003.

[19] P.W. Cooper and S.R. Kurowski. Introduction to the technology of explosives. *Wiley-VCH, Inc., USA*, 1996.

[20] F. Friedlander. The diffraction of sound pulses (I). Diffraction by a semi-infinite plane. *The Royal Society*, 186, 1946.

[21] S.E. Rigby, A.Tyas, S.S Clarke, S.D. Fay, J.J. Reay, J.A. Warren, and D.J. Pope. A review of UFC 3-340-02 blast wave clearing predictions. *16th International Symposium on the Interaction of the Effects of Munitions with Structures (ISIEMS16) Destin, Florida, USA.*, 2015.

[22] US Department Of Defense. Structures to resist the effects of accidental explosions. *United States of America Department of Defense*, Report No. UFC 3-340-02, 2008.

[23] N. Jackson and R.K. Dhir. Civil engineering materials – Fifth Edition. *Palgrave, Basingstoke, UK*, 1996.

[24] W. Powrie. Soil mechanics, concepts and applications – Second Edition. *Spon Press, Abingdon, Oxon, UK*, 2002.

[25] S. Clarke, J. Warren, and A. Tyas. The influence of soil density and moisture content on the impulse from shallow buried explosive charges. *14th International Symposium on Interaction of the Effects of Munitions with Structures (ISIEMS14), Seattle, USA*, 2011.

[26] M. Rein. Phenomena of liquid drop impact on solid and liquid surfaces. *Fluid Dynamics Research*, 12:61–93, 1993.

[27] S. Clarke, J.A. Warren, S.D. Fay, S.E. Rigby, and A. Tyas. The role of geotechnical parameters on the impulse generated by buried charges. *The 22nd International Symposium on Military Aspects of Blast and Shock (MABS22), Bourges, France*, 2012.

[28] S.D. Clarke, S.D. Fay, A. Tyas, J. Warren, S. Rigby, I. Elgy, and R. Livesey. Repeatability of buried charge testing. *23rd International Symposium on Military Aspects of Blast and Shock (MABS23), Halifax, Nova Scotia, Canada*, 2014.

[29] S.D. Clarke, S.E. Rigby, S.D. Fay, A. Tyas, J.A. Warren, M.Gant, , R. Livesey, and I. Elgy. 'bubble-type' vs 'shock-type' loading from buried explosives. *16th International Symposium for the Interaction of the Effects of Munitions with Structures (ISIEMS16), Florida, USA*, 2015.

[30] S.D. Clarke, S.D. Fay, J.A. Warren, A. Tyas, S.E. Rigby, J.J. Reay, R. Livesey, and I. Elgy. Geotechnical causes for variations in output measured from sallow buried charges. *International Journal of Impact Engineering*, 86:274–283, 2015.

[31] S.D. Clarke, S.D. Fay, J.A. Warren, A. Tyas, S.E. Rigby, J.J. Reay, R. Livesey, and I. Elgy. Predicting the role of geotechnical parameters on the output from shallow buried explosives. *International Journal of Impact Engineering*, 102:117–128, 2016.

[32] S. Clarke, S. Rigby, A. Barr, A. Tyas, J. Warren, and I. Elgy. Characterisation of sandy-gravel across the scales. *Mach Conference 2018, Baltimore, USA*, 2018.

[33] C. Aksit. AEP-55: Procedures for evaluating the protection level of logistic and light armoured vehicles, Volume 2 For mine threat. *North Atlantic Treaty Organization (NATO)*, 2011.

[34] B. Hopkinson. A method of measuring the pressure in produced the detonation if high explosives or by the impact of bullets. *Royal Society Publishing*, 213:497–508, 1914.

[35] D.H. Edwards, G.O. Thomas., A. Milne, G. Hooper, and D. Tasker. Blast wave measurements close to explosive charges. *Shock Waves*, 2:237–243, 1992.

[36] L.C.Taylor, W.L. Fourney, and H.U. Leiste. Pressures on targets from buried explosions. *Proceedings of the IMPLAST 2010 Conference, Rhode Island, USA*, 2010.

[37] P. Horowitz and W. Hill. The art of electronics. *Cambridge University Press, Cambridge, UK*, Second Edition, 1989.

[38] A.L. Window and G.S. Holister. Strain gauge technology. *Applied Science Publishers Ltd., Barking, Essex, UK*, 1982.

[39] S.E. Rigby, A.Barr, and M. Clayton. A review of Pochhammer-Chree dispersion in the Hopkinson bar. *Engineering and Computational Mechanics*, 171:3–13, 2018.

[40] L. Pochhammer. Über die fortpflanzungsgeschwindigkeiten kleiner schwingungen in einem unbegrenzten isotropen kreiszylinder. *Journal für die reine und angewandte Mathematik*, 62:324–336, 1876.

[41] C. Chree. The equations of an isotropic elastic solid in polar and cylindrical co-ordinates. *Transactions of the Cambridge Philosophical Society*, 14:250–369, 1889.

[42] A. Neuberger, S. Peles, and D. Rittel. Scaling the response of circular plates subjected to large and close-range spherical explosions. Part I: Air-blast loading. *International Journal of Impact Engineering*, 34:859–873, 2007.

[43] A. Neuberger, S. Peles, and D. Rittel. Scaling the response of circular plates subjected to large and close–range spherical explosions. Part II: Buried charges. *International Journal of Impact Engineering*, 34:874–882, 2007.

[44] D.M. Bergeron and J.E. Trembley. Canadian research to characterize mine blast output. *16th International Symposium on the Military Aspects of Blast and Shock (MABS16), Oxford, UK*, 8:1–11, 2000.

[45] S.L. Hlady. Effect of soil parameters on landmine blast. *18th International Symposium on the Military Aspects of Blast and Shock (MABS18), Bad Reichenhall, Germany.*, 2004.

[46] J.Q. Ehrgott. Tactical wheeled vehicle survivability: Results of experiments to quantify aboveground impulse. *US Army Corps of Engineers, Engineer Research and Development Center*, ERDC/GSL TR-10-7, 2010.

[47] J.Q. Ehrgott, R.G. Rhett, S.A. Akers, and D.D. Rickman. Design and fabrication of an impulse measurement device to quantify the blast environment from a near-surface detonation in soil. *Experimental Techniques*, 35:51–62, 2011.

[48] S. Xu, X. Deng, V. Tiwari, M.A. Sutton, W.L. Fourney, and D. Bretall. An inverse approach for pressure load identification. *International Journal of Impact Engineering*, 51:815–830, 2010.

[49] E.G. Pickering, S. Chung Kim Yuen, G.N. Nurick, and P. Haw. The response of quadrangular plates to buried charges. *International Journal of Impact Engineering*, 49:103–114, 2012.

[50] C.E. Anderson, T. Behner, C.E. Weiss, S. Chocron, and R.P. Bigger. Mine blast loading: Experiments and simulations. *US Army Tank–Automotive Research, Development and Engineering Center*, Report No. 8.12544/011, 2010.

[51] W.H. Jack and B.F. Armendt Jr. Measurements of normally reflected shock parameters from explosive charges under simulated high altitude conditions. *U.S. Army Materiel Command, Ballistics Research Laboratories, Aberdeen Proving Ground, Maryland, USA*, Report No. 1280, 1965.

[52] W.E. Baker. Prediction of scaling of reflected impulse from strong blast waves. *International Journal of Mechanical Science*, 9:45–51, 1967.

[53] P.S. Westine. The impulse imparted to targets by the detonation of landmines. *Southwest Research Institute, San Antonio, Texas, USA*, 1972.

[54] P.S. Westine and G.J Friesenhahn. Free-field ground shock pressures from buried detonations in saturated and unsaturated soils. *Southwest Research Institute, San Antonio, Texas, USA*, 1983.

[55] W.L. Fourney, R.D Dick, X.J. Wang, and Y. Wei. Fragmentation mechanism in crater blasting. *Internationl Journal of Rock Mechancis and Mining Sciences and Geomechanics*, 30:413–429, 1993.

[56] W.L. Fourney, U. Leiste, R. Bonenberger, and D.J. Goodings. Explosive impulse on plates. *Internationl Journal of Blasting Fragmentation*, 9:1–17, 2005.

[57] W.L. Fourney, U. Leiste, R. Bonenberger, and D.J. Goodings. Mechanism of loading on plates due to explosive detonation. *Internationl Journal of Blasting Fragmentation*, 9:205–217, 2005.

[58] E.G. Pickering, S. Chung Kim Yuen, and G.N. Nurick. The influence of the the height of burial of buried charges - some experimental observations. *International Journal of Impact Engineering*, 58:76–83, 2013.

[59] P.S. Westine, B.L. Morris, P.A. Cox, and E.Z Polch. Development of a computer program for floor plate response from land mine explosions. *Southwest Research Institute, San Antonio, Texas, USA.*, 1985.

[60] V. Joynt. Armoured fighting vehicle 2010. *MURI Lecture 8 April 2010*, 2010.

[61] W. L. Fourney, H. U. Leiste, A. Hauch, and D. Jung. Distribution of specific impulse on vehicles subjected to IEDs. *Proceedings for the IMPLAST 2010 Conference, Rhode Island, USA*, 2010.

[62] A. Tyas and A.J. Watson. An investigation of frequency domain dispersion correction of pressure bar signals. *International Journal of Impact Engineering*, 25:87–101, 2001.

[63] L.C. Taylor, W.L. Fourney, U.Leiste, and B.Cheeseman. Loading mechanisms from shallow buried explosives. *Proceedings of the 34th annual conference on explosives and blasting techniques*, 2008.

[64] A. Tyas. Experimental studies of direct pressure measurements of loading from shallow buried explosive charges. *Blastech Limited Report, Sheffield, UK*, Report No. BT-DPD-055, 2010.

[65] V. Tiwari, M.A. Sutton, S.R. McNeill, S. Xu, X. Deng, W.L. Fourney, and D. Bretall. Application of 3D image correlation for full-field transient plate deformation measurements during blast loading. *International Journal of Impact Engineering*, 36:862–874, 2009.

[66] M.A. Sutton, X.M. Deng, V. Tiwari, X. Zhao, W.L. Fourney, and H.U. Leiste. Scaling of blast loading experiments for buried explosives. *Proceedings of the IMPLAST Conference 2010, Rhode Island, USA*, 2010.

[67] M. Tyler-Street and P.J. Leerdam. Implementation of a user defined mine blast model in LSDYNA. *The 22nd International Symposium on Military Aspects of Blast and Shock (MABS22), Bourges, France*, 2012.

[68] B.J. Hinz. Experimental and numerical investigations of shallow buried explosive blast effects. *ME-790 Seminar*, South Dakota School of Mines and Technology, 2007.

[69] G.J. McShane, V.S. Deshpande, and N.A. Fleck. A laboratory-scale buried charge simulator. *International Journal of Impact Engineering*, 62:210–218, 2013.

[70] S. Park, T. Uth, N.A. Fleck, H.N.G. Wadley, and V.S. Deshpande. Sand column impact onto a Kolsky pressure bar. *International Journal of Impact Engineering*, 62:229–242, 2013.

[71] A.D. Barr. Strain-rate effects in quartz sand. *PhD Thesis, The University of Sheffield, Sheffield, UK*, 2016.

[72] A.D. Barr, S.D. Clarke, M. Petkovski, A. Tyas, S.E. Rigby, J.Warren, and S.Kerr. Effect of strain rate and moisture content on the behaviour of sand under one-dimensional compression. *Experimental Mechanics*, 56:1625–1639, August 2016.

[73] A.D. Barr, S.D Clarke, A. Tyas, and J.A. Warren. Effect of moisture content on high strain rate compressibiliy and particle breakage in loose sand. *Experimental Mechanics*, 58:1331–1334, 2018.

[74] M. Grujicic, B. Pandurangan, G.M. Mocko, S.T. Hung, B.A. Cheeseman, W.N. Roy, and R.R. Skaggs. A combined multi-material euler/lagrange computational analysis of blast loading resulting from detonation of buried landmines. *Multidiscipline Modeling in Materials and Structures*, 4:105–124, 2008.

[75] M. Grujicic, B. Pandurangan, R. Qiao, B. Cheeseman, W. Roy, R. Skaggs, and R. Gupta. Parametrization of the porous–material model for sand with different levels of water saturation. *Soil Dynamics and Earthquake Engineering*, 28:20–35, 2008.

[76] D.M. Fox, X. Huang, D. Jung, W.L. Fourney, U. Leiste, and J.S. Lee. The response of small scale rigid targets to shallow buried explosive detonations. *International Journal of Impact Engineering*, 38:882–891, 2011.

[77] D.M. Fox, S.A. Akers, U.H. Leiste W.I. Fourney, J.E. Windham, J.S. Lee, J.Q. Ehrhott, and L.C. Taylor. The effects of air filled voids and water content on the momentum transferred from a shallow buried explosive to a rigid target. *International Journal of Impact Engineering*, 69:182–193, 2014.

[78] D.M. Fox and J.S. Lee. Application of an arbitrary lagrangian eulerian method to describe high velocity gas-particle flow behaviour. *Army Research Laboratory*, Report No. ARL–RP–338, 2011.

[79] D.M. Fox and J.S. Lee. The influence of water, dry sand, and unsaturated sand constitutive behaviour on the blast response of a rigid target. *International Journal of Impact Engineering*, 65:163–173, 2014.

[80] D. Steinberg. Spherical explosions and the equation of state of water. *Lawrence Livermore National Laboratory*, Report No. UCID-20974, 1987.

[81] P.S. Follansbee and C. Frantz. Wave propagation in the split Hopkinson pressure bar. *Journal of Engineering Materials and Technology*, 105:61–66, 1983.

[82] D.A. Gorham. A numerical method for the correction of dispersion in pressure bar signals. *Journal of Physics E: Scientific Instruments*, 16:477–479, 1983.

[83] A. Tyas and A.J. Watson. A study of the effect of spatial variation of load in the pressure bar. *Measurement Science and Technology*, 11:1539–1551, 2000.

[84] S.D. Fay, J. Warren, and S.D. Clarke. *The characterisation of blast loading, end of year one report*, volume BT-141-DSTL-P3v2.0. Blastech Ltd., Sheffield, UK., 2013.

[85] British Standard Technical Committee B/525. BS 8110–1:1997: Structural use of concrete. part 1: Code of practice for design and construction. *British Standards Institution*, 2007.

[86] British Standard Technical Committee ISE/9/1. BS 8666:2005: Scheduling, dimensioning, bending and cutting of steel reinforcement of concrete – Specification. 2008.

[87] C. Arya. Design of structural elements – Second Edition. *Spon Press, Abingdon, Oxon, UK*, 2003.

[88] A. Tyas, T. Bennett, J. Warren, S.D. Fay, and S.E. Rigby. Clearing of blast waves on finite-sized targets - An overlooked approach. *Applied Mechanics and Materials*, 82:669–674, 2011.

[89] J.O. Hallquist. LS-DYNA theory manual. *Livermore Software Technology Corporation, Livermore, California, USA*, 2006.

[90] G. Randers-Pehrson and K.A. Bannister. Airblast loading model for DYNA2D and DYNA3D. *US Army Reaserch Laboratory*, Report No. ARL-TR-1310, 1997.

[91] British Standard Technical Committee B/526/1. BS 5930:1999 + A2:2010: Code of practice for site investigations. *British Standards Institution*, 2010.

[92] S.E. Rigby and P.W. Sielicki. An investigation of tnt equivalence of hemispherical pe4 charges. *Engineering Transactions*, 62, 4:423–435, 2014.

[93] V.I. Nifad'ev and N.M. Kalinina. Detonation mechanism in explosive mixtures containing polystyrene foam. *Combustion, Explosion and Shock Waves*, 28:650–654, 1992.

[94] A. Tyas, J. Reay, J.A. Warren, S.E. Rigby, S.D. Clarke, S.D. Fay, and D.J. Pope. *16th International Symposium on the Interaction of the Effects of Munitions with Structures (ISIEMS16) Destin, Florida, USA*.

[95] B. Hopkinson. British ordnance board minutes 13565. 1915.

[96] S.E. Rigby, S.D. Fay, A. Tyas, S.D. Clarke, J.J. Reay, J.A. Warren, M. Gant, and I. Elgy. Influence of particle size distribution on the blast pressure profile from explosives buried in saturated soils. *Shock Waves*, 28:613–626, 2017.

[97] E. Fermi. Thermodynamics. *Lightning Sources UK Ltd, Milton Keynes, UK*, 1937.

Appendix A

Tabulated peak and mean peak pressure and impulse data

A.1 Introduction

Chapter 4 provides much data for a range of charge confinement and geological states of soil. Peak pressure, mean peak pressure, peak impulse and mean peak impulse data is tabulated for each of the test in the parametric study (Tests 41–91) and presented in Tables A.3, A.4, A.5 and A.6. For convenience, an outline of the parameters studied in each test and relevant series are repeated here and presented in Tables A.1 and A.2.

Table A.1: Outline of Tests 41–44 - Influence of charge encasement and shape.

Test number	Encasement	Shape	SO (mm)
41	No case	3:1 cylinder	168
42	No top	3:1 cylinder	168
43	Full case	3:1 cylinder	165
44	No case	Sphere	168

Table A.2: Outline of Series A-K - Investigation of explosive-sand interaction.

Tests	Series	Soil type	w(%)	Bulk density	Dry density	Variable
45-46	A	Air	-	-	-	No soil
47-48	B	LB	2.45 %	1.635	1.600	Soil to charge base
49-50	C	LB	2.45 %	1.635	1.600	No overburden
51-57	D	LB	2.45 %	1.635	1.600	Baseline
58-62	E	LB	2.45 %	1.635	1.600	Increased overburden
63-67	F	LB	4.76 %	1.670	1.600	Increased moisture content
68-72	G	LB	25.0 %	1.990	1.600	Full saturation
73-74	H	Water	100 %	-	-	Water
75-81	I	STANAG	14.0 %	2.100	1.806	Soil type (full saturation)
82-86	J	LB	2.45 %	1.635	1.600	Reduction in standoff
87-91	K	LB	2.45 %	1.635	1.600	Increased standoff

Table A.3: Peak pressure for all HPBs, tests 41–91.

		Peak pressrue (MPa)																
		x-x (mm)									y-y (mm)							
Test	Series	-100	-75	-50	-25	0	25	50	75	100	-100	-75	-50	-25	25	50	75	100
41	-	-	-	-	116.0	126.3	142.7	138.7	74.0	15.8	12.5	35.2	84.1	245.6	88.1	72.9	57.7	20.2
42		21.2	62.5	58.5	85.3	108.8	160.0	68.4	70.6	13.0	21.9	50.9	81.1	98.6	137.6	84.1	58.4	13.7
43		-	-	-	335.2	303.4	294.6	257.8	122.8	38.7	41.6	138.1	276.5	318.2	340.0	307.5	126.8	34.1
44		26.4	26.9	55.8	39.6	64.7	73.9	37.2	26.7	21.3	20.0	43.7	91.2	122.8	70.8	34.0	29.7	26.7
45	A	15.7	57.0	47.5	108.9	140.9	152.0	74.0	63.8	18.5	16.5	62.6	112.2	193.9	227.4	103.8	81.7	12.9
46		13.3	47.9	83.4	116.8	149.5	132.5	58.8	62.6	28.1	18.6	38.6	114.4	174.9	160.8	103.3	32.8	10.6
47	B	13.7	47.4	109.0	114.3	186.3	140.4	118.1	40.8	20.6	21.6	48.8	133.2	170.0	195.5	64.9	31.9	29.7
48		16.4	37.6	119.5	109.6	178.3	193.4	92.5	77.6	15.7	16.3	35.4	211.1	165.2	122.8	58.5	82.9	17.7
49	C	7.3	13.7	71.9	57.7	264.2	240.5	135.1	46.7	8.2	7.2	14.6	179.8	232.8	235.5	187.8	29.5	11.9
50		3.5	7.7	23.2	42.3	145.5	201.5	63.3	40.6	24.3	9.1	20.9	65.2	162.2	222.2	144.2	18.8	12.2
51	D	33.2	141.5	73.1	64.8	119.1	161.6	106.8	71.5	29.7	43.7	35.6	142.4	205.6	94.8	98.6	20.1	78.4
52		44.1	15.6	89.4	28.6	221.6	81.5	80.5	78.0	71.2	125.4	40.4	78.0	117.6	213.9	125.7	120.0	14.7
53		-	-	-	-	-	-	-	-	-	-	-	-	-	-	-	-	-
54		67.5	72.6	72.7	73.0	159.6	151.9	87.0	107.7	47.5	71.2	53.1	120.5	144.1	148.1	111.0	29.5	80.2
55		28.6	39.6	90.6	114.6	171.6	151.7	91.2	131.3	26.9	23.2	204.5	152.8	168.8	141.7	70.2	115.6	33.0
56		27.5	32.4	120.7	77.9	112.7	107.3	70.3	101.8	34.5	33.8	47.6	134.7	180.4	117.7	101.2	61.9	27.2
57		33.0	38.7	70.9	113.6	166.3	147.7	70.8	106.6	44.4	45.9	61.6	115.2	155.4	175.0	83.8	41.9	47.4
58	E	-	-	-	-	-	-	-	-	-	-	-	-	-	-	-	-	-
59		94.7	-	75.8	36.6	59.9	-	38.8	38.8	41.8	51.0	40.2	33.5	90.8	125.0	45.3	-	-
60		187.2	24.9	69.0	190.2	202.2	106.9	46.6	37.0	43.8	22.0	95.5	64.2	140.5	116.9	104.8	225.4	8.9
61		47.0	40.0	77.2	102.9	54.8	105.4	31.5	18.3	21.5	46.0	182.1	56.7	152.2	119.1	149.7	24.5	17.3
62		34.3	24.2	33.2	81.4	45.3	92.8	65.5	82.6	52.7	91.8	80.3	103.5	151.1	173.3	85.6	75.8	57.0
63	F	32.4	25.5	91.6	119.4	144.3	163.0	155.3	45.2	24.2	43.9	-	153.1	148.0	113.3	78.1	57.2	18.6
64		66.6	40.0	119.4	233.0	70.7	78.0	119.5	39.1	74.1	14.7	35.8	71.1	75.6	75.6	97.5	69.8	150.1
65		-	-	-	-	-	-	-	-	-	-	-	-	-	-	-	-	-
66		29.5	55.5	90.2	94.1	272.0	118.5	54.8	91.3	70.8	50.1	38.1	54.2	187.5	201.1	86.7	108.0	53.5
67		-	-	-	-	-	-	-	-	-	-	-	-	-	-	-	-	-
68	G	94.6	208.5	197.2	301.1	309.5	325.3	242.5	158.2	115.6	117.8	208.1	232.3	159.3	359.6	255.3	219.1	118.7
69		-	-	-	-	-	-	-	-	-	-	-	-	-	-	-	-	-
70		90.8	192.5	243.5	170.3	326.6	268.6	304.3	185.8	107.1	105.8	181.2	275.8	303.6	278.6	154.6	227.0	96.1
71		76.2	183.3	299.8	358.2	372.5	402.8	282.9	167.6	123.2	94.9	185.0	143.4	332.3	142.5	223.8	199.0	125.5
72		60.3	123.4	198.8	281.9	92.6	238.2	261.4	174.6	141.3	93.2	155.8	212.1	430.4	91.7	301.7	191.0	110.2
73	H	95.8	154.2	230.1	238.7	326.3	320.7	262.0	166.1	90.6	111.8	162.7	279.1	404.3	353.7	275.6	160.4	90.2
74		93.0	174.4	230.0	259.4	330.6	215.5	251.6	191.4	92.3	87.2	163.2	231.0	394.9	343.7	300.6	181.1	99.5
75	I	36.7	255.6	244.9	252.1	252.3	412.6	143.9	238.0	129.6	45.2	268.9	368.3	195.6	242.9	127.3	118.2	211.3
76		314.2	24.6	283.0	-	250.4	391.6	161.2	78.9	124.1	97.6	56.3	83.3	89.3	312.5	377.0	49.5	32.4
77		89.6	213.3	367.1	357.2	189.9	336.7	277.2	62.4	159.5	86.2	365.8	150.1	458.8	463.0	314.4	104.0	37.8
78		296.9	175.9	88.6	114.9	137.6	188.4	190.8	283.5	98.5	76.5	271.5	107.8	489.9	307.6	113.1	95.0	36.5
79		55.5	138.6	299.9	342.6	361.7	494.6	145.5	93.9	102.1	97.8	227.8	95.3	263.3	455.9	77.3	259.1	80.1
80		33.9	278.2	220.8	225.0	483.1	242.5	245.7	67.2	21.5	154.5	126.3	130.9	501.6	300.0	175.7	90.0	41.3
81		36.4	133.9	105.4	358.3	68.6	290.8	239.4	64.5	30.5	145.3	243.8	360.5	549.5	89.2	165.4	109.0	100.1
82	J	21.0	97.7	168.0	193.4	237.9	266.4	158.0	53.4	54.9	31.1	61.6	210.0	249.6	171.6	178.9	75.3	-
83		25.4	70.2	119.0	168.3	208.3	183.8	111.8	81.3	68.6	44.3	128.6	180.5	296.3	227.6	147.5	121.8	58.9
84		38.7	83.9	95.5	171.8	229.7	182.2	85.6	87.0	17.6	67.2	158.4	153.1	281.2	236.1	121.1	43.3	47.1
85		69.1	89.3	167.6	263.7	181.9	209.6	221.5	90.9	38.0	29.4	128.0	215.1	257.9	251.5	153.5	88.9	49.7
86		57.6	58.8	265.1	158.7	232.6	332.8	122.9	51.4	36.0	36.5	64.1	179.2	343.2	240.9	174.3	64.4	42.1
87	K	22.7	40.6	50.2	50.5	69.5	81.0	76.3	85.4	42.8	16.0	42.3	57.8	85.1	62.9	79.9	69.7	59.9
88		55.3	40.4	67.7	92.6	70.6	93.8	37.3	68.0	57.0	30.8	116.8	69.3	129.9	71.4	49.8	51.2	20.7
89		18.0	28.3	42.0	43.0	49.1	95.8	52.6	74.7	71.2	20.1	69.5	111.7	74.0	105.7	50.3	50.0	28.1
90		19.6	29.3	89.7	92.2	102.7	72.5	37.3	41.9	21.7	33.2	20.5	74.3	109.2	79.2	31.9	28.3	33.7
91		40.0	13.6	113.4	86.7	62.2	104.9	42.3	34.7	14.1	8.8	15.3	44.0	164.4	107.1	88.7	47.2	26.4

Table A.4: Mean peak pressure for test series A–K.

	Mean peak pressure (MPa)										
Bar position	A	B	C	D	E	F	G	H	I	J	K
0	145.2	182.3	204.9	158.5	90.6	162.3	275.3	328.4	249.1	218.1	70.8
25	158.4	151.4	174.3	130.7	119.0	133.9	277.8	316.4	323.2	234.3	90.1
50	87.2	113.3	108.8	98.3	67.6	97.6	239.3	257.5	202.1	161.4	63.3
75	44.5	50.3	24.1	73.7	70.7	55.0	185.0	169.2	160.5	84.9	48.4
100	16.8	18.9	10.5	31.8	54.5	52.4	104.5	95.0	76.4	43.9	32.0

Table A.5: Peak impulse for all HPBs tabulated, tests 41–91.

		Peak impulse (MPa.ms)																
		x-x (mm)									y-y (mm)							
Test	Series	-100	-75	-50	-25	0	25	50	75	100	-100	-75	-50	-25	25	50	75	100
41	-	-	-	-	1.938	2.622	2.928	2.057	1.442	0.652	0.531	1.003	1.907	3.501	2.356	1.555	1.349	0.610
42		1.625	1.795	2.872	3.202	3.524	3.662	2.794	1.462	1.403	1.738	2.168	2.972	3.298	3.608	2.408	2.577	1.523
43		-	-	-	3.637	4.452	3.841	2.859	1.284	0.822	1.424	1.855	9.323	7.044	4.523	3.722	1.740	0.988
44		1.244	0.950	1.471	1.506	1.520	1.675	1.043	0.696	1.014	0.939	0.929	2.159	2.620	1.875	1.197	1.664	0.735
45	A	2.076	2.702	3.448	3.821	4.854	4.586	3.332	2.221	2.119	2.043	2.173	4.539	14.33	4.999	3.263	3.549	2.366
46		1.246	1.829	2.539	4.045	5.389	4.101	2.273	2.352	2.502	2.529	2.316	4.174	12.75	4.843	3.385	3.044	2.215
47	B	1.431	1.724	3.329	3.637	5.176	4.081	3.906	1.608	2.053	2.052	2.547	3.630	5.903	4.430	3.011	2.538	2.100
48		1.799	1.863	3.555	3.193	4.592	5.016	4.001	1.866	1.716	1.530	1.969	5.095	5.854	3.669	2.697	3.097	1.961
49	C	1.392	2.290	4.102	3.798	8.462	9.144	5.859	2.910	2.023	1.508	2.308	6.338	11.24	8.820	6.087	3.445	2.451
50		1.034	1.447	2.817	4.626	7.008	7.631	4.998	3.873	2.957	1.780	2.530	4.684	6.577	7.749	5.953	3.034	2.159
51	D	1.729	3.663	3.665	3.618	5.411	6.621	3.764	3.210	2.041	2.376	2.139	4.346	7.702	4.574	4.870	2.078	3.050
52		1.387	1.780	3.147	2.420	6.735	4.005	3.459	4.107	3.019	2.646	1.477	3.284	5.325	7.275	6.257	3.252	2.708
53		-	-	-	-	-	-	-	-	-	-	-	-	-	-	-	-	-
54		1.507	2.804	3.377	3.384	4.820	4.744	3.426	3.105	1.814	2.137	2.361	3.790	5.786	5.199	4.763	2.113	2.795
55		1.622	2.397	4.289	3.676	5.725	4.931	3.772	3.197	1.543	1.760	2.667	5.038	5.507	5.646	3.951	3.461	2.582
56		1.528	2.198	3.785	4.079	5.324	5.303	3.533	2.867	2.308	1.913	2.364	4.804	5.740	5.034	4.153	1.554	2.354
57		2.088	3.507	4.341	4.858	6.453	5.976	4.302	4.577	2.737	3.391	3.863	3.789	5.347	6.162	4.947	3.666	3.256
58	E	-	-	-	-	-	-	-	-	-	-	-	-	-	-	-	-	-
59		3.078	-	3.738	2.802	3.084	-	2.380	3.022	2.112	2.450	2.593	2.662	5.105	4.971	3.402	-	-
60		4.428	1.876	2.973	6.672	7.260	3.803	2.260	2.577	2.870	1.912	2.773	2.932	4.116	3.976	4.219	6.577	1.397
61		3.247	2.292	3.619	3.685	3.730	3.434	2.177	2.015	1.757	2.594	4.180	3.492	5.011	4.911	3.398	2.109	2.177
62		2.600	1.912	3.731	3.793	3.495	4.485	2.396	2.505	2.134	3.237	3.986	4.901	3.951	4.587	2.748	3.095	3.565
63	F	0.721	2.268	3.941	4.243	5.842	4.852	4.871	2.735	1.568	1.537	-	3.826	4.460	4.912	2.965	2.245	1.554
64		1.469	2.633	5.276	6.052	3.567	3.503	4.422	2.460	2.024	1.668	2.290	4.163	4.058	4.042	3.872	2.317	2.214
65		-	-	-	-	-	-	-	-	-	-	-	-	-	-	-	-	-
66		1.238	2.682	4.768	4.430	7.953	4.607	2.540	3.133	1.635	2.426	2.371	3.316	5.855	6.300	3.282	3.413	2.283
67		-	-	-	-	-	-	-	-	-	-	-	-	-	-	-	-	-
68	G	3.555	4.851	4.870	6.172	6.136	8.272	6.000	4.234	7.845	3.140	4.669	4.769	4.938	7.115	5.453	4.429	3.906
69		-	-	-	-	-	-	-	-	-	-	-	-	-	-	-	-	-
70		3.100	4.900	4.937	4.406	7.770	5.124	7.830	4.569	4.510	3.973	5.358	5.458	6.428	8.399	4.788	4.559	3.265
71		2.527	4.096	6.646	8.443	6.657	5.231	4.796	4.639	3.111	3.161	4.765	4.311	5.937	6.571	5.622	4.877	3.094
72		3.116	3.659	5.437	5.973	3.667	6.983	5.122	4.621	4.481	4.129	5.512	4.795	-	3.317	8.584	4.109	3.822
73	H	3.651	4.089	5.204	4.994	9.605	8.103	4.414	3.689	3.002	4.137	4.222	6.501	17.02	8.222	4.643	4.319	3.391
74		4.931	4.232	4.599	5.350	8.939	3.317	4.703	4.240	3.424	3.385	4.474	6.390	14.65	8.039	5.811	5.021	3.984
75	I	3.159	8.471	8.771	7.140	5.894	-	2.913	7.875	3.707	2.980	8.434	-	4.759	4.422	3.736	4.383	7.641
76		12.67	1.792	8.702	-	8.133	10.72	6.343	6.378	6.457	4.292	2.608	4.332	4.496	12.42	16.55	3.126	4.350
77		4.218	7.750	-	12.24	10.25	9.583	9.882	2.888	9.990	5.218	-	4.494	-	12.44	7.529	2.213	2.330
78		11.12	6.175	3.933	4.071	5.802	5.624	8.921	9.513	4.499	4.443	12.40	4.066	-	7.860	4.694	5.076	2.602
79		3.214	4.560	9.727	16.00	9.988	-	5.014	5.017	5.408	8.237	7.444	4.540	8.755	9.455	3.252	9.271	4.139
80		2.116	14.33	4.338	4.577	22.21	5.854	5.752	2.955	2.255	4.194	4.123	4.289	15.49	6.936	4.307	3.909	1.753
81		2.240	6.400	5.052	9.660	4.426	8.034	10.70	3.998	3.209	5.234	9.429	10.49	-	3.435	8.518	6.009	7.280
82	J	2.289	3.424	5.275	5.827	7.742	8.568	4.428	3.394	2.546	2.487	3.644	6.420	8.874	6.445	6.350	3.129	-
83		2.001	3.150	5.762	6.747	7.743	6.541	3.989	3.172	2.462	2.312	3.371	6.893	10.20	8.077	5.985	3.136	2.653
84		2.213	3.643	4.783	6.232	7.680	6.201	3.926	4.107	2.075	2.514	4.593	5.846	9.539	8.338	5.380	2.753	2.500
85		3.603	3.870	6.306	6.669	6.684	6.452	6.058	3.915	3.012	2.661	4.236	7.505	9.272	8.745	6.483	-	-
86		2.118	2.699	6.367	4.918	6.877	9.823	5.233	2.973	2.442	2.522	2.420	5.812	-	7.690	5.379	3.862	1.579
87	K	1.922	2.680	3.735	3.417	3.492	3.994	3.148	3.081	2.611	2.133	3.026	3.521	4.165	3.512	4.221	2.727	-
88		2.212	2.345	3.823	3.582	3.828	3.760	2.644	2.258	2.110	1.940	2.825	3.165	4.425	3.161	2.828	-	-
89		1.841	2.562	3.566	2.690	3.171	4.304	3.222	2.991	2.558	2.292	2.463	3.853	4.149	4.624	4.120	2.918	-
90		2.014	2.668	4.238	3.195	3.672	3.491	2.159	2.638	2.184	2.505	2.048	3.898	4.498	3.889	3.249	-	-
91		1.729	1.913	3.796	3.753	3.647	3.846	3.047	2.786	2.181	1.901	2.057	3.038	5.413	4.476	4.155	-	-

Table A.6: Mean peak impulse for test series A–K.

	Mean peak impulse per series (MPa.ms)										
Bar position	A	B	C	D	E	F	G	H	I	J	K
0	5.122	4.884	7.735	5.745	4.392	5.787	6.058	9.272	9.529	7.345	3.562
25	6.684	4.473	7.449	5.121	4.353	4.776	6.221	8.712	8.362	7.640	3.917
50	3.369	3.653	5.105	4.119	3.189	3.937	5.589	5.283	6.571	5.709	3.471
75	2.272	2.152	2.730	2.850	2.965	2.595	4.615	4.286	6.168	3.447	2.587
100	2.137	1.830	1.913	1.551	2.637	1.695	3.796	3.738	4.963	2.444	2.142

Appendix B

Commissioning test data

Chapter 3 describes the commissioning phase of this experimental work. The test configuration was refined from the initial CoBL apparatus and test set-up concept design to the final configuration used in the parameter study. Pressure–time data is presented for each test (Tests 1–40) from these commissioning tests. For convenience a table describing each test is repeated here, see Table B.1. The HPB arrangements were altered at various stages in the commissioning tests to maximise data capture for this mechanistic study. A diagram of the updated HPB arrangement is repeated where the HPB arrangements were modified.

Table B.1: Summary of commissioning tests.

Test number	Soil condition	Mass (g)	Case/ geometry	Detonator orientation	Detonator type	SO (mm)	OVB (mm)	Refinement
1–3	Air	100	Sph	Base	Non-el	75	-	Non-el
4–6	Air	100	Sph	Base	Electric	75	-	Electric
7–9	LB	78	Full	Top	Electric	69	25	Det orientation
10–14	LB	78	Full	Base	Non-el	69	25	Det orientation, case top
15–18	LB	53	No top	Base	Non-el	69	28	Charge mass
19–28	LB	53	No top	Base	Non-el	69	28	HPB array
29–34	LB	78	No top	Base	Non-el	140	28	Charge mass, stand off, soil container
35–40	LB, air	78	No top	Base	Non-el	140	28	Dispersion

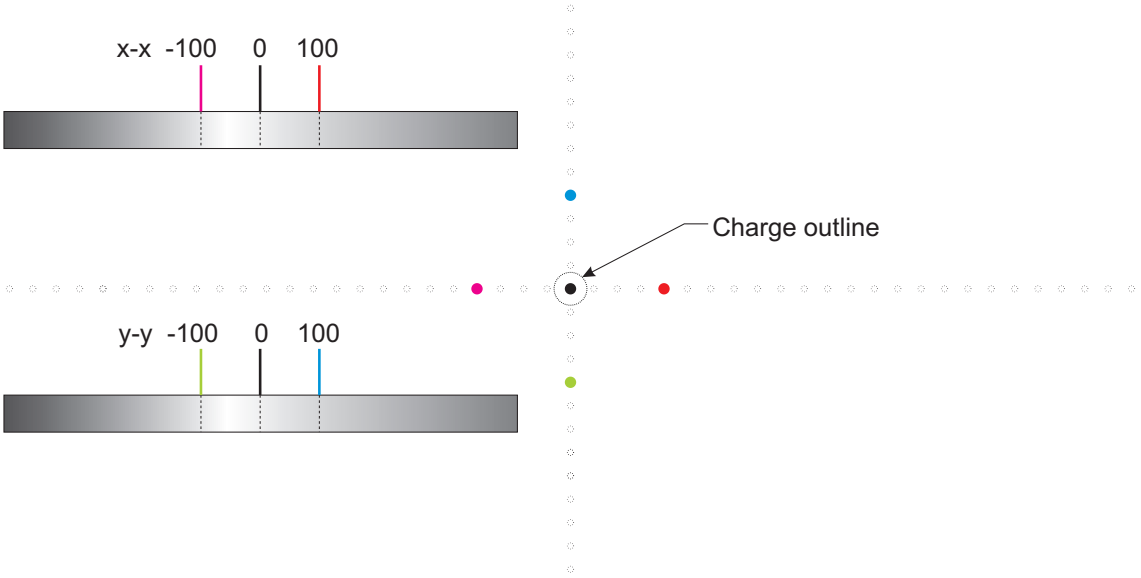

Figure B.1: HPB set-up for tests 1–6.

B.0.1 Pressure–time waveforms for Tests 1–6

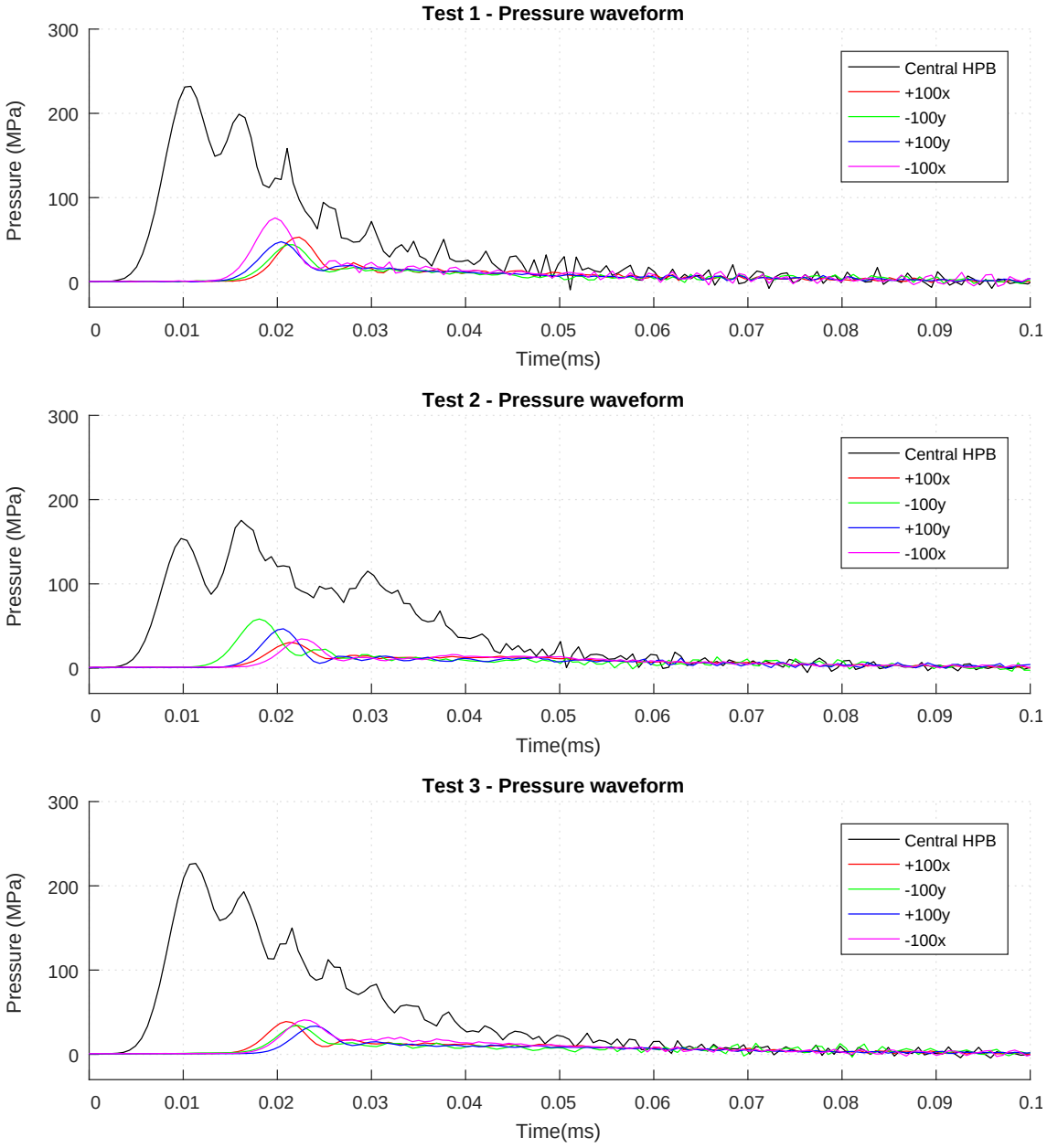

Figure B.2: Pressure-time histories of Tests 1–3.

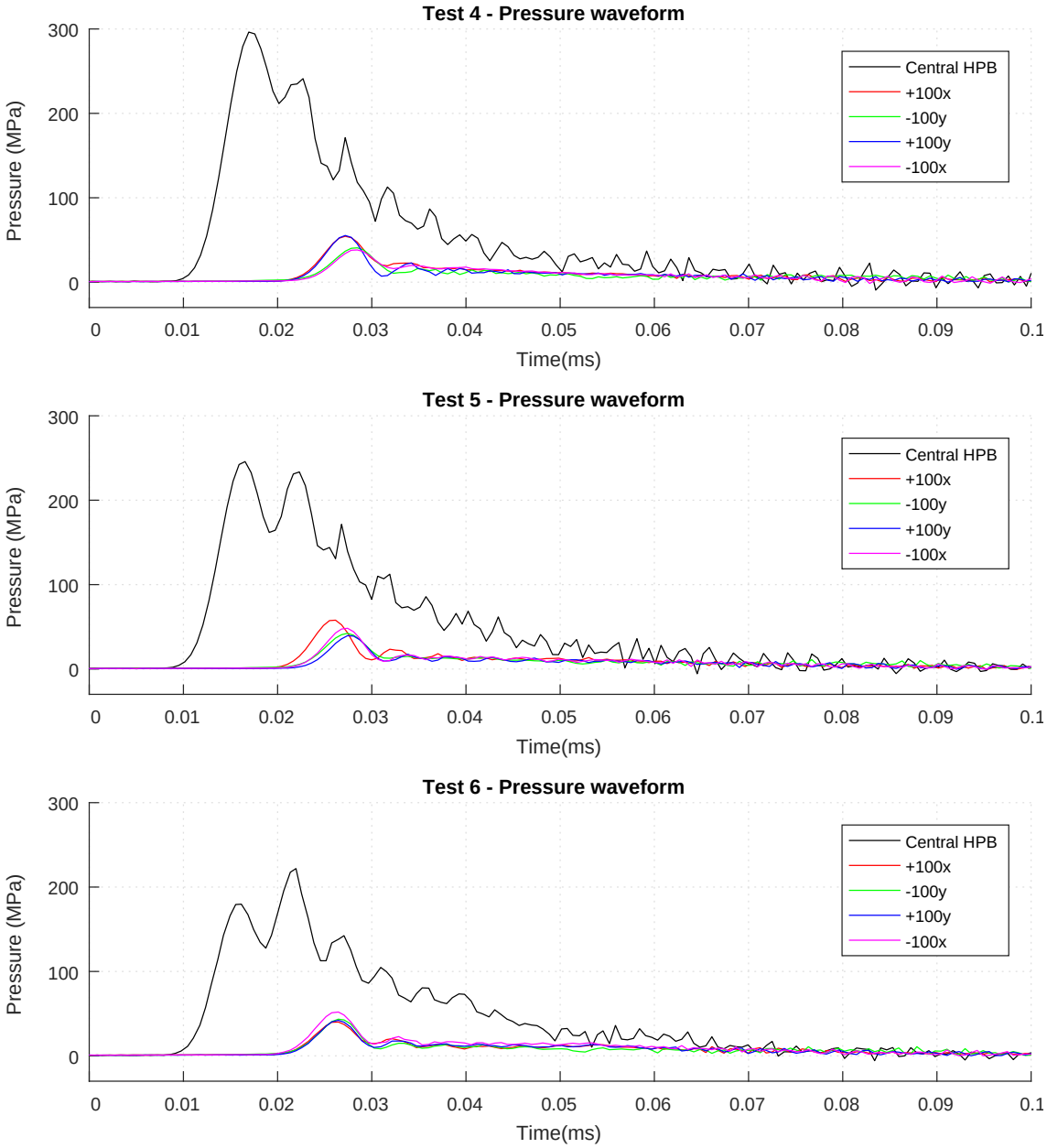

Figure B.3: Pressure-time histories of Tests 4–6.

B.0.2 Pressure–time waveforms for Tests 7–18

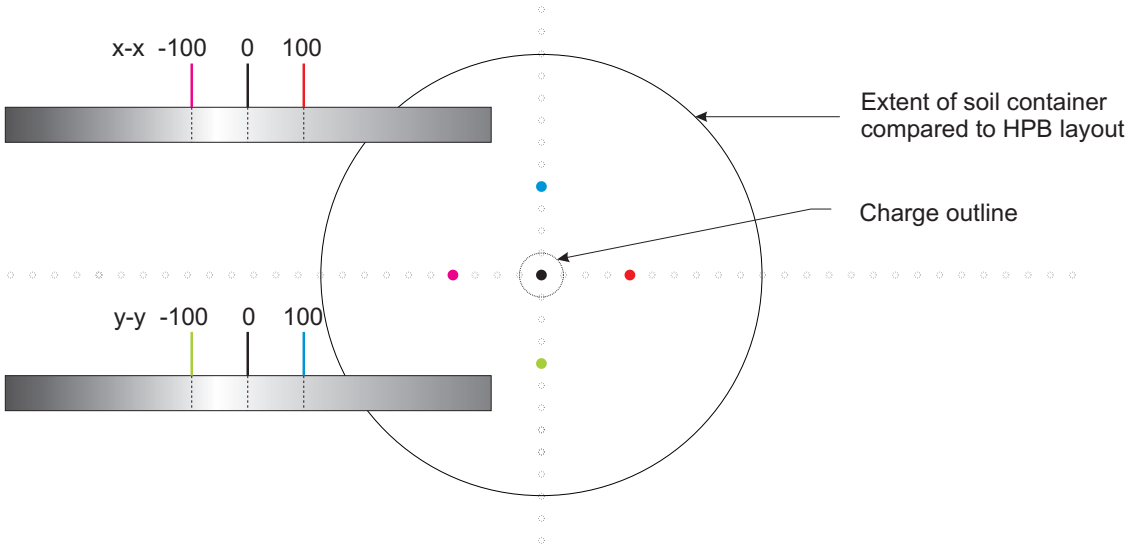

Figure B.4: HPB set-up for tests 7–18.

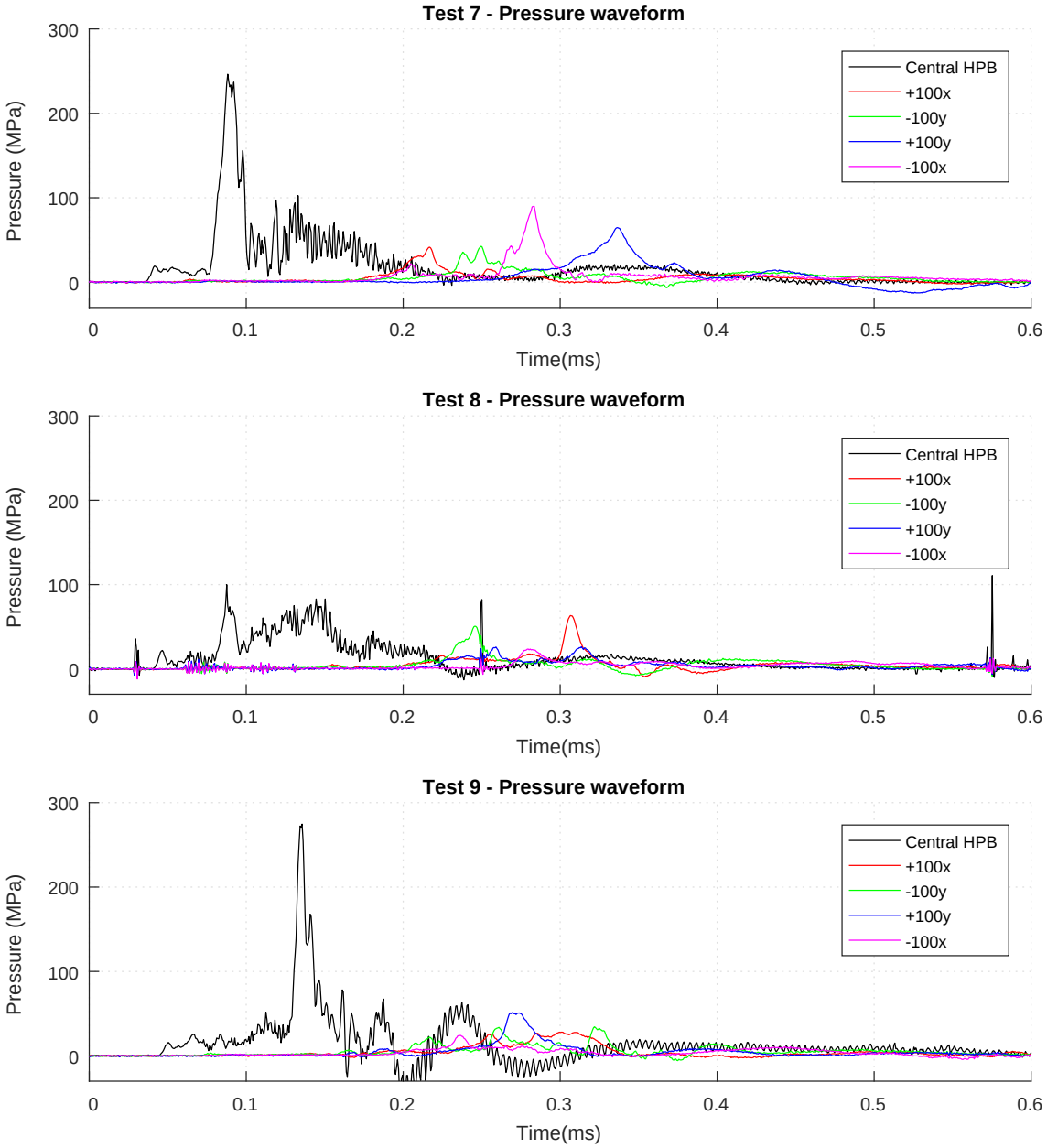

Figure B.5: Pressure-time histories of Tests 7–9.

Note: Test 10 was a misfire.

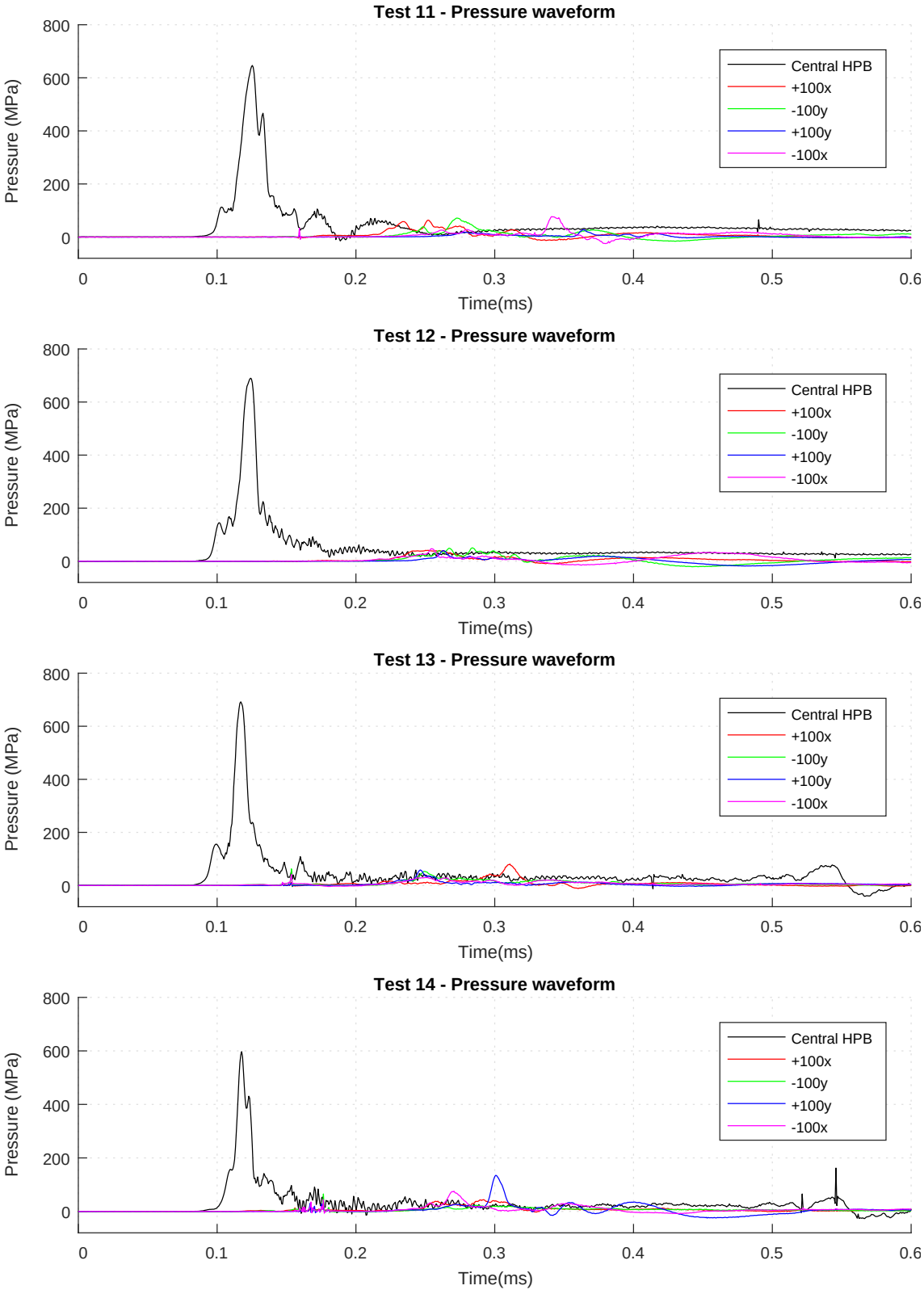

Figure B.6: Pressure-time histories of Tests 11–14.

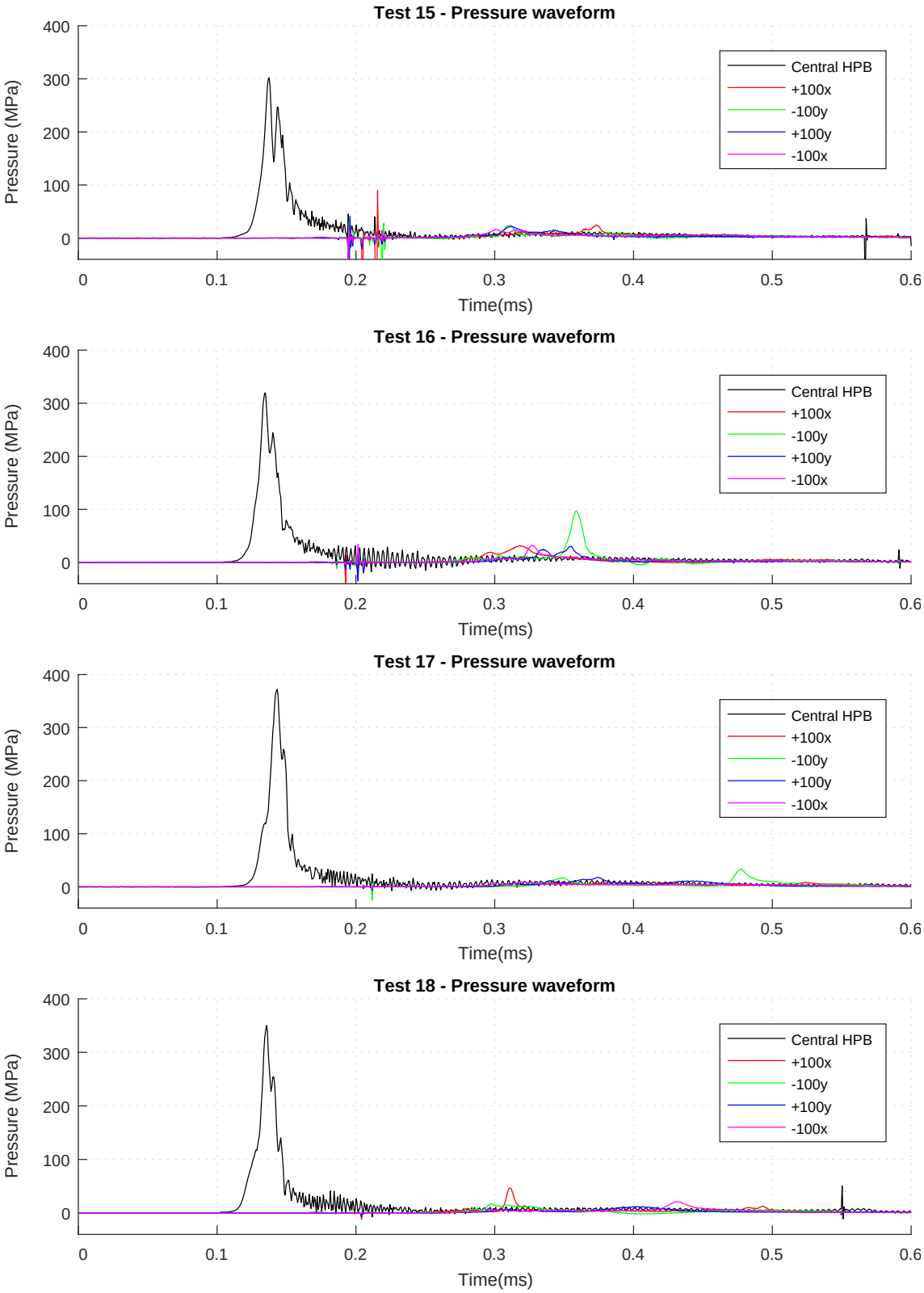

Figure B.7: Pressure-time histories of Tests 15–18.

B.0.3 Pressure–time waveforms for Tests 19–28

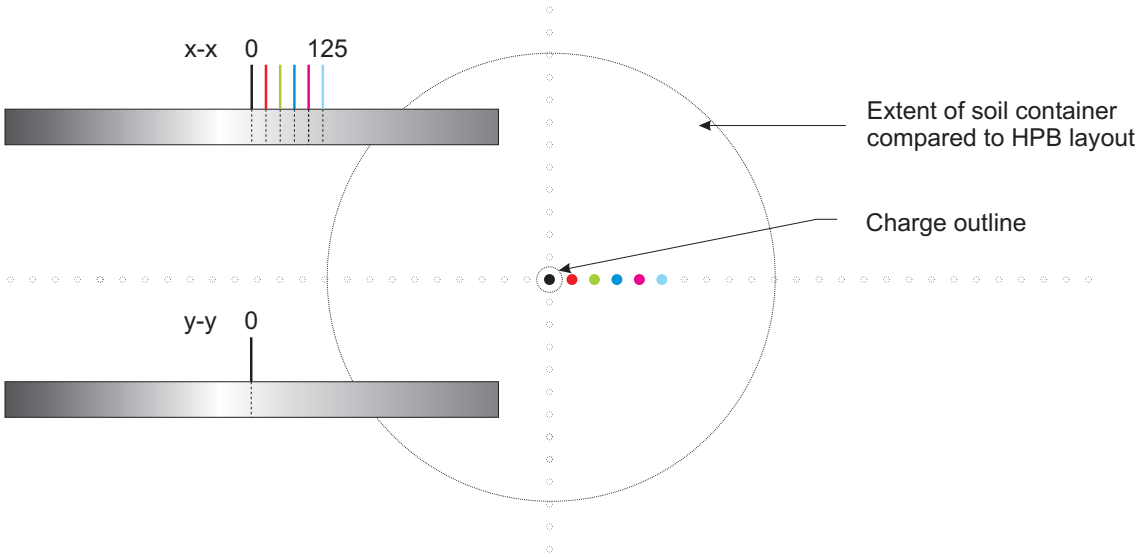

Figure B.8: HPB set-up for tests 19–24 and 25–28 right hand column.

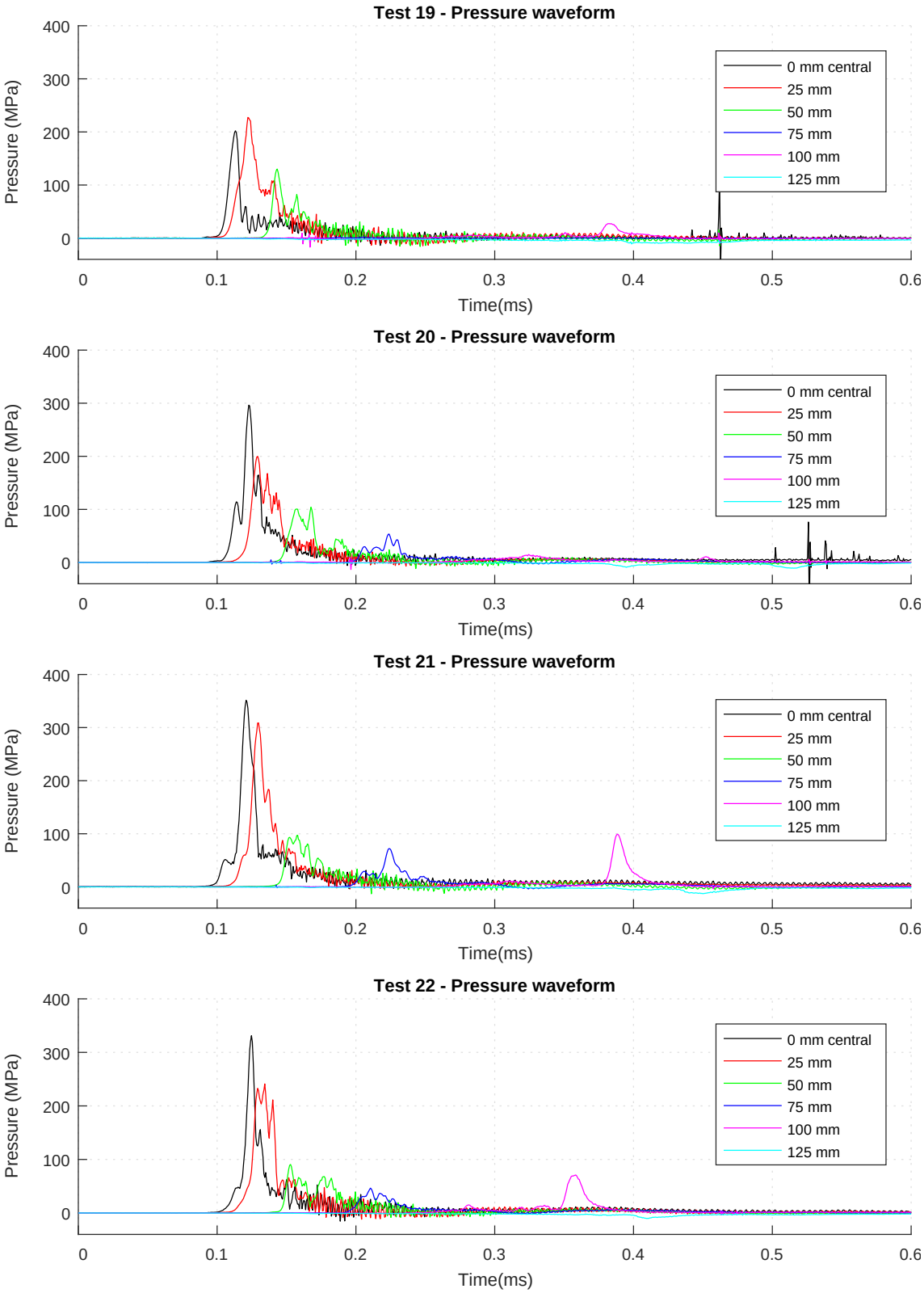

Figure B.9: Pressure-time histories of Tests 19–22.

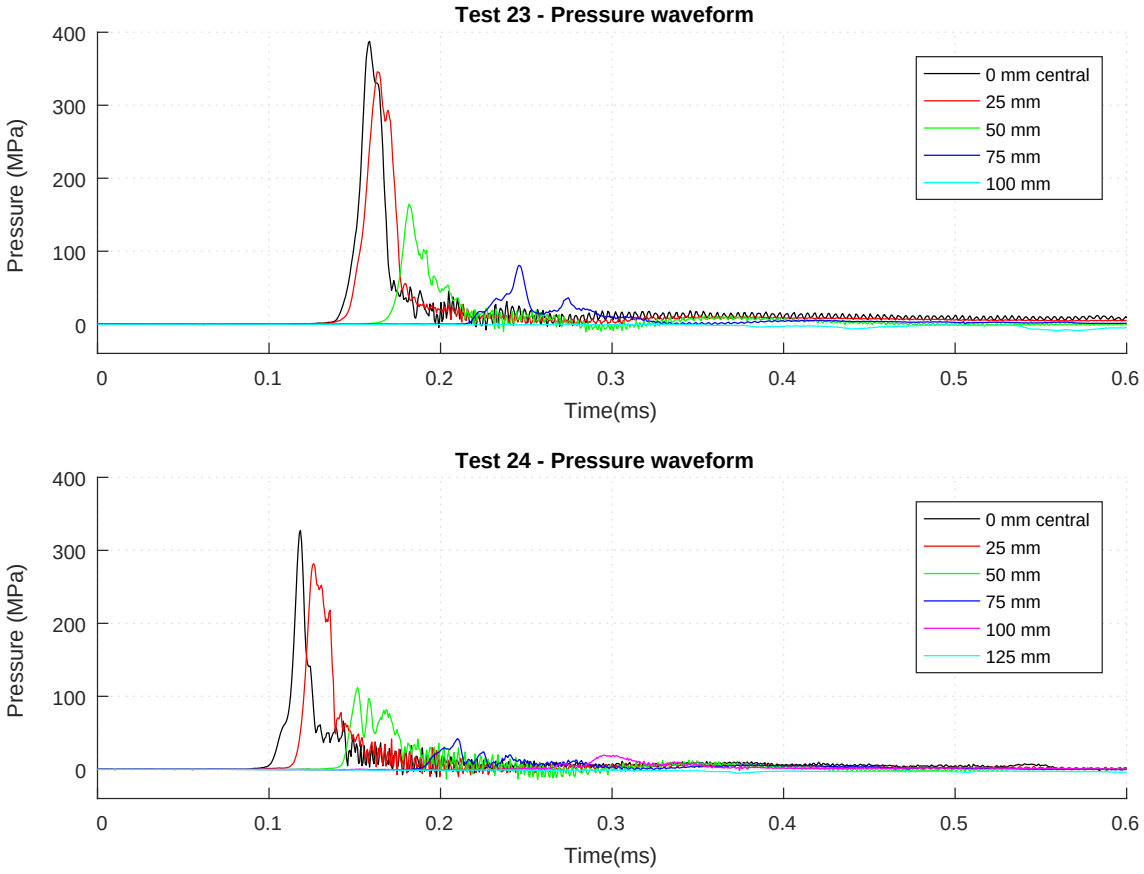

Figure B.10: Pressure-time histories of Tests 23–24.

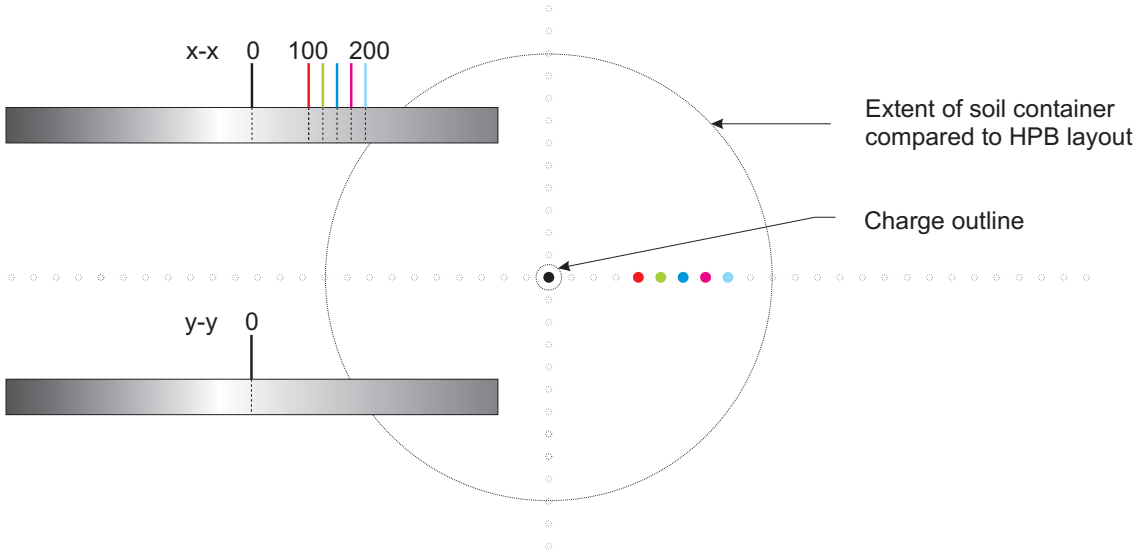

Figure B.11: HPB set-up for tests 25–28 left hand column.

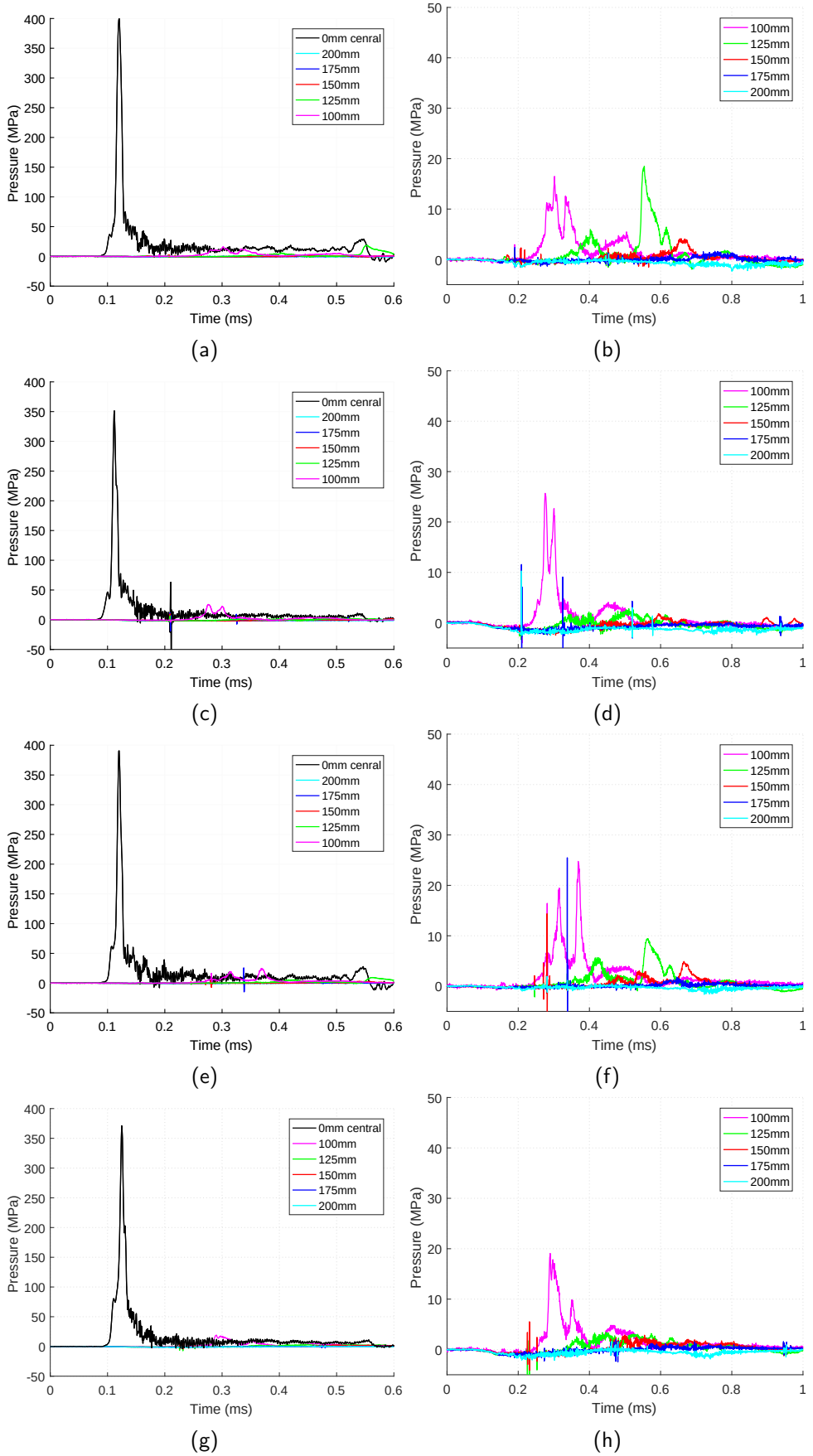

Figure B.12: Pressure-Time,Test 25–28 left column 0 mm (central) and 100–200 mm HPBs, right column 100–200 mm HPBs, (a) and (b) Test 25, (c) and (d) Test 26, (e) and (f) Test 27, (g) and (h) Test 28.

B.0.4 Pressure–time waveforms for Tests 29–33

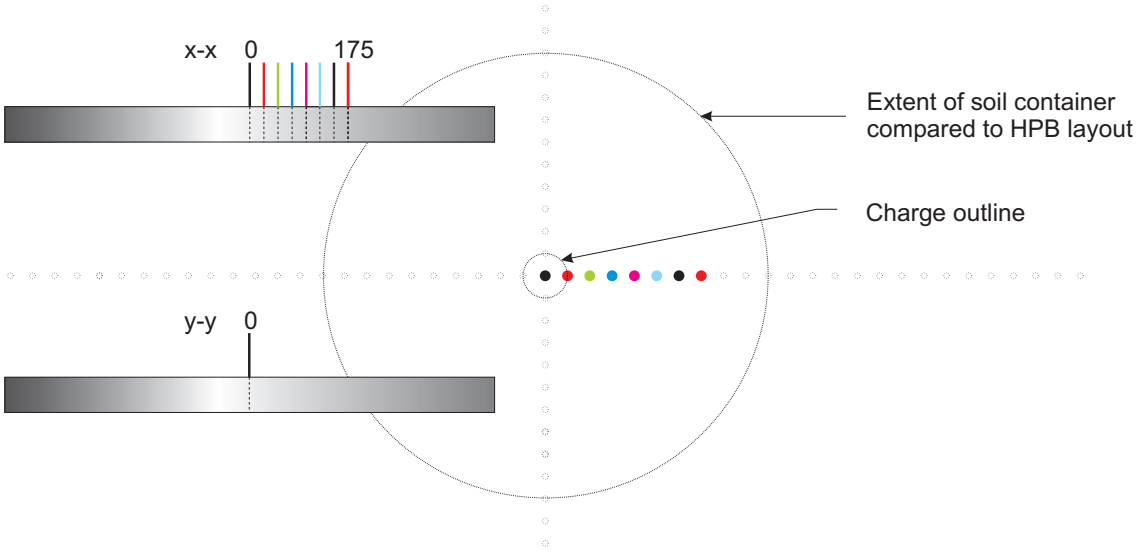

Figure B.13: HPB set-up for Tests 29–33.

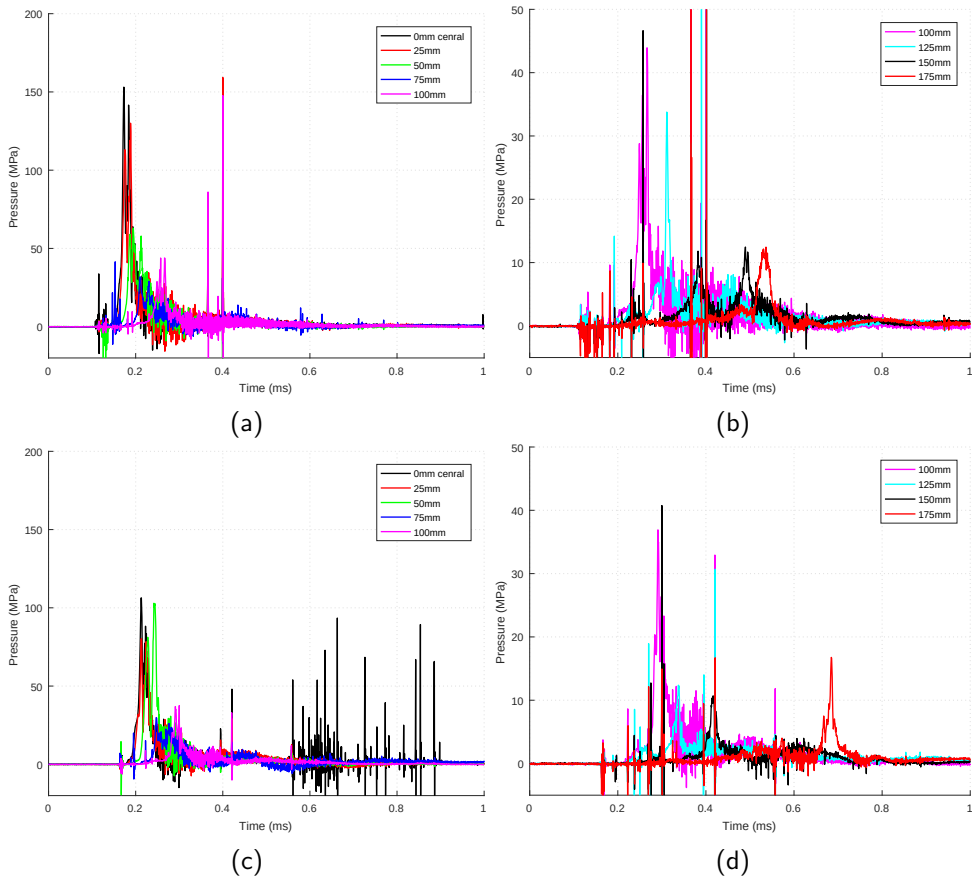

Figure B.14: Pressure-Time,Test 29–30 left column 0–100 mm HPBs, right column 100–175 mm HPBs, (a) and (b) Test 29, (c) and (d) Test 30.

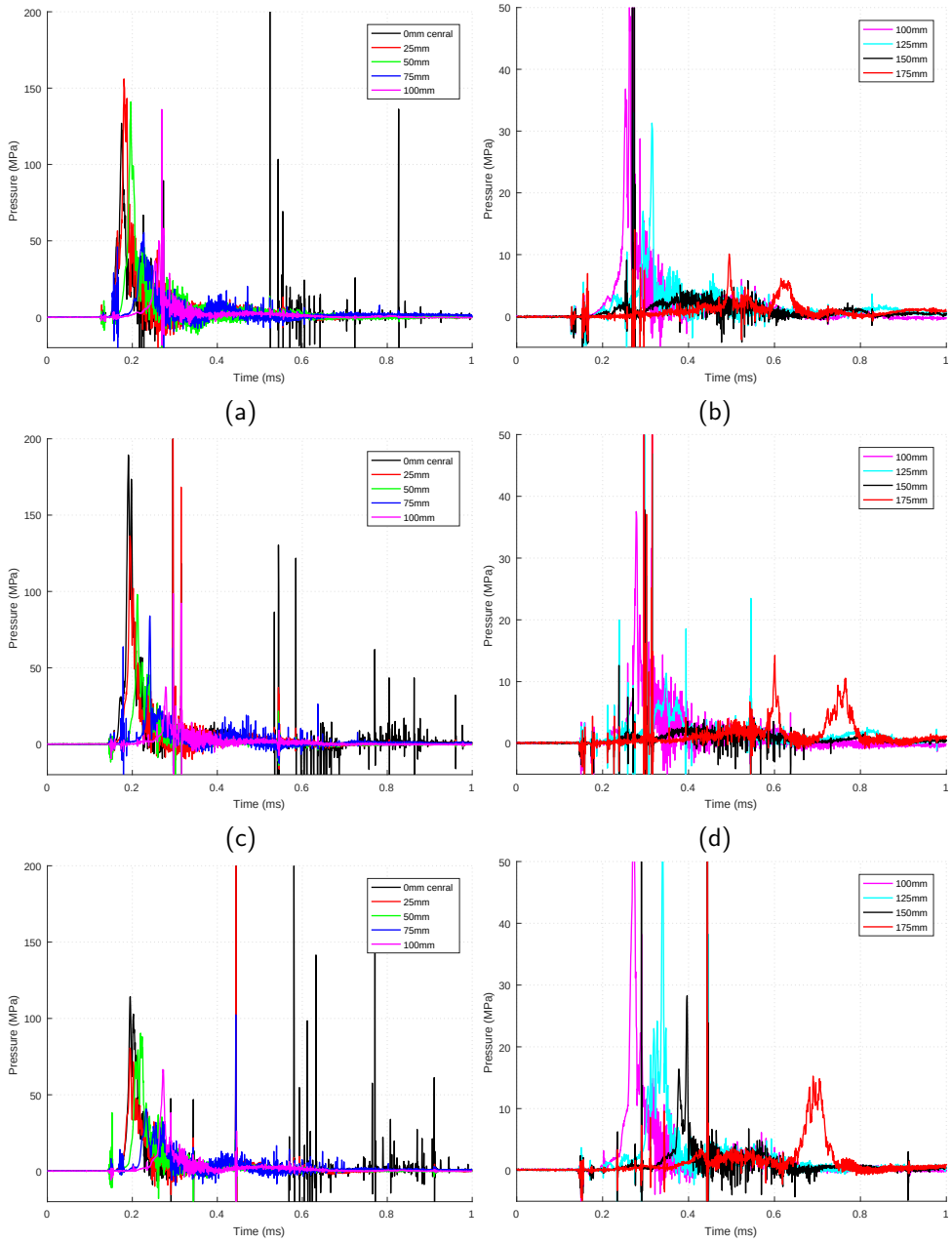

Figure B.15: Pressure-Time,Test 31–33 left column 0–100 mm HPBs, right column 100–175 mm HPBs, (a) and (b) Test 31, (c) and (d) Test 32, (e) and (f) Test 33.

B.0.5 Pressure–time waveforms for Test 34

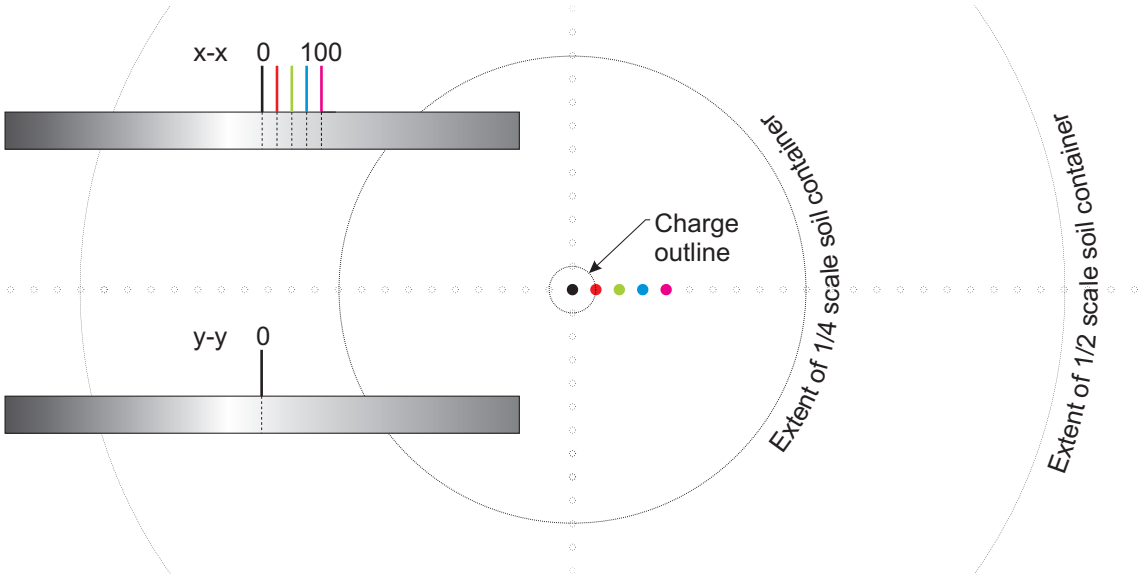

Figure B.16: HPB set-up for test 34.

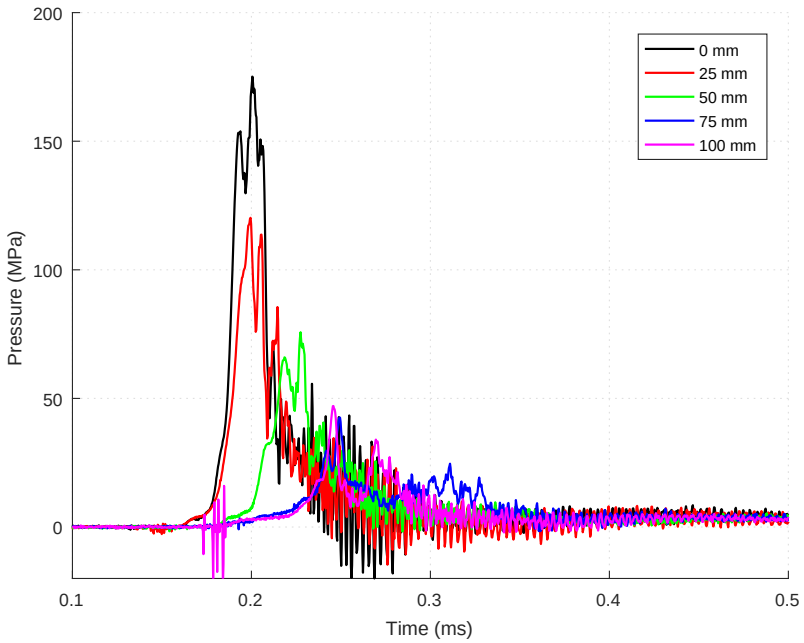

Figure B.17: Pressure-time histories of Test 34.

B.0.6 Pressure–time waveforms for Tests 35–40

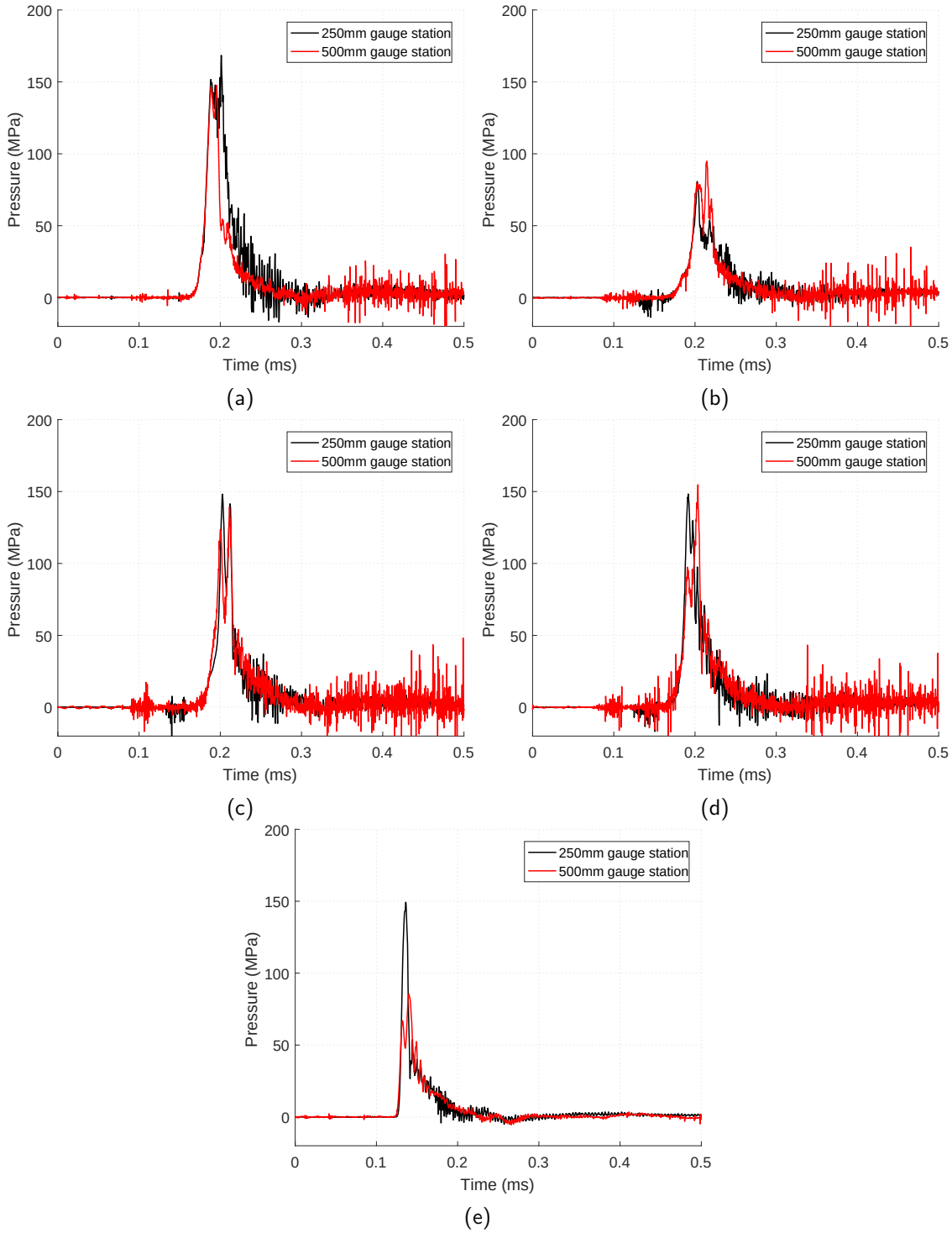

Figure B.18: Pressure waveforms of Tests 35, 36, 38–40 at the central HPB. Two gauges placed on each gauge station at 250 mm and 500 mm from impact face. (a) Test 35, (b) Test 36, (c) Test 38, (d) Test 39, (e) Test 40. Note during the firing of Test 37 a power failure wiped data in volatile oscilloscope memory.

Appendix C

Parameter study data

The parametric study presented in Chapter 4 investigates a range of parameters for buried blast loading on a horizontal plane. Pressure–time data is presented here for each of the 50 tests for each axis of the HPB array. Due to the ultra aggressive blast environment and physical environment that the HPBs were subject to in certain test series, it was productive to apply a Butterworth filter to the data to assist in clear analysis of general mechanistic trends. Both raw and Butterworth filtered pressure–time data are presented here. For convenience tables describing each test the in the parametric study are repeated here, see Tables C.1 and C.2.

Table C.1: Outline of Tests 41–44 - Influence of charge encasement and shape.

Test number	Encasement	Shape	SO (mm)
41	No case	3:1 cylinder	168
42	No top	3:1 cylinder	168
43	Full case	3:1 cylinder	165
44	No case	Sphere	168

Table C.2: Outline of Series A-K - Investigation of explosive-sand interaction.

Tests	Series	Soil type	w(%)	Bulk density	Dry density	Variable
45-46	A	Air	-	-	-	No soil
47-48	B	LB	2.45 %	1.635	1.600	Soil to charge base
49-50	C	LB	2.45 %	1.635	1.600	No overburden
51-57	D	LB	2.45 %	1.635	1.600	Baseline
58-62	E	LB	2.45 %	1.635	1.600	Increased overburden
63-67	F	LB	4.76 %	1.670	1.600	Increased moisture content
68-72	G	LB	25.0 %	1.990	1.600	Full saturation
73-74	H	Water	100 %	-	-	Water
75-81	I	STANAG	14.0 %	2.100	1.806	Soil type (full saturation)
82-86	J	LB	2.45 %	1.635	1.600	Reduction in standoff
87-91	K	LB	2.45 %	1.635	1.600	Increased standoff

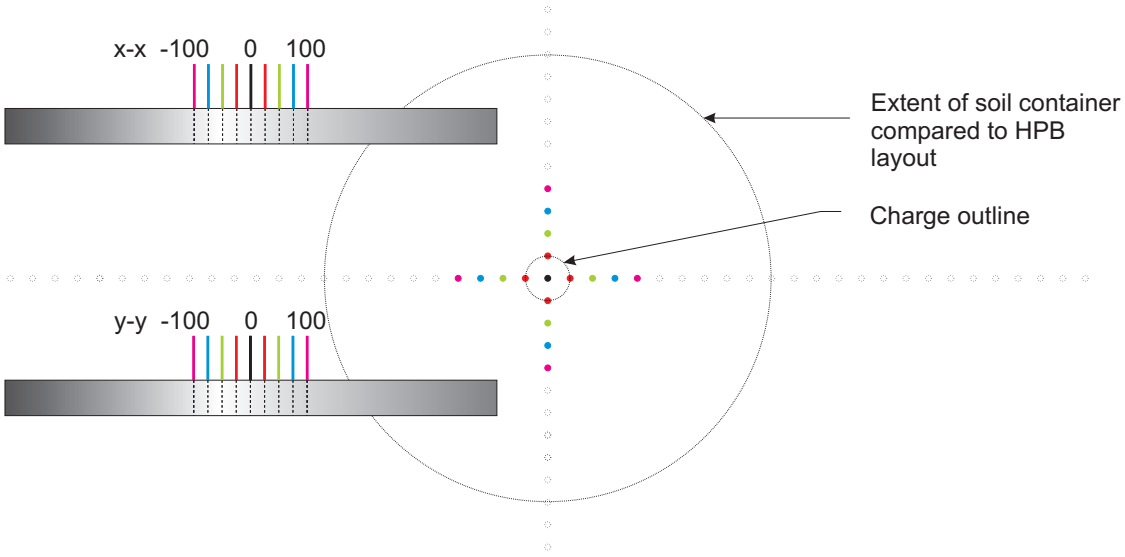

Figure C.1: HPB set-up for tests 41-91 with comparison of charge and soil container geometry.

C.0.1 Pressure–time waveforms for Tests 41–44

Note: In Test 41, failure of a single oscilloscope lost data for the -x ray of HPBs.

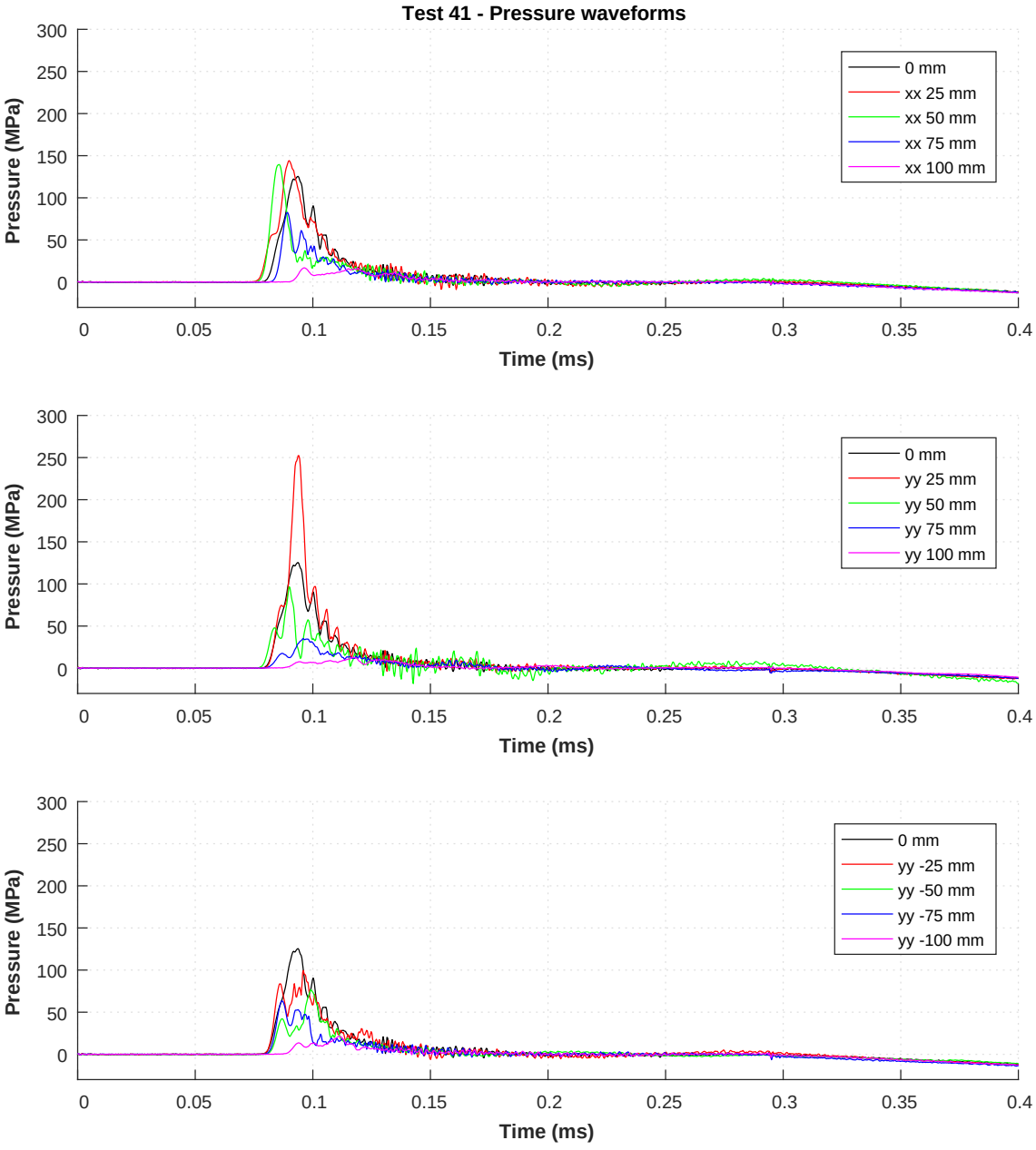

Figure C.2: Pressure-time waveform of Test 41.

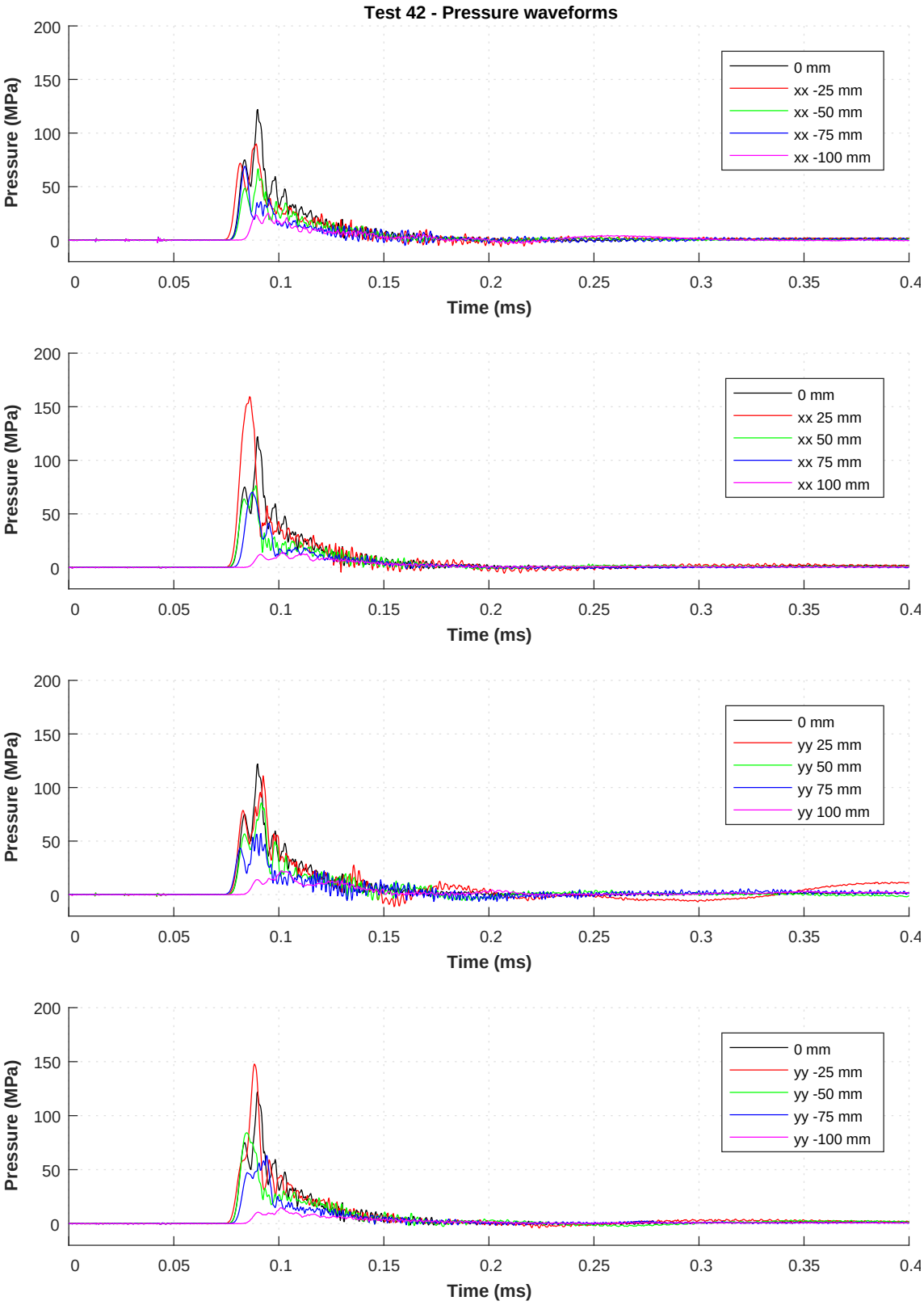

Figure C.3: Pressure-time waveform of Test 42.

Note: In Test 43, failure of a single oscilloscope lost data for the -x ray of HPBs. Following this failure the oscilloscope was replaced.

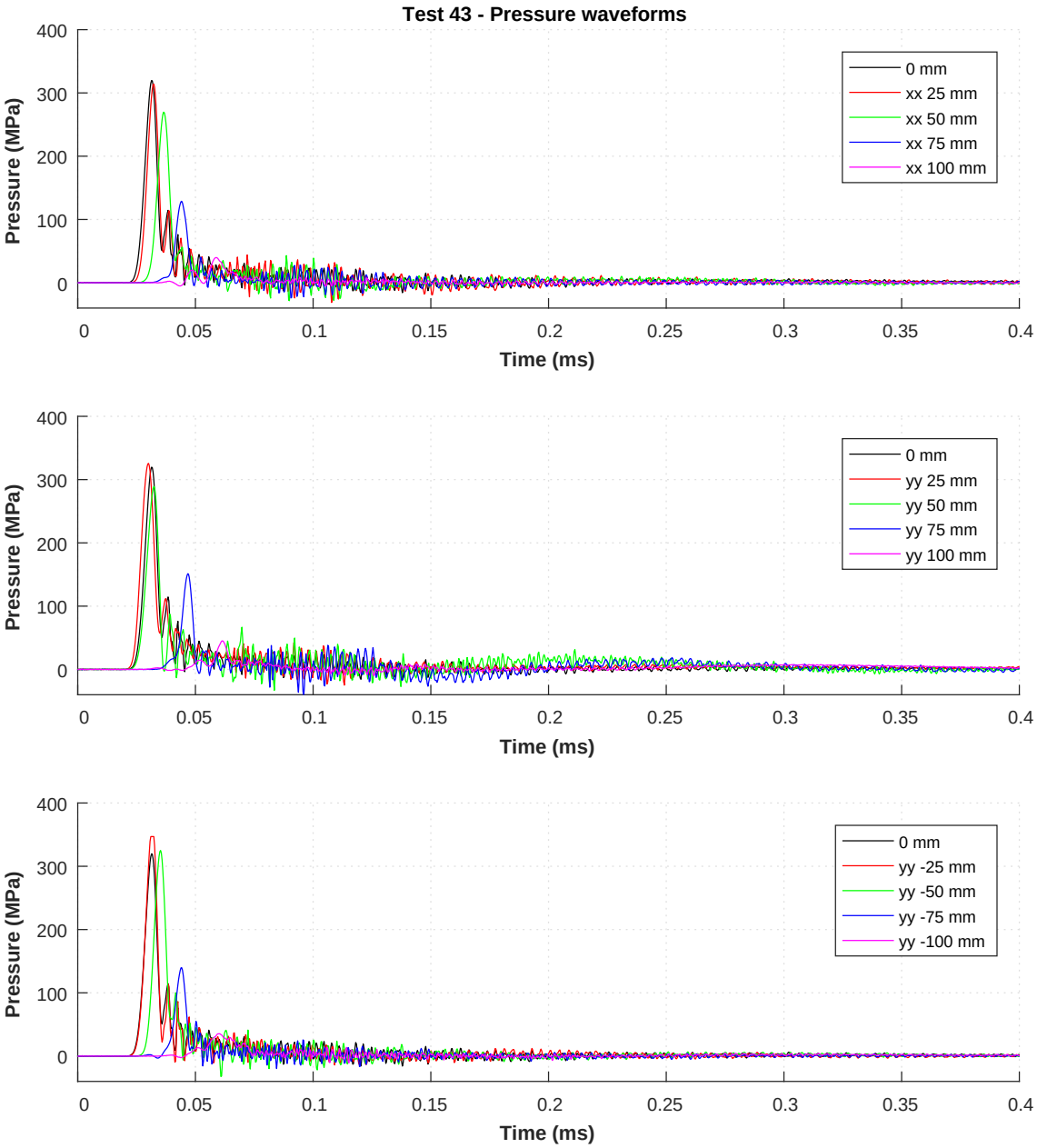

Figure C.4: Pressure-time waveform of Test 43.

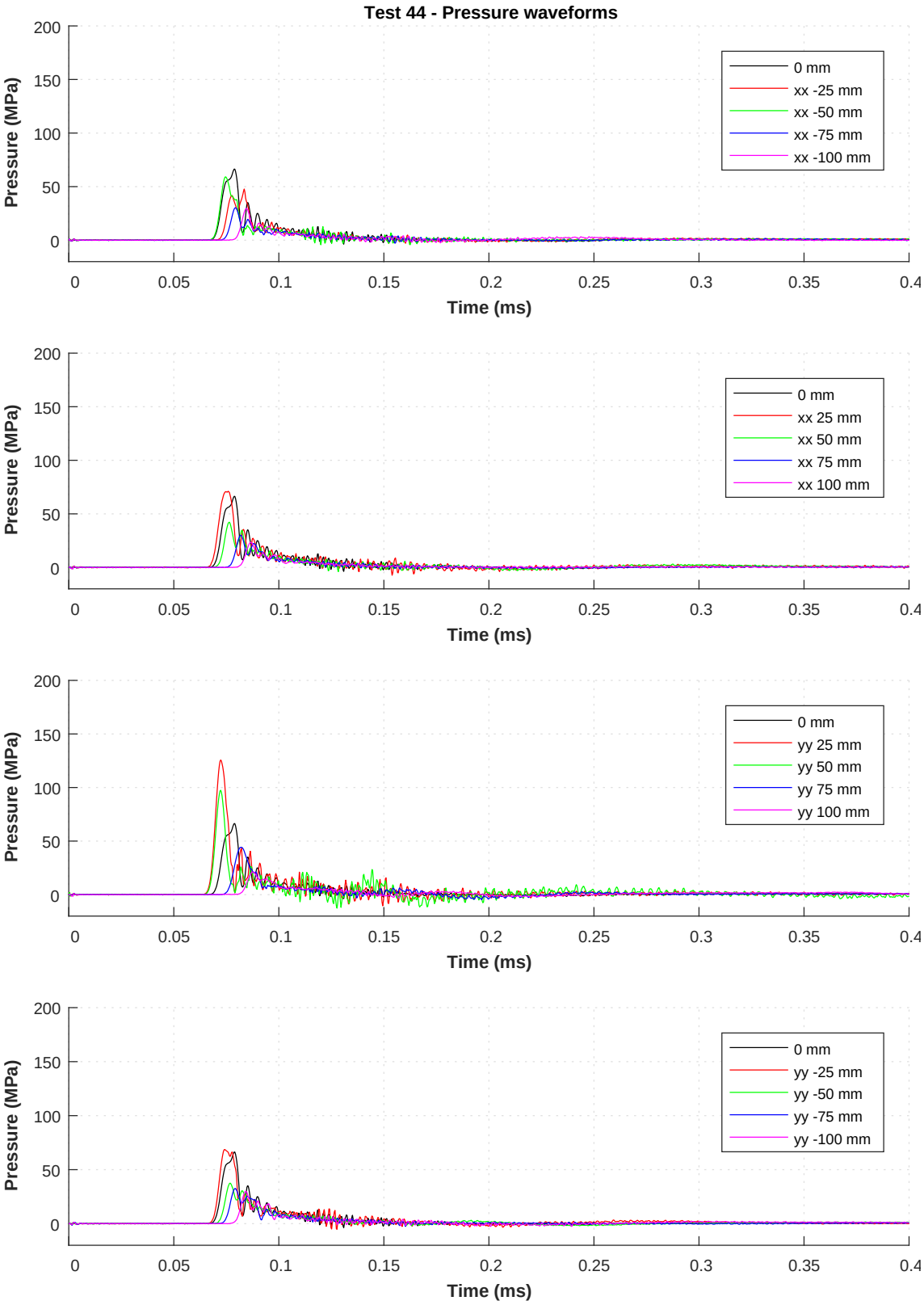

Figure C.5: Pressure-time waveform of Test 44.

C.0.2 Series A – Pressure-time waveforms for Tests 45–46

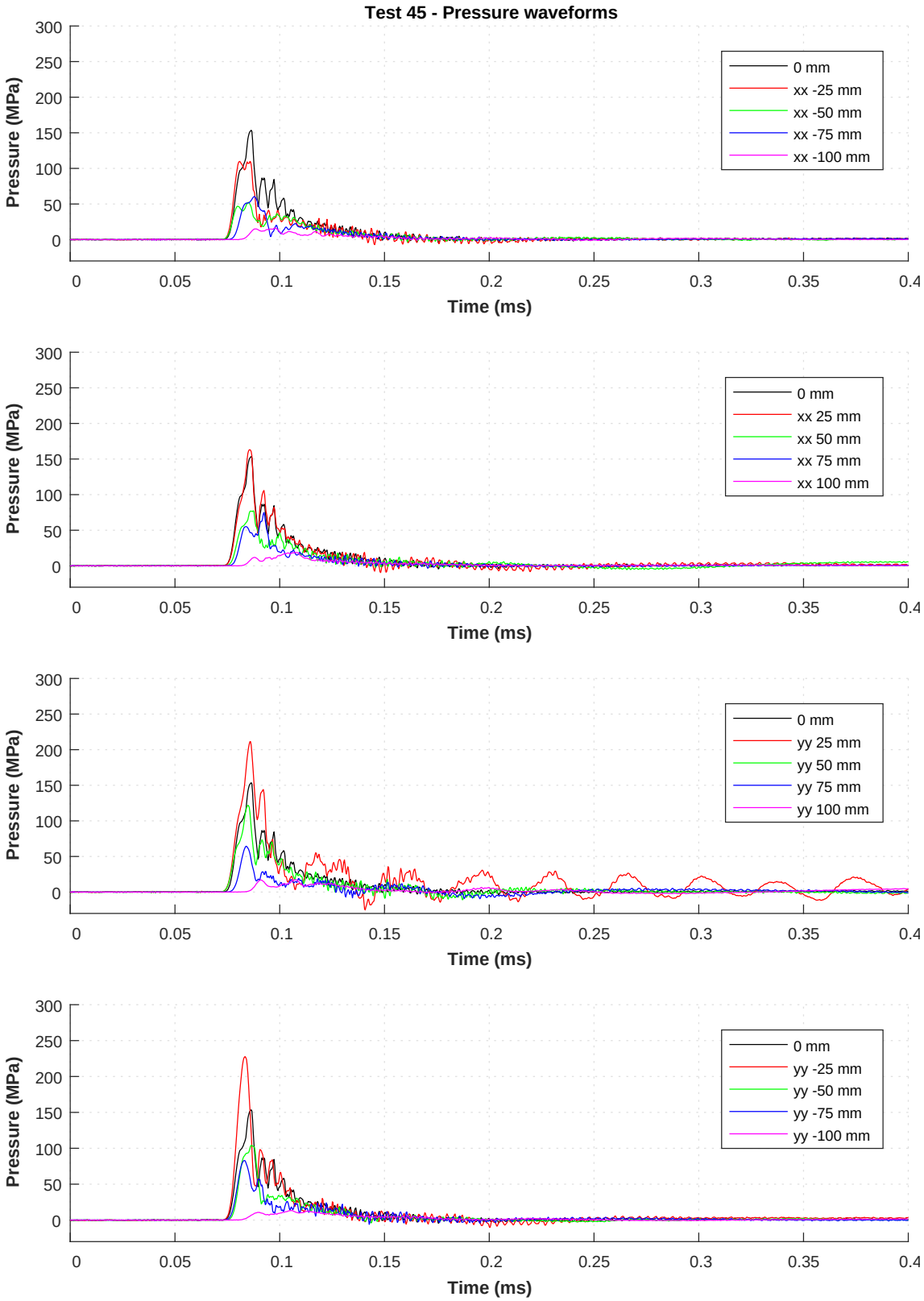

Figure C.6: Pressure-time waveform of Test 45.

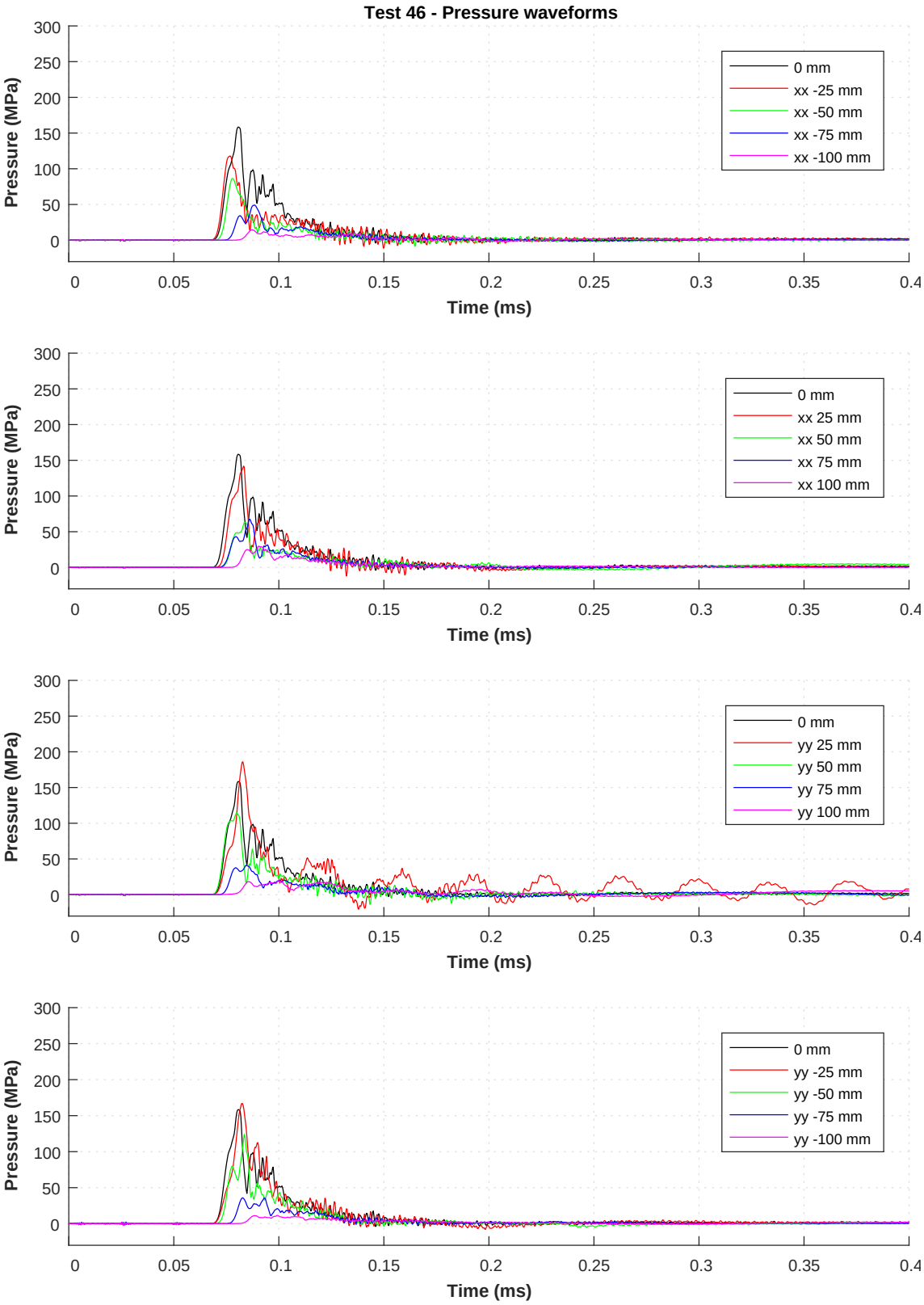

Figure C.7: Pressure-time waveform of Test 46.

C.0.3 Series B – Pressure-time waveforms for Tests 47–48

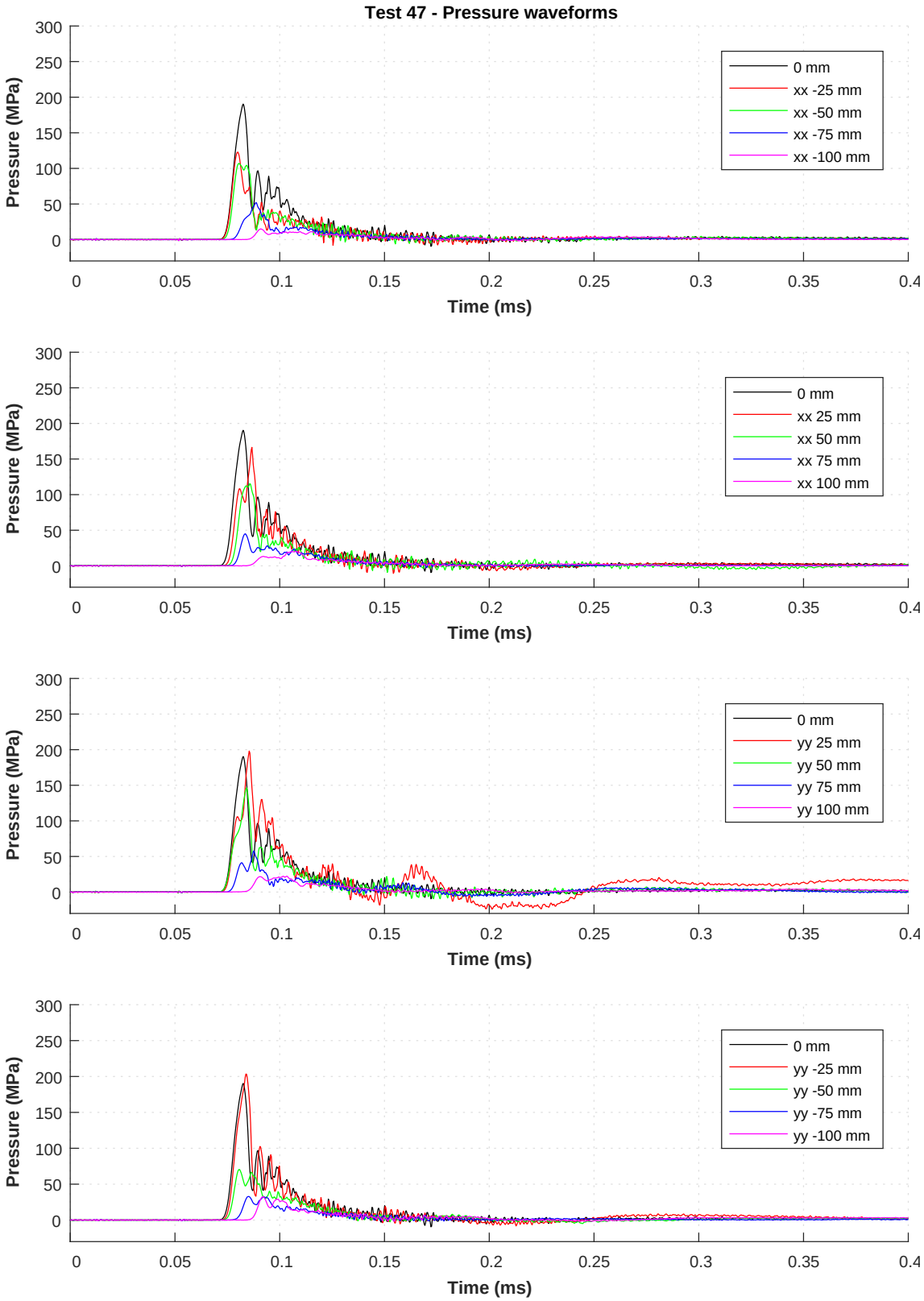

Figure C.8: Pressure-time waveform of Test 47.

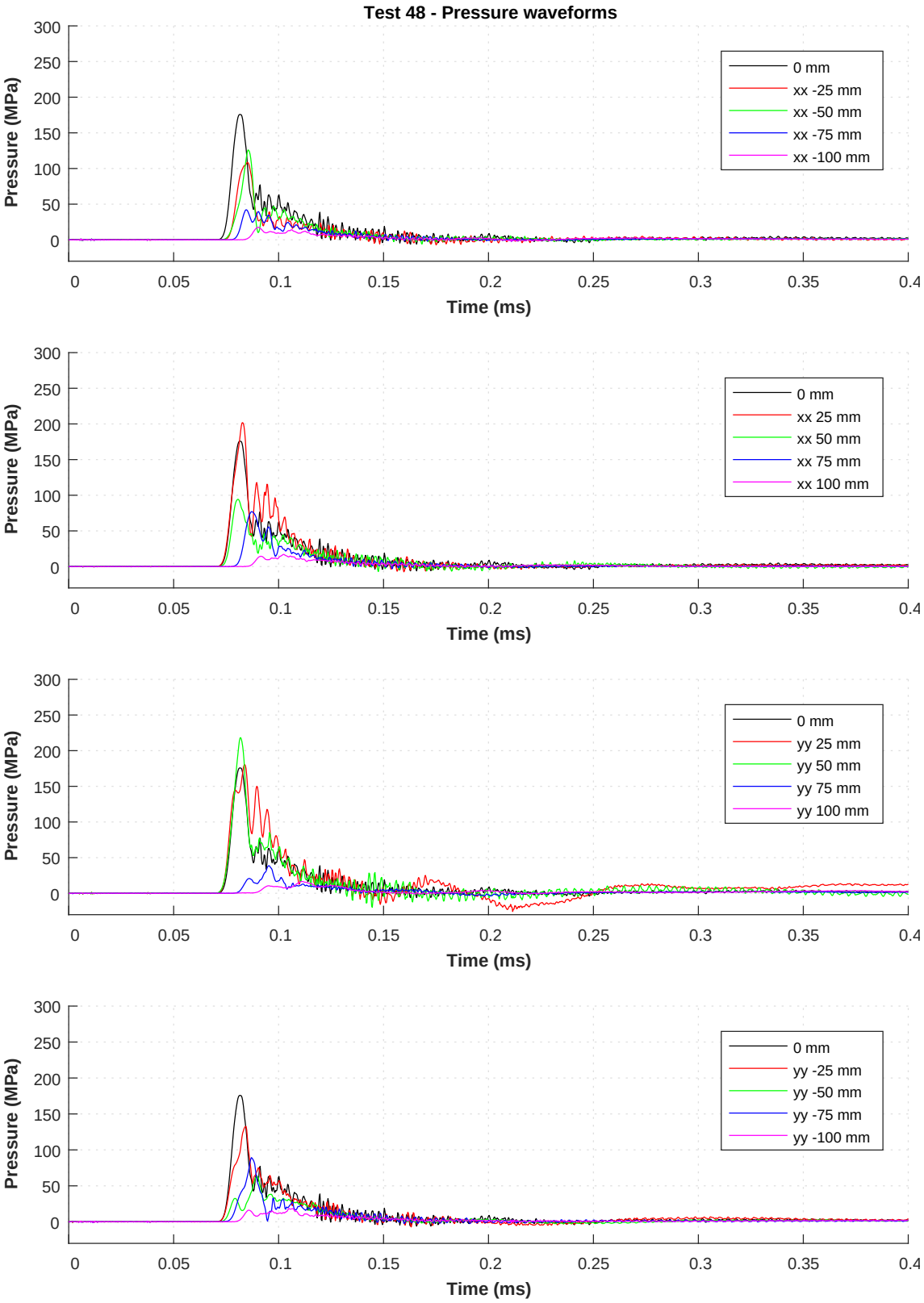

Figure C.9: Pressure-time waveform of Test 48.

C.0.4 Series C – Pressure-time waveforms for Tests 49–50

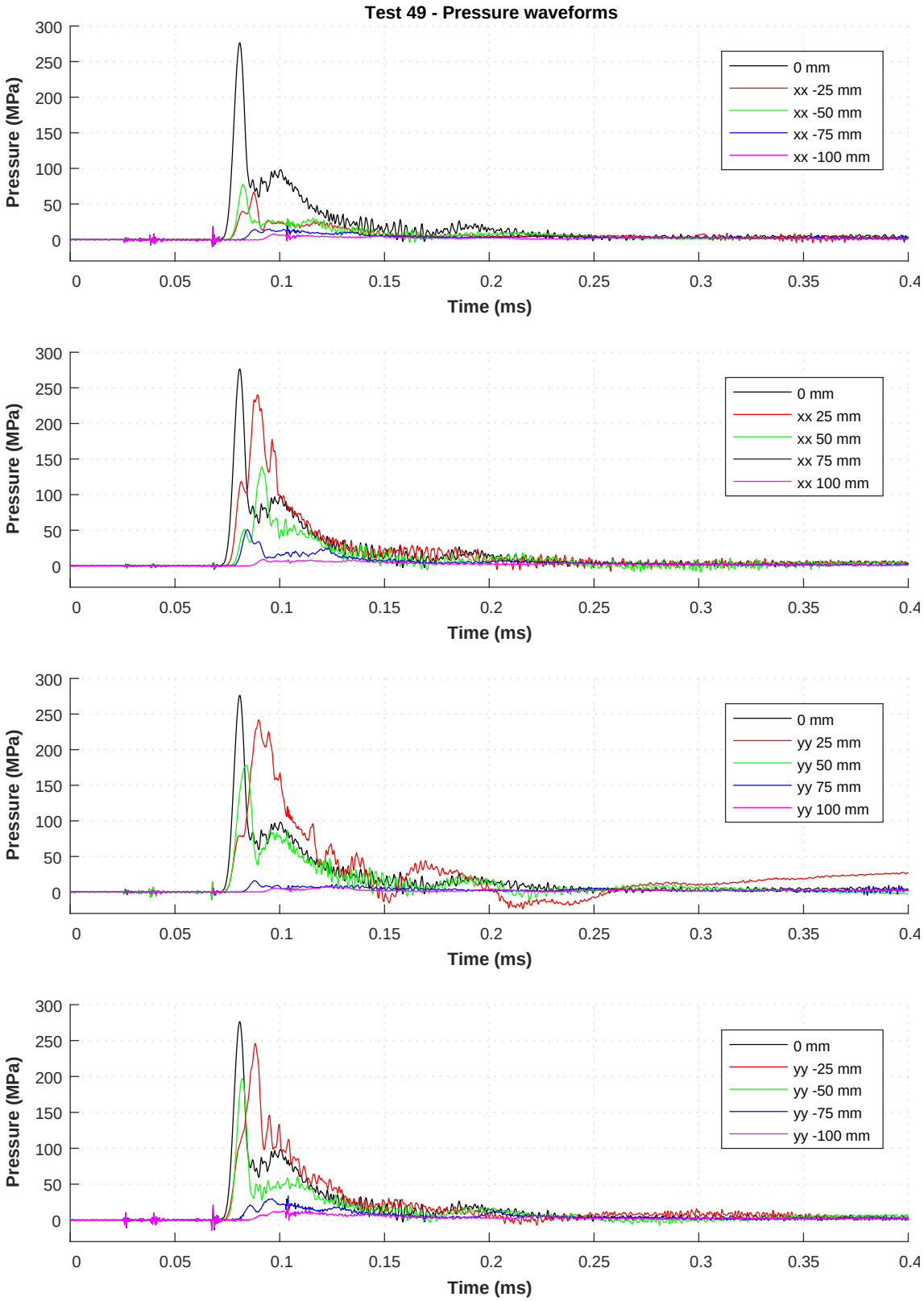

Figure C.10: Pressure-time waveform of Test 49.

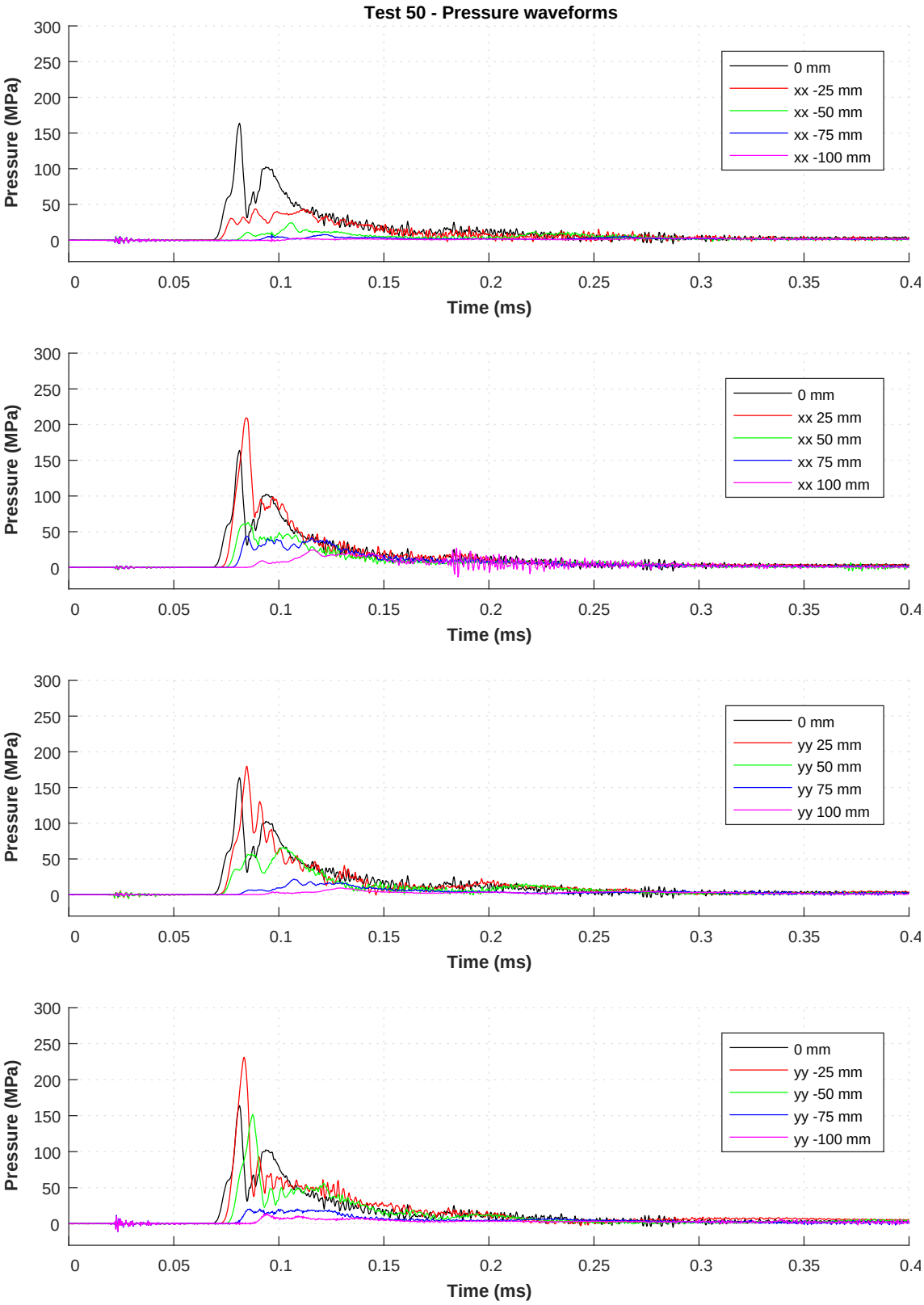

Figure C.11: Pressure-time waveform of Test 50.

C.0.5 Series D – Pressure-time waveforms for Tests 51–57

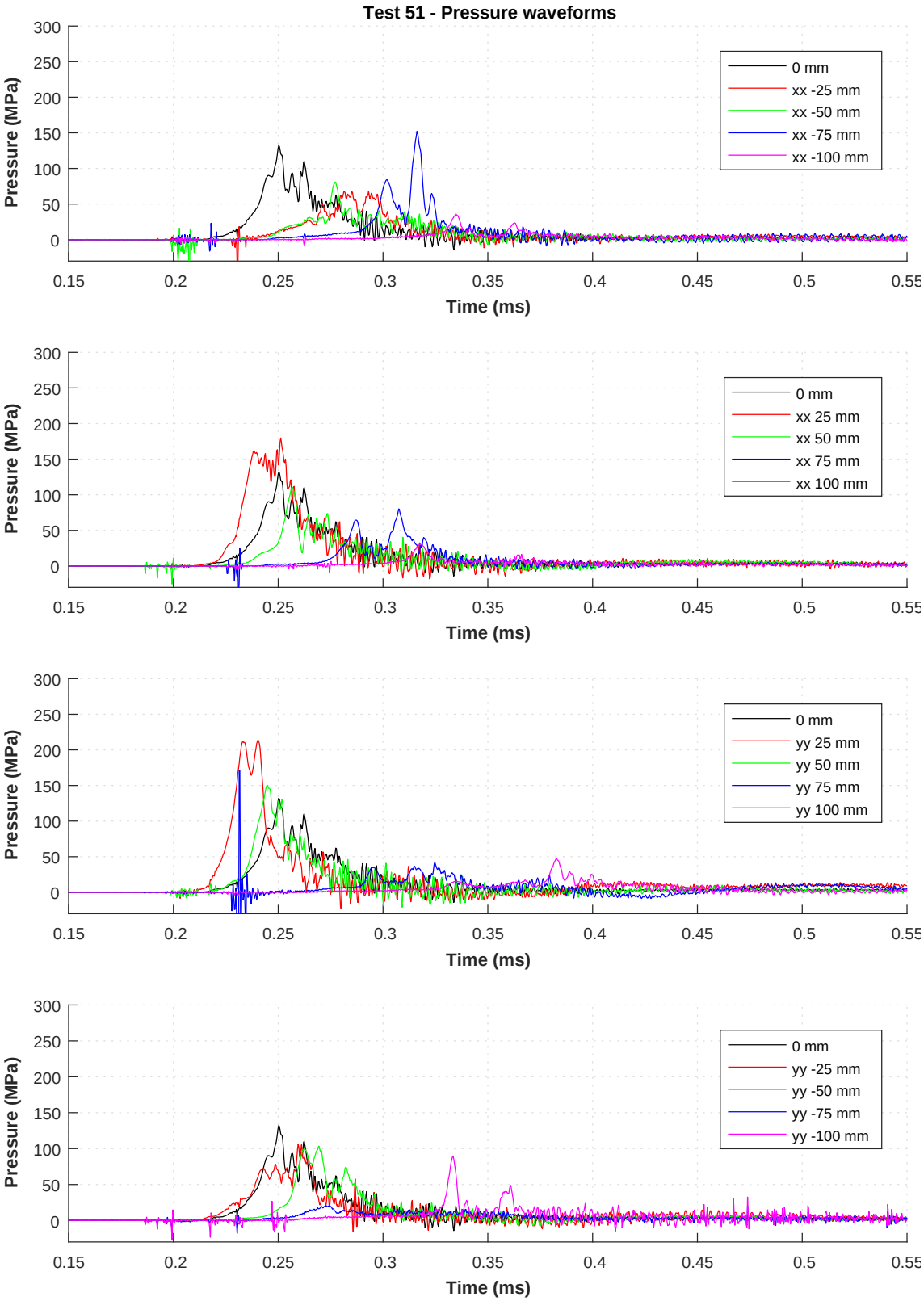

Figure C.12: Pressure-time waveform of Test 51.

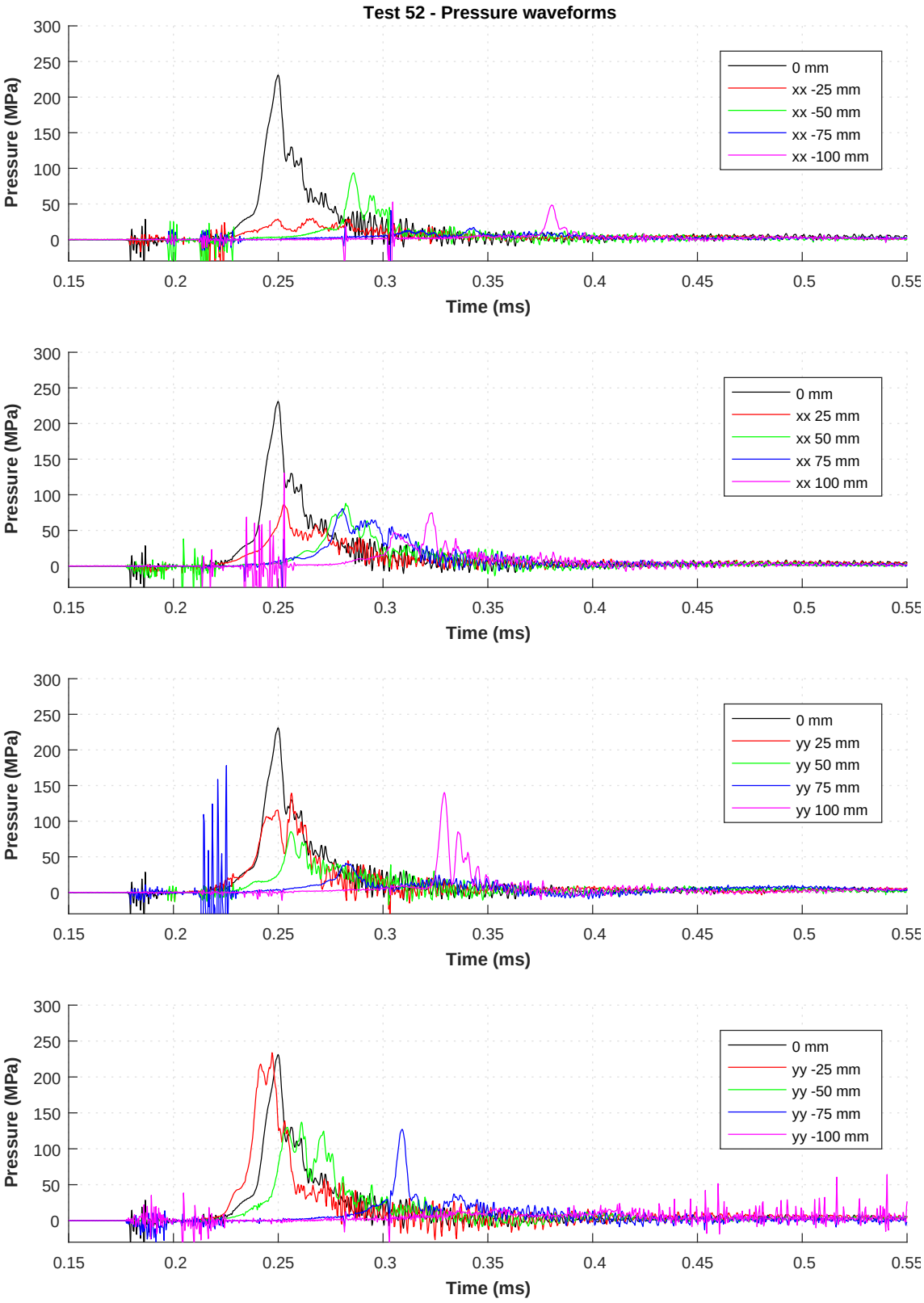

Figure C.13: Pressure-time waveform of Test 52.

Note: No data was captured for Test 53.

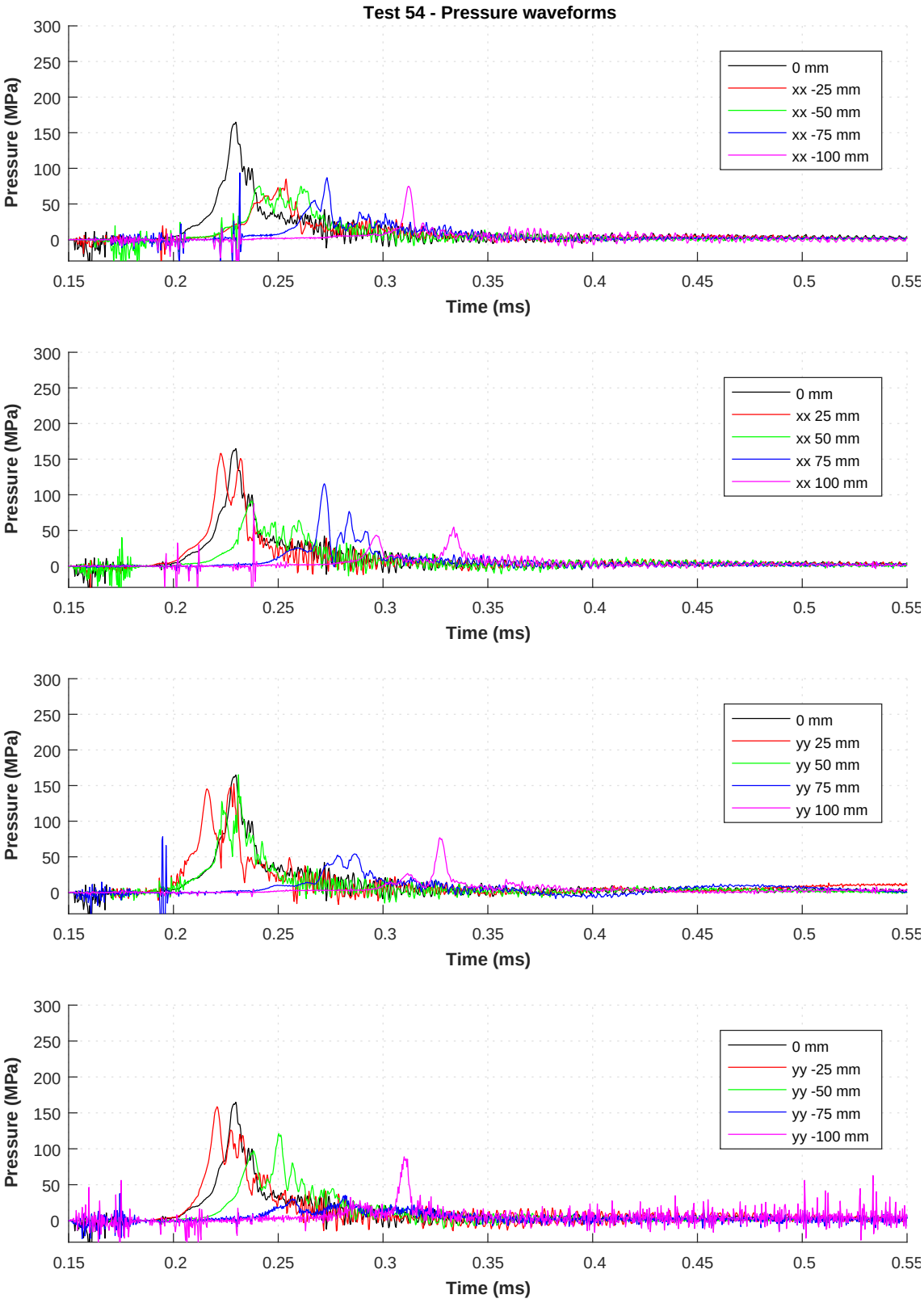

Figure C.14: Pressure-time waveform of Test 54.

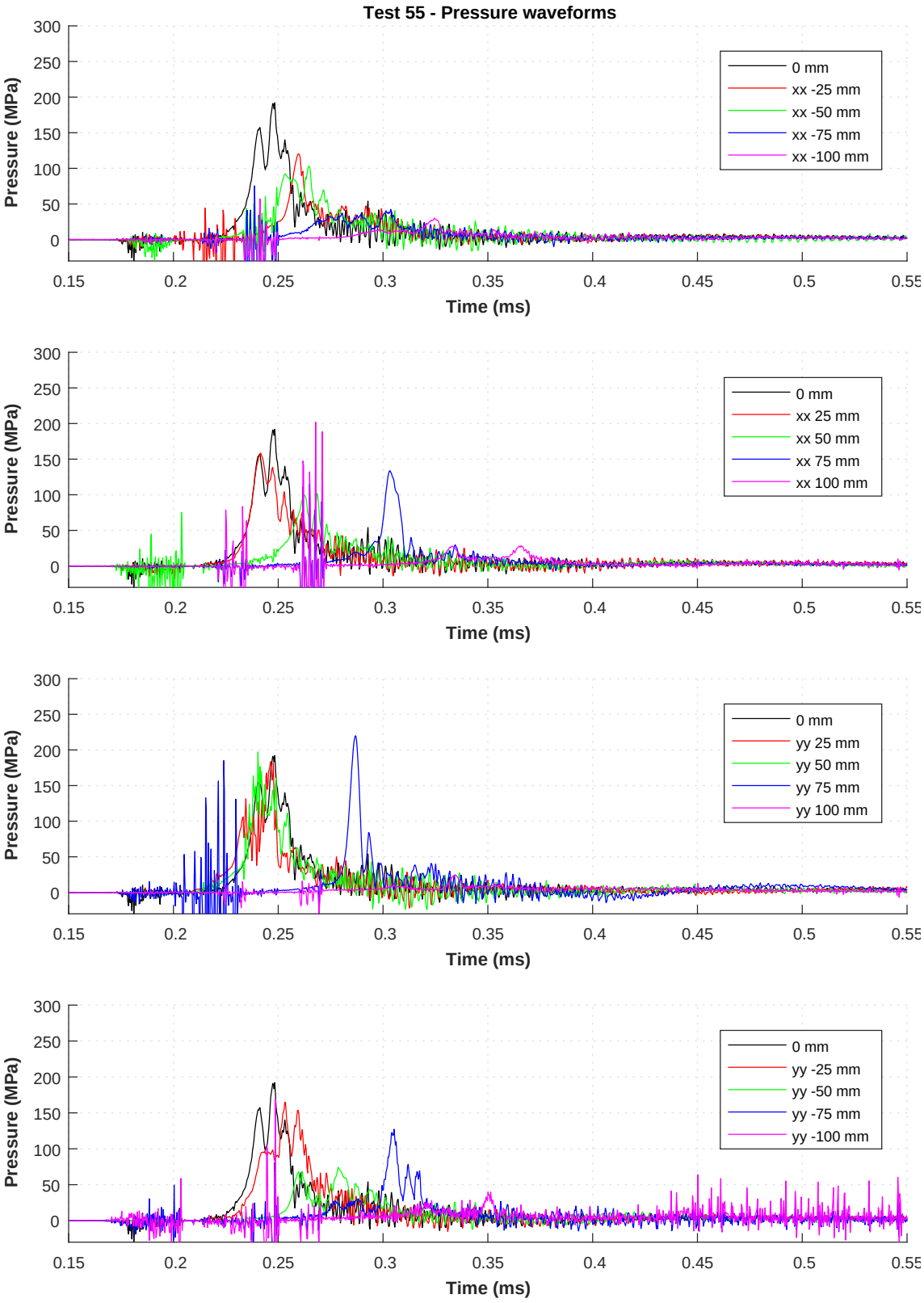

Figure C.15: Pressure-time waveform of Test 55.

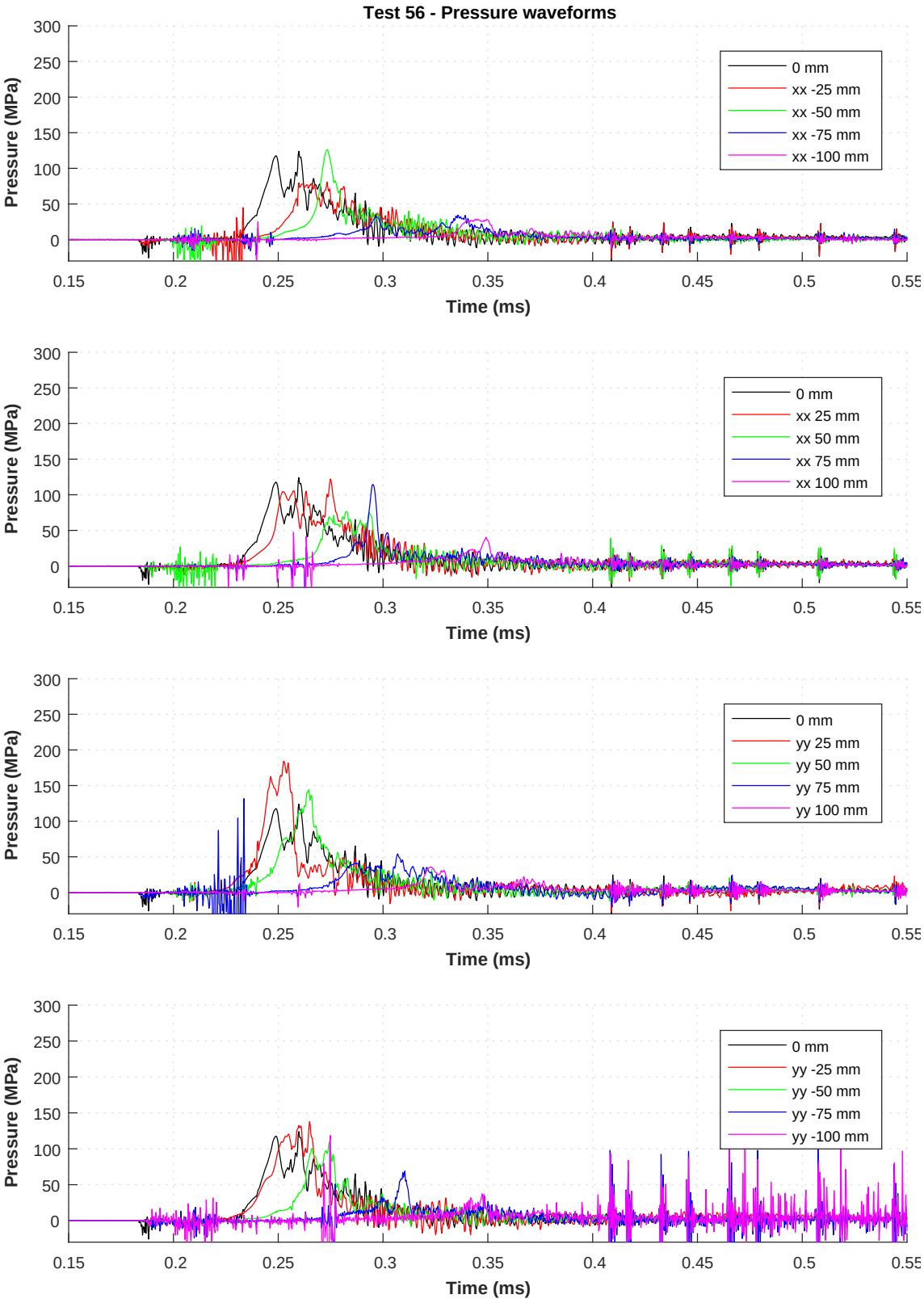

Figure C.16: Pressure-time waveform of Test 56.

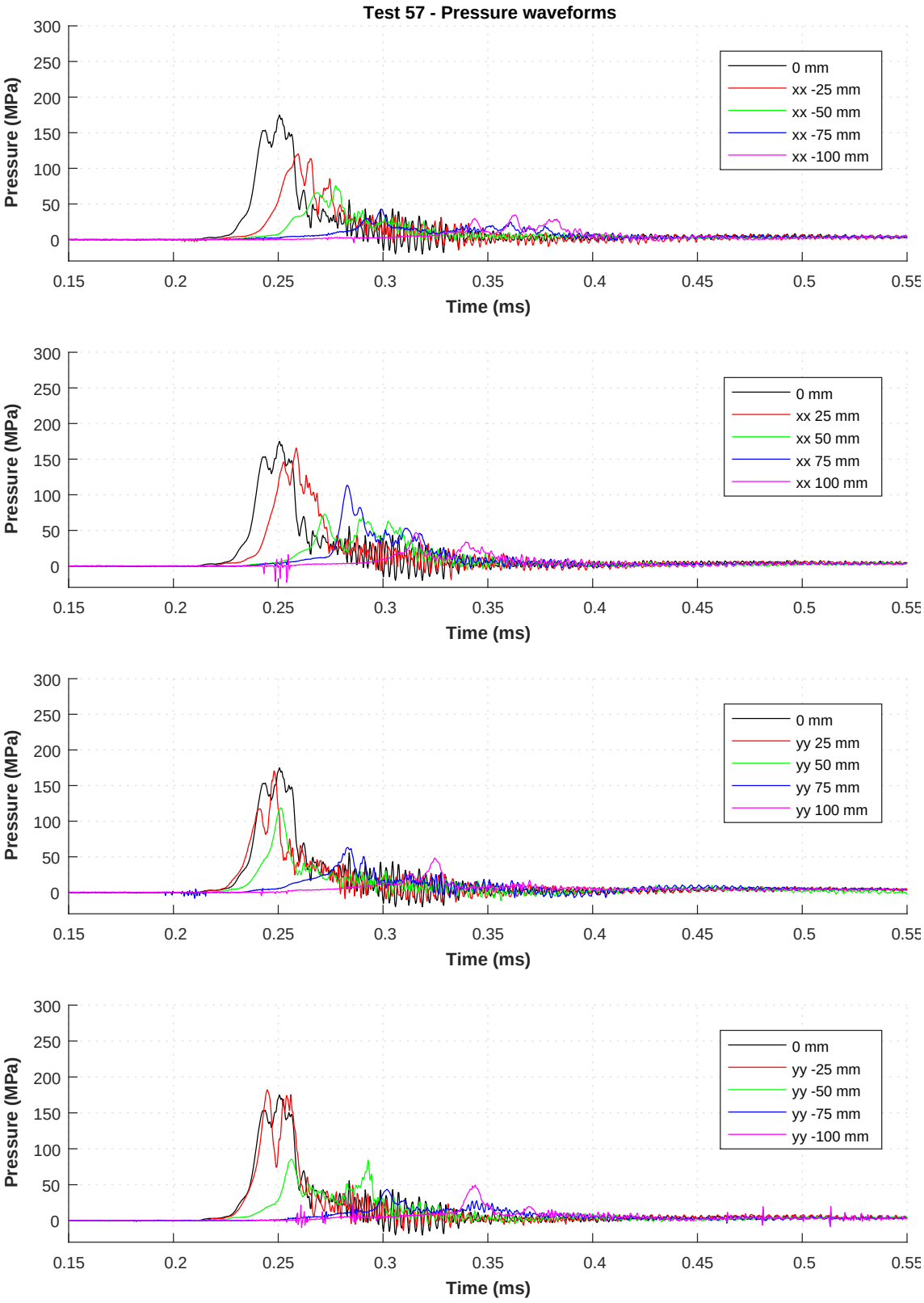

Figure C.17: Pressure-time waveform of Test 57.

C.0.6 Series E – Pressure-time waveforms for Tests 58–62

Note: No data was captured for Test 58.

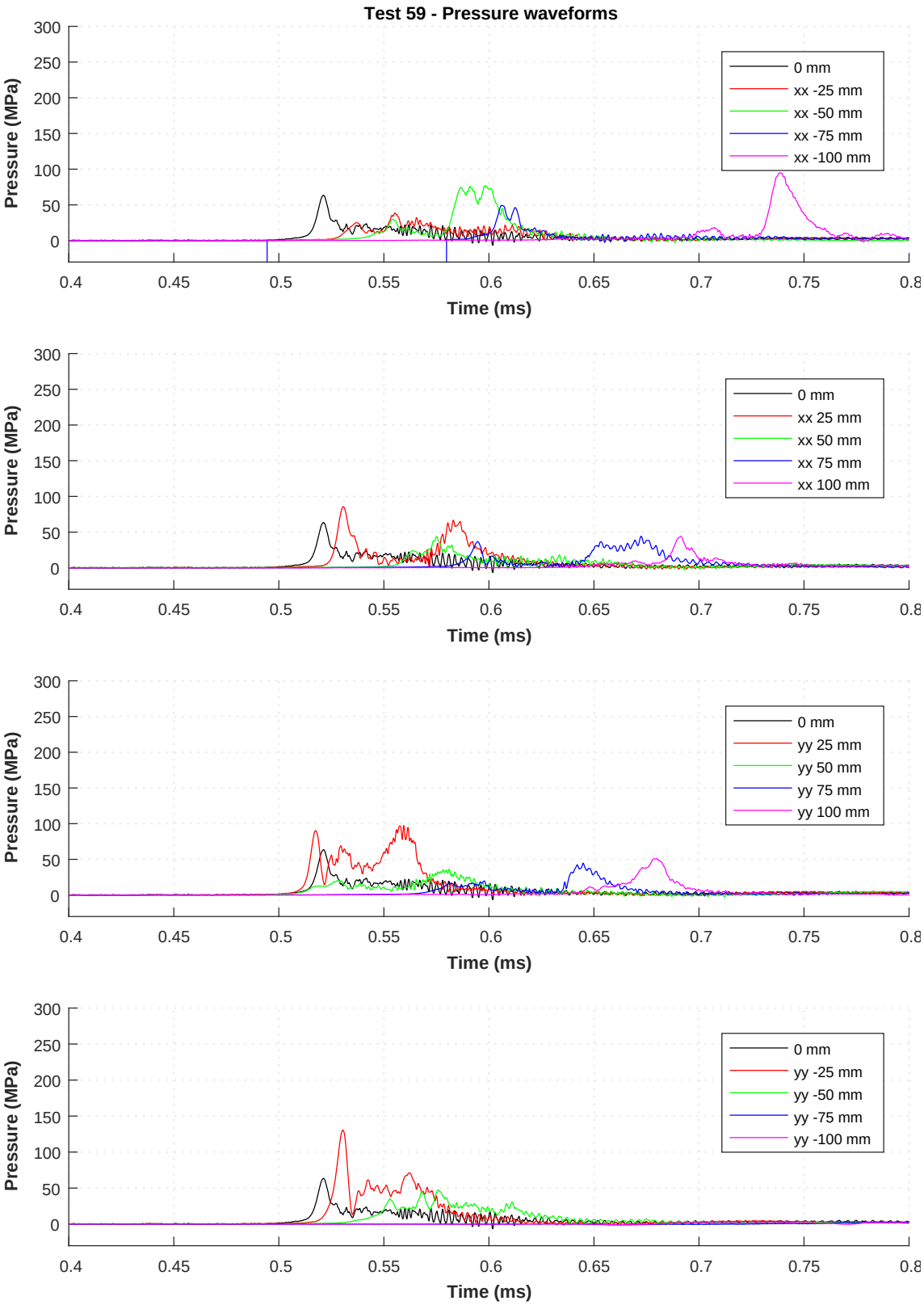

Figure C.18: Pressure-time waveform of Test 59.

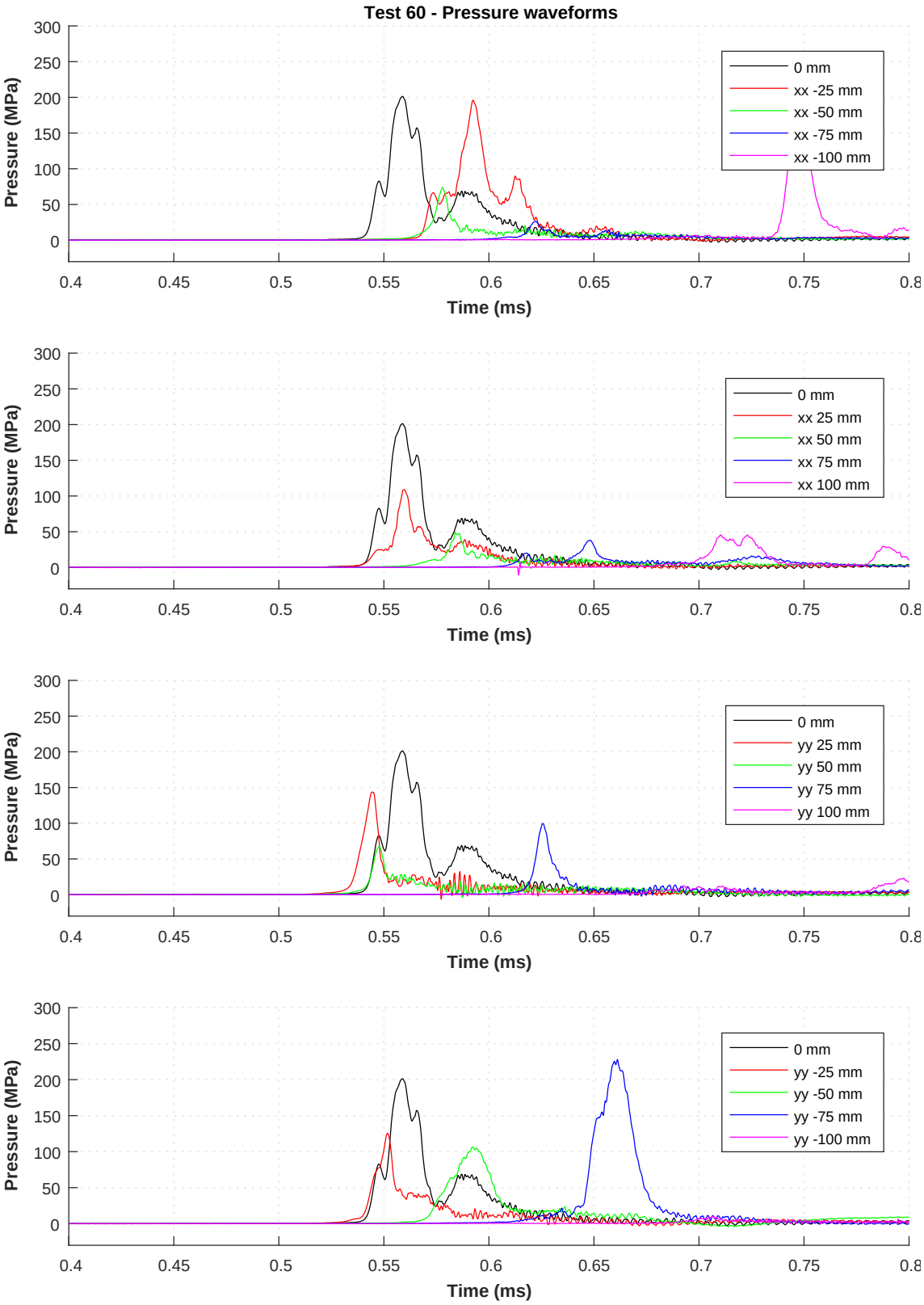

Figure C.19: Pressure-time waveform of Test 60.

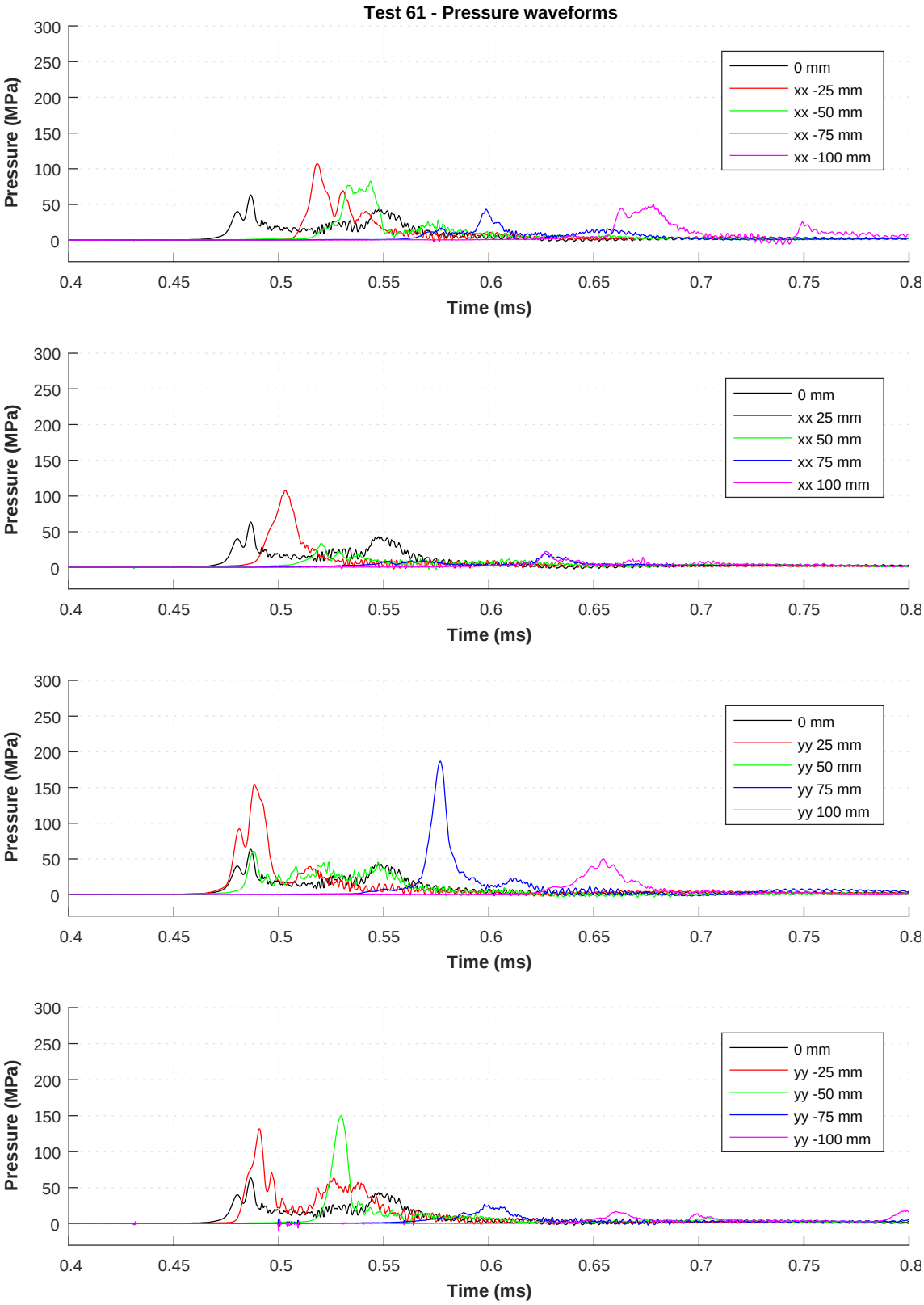

Figure C.20: Pressure-time waveform of Test 61.

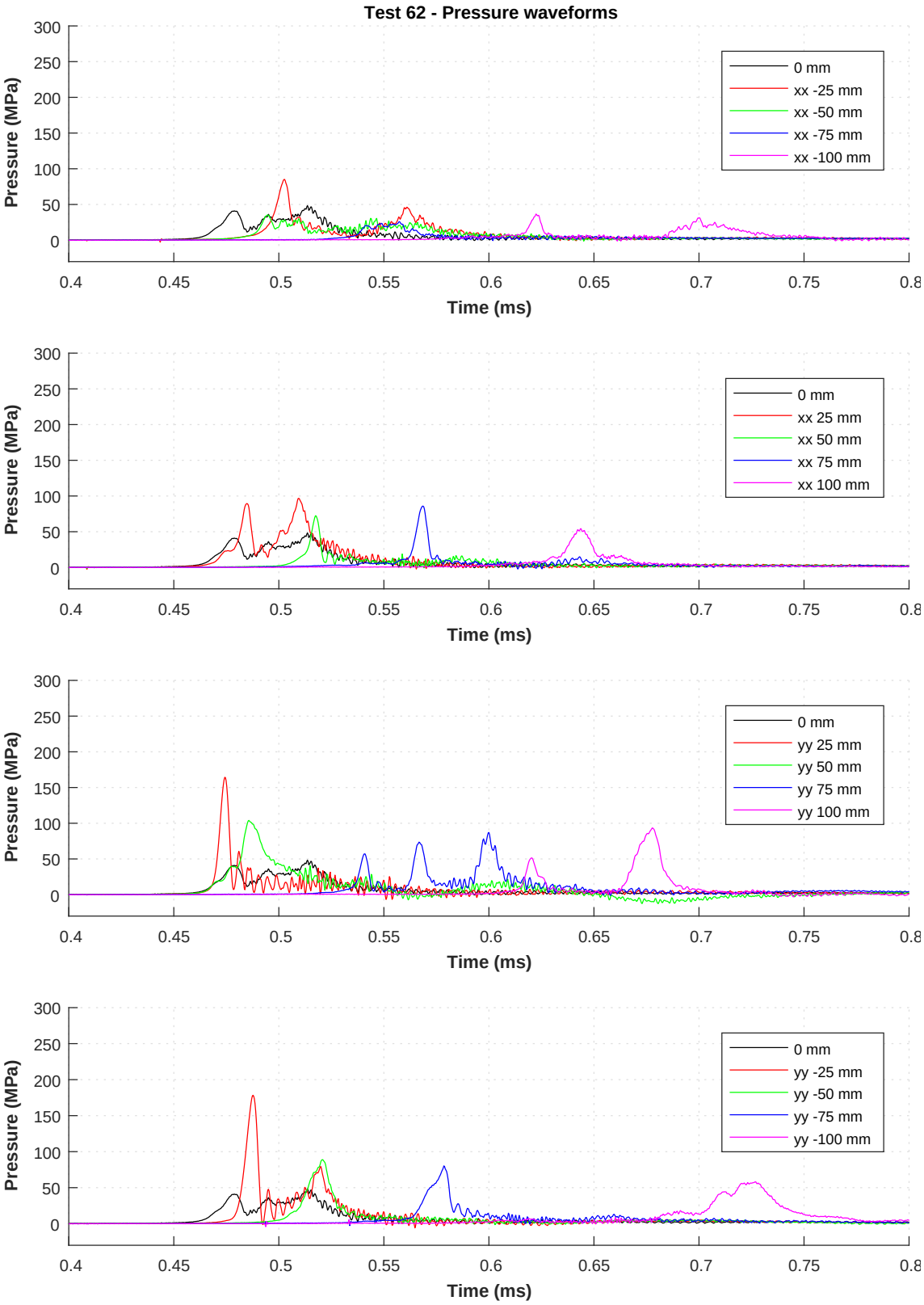

Figure C.21: Pressure-time waveform of Test 62.

C.0.7 Series F – Pressure-time waveforms for Tests 63–67

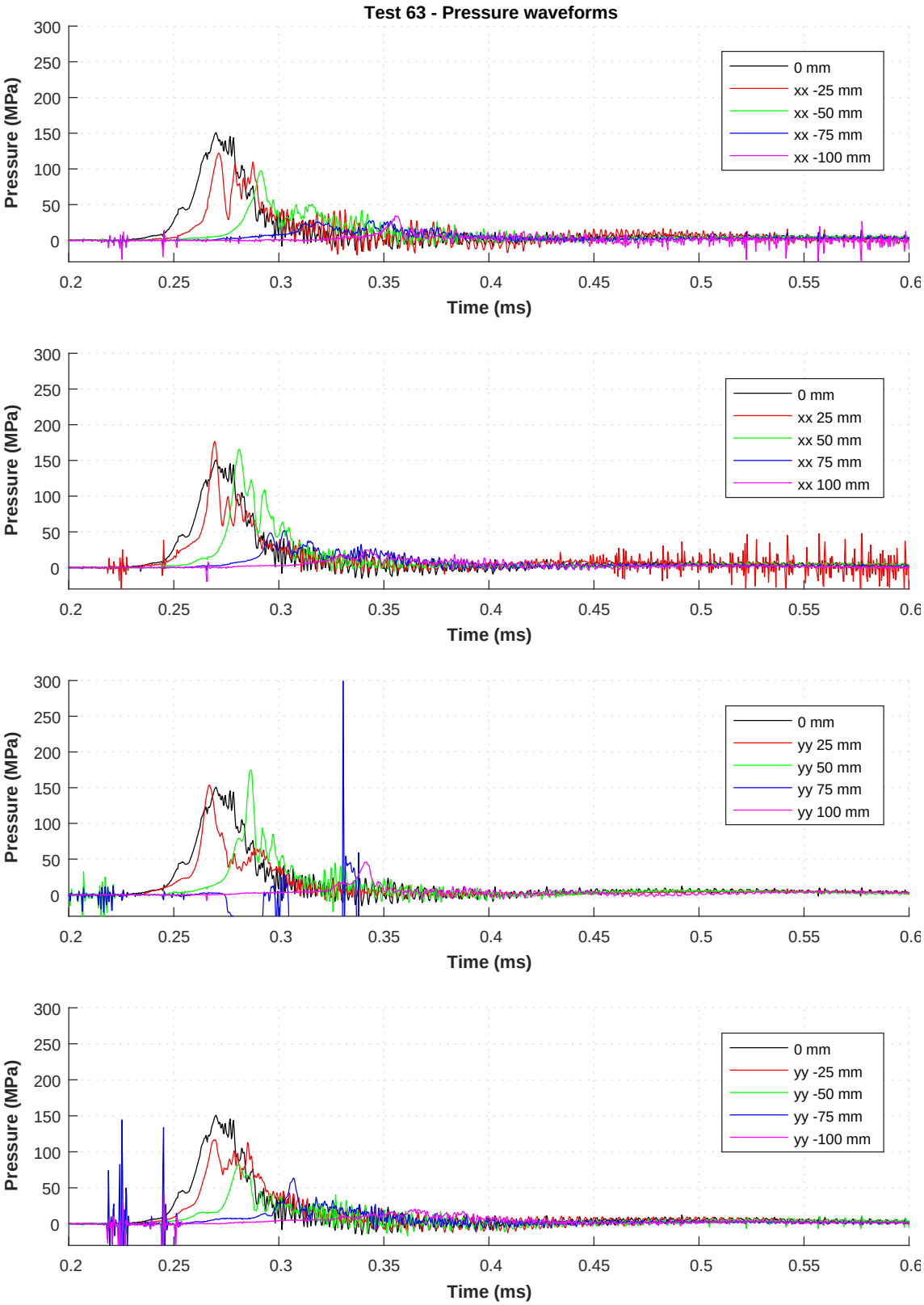

Figure C.22: Pressure-time waveform of Test 63.

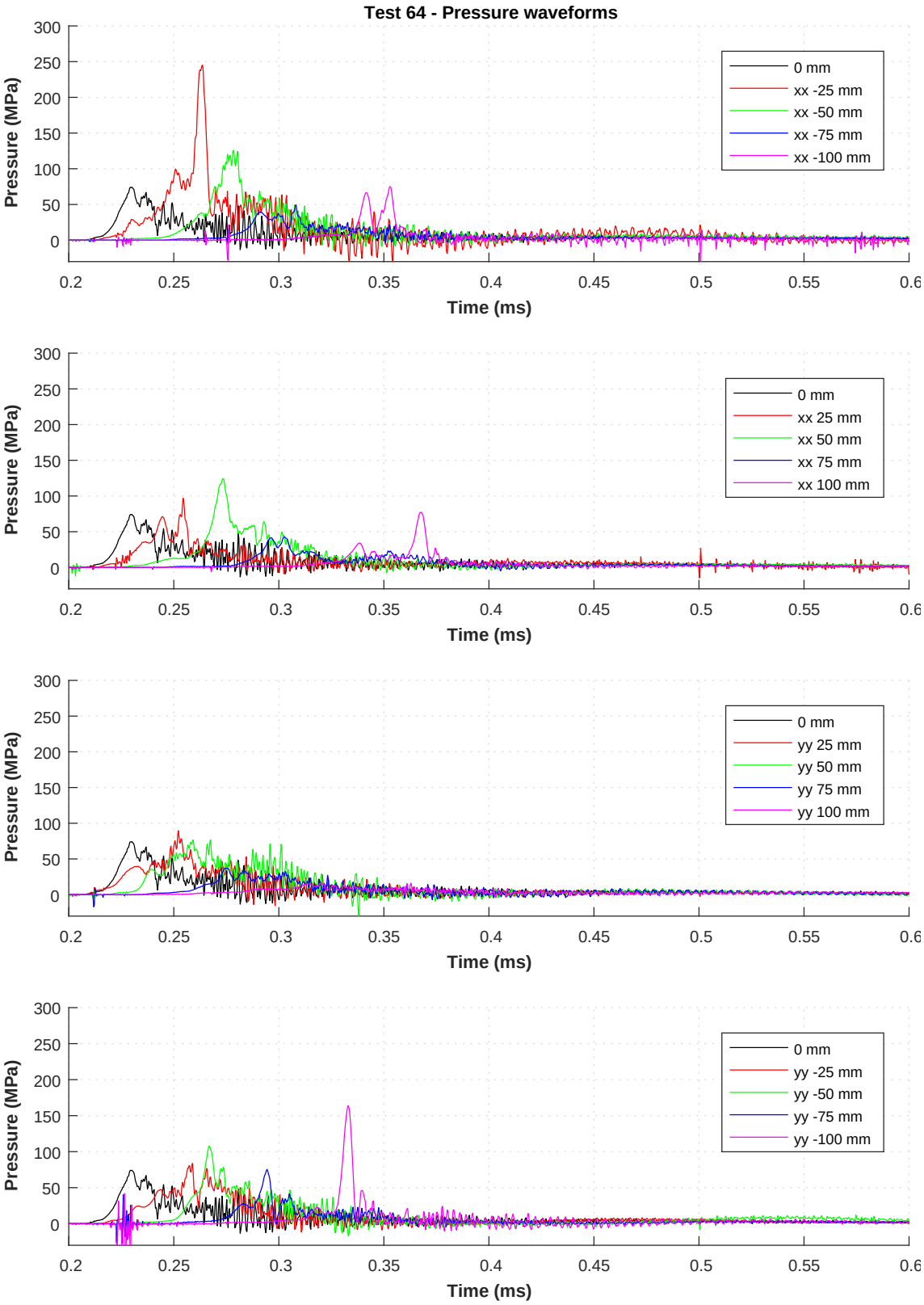

Figure C.23: Pressure-time waveform of Test 64.

Note: No data was captured for Test 65.

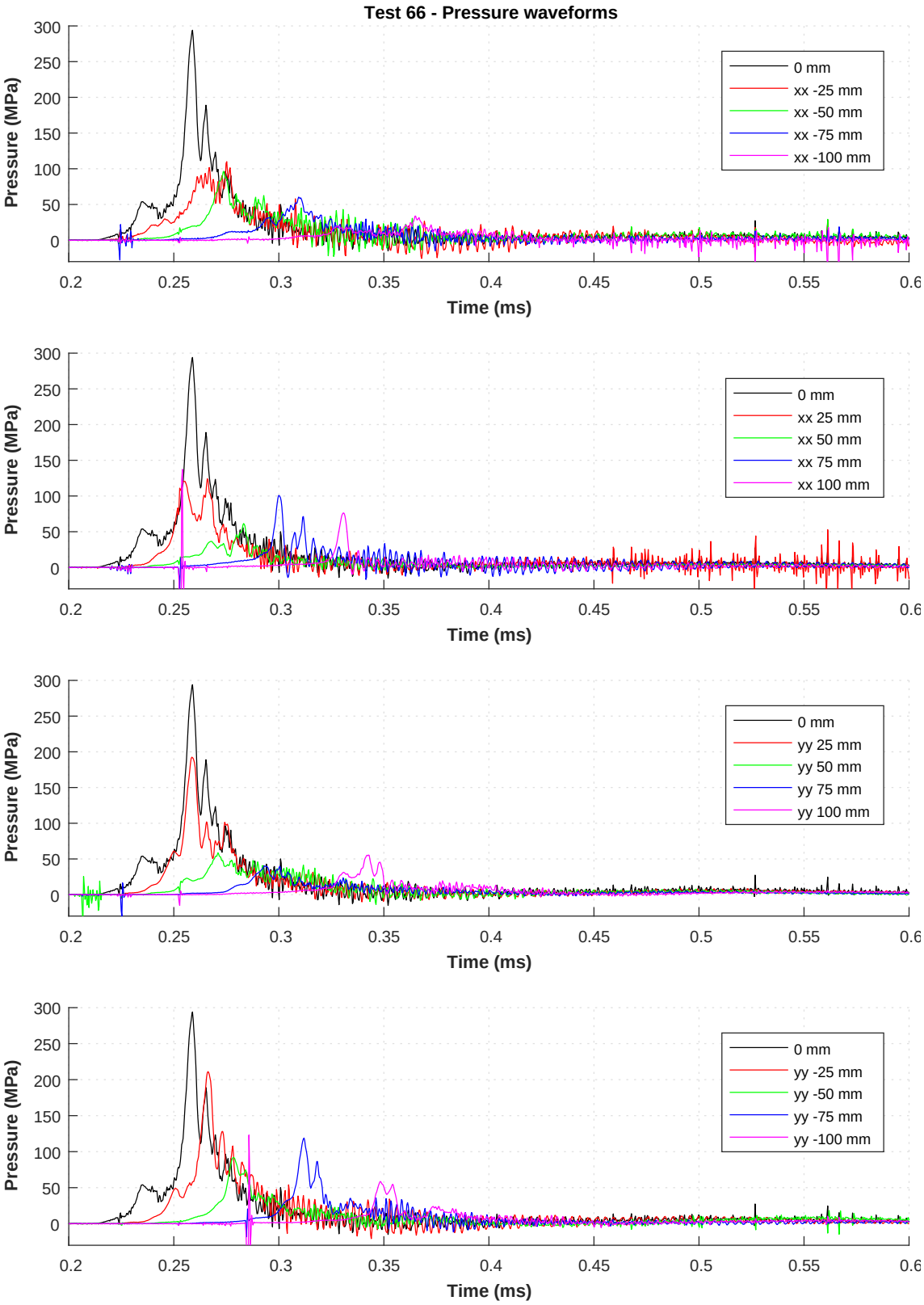

Figure C.24: Pressure-time waveform of Test 66.

Note: No data was captured for Test 67.

C.0.8 Series G – Pressure-time waveforms for Tests 68–72

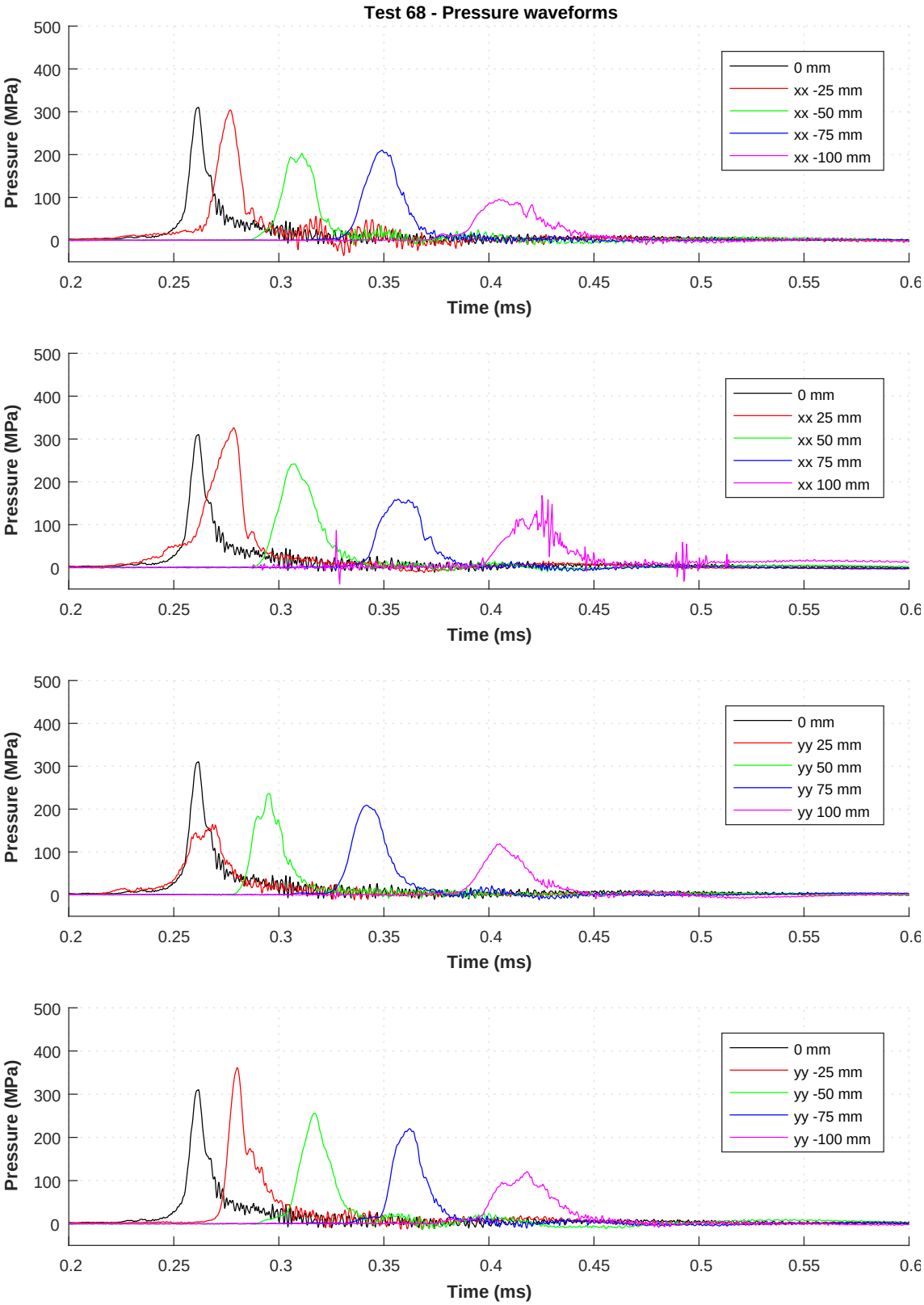

Figure C.25: Pressure-time waveform of Test 68.

Note: No data was captured for Test 69.

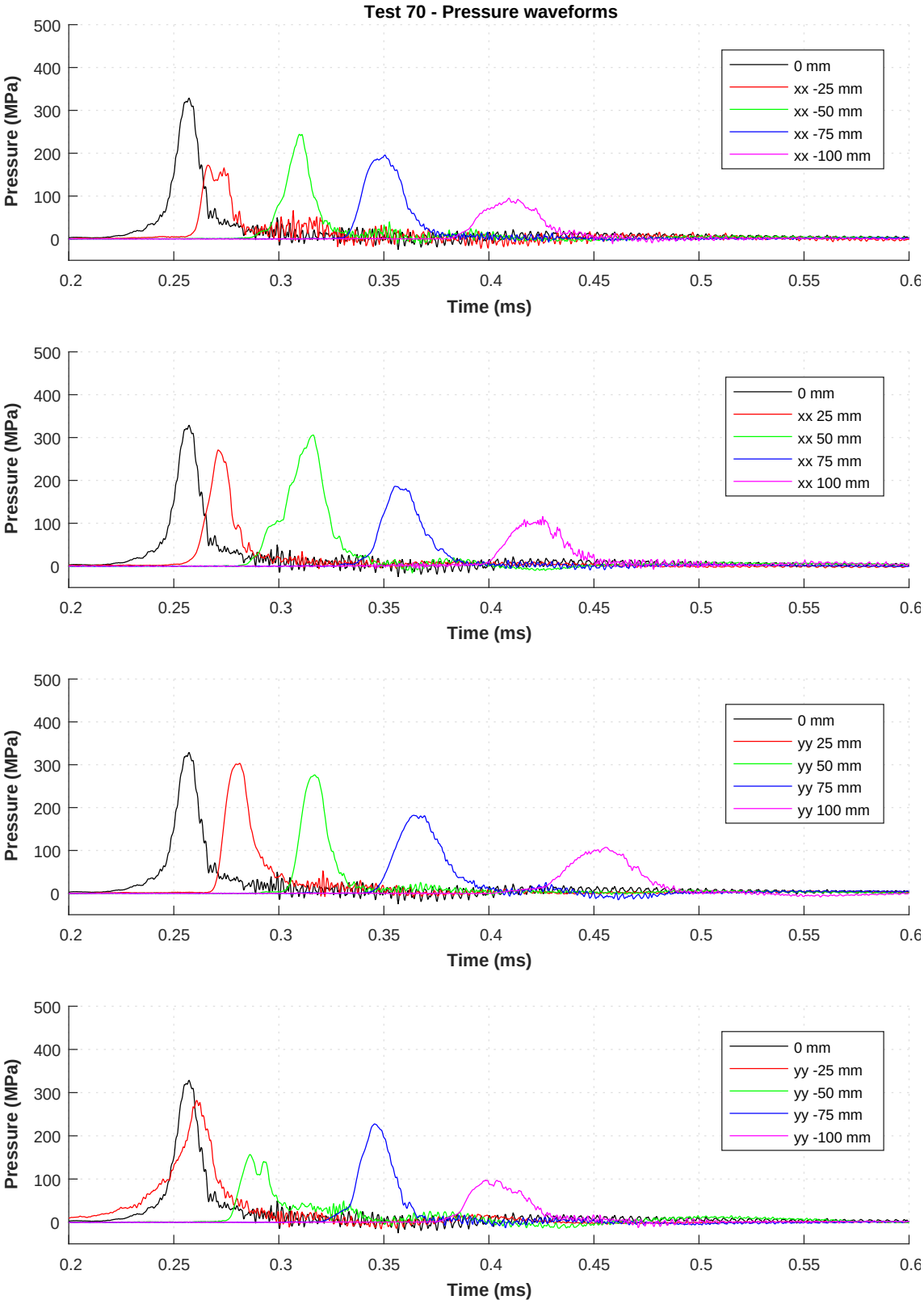

Figure C.26: Pressure-time waveform of Test 70.

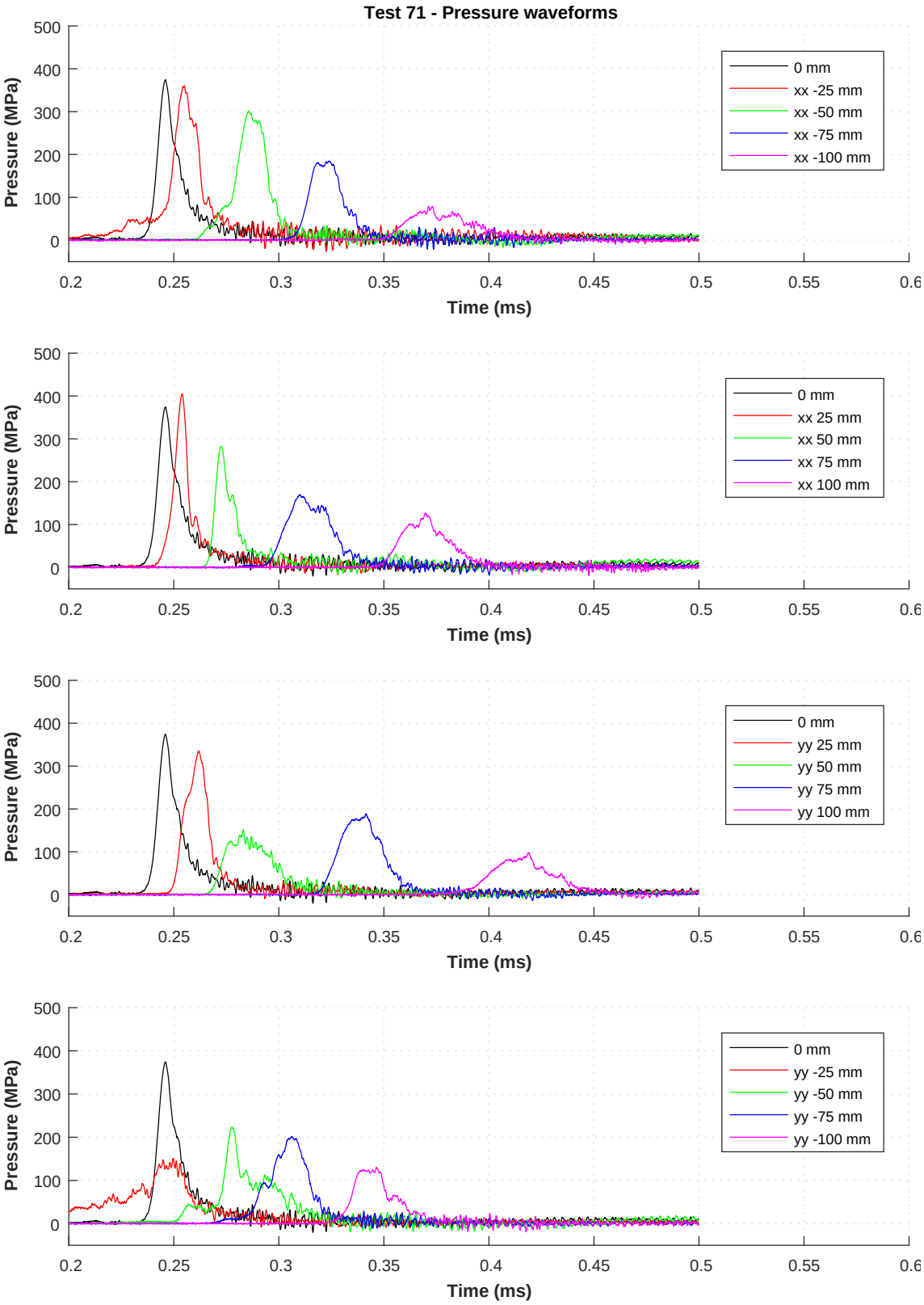

Figure C.27: Pressure-time waveform of Test 71.

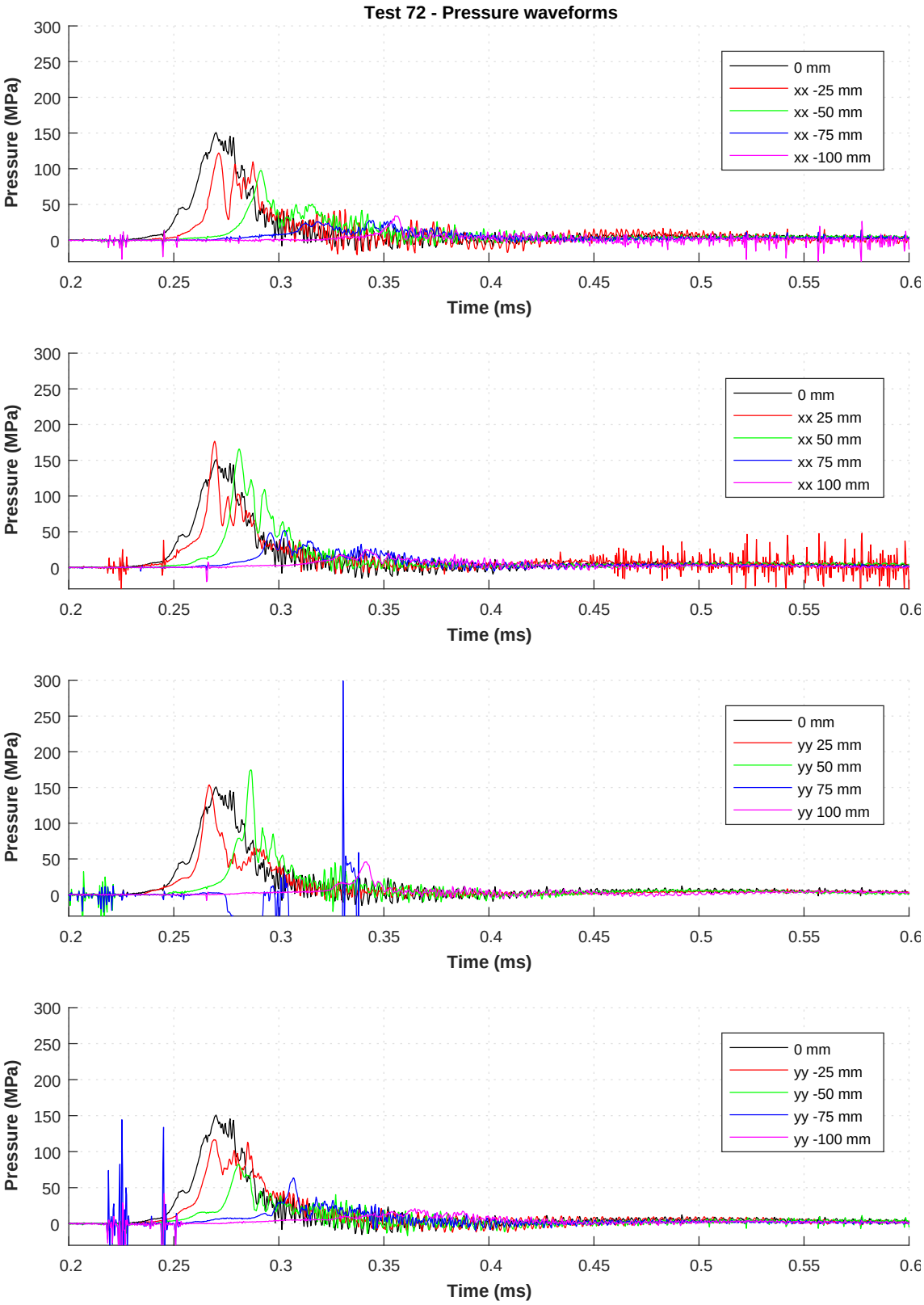

Figure C.28: Pressure-time waveform of Test 72.

C.0.9 Series H – Pressure-time waveforms for Tests 73–74

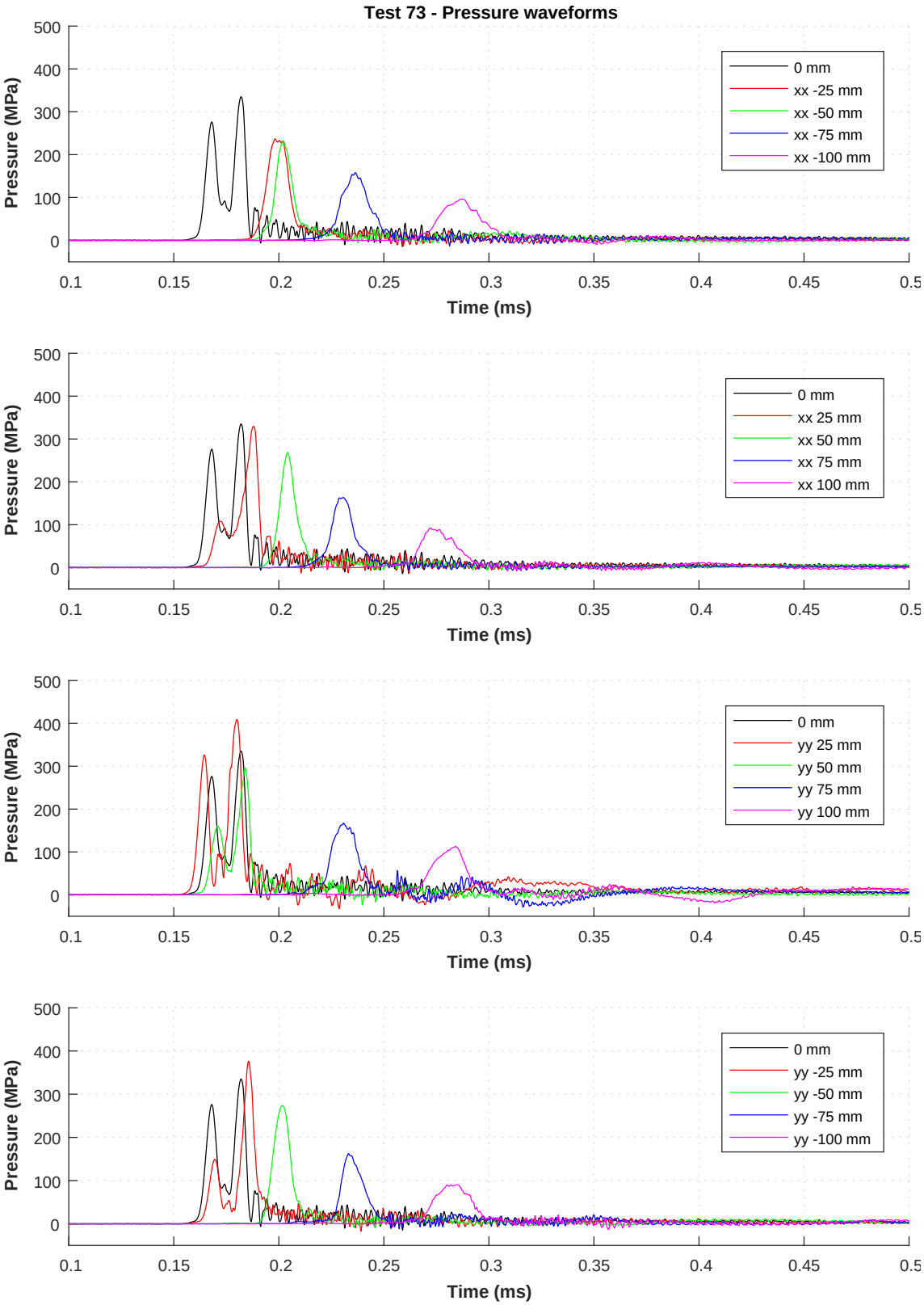

Figure C.29: Pressure-time waveform of Test 73.

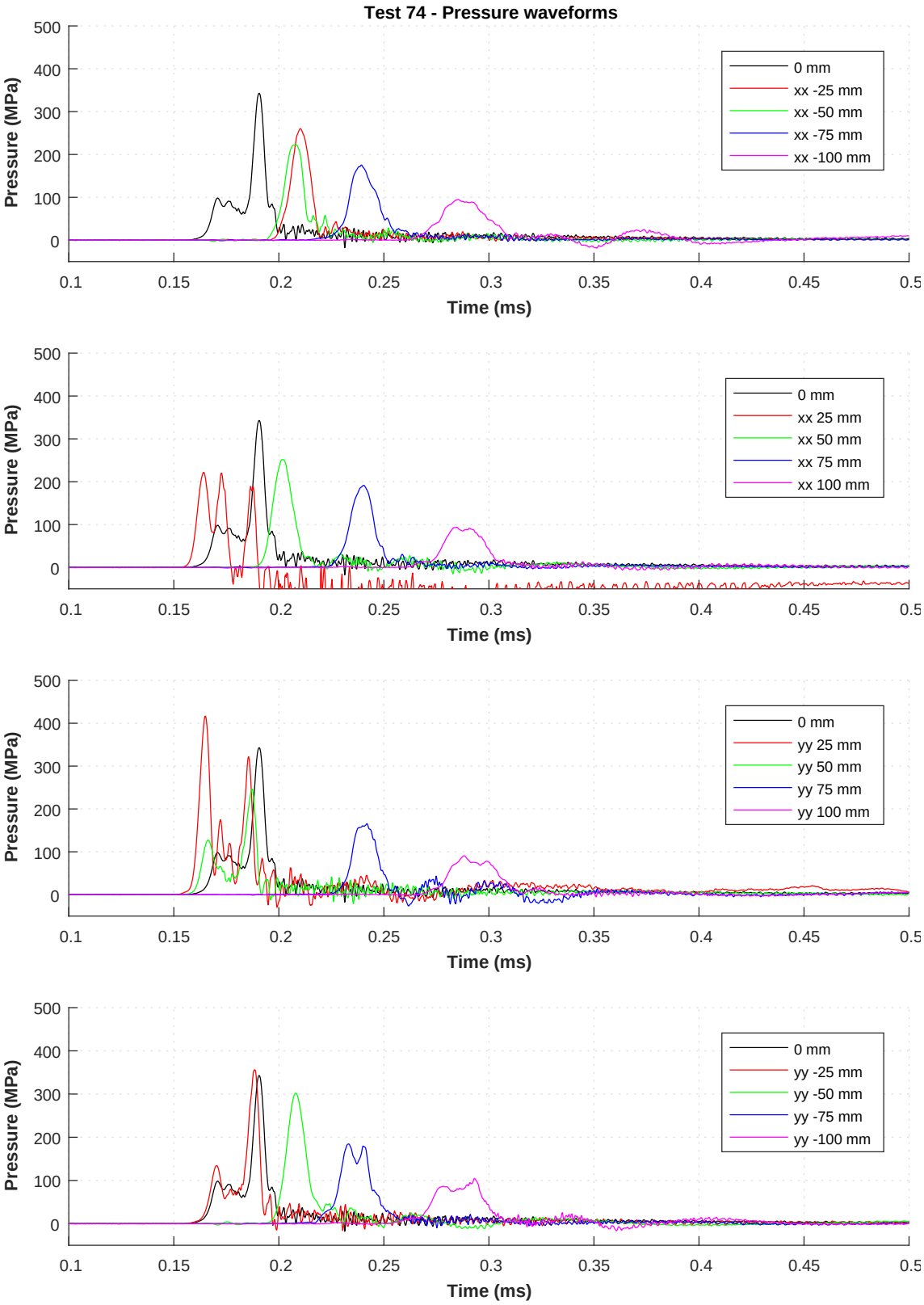

Figure C.30: Pressure-time waveform of Test 74.

C.0.10 Series I – Pressure-time waveforms for Tests 75–81

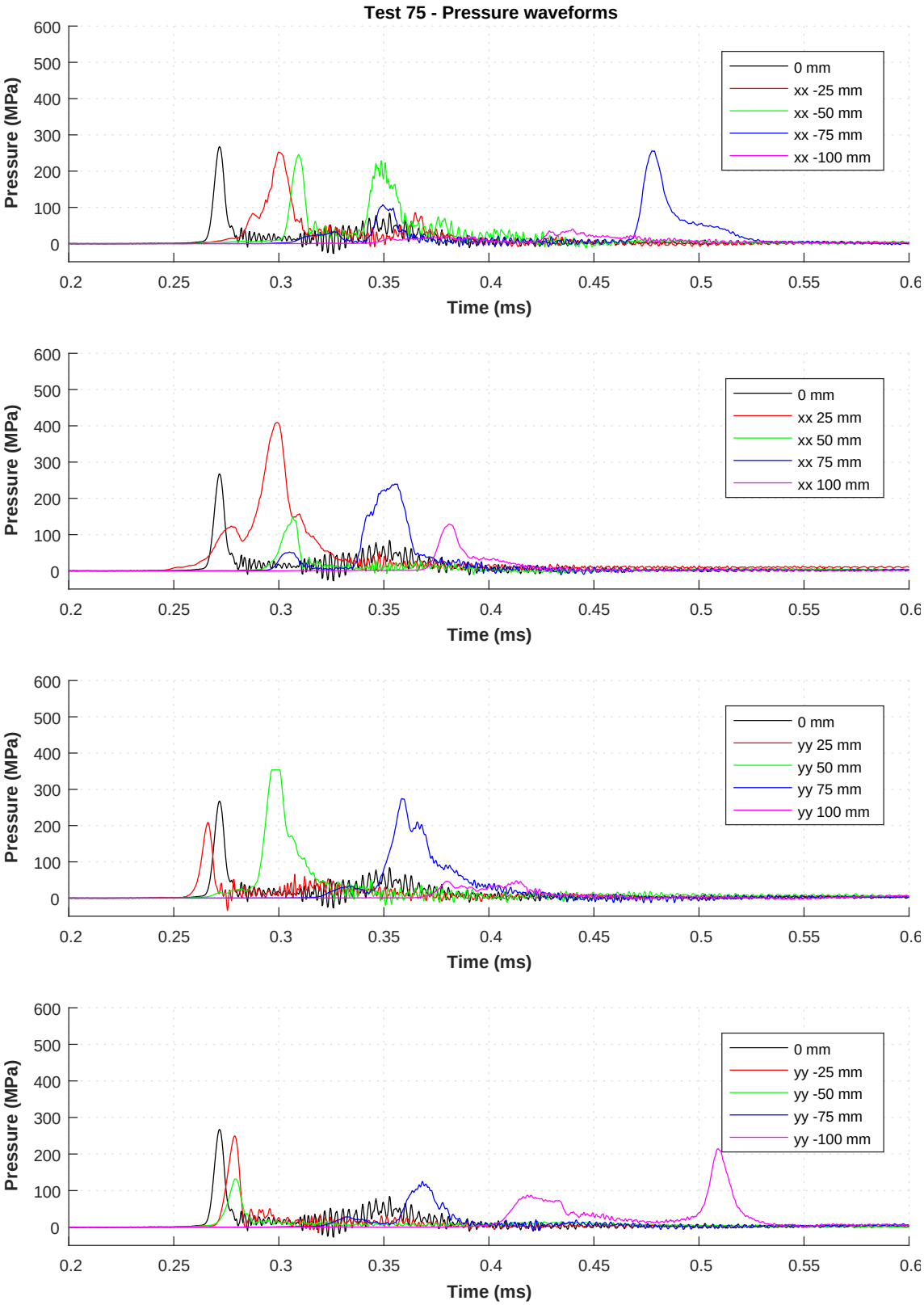

Figure C.31: Pressure-time waveform of Test 75.

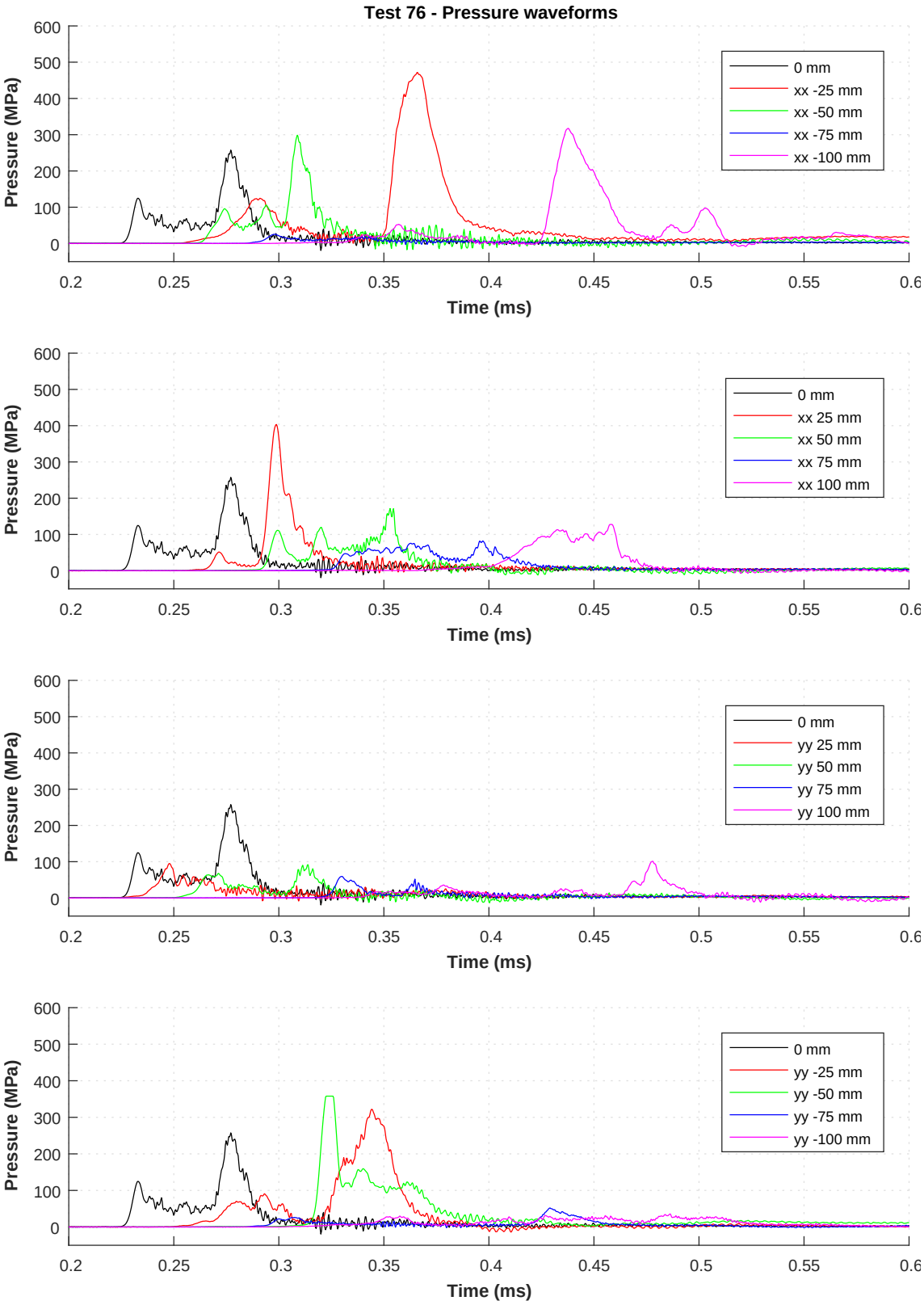

Figure C.32: Pressure-time waveform of Test 76.

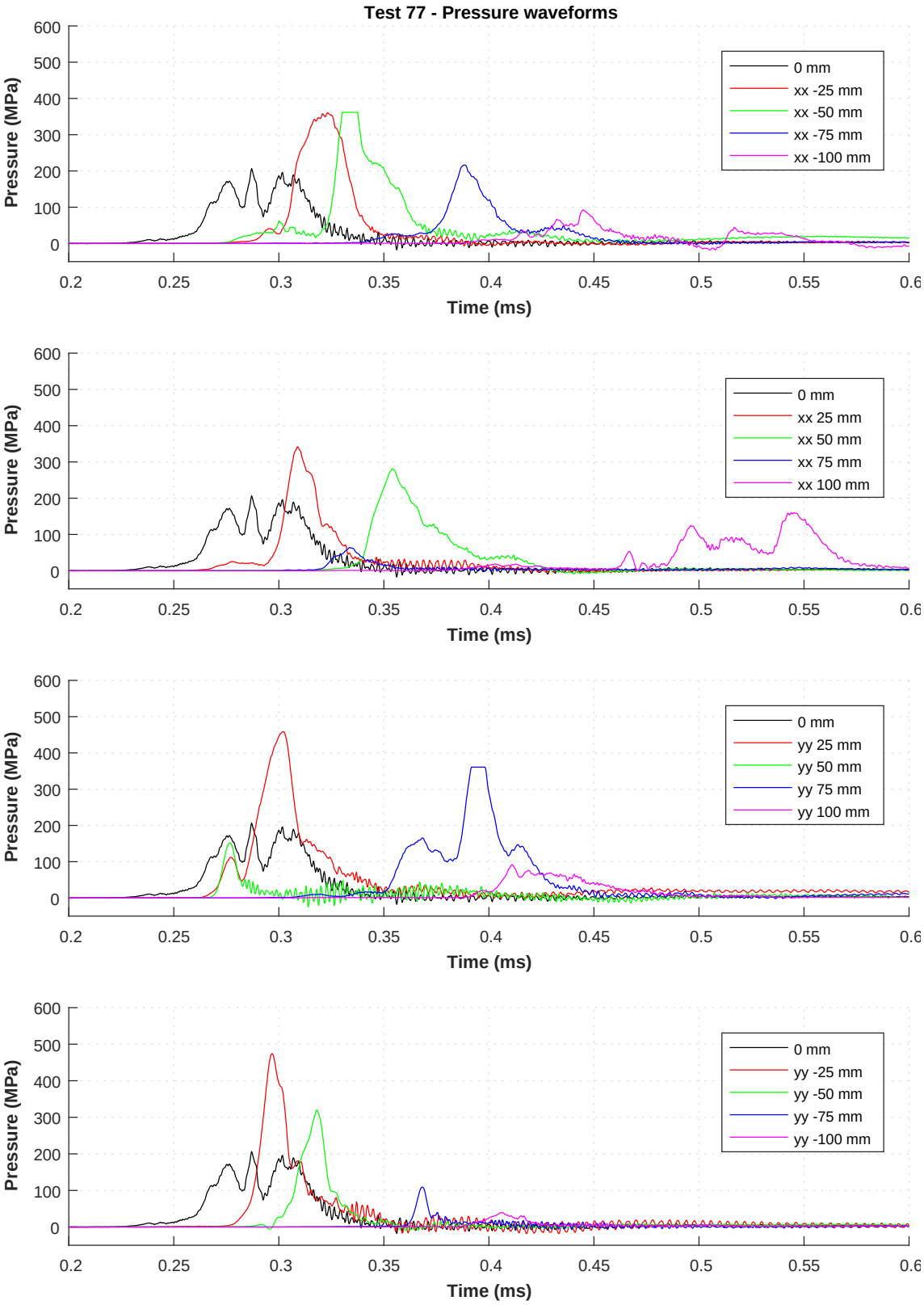

Figure C.33: Pressure-time waveform of Test 77.

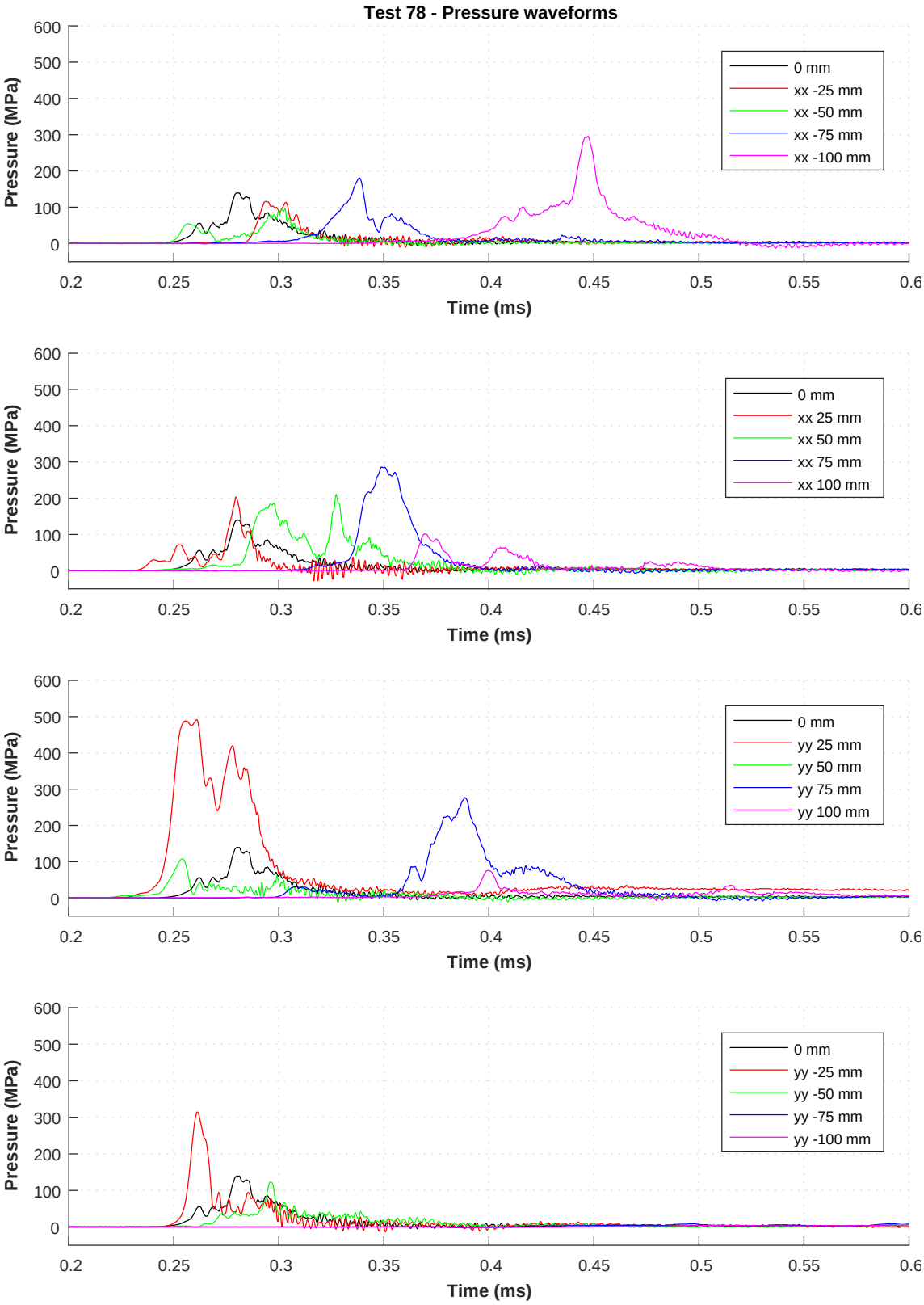

Figure C.34: Pressure-time waveform of Test 78.

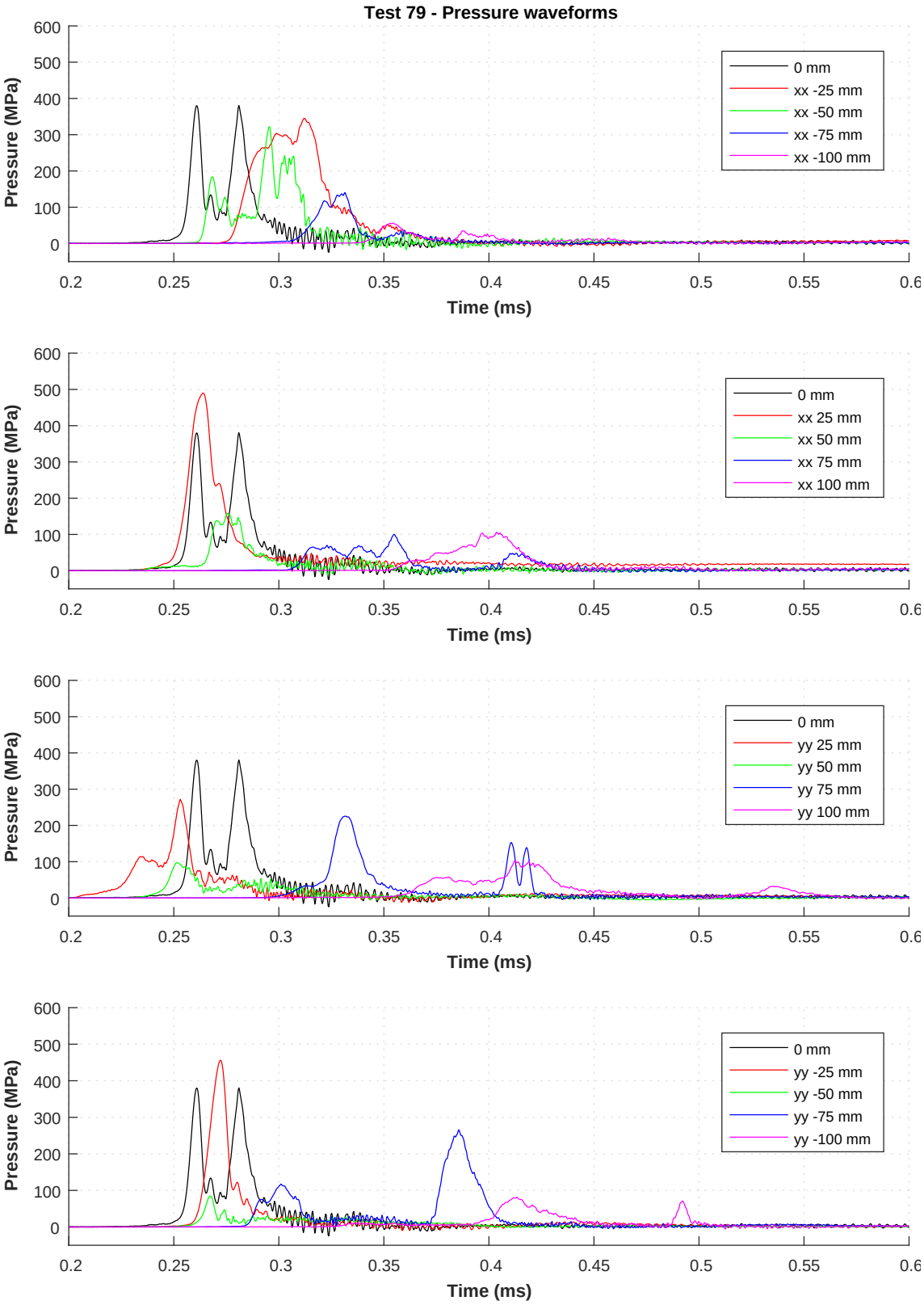

Figure C.35: Pressure-time waveform of Test 79.

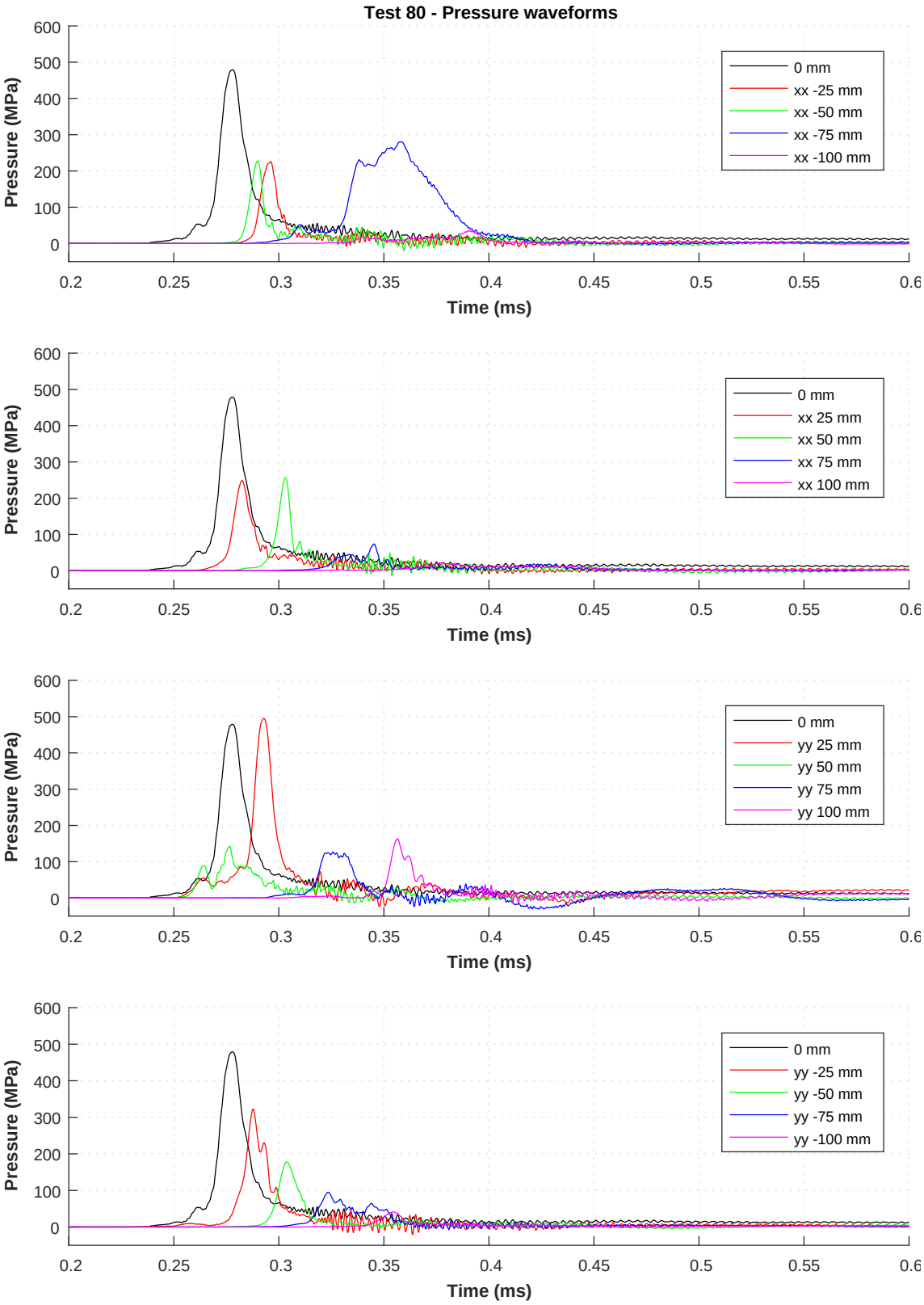

Figure C.36: Pressure-time waveform of Test 80.

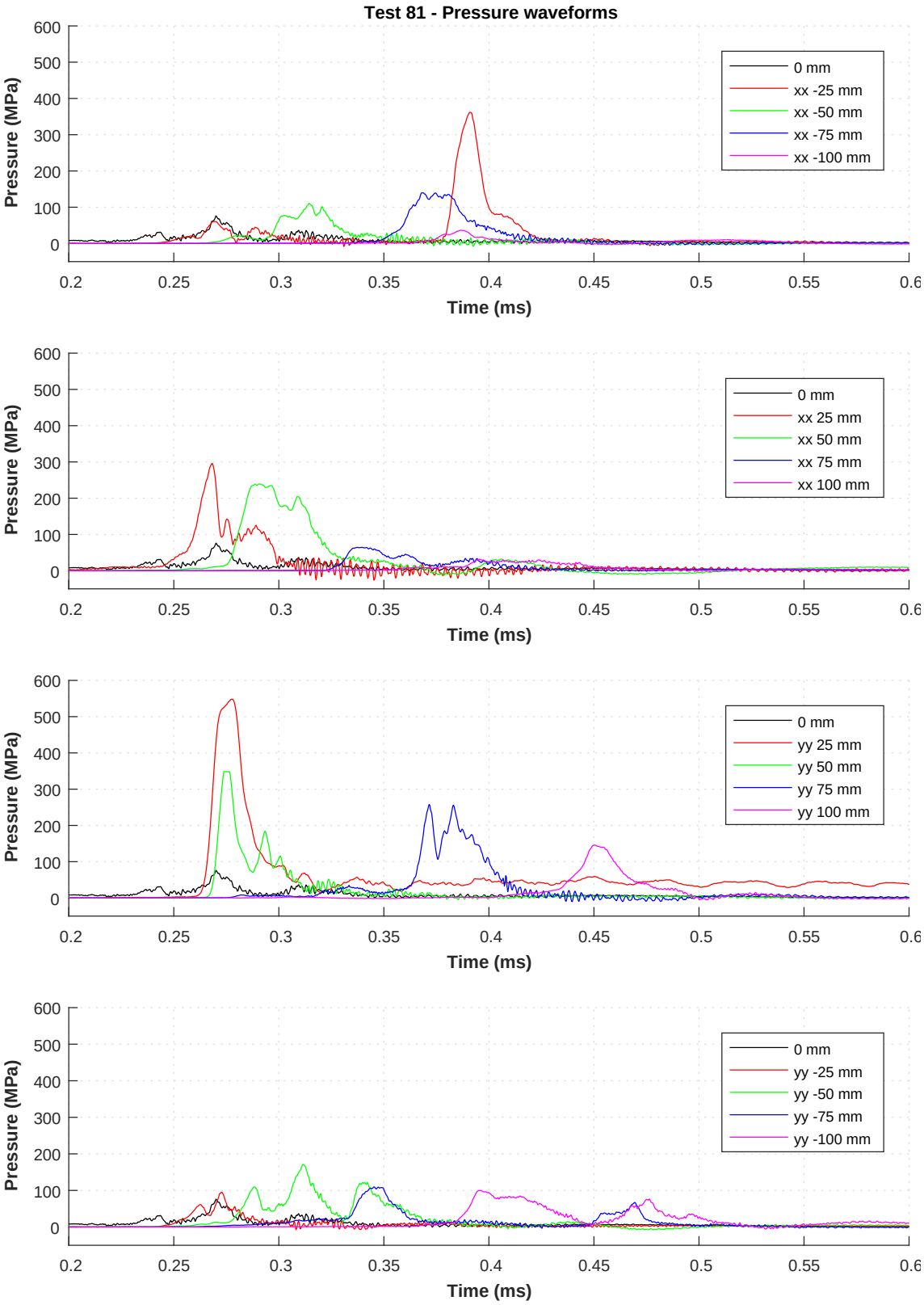

Figure C.37: Pressure-time waveform of Test 81.

C.0.11 Series J – Pressure-time waveforms for Tests 82–86

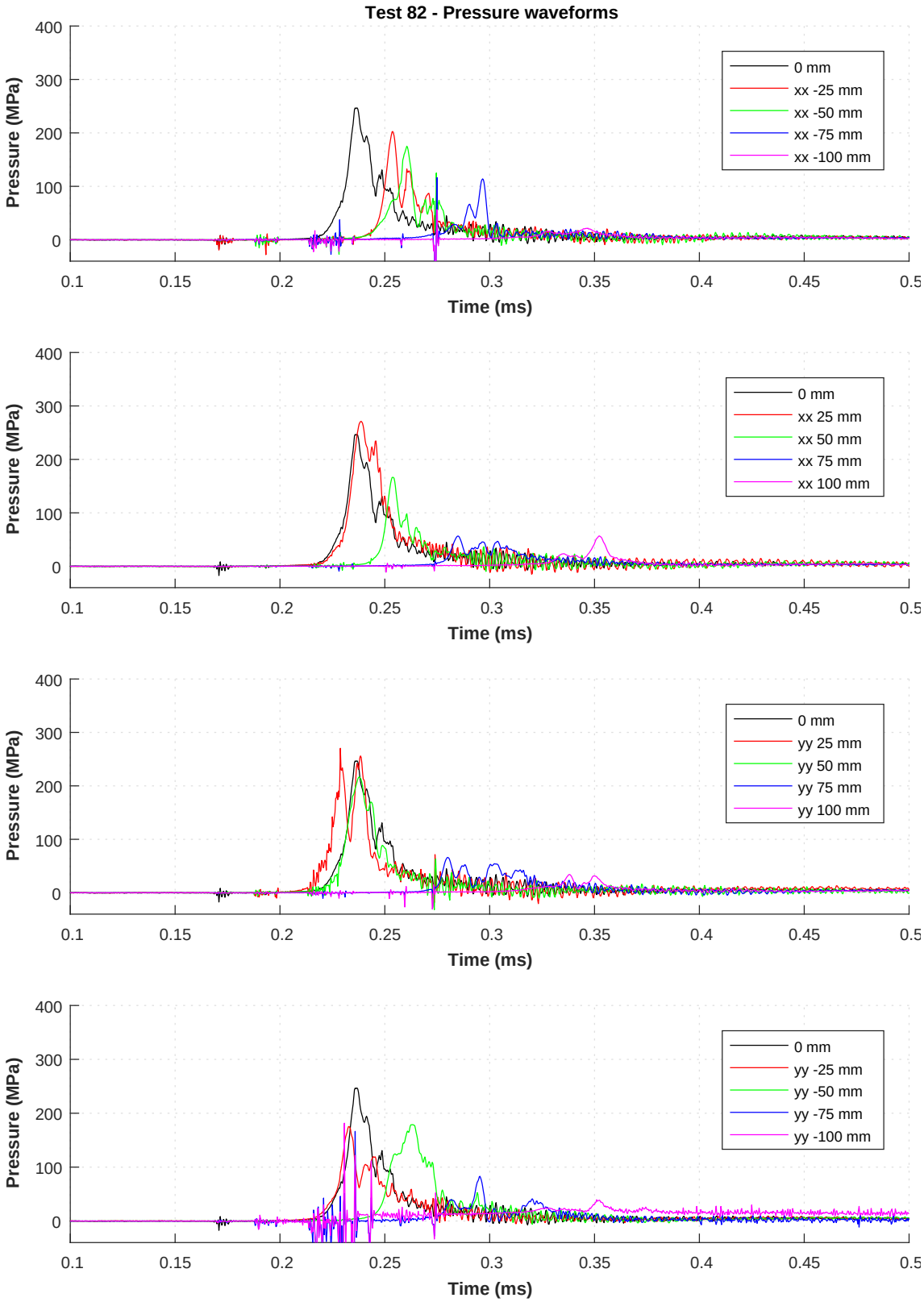

Figure C.38: Pressure-time waveform of Test 82.

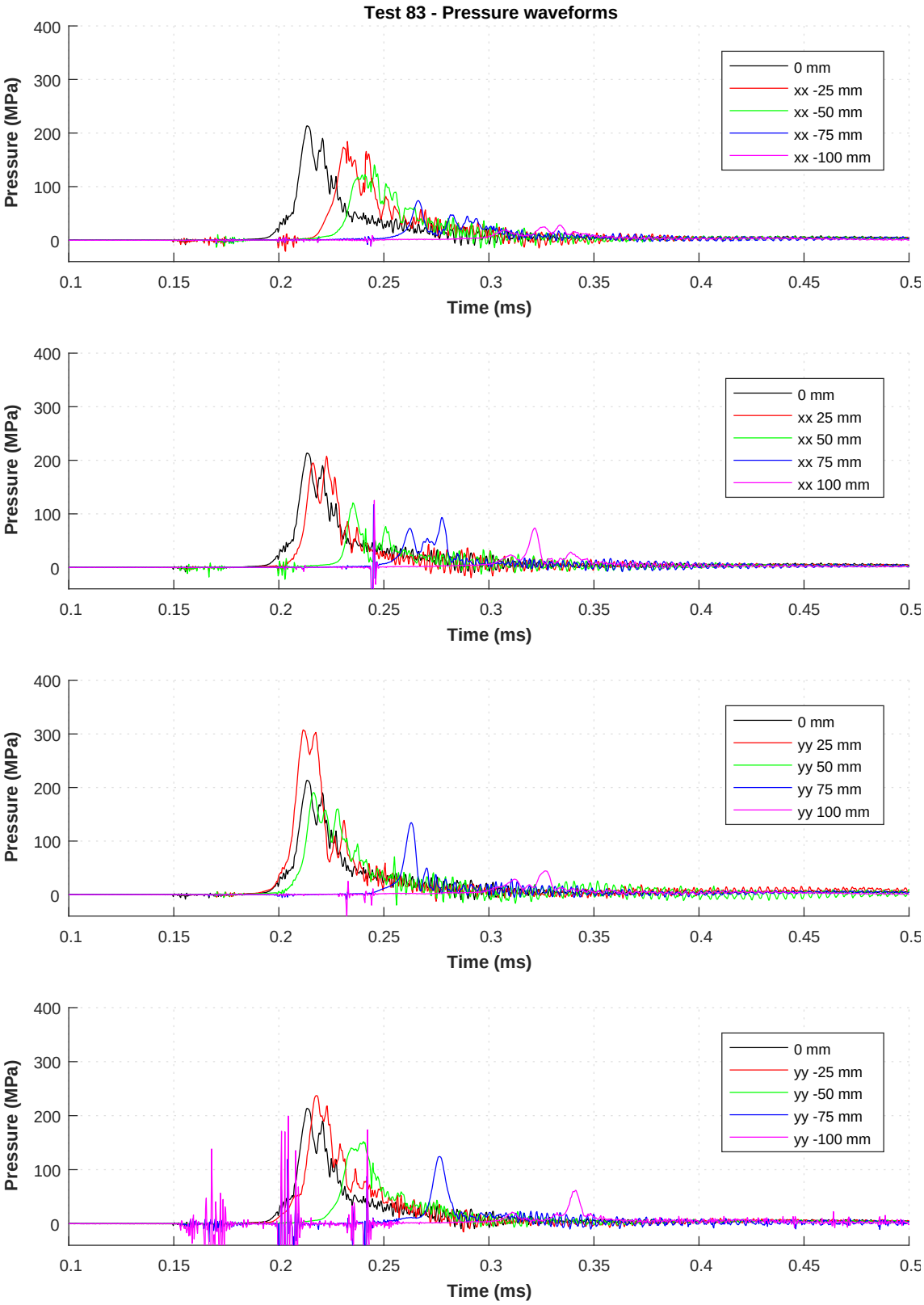

Figure C.39: Pressure-time waveform of Test 83.

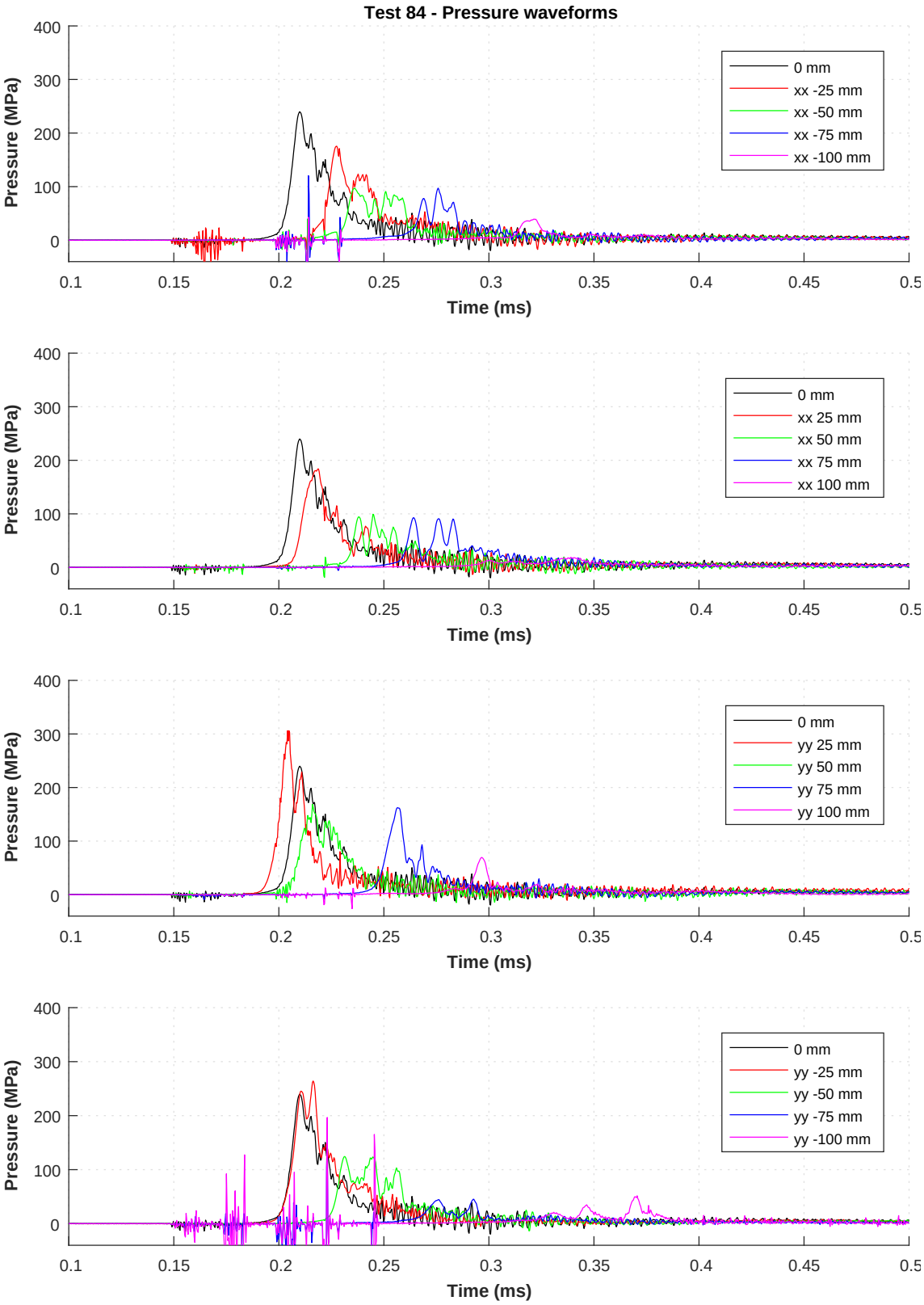

Figure C.40: Pressure-time waveform of Test 84.

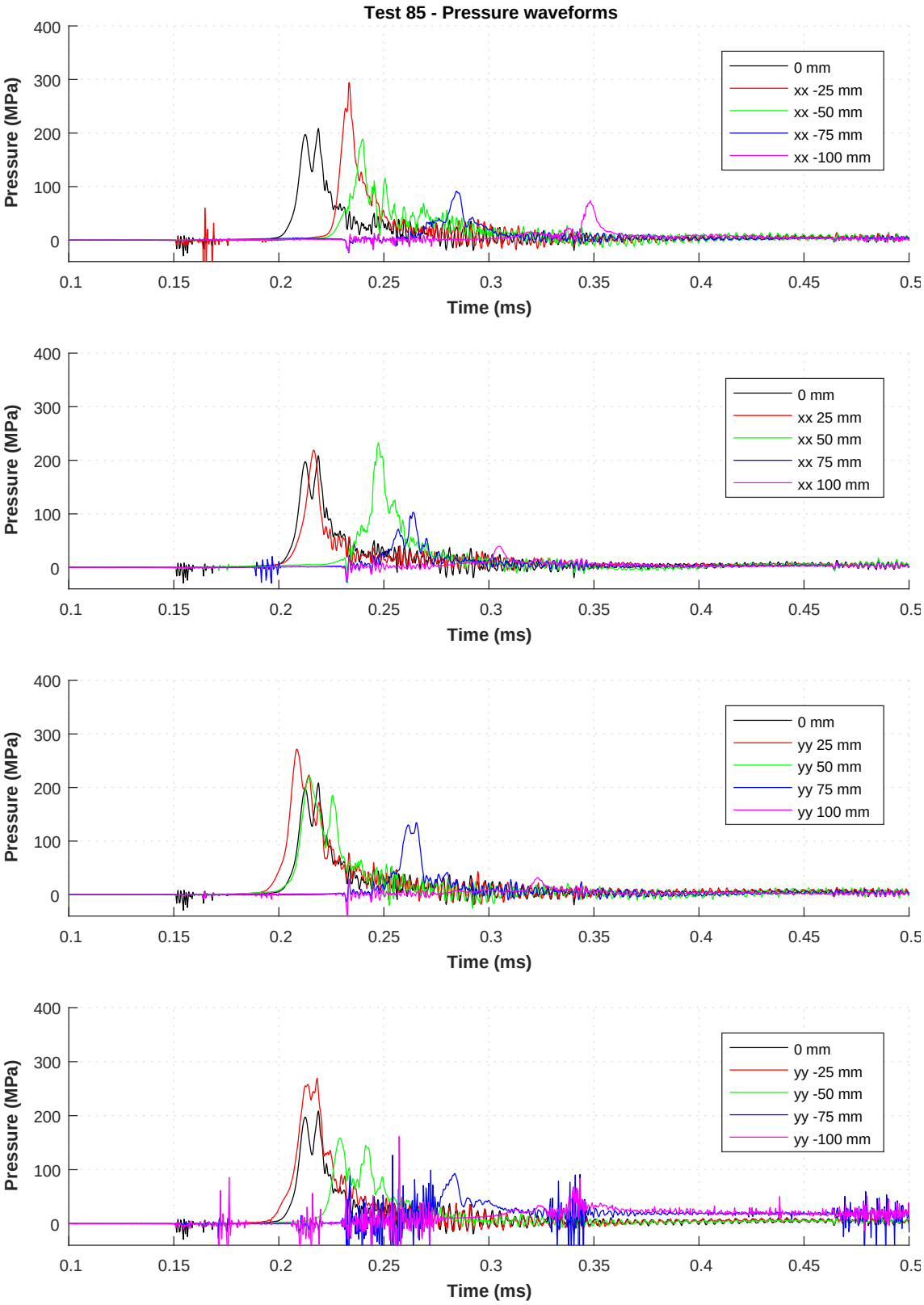

Figure C.41: Pressure-time waveform of Test 85.

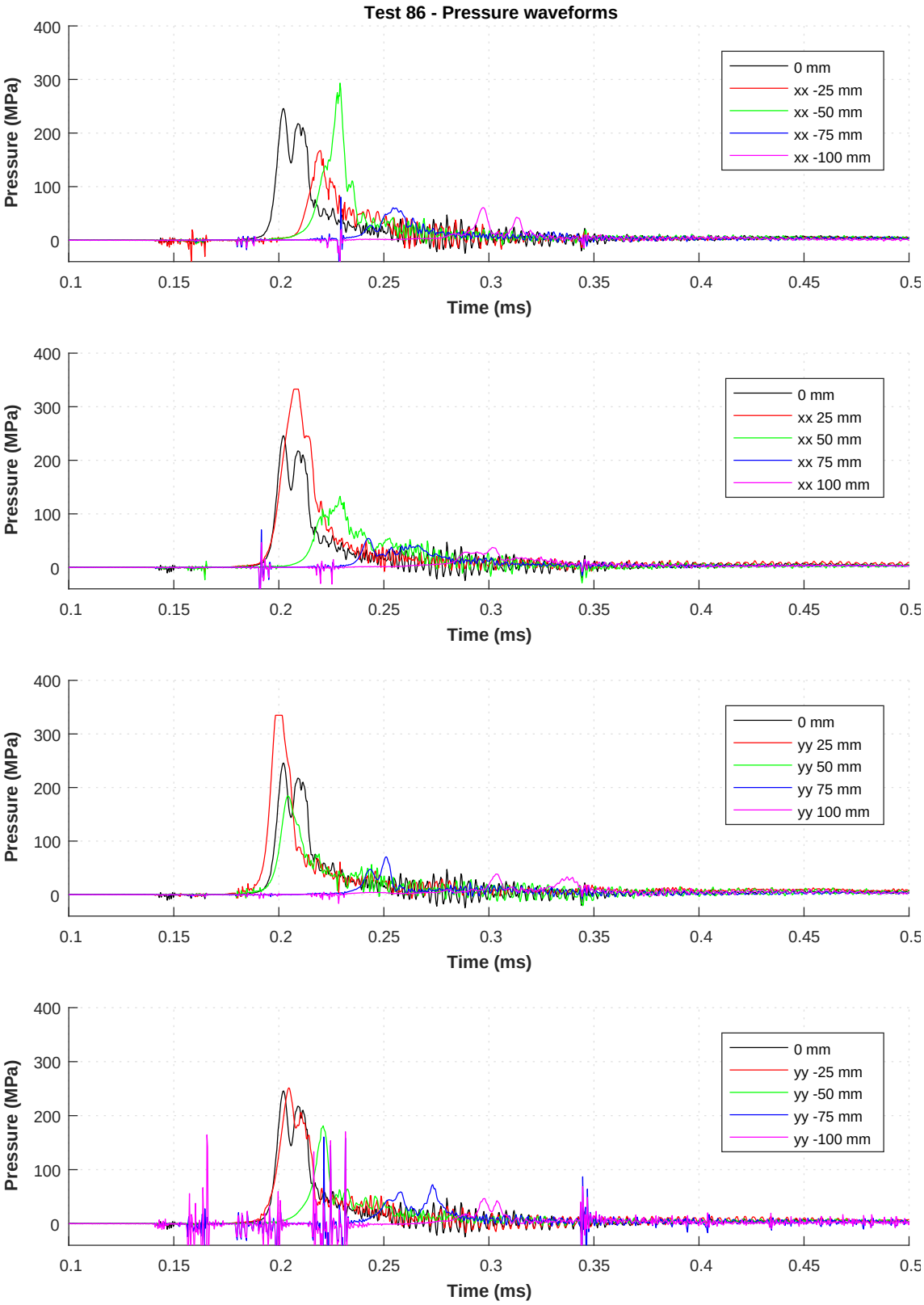

Figure C.42: Pressure-time waveform of Test 86.

C.0.12 Series K – Pressure-time waveforms for Tests 87–91

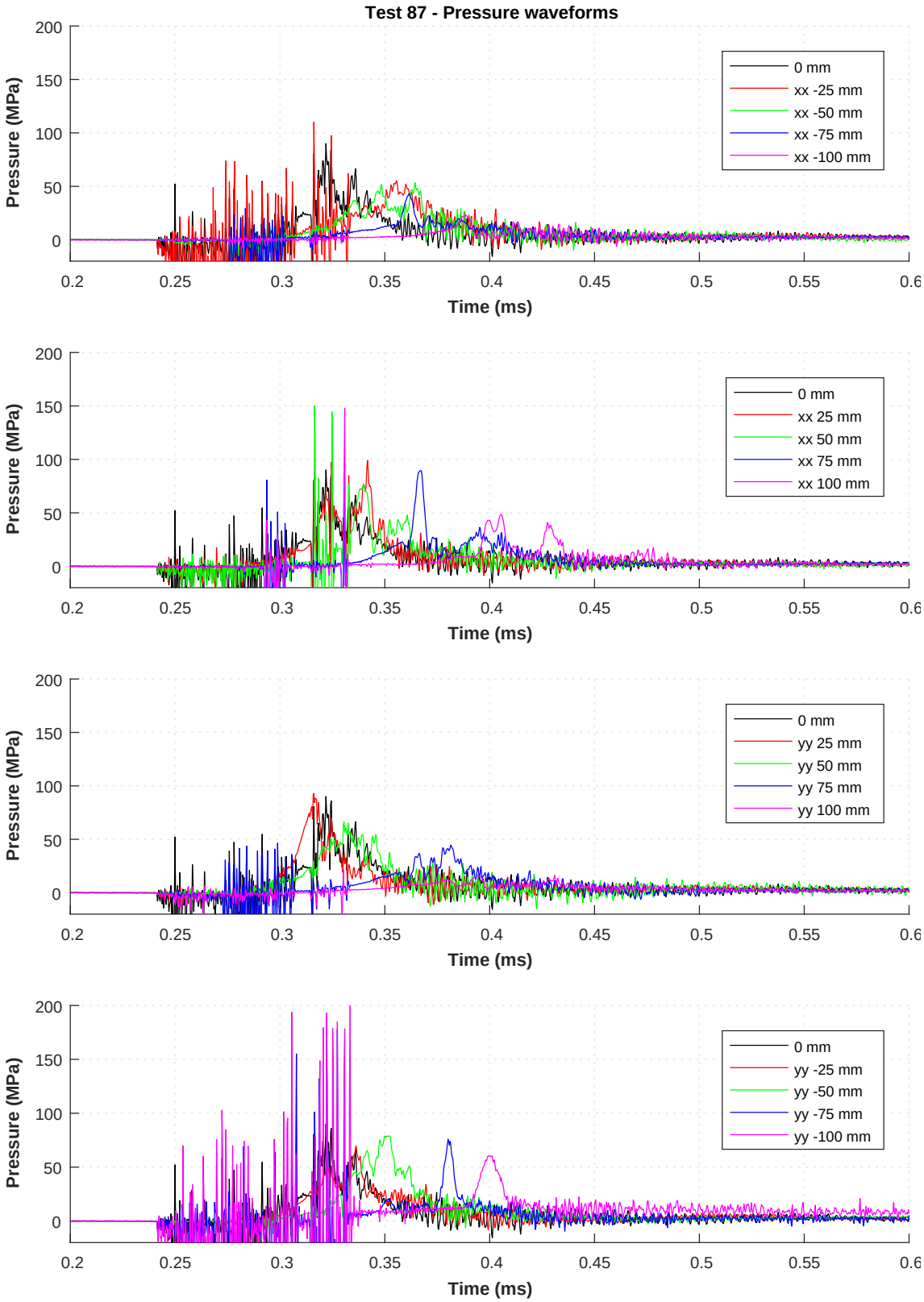

Figure C.43: Pressure-time waveform of Test 87.

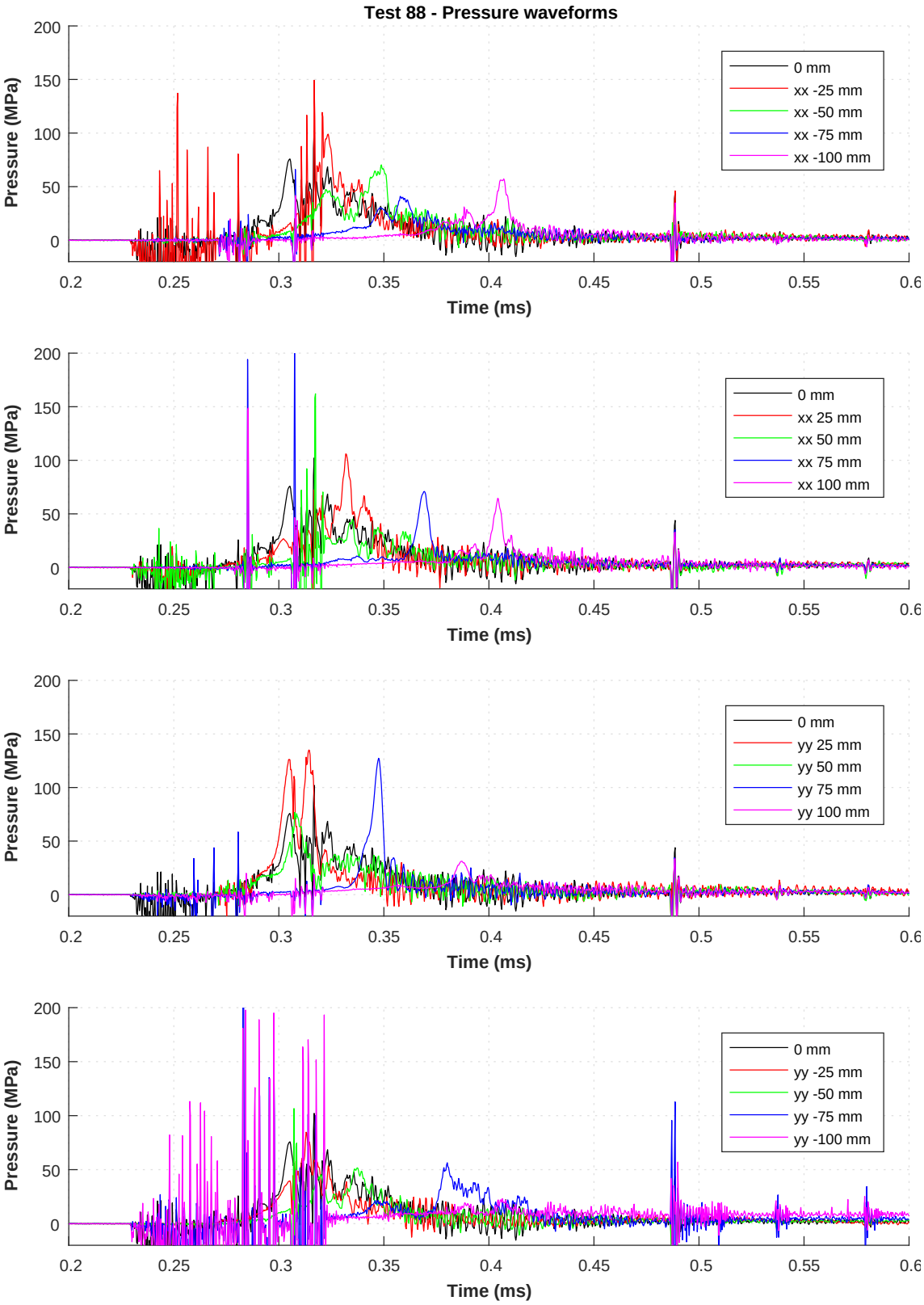

Figure C.44: Pressure-time waveform of Test 88.

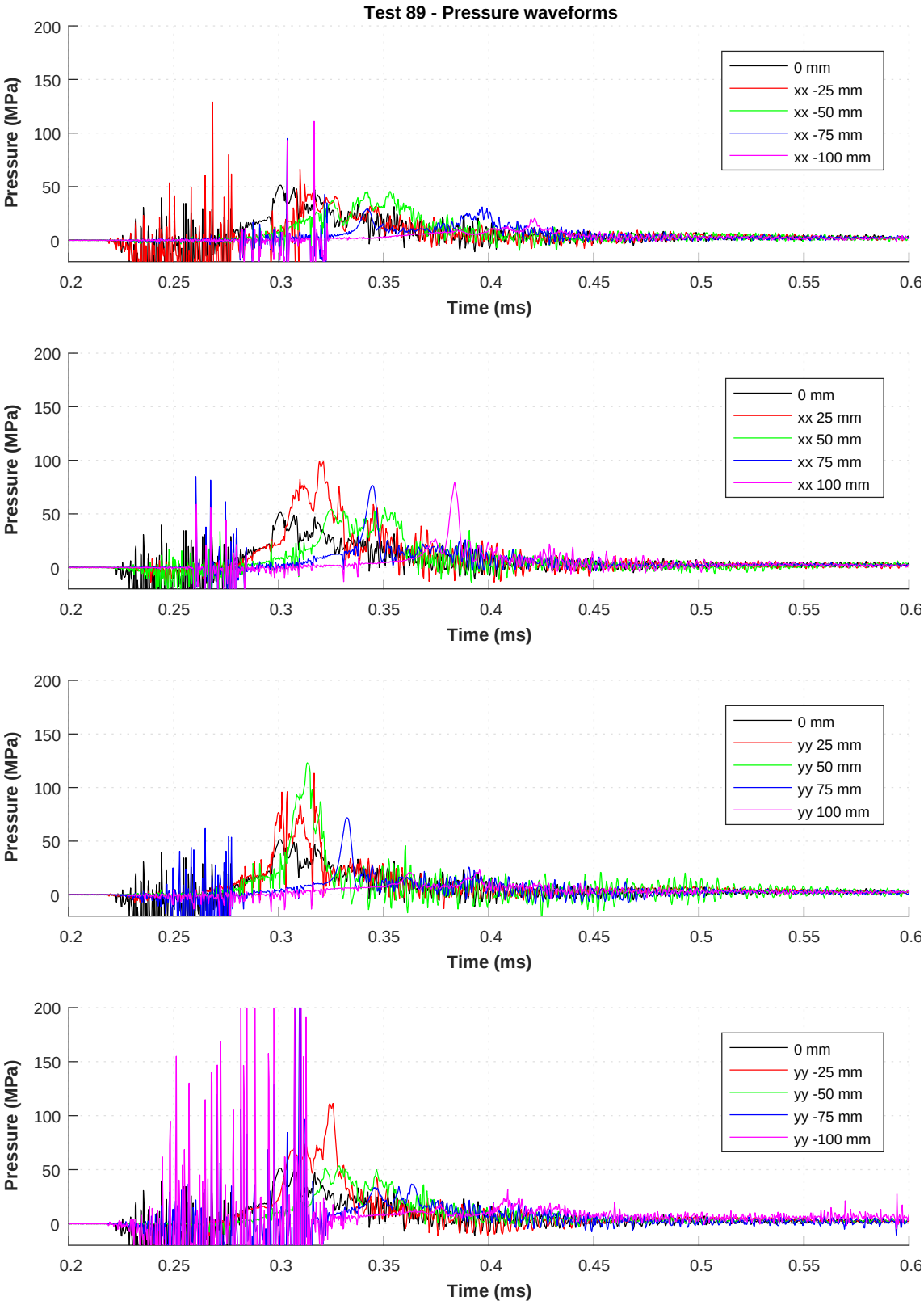

Figure C.45: Pressure-time waveform of Test 89.

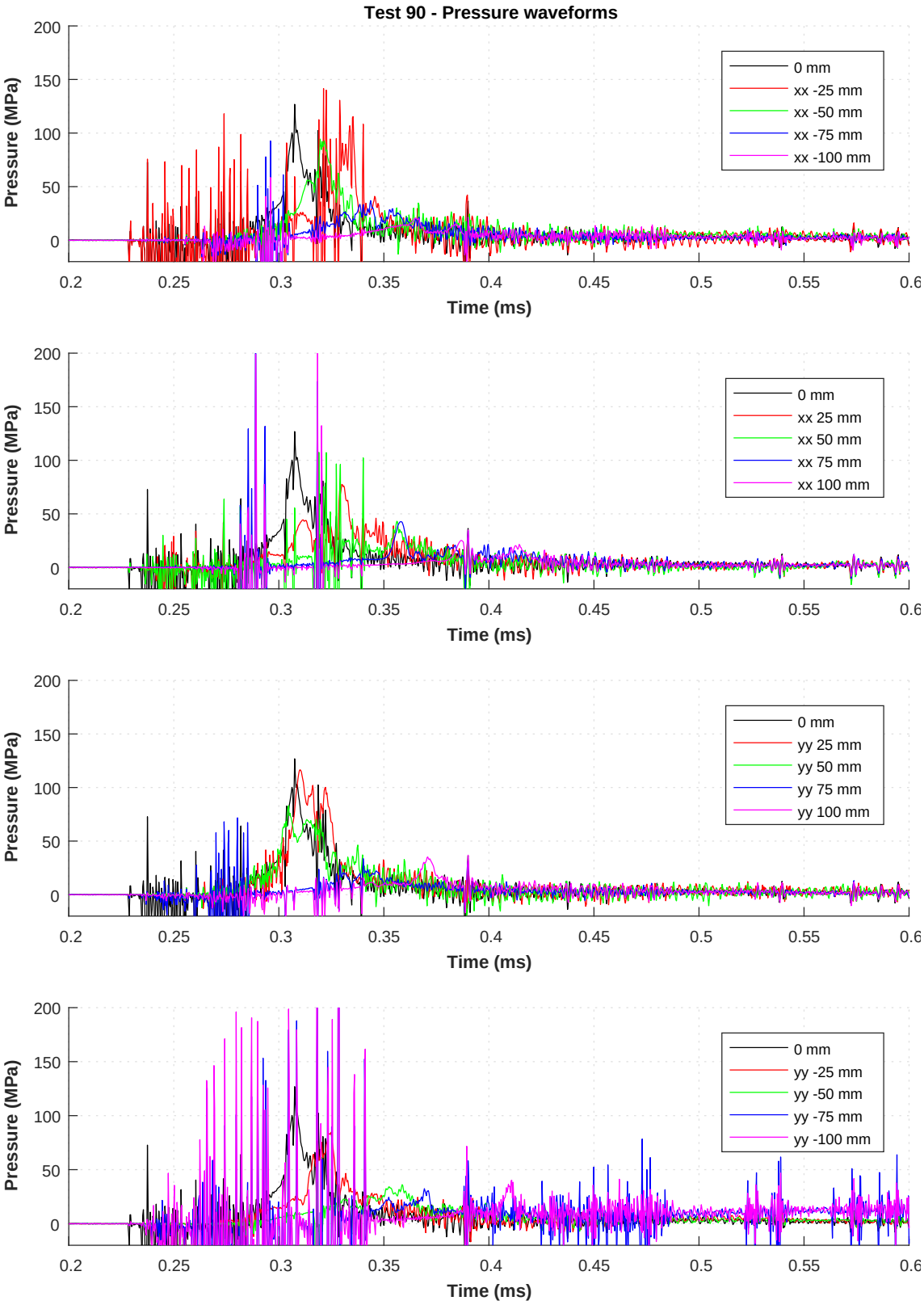

Figure C.46: Pressure-time waveform of Test 90.

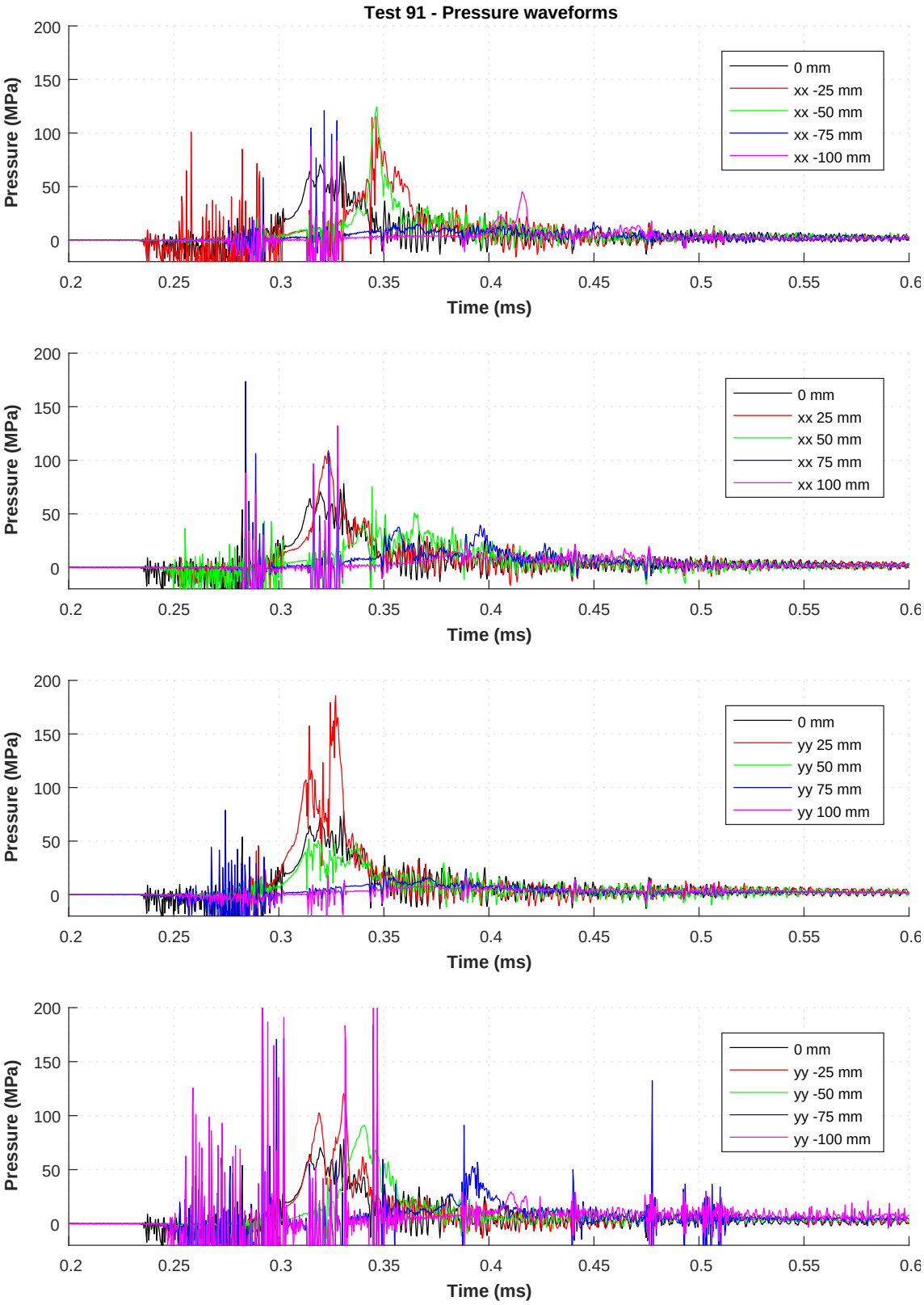

Figure C.47: Pressure-time waveform of Test 91.

C.1 Parameter study data with Butterworth filter

C.1.1 Pressure–time waveforms for Tests 41–44

Note: In Test 41, failure of a single oscilloscope lost data for the -x ray of HPBs.

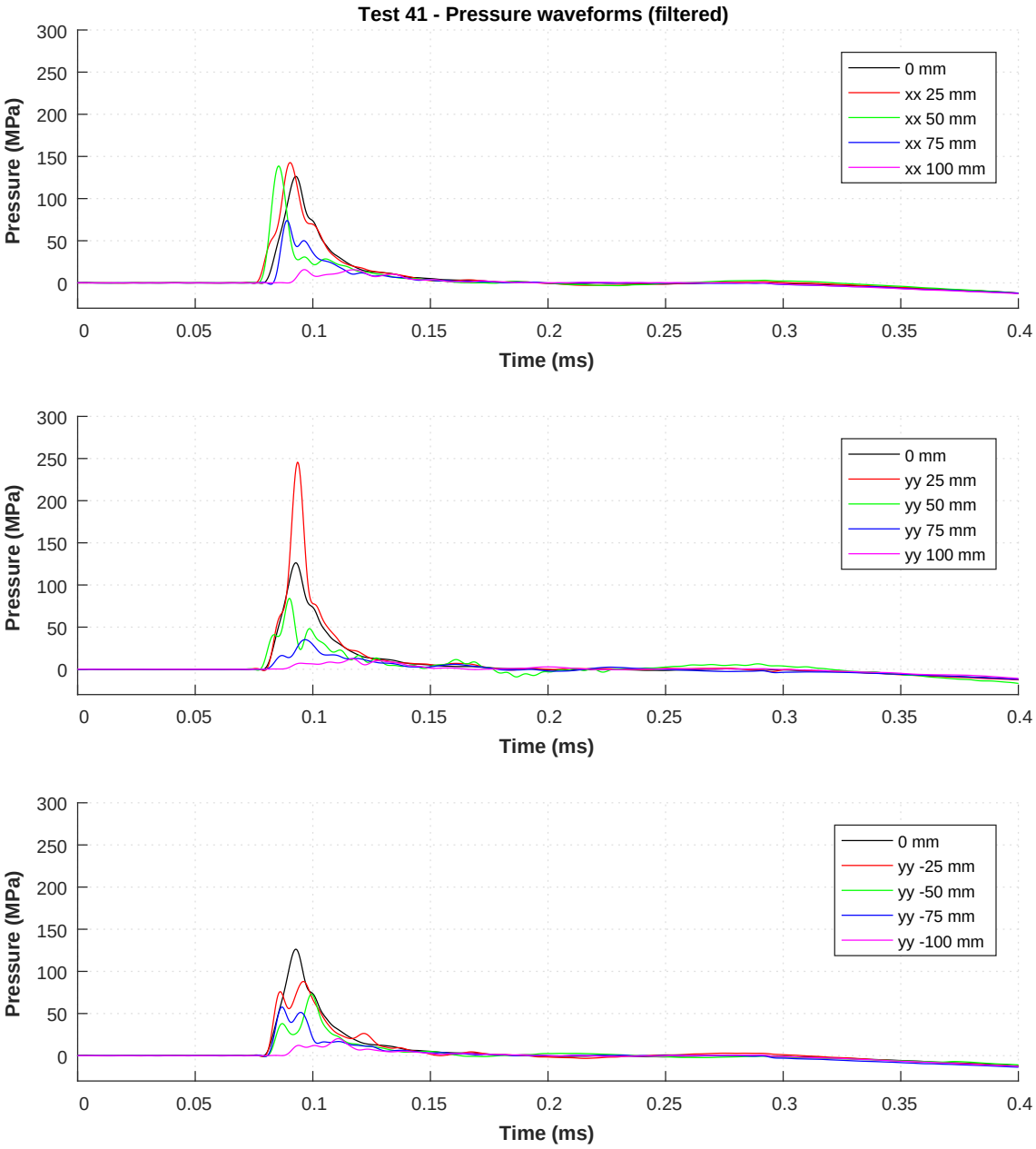

Figure C.48: Pressure-time waveform of Test 41.

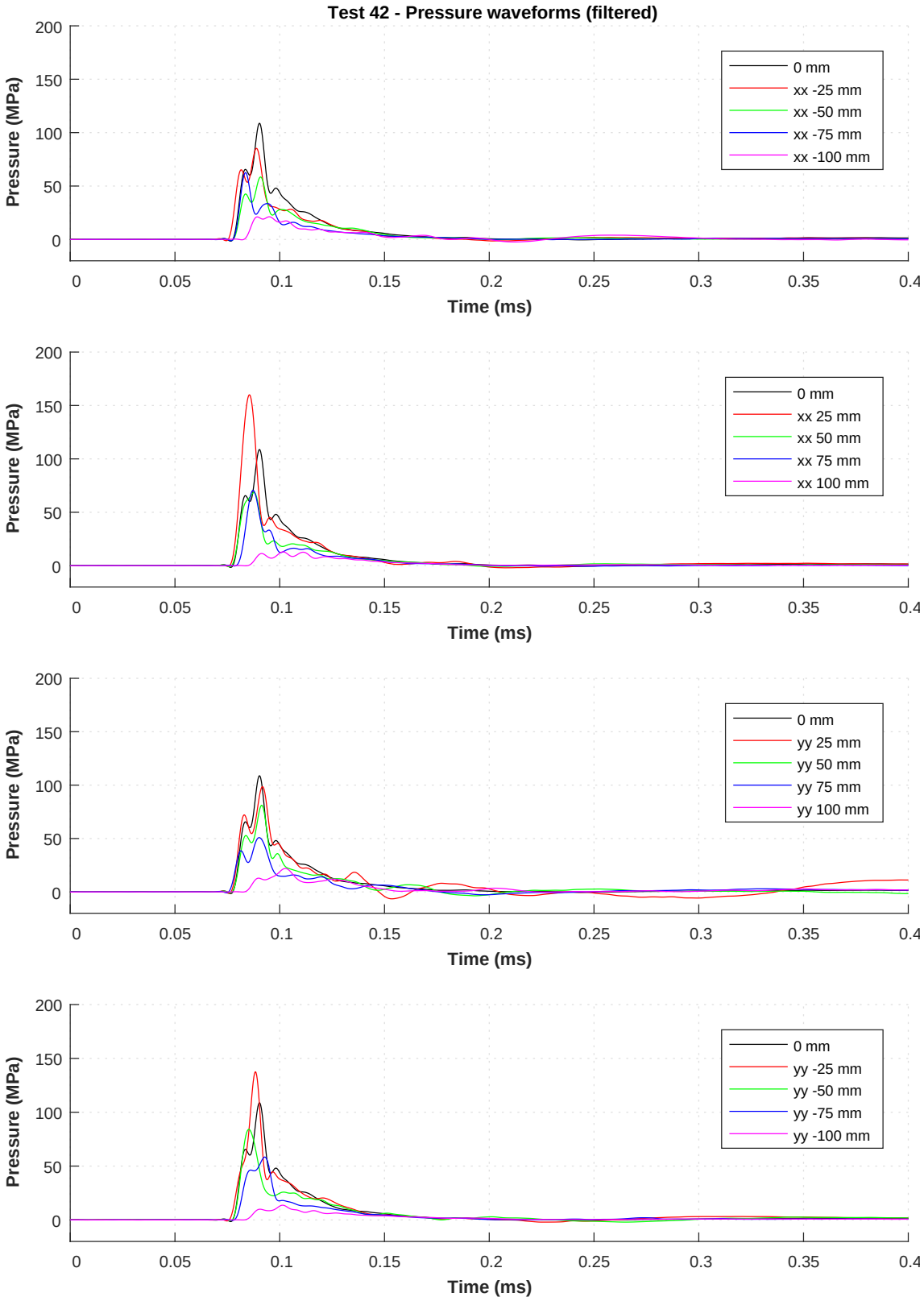

Figure C.49: Pressure-time waveform of Test 42.

Note: In Test 43, failure of a single oscilloscope lost data for the -x ray of HPBs. Following this failure the oscilloscope was replaced.

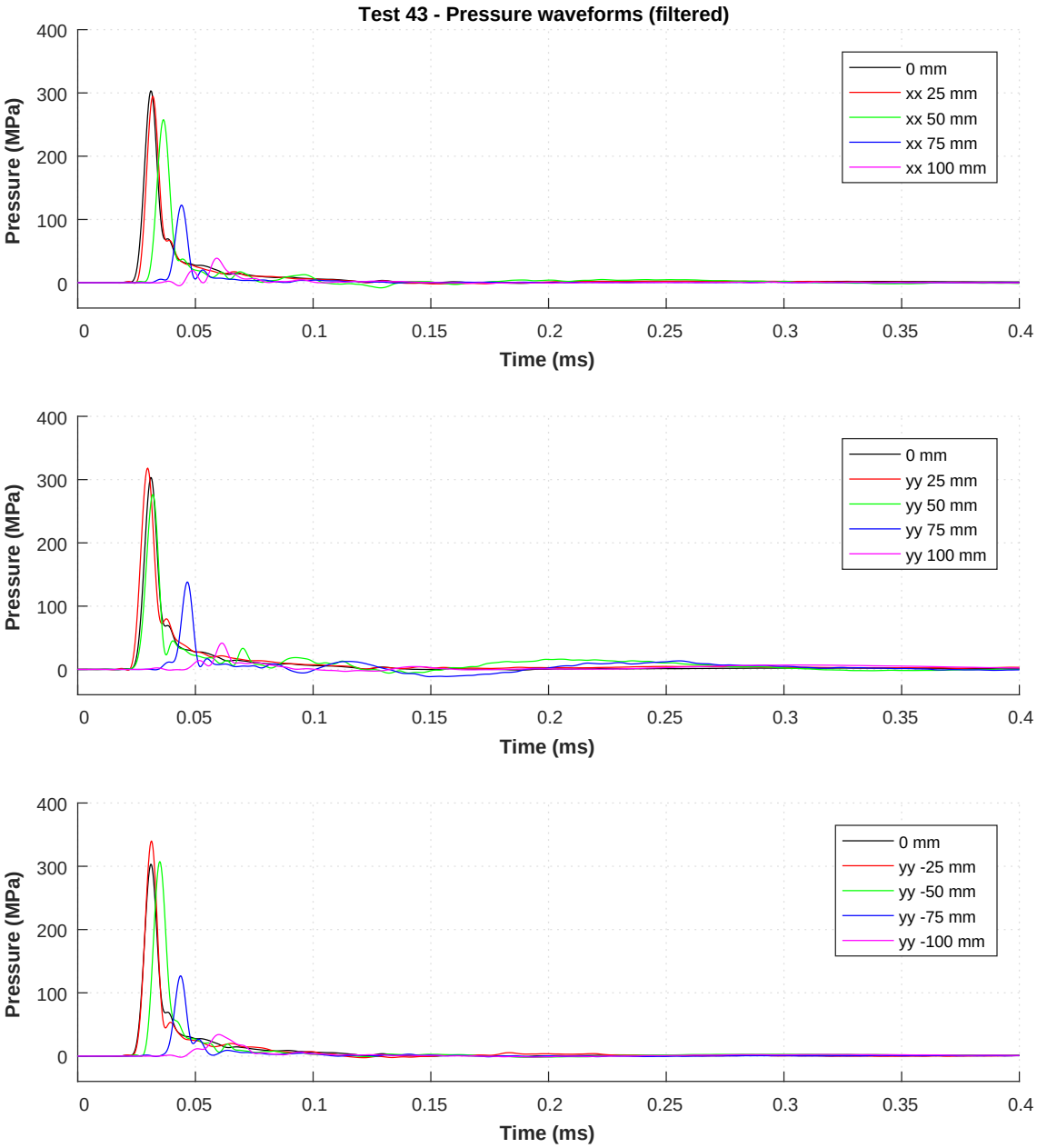

Figure C.50: Pressure-time waveform of Test 43.

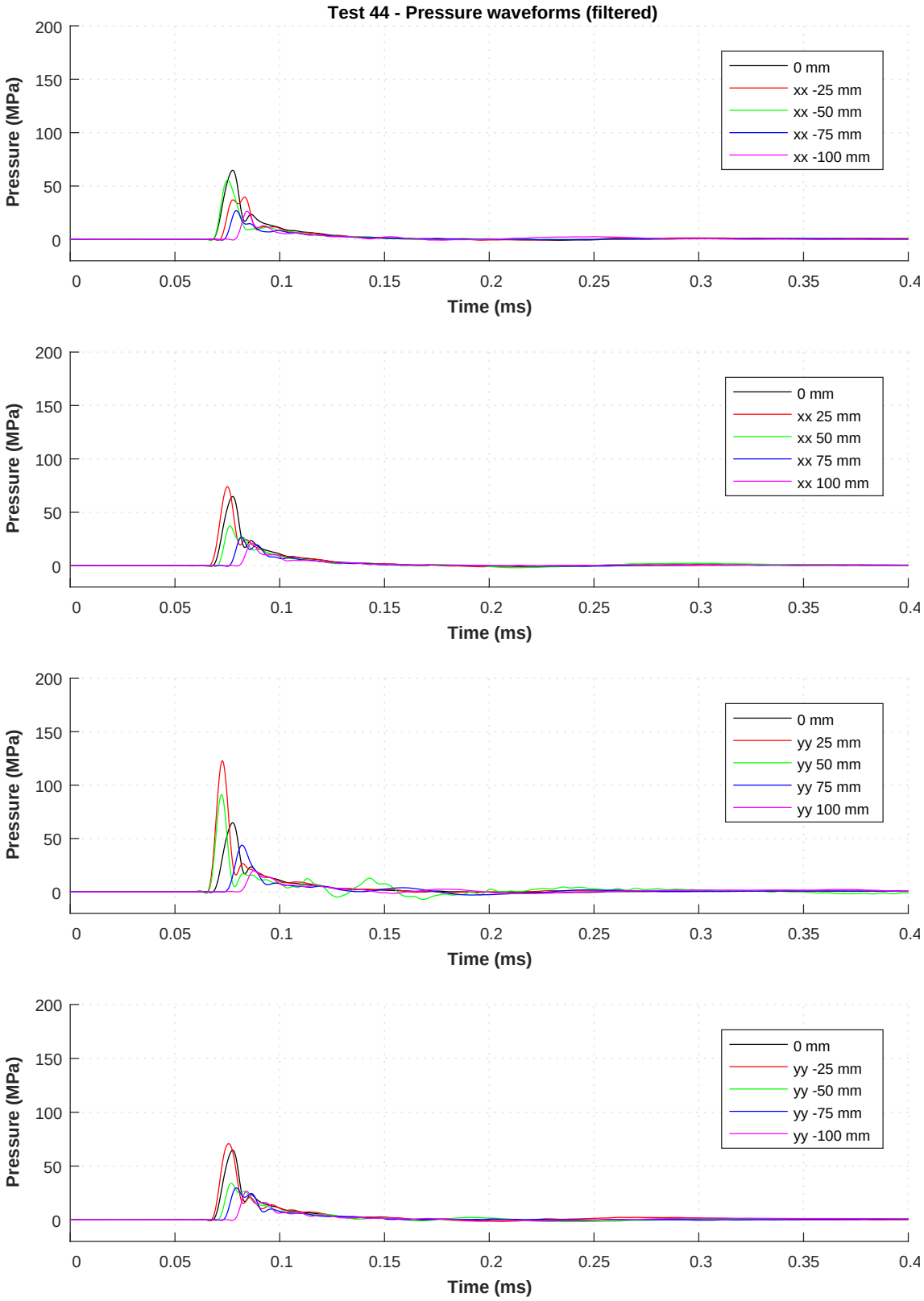

Figure C.51: Pressure-time waveform of Test 44.

C.1.2 Series A – Pressure-time waveforms for Tests 45–46

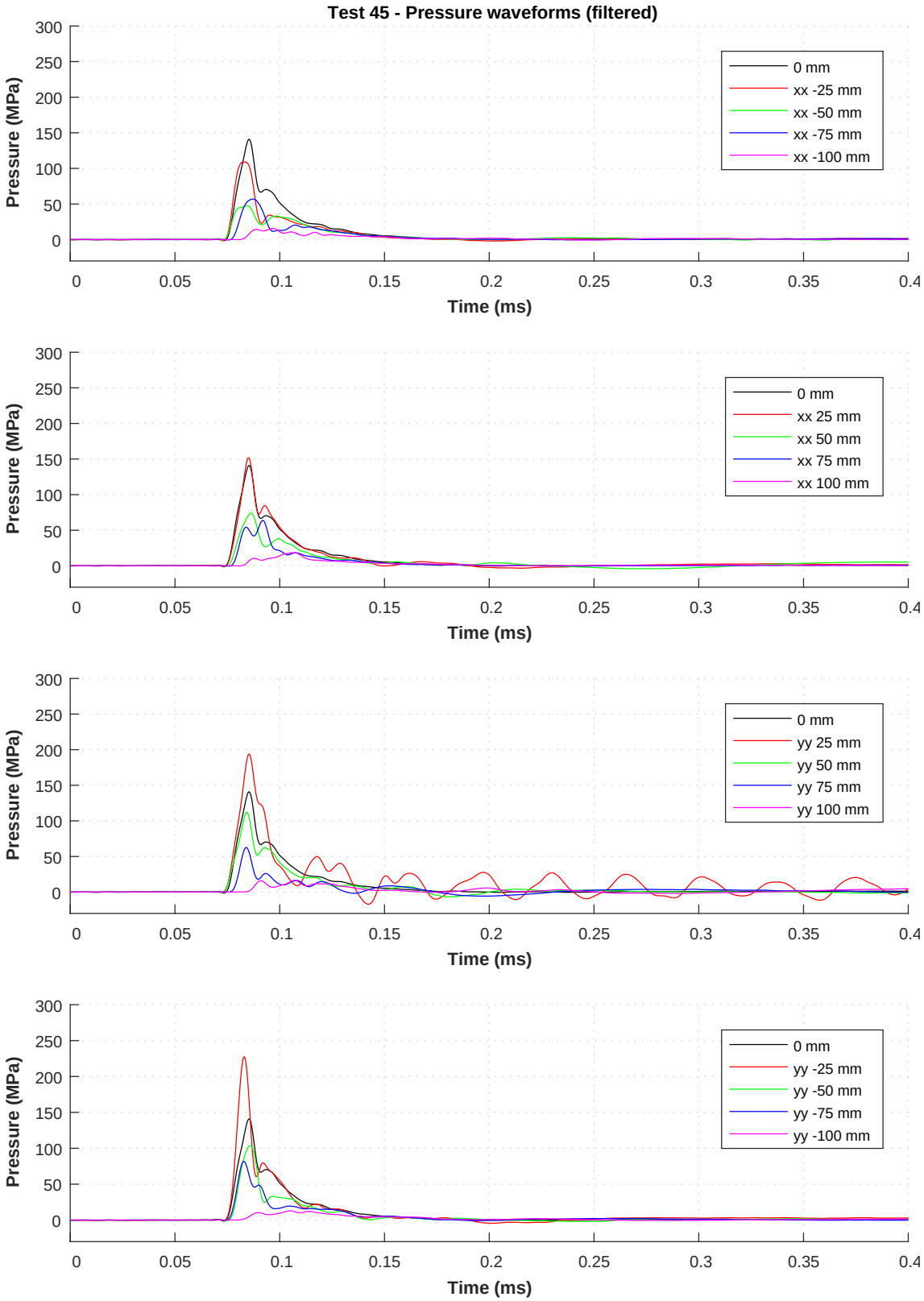

Figure C.52: Pressure-time waveform of Test 45.

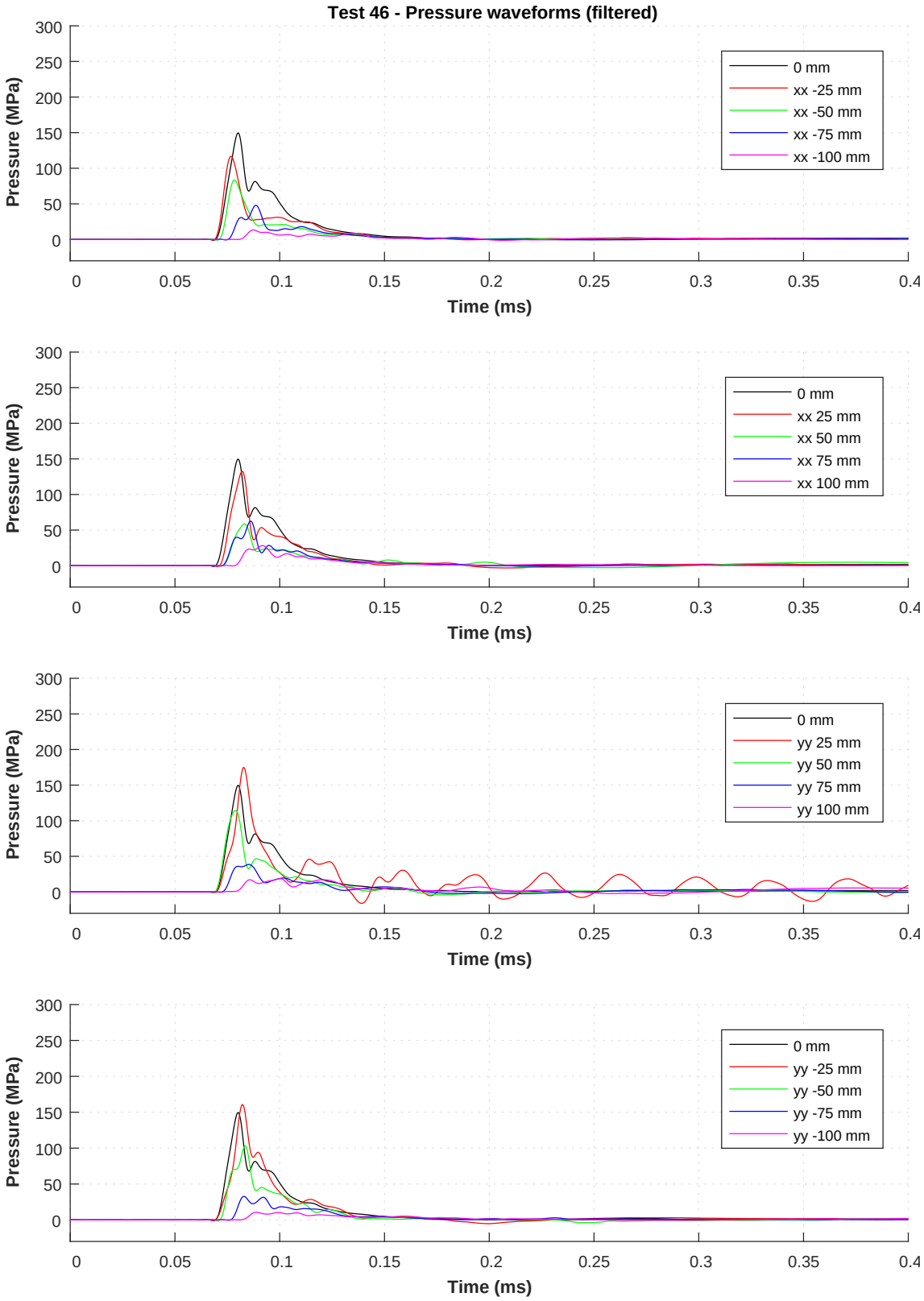

Figure C.53: Pressure-time waveform of Test 46.

C.1.3 Series B – Pressure-time waveforms for Tests 47–48

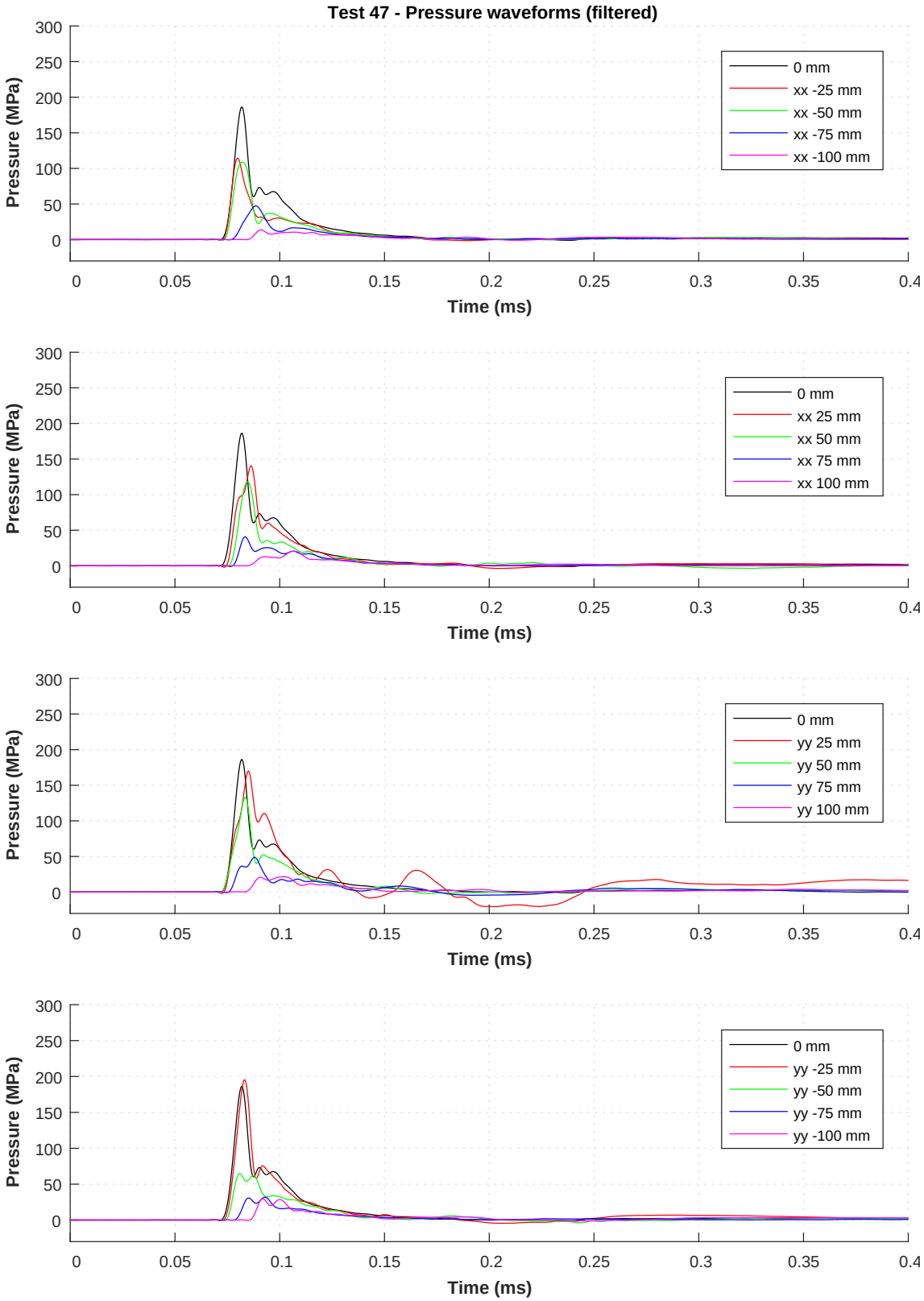

Figure C.54: Pressure-time waveform of Test 47.

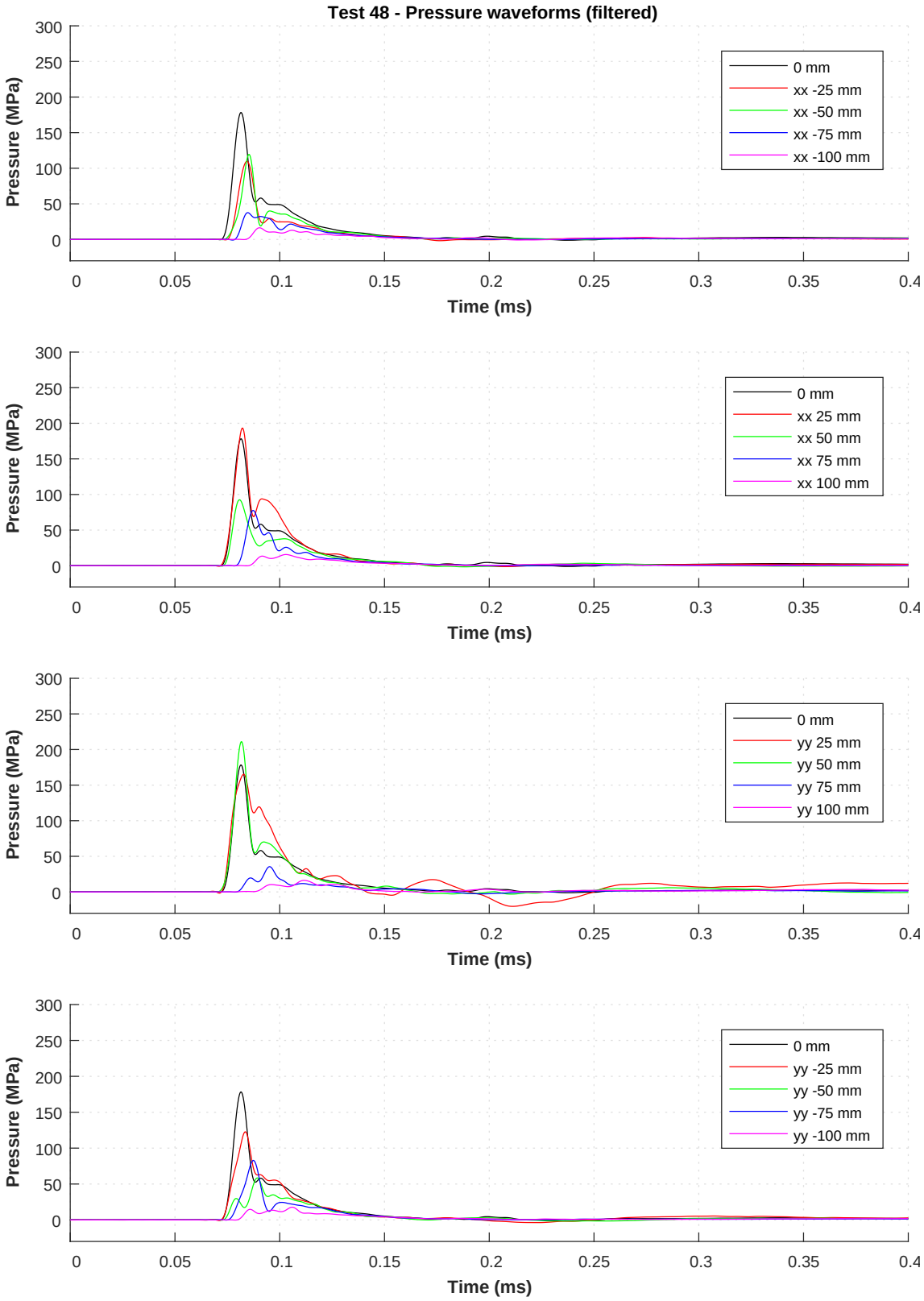

Figure C.55: Pressure-time waveform of Test 48.

C.1.4 Series C – Pressure-time waveforms for Tests 49–50

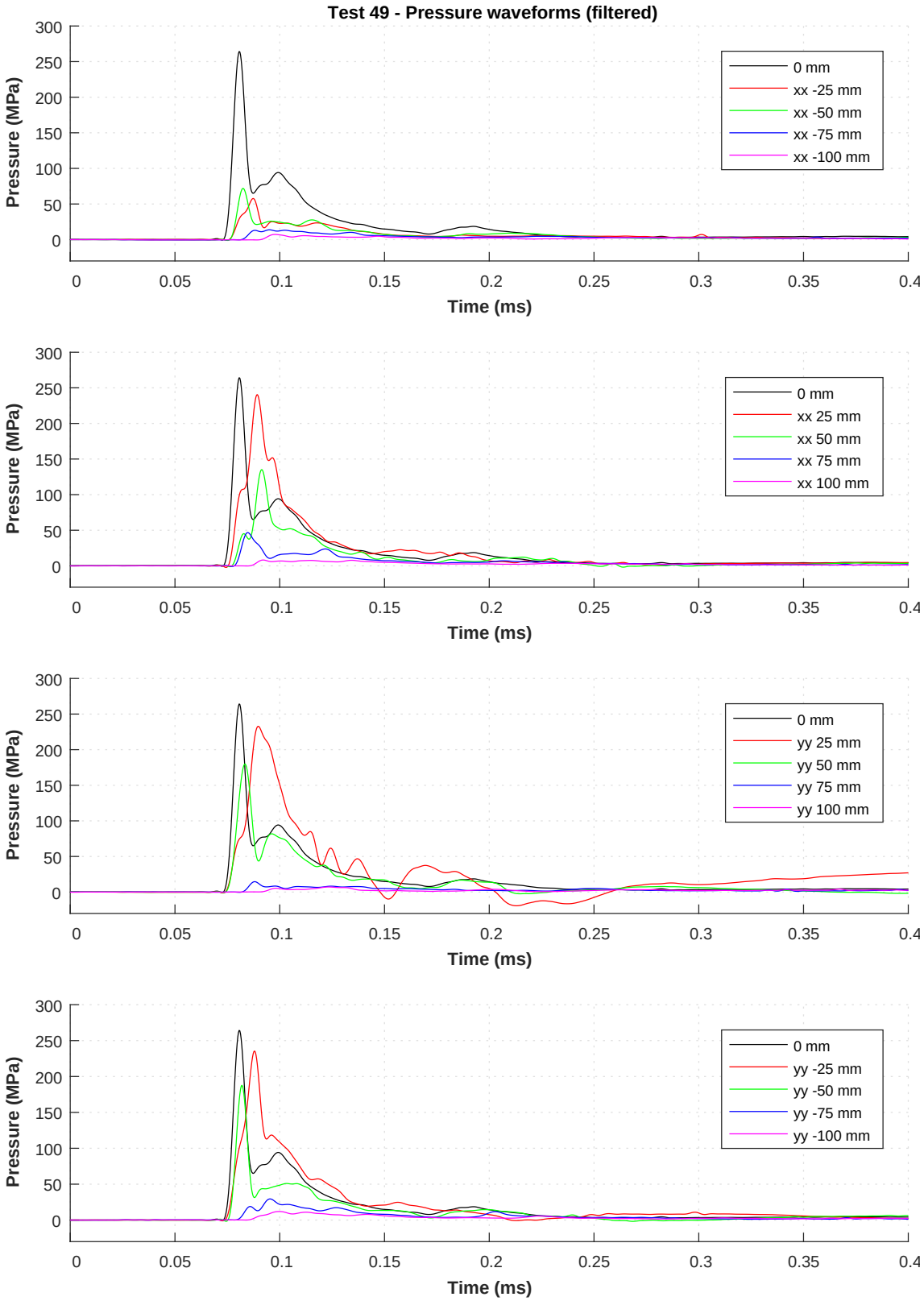

Figure C.56: Pressure-time waveform of Test 49.

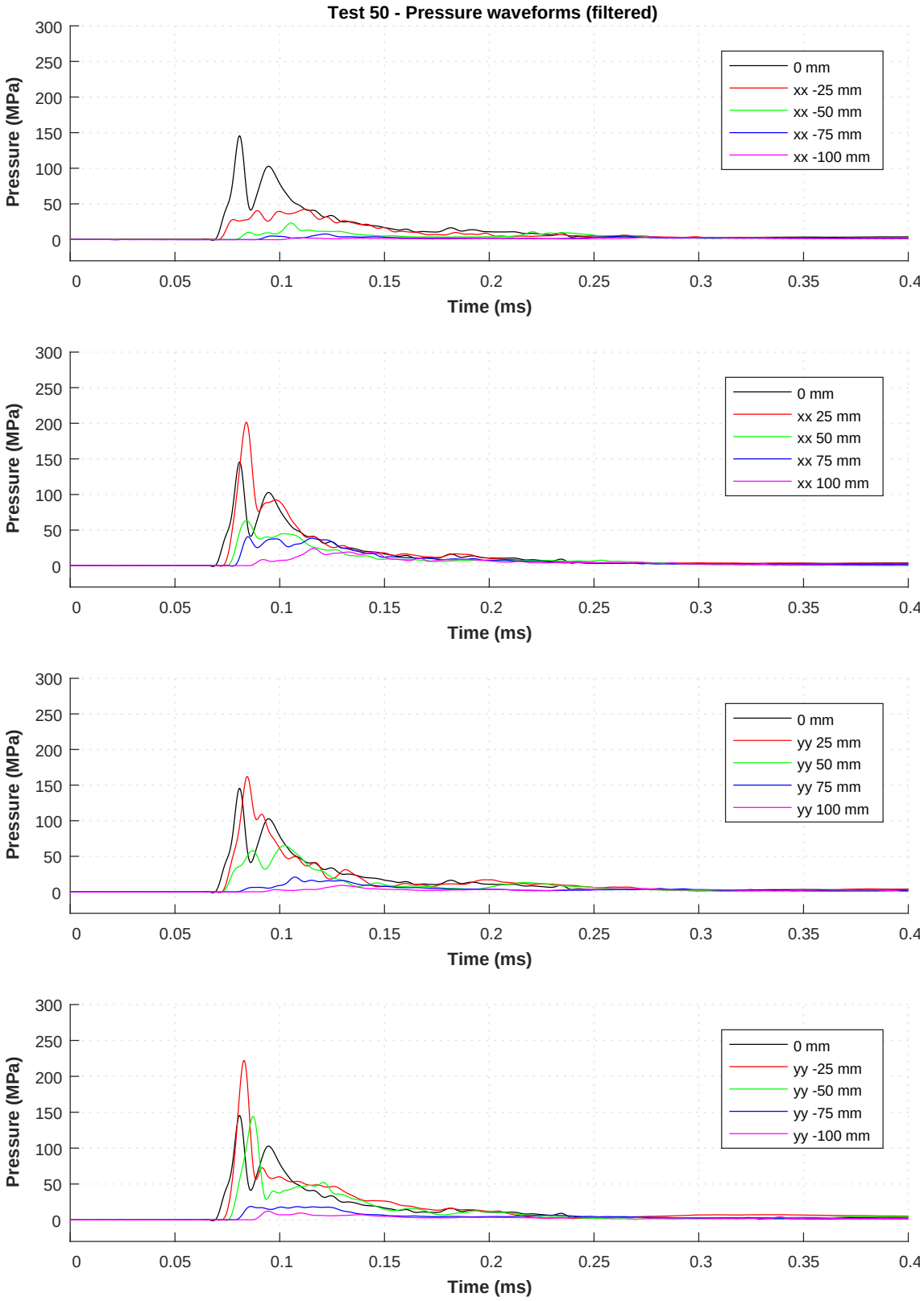

Figure C.57: Pressure-time waveform of Test 50.

C.1.5 Series D – Pressure-time waveforms for Tests 51–57

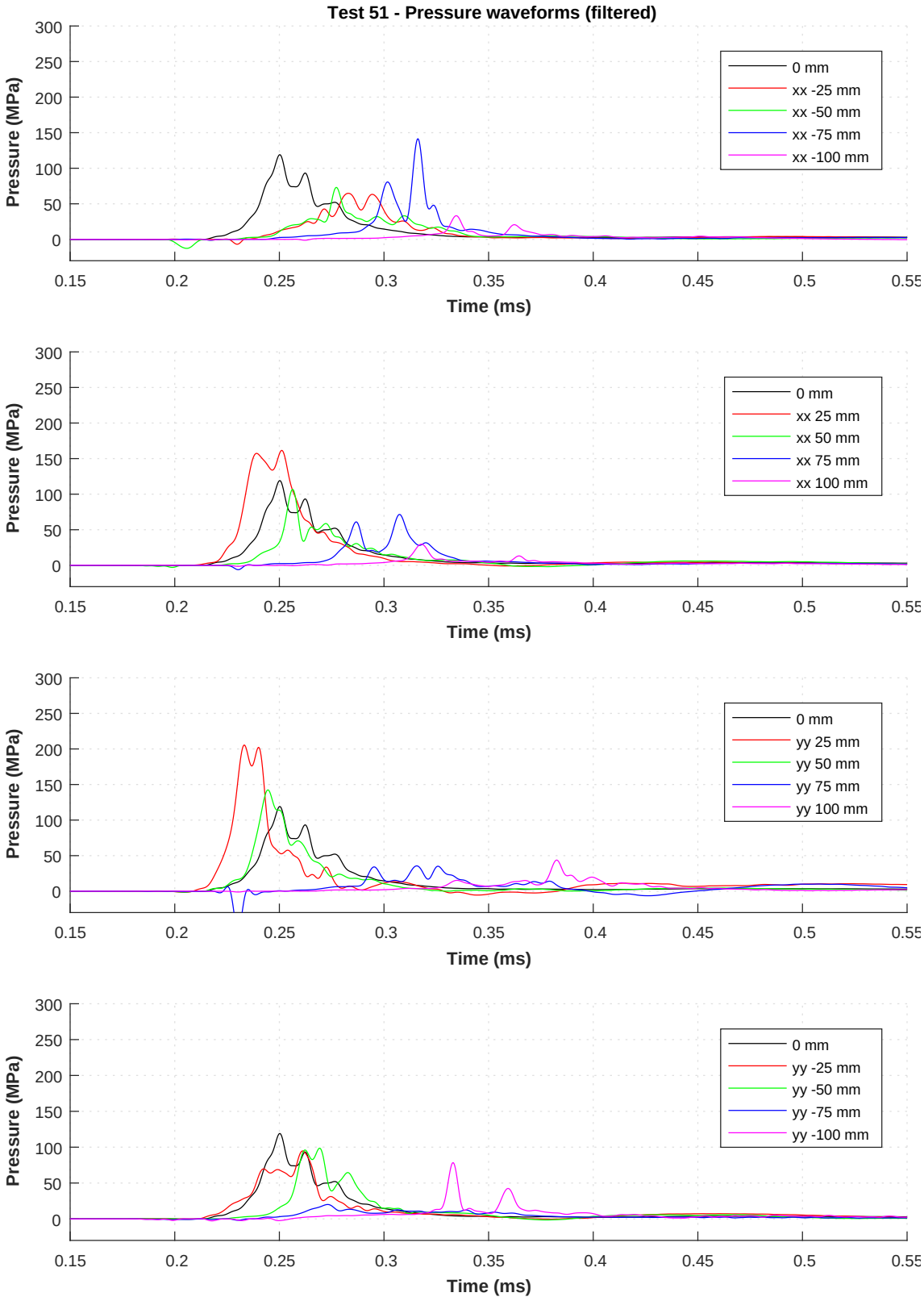

Figure C.58: Pressure-time waveform of Test 51.

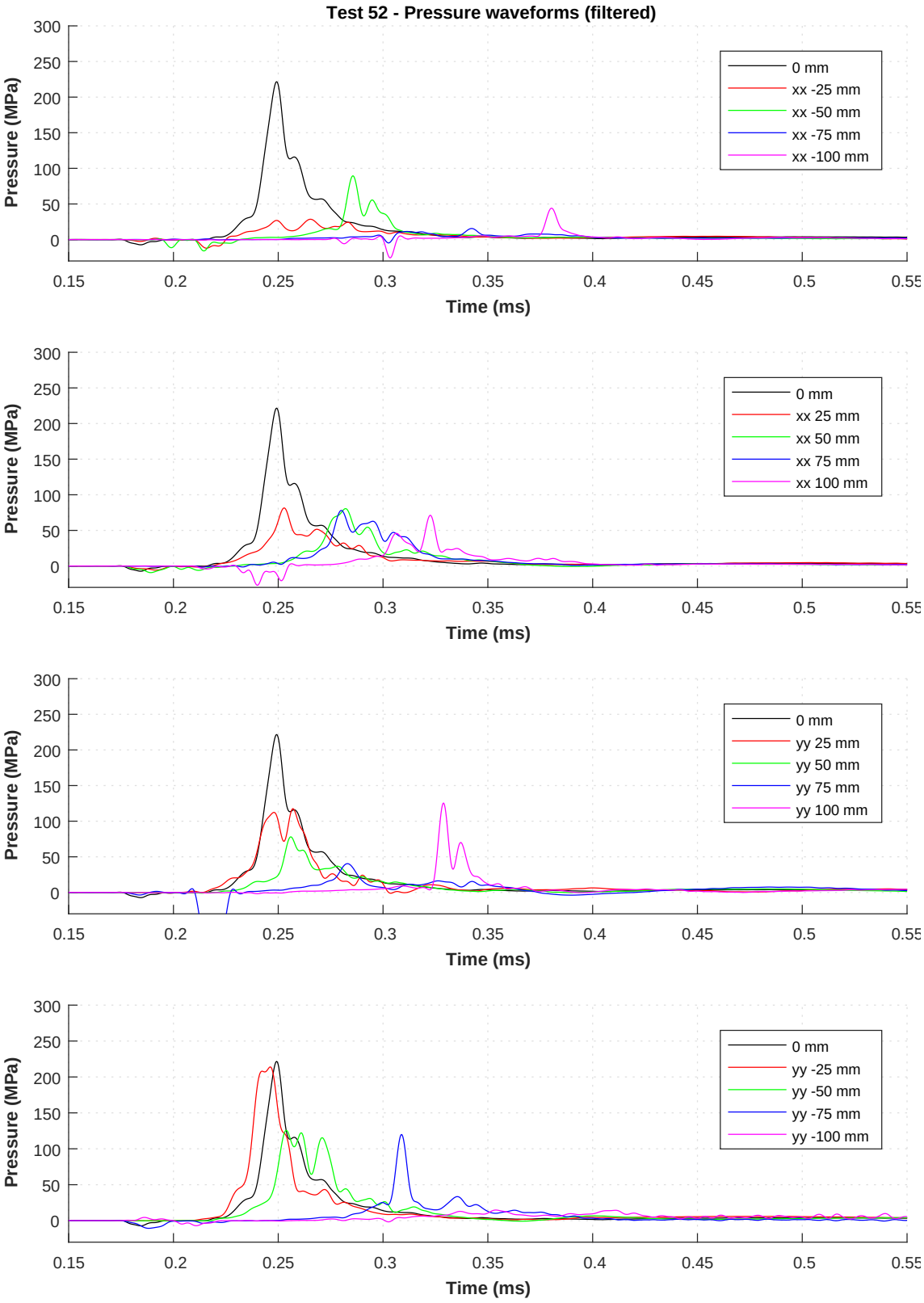

Figure C.59: Pressure-time waveform of Test 52.

Note: No data was captured for Test 53.

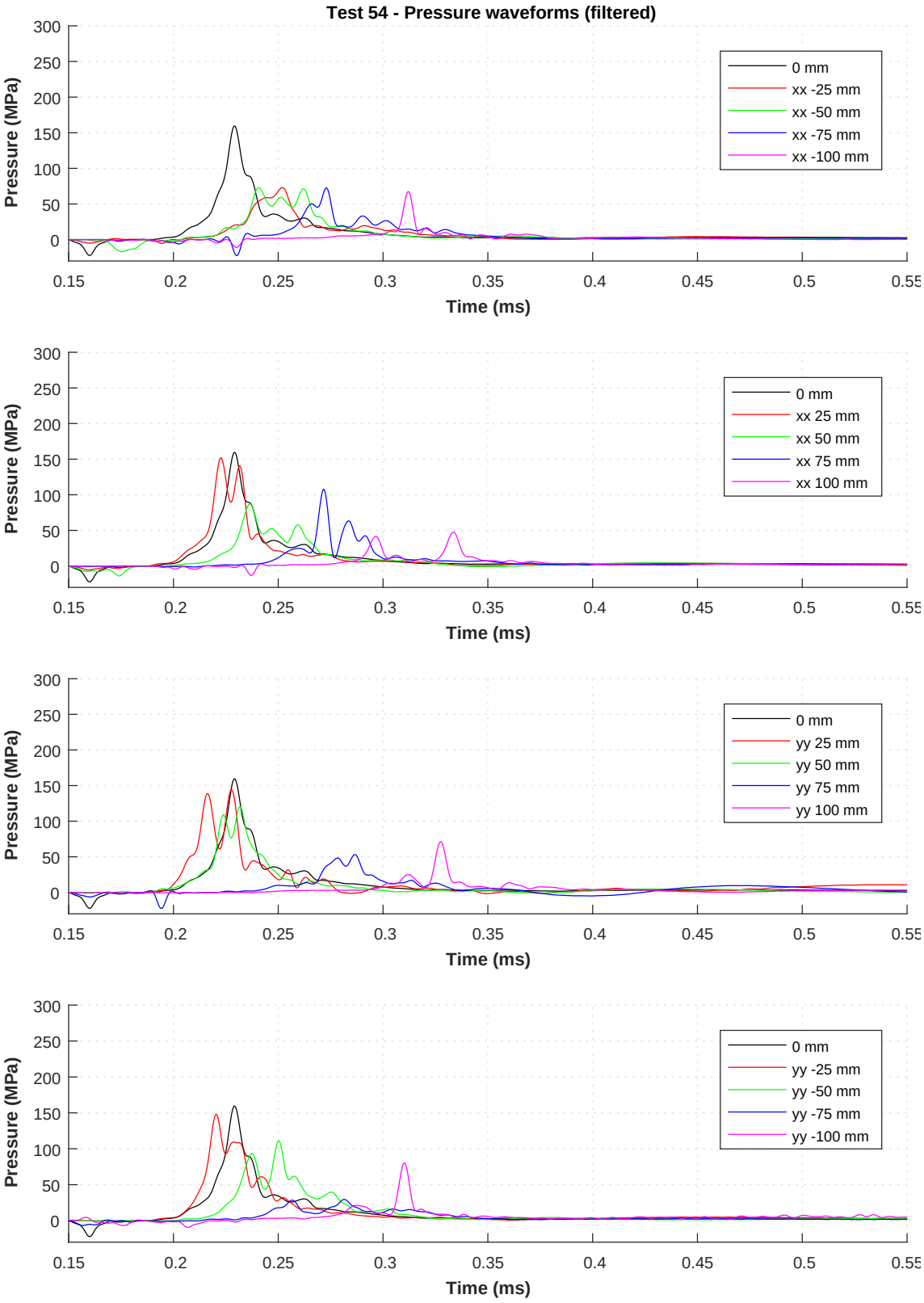

Figure C.60: Pressure-time waveform of Test 54.

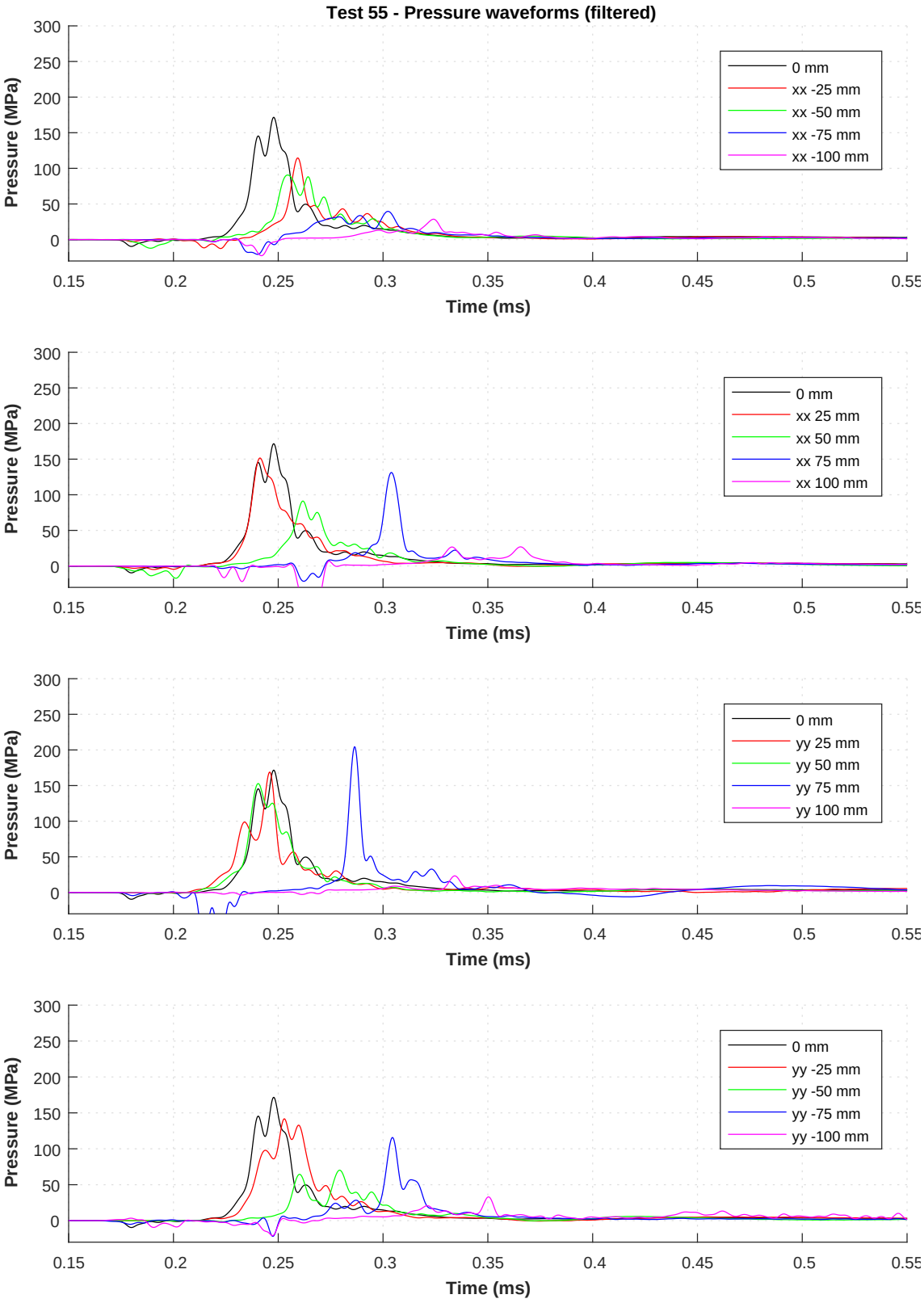

Figure C.61: Pressure-time waveform of Test 55.

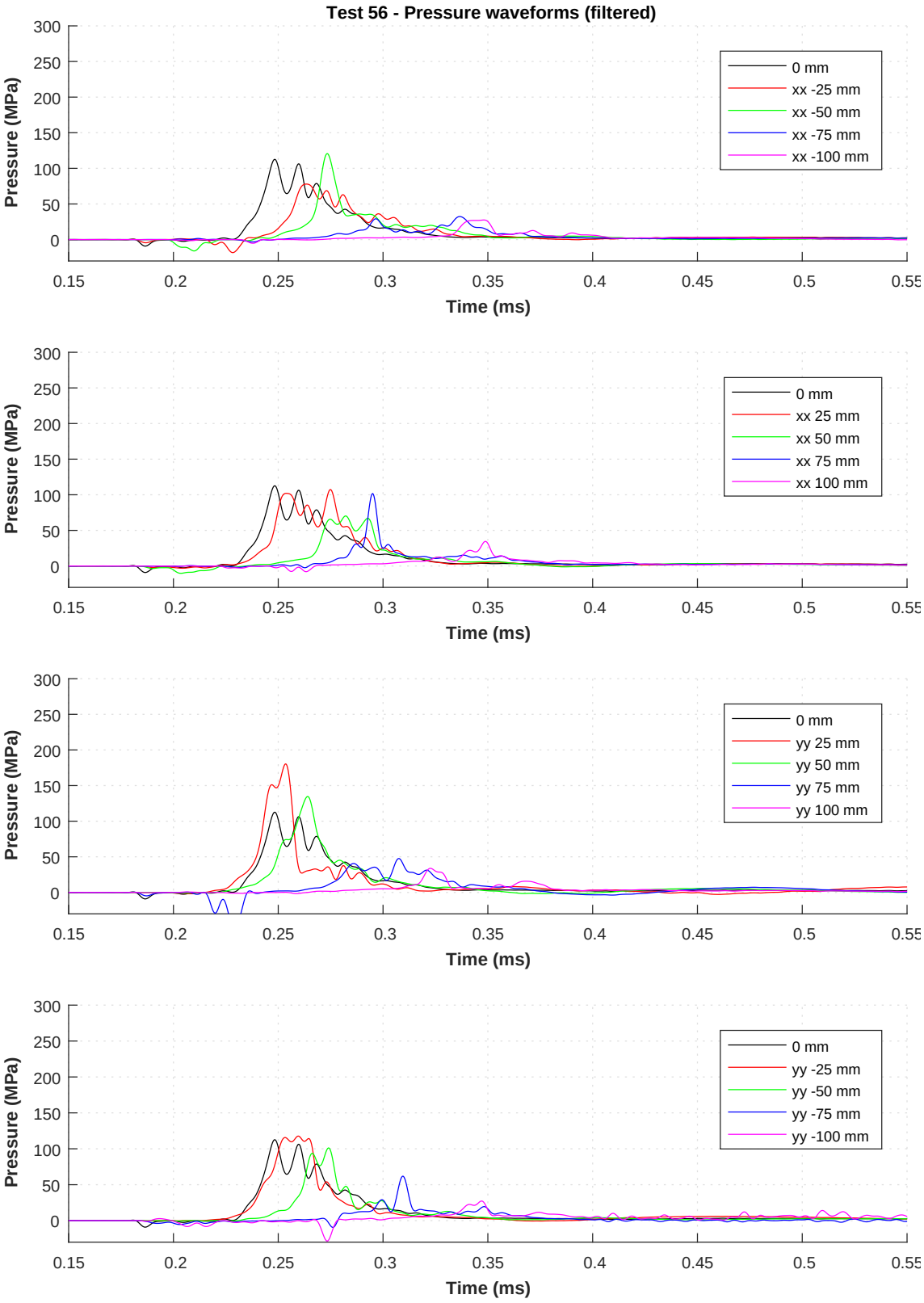

Figure C.62: Pressure-time waveform of Test 56.

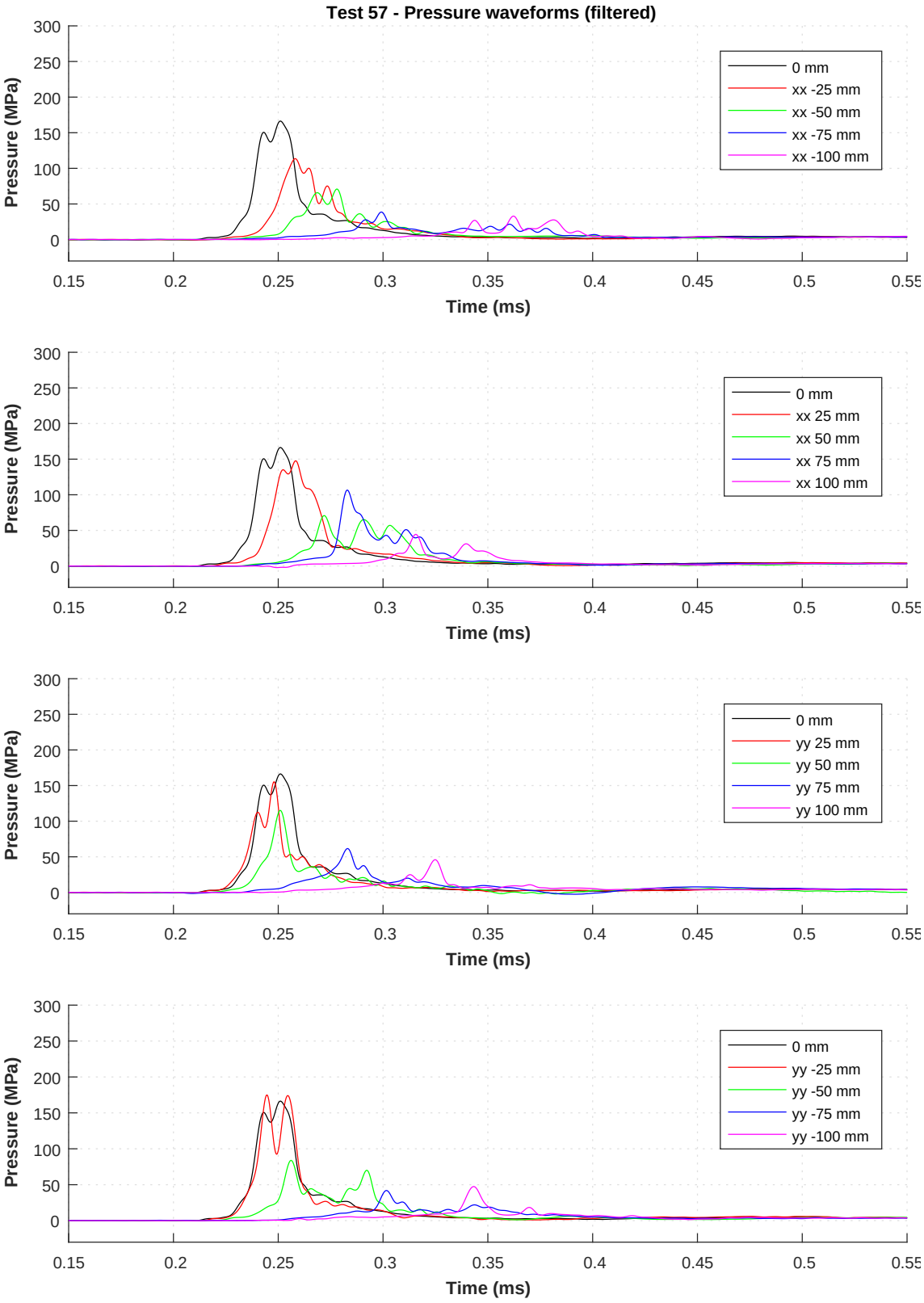

Figure C.63: Pressure-time waveform of Test 57.

C.1.6 Series E – Pressure-time waveforms for Tests 58–62

Note: No data was captured for Test 58.

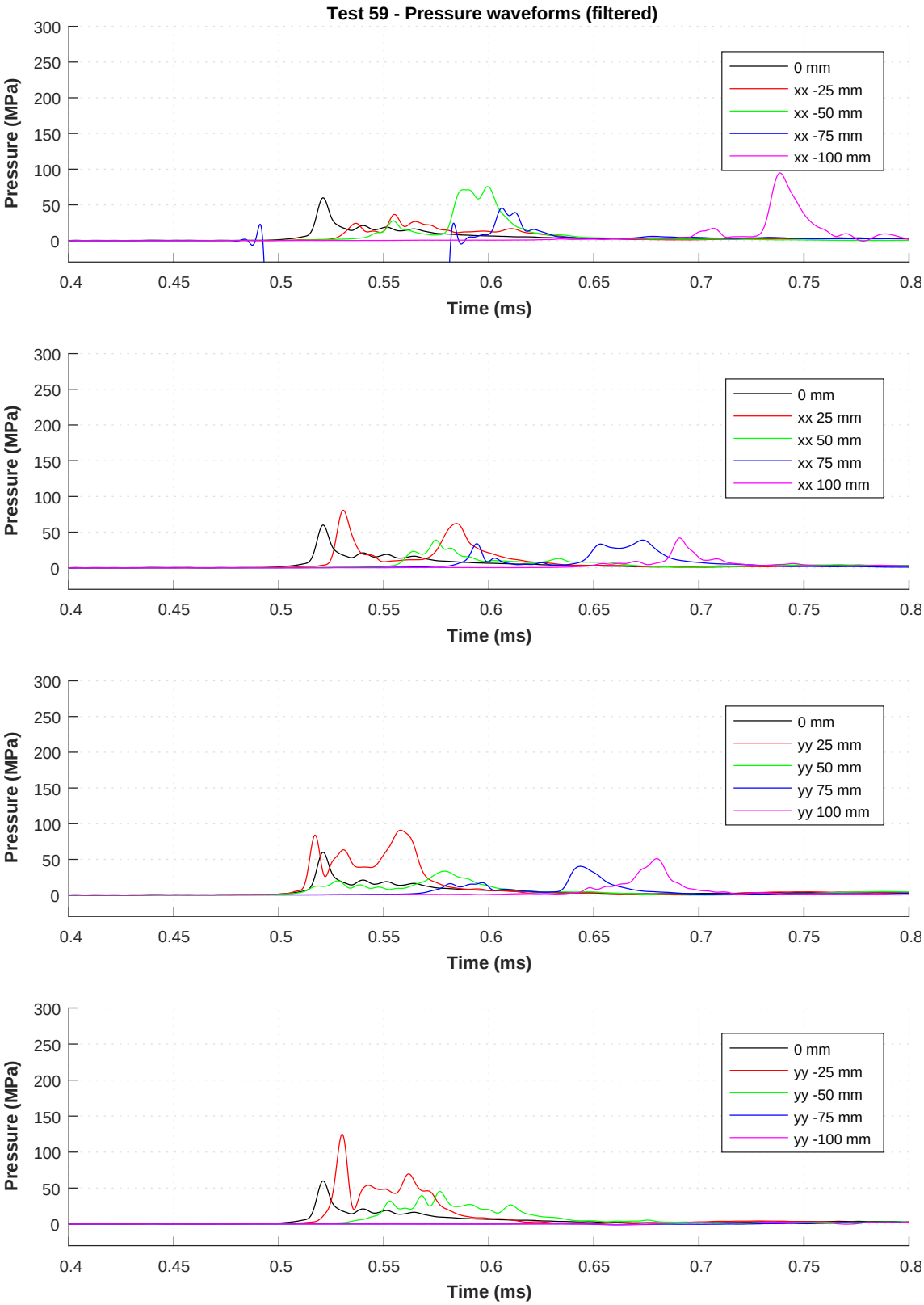

Figure C.64: Pressure-time waveform of Test 59.

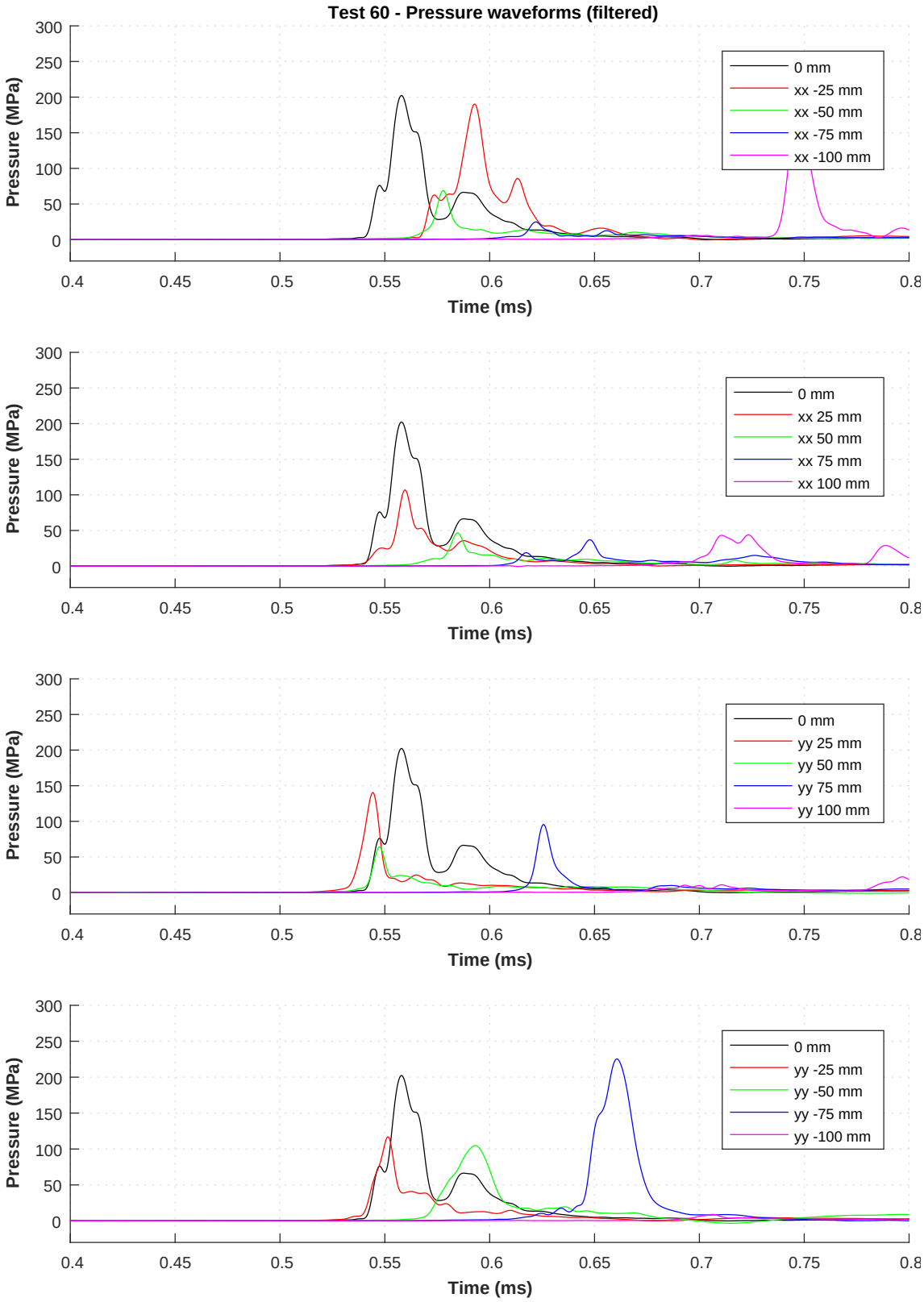

Figure C.65: Pressure-time waveform of Test 60.

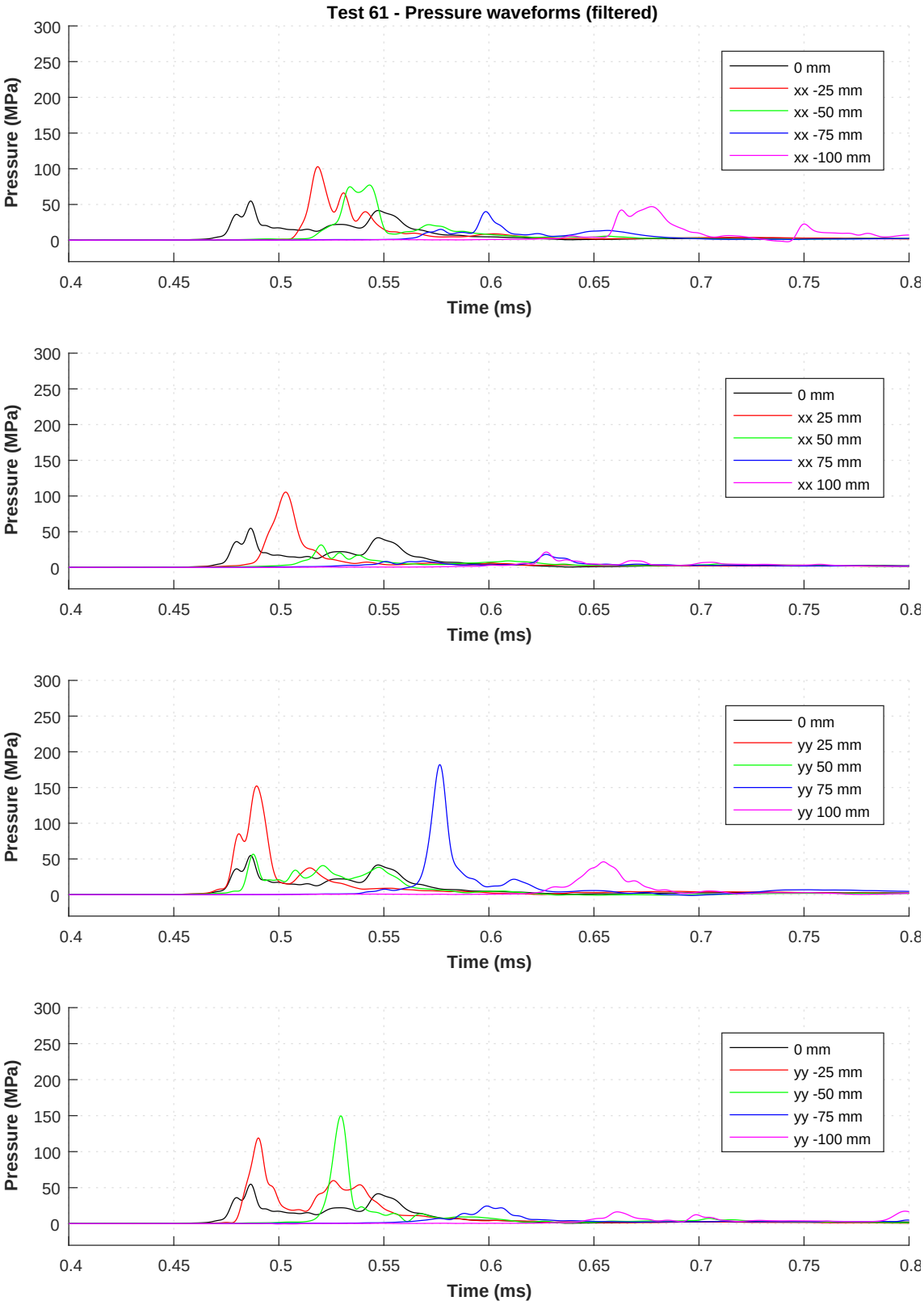

Figure C.66: Pressure-time waveform of Test 61.

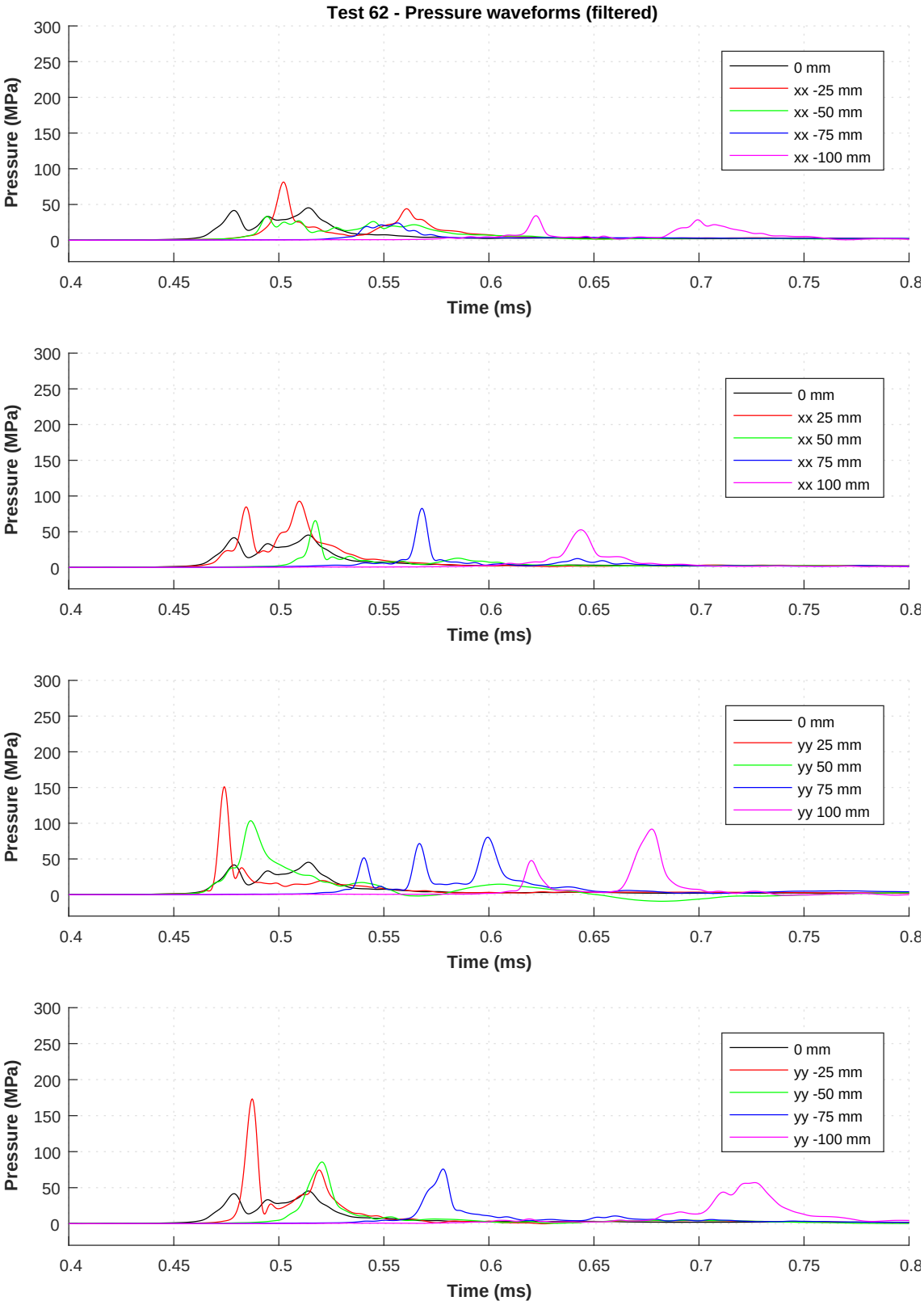

Figure C.67: Pressure-time waveform of Test 62.

C.1.7 Series F – Pressure-time waveforms for Tests 63–67

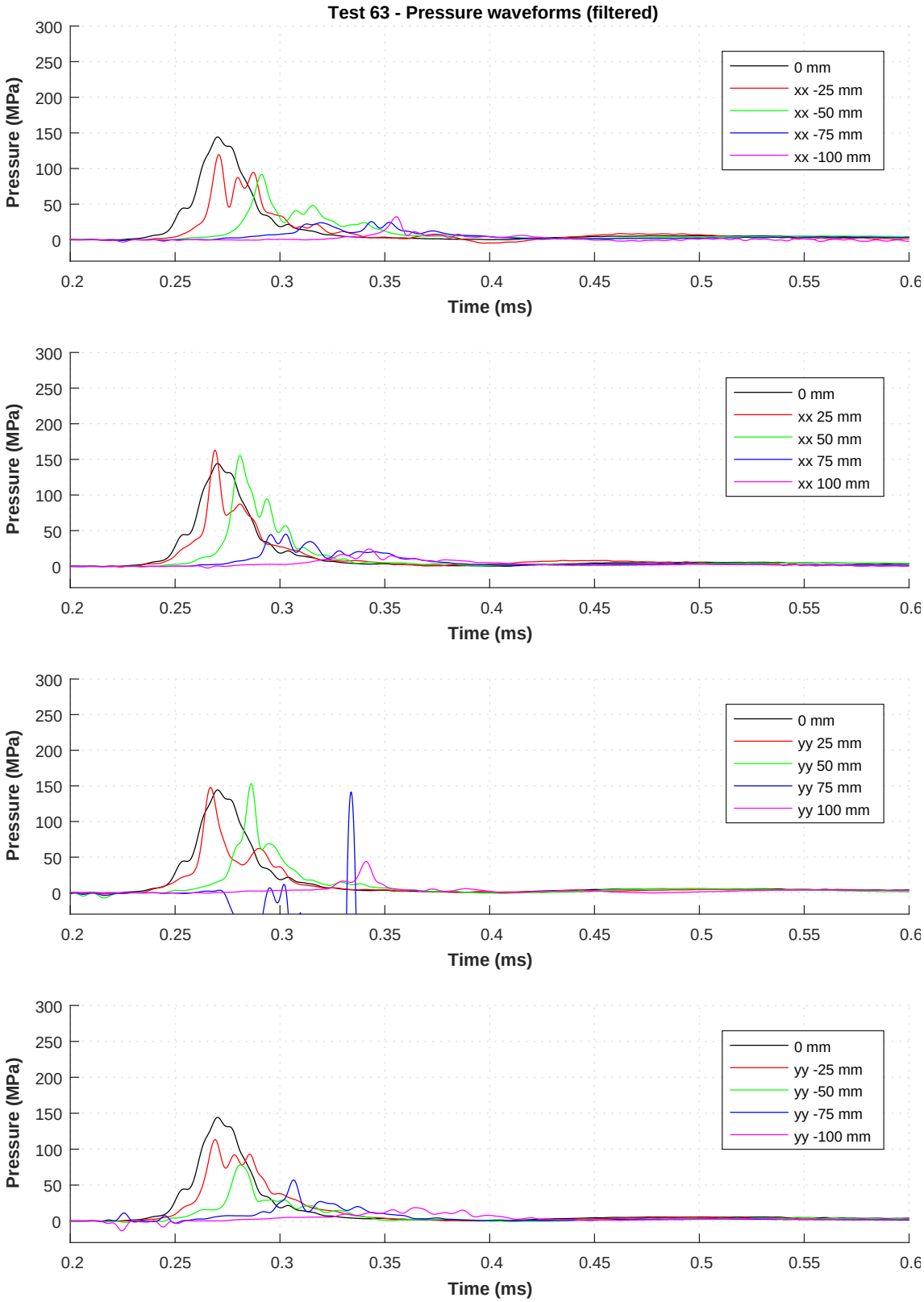

Figure C.68: Pressure-time waveform of Test 63.

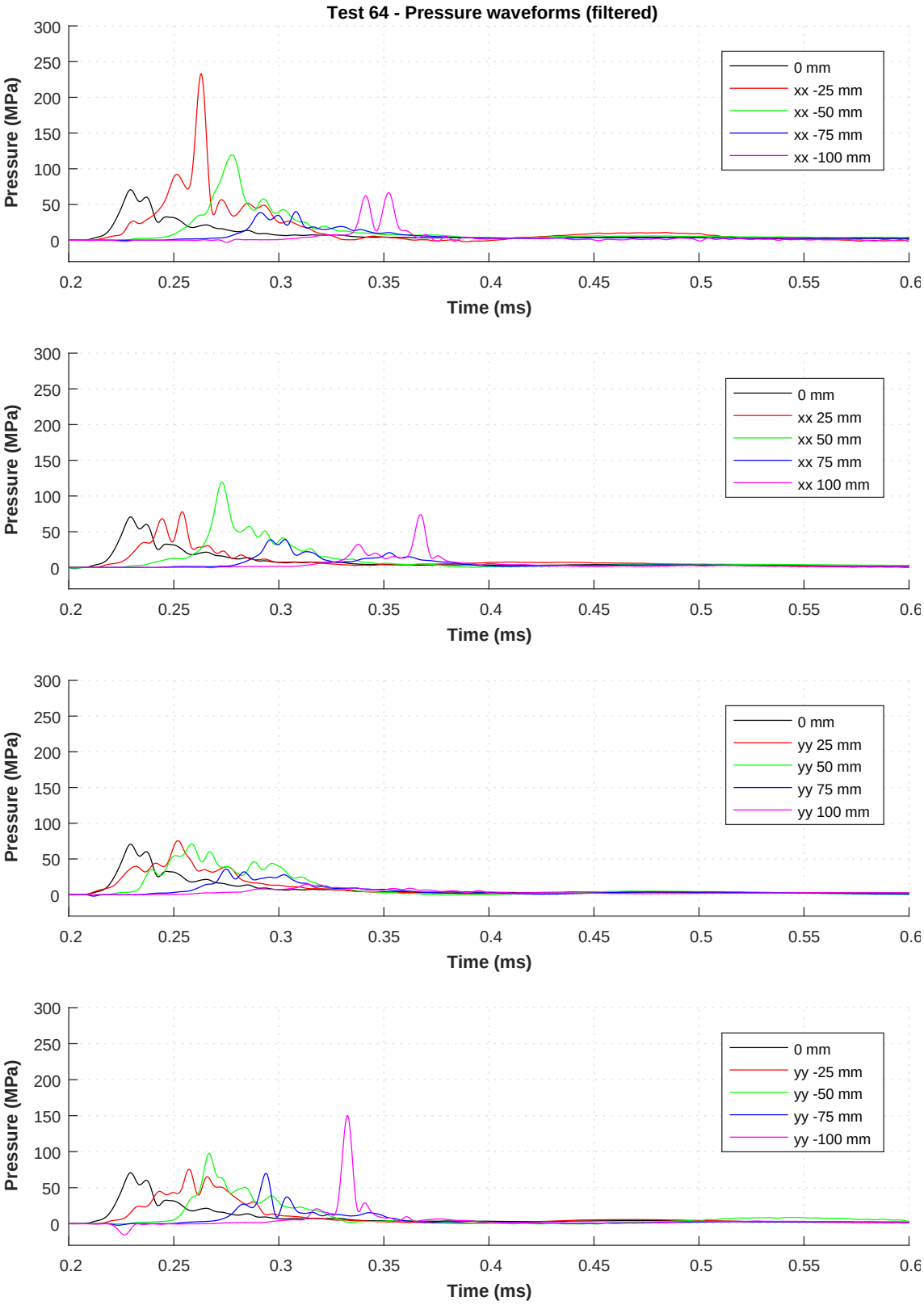

Figure C.69: Pressure-time waveform of Test 64.

Note: No data was captured for Test 65.

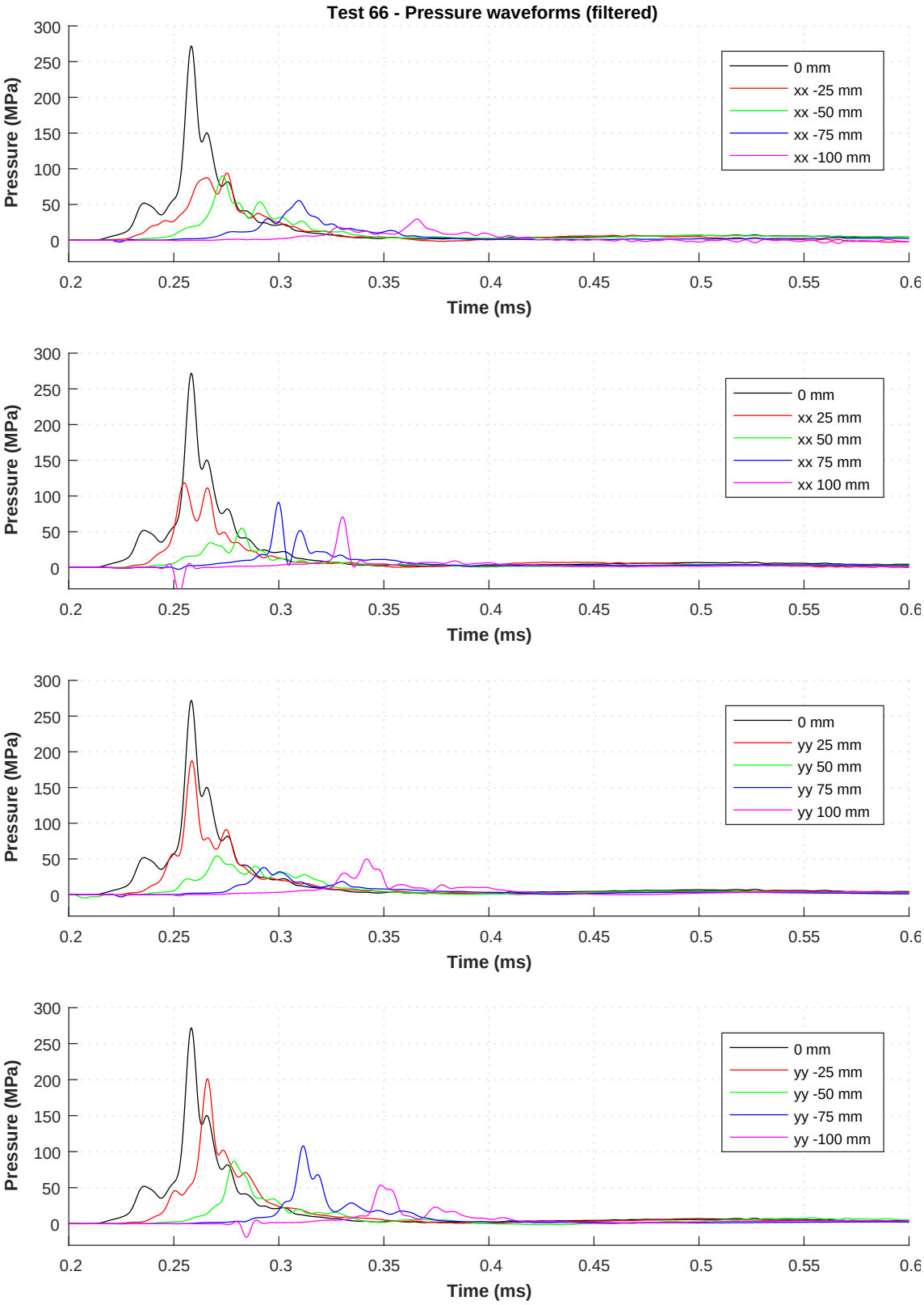

Figure C.70: Pressure-time waveform of Test 66.

Note: No data was captured for Test 67.

C.1.8 Series G – Pressure-time waveforms for Tests 68–72

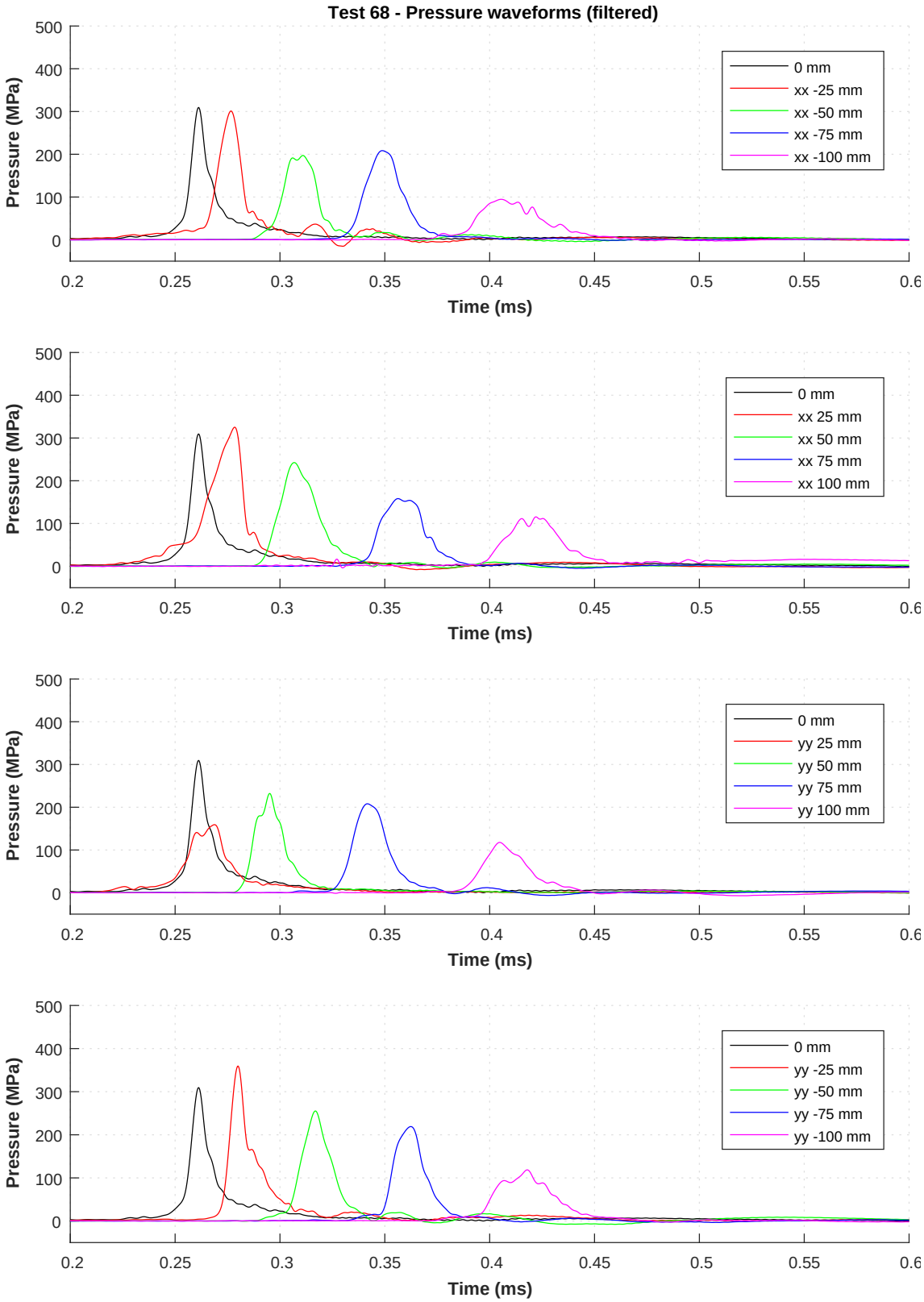

Figure C.71: Pressure-time waveform of Test 68.

Note: No data was captured for Test 69.

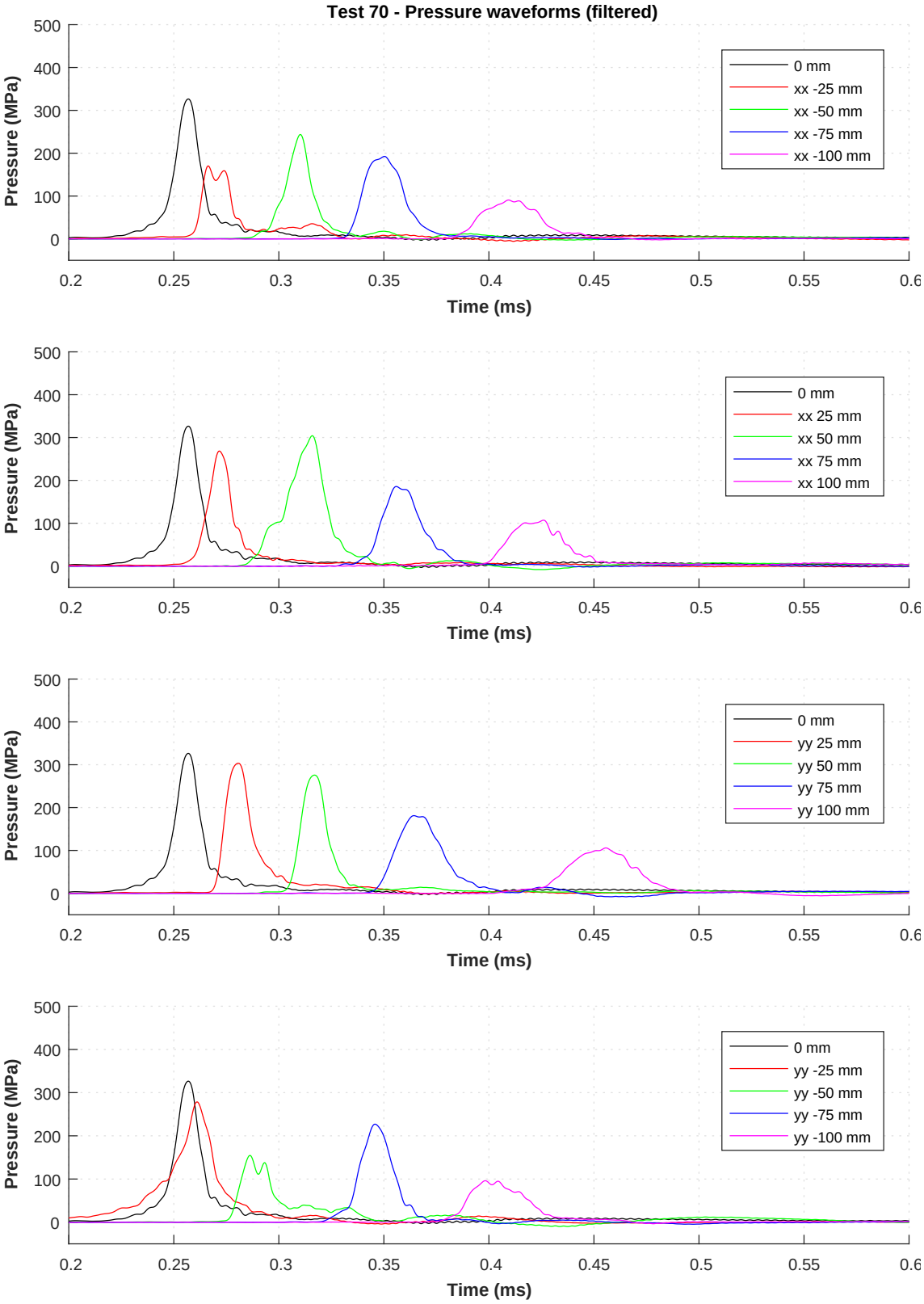

Figure C.72: Pressure-time waveform of Test 70.

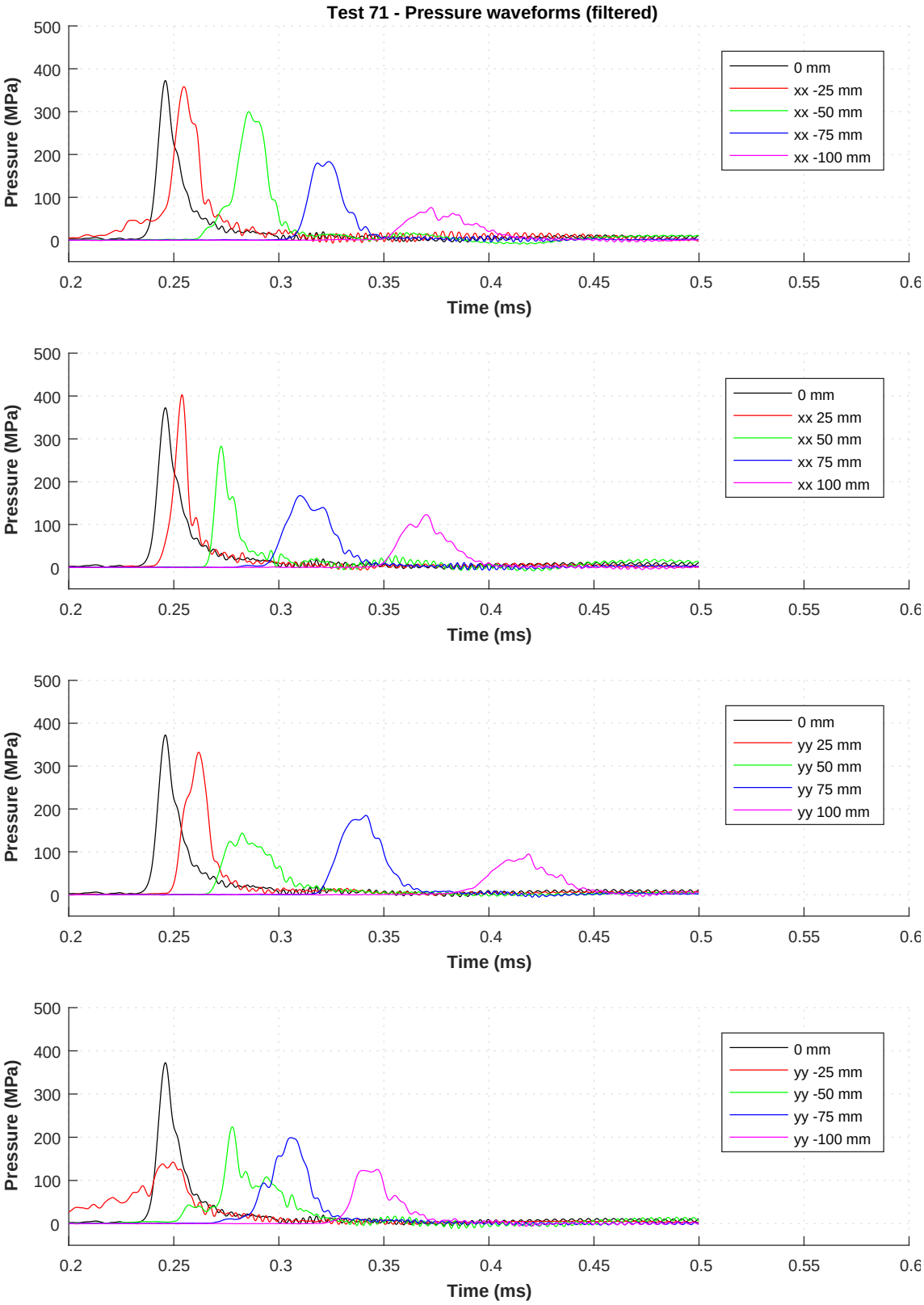

Figure C.73: Pressure-time waveform of Test 71.

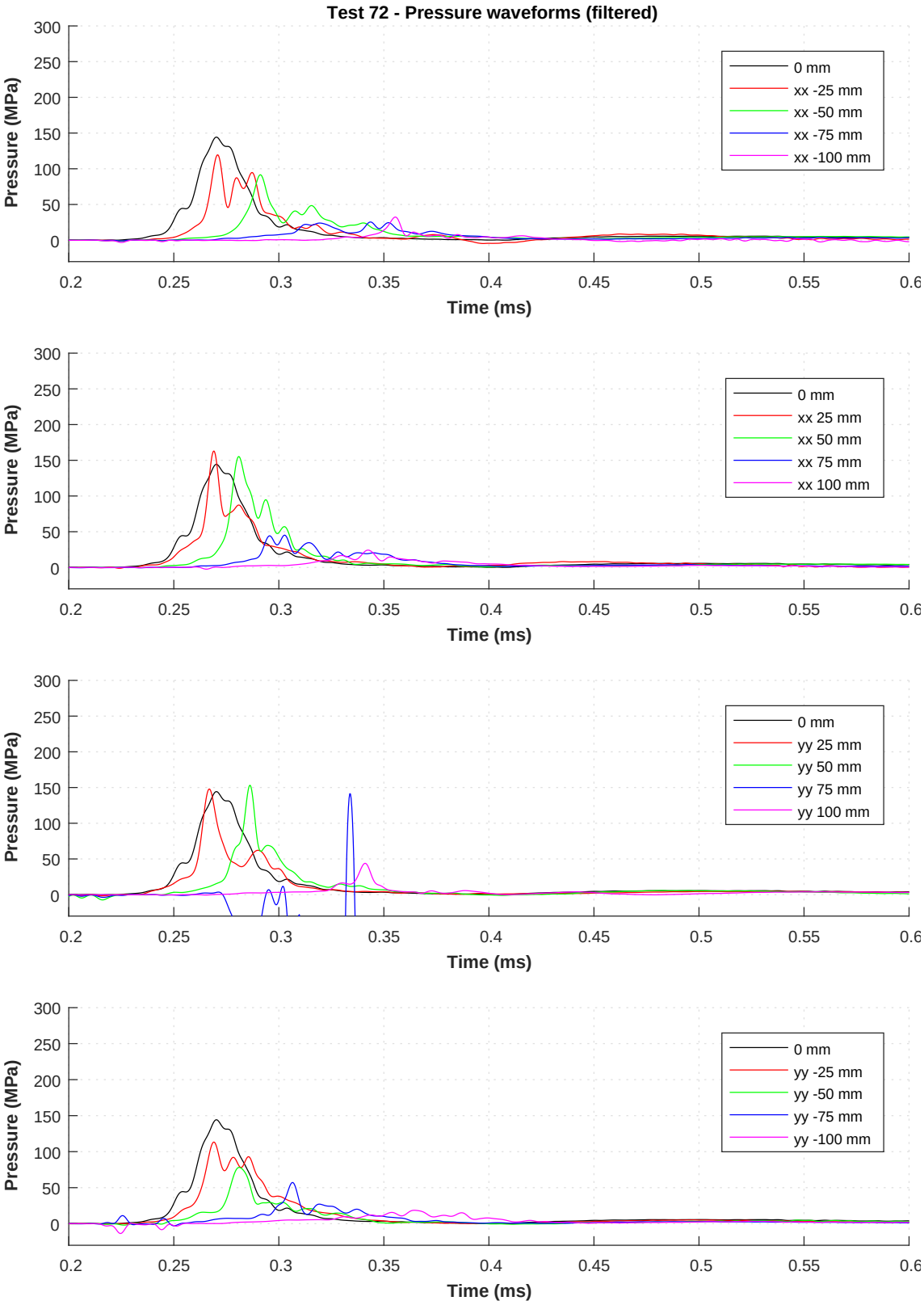

Figure C.74: Pressure-time waveform of Test 72.

C.1.9 Series H – Pressure-time waveforms for Tests 73–74

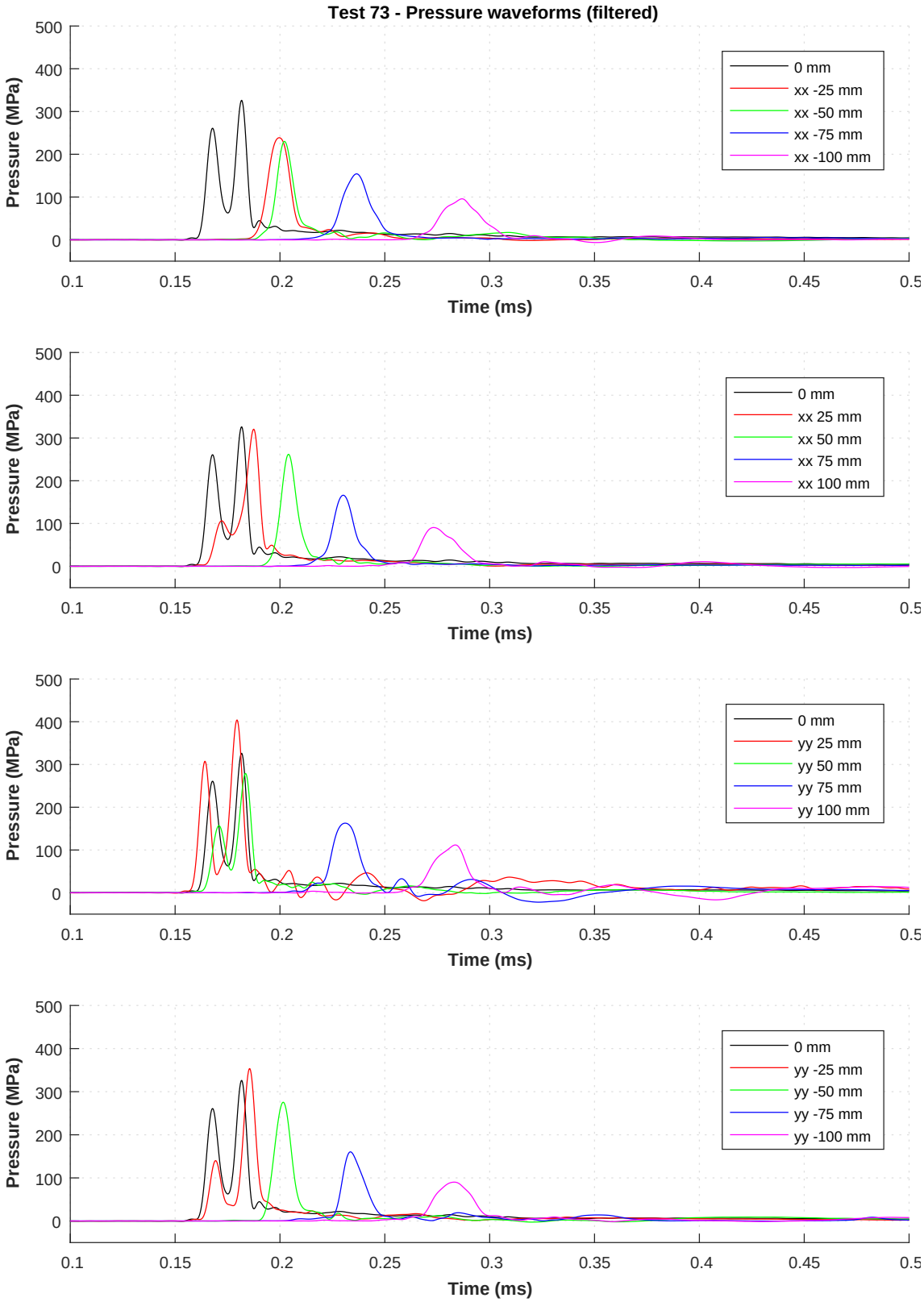

Figure C.75: Pressure-time waveform of Test 73.

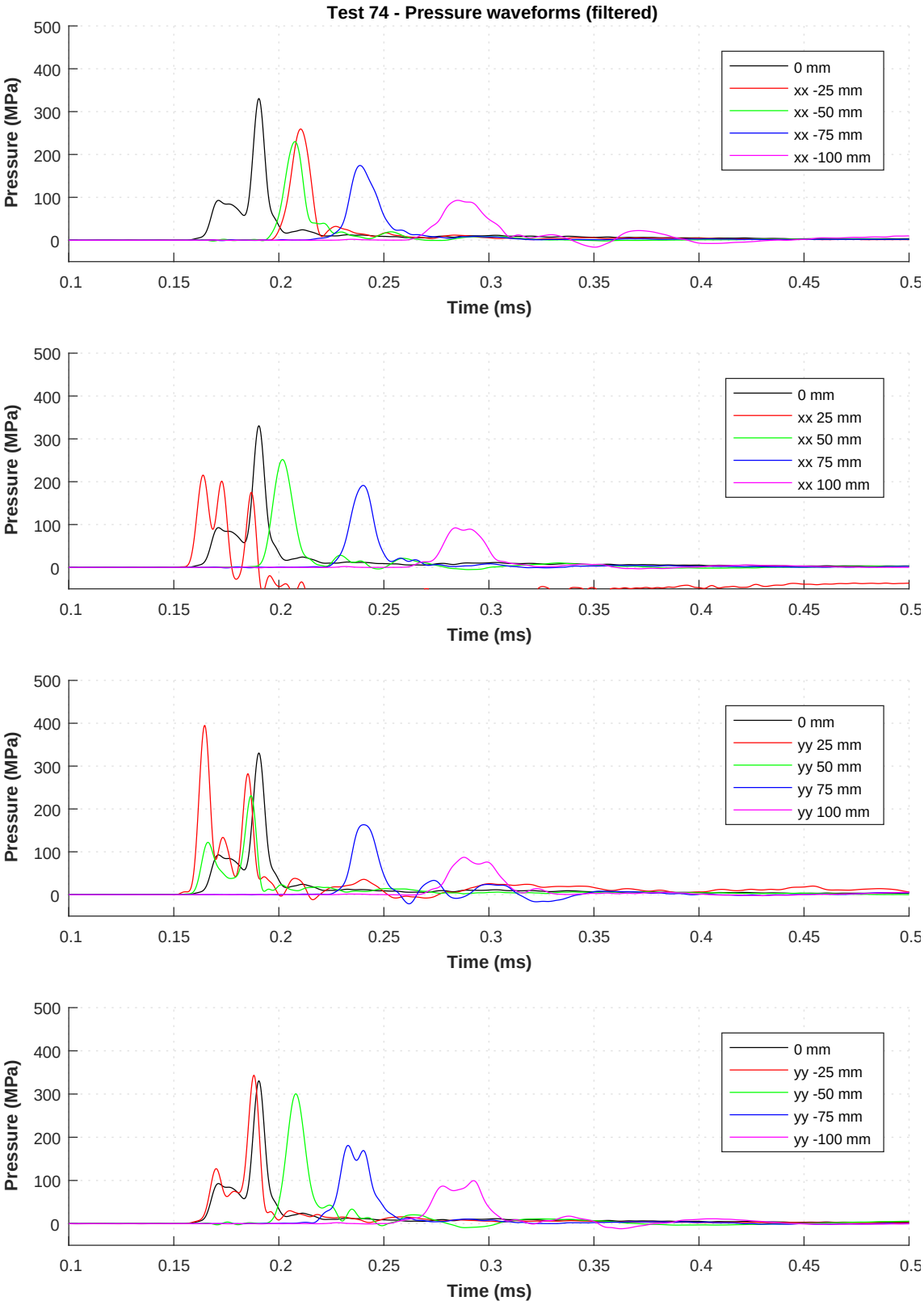

Figure C.76: Pressure-time waveform of Test 74.

C.1.10 Series I – Pressure-time waveforms for Tests 75–81

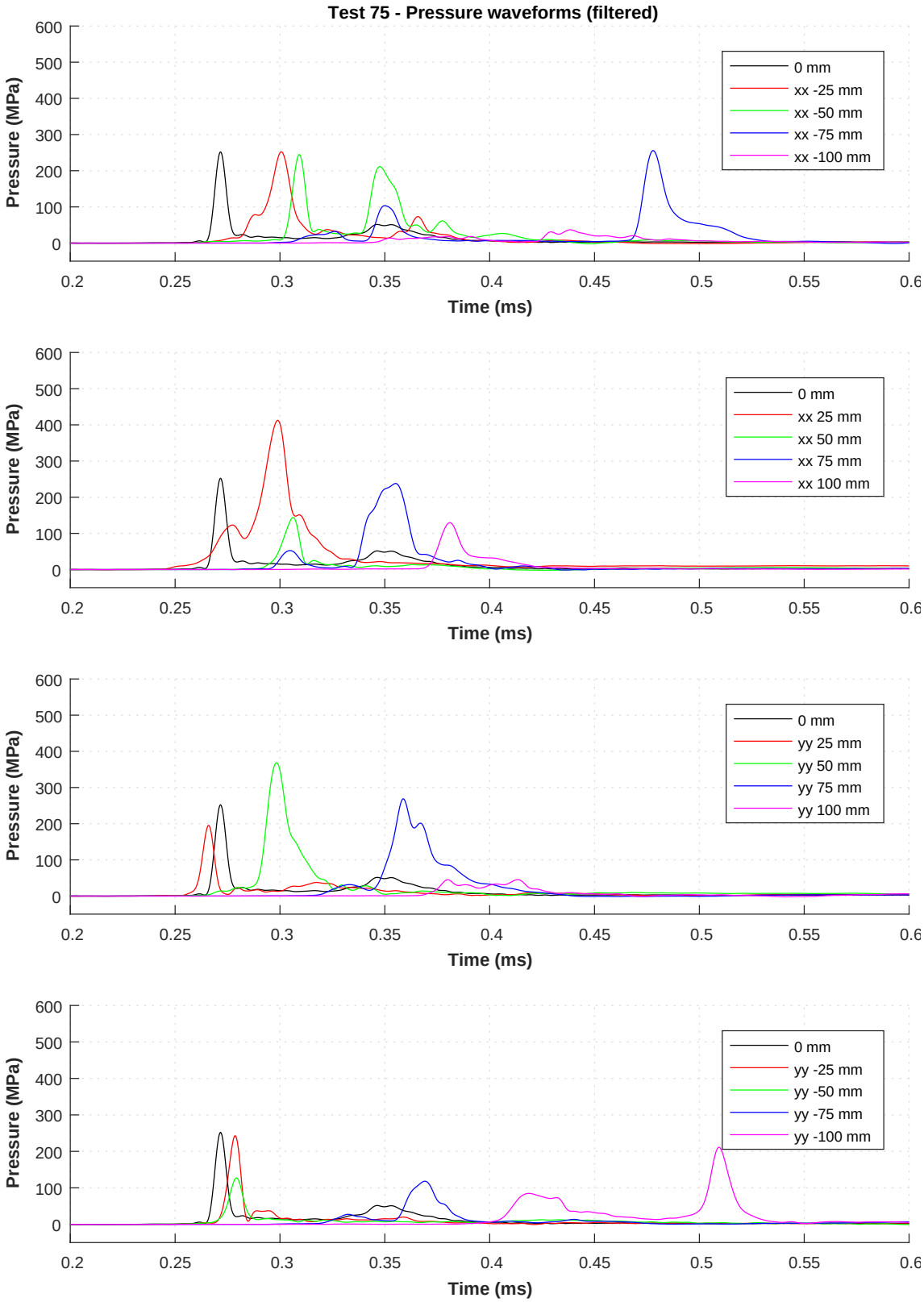

Figure C.77: Pressure-time waveform of Test 75.

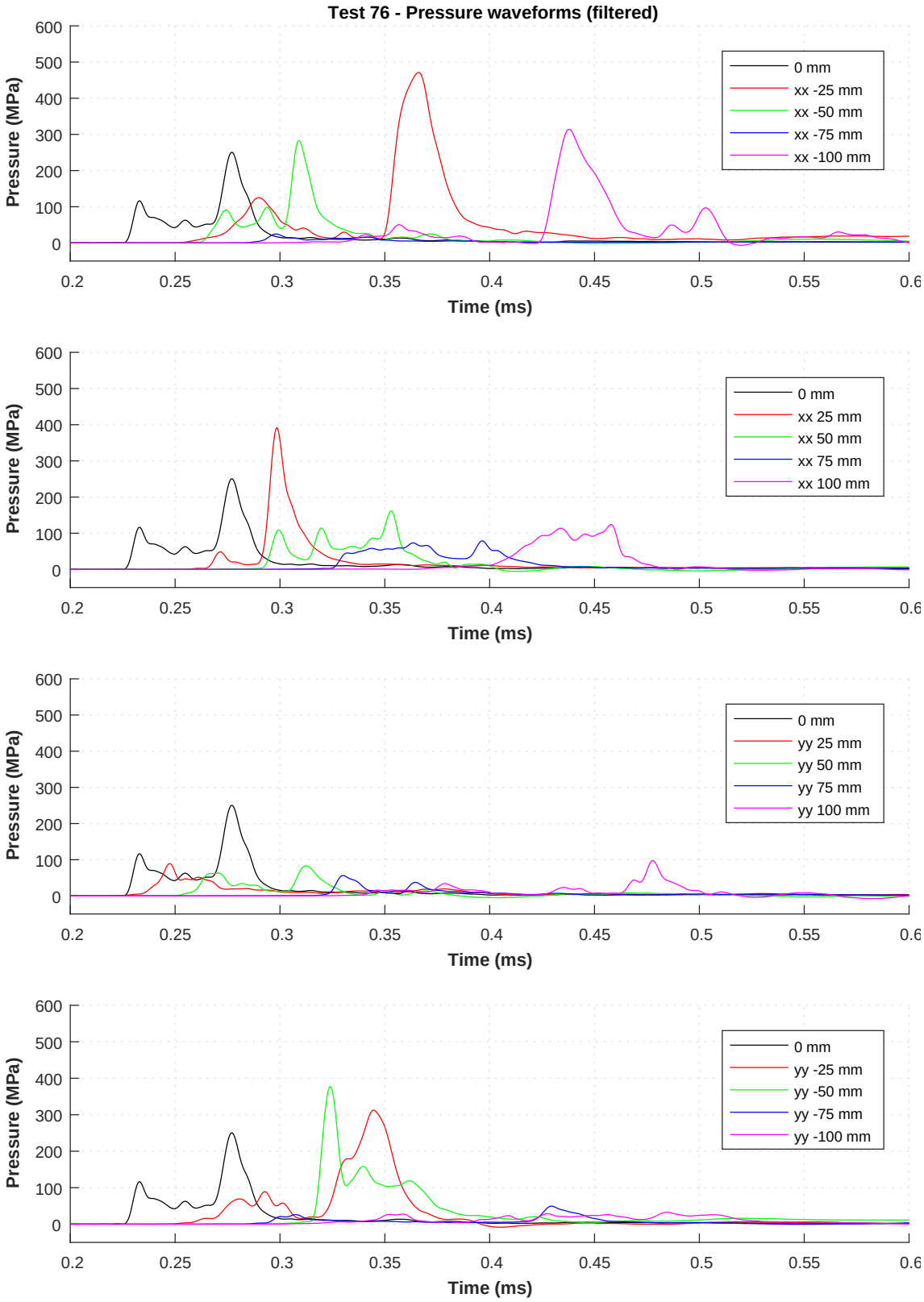

Figure C.78: Pressure-time waveform of Test 76.

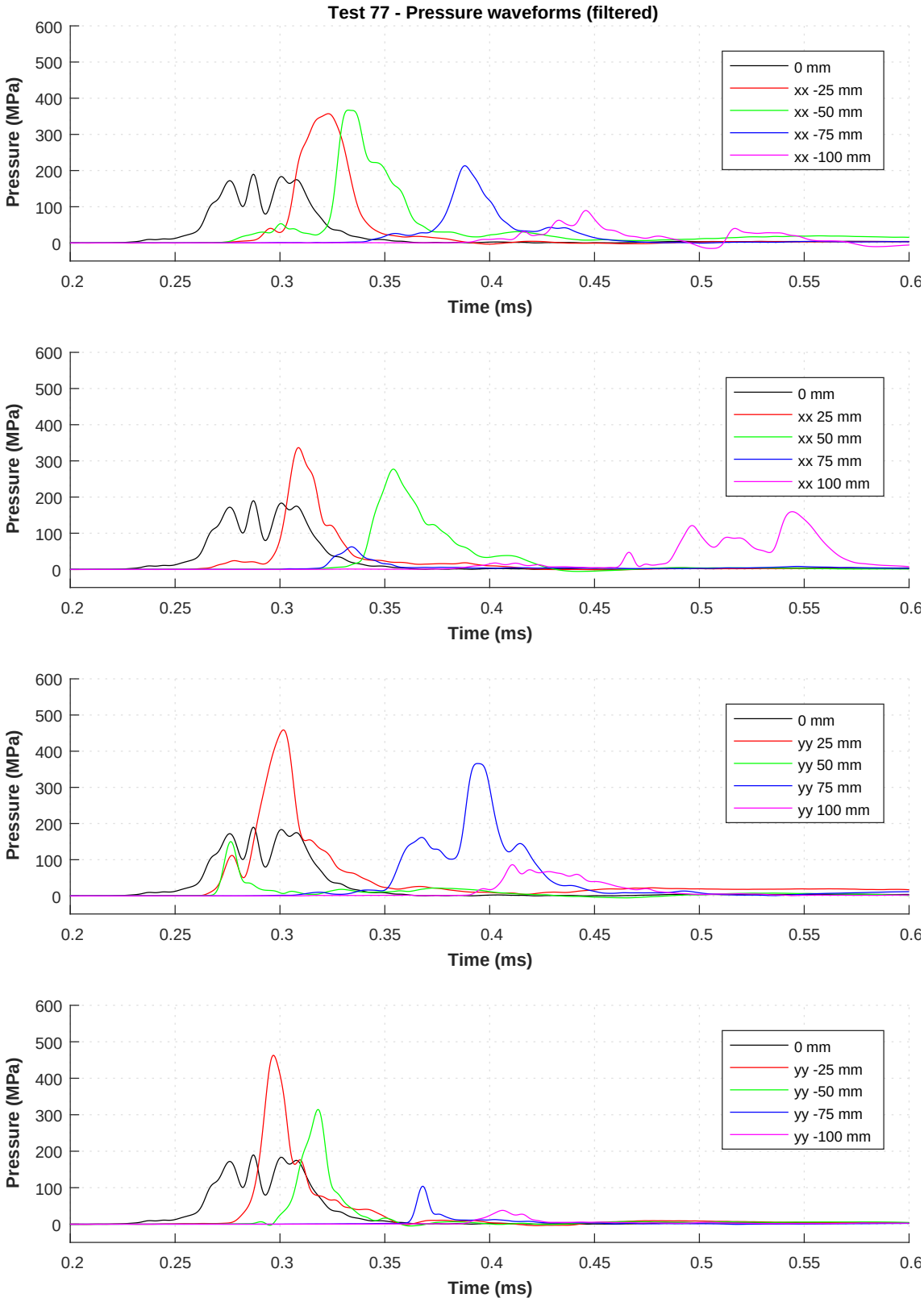

Figure C.79: Pressure-time waveform of Test 77.

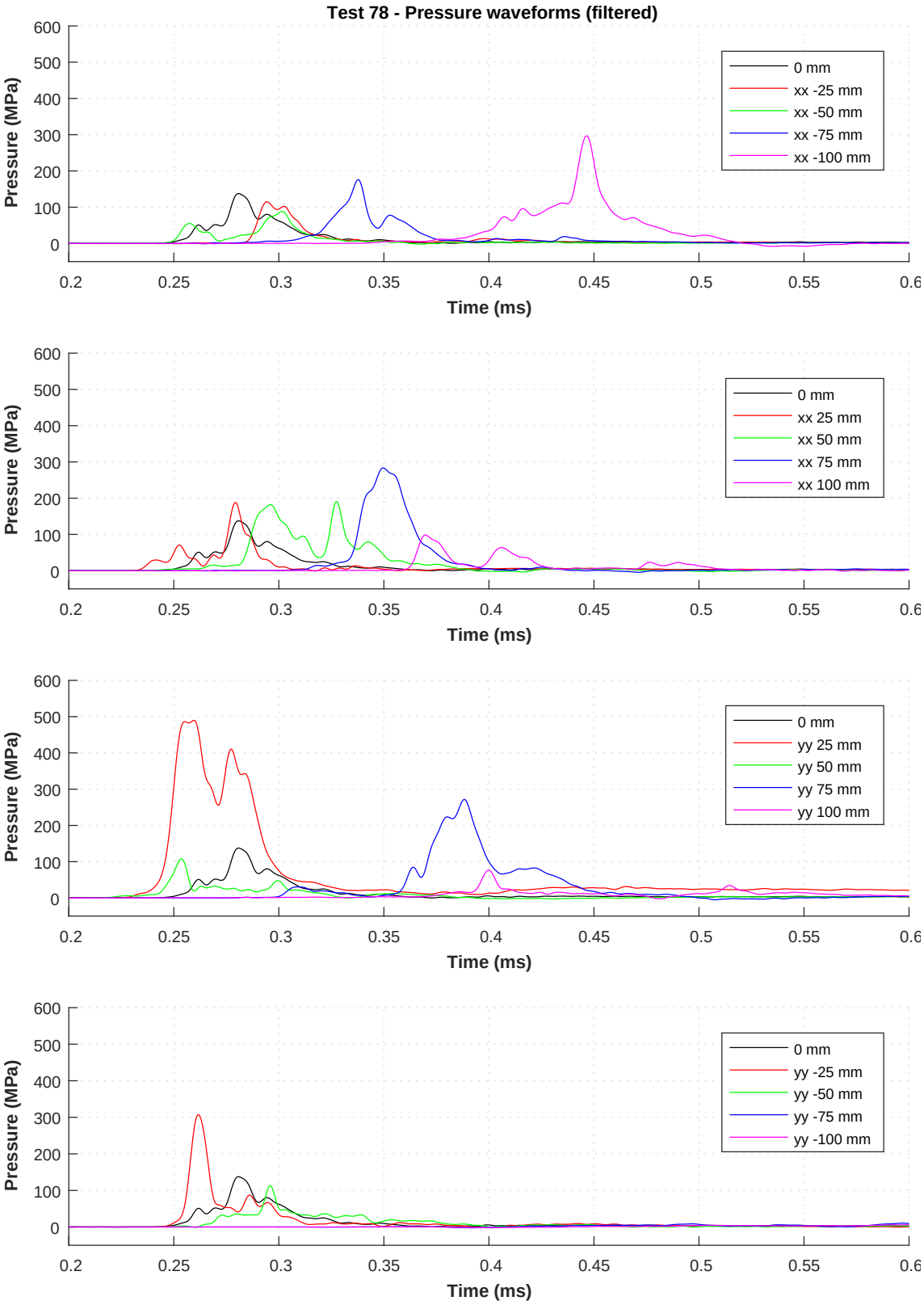

Figure C.80: Pressure-time waveform of Test 78.

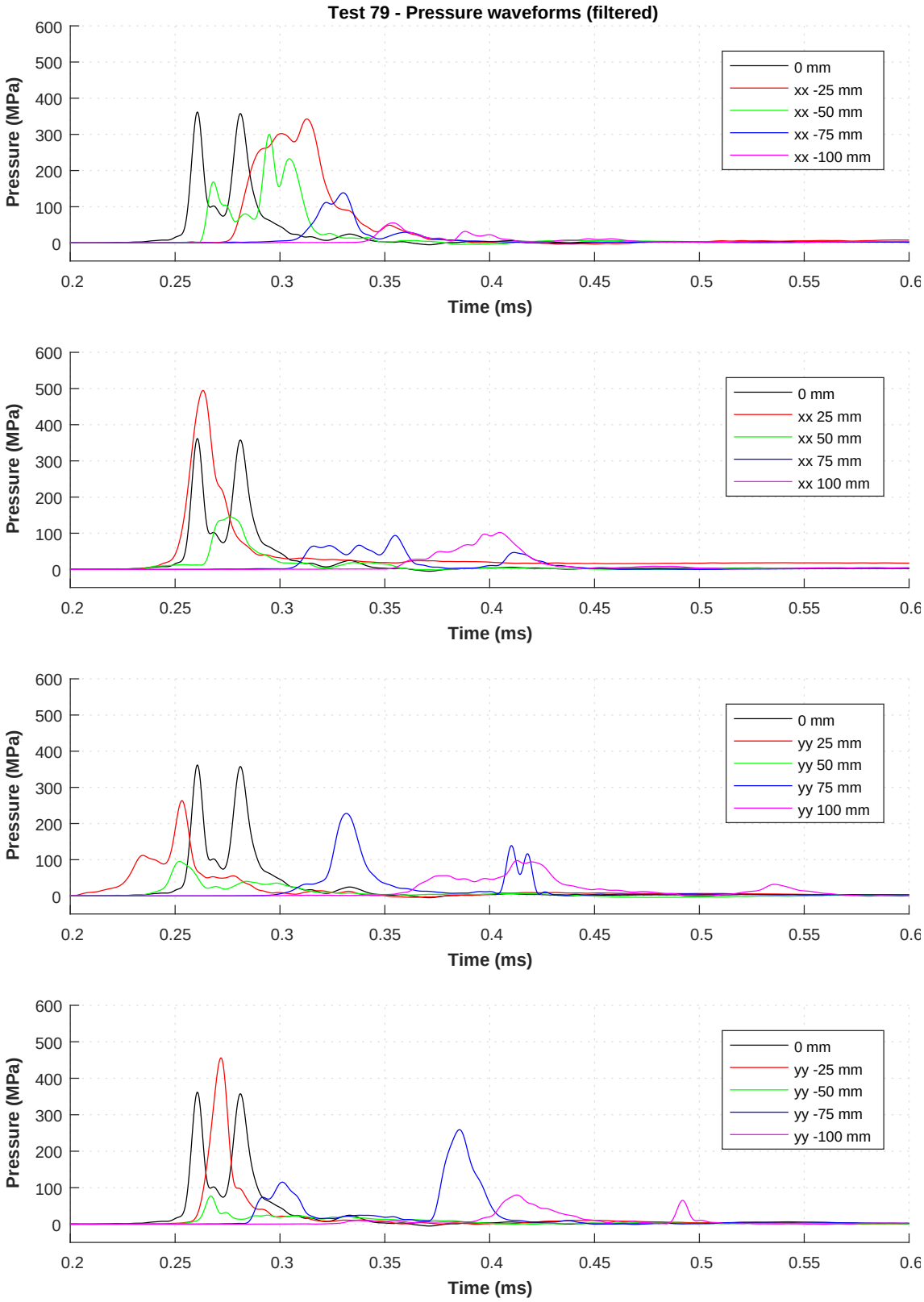

Figure C.81: Pressure-time waveform of Test 79.

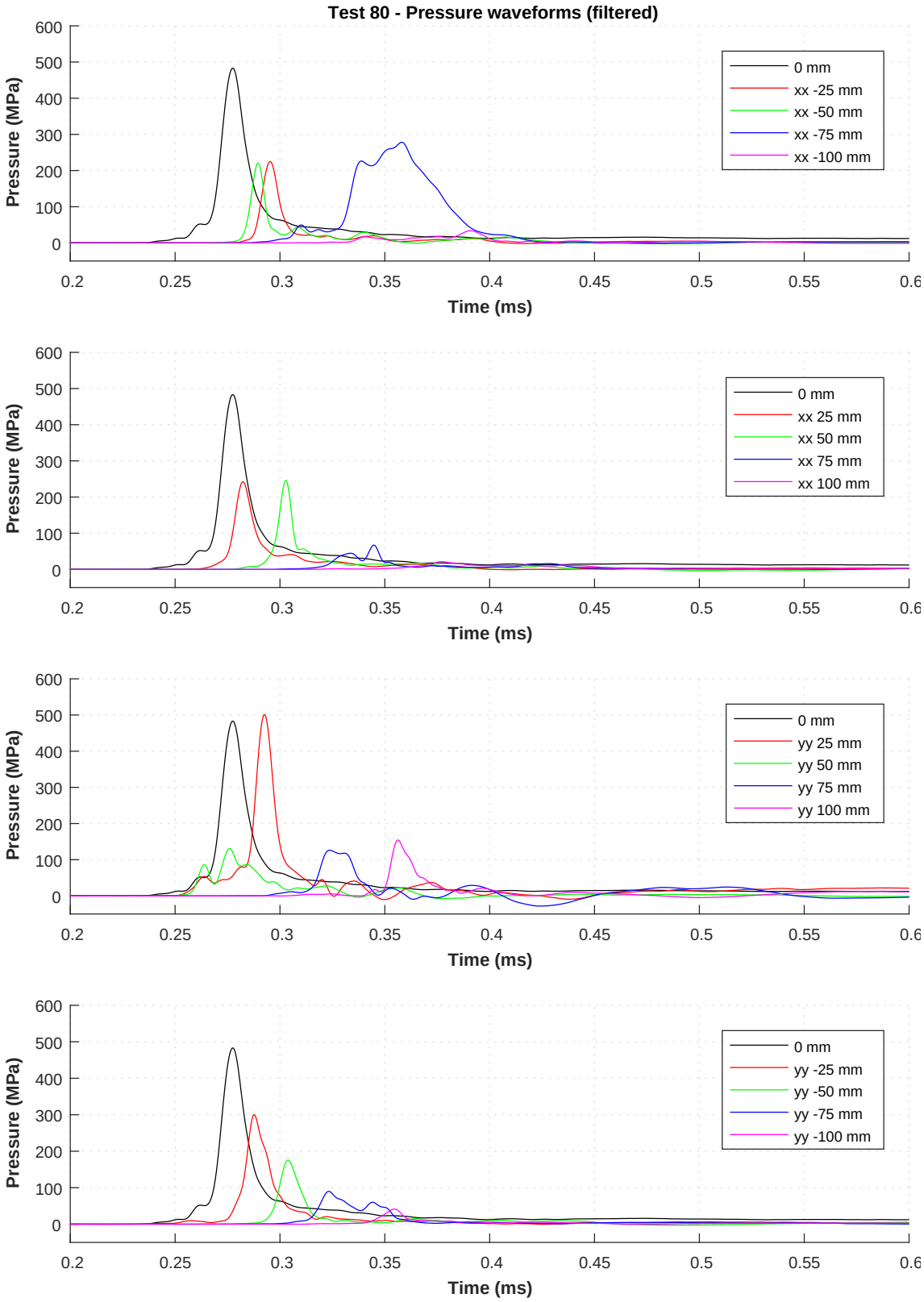

Figure C.82: Pressure-time waveform of Test 80.

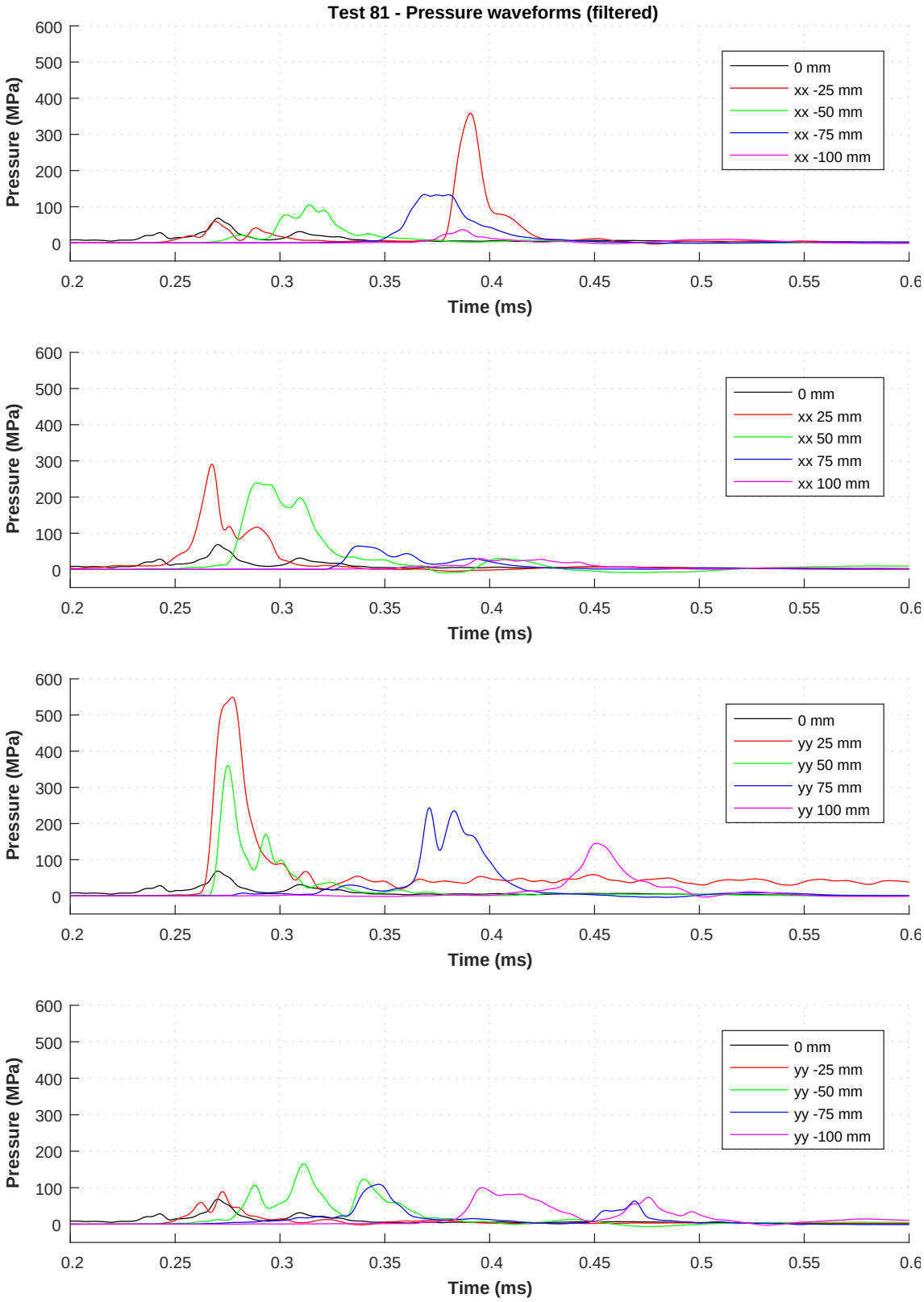

Figure C.83: Pressure-time waveform of Test 81.

C.1.11 Series J – Pressure-time waveforms for Tests 82–86

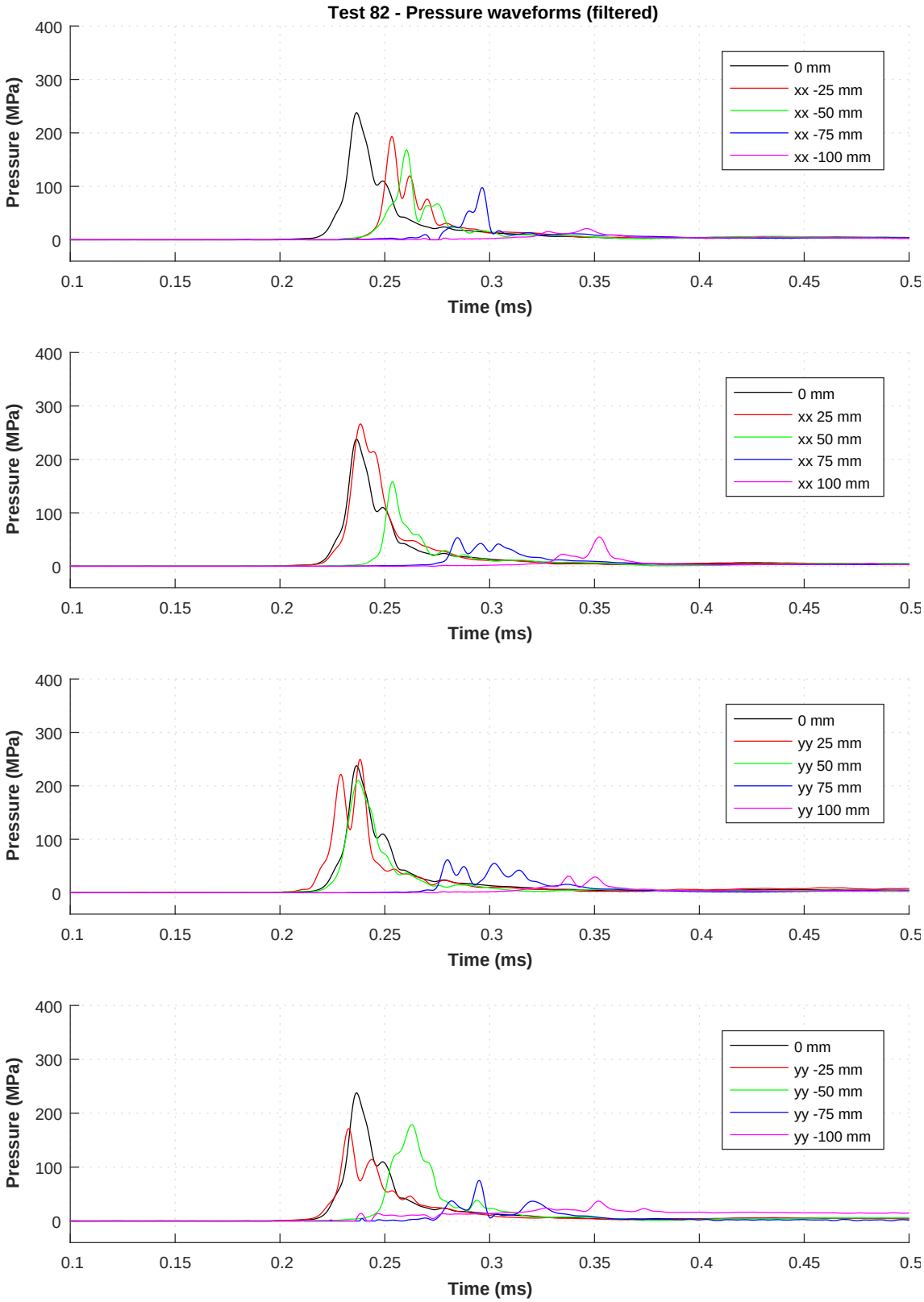

Figure C.84: Pressure-time waveform of Test 82.

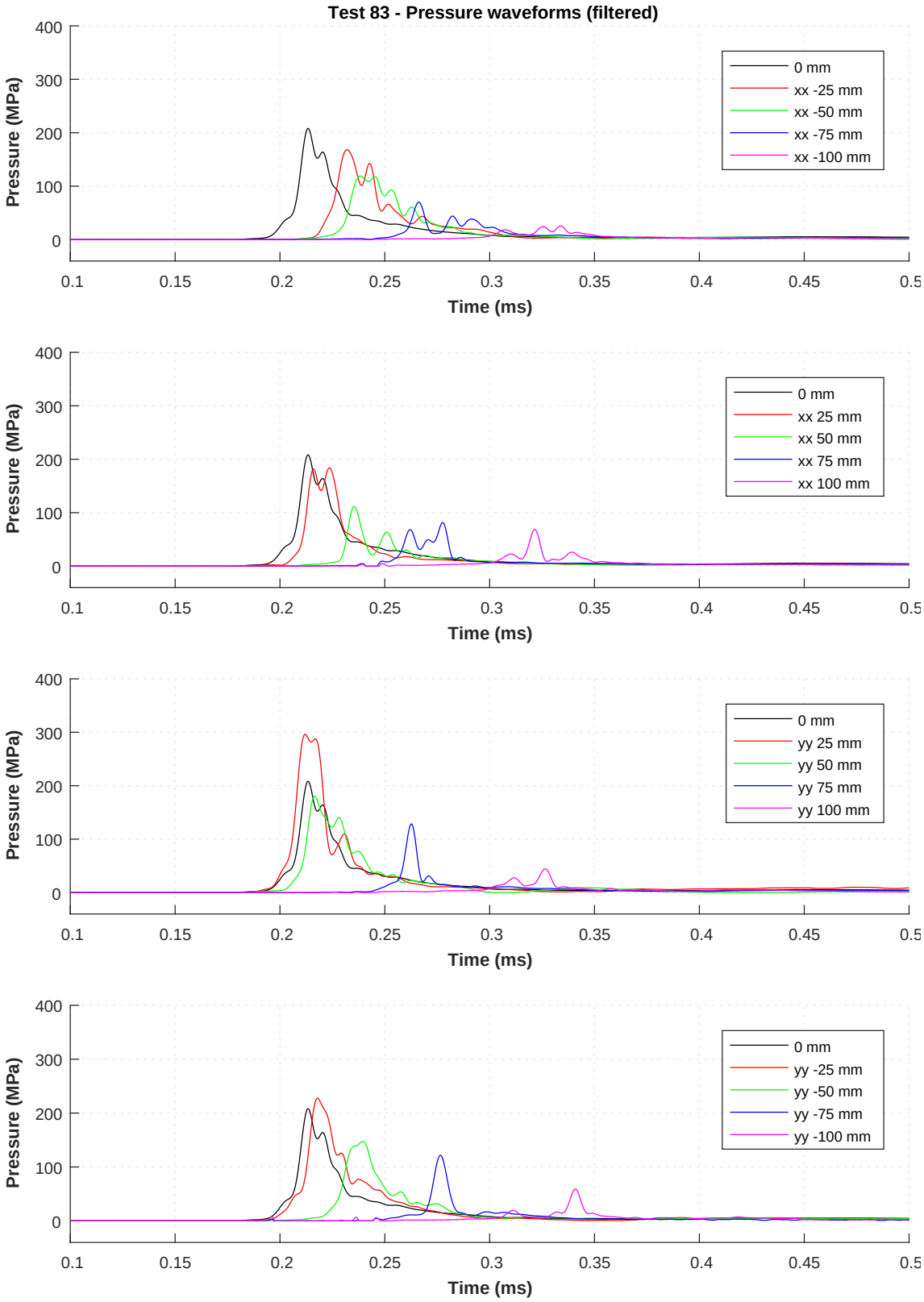

Figure C.85: Pressure-time waveform of Test 83.

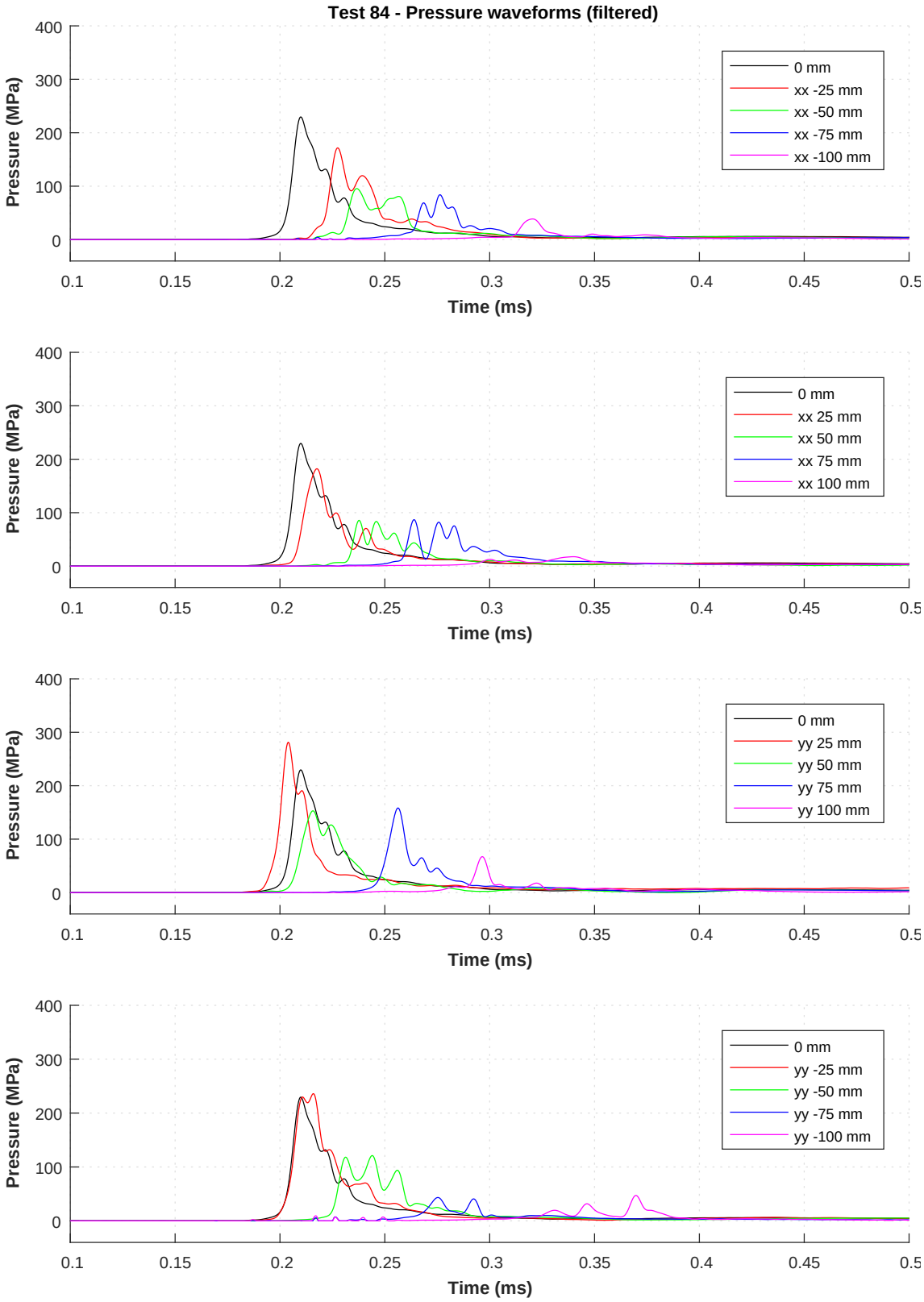

Figure C.86: Pressure-time waveform of Test 84.

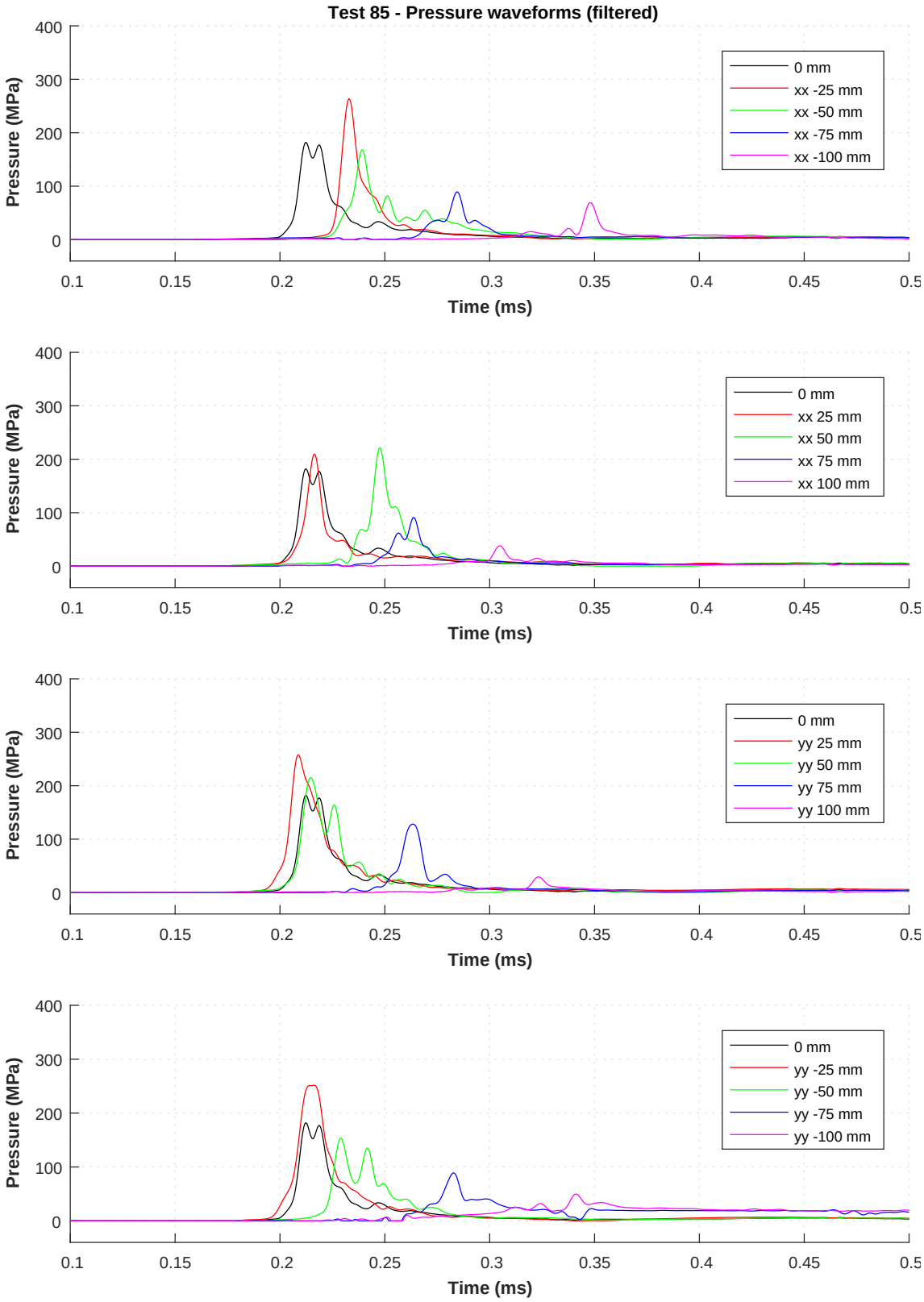

Figure C.87: Pressure-time waveform of Test 85.

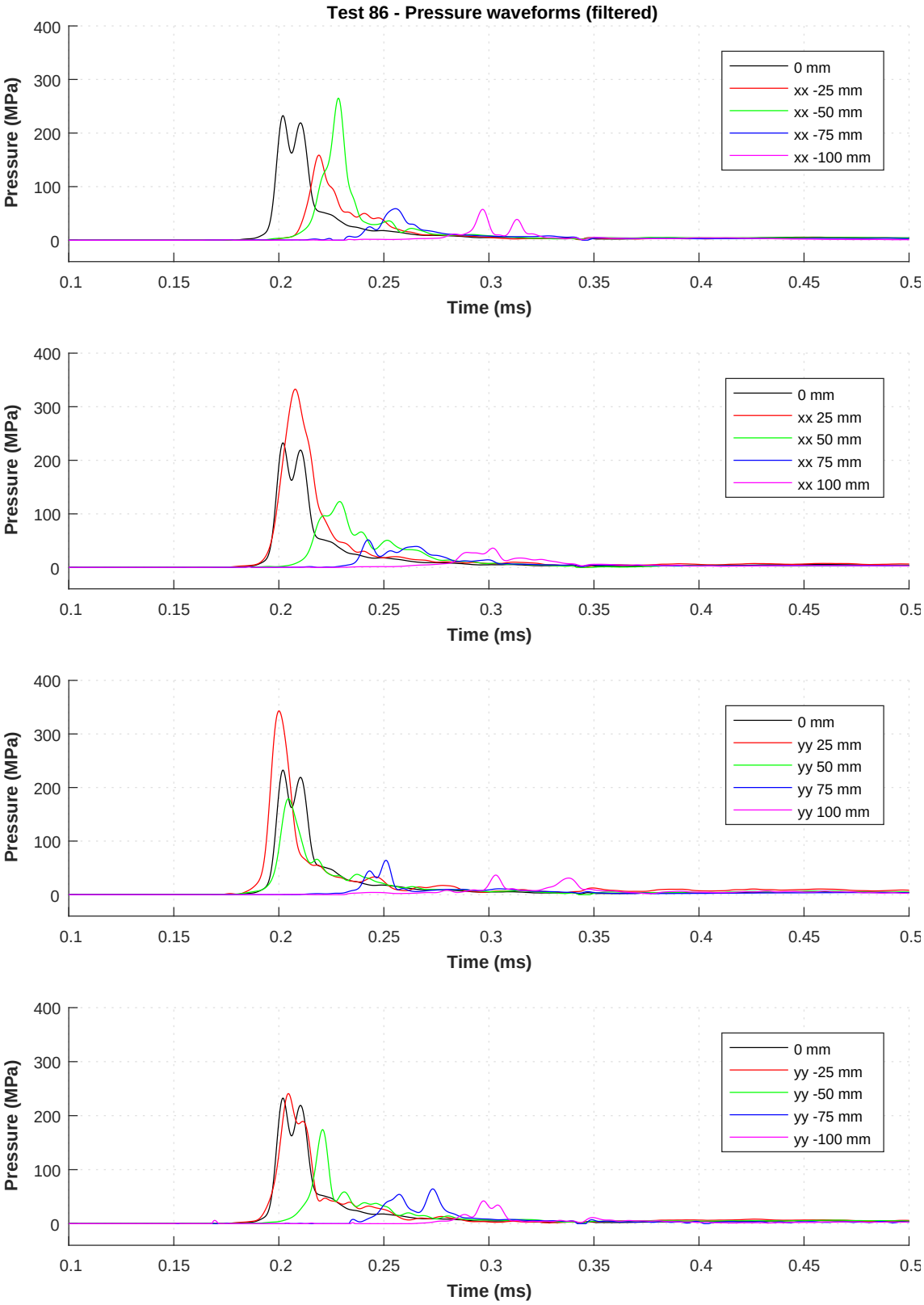

Figure C.88: Pressure-time waveform of Test 86.

C.1.12 Series K – Pressure-time waveforms for Tests 87–91

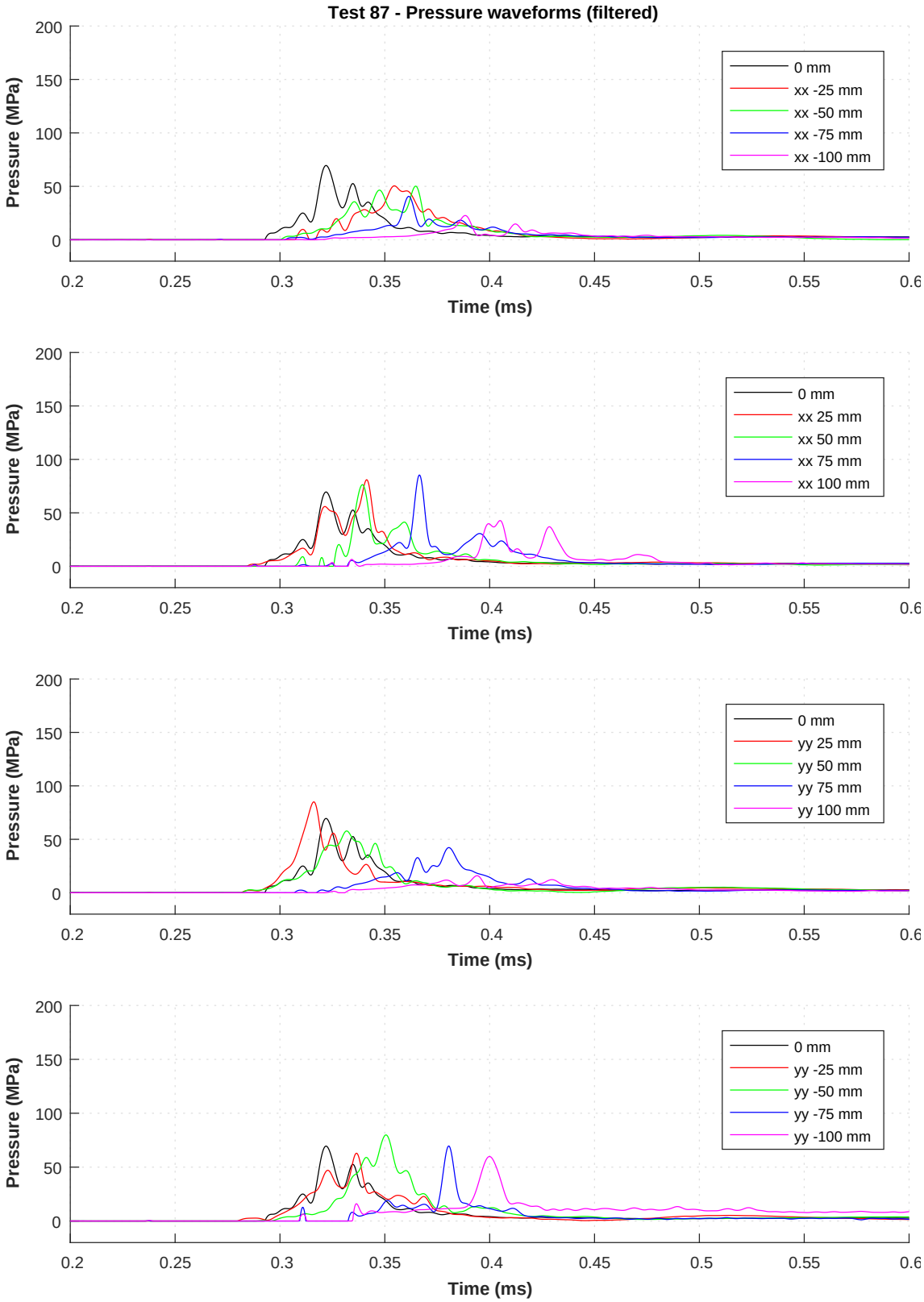

Figure C.89: Pressure-time waveform of Test 87.

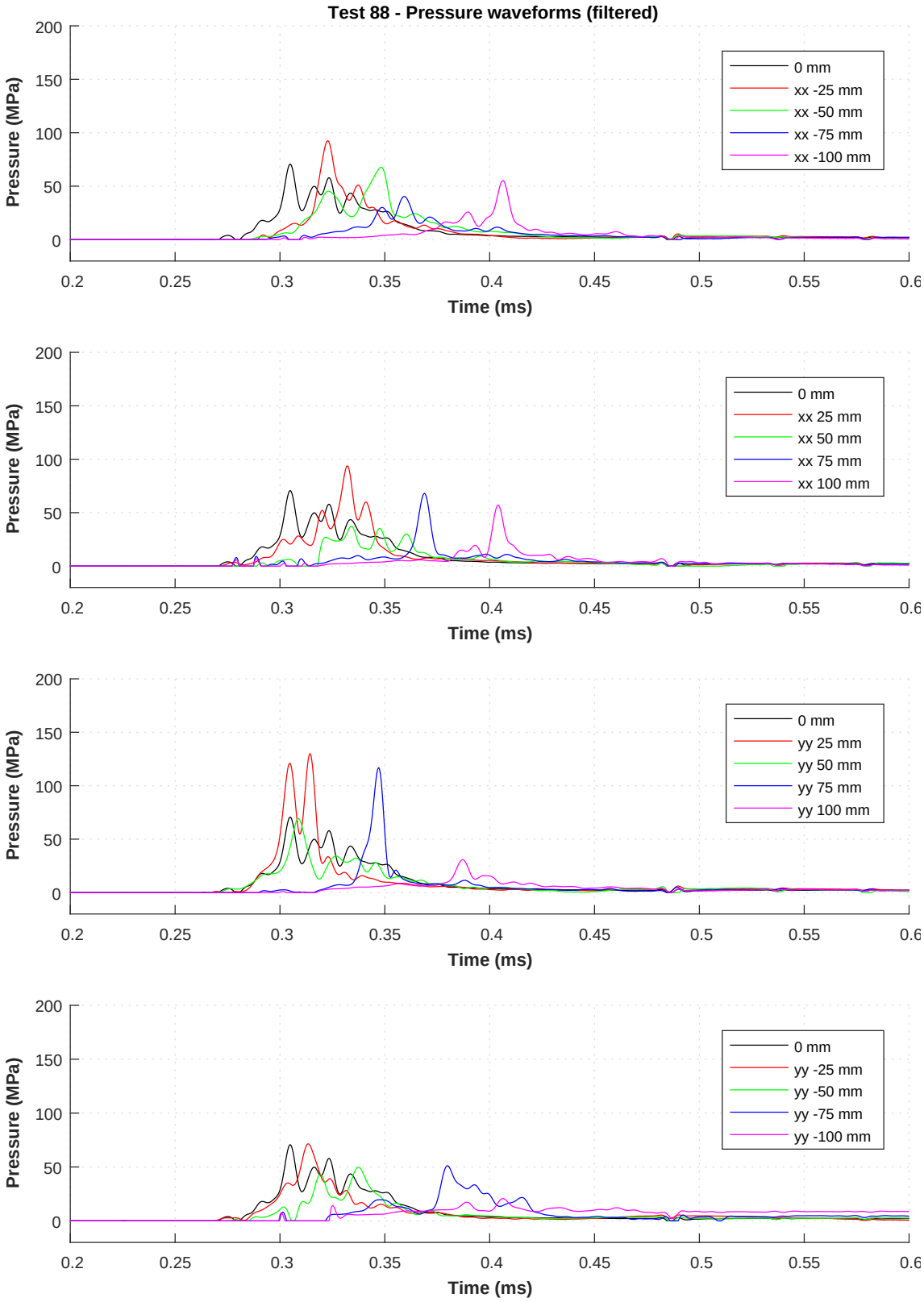

Figure C.90: Pressure-time waveform of Test 88.

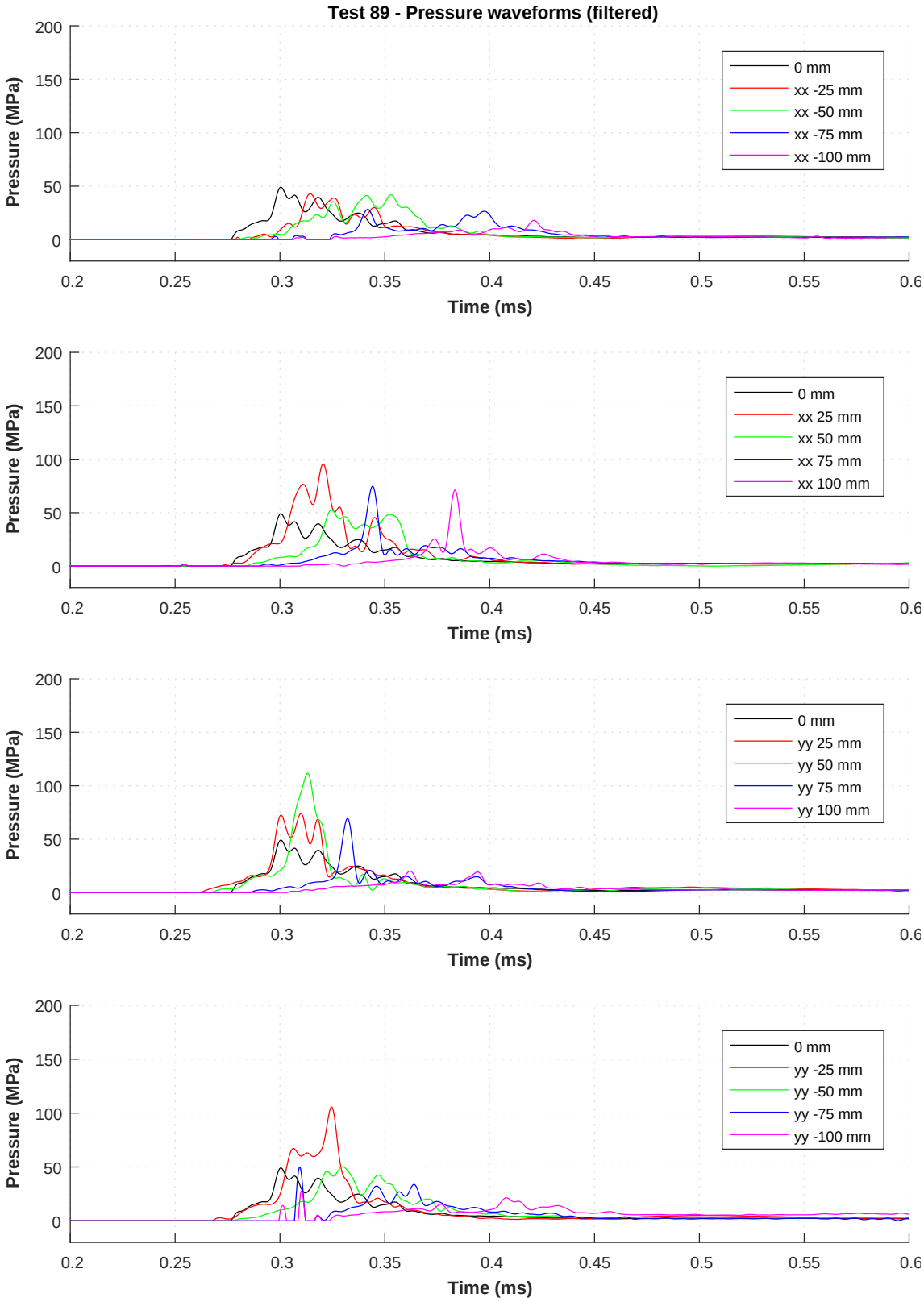

Figure C.91: Pressure-time waveform of Test 89.

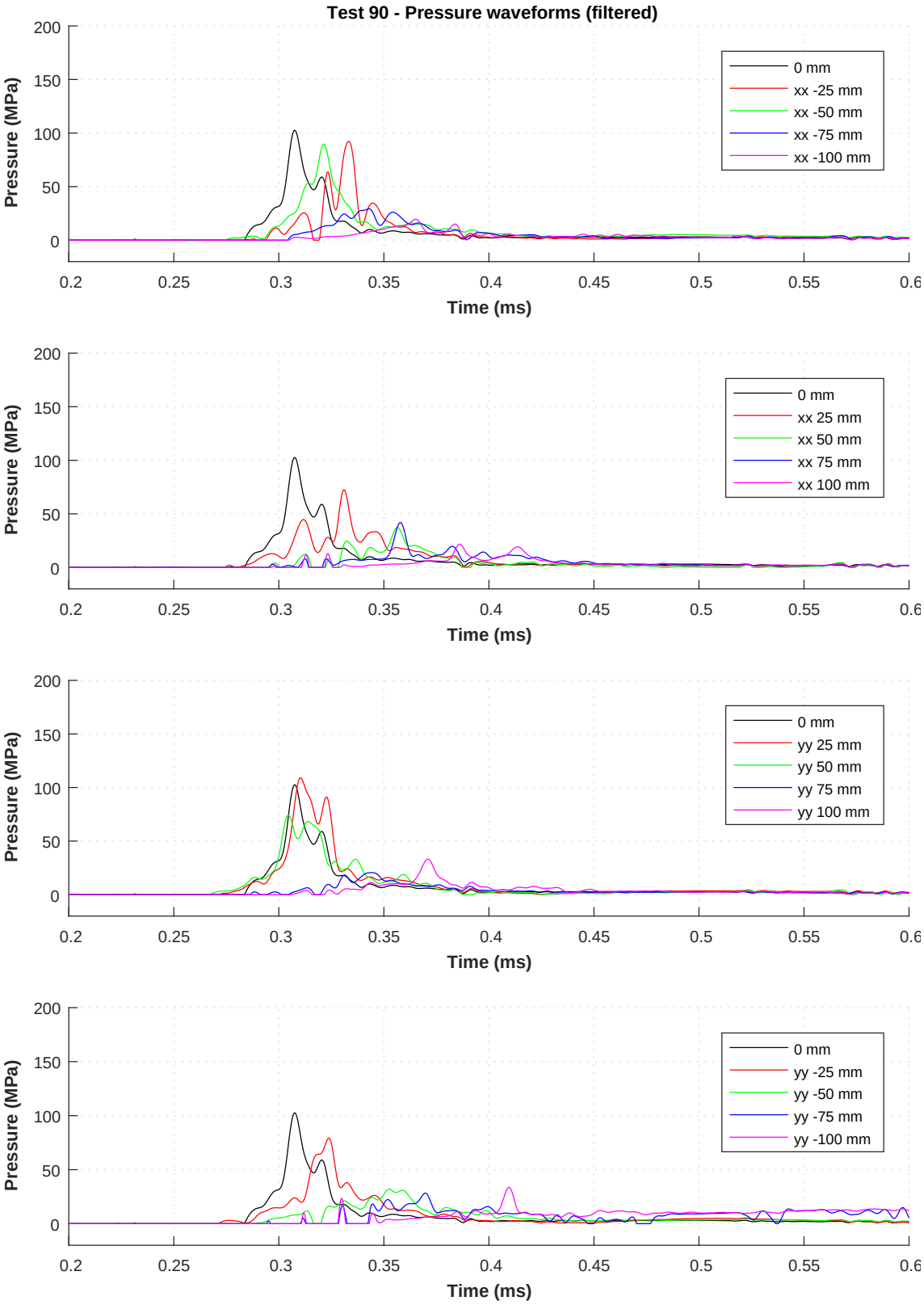

Figure C.92: Pressure-time waveform of Test 90.

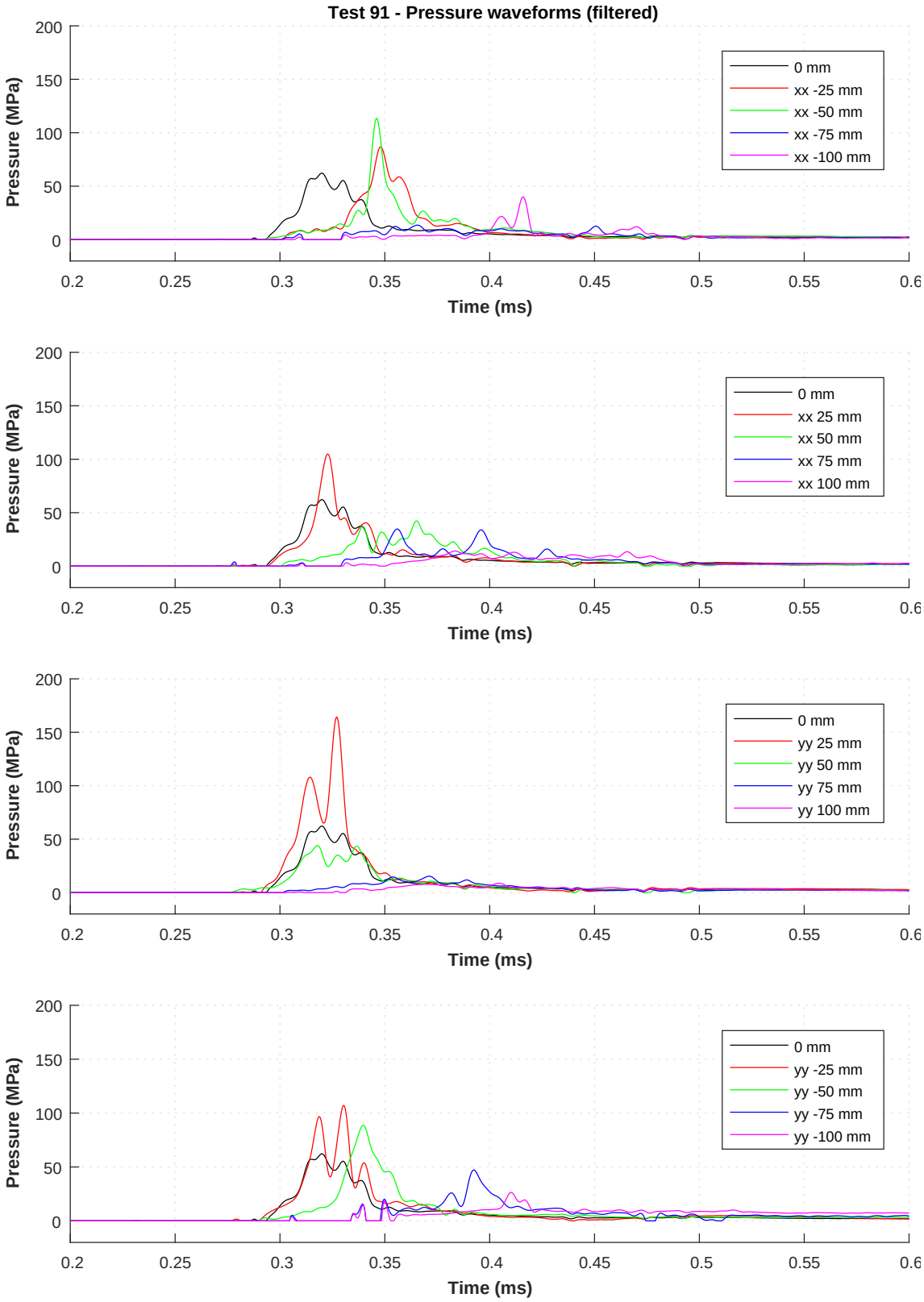

Figure C.93: Pressure-time waveform of Test 91.

Appendix D

Trials apparatus technical drawings

D.1 Introduction

During the commissioning phase of the CoBL project, detailed design of the concrete test frame, steel target and steel HPB receiver was undertaken. The technical drawings and reinforcement schedule used for the tender process and for construction of the CoBL apparatus are presented here.

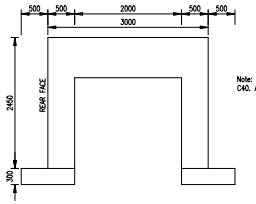

TRAIL FRAME – ELEVATION

SCALE 1:50

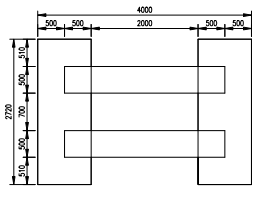

TRAIL FRAME – PLAN

SCALE 1:50

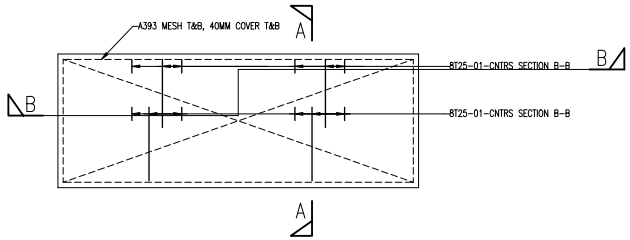

PAD FOUNDATION REINFORCMENT DETAIL

SCALE 1:20

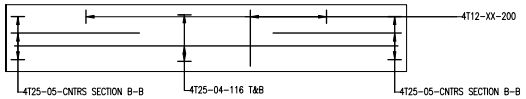

BEAM REINFORCMENT DETAIL PLAN

SCALE 1:20

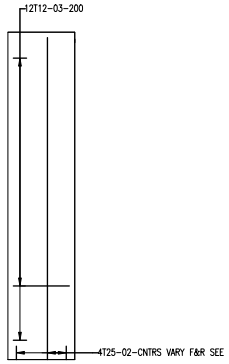

COLUMN REINFORCMENT DETAIL – REAR FACE SHOWN

SCALE 1:20

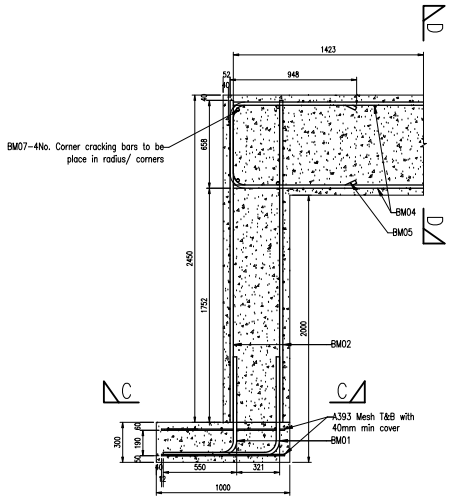

SECTION A-A

SCALE 1:20

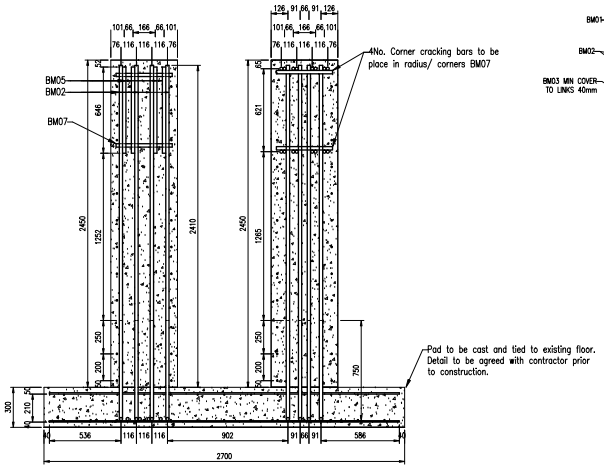

SECTION B-B

SCALE 1:20

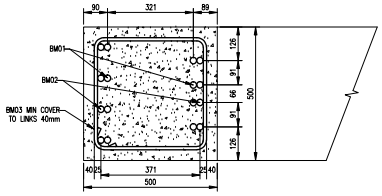

SECTION C-C

SCALE 1:10

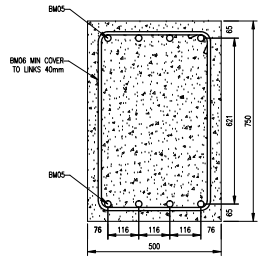

SECTION D-D

SCALE 1:10

NOTES:-

1. This drawing is not to be scaled, if in doubt ask!
2. This drawing is to be read in conjunction with all relevant Blastech drawings and specifications.
3. All dimensions are in millimetres unless otherwise stated.
4. All concrete to be grade C40.
5. All reinforcment to be high tensile 460N/mm^2.

REFERENCE DRAWINGS:-

Revisions	Date	Initial	CAD File Ref: Suffix
Pad geometry change, reinforcment – total revision	18/10/12	SF	1.1

Client:

DSTL

Project:

CoBL

Title:

CoBL TRIAL FRAME AND APPARATUS

DRAWN BY :	SF	CHECKED BY :	AT, JW
SCALE :	AS STATED	DATE :	16/07/12

DRAWING NUMBER :

BT137/1/A1/001 REV1.1

FILE NAME: -

Blastech

Blast & High Velocity Impact Testing

The Sheffield Bioincubator
40 Leavygreave Road
Sheffield
S3 7RD
Tel. +44 (0)114 222 4438
email: rmcmaster@sheffield.ac.uk

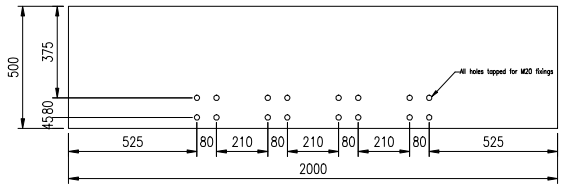

HOLE DIMENTSIONS

SCALE 1:20

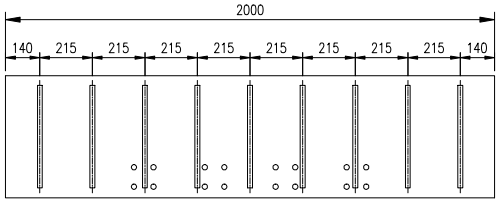

INTERFACE PLATE – PLAN

SCALE 1:20

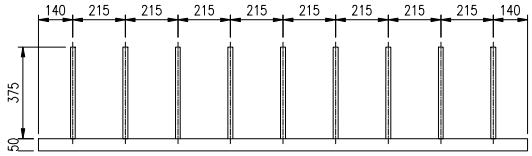

INTERFACE PLATE – ELEVATION SIDE

SCALE 1:20

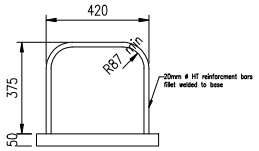

INTERFACE PLATE – ELEVATION END

SCALE 1:20

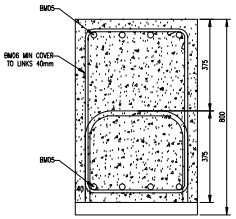

SECTION D–D

SCALE 1:10

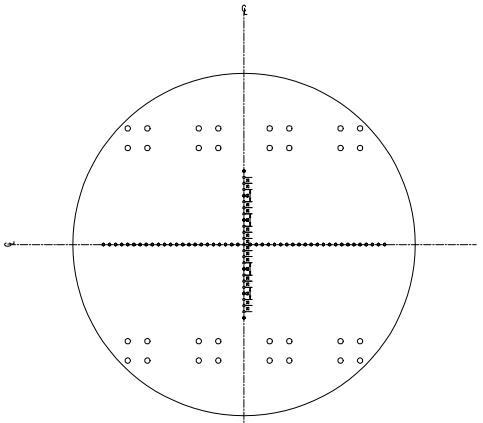

TARGET PLATE ADDITIONAL HOLES – PLAN

SCALE 1:10

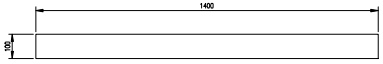

TARGET PLATE – ELEVATION

SCALE 1:10

NOTES:–

1. This drawing is not to be scaled, if in doubt ask!
2. This drawing is to be read in conjunction with all relevant Blastech drawings and specifications.
3. All dimensions are in millimetres unless otherwise stated.
4. All concrete to be grade C40.
5. All reinforcment to be high tensile 460N/mm^2.

REFERENCE DRAWINGS:–

Revisions	Date	Initial	CAD File Ref: Suffix
Additional holes in target plate	01–08–13	SF	1.5
Addition of report figures	29–06–13	SF	D
Dim correction on target plate and addition of centre line	04–12–12	SF	C
Addition of target plate	25–11–12	SF	B

Client: DSTL

Project: CoBL

Title: CoBL TRIAL APPARATIS STEEL WORK

DRAWN BY :	SF	CHECKED BY :	–
SCALE :	AS STATED	DATE :	07/11/12

DRAWING NUMBER : BT141/1/A1/002V1.5

FILE NAME: –

Blastech
Blast & High Velocity Impact Testing

The Sheffield Bioincubator
40 Leavygreave Road
Sheffield
S3 7RD
Tel. +44 (0)114 222 4438
email: rmcmaster@sheffield.ac.uk

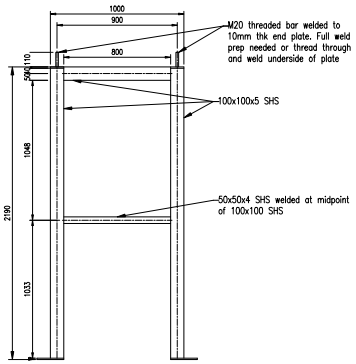

ELEVATION – SIDE

SCALE 1:20

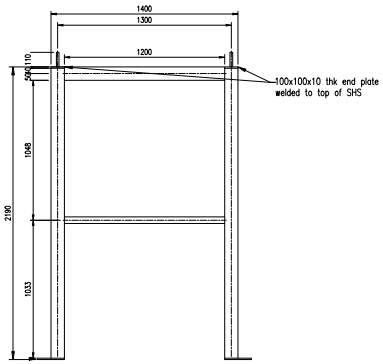

ELEVATION – FRONT/REAR

SCALE 1:20

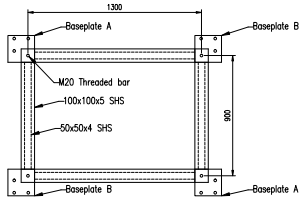

HOPKINSON BAR RECIVER FRAME – PLAN

SCALE 1:20

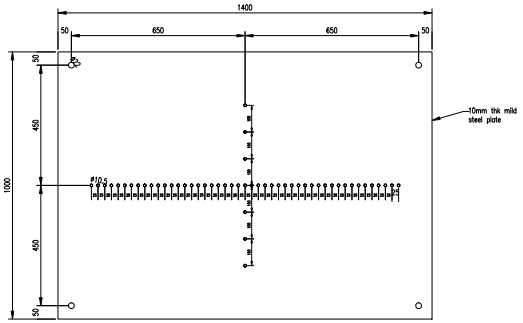

HOPKINSON BAR RECIVER PLATE– PLAN

SCALE 1:10

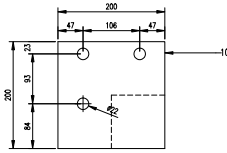

BASE PLATE A – PLAN

SCALE 1:5

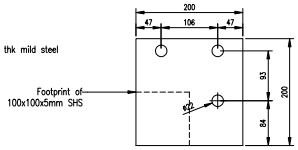

BASE PLATE B – PLAN

SCALE 1:5

NOTES:–

1. This drawing is not to be scaled, if in doubt ask!
2. This drawing is to be read in conjunction with all relevant Blastech drawings and specifications.
3. All dimensions are in millimetres unless otherwise stated.
4. All concrete to be grade C40.
5. All reinforcment to be high tensile 460N/mm^2.

REFERENCE DRAWINGS:–

Revisions	Date	Initial	CAD File Ref: Suffix
–	–	–	–

Client: DSTL

Project: CoBL

Title: HOPKINSON BAR RECEIVER

DRAWN BY :	SF	CHECKED BY :	–
SCALE :	AS STATED	DATE :	09/01/13

DRAWING NUMBER : BT141/1/A1/003

FILE NAME: –

Blastech
Blast & High Velocity Impact Testing

The Sheffield Bioincubator
40 Leavygreave Road
Sheffield
S3 7RD
Tel. +44 (0)114 222 4438
email: rmcmaster@sheffield.ac.uk

Blastech
Blast & High Velocity Impact Testing
The Sheffield Bioincubator
40 Leavygreave Road
Sheffield
S3 7RD
Tel. +44 (0)114 222 4438
email: rmcmaster@sheffield.ac.uk

CONTRACT		DRG No.
CoBL Design of trial apparatus		BT-141-xx
PREPARED	**DATE**	**SHEET No.**
SF	14/10/12	1 OF 1
CHECKED	**REV. DATE**	**REVISION**
AT JW		

Member	Bar Mark	Type and Size	No. of Mbrs	No. of Bars in Each	Total No.	Length of each Bar mm †	Shape Code	A mm*	B mm*	C mm*	D mm*	E/R mm*	REV
Pad	01	T25	2	16	32	1204	11	552	720				
Pad	02	T10	2	28	56	780	21	300	220	300			
Pad	03	T10	2	16	32	760	21	300	200	300			
Column	04	T25	4	8	32	2710	00	2710					
Column	05	T12	4	13	52	1805	51	420	420	100	100		
Beam	06	T25	2	8	16	2000	00	2000	X				
Beam	07	T25	2	8	16	2405	21	948	646	948			
Beam	08	T12	2	10	20	2305	51	420	670	100	100		
Beam	09	T25	2	8	16	420	00	420					

† Specified in multiples of 25mm * Specified in multiples of 5mm

Scheduled in accordance with BS8666:2005